Study of the Mechanical Response of Ply-Level Hybrid Composites under Quasi-Static and Dynamic Loadings

Maria Demsa Demsa Casapu

THESE DE DOCTORAT EN COTUTELLE PREPAREE A

L'ECOLE NATIONALE SUPERIEURE DE TECHNIQUES AVANCEES BRETAGNE

ECOLE DOCTORALE N° 648
Sciences pour l'Ingénieur et le Numérique
Spécialité : Mécanique des Solides, des Matériaux, des Structures et des Surfaces

ET L' UNIVERSITE NATIONALE POLYTECHNIQUE DES SCIENCES ET TECHNOLOGIES DE BUCAREST

Par
Maria DEMȘA (CASAPU)

Study of the Mechanical Response of Ply-Level Hybrid Composites under Quasi-Static and Dynamic Loadings

Thèse présentée et soutenue à « Bucarest », le « 20 décembre 2023 »
Unité de recherche : Institut de Recherche Dupuy de Lôme - UMR CNRS 6027

Rapporteurs avant soutenance :

Michel Boustie Directeur de recherche CNRS à ENSMA, Chasseneuil du Poitou, France
Adriana Ștefan Directeur de recherche à INCAS, Bucarest, Romania

Composition du Jury :

Président :	Daniel-Eugen Crunțeanu	Professeur à UNSTPB, Bucarest, Romania
Examinateurs :	Nachum Frage	Professeur à Ben-Gurion University of the Negev, Be'er Sheva, Israel
	Raluca Maier	Directeur de recherche à COMOTI, Bucarest, Romania
Dir. de thèse :	Michel Arrigoni	Professeur à ENSTA Bretagne, Brest, France
Co-dir. de thèse :	Ion Fuiorea	Professeur à UNSTPB, Bucarest, Romania)

Invité(s)
Ciprian-Marius Larco Maitre de conférences à ATM, Bucarest, Romania

ACKNOWLEDGEMENTS

I want to express my deep appreciation to my thesis advisors, Professor Ion Fuiorea and Professor Michel Arrigoni, for their constant support and guidance throughout these years. Their expertise and encouragement shaped not only my research but also my growth as a scholar.

I would like to express my appreciation to the members of my doctoral guidance committee, Associate Professor Mihai Mihăilă-Andres, Senior Lecturer Paul Roșu, Associate Professor Laurențiu Moraru, Professor Christine Espinosa, and Senior Scientiffic Researcher Raluca Maier for their valuable feedback that greatly improved this research.

Special thanks are due to Claudiu Bădulescu, Julien le Clanche, Celia Caer, Raphael Poncin from ENSTA Bretagne for their generous support, information and guidance in using the experimental testing equipment which played a crucial role in completing this work.

I am grateful to ENSTA Bretagne, the National University for Science and Technology POLITEHNICA Bucharest, and the Military Technical Academy "Ferdinand I" Bucharest for providing a supportive research environment and access to the necessary facilities and resources, and Belcoavia S.R.L. in Romania for manufacturing the composite plates needed in this research. Moreover, I express my gratitude to Campus France, for financial support during mobilities at ENSTA Bretagne.

Heartfelt thanks go to my family and friends, especially to my husband Alex, for their unwavering encouragement and understanding during the challenging phases of this academic pursuit. Their belief in my abilities kept me motivated and focused.

Lastly, I wish to express my gratitude to all those who, directly or indirectly, contributed to this research. Your support, no matter how small, made a significant impact on this journey.

ABSTRACT

In the context of the increased use of carbon fiber-reinforced composites in the aerospace industry, this thesis investigates the influence of inter-ply hybridization, involving variations in carbon fiber type and ply thickness, on the internal structure, mechanical properties, and dynamic responses of unidirectional carbon fiber-reinforced composites. Focused on aerospace applications, the study utilizes two types of unidirectional carbon fiber prepregs with distinct fiber types and ply thicknesses, manufacturing both reference and hybrid laminates.

The research objectives encompass comprehensive material characterization under quasi-static and dynamic loading conditions. Experimental analyses include monotonic on and off-axis quasi-static tests, off-axis cyclic load-unload tensile tests, coupled damage-plasticity model development, shockwave propagation assessment, dynamic tensile strength evaluation, and examination of damage position and threshold variations.

Beyond contributing to the fundamental understanding of unidirectional composites, this research introduces insights into ply-level hybridization, offering potential applications in complex structures. As the aerospace industry demands materials with enhanced mechanical performance, this thesis provides valuable insights for advancing composite material design and application.

REZUMAT

În contextul utilizării tot mai extinse în industria aerospațială a materialelor compozite ranforsate cu fibră de carbon, această teză se concentrează pe evaluarea impactului hibridizării la nivelul laminei, incluzând variații atât în tipul de fibră de carbon precum și în grosimea laminei. În mod specific, acest studiu introduce o abordare de hibridizare la nivelul laminei cu întreaga compoziție din fibră de carbon, pentru a investiga modul în care hibridizarea influențează structura internă, proprietățile mecanice și răspunsurile dinamice ale materialelor compozite ranforsate cu fibră de carbon, având structură unidirecțională.

Două tipuri de țesături unidirecționale preimpregnate cu rășină (prepreg), diferențiate prin tipul de fibră de carbon și grosimea stratului (~140 μm și ~560 μm), sunt utilizate pentru fabricarea laminatelor compozite. Prepreg-urile diferă nu numai în grosime, ci și în calitatea și costul fibrelor. Unul dintre ele conține o fibră standardizată cu proprietăți mecanice bine cunoscute, în timp ce al doilea prepreg cuprinde fibre nestandardizate, având furnizate de producător doar valorile minime potențiale ale proprietăților mecanice. Sunt fabricate atât laminate de referință, create dintr-un singur tip de prepreg, cât și configurații hibride, combinând cele două tipuri de prepreg.

Pentru a evalua efectele hibridizării, a fost realizată o caracterizare cuprinzătoare a materialului, acoperind atât condiții de încărcare cvasi-statice, cât și condiții dinamice, cu viteze de deformație foarte mari, de ordinul 10^5 s^{-1}. Obiectivele cercetării includ caracterizarea experimentală a proprietăților materialelor, evaluarea răspunsului mecanic prin diferite tipuri de teste de tracțiune, investigarea răspunsurilor nelineare în cazul încărcării pe o direcție diferită de cea a fibrelor, dezvoltarea unui model cuplat de deteriorare-plasticitate, evaluarea propagării undelor de șoc în lungul fibrelor și pe direcție perpendiculară a fibrelor, inducerea delaminării la viteze mari de deformație și examinarea diferențelor în poziția planului de rupere și pragul de deteriorare între diferitele configurații de compozite.

Pe lângă evaluarea efectelor hibridizării, aceste obiective contribuie la caracterizarea fundamentală a materialelor compozite ranforsate cu fibre unidirecționale, facilitând incorporarea lor în structuri complexe și sporindu-le potențialul de utilizare în diverse aplicații.

Teza este structurată sistematic în funcție de principalele campanii experimentale, în baza complexității și a categoriilor de viteză de deformație. Capitolul inițial include o analiză a literaturii de specialitate, acoperind subiecte precum materialele compozite ranforsate cu fibră de carbon și comportamentul mecanic în condiții de încărcare cvasi-statice și în condiții dinamice, dar și fundamentele teoretice necesare pentru analiza realizată în capitolele ulterioare.

Capitolul al doilea cuprinde o descriere amănunțită a materialelor, abordarea de hibridizare, precum și caracterizarea proprietăților fizice ale laminatelor și analiza structurii lor interne.

Al treilea capitol include o analiză cuprinzătoare a performanței mecanice în cazul încărcărilor cvasi-statice, incluzând teste monotone de tracțiune pe direcția axei principale și în afara acesteia, analiza deformațiilor și simularea răspunsului mecanic în afara axei principale utilizând un model cuplat de deteriorare-plasticitate.

Capitolul final abordează încărcările dinamice la viteze mari de deformație, esențiale pentru proiectarea componentelor aeriene supuse unor impacturi mecanic puternice. Acesta implică teste cu unde de șoc induse cu laser atât pe direcția fibrelor, cât și perpendicular pe direcția

acestora, și teste cu impact de bilă de oțel pentru investigații suplimentare privind propagarea deteriorării și capacitatea de absorbție a energiei a laminatelor unidirecționale.

În ansamblu, această cercetare contribuie semnificativ la înțelegerea comportamentului mecanic al materialelor compozite ranforsate cu fibre unidirecționale printr-o abordare experimentală cuprinzătoare. Introducerea hibridizării la nivelul laminei oferă perspective noi asupra proiectării materialelor compozite, subliniind impactul acestui tip de hibridizare asupra comportamentului mecanic și propagării undelor de șoc prin material.

RÉSUMÉ

Au cours de la dernière décennie, le trafic aérien mondial a enregistré une croissance significative, à l'exception des périodes de confinement liées à la pandémie, entraînant une augmentation des émissions de carbone du secteur de l'aviation. Pour répondre aux contraintes écologiques et faire face à la demande croissante de fabrication d'aéronefs, les fabricants se sont engagés dans une course concurrentielle où des solutions rentables et fiables à zéro défaut sont cruciales. Une évolution notable est l'utilisation accrue de matériaux composites légers dans l'industrie aéronautique, offrant des avantages tels que la réduction de la consommation de carburant et des émissions de CO_2. Ces matériaux présentent des propriétés mécaniques supérieures, notamment un remarquable rapport résistance-poids et une résistance à la corrosion, les rendant très attrayants pour la conception d'aéronefs modernes.

L'utilisation des matériaux composites a évolué depuis les structures d'aéronefs secondaires vers des structures primaires telles que les ailes et les fuselages. Malgré ces avancées, des défis persistent dans la compréhension et l'amélioration de la réponse des matériaux composites à différentes conditions de charge. La recherche s'est concentrée sur l'hybridation avec différents types de fibres ou composants métalliques pour pallier la faible résistance à la rupture et le comportement cassant des composites en fibres de carbone. Bien que l'hybridation offre un équilibre entre coût et performance, des méthodes alternatives telles que l'hybridation au niveau des plis avec des composites en fibres de carbone exclusives sont explorées pour surmonter les limitations et réduire les coûts de fabrication sans compromettre les performances techniques.

La durée de vie opérationnelle des aéronefs expose ces derniers à des charges dynamiques, avec des défis critiques tels que les dommages potentiels causés par des objets étrangers comme les impacts d'oiseaux. Assurer l'intégrité structurelle de composants clés tels que les aubes de turbine de moteur à réaction et les bords d'attaque des ailes est essentiel. Les exigences de certification rigoureuses de l'industrie aérospatiale nécessitent l'utilisation de puissantes méthodes de simulation numérique pour comprendre le comportement des matériaux sous des charges dynamiques, offrant des perspectives pour concevoir des structures plus solides et plus sûres.

Cependant, des lacunes subsistent dans la compréhension actuelle, nécessitant des modèles mécaniques spécifiques incluant des lois de comportement, une équation d'état et un modèle de dommage pour les matériaux composites étudiés. L'absence d'une description complète des matériaux composites par équation d'état et de modèles de délamination validés pour des charges à haute vitesse de déformation souligne l'importance du test des ondes de choc induites par laser pour obtenir des données pertinentes pour la caractérisation des matériaux à haute vitesse de déformation et valider les modèles numériques. Comprendre les conditions du début du dommage est crucial pour évaluer la survie des structures composites et identifier les conditions de charge responsables.

Dans le contexte de l'utilisation croissante de composites renforcés de fibres de carbone dans l'industrie aérospatiale, l'objectif principal de cette thèse est d'évaluer l'impact de l'hybridation intra-pli impliquant des variations à la fois du type de fibre de carbone et de l'épaisseur du pli. Spécifiquement, cette étude introduit une approche d'hybridation intra-pli

exclusive en carbone pour examiner son influence sur la structure interne, les propriétés mécaniques et les réponses dynamiques des composites en fibres de carbone unidirectionnelles.

Pour atteindre cet objectif, une caractérisation complète des matériaux est réalisée, couvrant à la fois des conditions de chargement quasi-statiques et dynamiques. Alignés sur l'objectif principal de cette thèse, les objectifs de recherche suivants ont été établis :

O1 – Caractérisation expérimentale de la structure interne et des propriétés physiques des matériaux composites en fibres de carbone unidirectionnelles de référence et d'hybridation intra-pli.

O2 – Évaluation de la réponse mécanique quasi-statique des laminés hybrides et de référence sous des essais de traction à axe sur et hors axe.

O3 – Investigation de la cause de la réponse non linéaire hors axe par le biais d'essais de traction cycliques hors axe et évaluation des déformations résiduelles et des variables de dommage.

O4 – Définition d'un modèle couplé dommage-plasticité pour prédire la réponse non linéaire hors axe des laminés.

O5 – Évaluation de la propagation des ondes de choc dans les matériaux de référence et d'hybridation intra-pli, dans la direction des fibres et perpendiculairement à la direction des fibres.

O6 – Induction de délaminage à des taux de déformation élevés et évaluation de la résistance dynamique à la traction.

O7 – Évaluation des différences de position et de seuil d’endommagement pour les différentes configurations des composites étudiés.

Outre l'évaluation des effets de l'hybridation, ces objectifs suivent également une caractérisation fondamentale des composites unidirectionnels. Cela permet d'incorporer ces matériaux dans des structures complexes, offrant une compréhension plus solide de leur réponse mécanique et améliorant leur potentiel dans diverses applications.

L'objectif 1 est orienté vers une exploration à l'échelle microscopique des implications de l'hybridation et de l'épaisseur du pli sur la structure du stratifié. En caractérisant expérimentalement la structure interne et les propriétés physiques des composites de référence et d'hybridation intra-pli, cet objectif cherche à révéler les changements matériels résultant de l'hybridation.

Passant à des évaluations plus macroscopiques, l'objectif 2 se penche sur l'évaluation des attributs mécaniques les plus fondamentaux des composites. À travers des essais de traction dans l’axe et hors axe, la réponse mécanique quasi-statique des laminés hybrides et de référence est examinée, fournissant des informations essentielles sur les capacités de charge dans différentes directions.

La réponse non linéaire hors axe est une considération cruciale en mécanique des composites. Pour y répondre, l'objectif 3 vise à démêler les complexités sous-jacentes à cette réponse en réalisant des essais de traction cycliques hors axe. De plus, les déformations résiduelles et les variables d’endommagement sont évaluées, contribuant à une compréhension plus approfondie du comportement des matériaux dans des conditions non linéaires. Comme les outils prédictifs sont cruciaux dans la conception des composites, l'objectif 4 vise à développer un modèle couplé endommagement-plasticité. Ce modèle vise à prédire la réponse non linéaire hors axe des laminés, offrant ainsi un outil utile pour des analyses approfondies sans nécessiter d'essais exhaustifs.

L'objectif 5 explore le comportement dynamique des composites unidirectionnels en examinant la propagation des ondes de choc dans les matériaux de référence et d'hybridation intra-pli. Cette évaluation couvre à la fois la direction des fibres et la direction perpendiculaire, offrant des perspectives sur des scénarios de chargement complexes et les effets à haute vitesse de déformation. Les objectifs 6 et 7 abordent l'aspect critique du comportement en cas de défaillance dans des conditions de chargement à haute vitesse de déformation. En induisant un délaminage à des taux de déformation élevés et en évaluant la résistance dynamique à la

traction, ces objectifs éclairent les mécanismes de défaillance dans des scénarios difficiles. De plus, ils explorent les différences de position de dommage et de seuil pour les différentes configurations des composites étudiées, contribuant à une compréhension holistique du comportement en cas de défaillance.

La thèse est structurée autour des principales campagnes expérimentales en fonction de leur complexité et des vitesses de déformation impliquées. Le premier chapitre propose une revue de littérature couvrant des sujets tels que les composites renforcés de fibres, le comportement mécanique sous des charges quasi-statiques et dynamiques, et les fondements théoriques nécessaires pour soutenir l'analyse réalisée dans cette étude.

Parmi les composites renforcés de fibres, ceux basés sur les fibres de carbone se distinguent comme particulièrement adaptés aux applications dans les structures aérospatiales. Bien que des propriétés mécaniques améliorées accompagnent les composites de fibres de carbone de meilleure qualité, elles s'accompagnent également de coûts élevés. Pour trouver un équilibre entre rentabilité et performances techniques, le concept d'hybridation a suscité une attention particulière. Cependant, l'hybridation avec d'autres types de fibres peut entraîner une perte notable de rigidité une fois que le composant plus faible échoue. Des recherches approfondies ont examiné les effets de l'hybridation de fibres de verre et de carbone sur les laminés composites, mais les études sur les composites hybrides en fibres de carbone exclusivement demeurent limitées. Une innovation récente a introduit la technique d'hybridation intra-pli pour les composites en fibre de carbone, impliquant la combinaison de préimprégnés avec des épaisseurs de plis différentes pour améliorer la réponse à la défaillance des composites en plis minces. Cependant, aucune recherche n'a jusqu'à présent porté sur l'hybridation intra-pli des composites en fibres de carbone en utilisant des fibres de qualités variées.

Dans le contexte des structures d'aéronefs, elles rencontrent souvent des charges d'impact à des taux de déformation variés pendant le service. Par conséquent, tout en évaluant les propriétés des matériaux composites conçus à des fins aérospatiales, une évaluation de leur réponse dynamique devient impérative aux côtés de leurs caractéristiques quasi-statiques. Différents chargements dynamiques peuvent conduire à des dommages d'impact à peine visibles au sein d'une structure, posant un risque car cela pourrait compromettre la capacité de charge structurelle. Dans ce contexte, la technique des ondes de choc induites par laser se révèle une approche appropriée et fiable pour caractériser le comportement dynamique des composites à des taux de déformation et de pressions très élevés rencontrés dans des situations d'impact à grande vitesse. De plus, elle permet d'évaluer la résistance dynamique à la traction des composites renforcés de fibres.

Avançant dans l'étude, le deuxième chapitre se concentre sur les matériaux utilisés dans la recherche, dans le but de fournir une description aussi complète que possible des matériaux utilisés dans cette étude et de fournir une caractérisation approfondie des propriétés et de la structure interne des composites unidirectionnels carbone/époxy hybrides au niveau des plis avec une disposition à 0°. Des propriétés physiques telles que la masse volumique, la fraction massique de fibres et la fraction volumique sont mesurées, tandis que la structure interne des composites est observée microscopiquement pour identifier d'éventuels défauts induits par l'hybridation et le processus de fabrication. De plus, une estimation du taux de vide constitué par la porosité est réalisée pour valider la qualité du stratifié. Cette évaluation vise à déterminer si taux de vide est suffisamment faible pour ne pas avoir d'impact sur les propriétés mécaniques des stratifiés testés.

Deux types de préimprégnés en fibres de carbone unidirectionnelles, ayant différents types de fibres de carbone et des épaisseurs de plis différentes, sont utilisés pour fabriquer les stratifiés composites : HSC-500-DT102S-40EF et UTS-150-DT120-32F, qui seront par la suite appelés préimprégnés HSC et UTS, en fonction du nom de leur type de fibre de carbone.

Outre la différence d'épaisseur, la principale différence de qualité des préimprégnés, et donc de leur prix, réside dans le fait que l'un a une fibre standardisée, avec des propriétés mécaniques bien connues, tandis que, pour l'autre préimprégné, la fibre n'est pas standardisée, et donc seules

les valeurs potentielles minimales de ses propriétés mécaniques sont fournies par le fabricant. Des matériaux de référence, fabriqués à partir d'un seul type de préimprégné, et des configurations hybrides, combinant les deux types de préimprégnés, sont fabriqués.

Pour réaliser une hybridation au niveau des plis à la fois en termes d'épaisseur et de type de matériau, pour un stratifié plus fin non symétrique désigné comme matériau H1, une séquence d'empilement de 2HSC+1UTS+1HSC+1UTS [0°] a été employée. Pour un stratifié plus épais symétrique désigné comme matériau H2, une séquence d'empilement de 1HSC+1UTS+2HSC+1UTS+1HSC [0°] a été adoptée. La séquence d'empilement des stratifiés hybrides a été initialement déterminée, et en fonction de la masse surfacique estimée fourni par les données des préimprégnés, le nombre de plis pour les stratifiés de type UTS a été choisi pour correspondre à la masse surfacique et à l'épaisseur du stratifié des échantillons H1 et H2 aussi précisément que possible. Par conséquent, des stratifiés composés de 13 et 17 plis UTS ont été fabriqués et étiquetés UTS13 et UTS17, respectivement. Comme le préimprégné HSC a des plis épais et une masse surfacique élevée, les stratifiés ont été fabriqués en utilisant le nombre de plis HSC dans chaque type de stratifié hybride, afin de déterminer s'il existe une différence de comportement mécanique en ajoutant simplement deux plis UTS supplémentaires. Les stratifiés HSC ont été construits avec 3 et 4 plis et seront désignés par HSC3 et HSC4, respectivement.

La masse volumique des échantillons composites a été mesurée selon deux approches : une méthode utilisant une balance de laboratoire et le principe d'Archimède, et une autre utilisant les mesures de masse et de volume des échantillons. De plus, une masse volumique théorique est estimée à l'aide des données de la fiche technique des préimprégnés.

La méthode de masse et de volume présente une plus grande variabilité des données, avec une barre d'erreur plus élevée par rapport à la méthode du principe d'Archimède. La principale cause de l'erreur plus élevée pour la méthode de masse et de volume est considérée comme le fait que, en raison du processus de découpe et des petites dimensions des échantillons, les bords ne sont pas parfaitement droits et parallèles, ce qui induit une erreur dans les mesures de la géométrie de l'échantillon, affectant ainsi le calcul du volume. Ainsi, les mesures de masse volumique par le principe d'Archimède ont été considérées comme plus fiables et ont été utilisées dans les calculs ultérieurs lorsque la masse volumique des stratifiés était nécessaire.

Selon le principe d'Archimède, les stratifiés testés ont des masses volumiques similaires, dans l'intervalle [1,478 ; 1,499] g/cm^3, se situant dans la plage de l'intervalle de la masse volumique théorique. Une différence maximale de 1,42 % a été trouvée entre les masses volumiques de H1 et H2, qui sont les plus basses et respectivement les plus élevées.

Pour déterminer le poids en fibres et la fraction volumique, la méthode de combustion est utilisée. Les échantillons composites ont été pesés avant et après la combustion pour déterminer la masse initiale M_i et la masse finale des fibres M_f. Pour le test, chaque échantillon a été placé dans un récipient en verre Duran® dans un four à moufle, à 400°C pendant 3 à 5 heures, selon le type de stratifié. La température a été choisie pour préserver les fibres de carbone non endommagées et pour rester également dans la plage de température recommandée du récipient en verre.

Après la procédure de combustion, les échantillons rectangulaires ont conservé leur forme jusqu'à ce qu'ils soient manipulés manuellement. Les fibres se sont facilement séparées les unes des autres et étaient flexibles. La fraction de poids moyen des fibres pour tous les stratifiés est dans l'intervalle W_f = [59 ; 65] %, les stratifiés HSC ayant la fraction de poids en fibres la plus basse et les stratifiés UTS la plus élevée, comme prévu d'après la fiche technique de préimprégnés. Les stratifiés hybrides H1 et H2 ont des valeurs intermédiaires par rapport aux stratifiés HSC et UTS, le stratifié H2 ayant une fraction de poids en fibres supérieure de 2 % à celle de H1.

En ce qui concerne la fraction volumique des fibres, les valeurs mesurées pour tous les stratifiés sont dans l'intervalle V_f = [49 ; 54] %, suivant le même ordre que pour la fraction de

poids en fibres. En reliant la densité des composites à leur fraction volumique en fibres correspondante, les valeurs se situent dans l'intervalle théoriquement établi.

Pour les observations microscopiques de la structure des stratifiés, des échantillons rectangulaires d'une longueur de 25 mm ont été découpés dans différentes régions des plaques composites. Les observations de la section transversale composite ont été effectuées à l'aide d'un microscope numérique de la série Keyence VHX-5000. Les échantillons doivent être préparés et soigneusement polis pour obtenir une image propre sans rayures. Tout d'abord, l'échantillon a été fixé dans un moule et incorporé dans de la résine de durcissement à froid. Après le durcissement de la résine, les échantillons ont été polis à l'aide d'un système de polissage LaboPol-30® et LaboForce-100® de Struers®. Les types d'éclairage annulaire et coaxial ont été utilisés pendant les observations, en fonction de ce qui donnait de meilleurs résultats pour les échantillons observés. Les vides ont été analysés en utilisant un éclairage coaxial, pour éviter de les confondre avec des poches de résine et vice versa.

Les observations microscopiques ont révélé des caractéristiques distinctes des composites UTS par rapport à ceux de HSC. Les composites UTS présentaient une plus grande uniformité dans leurs plis et une ondulation réduite des plis, bien qu'ils aient montré un pourcentage plus élevé de vides inter-plis par rapport aux composites HSC. L'analyse de la structure interne des stratifiés hybrides indiquait des améliorations en termes de mélange des plis, de zones riches en résine et d'ondulation des plis par rapport aux stratifiés HSC.

Les vides dans les matériaux composites sont considérés comme l'un des défauts de fabrication les plus nuisibles, car un pourcentage accru de vides peut affecter les propriétés mécaniques du matériau renforcé par des fibres. Étant donné que des préimprégnés et une cuisson en autoclave ont été utilisées dans le processus de fabrication, une faible porosité est attendue. Par conséquent, pour une meilleure précision et la possibilité d'étudier la position et la forme des vides au sein des composites, une microscopie numérique 2D et un traitement d'image sont utilisés. À cette fin, des images microscopiques des échantillons sous lumière coaxiale ont été enregistrées et traitées ultérieurement à l'aide du logiciel ImageJ. Dans cette approche en 2D, le contenu en vide est estimé en tant que fraction de la surface totale de l'échantillon.

Pour tous les composites examinés, le contenu en vide estimé est resté inférieur à 1 %, ce qui est indicatif d'une bonne qualité des composites. Cette faible porosité suggère que les propriétés mécaniques de ces composites devraient rester inchangées par les vides.

Le troisième chapitre englobe l'ensemble des analyses expérimentales réalisées dans le régime quasi-statique. Cela implique l'étude du comportement mécanique en traction tant en axe longitudinal qu'en axe transversal, ainsi que l'évaluation de l’endommagement par des essais cycliques de charge-décharge et la prédiction du comportement non linéaire en traction hors axe. Alors que le troisième chapitre est dédié aux essais quasi-statiques, le quatrième et dernier chapitre contient les résultats liés aux charges dynamiques à des taux de déformation élevés.

Des essais monotones quasi-statiques en traction en axes longitudinal et transversal ont été réalisés et surveillés en déplacement à 1 mm/min, afin d'évaluer le comportement dans le plan des laminés hybrides et de référence. L'évaluation et l'analyse des résultats ont conduit à l'atteinte de l'objectif numéro 2. Des laminés de référence de différentes épaisseurs ont été testés à des fins de comparaison, et également pour évaluer les éventuels effets d'épaisseur sur la réponse mécanique en traction hors axe. La Corrélation d'Images (Digital Image Correlation, DIC) [1] a été utilisée pour l'analyse complète des déformations en champ. Cependant, la configuration n'a permis que la moitié de la longueur utile du laminé à être dans le champ de vision du système DIC. Une méthode successive de régression linéaire a été proposée dans cette thèse et utilisée pour l'évaluation du module d'Young apparent dans les échantillons en traction hors axe. Cette méthode offre l'avantage de minimiser les erreurs induites par la sélection manuelle des données dans la région de réponse linéaire de la courbe contrainte-déformation en traction hors axe.

Les propriétés de traction dans le plan des composites fabriqués ont été obtenues à partir d'essais de traction quasi-statiques. Aucun effet d'épaisseur n'a été observé sur la réponse contrainte-déformation en traction quasi-statique, tant en charge longitudinale que transversale. Pour une épaisseur et une géométrie d'échantillon équivalentes, les composites hybrides ont présenté une contrainte à la rupture à 0° améliorée par rapport à la résistance estimée sur la base de la fonction d'échelle de Kawai [2]. Pour la contrainte à la rupture transversale, une dispersion élevée des données a été obtenue car la plupart des échantillons ont échoué près des mors de la machine (~ 4 sur 7 échantillons). Les propriétés dans le plan des matériaux étudiés sont similaires à d'autres travaux publiés réalisés sur des matériaux composites similaires renforcés de fibres de carbone unidirectionnelles.

Les résultats hors axe ont montré que tous les composites testés présentaient un comportement contrainte-déformation non linéaire, le degré de non-linéarité diminuant à mesure que l'angle hors axe augmentait. Dans la région de réponse linéaire, des différences mineures ont été observées entre les laminés, tandis que dans la région de réponse non linéaire, les laminés HSC ont montré un durcissement sous contrainte par rapport aux laminés UTS, mais avec une plus faible déformation à la rupture. Les épaisseurs n'ont montré aucun effet significatif sur la réponse contrainte-déformation en traction hors axe quasi-statique dans la région de réponse linéaire. Cependant, de légères différences de niveaux de contrainte ont été notées pour les laminés ayant le même matériau mais des épaisseurs différentes dans la région de réponse non linéaire.

Les résultats expérimentaux ont révélé une dégradation des modules élastiques hors axe avec l'augmentation des angles hors axe, conformément aux prédictions utilisant l'équation de transformation. Une dégradation similaire a été observée dans la résistance hors axe. Le module de cisaillement dans le plan a été évalué en utilisant des essais de traction à divers angles hors axe, et le module extrait de l'essai hors axe à 45° a été sélectionné pour des calculs ultérieurs, suivant les recommandations de Pindera [3].

Dans l'ensemble, l'approche d'hybridation a présenté des avantages notables en termes de comportement de durcissement sous contrainte et de contrainte à la rupture accrue par rapport aux laminés de référence. De plus, les laminés hybrides ont montré un comportement semblable à celui d'un système isotrope transverse.

De plus, des essais cycliques de charge-décharge hors axe ont été réalisés pour enquêter sur la cause de la réponse non linéaire et atteindre l'objectif 3. Après analyse des résultats, il a été conclu que la non-linéarité est causée par une combinaison de dommages internes et de déformation résiduelle. L'évolution de la variable d'endommagement et de la déformation résiduelle accumulée a été quantifiée en analysant la réponse contrainte-déformation de charge/décharge incrémentale des échantillons testés. Dans l'ensemble, les laminés UTS ont les déformations résiduelles les plus élevées dans tous les cas de test, suggérant que la matrice dans le préimprégné UTS présente une caractéristique de plasticité intrinsèquement plus élevée par rapport aux laminés HSC, tandis que les laminés hybrides présentent les plus faibles déformations résiduelles de tous les matériaux. Pour l'estimation de la variable d'endommagement, trois méthodes sont utilisées : Ladeveze [4], Fitoussi [5] et Régression (proposé dans cet étude). Parmi ces méthodes, la méthode de Régression est peu fiable avec les données expérimentales obtenues pour extraire le module d'élasticité des cycles de charge/décharge et estimer les variables de dommage pour les matériaux utilisés dans cette étude, car la variable de dommage change à un taux irrégulier lorsque les niveaux de contrainte augmentent, donnant également des valeurs négatives et des barres d'erreur élevées.

Les paramètres nécessaires pour définir un modèle constitutif non linéaire pour prédire le comportement hors axe des composites hybrides unidirectionnels au niveau des plis ont été déterminés à partir des données expérimentales sur la déformation résiduelle et la variable de dommage, atteignant ainsi l'objectif 4. Pour les prédictions du comportement hors axe des composites étudiés, seules les variables de dommage données par les méthodes de Ladeveze et Fitoussi sont prises en compte. Dans l'ensemble, une bonne prédiction a été obtenue, avec des

écarts par rapport aux résultats expérimentaux dans la région de réponse non linéaire. En augmentant la valeur de b_2 de 0,05 à 0,2, de meilleures prédictions sont obtenues pour tous les laminés. De plus, des prédictions pour des laminés de référence plus épais ont été effectuées en utilisant les paramètres de dommage et de plasticité des laminés plus minces du même matériau de préimprégné. Les résultats des prédictions ont été améliorés pour le laminé UTS17 et étaient satisfaisants pour le HSC4, confirmant que pour des laminés avec une différence d'épaisseur allant jusqu'à 0,7 mm, l'utilisation des mêmes paramètres de plasticité et de dommage offre des prédictions satisfaisantes. De plus, des prédictions de la réponse hors axe des laminés hybrides ont été réalisées en utilisant les paramètres d'endommagement des laminés hybrides et les paramètres de plasticité des laminés HSC. Dans la région de réponse non linéaire, les prédictions ont été considérablement améliorées, soulignant l'importance des paramètres de plasticité et suggérant que l'adoucissement dans la région de réponse non linéaire est principalement causé par la plasticité de la matrice et, dans le cas des laminés hybrides testés, la réponse plastique est principalement gouvernée par la matrice dans les plis HSC.

Bien que le troisième chapitre soit consacré aux essais quasi-statiques, le quatrième et dernier chapitre présente les résultats liés aux chargements dynamiques à taux de déformation élevés. Le complément dans le régime dynamique de la caractérisation mécanique des matériaux étudiés est nécessaire pour la conception de composants de structures d'aéronefs, car ils peuvent être soumis à des charges intenses et impulsionnelles telles que des impacts mécaniques à grande vitesse. Ces impacts peuvent survenir lors de la rupture d'une aube de turbine ou d'un impact balistique, par exemple. Dans ce chapitre, la réponse dynamique à des taux de déformation très élevés ($> 10^5\ s^{-1}$) est évaluée. Comme le matériau composite d'intérêt est unidirectionnel, cette étude considère également l'évaluation de la propagation des ondes de choc dans la direction des fibres.

Dans cette approche, dans la première partie du quatrième chapitre, des ondes de choc induites par laser sont choisies pour produire des charges mécaniques intenses et impulsives. Ainsi, deux types de tests au laser sont effectués : un dans la direction des fibres (dans le plan), et un perpendiculaire à la direction des fibres (hors du plan).

Les échantillons pour les tests d'ondes de choc induites par laser ainsi que le dispositif expérimental sont décrits dans ce chapitre. Les méthodes utilisées pour le traitement et l'analyse des données sont détaillées. Les résultats expérimentaux et les discussions pour chaque type de test au laser sont présentés, ainsi qu'une analyse de la réponse du matériau hybride par rapport aux laminés de référence. Des paramètres tels que la vitesse du son, la résistance dynamique à la traction et le taux de déformation lors de la rupture sont évalués à partir des signaux de vitesse mesurées à l'arrière des échantillons. Une analyse microscopique des coupes transversales près du centre du foyer d'impact du laser a été réalisée pour l'analyse des dommages des échantillons impactés dans la direction hors du plan.

La deuxième partie du quatrième chapitre décrit des essais d'impact de billes d'acier sur l'une des plaques composites hybrides (H2), accompagnés de quelques résultats expérimentaux. Ce type de test est exploré pour fournir un aperçu supplémentaire de la propagation des dommages lors d'un impact avec un objet étranger, ainsi que de la capacité d'absorption d'énergie des laminés unidirectionnels. Il sert de première étape fondamentale pour des analyses structurales futures, impliquant des vitesses de déformation modérées ($<10^3\ s^{-1}$).

Des tirs d'impact laser dans la direction des fibres (dans le plan) ont été réalisés sur les matériaux à trois niveaux d'énergie différents. En analysant le signal de vitesse à l'arrière du matériau, enregistré par interférométrie laser-Doppler à l'aide d'une sonde de vélocimétrie hétérodyne, une diminution de la vitesse maximale du premier pic avec la diminution du niveau d'énergie a été observée. Un signal d'écaillage dû à l'expulsion de la couche d'or déposée sur la face arrière pour augmenter la réflectivité a été remarqué pour deux échantillons H1, ce qui a légèrement influencé l'extraction du signal de vitesse à l'arrière.

La période de propagation a été extraite par analyse FFT, et la vitesse du son a été évaluée entre 10 km/s et 11 km/s, selon le type de laminé, avec des laminés UTS ayant la plus grande

vitesse du son dans la direction des fibres. En comparant la vitesse théorique longitudinale du son avec les données expérimentales, il a été observé qu'en utilisant les propriétés de la fibre de carbone pour estimer la vitesse longitudinale du son plutôt que les propriétés quasi-statiques du laminé, des résultats plus proches sont obtenus.

Bien que les signaux de vitesse à l'arrière n'aient montré que l'expulsion de la couche d'or, les échantillons tirés à 75% et 100% de l'énergie maximale ont montré des signes visibles de dommages, mais non sous forme d'écaillage, mais de fissuration de la matrice et de rupture des fibres. Outre la fissure principale de la matrice, d'autres lignes minces de propagation de fissures de la matrice ont pu être observées pour tous les échantillons inspectés tirés avec un niveau d'énergie supérieur à 75%. Comme des observations microscopiques ont été effectuées dans le plan de rupture de l'un des échantillons H1, il a été observé que certaines fibres étaient cassées, la plupart d'entre elles plus près de la face arrière. Des faisceaux de fibres cassées ont également pu être identifiés. Bien que certaines fibres soient cassées, il n'y avait pas de plan de fracture clair pour toutes, probablement pourquoi un signal de spallation clair n'a pas pu être obtenu pour la vitesse à l'arrière.

En analysant les signaux de vitesse à l'arrière pour les tests d'impact laser hors du plan (c'est-à-dire la direction de la propagation de l'onde de choc est normale au plan du pli), il a été observé que le premier pic avait une amplitude plus faible avec la diminution du niveau d'énergie et de la densité de puissance du tir laser. De plus, les tirs laser à des niveaux d'énergie élevés présentaient un signal d'écaillage. En évaluant les effets de l'épaisseur de l'échantillon sur le signal de vitesse à l'arrière, il a été observé que l'augmentation de l'épaisseur entraîne un retard dans l'arrivée de l'onde de choc et une diminution de la vitesse maximale du premier pic, causée par l'atténuation de l'onde de choc.

Pour le matériau H1, l'influence de l'impact sur l'une ou l'autre face de l'échantillon a également été étudiée. En comparant les signaux de vitesse à l'arrière pour les tirs sur la face UTS avec les signaux pour les tirs sur la face HSC du matériau H1, une différence claire de valeurs de la vitesse maximale du premier pic a été observée pour tous les échantillons testés en 2021, les tirs sur la face UTS ayant une vitesse maximale plus élevée. Cependant, pour les tirs effectués en 2022, aucune différence significative dans la vitesse maximale n'a été observée.

La vitesse du son dans la direction hors du plan a été évaluée en mesurant la différence de temps entre le premier et le deuxième débouché de l'onde de choc pour les tirs qui n'ont produit aucun dommage dans les composites, donnant des valeurs moyennes entre 2,75 km/s et 2,91 km/s, sans différences significatives entre les laminés de référence. La résistance dynamique à la traction a été évaluée à partir des tirs qui présentaient un signal clair d'écaillage selon l'approche de Novikov [6] et a été estimée entre 289 MPa et 317 MPa, avec des taux de déformation moyens pendant la rupture de spallation entre 1,75e+05 s^{-1} et 1,91e+05 s^{-1}.

Par une observation microscopique des coupes transversales près de l'axe central du foyer d'impact laser, une partie des échantillons qui présentaient un signal d'écaillage a été analysée plus en détail pour confirmer la présence de dommages à l'intérieur des échantillons. Bien qu'une délamination entre les plis soit attendue dans la plupart des cas, pour tous les laminés sauf H1 impacté sur la face HSC, les dommages se présentaient sous la forme d'une fissure intraplaque de la matrice, donc d'un écaillage. Les laminés UTS présentaient un écaillage dans l'avant-dernier pli, tandis que les échantillons HSC et les laminés hybrides montraient des dommages dans le dernier pli HSC. Les dommages étaient principalement situés à des positions similaires par rapport à la face arrière, à environ 250 µm. Pour H1 impacté sur la face HSC, les dommages se présentaient sous forme de délamination entre les derniers plis HSC et UTS. Cette occurrence était plus régulière, visible et étendue par rapport à l'écaillage observé dans le cas des échantillons H1 impactés sur la face UTS.

Des seuils d'endommagement ont été établis pour chaque matériau, et les laminés UTS se sont avérés avoir le seuil d'endommagement le plus élevé, ce seuil étant également influencé par l'épaisseur de l'échantillon. Les évaluations des dommages révèlent que des charges de courte durée et à haute énergie peuvent entraîner des dommages substantiels à l'intérieur de

l'échantillon composite. Ces dommages se manifestent souvent sous forme de problèmes liés à l'impact à peine visibles à l'œil nu et difficiles à détecter. De plus, de tels dommages ont le potentiel de compromettre l'intégrité structurelle du matériau.

Des tests d'impact de billes d'acier ont également été effectués sur le matériau hybride H2. Quatre tests ont été réalisés à différentes pressions de chargement dans le lanceur « Tonnerre de Brest » de l'ENSTA Bretagne. Pour le premier tir, avec une vitesse avant l'impact de 170 m/s, la balle a traversé le composite, causant des dommages sous forme de stries d'une largeur d'environ 3 mm atteignant les pattes d'extrémité. Pour le deuxième tir, une pression plus basse a été utilisée pour éviter d'endommager les pattes d'extrémité. La balle a eu une vitesse d'impact de 107 m/s et a rebondi. Seules des fissures de la matrice le long des fibres ont été observées, près des pattes d'extrémité mais sans les atteindre. Pour les deux tirs suivants, avec des pressions encore plus faibles et des vitesses d'impact correspondantes de 56 m/s et 39 m/s, aucun dommage apparent n'a été observé, à l'exception de la marque laissée par la balle au point d'impact. Le test d'impact de bille d'acier était destiné à être un test structurel pour une validation ultérieure par simulation numérique et a montré que le matériau H2 absorbe près de 90% de l'énergie cinétique incidente, pour toutes les vitesses d'impact testées.

En conclusion de ce travail de recherche présenté dans cette thèse, les apports ont contribué à la compréhension du comportement mécanique des matériaux composites unidirectionnels, et ont introduit également le concept d'hybridation au niveau du pli, tant en termes d'épaisseur de pli que de type de fibre de carbone, en abordant les effets d'une telle hybridation. Les objectifs ont été atteints, ainsi que l'objectif principal de l'étude.

En tenant compte les objectifs de cette thèse, les contributions originales suivantes sont mises en évidence :

1. Introduction d'une nouvelle approche d'hybridation au niveau du pli, en considérant des fibres de carbone de différentes qualités en plus de l'épaisseur de pli différente, dans le but de réduire les coûts ;
2. Mise en œuvre d'une procédure de régression linéaire successive, pour déterminer la région de réponse linéaire de la réponse non linéaire hors axe, afin de déterminer le module d'Young apparent et le coefficient de Poisson ;
3. Utilisation et comparaison de trois méthodes distinctes d'évaluation de la variable d'endommagement à partir d'essais de traction cyclique, et leurs effets sur les modèles de prédiction ;
4. Utilisation de paramètres d'endommagement et de plasticité provenant de laminés plus minces pour prédire le comportement non linéaire de laminés plus épais du même type de préimprégné ;
5. Essais utilisant des ondes de choc induites par laser dans la direction des fibres, en considérant une nouvelle méthode d'obtention d'un échantillon d'essai viable à partir de laminés unidirectionnels minces ;
6. Analyse de l'impact du laser sur les faces opposées de laminés avec une séquence d'empilement asymétrique ;
7. Synthèse des campagnes expérimentales et analyse des effets d'hybridation au niveau du pli entièrement en carbone sur la réponse mécanique des composites en fibres de carbone sous chargement quasi-statique et dynamique à haut taux de déformation.

Le travail de cette thèse ouvre des perspectives intéressantes, parmi lesquelles la modélisation numérique de l'impact laser, à la fois dans la direction des fibres et dans la direction hors du plan, calibrée à l'aide des données expérimentales de ce travail, fournirait des informations précieuses et des perspectives supplémentaires sur la propagation des ondes de choc à l'intérieur des laminés, les effets de l'orientation des fibres et les effets d'hybridation supplémentaires sur la propagation des ondes de choc.

[1] M. Merzkirch and T. Foecke, "10° off-axis testing of CFRP using DIC: A study on

strength, strain and modulus," *Composites Part B Engineering*, vol. 196, Sep. 2020, doi: 10.1016/j.compositesb.2020.108062.

[2] M. Kawai, K. Watanabe, H. Hoshi, E. Hara, and Y. Iwahori, "Effect of specimen size on longitudinal strength of unidirectional carbon/epoxy composite laminates (part 1, unnotched strength)," *Advanced Composite Materials*, vol. 28, pp. 53–71, Feb. 2019, doi: 10.1080/09243046.2018.1458269.

[3] M. J. Pindera and C. T. Herakovich, "Shear characterization of unidirectional composites with the off-axis tension test," *Experimental Mechanics*, vol. 26, no. 1, pp. 103–112, 1986, doi: 10.1007/BF02319962.

[4] P. Ladeveze and E. LeDantec, "Damage modelling of the elementary ply for laminated composites," *Composites Science and Technology*, vol. 43, no. 3, pp. 257–267, Jan. 1992, doi: 10.1016/0266-3538(92)90097-M.

[5] J. Fitoussi, F. Meraghni, Z. Jendli, G. Hug, and D. Baptiste, "Experimental methodology for high strain-rates tensile behaviour analysis of polymer matrix composites," *Composites Science and Technology*, vol. 65, no. 14, pp. 2174–2188, Nov. 2005, doi: 10.1016/J.COMPSCITECH.2005.05.001.

[6] I. A. . Novikov S.A., Divnov I.I., "The Study of Fracture of Steel, Aluminum, and Copper under Explosive Loading," *Physics of Metals and Metallography.*, vol. 21(4), pp. 608–6015, 1966.

TABLE OF CONTENTS

INTRODUCTION

In the last decade, except during the pandemic lockdown, global air traffic has increased in power law [1]. In addition, air traffic is pointed out by its significant contribution to carbon emissions. To comply with ecological constraints and to supply air transport companies with the increasing demand for aircraft manufacturing, manufacturers are leading a commercial competition in which cost-effective solutions constrained with zero-fault reliability are key solutions. In this race, the use of composite materials in the aeronautic industry increased. As they are lightweight, they help decrease fuel consumption [2] and CO_2 emissions [3]. Their mechanical properties are superior to traditional metals and can be tailored for a specific application [4]–[6]. Their remarkable strength-to-weight ratio, high specific modulus, and inherent corrosion resistance make them highly appealing for modern aircraft design.

As knowledge and development of the materials have improved, composite materials have been used not only in secondary aircraft structures, but their use in primary structures such as wings and fuselages has increased. For example, Airbus first used composite materials in 1983 on the A310-200 aircraft, when the spoilers, airbrakes, and rudder were made of sandwich carbon fiber reinforced plastics. The evolution continued and on the A350 XWB, the entire fuselage and wing skins – more than half of the structure – are made from carbon-fiber composites, as can be seen in [7]. Besides their use to manufacture the main components of the aircraft's structure, carbon fiber composite materials have also been used lately for jet engine components, such as fan blades [8], [9] and fan case structures [10].

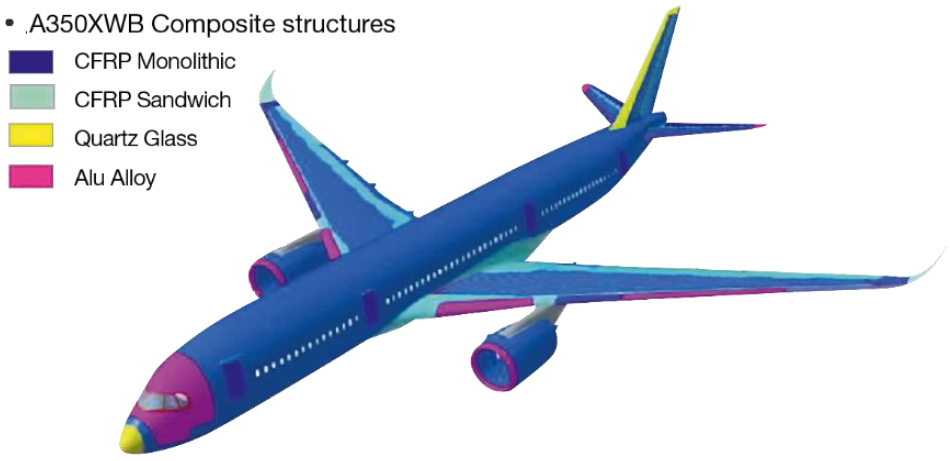

Fig. 1. Composite use in A350XWB [7]

Although composite materials have made a breakthrough in aviation materials, the complexities associated with their response to different loading cases and methods of improving their response to loads without increasing their cost are still being researched. As carbon fiber composites have low failure strain and exhibit a brittle behavior [11], hybridization with other types of fibers [12]–[16] or metallic components [17], [18] has been studied to alleviate some of these drawbacks. Hybridization could also offer a good balance between cost and

performance. However, the use of a metallic component is not suitable for lightweight applications, leaving hybridization with other fiber types as a viable solution.

As different fiber reinforcements have different mechanical properties, the most common attempt to improve or tailor the response of the composite to a specific load is by hybridization of the material, either intra-ply [15] or inter-ply [13], using two different types of fiber reinforcements. However, different fiber hybrid composites usually show a major load drop at the failure of the lower strain component, reducing the overall strength of the composite [19]–[21]. Consequently, this limitation restricts their application in high-added-value technologies. To address this challenge, alternative hybridization methods have been explored in recent years. These methods aim to customize composite responses without altering the fiber type. Nonetheless, few studies are focused on the mechanical behavior of all-carbon fiber hybrid composites. After the development of thin-ply composites, which can enhance the mechanical and weight performance of the composites [22], compared to traditional thick-ply composites, another type of ply-level hybridization has been proposed consisting of mixing plies of different thicknesses in an attempt to obtain a targeted response of the material, without the use of other matrix or fiber reinforcements [23]. In light of these considerations, the integration of ply-level hybridization with all-carbon hybrid composites emerges as a promising avenue. This technique holds the potential to reduce manufacturing costs without compromising on superior technical performance.

The operational lifespan of aircraft exposes them to dynamic loadings, presenting a series of critical challenges. Jet engine blades and key aircraft components, notably the wing leading edge, face potential damage from foreign objects, such as bird strikes. These impacts, occurring at speeds reaching up to 305 m/s, can inflict significant harm on the aircraft's structural integrity [24]. Moreover, a pressing concern involves containing a malfunctioning fan blade within the engine, safeguarding passengers and the airframe from harm. Achieving this dual objective requires the fan case structure to not only endure the impact but also maintain its structural stability during engine shutdown. Consequently, a comprehensive understanding of the dynamic behavior of materials used in the aerospace industry becomes imperative for designing structures that can withstand dynamic loads effectively.

As the aerospace industry has strong certification requirements and experimental tests can be quite expensive to perform for various load cases, it is necessary to use the ability of powerful computational methods to simulate the mechanical behavior of composites at the appropriate scale. These models provide an in-depth understanding of material deformation and failure that can be used to rethink the design approach in order to create stronger and safer structures and enhance maintenance under operational conditions. However, in order to model the response of the structure subjected to dynamic loading, a specific mechanical model including constitutive law, equation of state, and damage model for the studied composite material is mandatory. Currently, there is no existing full description of composite materials by equation of state. In addition, there are no delamination models validated for high-strain rate loading. Therefore, the laser-induced shockwaves test can be an appropriate method for obtaining relevant data for material characterization at high strain rate loading, as well as information regarding the delamination threshold of the material subjected to dynamic loading in order to validate numerical models [25]. It is important to know the conditions of incipient damage in order to evaluate the survivability of the composite structure, as well as the loading conditions responsible for it.

In this context, the primary aim of this thesis is to assess the impact of hybridization involving variations in both carbon fiber type and ply thickness. Specifically, this study introduces an all-carbon ply-level hybridization approach to investigate how it influences the internal structure, mechanical properties, and dynamic responses of unidirectional carbon fiber composites. To achieve this, a comprehensive material characterization is conducted, encompassing both quasi-static and dynamic loading conditions.

Aligned with the main objective of this thesis, the subsequent research goals were established:

- **O1 –** Experimental characterization of internal structure and physical properties of reference and ply-level hybrid unidirectional carbon composite materials
- **O2 –** Evaluate the quasi-static mechanical response of hybrid and reference laminates under on and off-axis tensile testing
- **O3 –** Investigate the cause of the nonlinear off-axis response through off-axis cyclic load-unload tensile tests and evaluate residual strains and damage variables
- **O4 –** Define a coupled damage-plasticity model to predict the nonlinear off-axis response of laminates
- **O5 –** Evaluate the shockwave propagation in the reference and ply-level hybrid materials, in the fiber direction and perpendicular to the fiber direction
- **O6 –** Induce delamination at high-strain rates and evaluate the dynamic tensile strength
- **O7 –** Evaluate the differences in damage position and threshold for the different configurations of the studied composites

Besides evaluating the effects of hybridization, these objectives also follow a fundamental characterization of unidirectional composites. This enables the incorporation of these materials into complex structures, providing a more robust understanding of their mechanical response and enhancing their potential across various applications.

Objective 1 is oriented towards a microscale exploration of the implications of both hybridization and ply thickness on the laminate structure. By experimentally characterizing the internal structure and physical properties of both reference and ply-level hybrid composite materials, this objective seeks to uncover the material changes resulting from hybridization.

Moving to more macroscopic assessments, Objective 2 delves into evaluating the most fundamental mechanical attributes of composites. Through on and off-axis tensile testing, the quasi-static mechanical response of hybrid and reference laminates is examined, providing essential insights into load-bearing capabilities in various loading directions.

The nonlinear off-axis response is a critical consideration in composite mechanics. Addressing this, Objective 3 aims to unravel the complexities underlying this response by conducting off-axis cyclic load-unload tensile tests. Additionally, residual strains and damage variables are evaluated, contributing to a deeper understanding of material behavior under nonlinear conditions. As predictive tools are invaluable in composite design, Objective 4 seeks to develop a coupled damage-plasticity model. This model is aimed at forecasting the nonlinear off-axis response of laminates, thereby providing a useful tool for comprehensive analyses without the need for exhaustive testing.

Objective 5 explores the dynamic behavior of the unidirectional composites by examining shockwave propagation in both reference and ply-level hybrid materials. This assessment spans both the fiber direction and the perpendicular direction, offering insights into complex loading scenarios and high-strain-rate effects. Objectives 6 and 7 address the critical aspect of failure behavior under high-strain-rate loading conditions. By inducing delamination at elevated strain rates and evaluating dynamic tensile strength, these objectives shed light on failure mechanisms in challenging scenarios. Moreover, they explore differences in damage position and threshold across different configurations of the studied composites, contributing to a holistic understanding of failure behavior.

The structure of this thesis is designed to organize the major experimental campaigns based on their complexity and strain rate category. The initial chapter offers a literature review covering topics such as fiber-reinforced composites, mechanical behavior under quasi-static and dynamic loading, and the theoretical foundation necessary to support the analysis conducted within this study.

Moving forward, the second chapter focuses on the materials employed in the research, the hybridization approach pursued, and the comprehensive characterization of physical properties like density and fiber volume content. Additionally, microscopic examinations of the internal structure are conducted, along with the identification of potential internal defects like voids and resin-rich regions.

The third chapter encompasses the complete range of experimental analyses carried out within the quasi-static regime. This involves studying both on and off-axis mechanical behavior, as well as assessing damage through cyclic load-unload testing and predicting nonlinear off-axis behavior. While the third chapter is dedicated to quasi-static testing, the fourth and final chapter contains the findings related to dynamic loading under high strain rates.

Detailed explanations of the testing setup and data processing for the laser-induced shockwaves technique are provided in the fourth chapter, along with the results obtained from impacts in both the fiber direction and perpendicular to it. The chapter also explores the setup and experimental findings of a steel ball impact test, which serves as a foundational step for future structural analyses.

CHAPTER 1. STATE OF THE ART AND THEORETICAL BACKGROUND

INTRODUCTION

This chapter provides the essential theoretical foundation for this thesis and discusses key research papers that are relevant to the subject. In accordance with the scientific approach followed in this work, first, the fiber-reinforced composite materials are reviewed, with an accent on the fiber-reinforced hybrid materials. The subsequent discussion encompasses the failure mechanisms inherent in fiber-reinforced composites, outlining the damages brought about by both low and high-velocity impacts.

Next, attention is directed towards describing the quasi-static response of unidirectional fiber-reinforced composites. This also involves a description of the theoretical formulations, testing protocols, and procedures for evaluating acquired data. Additionally, a comprehensive overview is provided concerning dynamic loading, centering on the fundamental principles of laser-induced shock wave theory.

1.1 FIBER-REINFORCED COMPOSITE MATERIALS

1.1.1 Generalities

A structural composite refers to a material system characterized by two or more phases at a macroscopic level. The purpose of such a system is to achieve mechanical performance and properties that surpass those of the individual constituent materials in isolation. Typically, one of these phases is discrete, exhibiting greater stiffness and strength – often referred to as the reinforcement phase. Meanwhile, the other phase, known as the matrix, remains continuous, featuring lesser stiffness and strength. The properties of the composite material are influenced by the attributes of its constituents, their geometries, and how the phases are distributed.

Fiber-reinforced composites can use different types of fibers as reinforcement, while the matrix is usually comprised of thermoset polymers or thermoplastics.

A large variety of fibers are available as reinforcement for composites, and each type of fiber has its advantages and disadvantages. Within this spectrum, the aerospace industry predominantly employs glass fibers, carbon fibers, aramid fibers, and ceramic fibers.

Glass fibers are the most commonly used in low to medium-performance composites because of their high tensile strength and low cost. They are limited in high-performance composite applications because of their relatively low stiffness and low fatigue endurance when compared to other fiber types [26], as well as rapid degradation of properties with exposure to severe hygrothermal conditions [27].

Kevlar fibers, the trade name for aramid fibers, have low density, about half that of glass fibers, high tensile strength, and excellent toughness and impact resistance [28]. However, Kevlar composites have very low longitudinal compressive and transverse tensile strengths and are sensitive to moisture absorption [6].

Carbon fibers are widely used for advanced composites and come in many forms with a range of stiffnesses and strengths depending on the manufacturing process [6]. Carbon fibers have been used in the aerospace industry, their application developing from small-scale technology demonstrators in the 1970s to large structures today, such as aircraft components

[11]. Carbon fibers are well-known for being strong yet lightweight, they have high tensile strength, high chemical resistance, high stiffness, low thermal expansion, and low weight properties. Their mechanical properties are superior compared to glass fibers [26] which is why carbon fiber composites gradually replaced glass fiber composites in the aerospace industry [2].

Ceramic fibers have been developed as reinforcement for composites to be used in applications requiring high-temperature resistance, such as jet engine applications [29]. The term "ceramic fibers" summarizes all non-metallic inorganic fibers (oxide or non-oxide), except fibers manufactured via solidification of glass melts. In general, ceramic fibers exhibit high values for tensile strength and modulus and can withstand higher temperatures than classical fibers [30]. The most common types of oxide ceramic fibers are based on alumina (Al_2O_3) or alumina/silica (Al_2O_3/SiO_2) ceramics and non-oxide ceramic fibers are most commonly based on silicon carbide (SiC) and Si-C-(N)-O materials. They can also contain titanium, aluminum, or zirconium [30]–[32].

Fig. 1.1 illustrates an Ashby diagram for the specific strength and stiffness of natural and synthetic fibers [33]. By analyzing the position of carbon, aramid, and glass fibers, it can be observed that carbon fibers offer the best strength-to-weight ratio among the presented fiber types.

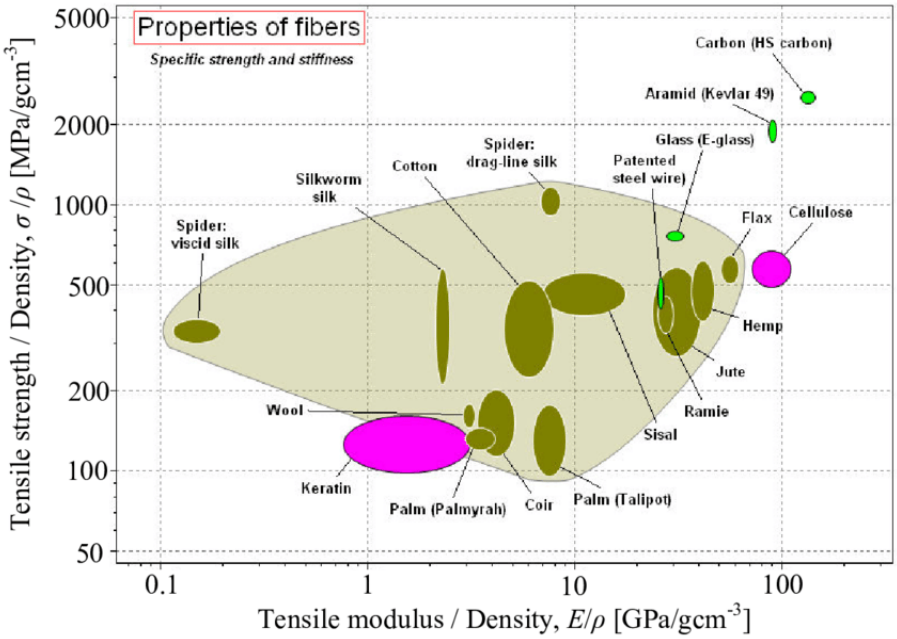

Fig. 1.1. Specific strength and stiffness of natural and synthetic fibers [33]

For the matrix component of fiber-reinforced composites, thermoset polymers and thermoplastics are commonly used, but among the two, the most predominant types are thermoset polymers. When using thermoset polymers as a matrix, the stiffness and load-bearing capability of the composite material is given by the fibers [31], and all the load acting on the matrix has to be transferred to the reinforcement via the interface. Thus, fibers must be strongly bonded to the matrix if their high strength and stiffness are to be imparted to the composite [11]. The most commonly used thermosets are unsaturated polyesters, epoxies, polyimides, and vinylesters [6].

Another type of matrix is the ceramic matrix, which, in contrast to the polymer matrix, has a load-bearing capability of its own. However, the use of monolithic ceramics is limited by their brittle fracture behavior. Therefore, the fiber is relied upon to bridge cracks or flaws in the matrix. However, the selection of fibers available for ceramic composites is much more limited, due to the higher temperatures required for composite processing [31]. Therefore, a compatibility analysis must be performed before combining fibers and ceramic matrix [34]. Some important types of ceramic materials are single oxides (Alumina, Silica, etc.), carbides

(Silicon carbide, Boron carbide), nitrides (Boron nitride, Silicon nitride), intermetallics (Nickel aluminide, Titanium aluminide) and elemental (Carbon, Boron) [32].

Advanced composite structures are usually in the form of unidirectional plies laminated together at various orientations, but they can also be used in the form of woven fabrics or textiles [6].

There are various methods to manufacture composite materials. They include hand lay-up, spray-up, vacuum bag and compression molding, pultrusion, injection molding, resin transfer molding (RTM) process, and autoclave processing [11], [35], [36]. The selection of a particular method depends on the materials used, the part design, and its application. In the aerospace industry, the dominant manufacturing method for composite structures is represented by the use of pre-impregnated fiber reinforcement (prepregs) and autoclave processing [37].

Prepregs, consisting of reinforcement fibers pre-impregnated with a precisely controlled amount of resin, offer superior uniformity and quality, ensuring consistent resin distribution and fiber impregnation [38]. Autoclave processing involves the curing of prepreg layups under elevated temperature and pressure conditions. This process facilitates resin consolidation, ensuring minimal void content and enhanced mechanical properties. The combination of prepregs and autoclave processing results in aerospace components with exceptional strength-to-weight ratios, thermal stability, and performance consistency, critical for aircraft and spacecraft applications [37].

1.1.2 Fiber-reinforced hybrid composite materials

Although carbon fiber composites exhibit superior mechanical properties compared to traditional metals and other types of fibers [4], they have low failure strain and exhibit a brittle behavior [11]. To alleviate some of these drawbacks, as well as to address cost-effectiveness and environmental impact while preserving technical performance, there has been significant interest in the concept of hybridization [39]–[41]. The aim is to mitigate costs or reduce the carbon footprint of materials while still maintaining the desired level of technical performance.

Hybridization can be seen at the structural scale to resist dynamic loads such as blast effects [42]. Hybridization with other types of fibers, either intra-ply or inter-ply, [12]–[16], or with metallic components [17], [18] has been studied as a method of increasing the damage tolerance and mechanical properties of carbon-fiber-reinforced composites. The use of a metallic component is not suitable for lightweight applications, and different fiber hybrid composites usually show a major load drop at the failure of the lower strain component, reducing the overall strength of the composite [19]–[21], and also limiting their use in high-added-value technologies. Therefore, other types of hybridizations have been researched in recent years to tailor the response of the composites, without changing the fiber type.

After the development of thin-ply composites, which can enhance the mechanical and weight performance of the composites [22], compared to traditional thick-ply composites, another type of hybridization has been proposed – ply-level hybridization – consisting of mixing plies of different thicknesses in an attempt to obtain a targeted response of the material, without the use of other matrix or fiber reinforcements [23]. Furtado et al. [43] studied the effect of ply-level hybridization on the tensile unnotched and notched response of composite laminates showing that an enhanced notched behavior without compromising the unnotched and fatigue responses of thin-ply composites can be obtained by combining thin off-axis and transverse plies with thicker 0° plies. Arteiro et al. [44] showed that a wise combination of thin transverse and off-axis plies with thicker 0° plies leads to improvements in the structural response of composite laminates, without affecting the in-plane elastic response or the laminate plain strengths. Sasikumar et al. [45] studied the effect of the ply thickness and ply level hybridization of the compression after impact strength of thin laminates concluding that ply hybridization appears to be a promising economic perspective in the quest to improve the compression after impact (CAI) strength of thin laminates. In these studies, the layup of the

composite plies was multidirectional and a specific response was envisioned, either the notched behavior or compression after impact strength.

While an extensive number of research papers address the effects of glass-carbon fiber hybridization on the mechanical response of the composite laminate, [13], [15], [16], [19], [20], [46]–[49], few studies reported the mechanical behavior of all-carbon fiber hybrid composites. Curtis and Browne et al. [39] mixed the standard quality carbon fiber plies in the principal load direction of a quasi-isotropic laminate with ultra-high performance carbon fibers, in an attempt to improve the overall mechanical response of the standard quality composite without significantly increasing manufacturing costs. The hybrid laminate showed a similar mechanical response to the reference material manufactured with only ultra-high-performance fibers, together with a cost reduction of 17% based only on prepreg costs. Naito et al. [50] combined high strength with high modulus carbon fibers and performed 0° quasi-static tensile testing. They determined an intermediate initial modulus for the hybrid composite, with a complicated stress-strain response due to the sudden load drop associated with failure of the lower strength, higher modulus carbon fiber. Czel et al. [51] used an all-carbon hybridization approach to obtain a pseudo-ductile failure response of the unidirectional carbon fiber composites by blocking low strain to failure, high and ultra-high modulus carbon fibers with outer layers of high strain to failure and intermediate modulus carbon fibers. They reported an improvement in the initial modulus compared to the baseline composite manufactured only with intermediate modulus carbon fiber in all hybrid configurations and pseudo-ductility was also demonstrated. Pseudo-ductility has also been previously reported by Amacher et al. [52] for a quasi-isotropic hybrid laminate combining plies of carbon fibers that have a difference in elastic modulus of around 100 GPa.

While these studies presented the effects of the hybridization of different types of carbon fiber with similar ply thickness, another type of all-carbon hybridization approach has been proposed by Furtado et al. [43]. To improve the notched response of thin-ply composites they introduced the concept of ply-level hybridization which consists of mixing in the same laminate prepregs with different ply thicknesses, without changing the fiber and matrix system. The effect of such a hybridization on the unnotched and notched response of quasi-isotropic laminates was studied and their work revealed that when using a selective hybridization, no significant difference was observed in the unnotched tensile strength. For the notched response, an improvement in strength was reported. Other studies on the effect of ply level hybridization were focused on compression after impact (CAI) strength improvement, with Sebaey et al. [53] reporting an increase of up to 15% in the CAI strength for quasi-isotropic laminates in which standard thickness plies were surrounded by thin plies. On the same subject, Sasikumar et al. [45] concluded that ply-level hybridization is a promising economic perspective to improve CAI strength, as they reported an increase of up to 40% for the CAI strength of hybrid laminates compared to the thin-ply baseline due to a balance between fiber damage and delamination. Yuan et al. [54] reported similar results by using numerical modeling.

While various studies focused on improving the notched response and compression after impact strength of all-carbon hybrid composites, no works have been found so far on the response under high-velocity impact and high-strain loading of such composites, most works being focused on the response of glass/carbon fiber hybridization [55]–[57] or of fiber-metal laminates [58]–[60]. Moreover, all mentioned works used a quasi-isotropic layup for the composite laminate, and all-carbon hybridization was made by replacing thin plies in 0° orientation or sets of thin-ply quasi-isotropic substructures by equivalent standard thickness plies. Regarding unidirectional composites, no results were reported in the case of the effects of a ply-level hybridization. However, Amacher et al. [61] performed a study on the effect of ply thickness on the mechanical response of unidirectional and quasi-isotropic carbon fiber laminates under quasi-static uniaxial tension and other test setups as well and reported that there is no significant difference between the properties of the unidirectional laminate derived from quasi-static tensile testing in the longitudinal and transverse direction for carbon fiber laminates

manufactured using prepregs with areal weights of 30 g/m^2, 100 g/m^2 and 300 g/m^2. Therefore, it can be implied that mixing prepregs of different thicknesses of the same prepreg system should not affect the in-plane properties of the composite. In the aforenamed studies, hybridization was obtained either in the thickness of the plies or in the type of carbon fiber used.

1.1.3 Failure Mechanism and Damage

1.1.3.1 Failure Mechanism

When a laminate undergoes various types of loading, whether in-plane or through-thickness, it is susceptible to the initiation and propagation of damage. This can ultimately lead to the failure of the composite structure. Additionally, the manufacturing process itself can introduce imperfections like voids and residual stresses, which may trigger early cracks within the matrix. Moreover, external environmental factors such as temperature and humidity can significantly influence the behavior of the composite. Common types of damage include fiber fracture, matrix cracking, fiber-matrix separation, and delamination, as illustrated in Fig. 1.2 [4].

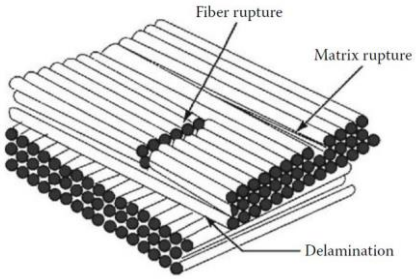

Fig. 1.2. Failure mechanism in fiber-reinforced composite materials [4]

The failure of composites does not happen abruptly. Typically, fracture mechanisms evolve hierarchically. Although their rate of propagation and mutual influence may be influenced by the microstructure, the sequence and location of their occurrence remain relatively consistent across various materials and loading conditions. Taking the example of a [0/90°] composite material subjected to longitudinal loading, we can identify five distinct stages of failure.

The first step represents the decohesion between the fiber and the matrix. It occurs as microcracks appear in the matrix at the scale of the fiber, mainly due to manufacturing residual stresses, as illustrated in Fig. 1.3 [62]. These microcracks will grow, causing the occurrence of the first cracks in the ply.

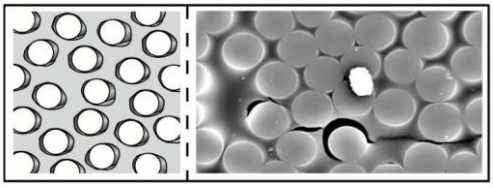

Fig. 1.3. Fiber-matrix decohesion [62]

The second step is represented by the propagation of the matrix crack. During the loading phase, the diffuse damage continues to propagate and develop into transverse and shear stresses. As loading intensifies, the damage propagates, resulting in transverse cracking in the ply perpendicular to the loading direction. In Fig. 1.4, matrix cracks parallel to the fiber are illustrated [63]. It can be observed that the cracks span the entire thickness of the ply.

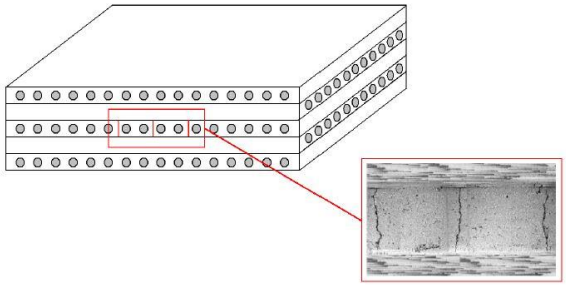

Fig. 1.4. Matrix cracking parallel to fibers [63]

The third step is represented by local delamination. Because of the stress concentration at the transverse crack tip, local delamination occurs at the interface between plies. The fourth step is represented by the fiber rupture. As the delamination prevents the transmission of the loads between the plies, the load will only be supported by part of the fibers, leading to their overload and fiber rupture. The final stage is represented by the entire failure of the material [62]. Fig. 1.5 illustrates the failure evolution of composite materials.

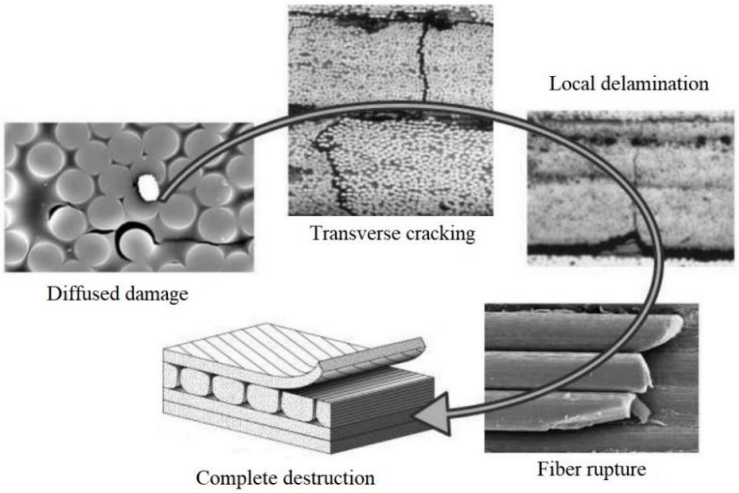

Fig. 1.5. Composite material failure evolution [62]

At the level of the laminate, there can be interlaminar damage that arises from the weakening of the bond between layers, particularly in the resin-rich regions. This type of failure is referred to as delamination. Delamination manifests as interlaminar cracks that emerge when the layers start to separate due to resin fracture. Following the initiation of damage, delamination can propagate under various modes, as depicted in Fig. 1.6: mode I involves crack opening, mode II entails sliding shear, and mode III is characterized by scissoring. Delamination doesn't typically propagate as a singular fracture mode; rather, it often represents a combination of these three modes, forming a mixed-mode pattern [63].

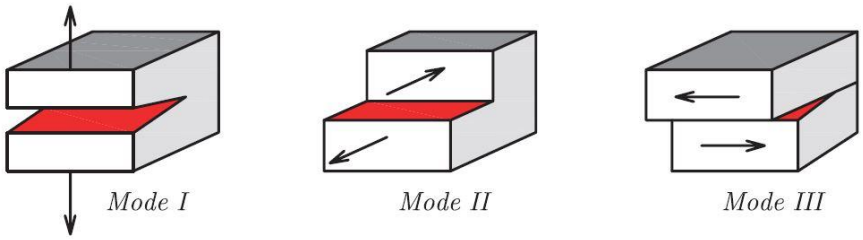

Fig. 1.6. Modes of delamination [64]

1.1.3.2 Impact damage

When subjected to impact loading, depending on the impact energy level, the impact damage in composite materials can be divided into three categories:

- Barely Visible Impact Damage (BVID) – this type of damage can occur under low-velocity and low-energy impact (1 to 5 J [65]) leading to an invisible impact damage underneath the surface of the laminate, such as a delamination between adjacent layers inside the material, which is difficult to detect visually [66].
- Visible Impact Damage (VID): With the increase of the impact energy, clear dents will occur on the laminate surface around the impact zone. In addition, the large internal delamination area or matrix cracking can be observed by C-scan or other scanning methods, or simply visible on semi-transparent composite materials.
- Perforation damage: It usually occurs when the laminate is subjected to high-velocity impact and the energy level is large enough to perforate the laminate, which often leads to complete failure of the material in the impact area, engendering a plume of debris.

Composite materials have several failure modes, and the strain rate sensitivity can result in a change from one failure mode to the other. The impact damage mechanism in a laminate is a very complex process as it represents a combination of matrix cracking, surface buckling, delamination, fiber shear-out, fiber fracture, etc., which usually all interact with each other [67].

Under low-velocity out-of-plane impact, the initial form of damage that emerges is matrix cracking in the transverse direction, followed by delamination if the loading persists.

Matrix cracking can materialize at various locations within the laminate: it can occur in the upper layers at the contact edges of the impactor or on the back face of the laminate, situated opposite the impactor's side.

Delamination arises when matrix cracking is present, typically due to the development of interlaminar normal and shear stresses at the interfaces between adjacent plies.

Consequently, a network of interconnected transverse matrix cracks and delamination forms within the laminate due to low-velocity impact, as depicted in Fig. 1.7. In thicker laminates, localized contact stresses lead to matrix cracks on the impacted surface of the laminate, initiating damage that progresses downward. Conversely, in thinner laminates, initial matrix cracking primarily results from bending stresses, initiating damage in the lowest layer of the laminate and propagating toward the impacted surface [65], [67]–[69].

Fiber failure follows delamination in the sequence of damage. Fibers positioned beneath the striker can fracture due to locally elevated stress, while fibers on the non-impacted surface fail as a consequence of substantial bending stresses.

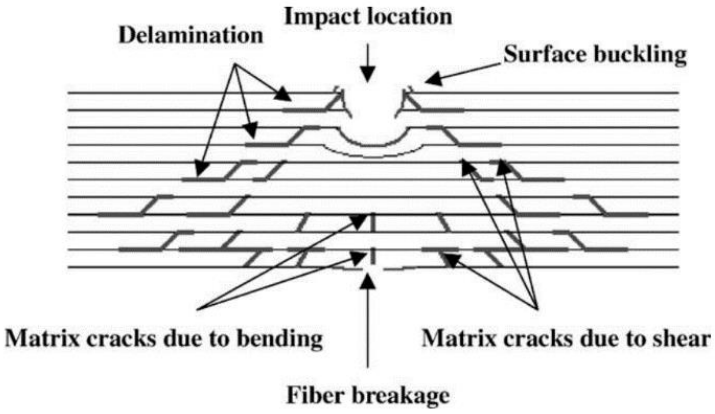

Fig. 1.7. Damage evolution in laminates under low-velocity impact [67]

Bieniaś et al. [70] investigated the behavior of carbon fiber reinforced polymer under low-energy impacts. They utilized microscopic observations of cross-sections within the impact

zone to visually assess the internal damage of the composites. Their findings indicated that under low-energy impacts (1.5 J), only a few transverse cracks and delamination instances emerged in the lower layer of the impacted region. As the impact energy increased to 2.5 J, there was a noticeable rise in composite structure deterioration, manifesting in both matrix cracking and delamination. Subsequently, with an impact energy of 5 J, the middle and lower sections experienced substantial degradation, leading to complete delamination of the composite. Interestingly, damage on the surface remained scarcely visible despite the significant internal effects. In their work, Rajput et al. [71] conducted drop weight tests on sandwich structures comprising carbon/epoxy composite face sheets of varying thicknesses and a consistent foam core thickness, using a range of impact energies. When subjected to lower impact energies (below 5.5 J), the structures exhibited barely visible impact damage (BVID). On the other hand, as the impact energy increased to approximately 15 J, visible impact damage (VID) became evident. Microscopy images of the impacted samples, specifically around the point of impact, are presented in Fig. 1.8. These images showcase the various types of damage discussed earlier. Notably, even for instances where no visible damage is apparent on the faces, the severity of delamination resulting from lower impact energy is considerable. This delamination could significantly compromise the material's resistance to subsequent loads.

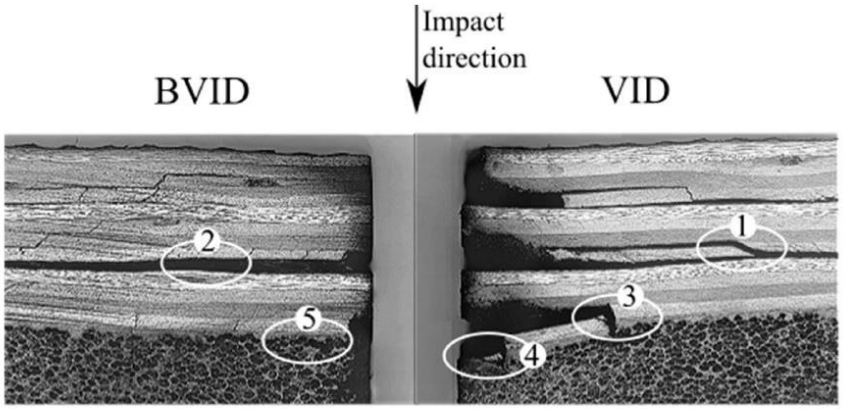

1: Transverse shear crack, 2: delamination, 3: fiber breakage, 4: core damage, 5: Face-core debonding

Fig. 1.8. Damage induced by drop-weight test [71]

For high-velocity and ballistic impact, the structure has less time to respond and therefore, the damage does not propagate as in the case of low-velocity impact. The architecture of the reinforcement can influence the energy absorption mechanism and also, for different materials such as carbon, glass, or Kevlar, different mechanisms can dominate [65], [68], [72].

In addition to the known energy absorption mechanisms in composite materials like delamination and matrix cracking, high-velocity impact loading introduces new forms of damage. This occurs because the impact energy is concentrated within a small area of the composite material. These emerging damage mechanisms include cone formation on the target's back face and shear plugging. In cases involving woven fibers, primary yarns/fibers can fracture, while secondary yarns experience deformation. Here, the fibers located below the projectile are referred to as primary yarns, while those away from the impact area are termed secondary yarns. The intense stresses at the impact point cause the target material to shear and be pushed forward, leading to the creation of a hole or plug. The size of this hole or plug grows as it penetrates deeper into the target material [65], [68], [73]–[75]. An example of typical damage modes that appear in the penetration process of a composite material is presented in Fig. 1.9.

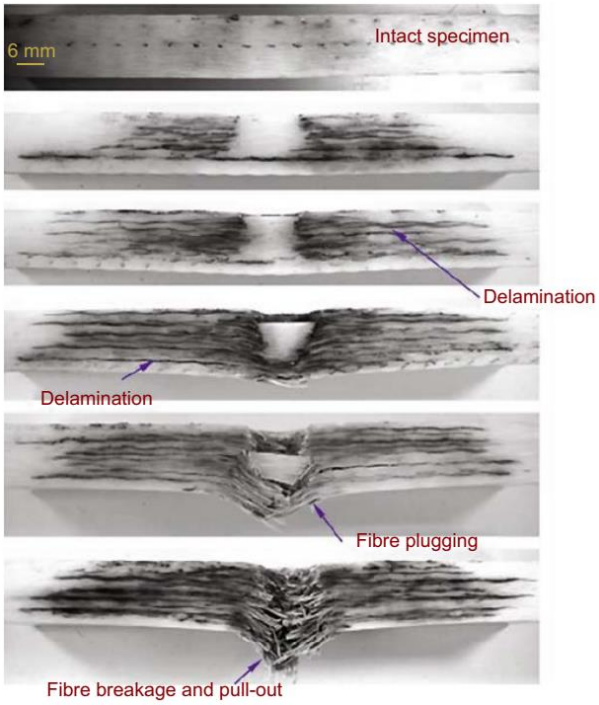

Fig. 1.9. Penetration process for fiber-reinforced composites [68]

The impact properties of the materials can be affected by various parameters of the target such as fiber properties, laminate thickness, and stacking sequence.

Naik et al. [72] investigated the response of woven E-glass/epoxy and T300 carbon/epoxy laminates to ballistic impact, utilizing a combination of analytical and experimental approaches. The study focused on 2 mm thick laminates and aimed to establish an analytical model for ballistic impact analysis solely based on the dynamic mechanical properties and fracture characteristics of the target material. In this context, the study evaluated the energy absorption capacity associated with various damage modes. The key findings indicated that under identical ballistic impact conditions, the ballistic limit is higher for E-glass/epoxy laminates compared to T300 carbon/epoxy laminates. Notably, for E-glass/epoxy laminates, the primary energy-absorbing mechanisms include energy dissipation through secondary yarn deformation and tensile failure of primary yarn. In contrast, T300 carbon/epoxy laminates primarily utilize shear plugging and secondary yarn deformation as the main energy-absorbing mechanisms. In a later study of thick composites, Naik et al. [75] concluded that for thick composites shear plugging represents the major failure mechanism for E-glass/epoxy as well. However, in thick UHMWPE composite laminates, delamination was found as the preponderant energy dissipating mechanism [76], when subjected to ballistic impact. Yashiro et al. [77] conducted a study on the effects of high-velocity impact on Carbon Fiber Reinforced Polymer (CFRP) laminates, focusing on both unidirectional and cross-ply configurations. The research findings indicated that as impact velocity increased, the extent of the damaged area also increased. However, despite these variations in damage size, the observed pattern of damage on the front and back faces remained consistent across different stacking sequences analyzed. A notable observation was the presence of substantial fiber breaks beneath the impact point, resulting in what appeared to be catastrophic ply failure in off-axis plies. Moreover, outside the region of ply failure, the phenomenon of delamination was observed, originating from the tips of matrix cracks. In a study conducted by Velmurugan et al. [78], the impact of fiber orientation and thickness on the response of CFRP composites to high-velocity impacts was investigated. For this purpose, woven carbon/epoxy laminates with four different orientations were fabricated, and laminates of different thicknesses were prepared for each orientation. The findings from ballistic impact tests revealed that the [0/90°] laminates exhibited higher resistance to impact at elevated velocities, leading to greater energy absorption capacity in comparison to the other investigated

laminates. Furthermore, the study observed a direct relationship between the ballistic limit and laminate thickness; as thickness increased, the ballistic limit also increased while the residual projectile velocity decreased. A similar trend of higher ballistic limits with increasing laminate thickness was also observed in woven glass fiber composites [79].

Spallation can also occur as a result of high-impact loads, thermal stresses, or shockwave propagation. In shock wave research, spallation is characterized by the separation of material along a plane that runs parallel to the wave front. It results from the occurrence of two release waves that results in a dynamic tensile stress in the wave front. This separation arises from the formation of dynamic tensile stress components oriented perpendicular to this plane [80]. In the case of composite materials, the spallation process often leads to the creation of voids or cracks between layers, leading to delamination and/or intra-ply failure when the shockwave propagates through the thickness of the laminate, and compromising the structural integrity of the material. Fig. 1.10 shows an example of spallation damage resulting from shockwave propagation [81]. It is a critical concern in composite structures, as it can significantly reduce the overall strength and performance of the material, potentially leading to catastrophic failure if not properly addressed, as it is not always visible on the exterior surface of the composite [81]. Conventional techniques for the study of spallation effects in composite materials include the plate impact method [82], laser-induced shock waves [25], and high pulsed power [83].

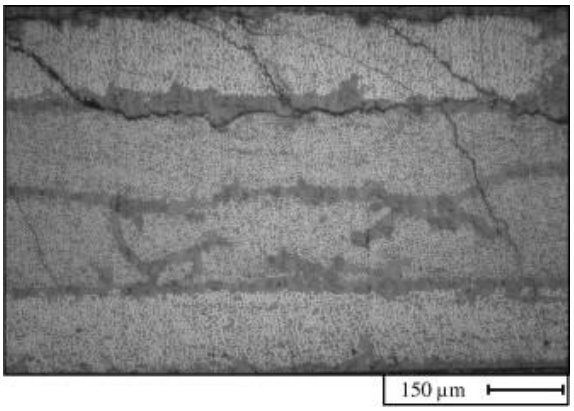

Fig. 1.10. Spallation and matrix crack damage resulting from laser-induced shockwaves [81]

1.2 QUASI-STATIC CONSTITUTIVE LAW AND DAMAGE FOR FIBER-REINFORCED COMPOSITES

Constitutive law

The unidirectional ply is a widely form of the elementary component of the fiber-reinforced composite laminates. Its cured mechanical characteristics are orthotropic, with higher mechanical performance in the longitudinal direction, also called fiber direction – designated as 1, than in the two other orthogonal directions, called transverse directions – designated as 2 and 3 (see Fig. 1.11). The elastic behavior of an orthotropic material is characterized by 9 elastic constants, and the constitutive equations (compliance matrix) for orthotropic materials, in terms of engineering constants, can be written in the form of equation (1.1) [65].

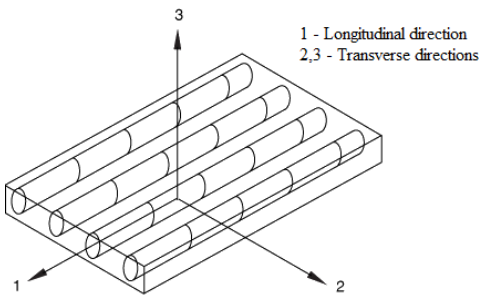

Fig. 1.11. Unidirectional ply axis system

$$\begin{bmatrix}\varepsilon_{11}\\ \varepsilon_{22}\\ \varepsilon_{33}\\ \gamma_{23}\\ \gamma_{13}\\ \gamma_{12}\end{bmatrix}=\begin{bmatrix}\frac{1}{E_{11}} & -\frac{\nu_{21}}{E_{22}} & -\frac{\nu_{31}}{E_{33}} & 0 & 0 & 0\\ -\frac{\nu_{12}}{E_{11}} & \frac{1}{E_{22}} & -\frac{\nu_{32}}{E_{33}} & 0 & 0 & 0\\ -\frac{\nu_{13}}{E_{11}} & -\frac{\nu_{23}}{E_{22}} & \frac{1}{E_{33}} & 0 & 0 & 0\\ 0 & 0 & 0 & \frac{1}{G_{23}} & 0 & 0\\ 0 & 0 & 0 & 0 & \frac{1}{G_{13}} & 0\\ 0 & 0 & 0 & 0 & 0 & \frac{1}{G_{12}}\end{bmatrix}\begin{bmatrix}\sigma_{11}\\ \sigma_{22}\\ \sigma_{33}\\ \tau_{23}\\ \tau_{13}\\ \tau_{12}\end{bmatrix} \quad (1.1)$$

Many unidirectional composites with fibers packed in a hexagonal array, or close to it, can be considered transversely isotropic, with the 2-3 plane (normal to the fibers) as the plane of isotropy [6]. Therefore, $E_{22}=E_{33}$, $G_{12}=G_{13}$, $\nu_{12}=\nu_{13}$ and G_{23} can be expressed in terms of transverse Young's modulus and Poisson's ratio by equation (1.2).

$$G_{23}=\frac{E_{22}}{2(1+\nu_{23})} \quad (1.2)$$

Based on the transverse isotropy of unidirectional composites and symmetry of the stiffness matrix, only five elastic parameters are necessary to identify the elastic behavior of the material [84]:

- E_{11} and E_{22} – Young's modulus in the longitudinal (1) and transversal (2) direction,
- G_{12} – shear modulus,
- ν_{12} and ν_{23} –longitudinal/transversal and transversal/transversal Poisson's coefficients.

To obtain these elasticity coefficients, various mechanical tests can be carried out on laminate composite, as will be discussed in the following sections.

In certain scenarios, the loading direction does not coincide with the principal directions of orthotropy (on-axis) of the unidirectional lamina. Consequently, it can be loaded at an arbitrary angle θ (off-axis) relative to the principal longitudinal direction (1 – axis). In this case, the relation between the in-plane stresses and strains in the principal material coordinates and those in loading direction coordinates (X – loading direction, Y – transverse to the loading direction) can be written in the form of equation (1.3) for stresses (σ – axial stress, τ – shear stress) and equation (1.4) for strains (ε – axial strain, γ – shear strain).

It is observed that strains undergo the same transformation as stresses when the tensor definition of shear strain is applied (equivalent to dividing the engineering shear strain by two).

$$\begin{bmatrix}\sigma_x\\ \sigma_y\\ \tau_{xy}\end{bmatrix}=\begin{bmatrix}\cos^2(\theta) & \sin^2(\theta) & -2\sin(\theta)\cos(\theta)\\ \sin^2(\theta) & \cos^2(\theta) & 2\sin(\theta)\cos(\theta)\\ \sin(\theta)\cos(\theta) & -\sin(\theta)\cos(\theta) & \cos^2(\theta)-\sin^2(\theta)\end{bmatrix}\begin{bmatrix}\sigma_{11}\\ \sigma_{22}\\ \tau_{12}\end{bmatrix} \quad (1.3)$$

$$\begin{bmatrix}\varepsilon_x\\ \varepsilon_y\\ \frac{\gamma_{xy}}{2}\end{bmatrix}=\begin{bmatrix}\cos^2(\theta) & \sin^2(\theta) & -2\sin(\theta)\cos(\theta)\\ \sin^2(\theta) & \cos^2(\theta) & 2\sin(\theta)\cos(\theta)\\ \sin(\theta)\cos(\theta) & -\sin(\theta)\cos(\theta) & \cos^2(\theta)-\sin^2(\theta)\end{bmatrix}\begin{bmatrix}\varepsilon_{11}\\ \varepsilon_{22}\\ \frac{\gamma_{12}}{2}\end{bmatrix} \quad (1.4)$$

1.2.1 On-axis behavior and testing

Numerous mechanical characteristics of composites can be deduced based on the properties of their constituents. However, due to the heightened sensitivity of certain parameters like strength, employing precise mathematical approaches may not always be feasible [85]. While

typical elastic property values for different fiber-reinforced composites are available in the literature, obtaining accurate properties tailored to the specific material in use is recommended. Hence, conducting direct experimental tests becomes essential to ensure precision in these properties. Quasi-static tension tests along 0° and 90° fiber orientations are performed with the use of electro-mechanical or hydraulic testing equipment, to determine the tensile properties in the longitudinal and transverse directions of the unidirectional laminates.

Longitudinal properties associated with loading in the fiber direction are dominated by the fibers, which are usually stronger, stiffer, and have a lower ultimate strain than the matrix [6]. To analyze the behavior of composite materials under tensile or compressive loading and compare the results with other studies, standard procedures must be followed. "ASTM D3039/D3039M - Standard Test Method for Tensile Properties of Polymer Matrix Composite Materials" [86] can be used for tensile loading as well as BS EN ISO 527-5:2009: Plastics. Determination of tensile properties. Test conditions for unidirectional fibre-reinforced plastic composites [87].

The behavior under tensile loading in the fiber direction is described as brittle linear-elastic which was confirmed by several experimental studies [88]–[92] for carbon/epoxy and glass/epoxy composites.

In the transverse to the fiber direction, the behavior of unidirectional composites, especially the strength, is dominated by the matrix and interfacial properties. Under tensile loading, the behavior of unidirectional composite materials is quasi-linear, with relatively low ultimate strengths and strains [6]. The same behavior was reported by Botelho et al. [92]and by Li and Lambros [93].

To extract the Young modulus, the axial stress-axial strain curves are plotted and approximated with a linear function whose slope represents the modulus of elasticity. The Poisson ratio can be computed using equation (1.5).

$$\nu_{lt} = \left|\frac{\varepsilon_t}{\varepsilon_l}\right| \tag{1.5}$$

where ε_l represents the strain in the longitudinal direction, which coincides with the loading direction, and ε_t represents the strain in the transverse direction, perpendicular to the loading direction. As various strain recordings are made and can give slightly different Poisson ratios, to get an average value for a test sample, the $\varepsilon_t - \varepsilon_l$ curve corresponding to the elastic region of the stress-strain curve can be approximated with a linear function to extract its slope as the Poisson ratio ν_{lt} [94].

In the case of failure stress in the fiber direction, thickness and size effects due to the geometry of the tested sample were reported in the literature. [95], [96]. Kawai et al. [96] proposed a geometrical scaling for the failure stress of the 0° tensile test specimens. Using equation (1.6), where σ_{ref} –failure stress of laminate with reference thickness, t_{ref} – reference laminate thickness, σ – calculated failure stress, t – laminate's thickness for which failure stress is calculated, m – fitting exponent, a 1D thickness scaling can be performed. If another dimension of the sample varies, such as the width, a 2D geometrical scaling can be performed. In this second scaling, the reference failure stress of laminate (with reference thickness) σ_{ref} is scaled based on the gauge area (length × width) of the new-dimension laminate A and the gauge area of reference laminate A_{UTS13}, using equation (1.7), where n_2 represents a fitting exponent. The exponent m from equation (1.6) is also scaled using equation (1.8), based on the initial exponent determined from the reference laminates m_{UTS}.

$$\frac{\sigma}{\sigma_{ref}} = \left(\frac{t}{t_{ref}}\right)^{-\frac{1}{m}} \tag{1.6}$$

$$\sigma_{ref} = \sigma_{UTS13}\left(\frac{A}{A_{UTS13}}\right)^{n_2} \tag{1.7}$$

$$-\frac{1}{m} = -\frac{1}{m_{UTS}}\left(\frac{A}{A_{UTS13}}\right)^{n_1} \tag{1.8}$$

1.2.2 Off-axis behavior and testing

To characterize the behavior of unidirectional composites, the off-axis tensile test has received much attention as it can be used to verify the applicability of tensor transformation equations for the elastic properties of the fiber composite [4], [97]. The off-axis tensile test also serves as a convenient method for estimating the in-plane shear properties, eliminating the need for specialized fixtures or composite samples designed specifically for this purpose [98]–[101]. Furthermore, the off-axis test can be employed to evaluate the strength properties of the composite in various in-plane loading directions. This capability is valuable for design and optimization purposes, enabling a comprehensive understanding of the material's behavior and facilitating informed decision-making.

From a macro-mechanical point of view, the off-axis mechanical properties of unidirectional fiber-reinforced composites are anisotropic due to variations in fiber orientation with respect to the loading axis. Moreover, several papers state that for most fiber orientations relative to the loading axis of unidirectional fiber composites, the axial stress-strain curves show a nonlinear behavior, and the angle between the fiber orientation and the loading direction significantly affects the degree of nonlinear response. Hahn et al. [102] showed that the behavior of laminates is affected by the nonlinear constituent laminae, by employing experiments and analytical models. Ogihara et al. [103] studied the nonlinear response of T300/2500 carbon/epoxy system under off-axis tensile loading, using cross-ply and woven laminates. In their work, the off-axis specimens showed apparent softening nonlinearity. Yokozeki et al. [104] investigated the nonlinear mechanical behaviors and strengths of CFRP unidirectional and multidirectional laminates under compressive loadings and measured the nonlinear mechanical properties of the unidirectional composites based on a one-parameter plasticity model combined with nonlinear elasticity. Predictions of compressive strength of unidirectional and multidirectional composites were performed, concluding that usage of experimental data of multidirectional laminates might be a better means to obtain the compressive strength of unidirectional composites for efficient composite structural design. In their experimental study, Cai et al. [105] investigated the off-axis tension responses of woven glass/epoxy composites. Both sets of specimens exhibited a nonlinear stress-strain relationship, and the study reported a decrease in elastic moduli as the off-axis angle increased. In a recent investigation by Ma et al. [106], the off-axis behavior of PEEK/AS4 unidirectional thermoplastic composites was examined. The study encompassed a fractographic analysis to explore the damage mechanisms occurring under a combined tension/shear stress state. The findings revealed that the material exhibited a linear-elastic relationship during the initial stage, followed by nonlinear behavior during the strain-hardening phase. The tension/shear coupling effect induced by combined tension and shear stress contributed to heightened nonlinearity and resulted in the generation of inhomogeneous strain fields. Studies of the nonlinear stress-strain behavior under high strain rate loading were performed by Koerber et al. [107], [108], using transverse tension and off-axis tension specimens. They also simulated the stress-strain response using a transversely isotropic elastic–viscoplastic constitutive model.

If the composite is transversely isotropic and the in-plane elastic properties are known (E_1 – elastic modulus in the fiber direction E_2 – elastic modulus in the transverse direction, ν_{12} – major Poisson ratio, G_{12} – in-plane shear modulus), the off-axis apparent elastic modulus E_x can be predicted using the transformation equation (1.9) and the apparent Poisson ratio ν_{xy} can be predicted by using equation (1.10), for any off-axis angle θ.

$$\frac{1}{E_x} = \frac{1}{E_1}\cos^4\theta + \left[\frac{1}{G_{12}} - \frac{2\nu_{12}}{E_1}\right]\sin^2\theta\cos^2\theta + \frac{1}{E_2}\sin^4\theta \tag{1.9}$$

$$\nu_{xy} = E_x \left[\frac{\nu_{12}}{E_1}(\sin^4\theta + \cos^4\theta) - \left(\frac{1}{E_1} + \frac{1}{E_2} - \frac{1}{G_{12}}\right)\sin^2\theta\cos^2\theta\right] \quad (1.10)$$

1.2.3 In-plane shear properties

The behavior of a unidirectional composite under in-plane shear loading is dominated by the matrix properties and the local stress distributions [6]. The shear behavior of unidirectional composite laminates can be decomposed into two parts, a linear behavior and a second nonlinear behavior followed by the rupture of the material, as was reported by several authors [109]–[112].

Various experimental approaches can be used to characterize the shear behavior of unidirectional composite materials, each having advantages and disadvantages, as a state of pure shear is difficult to obtain experimentally.

ASTM D4255/D4255M [113] and ASTM D5379/D5379M [114], also known as the Iosipescu test [115], are examples of standardized tests for the shear characterization of composite materials, but they require specialized fixtures for the testing machine and specific shapes for the samples. Another standardized method is ASTM D3518/D3518M [116], which requires a ±45° cross-ply laminate that is symmetrically laminated about its midplane.

Despite lacking standardization, the off-axis tensile test has received significant interest as a means of establishing a straightforward method for characterizing the shear properties of composite materials. The 10° off-axis test was studied by Chamis et al. [100] and was considered suitable for shear characterization and was also recommended as a potential standardized test. In another, more recent, extensive study of the 10° off-axis test [117], the authors used Digital Image Correlation (DIC) to emphasize the non-uniformity of the displacement field and strain contour in the 10° specimen induced by end constraints. This effect was observed and quantified by Pindera et al. [98] who conducted a study on seven off-axis configurations 5°, 10°, 15°, 30°, 45°, 60°, and 75°. The authors concluded that in the region of an off-axis angle smaller than 30°, the shear stress induced by end-constraints in the presence of shear coupling induces an error in the determination of intralaminar shear modulus G_{12} and a correction factor should be used. They also noted that the 45° specimen is an excellent specimen for accurate determination of G_{12}, as the error due to shear stress vanishes in calculating G_{12}. In terms of shear strength, the 10° configuration yields considerably higher shear stress at failure than 45°, therefore being preferred for estimating the shear strength. In a later study, Pindera et al. [99] compared the off-axis test with the Iosipescu test concluding that the best outcome would be by using the 45° off-axis test for determining the intralaminar shear modulus and the 0° Iosipescu test for shear strength. A similar comparison was made by Pierron et al. [118] having a similar conclusion, that both tests can be used for initial shear modulus determination for carbon/epoxy specimens.

When the shear strength cannot be accurately evaluated experimentally, to obtain an approximate shear strength, the Tsai-Hill failure criterion for uniaxial off-axis strength [97] represents an alternative. The Tsai-Hill failure criterion is detailed in equation (1.11), in which θ is the off-axis angle, X is the failure stress in the fiber direction, Y is the failure stress in the direction perpendicular to the fiber and S represents the shear failure stress or shear strength. The shear strength S is adjusted so that the failure stress prediction using the Tsai-Hill criterion fits the off-axis experimental data for failure stress.

$$\frac{\cos^4\theta}{X^2} + \left[\frac{1}{S^2} - \frac{1}{X^2}\right]\cos^2\theta\sin^2\theta + \frac{\sin^4\theta}{Y^2} = \frac{1}{\sigma_{xx}^2} \quad (1.11)$$

The shear stress τ_{12} in a composite ply with fibers oriented at an angle θ from the direction of the load can be evaluated by using a coordinate transformation. The simplified equation (1.12) can be used in which the end-constraints effects are ignored [98]. For θ = 45°, the in-plane shear stress is half of the tensile stress σ_x.

$$\tau_{12} = -\sigma_x \cdot \cos\theta \cdot \sin\theta \tag{1.12}$$

The in-plane engineering shear strain γ_{12} can be evaluated based on the structural-axes strains by using equation (1.13) [100].

$$\gamma_{12} = (\varepsilon_y - \varepsilon_x)\sin 2\theta + \gamma_{xy}\cos 2\theta \tag{1.13}$$

In equations (1.11), (1.12), and (1.13), the notations are as follows: x and y are the structural directions, with x in the loading direction; 1 and 2 are the axes of the composite coordinate system, with 1 in the fiber direction.

The in-plane shear modulus G_{12} can be determined from the slope of the tangent to the shear stress- shear strain plot, in the linear response region.

1.2.4 Damage assessment by cyclic load-unload off-axis test

Different models used to predict the nonlinear behavior of unidirectional fiber-reinforced composites loaded off-axis attribute the nonlinearity of the response either to plastic deformation of the matrix [107], [119]–[121], to internal damage and stiffness reduction [122], [123] or both [124]–[129].

To investigate the cause for nonlinear behavior in off-axis tests for the composite materials, cyclic load-unload tests can be performed, with the amplitude of the stress level increasing for each cycle. This approach has been proposed by Ladeveze and Le Dantec [129] and they associated the stiffness reduction with a damage variable, based on continuum damage mechanics, while a plasticity model takes into account the residual strains with complete unloading. The number of cycles is limited to a maximum of six, to avoid low cycle fatigue phenomenon effects [129]. The damage variable can be calculated from the cyclic load-unload tests using equation (1.14), where E_i represents the modulus of the ith cycle and E_0 represents the initial elastic modulus of the first cycle. The damage variable provides an indirect measurement of physical damage in composite laminates [130]. The residual strain (or plastic strain), needed for identifying the parameters for a plasticity model, can be extracted as well from the cyclic load-unload modulus using relation (1.15) where σ_i is the maximum stress in the ith cycle, which should be as close as possible to the maximum stress levels imposed in the test setup.

$$D = 1 - \frac{E_i}{E_0} \tag{1.14}$$

$$\varepsilon_{res} = \varepsilon_i - \frac{\sigma_i}{E_i} \tag{1.15}$$

In Ladeveze's work, the elastic modulus of the cycle E_i is evaluated as the unloading chord modulus from the endpoints of the loading and unloading part of the ith cycle, as shown in Fig. 1.12a, such that the effects of the load-unload hysteresis are minimized [128]. The same suggestion is given by Lemaitre and Chaboche [131]. Ladeveze's approach to elastic modulus evaluation was also used by Zhai et al. [132] to determine damage parameters for a coupled damage-plasticity model, for nonlinear off-axis behavior prediction of quasi-UD E-glass fabric reinforced polypropylene composites. In other works [133]–[135], the same approach was used to evaluate the in-plane shear modulus degradation. Fuller et al. [136] used a similar approach to show that the $[\pm 26_5]_s$ and $[\pm 27_5]_s$ layups of thin-ply carbon-fiber specimens retain most of their initial stiffness after multiple cyclic load-unload testing while exhibiting pseudo-ductility. However, they considered that by calculating the chord modulus of each cycle from a higher applied stress than the previous one, an overestimation of the stiffness loss would be induced, and used a secant modulus up to a constant value of applied stress.

While Ladeveze's approach is widely used in the literature, two other proposals for the evaluation of the elastic modulus of the cycle were found, which are less researched. Fitoussi et al. [137] and Hug [138] suggested taking the cycle modulus as the slope of a linear regression

of the loading curve of the cycle, taken between $\sigma_{xi}/10$ and $\sigma_{xi}/2$. An illustration of this method is found in Fig. 1.12b. Castres [84] suggested another approach, by applying a successive linear regression on the loading curve of each cycle and selecting the modulus as the slope of the linear regression that has a maximum coefficient of determination R^2, denoted as the Regression method. By considering the tangential modulus of the loading curve, the stress level of the cycle should not influence the modulus evaluation. Compared to the chord modulus, which provides an overall measure of how the material's stiffness changes as it undergoes loading and unloading, capturing the cumulative effect of these changes throughout the cycle, the tangential modulus offers a localized measure of the material's stiffness during the initial loading phase of the cycle. However, it does not account for the energy dissipation and the differences between loading and unloading behavior.

In the Regression method employed in this work, for each loading curve of each cycle, successive least-squares linear regressions are employed. For a given cycle, a regression is calculated using an initial selection of the first few experimental points from the entire loading curve. Subsequent regressions are computed by adding additional experimental points with each increment. For each regression, the coefficient of determination R^2 is determined, indicating the correlation between experimental data and the linear fit. A value of 1 indicates a perfect fit. In this procedure, the dataset points from the loading curve with the highest R^2 are identified, and the apparent modulus is then determined as the slope of the linear fit for the data points associated with the highest R^2 regression.

The distinction between the Fitoussi method and the Regression method lies in the data points from the loading curve used to assess the modulus. The Fitoussi method employs linear regression within predetermined bounds on the loading curve, regardless of the fit's quality. In contrast, the Regression method selects the set data points from the same loading curve that offers the best correlation to a linear regression. While Eliopoulos and Philippidis [139] also determined the cycle elastic modulus for stiffness degradation analysis as the slope of the linear regression model of each stress-strain loop, no mention is made in their work as to whether any bounds or additional criteria were imposed for the regression.

Regardless of the method for extracting the cycle modulus, in these methods, the residual strain is extracted in the same manner as in Ladeveze's work. The three methods for evaluating the elastic modulus of the cycle, thus the damage variable, will be referred to in this work as the Ladeveze method, the Fitoussi method, and the Regression method.

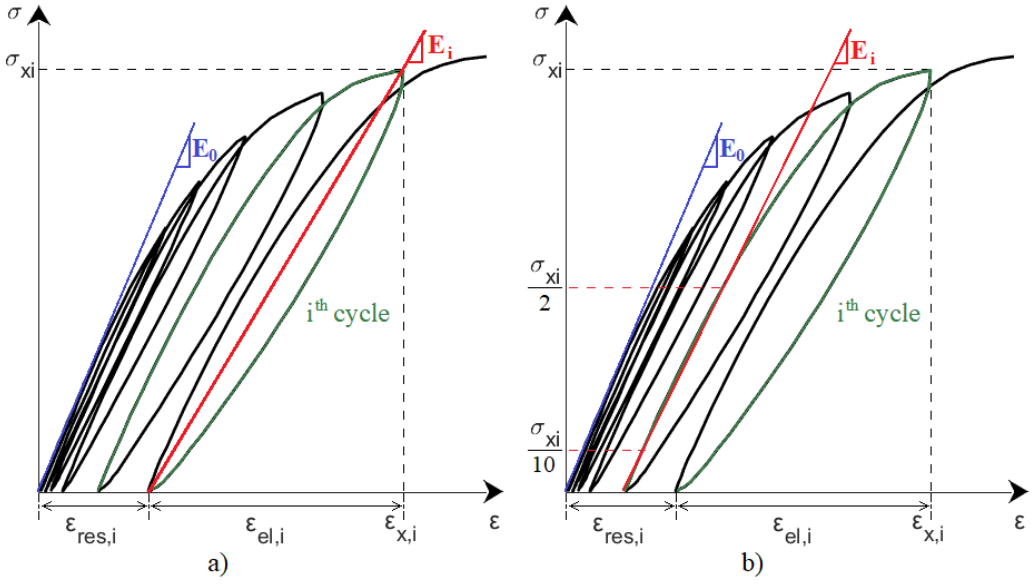

Fig. 1.12. Methods of determination of damage variable D and residual strain ε_{res} from load-unload cycles; a) Ladeveze's method, b) Fitoussi's method

1.2.5 Nonlinear constitutive model formulation

Ladeveze's approach to damage formulation has been used and refined by different authors to develop a coupled damage-plasticity nonlinear constitutive model and determine the needed parameters. Xie et al. [140] studied the off-axis nonlinear behavior of 3D needled C/C-SiC composites and proposed a different formulation of the damage variable, in the form of a Weibull distribution function of the effective stress of the composite material. In terms of the plasticity approach for developing an elasto-plastic damage model for the studied material, they used Cho's yield function [120] which is an extension of the one used by Sun and Chen's one-parameter plasticity model [119]. In Cho's yield function, both deviatoric and dilatational deformations are considered while in Sun and Chen's one-parameter plasticity model only deviatoric deformations are taken into account. The off-axis and cyclic load-unload tensile behavior and residual strain of 3D Needle C/SiC composites have also been studied by Liu et al. [141].

Zhai et al. [132] adapted Xie's damage formulation and Cho's yield function to characterize the nonlinear response of quasi-unidirectional E-glass fabric composites and determined the parameters for the model from cyclic load-unload tensile tests. They also extended the model formulation to include the temperature-dependent response under off-axis loading of the same material [142].

Wang et al. [143], [144] studied and modeled the tension-compression asymmetry in plastic strain and hysteresis behavior of unidirectional HTS40/PA6 composites by analyzing the off-axis load-unload response under tension and compression. Their model splits the strain components into three components: an elastic component, a plastic component, and an anelastic strain component, considered to be due to the nonlinear unloading. This anelastic strain component is recoverable like an elastic strain during the loop but dissipates energy as plastic strain. O'Brien et al. [145] modeled the nonlinear shear stress-strain response of hybrid fiber-metal composites by finite element analysis, starting from the model proposed by Paepegem et al. [134], [146]. In their phenomenological model, the shear damage variable and shear plastic strain are extracted in the same manner as the cycle modulus and residual strain in Ladeveze's work (Fig. 1.12a) but in terms of the constitutive model, they express the shear damage variable and permanent shear strain as a function of the total shear strain and propose a different formulation compared to previously mentioned papers. Another phenomenological model, which decomposes the total strain into three components, has been proposed by Fallahi and Taheri-Behrooz [147].

A coupled damage-plasticity model similar to the one proposed by Zhai et al.[132] can be defined, to model and predict the off-axis nonlinear behavior of unidirectional composite materials. In the model, the nonlinear off-axis behavior exhibited by the unidirectional fiber composites is attributed to both damage and plasticity. The damage is characterized by stiffness loss with each load-unload cycle, and plasticity is defined by the residual strains with complete unloading.

To account for the influence of both parameters, the incremental strain is decomposed into elastic and plastic strain increments, as proposed by Sun et al [119]. Equation (1.16) shows the components of the incremental strain, where ε_x represents the macroscopic axial strain, ε_x^e is the elastic strain, and ε_x^p is the plastic strain component.

$$d\varepsilon_x = d\varepsilon_x^e + d\varepsilon_x^p \tag{1.16}$$

1.2.5.1 Plastic strain formulation

By using an associated flow rule, the incremental plastic strain can be written in terms of the stress σ_{ij} (i, j = 1, 2, 3) in the principal material directions, the plastic potential function f and a scalar function of proportionality λ, as shown in equation (1.17) [119], [120], [140].

$$d\varepsilon_x^p = \frac{\partial f}{\partial \sigma_{ij}} d\lambda \tag{1.17}$$

Cho's [120] plastic potential function formulation is employed in this study, as it accounts for both deviatoric and dilatational deformations. In the case of plane stress-state, $\sigma_{33} = \sigma_{13} = \sigma_{23} = 0$, and transversely isotropic composites, the plastic potential function is defined as shown in equation (1.18), where σ_{ij} (i, j = 1, 2, 3) are the stresses in the material principal directions, a_1, a_2, and a_6 represent plastic anisotropy parameters, μ is an elastic anisotropy parameter defined by Chen and Sun [148], and b_1 and b_2 also represent plastic anisotropy parameters, for the dilatational component of the plastic potential function.

$$f = \sqrt{a_1[(\sigma_{11} - \mu\sigma_{22})^2] + a_2\sigma_{22}^2 + a_6\sigma_{12}^2} + b_1\sigma_{11} + b_2\sigma_{22} \tag{1.18}$$

For unidirectional composites manufactured using carbon fibers, the stress-strain behavior in the fiber direction is linear. Thus, it can be assumed that there is zero plastic deformation in the fiber direction [119]. This condition is expressed as in equation (1.19) and leads to $a_1 = b_1 = 0$. Without loss of generality, $a_6 = 1$ [120], and a two-parameter, simplified expression for the plastic potential function f is obtained and shown in equation (1.20).

$$d\varepsilon_{11}^p = \frac{\partial f}{\partial \sigma_{11}} d\lambda = 0 \tag{1.19}$$

$$f = \sqrt{a_2\sigma_{22}^2 + \sigma_{12}^2} + b_2\sigma_{22} \tag{1.20}$$

The effective stress $\overline{\sigma}$ is defined as being equal to the plastic potential function f, and the proportionality factor is derived from the increment of plastic work per unit volume dW^p, defined in equation (1.22), where $d\bar{\varepsilon}_p$ represents the incremental effective plastic strain.

$$\overline{\sigma} = f \tag{1.21}$$

$$dW^p = \sigma_{ij} d\varepsilon_{ij}^p = \bar{\sigma} d\bar{\varepsilon}_p \tag{1.22}$$

Substituting into equation (1.17), the scalar function of proportionality is given by:

$$d\lambda = d\bar{\varepsilon}_p \tag{1.23}$$

Sun and Chen [119] proposed using a power-law function to fit the master effective stress–effective plastic strain curve, as for fiber composites there is no well-defined yield point and nonlinearity appears gradually. Thus, the effective plastic strain can be expressed as shown in equation (1.24), where the coefficients *A* and *n* are to be determined from experimental data.

$$\overline{\varepsilon_p} = A(\overline{\sigma})^n \tag{1.24}$$

Moreover, for off-axis tensile tests, with θ as the off-axis angle, the applied axial stress σ_x has to be transformed into the stress components in the principal material direction:

$$\begin{aligned} \sigma_{11} &= \sigma_x \cos^2\theta \\ \sigma_{22} &= \sigma_x \sin^2\theta \\ \sigma_{12} &= -\sigma_x \sin\theta \cos\theta \end{aligned} \tag{1.25}$$

Substituting equation (1.25) into equations (1.20) and (1.21), the effective stress can be expressed in terms of off-axis angle and applied stress as:

$$\overline{\sigma} = h(\theta)\sigma_x \tag{1.26}$$

where

$$h(\theta) = \sqrt{a_2 \sin^4\theta + \sin^2\theta \cos^2\theta} + b_2 \sin^2\theta \tag{1.27}$$

Moreover, the effective plastic strain increment $d\bar{\varepsilon}_p$ can be derived from the measured plastic strain increment $d\varepsilon_x^p$ as:

$$d\bar{\varepsilon}_p = \frac{d\varepsilon_x^p}{h(\theta)} \tag{1.28}$$

For proportional loading, equation (1.28) can be integrated into [120]:

$$\bar{\varepsilon}_p = \frac{\varepsilon_x^p}{h(\theta)} \tag{1.29}$$

For each load-unload cycle, the effective plastic strain and effective stress can be calculated from the experimental axial stress and axial plastic strain, also referred to as residual strain. Regardless of the off-axis angle, the curve $\overline{\sigma} - \overline{\varepsilon_p}$ should be almost the same [119]. Therefore, by trial and error, a_2 and b_2 are tuned so that $\overline{\sigma} - \overline{\varepsilon_p}$ curves from different off-axis tests are as coincident as possible. After a_2 and b_2 are determined, the curve $\overline{\sigma} - \overline{\varepsilon_p}$ is fitted with the power function in equation (1.24), and *A* and *n* parameters are extracted.

1.2.5.2 Elastic strain formulation and nonlinear coupled damage-plasticity constitutive model

Using the formulation of the damage variable in equation (1.14), the elastic strain increment from equation (1.16) can be written as

$$d\varepsilon_x^e = \frac{d\sigma_x}{(1-D)E_0} \tag{1.30}$$

where D represents the damage variable, E_0 is the initial elastic modulus of the undamaged material, and σ_x is the applied axial stress.

To incorporate the damage variable *D* into a constitutive model, Xie et al. [140] proposed expressing the damage variable in terms of the effective stress, in the form of a Weibull

distribution function, similar to the formulation of the failure probability. The expression of the damage variable is shown in equation (1.31), where n_e and σ_e are parameters that can be determined by fitting the experimental data, and $\bar{\sigma}$ represents the effective stress.

$$D = 1 - \exp\left(-\left(\frac{\bar{\sigma}}{\sigma_e}\right)^{n_e}\right) \tag{1.31}$$

Based on previous equations, the expression of the axial strain can be written in terms of the applied stress, the off-axis angles, and the parameters for the constitutive model as written in equation (1.39).

$$\varepsilon_x = \frac{\sigma_x}{E_x \cdot exp\left(-\left(\frac{\sigma_x h(\theta)}{\sigma_e}\right)^{n_e}\right)} + A\sigma_x^n\left(h(\theta)\right)^{n+1} \tag{1.32}$$

The apparent elastic modulus E_x can be evaluated using the transformation equation (1.9), based on the in-plane mechanical properties.

1.3 DYNAMIC LOADING OVERVIEW

1.3.1.1 Generalities

In general, the fluid-structure interaction and impact response of materials can be described by their physical modifications after being recovered (melting, deformation, cracks, …). They are classified depending on the velocity of the projectile [65].

- **Low-velocity impacts** are considered to occur at velocities below 10 m/s;
- **Intermediate-velocity impacts**, which represent a transition regime between low and high-velocity impacts, are at velocities between 10 m/s and 50 m/s.
- **High-velocity impacts** range from 50 m/s up to 1000 m/s.
- **Hyper-velocity impact,** at velocities above 1000 m/s.

This classification is based on the fact that energy transfer between projectile and target, energy dissipation, and damage propagation mechanisms undergo drastic changes as the velocity of the projectile increases [72].

The material response depends on the stress intensity - and its duration - and also, the stress or strain rate. In low-velocity impact, the structure has more time to respond to the impactor and as a consequence, more impact energy can be absorbed by the structure which can also lead to extensive damage within the structure [68].

With the increase of the impact velocity of the projectile, the shock-induced stress increases, and thus the damage in the composite structure is more localized [149]. In high-velocity impact, the structure has less time to respond to the sudden load, as the response of the material is dominated by the stress-wave propagation through the target's thickness [68], therefore leading to a local deformation at the impact point, and often perforation of the structure [150]. Thus, understanding perforation mechanism and failure is important when studying materials intended to be used in applications where high-velocity impact represents a threat.

Moreover, when a material is subjected to impact, it undergoes large amounts of strain, depending on the strain rate and the magnitude of the impact [65]. The material must therefore be mechanically characterized at the strain rates of the intended application.

Ballistic impact is generally a low-mass high-velocity impact caused by a propelling source [72]. The ballistic limit velocity, v_{50}, is the velocity at which a specific projectile is expected to perforate the target half of the time [151] while the ballistic limit of a target is defined as the maximum velocity of a projectile at which the complete perforation takes place with zero exit velocity [72], [152].

Impact energy is the maximum kinetic energy of the impactor at the time of impact into the sample. For impacts without perforation of the target, it also represents the energy introduced into the specimen [153].

The absorbed or transmitted energy by the target represents the loss in kinetic energy through elastic and plastic deformations and other energy absorption mechanisms while the residual kinetic energy is the remaining energy of the projectile after the ballistic impact [154].

The impact energy (E_i), residual energy (E_r), and absorbed energy (E_t) can be calculated based on the velocities before impact (v_0) and the velocity at the exit, or residual velocities (v_r), after perforation of the target by the projectile of mass m using equations (1.33) - (1.35). The percentage change in kinetic energy (ΔE_f) can be evaluated using equation (1.36).

$$E_i = \frac{1}{2} m v_0^2 \tag{1.33}$$

$$E_r = \frac{1}{2} m v_r^2 \tag{1.34}$$

$$E_t = \frac{1}{2} m v_0^2 - \frac{1}{2} m v_r^2 \tag{1.35}$$

$$\Delta E_f = \frac{E_t}{E_i} \cdot 100 \tag{1.36}$$

In the aircraft industry, structures are subjected to different types of loads that occur at different velocities. Low-velocity impact may occur during the ground service of an aircraft (tool-drop), during lofting stones, and other foreign objects from the runway during aircraft take-off. While a small tool drop on the airplane structure can induce strain rates between $1 s^{-1}$ and $10\ s^{-1}$ [155], runway debris impact velocity can reach up to 50 m/s and therefore induce higher strain rates than tool drops. During flight, birds can strike at high velocities with corresponding strain rates of $300\ s^{-1}$ [156]. Even though these strain rates are higher than the ones that tool drops and runway debris induce, they are still in the intermediate strain rate category (1 to $500\ s^{-1}$). High and very high strain rates occur at high-velocity impacts such as projectile, ice stone impact, or turbine blade containment, the actual category depends on the

impact velocity and object size. Fig. 1.13, adapted from [84], [157], [158], illustrates the dynamic strain rate range as well as corresponding loads on composite materials for aircraft structures.

1.3.1.2 Experimental testing techniques for dynamic loading

For low strain rates, below 10 s^{-1}, servohydraulic machines can be used. They are not suitable for higher strain rates because of the inertial effects of the heavy load cells and grip [159].

Daniel et al. [24], described a method for testing composite materials in compression at strain rates up to approximately 230 s^{-1}. The method utilizes a thin ring specimen loaded dynamically by an external pressure pulse applied explosively through a liquid. Strains in the composite specimen and in a steel calibration ring were recorded with a digital processing oscilloscope.

A brief description of another method to test composites at intermediate and high strain rates is given in [73]. The Hopkinson bar technique permits the determination of the variation of basic material properties as a function of strain rate. Several types of Hopkinson bars are currently employed; these include the punchloaded Hopkinson bar, the compression bar, the tensile bar, and the Hopkinson bar shear test. The setup and experimental procedures associated with these tests are detailed in [160]. Strain rates approaching 1000 s^{-1} can then be achieved using gas-driven projectiles to accelerate the weighbar and, in turn, load the input bar. The inertia of the inertia bar then enables the test coupon to be loaded dynamically. Strain gauges bonded to the input and inertia bars enable the incident and reflected stress waves to be analyzed and permit the determination of a dynamic stress/strain curve for the material. The Hopkinson-bar tensile test is destructive. Care has to be taken in order to ensure that the interface between the specimen and loading bars is good, otherwise, a shear failure within the gripping section is likely to occur. Further, in order to minimize stress concentrations associated with the gripping area, relatively long specimens (approximately 60 mm) are required when testing composite materials [73], [161].

Besides the Hopkinson bar technique, Hsiao et al. [159] used a drop tower for dynamic compressive testing of thick composites. This method has a series of advantages, such as easy variation of strain rate, low cost, and adaptability to different specimen geometries. The drop weight is guided along two long guide rods through bearing assemblies. It is raised and released using an electromagnet. The dynamic impact force was measured in two different ways. Initially, it was measured with an accelerometer mounted on the top of the drop weight and the results were compared with values obtained more directly from strain readings on the steel portion of the specimen. The major problem in the use of a drop tower apparatus is the presence of vibration stress waves superimposed on the stress-strain curves. Therefore, measures must be taken in order to limit their effects.

For high-velocity impact studies, the single-stage gas gun is generally used. The specimen is clamped between frames to be kept in position while being hit by the projectile. The projectile's velocity can be modified by varying the pressure of the gas in the firing chamber. Different types of projectiles can be used, depending on the requirements of the experimental campaign [162]–[164]. Recently, Caisso et al. [165] proposed an experimental and numerical investigation of a soft projectile impact by subjecting blade parts to three-point bending (SPITPB) test for adhesion assessment under soft projectiles supposed to be surrogate of a bird. Besides gas guns, a universal receiver powder gun can also be used to evaluate the ballistic behavior of composites. It can also be customized for different testing conditions [65].

For very high strain rates and shockwave studies, plate-impact techniques can be used. With this technique, a metallic or polymeric flyer plate hits the tested target at an impact velocity ranging from a few tens of meters per second to a few thousand meters per second. Millet et al. [166] and Jaulin et al. [167] studied the response of two-dimensional carbon fiber epoxy composite using shock stresses induced by the impact of a flyer plate in the velocity range 225–

1125 m/s, in the fiber direction and the through-thickness direction. Lässig et al. [168] proposed with this method a shock equation of state for Dyneema HB26, a UHMWPE composite dedicated to ballistic protection. The same technique was employed by Hazell et al. [169] to study the effect of specimen thickness on the shock propagation in a woven laminate and along the fiber. The dynamic response of carbon fiber reinforced epoxy was studied by means of plane plate impact by Alexander et al. [170]. The observed mechanisms of the experimental shockwave response were supported and validated by micromechanics simulation results.

Another method of generating very high strain rate loadings is by using laser-induced shockwaves [81]. This technique was initially developed for studying bonded material adhesion. It was employed for composite material bonding assessment [171], delamination observation under out-of-plane high strain rate loading [158], [172], controlled delamination in carbon fiber composites [173], and delamination in UHMWPE composites [25]. Extended details are given in section 1.4.

Fig. 1.13 summarizes the test methods used for generating various strain rate categories.

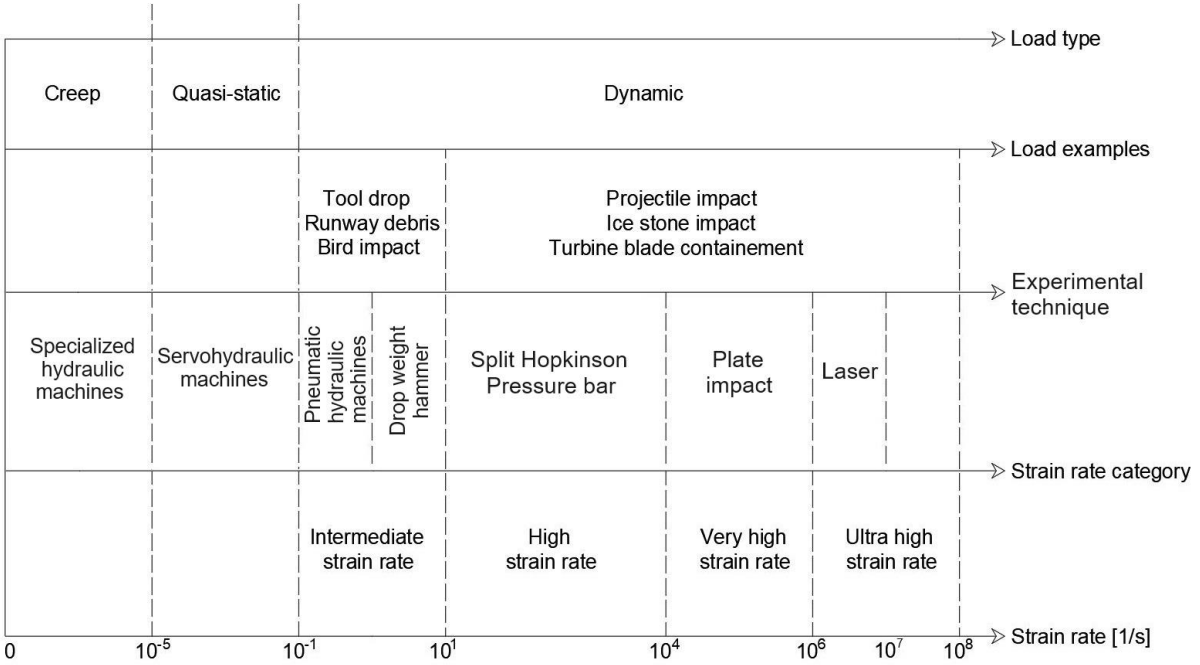

Fig. 1.13. Load examples and experimental techniques for different strain rate categories

1.3.1.3 Strain rate effects on fiber-reinforced composite materials

Numerous investigations have tackled the issue of composite material response under different strain rate conditions, revealing a noticeable impact of strain rate on the mechanical characteristics of these materials.

Harding and Welsh [161] showed that the influence of the strain rate is barely observed in tensile loading in the longitudinal direction of unidirectional carbon/epoxy composites. Kwon et al. [174] reported the same behavior for the tensile loading at various strain rates in the longitudinal direction.

In [175], Ou and Zu investigated the effects of intermediate strain rate on the mechanical properties of unidirectional glass fiber reinforced polymer (GFRP). The tensile strength increases remarkably from quasi-static to dynamic condition and Young's modulus also increased with increasing strain rate over the strain rate range of 40 –160 s^{-1}. They also concluded that the failure patterns of the tested GFRP specimens are also strain rate dependent: at low strain rate, the fracture surface is more localized while at higher strain rates it expands to the entire gauge section at higher strain rate, which leads to an increase in energy absorption. Similar results were reported by Shokrieh and Omidi [89].

For tensile loading in the transverse direction for unidirectional composites, strain rate sensitivity is more pronounced [174]. An increasing modulus and strength for increasing strain rates for unidirectional carbon/epoxy was reported by Gilat et al. [176] but he also reported no considerable effect on the failure strain, for strain rates between 10^{-5} s^{-1} and 400 s^{-1}.

Lifshitz and Leber [177] studied the interlaminar tensile strength and modulus of unidirectional composite material at various strain rates and reported that the stress-strain relation is linear to fracture and there is a value increase of ultimate strength and modulus with increasing strain rate.

For the transverse compressive behavior, Hsiao and Daniel [159] showed that transverse strength, which is a matrix-dominated property, shows nearly a two-fold increase from the quasi-static value. The initial modulus follows a similar trend, although not as pronounced, with an increase of up to 37%. The ultimate strain shows no strain rate effect at all. Koerber et al. [110] performed high strain rate experiments on unidirectional carbon-epoxy composites, with strain rates up to 350 s^{-1}, and observed that the transverse compression modulus of elasticity, yield strength, and failure strength exhibit growth of 12%, 83%, and 45% respectively.

To determine the shear behavior of unidirectional composite materials, most authors used ± 45° laminates for testing. Both Gilat et al. [176] and Hsiao and Daniel [159] reported that the shear stress-strain behavior shows high nonlinearity with a plateau region at a stress level that increases significantly as the strain rate increases. An increase of both strength and modulus with increasing strain rate was reported, and Koerber et al. [110] mentioned increases of 25, 88, and 42% for the in-plane shear modulus of elasticity, yield strength, and pure failure strength, respectively.

1.4 GENERALITIES ON LASER-INDUCED SHOCKWAVES

1.4.1 Principle and description of laser-induced shockwaves

Laser-induced shockwaves have been used to induce a dynamic loading in materials since the first work of White in 1963 [178]. Later on, the possibility of measuring the free-surface velocity extended its application [179], [180]. Several studies addressed the dynamic loading and failure of metallic materials in the 90s [179]–[182] and also the adherence of thin film coatings [183].

A technique was developed for studying the adhesion of bonded materials using laser-induced shockwaves in the early 2000s. LASAT (LASer Adhesion Test) was used to test the adhesion of ceramic coating to metals [184]. The bonding between aluminum plates was also addressed [185] as well as the bonding of composite materials [171], [172] and more recently, Ducousso et al. [186] used this technique to evaluate the mechanical strength of an aeronautical-quality bond between titanium alloy and a 3D woven carbon/epoxy composite material. Additionally, this technique has the advantage of not inducing any mechanical contact. The laser-induced shock technique was also used in weak-bond inspection in CFRP adhesively bonded composites [187].

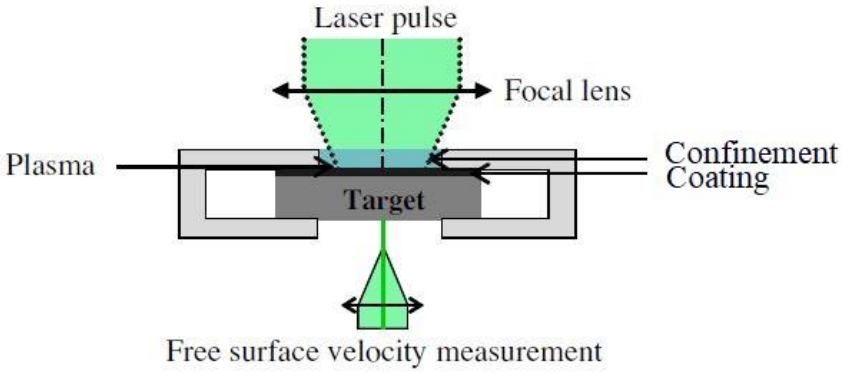

Fig. 1.14. Experimental setup for laser-induced shockwaves (not at scale) [172]

The principle of generating a shockwave by using laser irradiation is well described in the earlier mentioned papers as well as in [188], therefore only a brief description will be given here. Fig. 1.14 illustrates a general experimental setup for laser-induced shockwave experiments and each element will be further discussed.

Laser-induced shockwaves are produced when focusing a short-duration (~ns) and high-energy (~ J) pulsed laser beam on a small solid surface. When focused on a material, the photonic energy is absorbed by condensed matter and as a consequence, the surface of the irradiated material is sublimated. The plasma resulting from the sublimation expanses rapidly, which induces a shockwave into the target material, similar to a surface explosion effect. The maximal pressure of this shockwave is called the ablation pressure and depends on the laser source characteristics and the irradiated material. The shockwave then propagates through the thickness toward the target's back face, according to the material properties. For these experiments, the concept of incident energy is less relevant than that of incident laser density of power (intensity), which takes into account not only the energy but also the laser irradiation time and the impacted surface. The density of power can be determined based on equation (1.37), where ϕ is the density of power, E represents the laser beam energy, τ is the pulse duration and S is the surface irradiated by the laser beam.

$$\phi\left(\frac{GW}{cm^2}\right) = \frac{E(J)}{\tau(ns)\cdot S(cm^2)} \tag{1.37}$$

The plasma expansion can be confined by adding a solid (glass) or liquid (water) transparent media to the laser irradiation on the irradiated surface, slowing down the plasma expansion. In Fig. 1.14 both a confinement medium as well as a coating layer are represented. Moreover, the confining medium has two major effects on the pressure generated. The first one is an increase of ablation pressure by a factor of 5 to 10 compared to direct ablation and the second one is related to shock duration, which is increased by a factor of 2 to approximately 3 in air [188], as illustrated in Fig. 1.15. The effects of water confinement on the laser-induced shockwave parameters have been studied by Berthe et al. [189] and both glass and water confinement were studied by Devaux et al. [190]. In both papers analytical relations to determine the pressure are explained. Berthe's analytical expression, equation (1.38), gives the ablation pressure in a water-confined medium as a function of the density of power ϕ, the reduced shock impedance Z between the target and the confining water, given by equation (1.39), where ρ_{0_i} – density of the material and C_{0_i} – the sound velocity in the material, and a coefficient α of laser-matter interaction which depends on the laser source. Berthe proposed a typical value α=0.25 and it was also confirmed to be close to 0.22 below 4 GW/cm² and 0.25 above by Arrigoni et al. [191].

$$P(GPa) = 0.01\sqrt{\frac{\alpha}{\alpha+3}}\cdot\sqrt{Z(g\cdot cm^{-2}\cdot s^{-1})}\cdot\sqrt{\phi(GW/cm^2)} \tag{1.38}$$

$$\frac{2}{Z} = \frac{1}{Z_{water}} + \frac{1}{Z_{target}} \; with \; Z_i = \rho_{0_i}\cdot C_{0_i} \tag{1.39}$$

The coating layer, or sacrificial layer, is usually used between the target surface and the confining medium in order to absorb the plasma-induced thermal effects [173]. Since the laser-matter interaction on composite materials can be difficult to assess and reproduce within various experimental campaigns due to the heterogeneity of the composite microstructure, the sacrificial layer can also be used to have a known pressure profile after a calibration has been performed on a sample made from the same material as the coating. In general, aluminum coating is used, as the laser-matter interaction for aluminum is well described in the literature.

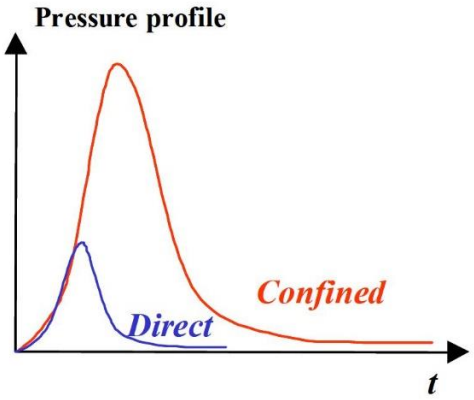

Fig. 1.15. Pressure profile for direct and confined ablation [188]

For composite materials, laser-induced shockwaves can be used to test the bonding between plies as well as to generate high out-of-plane tensile loadings, which are difficult to reproduce with conventional machines. Moreover, the influence of anisotropy of composite materials in shock propagation can be studied and by measuring the back-face velocity, the out-of-plane damage threshold of the material can be identified by an inverse approach.

1.4.2 Shockwave propagation

In order to bring a simplified understanding of shock propagation, conservation laws in 1D geometry are applied to the case of the propagation of a shock wave, treated as a discontinuity, as illustrated in Fig. 1.16. The parameters ahead of the shock front are pressure P_0, temperature T_0 and density ρ_0, and material velocity u_0 (assumed to be zero here). The corresponding parameters behind the shock front are P, T and ρ . The front velocity is D, and behind it, the material velocity is u.The expressions for conservation of mass, momentum and energy across a shock front are also known as Rankine-Hugoniot relations.

$$\text{Mass conservation: } \rho_0 D = \rho(D-u) \tag{1.40}$$

$$\text{Momentum conservation: } P - P_0 = \rho_0 D u \tag{1.41}$$

$$\text{Energy conservation: } Pu = \frac{1}{2}\rho_0 D u^2 + \rho_0 D(E - E_0) \tag{1.42}$$

By making substitutions, a more common form of the equation of energy can be obtained.

$$E - E_0 = \frac{1}{2}(P + P_0)\left(\frac{1}{\rho_0} - \frac{1}{\rho}\right) \tag{1.43}$$

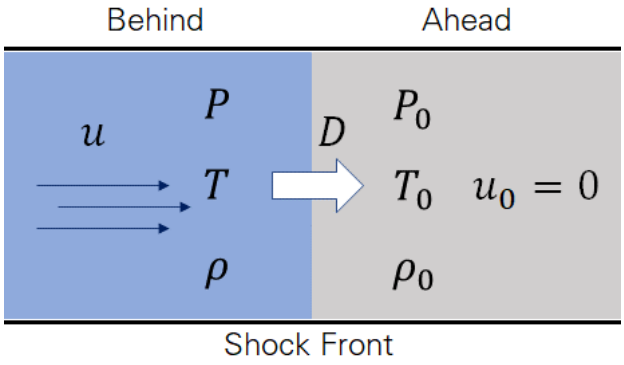

Fig. 1.16. 1D shockwave propagation

The system of three equations, (1.40), (1.41), (1.43) introduces five variables, P, ρ, E, u, D. A fourth relation is the equation of state that brings the description of the mater under a thermodynamic state (P, ρ, E). A closure relation, equation (1.44), describes the dependency of the shock velocity D with the material velocity u, where C_0 and s are characteristic constants

of the material that can be determined experimentally. C_0 is also referred to as the hydrodynamic speed of sound and can be calculated based on equation (1.52), where C_L and C_T are the longitudinal and transversal speed of sound.

$$D = C_0 + s \cdot u \tag{1.44}$$

$$C_0 = \sqrt{C_L^2 - \frac{4}{3}C_T^2} \tag{1.45}$$

For isotropic materials, the longitudinal speed of sound can be estimated based on the elastic modulus of the material (E) and its initial density ρ_0 using equation (1.46). However, composite materials have orthotropic properties, hence the same equation cannot be used. For unidirectional composites, the longitudinal speed of sound in the fiber direction can be determined using equation (1.47), while the longitudinal speed of sound in the direction perpendicular to the fiber can be calculated using equation (1.48) [97], [192].

$$C_L = \sqrt{\frac{E}{\rho_0}} \tag{1.46}$$

$$C_L = \sqrt{\frac{E_{11}}{\rho_0(1 - \nu_{12}\nu_{21})}} \tag{1.47}$$

$$C_L = \sqrt{\frac{E_{22}}{\rho_0(1 - \nu_{12}\nu_{21})}} \tag{1.48}$$

Substituting equation (1.44) in equation (1.41), one can express the pressure versus material velocity as a polynomial of second-degree using equation (1.49), also called shock polar in the *P-u* plane. The shock polar curve is characteristic of each material. The straight line joining the initial and the final shock states is the Rayleigh line and its slope represents the shock impedance $Z = \rho_0 \cdot D$. For moderate pressure, in order to simplify the calculus, the shock impedance is often reduced to the acoustic impedance $Z = \rho_0 \cdot C_0$, therefore the shock polar becomes a straight line. The compression and expansion waves

$$P - P_0 = \rho_0 C_0 u + \rho_0 s u^2 \tag{1.49}$$

The speed of sound in the compressed material behind the advancing shock front exceeds the shock front velocity. This results in a catch-up of the release wave (expansion wave) moving into the shocked region.

The primary shock propagates at the speed D_{01}. During the pressure release phase, a bundle of release waves propagates behind the shock front, propagating through a denser medium than the one through which the primary shock front propagates. The peak of the release wave bundle travels at C_1+u_1, faster than the shock front, while the base of the release travels at C_0+u_0, slower than the shock front. Consequently, the peak of the release wave catches up with the shock front and absorbs it, which leads to shock attenuation, often called hydrodynamic attenuation [193], while the base spreads out. This phenomenon is illustrated in Fig. 1.17., where *P* represents the pressure and *x* the distance. For this reason, when the shock wavelength is short with respect to the target thickness, it results in a rapid attenuation of the stress level.

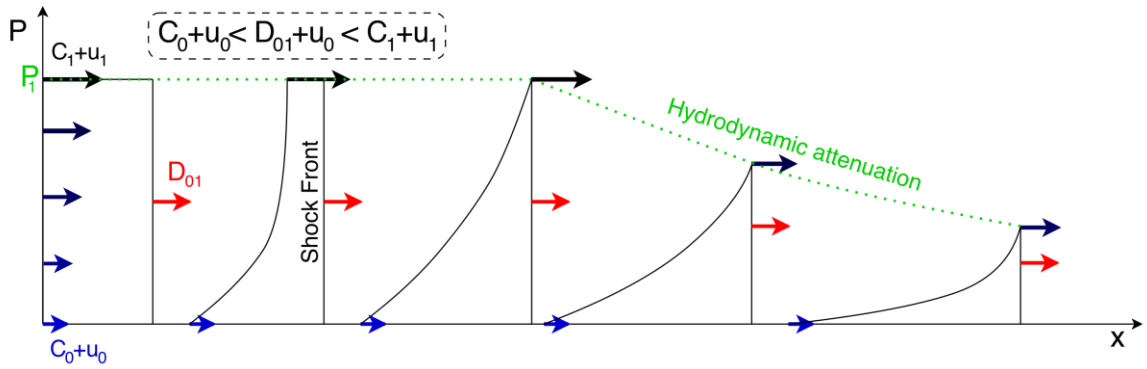

Fig. 1.17. Diagram of spatial pressure profiles of a shock wave subjected to hydrodynamic attenuation

The Hugoniot elastic limit (σ_{HEL}) is a fundamental dynamic material property of solid materials that characterizes the dynamic yield strength of the material [194]. It represents the highest stress level that a material can experience while still maintaining purely elastic behavior, meaning that it returns to its original shape once the shock is removed. Beyond the Hugoniot elastic limit, the material starts to undergo plastic deformation and permanent changes in its structure. As the hydrodynamic pressure increases during the shock application, it crosses the Hugoniot elastic limit σ_{HEL} and brings the material into permanent deformation. This behavior is manifested by the appearance of an elastic precursor.

The precursor is an elastic wave that travels faster than the main shock wave, with the longitudinal speed of sound C_L, and can provide valuable information about the material's behavior under extreme conditions. In essence, the elastic precursor is a distinctive feature of the initial stages of shock propagation, representing the rapid compression and subsequent elastic relaxation that occurs before the full impact of the shock wave is felt.

In the case of perfect elastoplastic behavior, this precursor results in a discontinuity in the rising front of the back-face velocity followed by a short plateau. In the case of viscoplastic behavior, the elastic precursor appears as a change in slope in the rising velocity front. The σ_{HEL} can be computed using equation (1.50), if the HEL material velocity is known. The HEL material velocity represents half of the back-face velocity at which the discontinuity in the rising front appears.

$$\sigma_{HEL} = \rho_0 D u_{HEL} \tag{1.50}$$

1.4.3 Tensile stress generation and velocity signal analysis for failure diagnosis

For simplicity reasons, the tensile stress and damage induced by a one-dimensional shock are explained for the case of a homogeneous target of finite thickness L, subjected to a loading of constant pressure P_1 for a period τ.

Fig. 1.18a illustrates the shockwave propagation in the time-position plane for the analytical representation of the phenomena and also the Pressure versus Particle velocity diagram (shock polar), in the case of no damage in the material. Initially in a resting state (0) with $P_0 = 0$, the material is then compressed from state (0) to state (1) at a given pressure P_1 by the incident shock front. When the pressure load is suddenly interrupted, a release wave (R_1) is generated, which relaxes the material to the initial state (0).

When the shockwave reaches the back-face, a free surface, it is reflected as a release wave (R_2) which propagates backward and brings the material to state (2) of $P_1 = 0$ but different than state (0), as it has a higher particle velocity, $u_2 = 2 \cdot u_1$. When the release wave (R_1) reaches the back-face, the free surface is decelerated.

Depending on the material properties (impedance, thickness, etc.), the two release waves can intersect inside the material thickness thus resulting in a state (3) with negative pressure. Considering the case of no attenuation, the negative pressure is equal to - P_1, thus it is correlated directly to the initial pressure load and therefore it is linked to the laser impact energy. The

crossing of these two waves can induce a local high tensile loading which could damage the material if the stress level exceeds the material damage threshold. From this point on, if the material is damaged, voids are created inside the material, adding an inner free surface that will affect wave propagation. Therefore, the two shockwaves propagate back and forth in the two separated sections of the material, as illustrated in Fig. 1.18b.

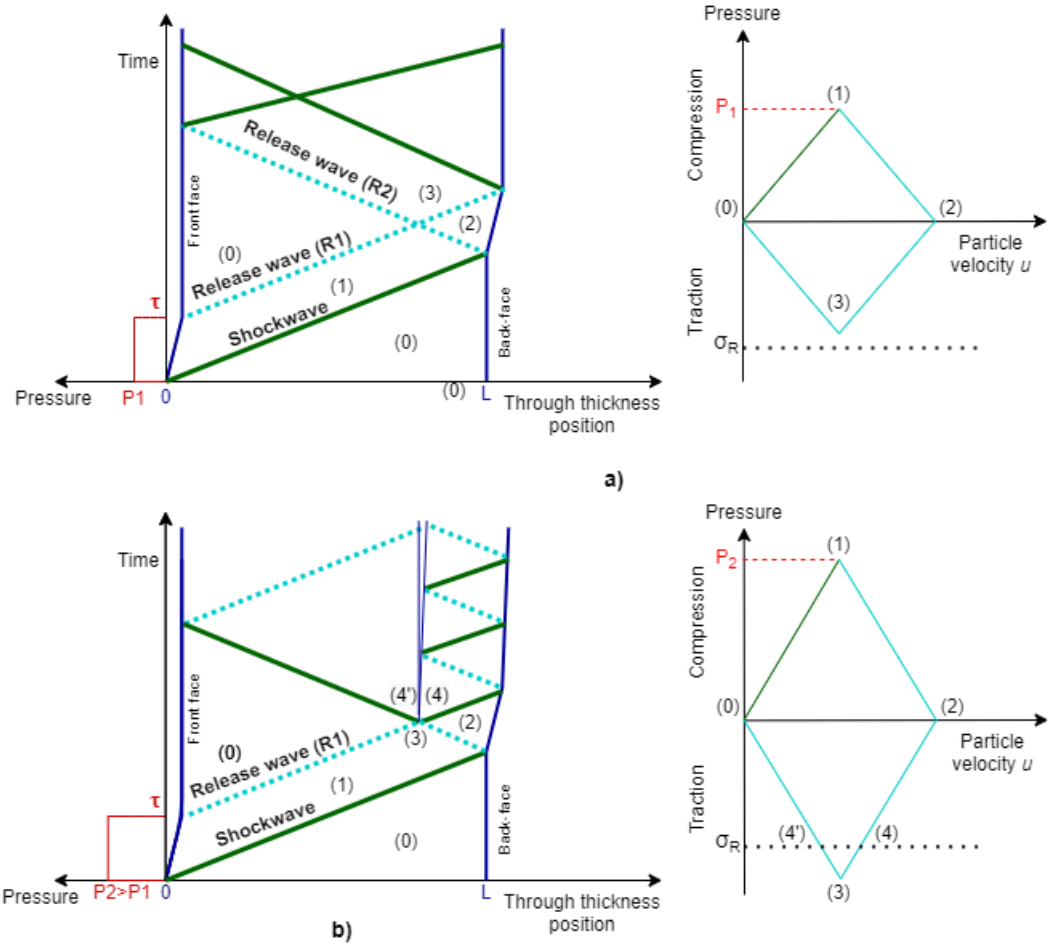

Fig. 1.18. Time-Position diagram of shockwave propagation through material thickness (left) and Pressure - Particle velocity diagram (right); a) no spall; b) spall

The two states -undamaged and damaged - illustrated in Fig. 1.18 can be highlighted without the need for damage inspection, with the use of back-face velocity measurement. The principle is very simple: each time the shockwave reaches the back face, a peak in the velocity measurement can be observed. An example is given in Fig. 1.19, where the back-face velocity measurement is illustrated in parallel with the Time-position diagram, for a better understanding of the correlation between the measurement and the shockwave propagation.

In the case of an undamaged sample, the two peaks exemplified in Fig. 1.19a represent the first and the second shock breakout. The time period $t_1 - t_3$ represents the shockwave back-and-forth propagation time. As it propagates, the shockwave attenuates, thus the second velocity peak is smaller in amplitude than the first one. This type of test and measurement can be used to determine the propagation speed of the shockwave. By knowing the sample thickness L and extracting the values of t_1 and t_3, the propagation speed can be calculated using equation (1.51).

$$C_L = \frac{2L}{t_3 - t_1} \tag{1.51}$$

In the second case, displayed in Fig. 1.19b, the tensile stress generated at the crossing of the release waves exceeds the strength of the material, and spallation of the material occurs. The wave that propagates in the spall has a much smaller period, therefore velocity peaks in the back-face velocity measurements are more frequent than in the case of no spall. This is the first

indication of a spall in the material. Moreover, the amplitude is smaller than the first peak and the velocity signal does not reach the 0 point before another peak appears. It oscillates around a mean velocity until the shockwave is attenuated. By using the spall signal, the thickness of the spall, L_{spall}, can be determined based on the propagation speed C_L and propagation time Δt between the first and second peak or the second and the third, if visible, by using equation (1.52).

$$L_{spall} = \frac{C_L \cdot \Delta t}{2} \tag{1.52}$$

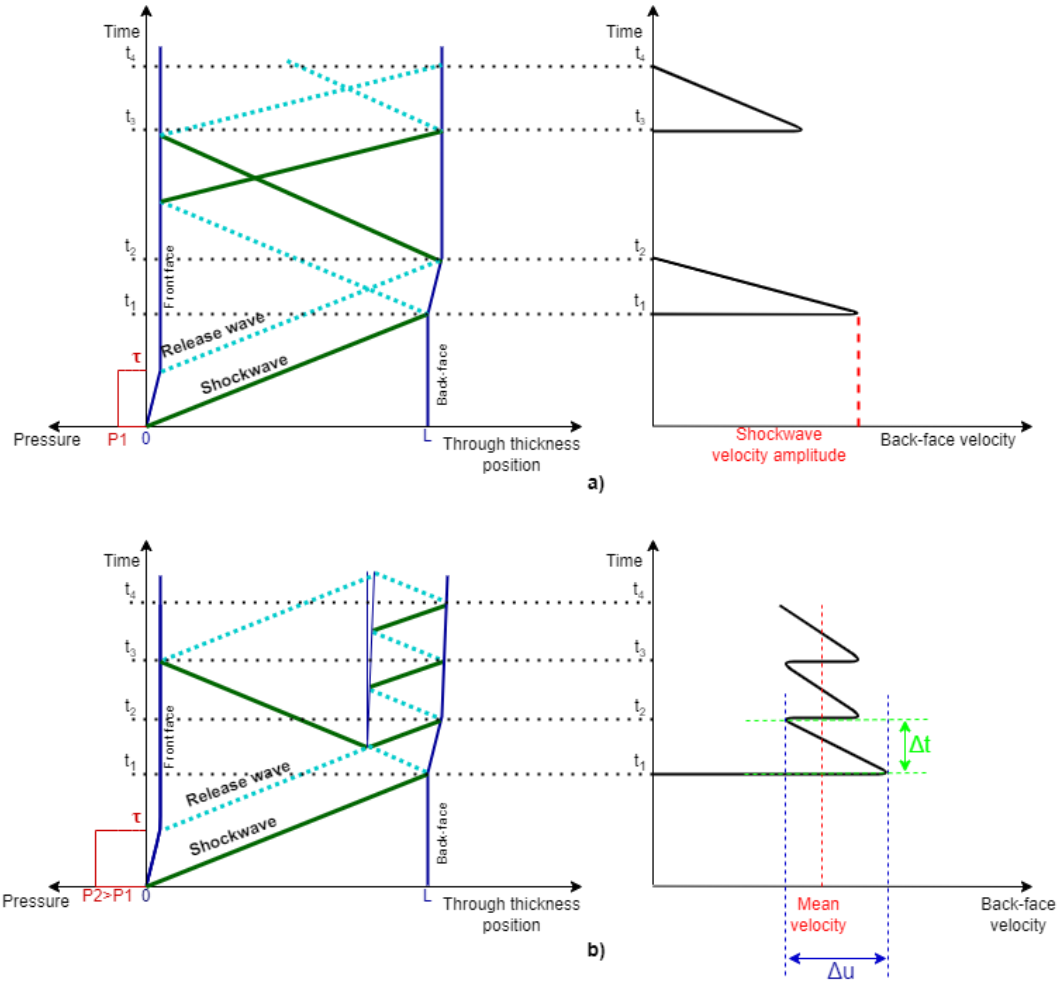

Fig. 1.19. Time-Position diagram of shockwave propagation through material thickness and corresponding back-face velocity measurement; a) no spall; b) spall

The dynamic tensile strength σ_{spall} can be evaluated within a homogenous material by equation (1.53), according to Novikov and Divnov [195], where ρ_0 – initial density of the material and C_0 – the sound velocity in the material and Δu represents the velocity pullback – the velocity gap measured between the maximum velocity of the first peak and the take-off point (the free-surface velocity just before the arrival of the spall pulse), illustrated in Fig. 1.19.

$$\sigma_{spall} = \frac{1}{2} C_0 \cdot \rho_0 \cdot \Delta u \tag{1.53}$$

This relation was extended for composite materials in [25], [172], [196] with the mention of a careful selection of velocity pullback, as for composite materials a small acceleration may appear after the first velocity peak due to a wave reflection in the outer epoxy layer.

The strain rate during delamination of the composite sample can also be estimated using the velocity pullback Δu [25], with the use of equation (1.54).

$$\dot{\varepsilon} = \frac{1}{2C_0} \cdot \frac{\Delta u}{\Delta t} \tag{1.54}$$

1.4.4 Back-face velocity measurement techniques

The measurement of the back-face velocity is of great interest for laser-induced shockwaves because it helps the understanding of the shockwave propagation through the material. It also offers information to be able to discriminate an unharmed sample from a spallation process during the shock experiment.

There are various methods of measurement based on the emission and reception of a laser beam. The most common methods are the Velocity Interferometer System for Any Reflector (VISAR)[197] and the Photon Doppler Velocimetry (PDV) [198].

The VISAR system is a time-resolved velocity measurement system that uses laser interferometry to measure the surface velocity of solids moving at high speeds. The VISAR measures the velocity of the moving surface by measuring the velocity-dependent phase change of laser light reflected from the surface. The reflectivity of the target is crucial for the proper functioning of the device and the measurement of displacement of the rear face is limited to one point [199].

Photonic Doppler velocimetry (PDV), also known as heterodyne velocimetry, is essentially a fiber-based Michelson interferometry and combines Doppler shifted light from a moving reflector with a reference source ($\lambda_0 \approx 1550$ nm), yielding a complete fringe when the reflector moves a distance $\lambda_0/2$. Therefore, the sample reflectivity influences the measurements. Unlike traditional displacement interferometry, which is impractical in most shock-wave experiments, PDV can be applied wherever VISAR is used [200]. The system is simpler to put in place because it is full fibered and requires lower powers than VISAR, but its temporal resolution depends on the sampling rate of the recording oscilloscope, which can make it expensive to compete against VISAR. The difficulty in using this technique stands in the post-processing of the data, which implies a frequency analysis of the recorded signal. Another disadvantage is the fact that the maximum measurable speed depends again on the sampling frequency of the oscilloscope associated with the measurement. Therefore, for high velocities experiments, the cost of the device increases.

1.4.5 Fiber-reinforced composites response under laser-induced shockwaves

In the early 1990s, Gilath et al. [201] studied the behavior of composite materials under laser shock and showed that the thickness of the unidirectional carbon/epoxy composite is linearly related to the incident threshold of delamination, in a monodimensional shock configuration, with a damage threshold of 1.5 kbar. A pressure decay as the shockwave passes through the target was reported.

The development of the LASAT technique also led to several studies of composite behavior under short and ultra-short shocks. Gay [202] studied the propagation of shockwaves between the different layers of a carbon fiber composite, in the through-thickness direction, and the resulting delamination. The dynamic strength between plies was evaluated at 292 MPa.

In the context of studying adhesive assemblies and detecting weak joints, Ecault [158] has shown a lot of interest in the behavior of composite materials under shocks in his thesis, both experimentally and through numerical simulations using LS-Dyna. The time-resolved experimental results were used to validate the numerical modeling of laser shock propagation in these materials, and parametric studies were performed, to evaluate the influences of pressure loading, interfaces, and anisotropic 2D effects, as well as elastic material parameters. Damage thresholds were established and the induced damage was investigated through microscopic and ultrasonic analysis.

Controlled delamination in carbon fiber composites using a symmetrical laser shock configuration was performed by Ghrib et al. [173] and laser-induced shockwave was also used as a delaminator for UHMWPE composites by Alil et al. [25]. In a more recent study, Scius-

Bertrand [203] used the LASAT technique for controlled delamination and disassembly of bonded composites. 3D woven and cross-ply composites were characterized and damage was assessed using various techniques such as X-ray micro-tomography, ultrasonics, and direct observations.

Besides classical fiber-reinforced composites, the effect of short dynamic loading on a woven hybrid basalt/carbon composite has been studied by Ferrante et al. [14] and concluded that the main damage type induced by laser impact is inter-ply delamination that follows the geometry of the woven.

Most numerical modelling of laser shock experiments on composite materials were validated only through the comparison of the computed free surface velocity and the measured one in the out-of-plane direction. This approach does not consider shock propagation along fibers and although it helps determining some mechanical characteristics, it is required to better understand shock propagation and consecutive damage in composite materials. Especially, recent studies focusing on the in-plane dynamic response of unidirectional carbon-fiber composites under laser-induced shockwaves are lacking.

SUMMARY

The first chapter of this thesis serves as a comprehensive review of the existing literature on composite materials, their hybridization and mechanical behavior, and offers a theoretical foundation on the key aspects related to characterizing fiber-reinforced composites under different loading conditions.

Among fiber-reinforced composites, those based on carbon fibers stand out as particularly suited for application in aerospace structures. While improved mechanical properties accompany higher-quality carbon fiber composites, they also come with elevated costs. To strike a balance between cost-effectiveness and technical proficiency, the concept of hybridization has gained considerable attention. Nonetheless, hybridizing with other fiber types may result in a notable loss of stiffness once the weaker component fails. Extensive research has investigated the effects of glass-carbon fiber hybridization on composite laminates, yet studies on all-carbon fiber hybrid composites remain limited. A recent innovation introduced the ply-level hybridization technique for all-carbon composites, involving the combination of prepregs with differing ply thicknesses to enhance the failure response of thin-ply composites. However, no research has thus far concentrated on ply-level hybridization of carbon-fiber composites using fibers of varied qualities.

In the context of aircraft structures, they often encounter impact loading at varying strain rates during service. Consequently, while assessing the properties of composite materials designed for aerospace purposes, an evaluation of their dynamic response becomes imperative alongside their quasi-static characteristics. Different dynamic loadings can lead to barely visible impact damage (BVID) within a structure, posing a risk as it might undermine the structural load-bearing capacity.

In this context, the laser-induced shockwave technique proves itself an appropriate and dependable approach to characterizing the dynamic behavior of composites under very high strain rates and pressures encountered in high-speed impact situations. Additionally, it allows for the assessment of the dynamic tensile strength of fiber-reinforced composites.

CHAPTER 2. TECHNICAL PERFORMANCES MEASUREMENTS OF THE MATERIALS

INTRODUCTION

The main objective of this chapter is to provide an as complete as possible description of the materials used in this study and to provide a thorough characterization of the properties and the internal structure of the ply-level hybrid carbon/epoxy unidirectional composites with 0° layup. Two different ply-stacking configurations are chosen for the hybrid configuration. Reference laminates are also manufactured from a single type of prepreg, with the purpose of providing a foundational benchmark against which the hybrid laminates could be compared. Furthermore, a comparison between the reference laminates is envisioned as well, intended to evaluate differences among laminates manufactured using high-quality carbon fiber and thinner ply prepregs, and those originating from prepregs with thicker plies, incorporating non-standardized carbon fibers.

Physical properties such as density, fiber weight, and volume fraction are measured, while the internal structure of the composites is observed microscopically to identify potential defects induced by hybridization and the manufacturing process. Furthermore, an estimation of the void content is conducted to validate the laminate quality in terms of void content. This assessment aims to determine whether the void content is sufficiently low to not impact the mechanical properties of the tested laminates.

The chapter follows this structure: the first section describes the composite material configurations used in this study, covering both reference and hybrid laminates. The second section outlines the experimental testing methods and data processing techniques. The third section presents the experimental results, followed by a concluding summary at the end of the chapter.

2.1 MATERIALS AND LAMINATE CONFIGURATIONS

Two types of unidirectional prepregs were used to manufacture the composite laminates, HSC-500-DT102S-40EF and UTS-150-DT120-32F, which will further be referred to as HSC and UTS prepregs, based on the name of their carbon fiber type. Both prepregs are produced by Delta-Preg® (Sant'Egidio alla Vibrata, Italy). The properties of the prepregs, detailed in Table 2.1, are taken from the manufacturer's datasheet.

The UTS fiber is produced by Teijin Tenax® (Tokyo, Japan) and has a longitudinal modulus of 245 GPa and a strength of 5100 MPa. The elongation at break is 2.1 % and the density is 1.78 g/cm^3. The HSC fiber is not standardized; therefore, the properties are only approximate. The longitudinal modulus is ≥ 230 GPa and the strength is ≥ 3800 MPa. The elongation at break is between 1.6% and 2.1%, and the density is not specified. The thermosetting epoxy matrix systems are both from Delta-Tech® (Altopascio, Italy), have a medium temperature curing, and are compatible to be cured together. DT102S is a thermosetting epoxy while DT120 is a toughened thermosetting epoxy with high impact strength.

The key distinction between the two prepregs lies in the fibers' quality: the UTS prepreg has a standardized fiber, with well-known mechanical properties, while for the HSC prepreg, the fiber is not standardized, therefore only the minimum potential values of its mechanical

properties are given by the manufacturer. This also implies a different cost/areal weight of the prepregs, with a cost/areal weight ratio of 1.6 for the UTS prepreg compared to the HSC one. Moreover, HSC prepreg has a dry fiber area weight of 500 g/m^2 and an estimated ply thickness of 0.560 mm while UTS prepreg has a much lower dry fiber areal weight, of 150 g/m^2 and an estimated ply thickness of 0.140 mm.

Table 2.1. Prepreg properties

Name	HSC-500-DT102S-40 EF (HSC)	UTS-150-DT120-32 F (UTS)
Fiber Name	High-strength carbon (HSC)[a)]	UTS50 F13
Fiber diameter	Not specified	7μm
Resin Name	DT102S	DT120
Dry fiber areal weight	500±20 g/m^2	150±5 g/m^2
Resin content [% by weight]	40±3 %	32±3 %
Laminate thickness	~0.560 mm	~0.140 mm

[a)] Not a standardized fiber

To achieve ply-level hybridization in both ply thickness and material type, for an unsymmetric, thinner laminate denoted as H1 material, a stacking sequence of 2HSC+1UTS+1HSC+1UTS [0°] was employed. For a symmetric, thicker laminate referred to as H2 material, a stacking sequence of 1HSC+1UTS+2HSC+1UTS+1HSC [0°] was adopted. The stacking sequence of the hybrid laminates was initially determined, and based on the estimated areal weight provided by the prepregs' data, the number of plies for the UTS type laminates was chosen to match the areal mass and laminate thickness of H1 and H2 samples as closely as possible. Consequently, laminates consisting of 13 and 17 UTS plies were manufactured and labeled as UTS13 and UTS17, respectively. As the HSC prepreg has thick plies and a high areal mass, the laminates were manufactured by using the number of HSC plies within each type of hybrid laminate, to assess if there is a difference in the mechanical behavior by just adding two additional UTS plies. The HSC laminates were constructed with 3 and 4 plies and will be referred to as HSC3 and HSC4, respectively.

Table 2.2. Laminate details

Laminate	Type of plies	Stacking sequence	Areal mass (estimated) [g/m^2]	Areal mass (measured) [g/m^2]	Laminate thickness [mm]
HSC3	Thick plies	HSC $[0°]_3$	2499±162	2465±41	1.69±0.02
HSC4	Thick plies	HSC $[0°]_4$	3332±216	3346±41	2.24±0.03
UTS13	Standard plies	UTS $[0°]_{13}$	2860±169	3046±41	2.10±0.05
UTS17	Standard plies	UTS $[0°]_{17}$	3740±221	4033±41	2.70±0.04
H1	Thick & Standard plies	2HSC+1UTS+1HSC+ 1UTS[0°]	2939±164	3250±41	2.19±0.03
H2	Thick & Standard plies	1HSC+1UTS+2HSC+ 1UTS+1HSC [0°]	3772±218	4080±41	2.7±0.01

The six different laminate configurations are illustrated in Fig. 2.1 and they are also described in Table 2.2, with their stacking sequence, estimated and measured areal mass, and average laminate thickness. The thickness of the laminate plate varies slightly, thus individual measurements are performed for each sample of the experimental testing campaigns. Uncertainties for the estimated areal mass are due to the tolerances given by the prepreg manufacturer for the prepreg dry areal mass and resin weight fraction. For the measured areal

mass uncertainties are given by the measuring equipment. The laminate thickness was measured for several samples of each material and the uncertainties are half the range between the maximum and minimum value. All laminate panels were cured in an autoclave, according to the prepreg manufacturer's specifications, and the laminate manufacturing was carried out by Belcoavia S.R.L (Livezile, Romania).

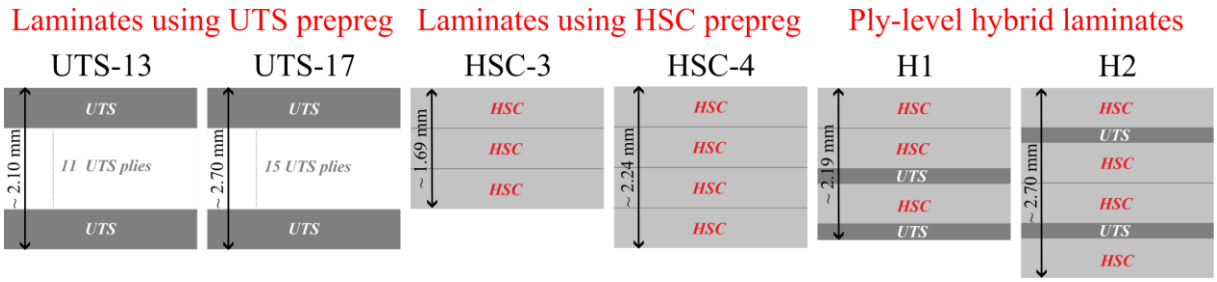

Fig. 2.1. Illustration of the stacking sequence of the manufactured laminates

2.2 EXPERIMENTAL METHODS AND DATA ANALYSIS

2.2.1 Density measurements

The density of the composite samples was measured using two approaches: a method using a laboratory scale and Archimedes' principle, and another using the mass and volume measurements of the samples. Small rectangular specimens were used, with an approximate dimension of 5 mm × 8 mm for H1 and H2 hybrid materials and 9 mm × 9 mm for the reference HSC and UTS laminates. Five samples were used for each laminate configuration.

The dimensions of the samples were measured using a micrometer resolution caliper with ±1 µm accuracy and the mass using a Precisa XT220A laboratory scale with weighing accuracy given at $\pm 10^{-5}$ g, at ENSTA Bretagne. For the density measurement using Archimedes' principle, the same Precisa XT220A laboratory scale was used, equipped with the density measurement kit using a double beaker configuration and distilled water at room temperature (~20ºC). From the methods exposed in the user manual, the mode "SOLID IN AIR" was selected. The setup of the scale with the double beaker is illustrated in Fig. 2.2a. A thermometer was used to monitor the water's temperature as it can cause density calculation errors when the ambient temperature is not accurate. Therefore, before starting the measurements, the temperature of the liquid was read and the scale was calibrated to modify the density of the water according to its temperature. The method involves two steps. The first step is to determine the mass of the solid in air, M_a. For this, the solid is placed in the top beaker, Fig. 2.2b. The second step involves the determination of the mass of the solid in water, M_w. For this, the solid is carefully placed in the bottom beaker, Fig. 2.2c. As soon as the reading is stable, it is saved. The scale displays the density of the material afterward. The density is calculated based on Archimedes' principle, using equation (2.1).

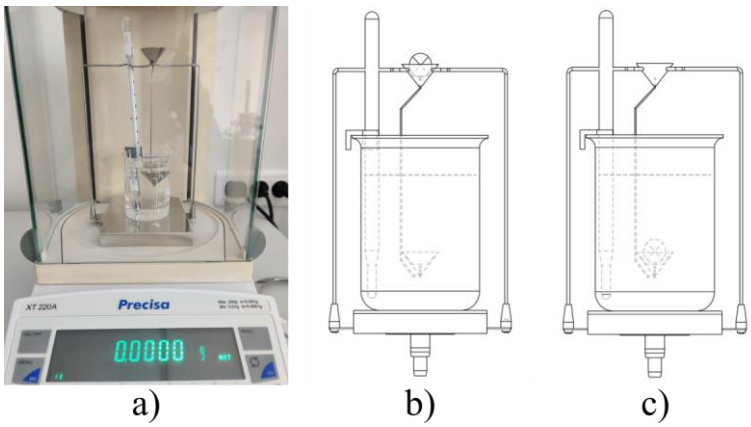

Fig. 2.2. a) Density measurement setup; b) sample in upper beaker; c) sample in the bottom beaker

$$\rho = \frac{M_a}{M_a - M_w} \cdot \rho_w \tag{2.1}$$

After analyzing the results of each method's distribution, a density value will be chosen for each composite. This selected value will be utilized in any future essential calculations. Moreover, a theoretical density is estimated using equation (2.2) [204]. As the precise density of the cured resins is not provided by the manufacturer, a theoretical density is computed by considering a range for the density of epoxy resins. This range is derived from the available datasheets related to epoxy resins. Since HSC carbon fibers are not standardized, there is no data available for their density. Discussions with the manufacturer of the prepregs implied that HSC fibers are similar to STS carbon fibers manufactured by Tenax®, which have the same density as UTS carbon fibers. Therefore, an interval for the theoretical density is calculated using an interval for the matrix density ρ_m = [1.15; 1.22] g/cm^3, the density of the UTS carbon fibers ρ_f = 1.78 g/cm^3 and an interval W_f = [60; 68] % for the fiber weight fraction, taken from the HSC and UTS prepreg data. It is expected that the fiber weight fraction for the hybrid configurations to be in this interval. The calculated theoretical density interval for the composite is ρ_{cTH} = [1.460; 1.552] g/cm^3.

$$\rho_{c\,TH} = \frac{1}{\frac{W_f}{\rho_f} + \frac{W_m}{\rho_m}} \tag{2.2}$$

2.2.2 Fiber weight fraction and fiber volume fraction

Although the burn-off method is more commonly used for the estimation of fiber volume fraction of glass-fiber composite materials [205]–[207], it has also been used by Francis et al. [208] for carbon fiber composites, and McDonough et al. also described a procedure to use the burn-off method for hybrid glass/carbon fiber composites as well [46].

ASTM D3171 – 15 standard [209] describes several procedures used to determine the constituent content of composite materials, including the calculation process. The guidelines of the burn-off procedure (Procedure G) [209] described in the standard were followed to determine the fiber content in the studied carbon fiber laminates because it was considered safer than the acid digestion procedure. As the small samples used for the density measurement were dried and used afterward in the burn-off test, their mass was smaller than the one proposed in the standard. Five samples were used for each laminate configuration.

The composite samples were weighed before burn-off and after, to determine the initial mass M_i and the final mass of the fibers M_f. For the test, each sample was put in a Duran glass container in a muffle furnace, at 400°C for 3h-5h, depending on the laminate type.

The temperature was selected to keep the carbon fibers undamaged and to also be in the recommended temperature range of the glass container. McDonough et al. [46] performed thermo-gravimetric analysis on carbon fibers and observed that at 600°C, there was a mass loss of around 0.04 mass fraction after 60 min, which indicated that part of the fibers was burnt as well. The analysis at 500°C showed only a slight decrease in mass at the beginning, which was attributed to moisture removal. Francis et al. [208] used a 450°C temperature for resin burn-off of carbon fiber composites. Therefore, it was concluded that a temperature of 400°C should not damage the carbon fibers. It was also in the range of operating temperatures for the glass container.

An initial test was performed to determine the duration of the burn-off procedure. An H1 sample, similar in size to the one used for the analysis, was put in the furnace at 400°C for 1 hour. Afterward, it was taken out, cooled, and weighed. The sample was put for another hour in the furnace at the same temperature. After the second burn-off step, it was weighed again and the mass was compared with the mass after 1 hour burn-off. Only a slight decrease in mass was observed. After an additional hour, the remaining fibers were flexible and broke apart from each other. No fiber matrix bonding was observed by microscopic observation, concluding that all

the resin burnt. Therefore, we concluded that 3 hours should be enough to burn the resin entirely. For HSC3 and UTS17, the time was increased to 4 hours. For HSC4, it was increased to 5 hours, as it was observed that some bonding between the fibers remained after only 3 hours of burn-off.

Equation (2.3) can be employed to calculate the fiber weight fraction, while equation (2.4) can determine the volume fraction provided the densities of both the fibers and the composite are known. In this case, the density of the composite is taken from the density measurements performed before burn-off. The carbon fiber density is approximated at ρ_f = 1.78 g/cm^3 from the manufacturer's data for UTS fibers and other fibers similar to HSC fibers.

$$wf[\%] = \frac{M_f}{M_i} \cdot 100 \tag{2.3}$$

$$V_f[\%] = \frac{M_f}{M_i} \cdot 100 \cdot \frac{\rho_{comp}}{\rho_f} \tag{2.4}$$

2.2.3 2D Microscopic Observations

For microscopic observations of the structure of the laminates, rectangular samples with a length of 25 mm were cut from different regions of the composite plates. A minimum of 4 samples were used for each laminate configuration.

The composite cross-section observations were performed using a Keyence VHX-5000 series digital microscope at ENSTA Bretagne. The samples must be prepared and thoroughly polished to have a clean image without scratches. First, the sample was fixed in a mold and embedded in cold-curing resin. Depending on the availability at the time of the observations, different cold-cure resin systems were used, as they do not affect the quality of the polishing/observations. The most often used was the KM-U Acrylic resin kit from Presi®. After the resin was cured, the samples were polished using a LaboPol-30® and LaboForce-100® polishing system from Struers®. The polishing method is detailed in APPENDIX A.

The microscope can be used with two types of lighting: annular and coaxial. Under the annular lighting of the microscope, the fibers are lighter, and the resin is dark and black. Unfortunately, under this type of light, voids are illustrated in black as well. Therefore, it is problematic to distinguish between resin pockets and voids within the cross-section. Under coaxial light, fibers are visualized as white, resin as light grey, and voids as black, as illustrated in Fig. 2.3. Both annular and coaxial lighting types were used during observations, depending on which gave better results for the observed samples. Voids were analyzed using coaxial lighting, to avoid mistaking them for resin pockets and vice versa.

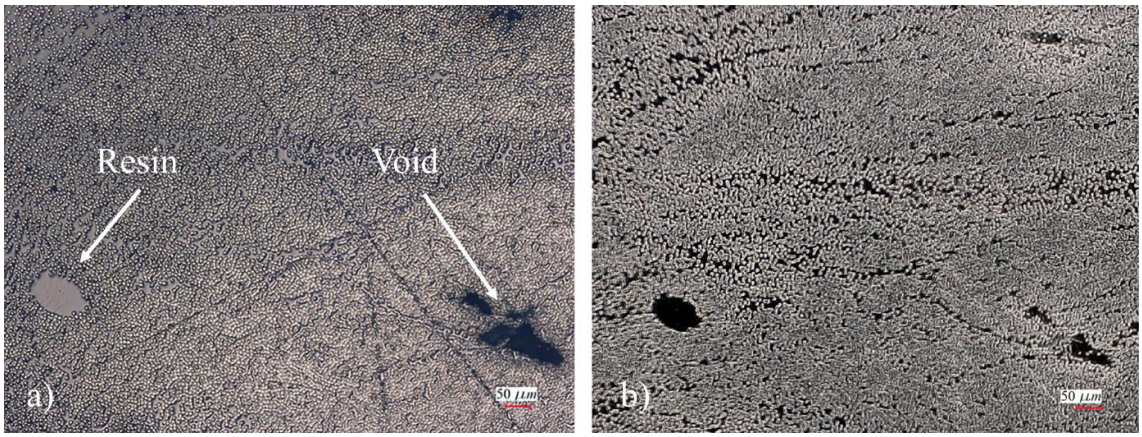

Fig. 2.3. Observation of resin pocket and void in a sample under a) coaxial light; b) annular light

2.2.4 Void content estimation

Voids in composite materials are considered one of the most harmful manufacturing defects, as an increased percentage of voids can affect the mechanical properties of the fiber-reinforced material.

Purslow [210] proposed a chart for estimating the quality and performance of a composite containing a certain void content level (V_v). The chart, shown in Table 2.3, illustrates that just a few fractions of a percentage increase in void content can lead to a significant drop in the quality of the composite.

Table 2.3. Purslow's composite quality chart based on void volume content V_v [210].

Grade name	Void content	Quality
Grade A	V_v<0.2%	Excellent
Grade B	0.2%<V_v<0.5%	Very good
Grade C	0.5<V_v<1%	Good
Grade D	1%<V_v<2%	Fair
Grade E	2%<V_v<5%	Poor
Grade F	V_v>5%	Very poor

Saenz-Castillo et al. [211] showed that critical void content values beyond which in-plane shear strength and in-plane shear modulus started to decrease were in the range of 1.2–2.7%, depending on the manufacturing process. Liu et al. [212] studied the effect of the cure cycle and void content on the mechanical properties of carbon fiber-reinforced composites, concluding that both the strengths and moduli decrease with increasing void content with a different drop-off rate. For an increase in void content from 0.6 to 3.2%, the interlaminar shear strength has a drop-off of 18%, the flexural strength falls by 22% while the tensile strength has a decrease of 14%. For the tensile modulus, it was concluded that it is insensitive to void content, as it had little decrease in value.

Other studies [213]–[215] also showed that an increased void content could affect the mechanical properties of the composites. Therefore, it is meaningful to investigate the void content of the studied composites to assess the quality of the composite and a possible decrease in mechanical properties due to the manufacturing process. The use of Purslow's quality criteria is then fully justified, in our opinion.

There are several methods by which the void content can be assessed. ASTM D2734 Standard Test Methods for Void Content of Reinforced Plastics [216] describes a method of evaluating the void content by comparing the theoretical density of the composite and constituents with the actual densities measured by various methods. It requires precise knowledge of the densities of both matrix and fibers, which, in the case of prepregs, is not always provided by the manufacturer of the resin system. Moreover, for low void contents, uncertainties induced by the assumption that the density of the resin is the same in the composite as it is in large cast mass get progressively more important. It could lower the void content from a real 0.2% to a calculated 0.1%. This method also gives information only on void content, without knowing void position – either interply or intraply, or void dimension and shapes.

Another used method is 2D digital microscopy and image processing [217]. 2D microscopy is limited to a cross-section of each coupon, therefore, involving an inherent bias error. However, microscopy can offer qualitative and quantitative information regarding the size, location, and morphology of voids or other defects [211]. In this 2D approach, the void content is estimated as an area fraction of the entire face of the sample. Regarding calculating void content, various types of image analysis methods are available. The "optical counting technique", described by Purslow [210], uses a statistical approach to estimate void content quickly. After applying a regular square grid pattern over the micrograph image, the void

content can be estimated by counting the fraction of the squares whose centers lie over a void. That fraction should equal the void content. Another method that should be more accurate and can be easily used due to image processing software is the "area fraction" method. It calculates the void content by determining the area fraction of the micrograph consisting of voids [211], [217].

Because prepregs and autoclave curing were used in the manufacturing process, a low void content is expected. Therefore, for better accuracy and the ability to investigate the position and shape of voids within the composites, 2D digital microscopy and image processing will be employed. For this, microscopic images of the samples under coaxial light were saved and further processed using ImageJ software [218].

In Fig. 2.4, the image treatments performed with ImageJ are presented. The image is transformed into greyscale, and a grey threshold is applied to select the black areas that denote the voids. Each void is covered in a red color, the threshold is applied, and a black-and-white image is obtained. By analyzing the ratio of black pixels over white ones, the software calculates the percentage area occupied by pores in the full image. The images were processed without scales, to not influence the analysis and the scale was added afterward.

The cross-section views from the microscopic observations were used for void content assessment. Therefore, a minimum of 4 samples were used for laminates that showed less variability in void content and up to 7 samples for UTS13 and UTS17, with high variability in data.

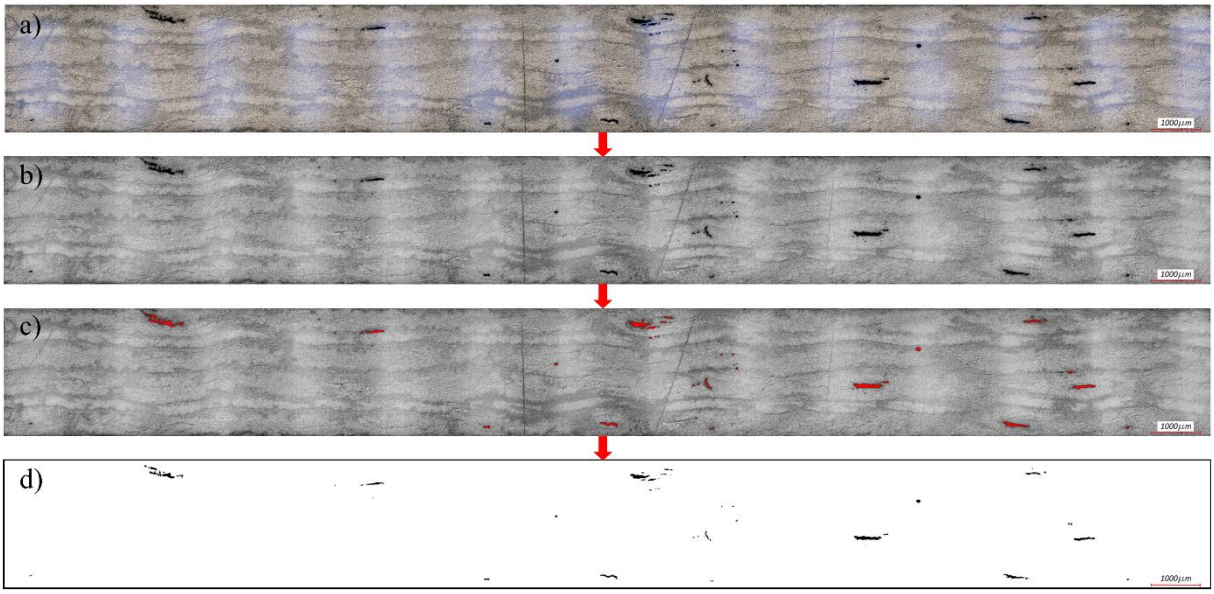

Fig. 2.4. A sequence of images showing the process of thresholding; a) Micrograph of the sample without image treatment; b) Greyscale image of micrograph; c) Selection of threshold level to separate voids from the background; d) Thresholded binary image with an estimated void content of 0.294%

2.3 EXPERIMENTAL RESULTS AND DISCUSSION

2.3.1 Density measurements

The average density measurements from both measuring approaches are presented in Table 2.4 and Fig. 2.5, with the error bars representing uncertainty in a measurement (half the range of the measured values). Different values of the density were obtained for the same samples using the two methods. The mass and volume method has a higher variability in data, with a higher error bar compared to Archimedes' principle method. Moreover, not all the density values from the mass and volume method are within the interval of the expected theoretical density, which also indicates faults in the method. The main cause of the higher error for the mass and volume method is considered to be the fact that due to the cutting process and the small dimensions of the samples, the edges are not perfectly straight and parallel, which induces

an error in sample geometry measurements, therefore affecting the volume calculation. Thus, the density measurements by Archimedes' principle were considered more reliable and were used in further calculations in which the density of the laminates was needed.

By Archimedes' principle, the tested laminates have similar densities, within the interval [1.478; 1.499] g/cm^3, being in the range of the theoretical density interval. A maximum difference of 1.42% was found between the densities of H1 and H2, which are the lowest and respectively the highest ones.

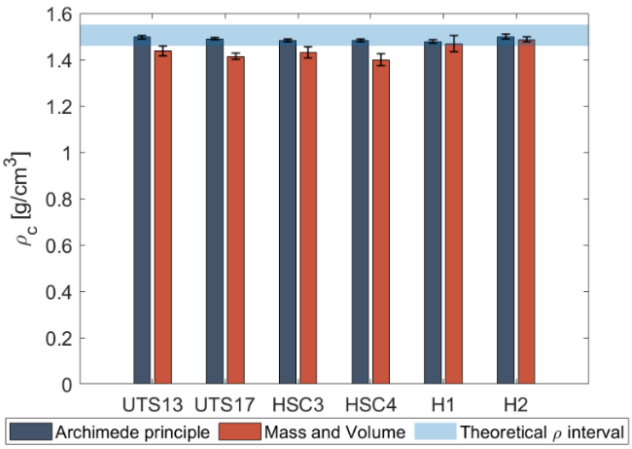

Fig. 2.5. Averaged measured densities for all laminates

Table 2.4. Averaged measured densities using mass and volume measurements and Archimedes' principle

Material	UTS13	UTS17	HSC3	HSC4	H1	H2
Archimedes principle	1.497 ± 0.009	1.490 ± 0.004	1.483 ± 0.005	1.483 ± 0.005	1.478 ± 0.007	1.499 ± 0.011
Mass & Volume measurements	1.438 ± 0.022	1.415 ± 0.014	1.432 ± 0.024	1.400 ± 0.025	1.470 ± 0.034	1.487 ± 0.011

2.3.2 Fiber weight and volume fraction

After the burn-off procedure, the rectangular samples preserved their shape until they were manually manipulated. The fibers broke apart with ease from each other and were flexible. Fig. 2.6a shows an example of a sample after burn-off while Fig. 2.6b shows a microscope image of the carbon fibers after burn-off. No matrix residue was identified for the observed fibers and the diameter of the fibers was measured randomly. No difference compared to the nominal diameter of the carbon fibers was identified. Table 2.5 summarizes the results of the burn-off tests and presents the average fiber weight and volume fraction for each laminate configuration, with the corresponding standard deviation and coefficient of variation (CV). The coefficient of variation is calculated as the ratio between the standard deviation and the mean value, and shows the relative dispersion of measurements around the average value. The average fiber weight fraction for all laminates is in the interval W_f = [59; 65]%, with HSC laminates having the lowest fiber weight fraction and UTS laminates the highest one, as expected from the prepreg datasheet. In Fig. 2.7a, the average measured values, with half the measurement range represented as error bars, are compared with the expected values from the prepreg datasheet. Except for the UTS prepregs, which have a lower fiber weight fraction than the expected value, suggesting an insufficient resin removal during the manufacturing process, for all other laminates, the expected values are within the uncertainties of the measured ones.

The hybrid laminates H1 and H2 have in-between values compared to HSC and UTS laminates, with H2 laminate having a fiber weight fraction higher than H1 by 2%. By analyzing Fig. 2.7a, it can be observed that H2 laminate has a higher average fiber weight fraction

compared to the expected value calculated from the prepreg datasheet, while H1 laminate has a lower fiber weight fraction compared to the expected one. Moreover, by analyzing the coefficient of variation in Table 2.5, it can be observed that H1 has a higher variability in measured data compared to H2 laminate. This suggests that both the manufacturing process and variability in measured data had an influence on the reversal of the order of the average fiber weight fraction of the hybrid laminates compared to the expected value.

Regarding the fiber volume fraction, the measured values for all laminates are within the interval V_f = [49; 54]%, having the same order as for the fiber weight fraction. Fig. 2.7b shows that by relating the density of the composites to their corresponding fiber volume fraction, the values are within the theoretically established interval.

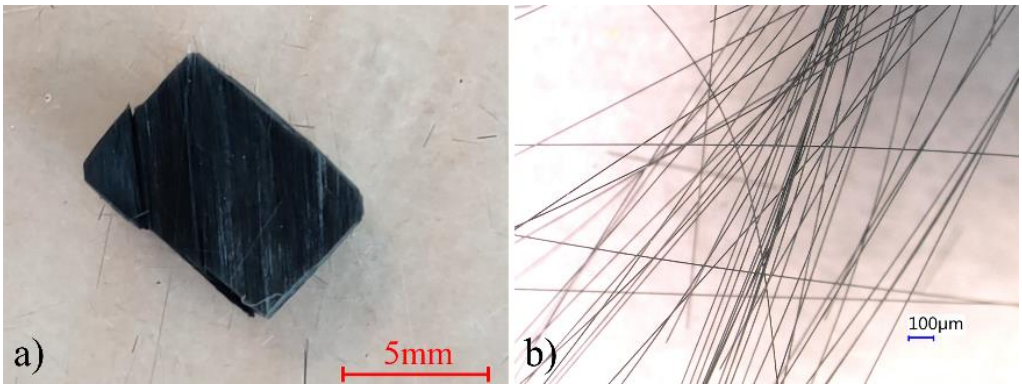

Fig. 2.6. Example of a sample after the burn-off procedure; a) entire sample; b) microscopic view of carbon fibers after burn-off

Table 2.5. Fiber weight and volume fraction results from the burn-off method

Material	UTS13	UTS17	HSC3	HSC4	H1	H2
Average Fiber Weight fraction [%]	64.76	64.08	59.83	59.19	60.6	61.83
Standard deviation [%]	0.76	0.51	1.33	0.57	0.89	0.41
Coefficient of variation [%]	1.17	0.80	2.23	0.97	1.47	0.67
Average Fiber Volume fraction [%]	54.46	53.67	49.84	49.31	50.32	52.14
Standard deviation [%]	0.71	0.48	1.26	0.49	0.87	0.52
Coefficient of variation [%]	1.31	0.91	2.53	0.99	1.73	1

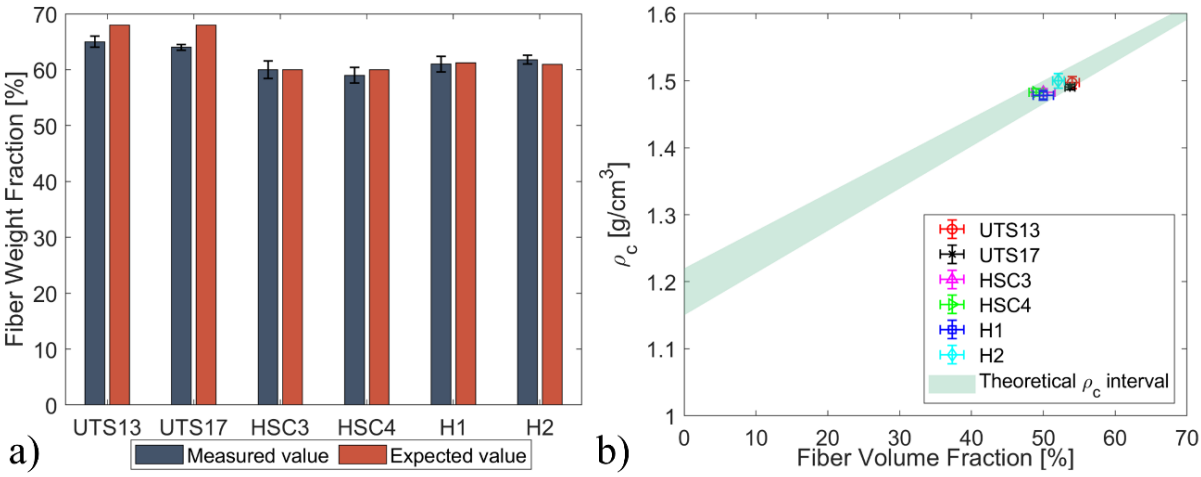

Fig. 2.7. a) Measured fiber weight fractions of manufactured composites and expected values based on prepreg datasheet; b) Density of the manufactured composites with respect to the fiber volume fraction (Archimedes principle method)

2.3.3 Microscopic observation

2.3.3.1 Microscopic observations on HSC laminates

Multiple observations were made on samples from both HSC3 and HSC4 laminates, and only a representative of each will be presented, with observations being valid for all samples. Fig. 2.8a and Fig. 2.9a show the assembly of microscopic images of an entire HSC3 sample and HSC4 sample respectively, with a close-up sample segment in Fig. 2.8b and Fig. 2.9b, for easier identification of the stacking sequence and defects. The thick HSC plies can be easily identified due to the resin-rich area at the interface between the plies. Moreover, ply waviness was observed in all HSC samples, with ply thickness variation. From multiple measurements in random positions, the HSC ply thickness varies between 510-600 µm, compared to the expected thickness from the prepreg datasheet, of 560 µm. Both intraply and interply voids were observed within the laminates, having an almost circular shape, with dimensions ranging from 71-521 µm for the observed samples.

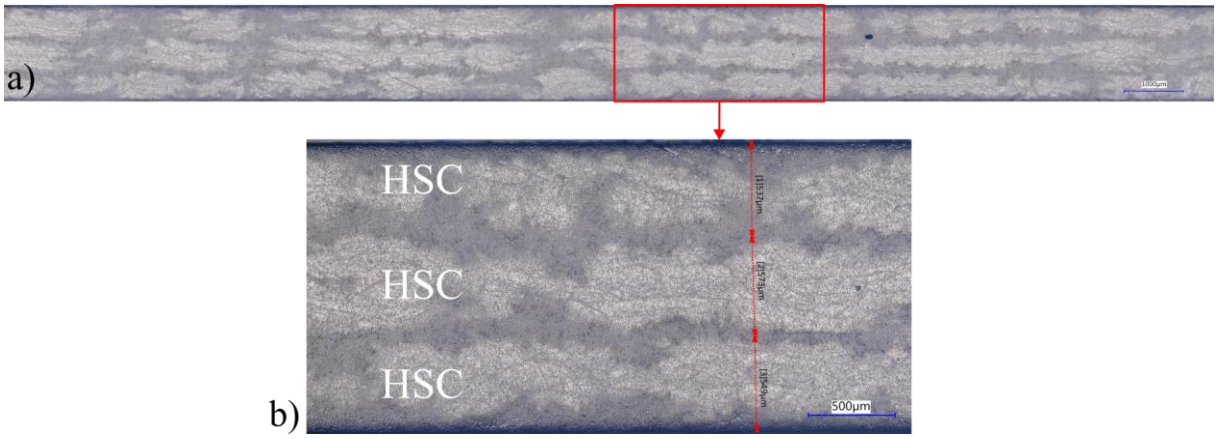

Fig. 2.8. Microscopic observation of HSC3 sample under coaxial lighting; a) view of entire sample; b) close-up view of the highlighted region with plies stacking sequence and thickness measurements

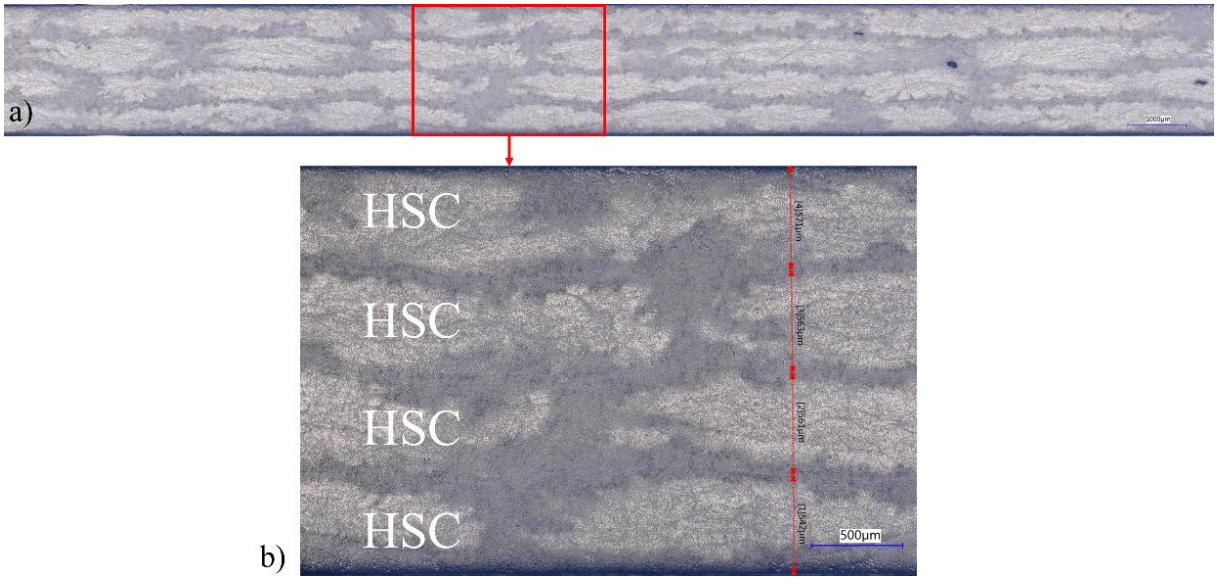

Fig. 2.9. Microscopic observation of HSC4 sample under coaxial lighting; a) view of entire sample; b) close-up view of the highlighted region with plies stacking sequence and thickness measurements

Regions of resin-rich areas and ply-mixing were also observed, which are more easily identified in Fig. 2.9b. In these regions, a localized low fiber volume fraction was observed. By performing image processing of such an area with the method described for void content estimation, a fiber volume fraction as low as 22% was obtained. The observed region and the

binary image, with fibers in black and resin in white, are depicted in Fig. 2.10. The scale was added after the image processing, to not influence the results.

The HSC carbon fiber diameter, as measured from the cross-section view, was found to be 7 µm, which is identical to the diameter of the UTS carbon fibers.

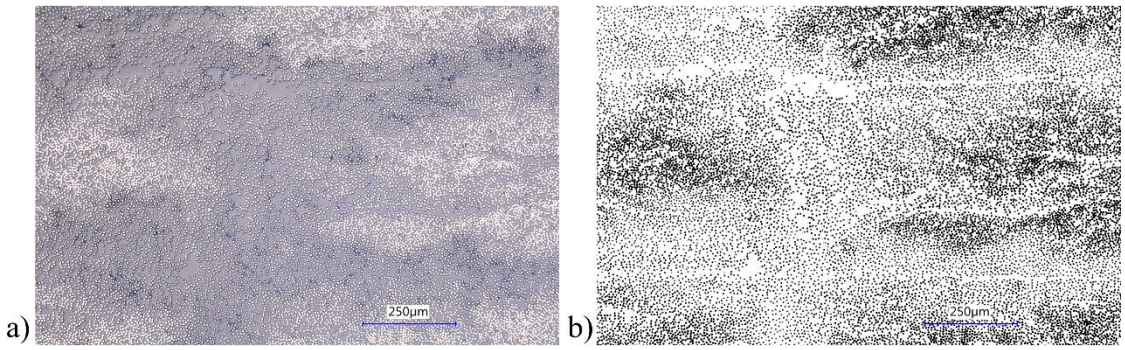

Fig. 2.10. An estimated fiber volume fraction of 22% from of a resin-rich region with ply-mixing inside an HSC4 laminate using image processing with ImageJ; a) original microscopic observation of the region; b) binary image with fibers as black and resin as white

2.3.3.2 Microscopic observations on UTS laminates

For UTS laminates, representative samples are illustrated in Fig. 2.11 for UTS13 and in Fig. 2.12 for UTS17. In both UTS laminates, the plies can still be identified, but it is not as straightforward as in HSC laminates. This is because there is no distinct resin-rich area at the interface to help with easy identification. Having thinner, more compact plies, less ply waviness was observed for UTS laminates compared to HSC laminates. Still, the ply thickness varies within the laminates, ranging from 130 µm to178 µm compared to an expected ply thickness of 140 µm. Moreover, the fiber distribution is more uniform and no regions of localized low fiber volume fraction were observed.

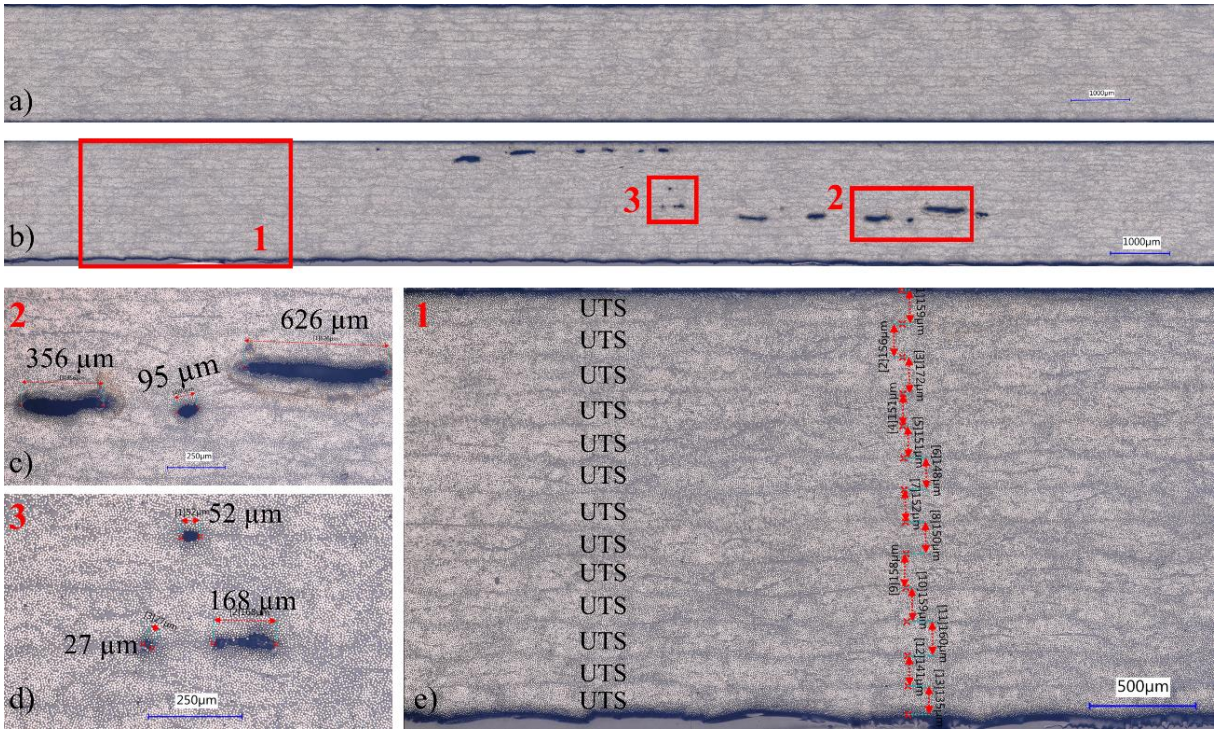

Fig. 2.11. Microscopic views of UTS13 samples under coaxial lighting; a) assembly for UTS sample free of voids; b) assembly view of UTS sample with multiple interply voids; c) close-up view of region 2 with voids dimensions measurements; d) close-up view of region 3 with voids dimensions measurements; e) close-up view of region 1 with plies stacking sequence and thickness measurements

In Fig. 2.11a, a UTS13 sample free of voids is presented while in Fig. 2.11b, a sample with multiple interply voids is shown. For UTS17, a sample with only a few small interply voids is depicted in Fig. 2.12a. When comparing UTS laminates to HSC laminates, it is observed that UTS laminates contain more interply voids, rather than intraply voids. This difference is likely a result of having a greater number of plies in the UTS laminates. Furthermore, the larger voids exhibit an elongated shape, while the smaller ones tend to be more circular, with specific dimensions (length or diameter) between 27 µm and 1460 µm.

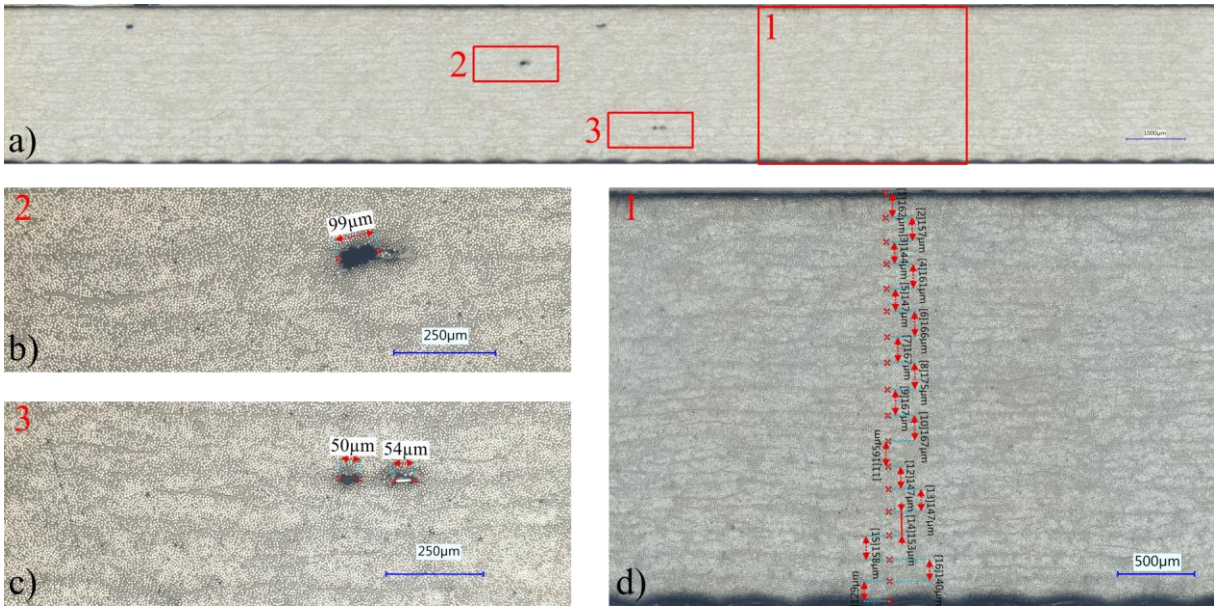

Fig. 2.12. Microscopic views of UTS17 samples under coaxial lighting; a) assembly for UTS17 sample; b) close-up view of region 2 with measurement of void; c) close-up view of region 3 with measurements of voids dimensions; d) close-up view of region 1 with ply thickness measurements

2.3.3.3 Microscopic views on H1 and H2 sample

By analyzing the microstructure of the two types of plies within the H1 composite laminate, a significant difference in the degree of heterogeneity between thick and thin plies was observed for all samples. While the UTS plies exhibit very few resin-rich regions, thus having a more even distribution of the fibers and a uniform distributed microstructure, the HSC plies have significantly more in-ply resin-rich regions, including resin pockets and small voids. Similar observations were made by Amacher et al. [61] when comparing microstructures of laminates made from plies of different thicknesses. Moreover, more resin-rich regions were observed at the interface between two HSC plies than at the interface between HSC and UTS plies.

While the overall thickness of the sample is mainly preserved, with only slight differences, it was observed that all the samples show ply waviness. It is considered to appear due to the thicker prepregs used [61]. Also, HSC laminates showed increased ply waviness compared to UTS laminates. Moreover, the waviness at the interface between the two adjacent HSC plies is more severe when compared to the waviness of the HSC ply placed between the UTS plies.

Fig. 2.13 illustrates the microscopic observations of an H1 sample under annular lighting. At the time of the observations, this type of lighting offered a better fiber/matrix contrast compared to the coaxial one. The stained, darker areas that can be seen in most images are a result of uneven drying and removal of the ethanol used to remove water stains after polishing. Several attempts were made, but it was not possible to entirely avoid the appearance of some stains.

As the assembly of the entire composite (Fig. 2.13a) does not offer a good visualization of the plies due to the need for a higher resolution, two areas with aforenamed defects were enlarged for visualization. Ply waviness and resin-rich areas within the thicker plies can be observed in Fig. 2.13b. Fig. 2.13c offers a better resolution of the resin-rich area and emphasizes the uneven fiber distribution in the thicker ply. Fig. 2.13d illustrates the stacking sequence of

the laminate and measurements of the ply thickness. Due to the waviness, the ply thicknesses vary along the cross-section. Moreover, by analyzing the sample under coaxial light, only one large void was identified in this cross-section. The void is illustrated in Fig. 2.13e, under annular light, and has a dimension of 289.5 × 63.4 µm.

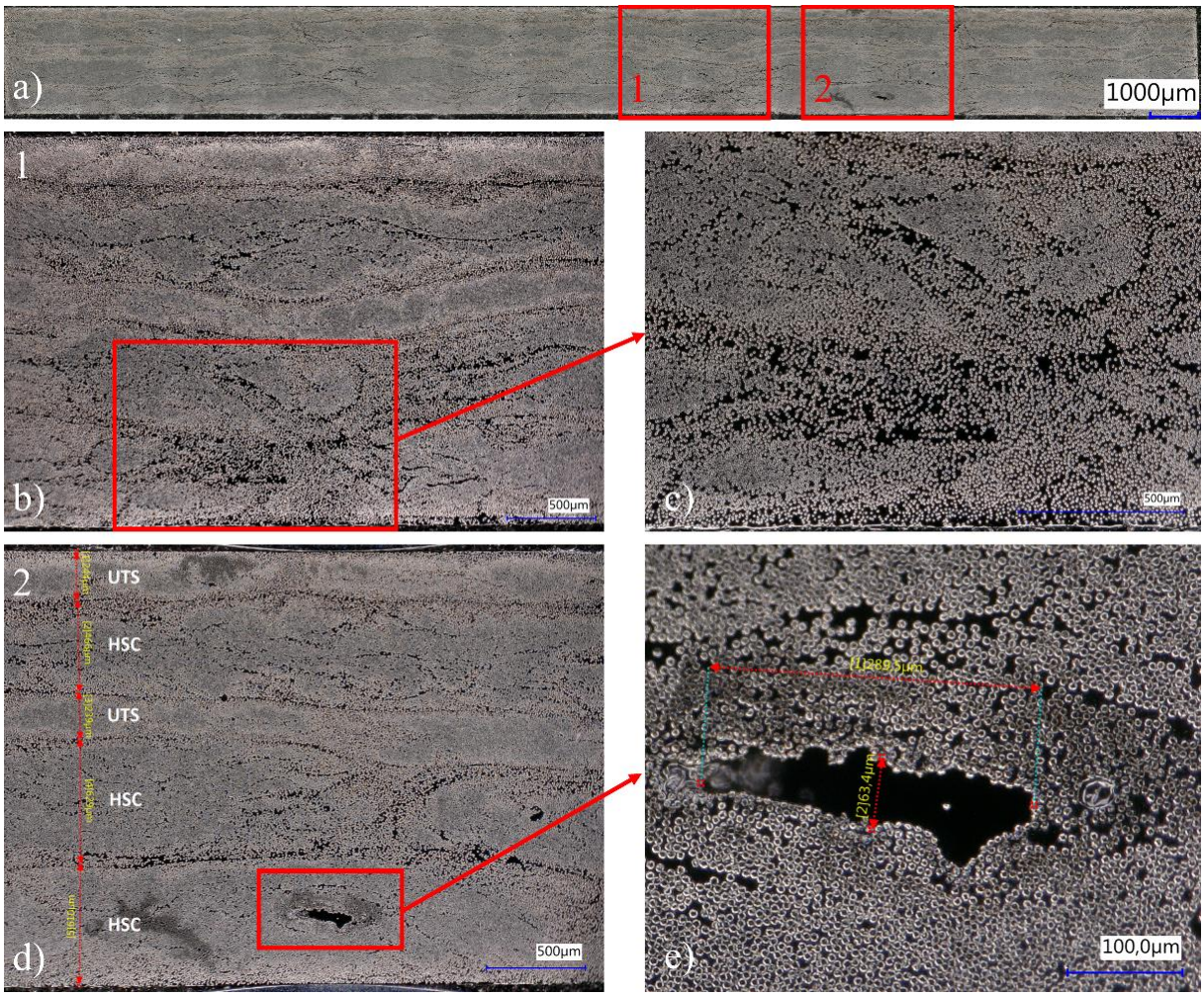

Fig. 2.13. Microscopic observations of H1 sample under annular lighting; a) assembly of the entire sample, b) resin-rich area and ply waviness, c) zoom on resin-rich area, d) laminate stacking sequence and thickness measurements, e) zoom on void with 289.5 µm in length

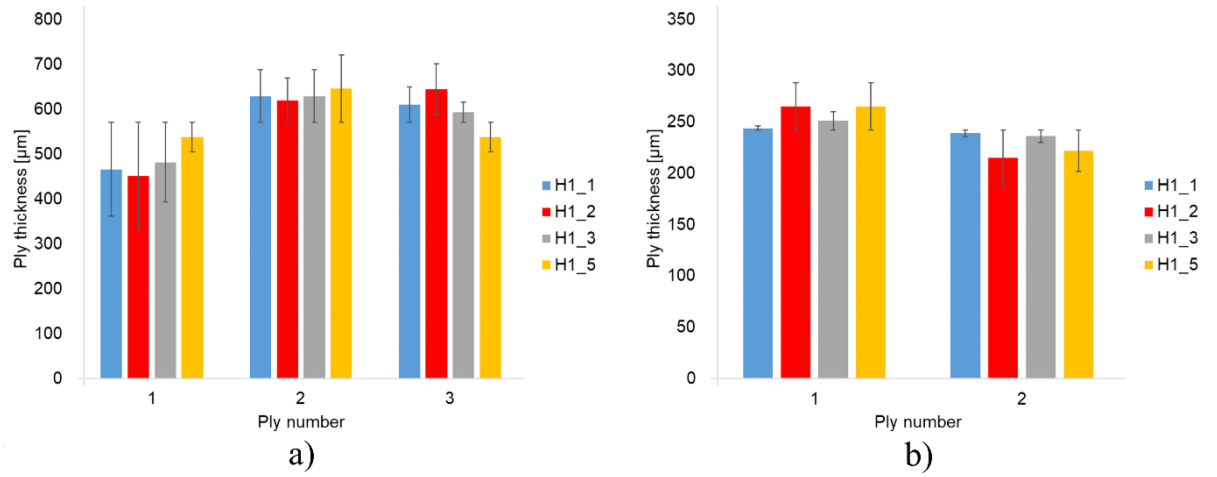

Fig. 2.14. H1 laminate ply thickness, with plies numbered from top to bottom and error bars representing the difference between the average measured thickness of the ply type and the actual thickness of the measured ply; a) HSC plies thickness; b) UTS plies thickness

Based on the ply thickness measurements from all samples, it was observed that the first ply of HSC, the one in between UTS plies, is generally thinner than the other two, as can be seen in Fig. 2.14a. Moreover, the thickness measurements of the HSC ply have a relative percentage difference with respect to the expected thickness value from the prepreg datasheet (560 µm) in between -19% and +15%, with an average thickness of 570.5 µm.

The variation of UTS plies thickness can be observed in Fig. 2.14b. The error bars in both figures represent the difference between the mean measured thickness of the ply type and the actual measured thickness. For the UTS plies, the difference in thickness between the plies is not as large as it is for the HSC plies, but the UTS plies are also thinner and more compact than the HSC ones. Still, the average thickness is 242 µm, compared to an expected thickness of 140 µm. The relative percentage difference with respect to the expected thickness value is much higher for UTS plies than for the HSC plies, between +53% and +89%. When looking at UTS laminates, a closer value of the actual ply thickness to the expected value was found. This suggests inconsistent resin removal from the different types of plies within the H1 laminate during the manufacturing process.

In general, for H2 laminates the same observations as for H1 material can be made regarding the difference in the homogeneity of the HSC and UTS plies, the interface between HSC and UTS plies compared to two adjacent HSC plies, and ply waviness. Voids were also observed within the samples under coaxial light, several in number compared to H1 material.

In Fig. 2.15, observations of an H2 sample are illustrated with the assembly of the entire sample in Fig. 2.15a, a close-up view under coaxial lighting of a region with multiple voids in Fig. 2.15b, and details of the composite stacking sequence are illustrated in Fig. 2.15c. By analyzing the thickness of the plies in two different sections of a region with a high ply waviness (Fig. 2.15c), the thickness of the HSC plies has a relative percentage difference with respect to the expected thickness value between -26% and +11%, with a maximum difference between the thickness of the same ply at different positions of 171 µm. From all measurements, the average thickness of the HSC plies is 555 µm, slightly lower than the expected value. Looking at Fig. 2.16a, we can see that there is no correlation between the thickness of the plies and their position in the analyzed samples, as could be observed for the H1 material. Moreover, only 3 plies out of 16 exceed 600 µm compared to 5 out of 12 for H1 material.

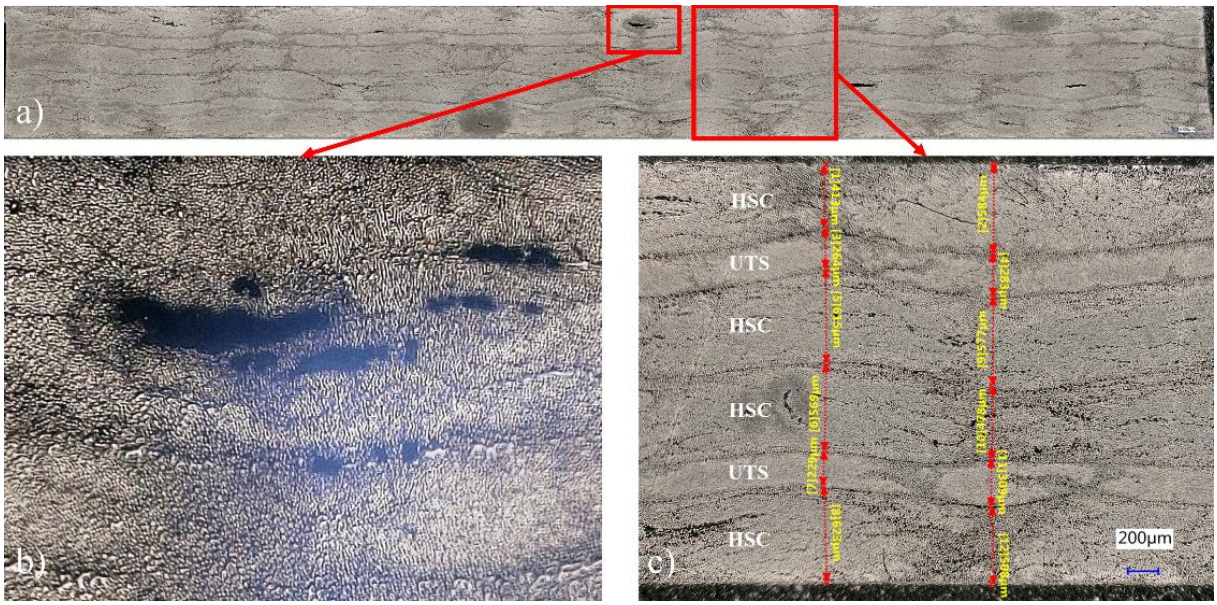

Fig. 2.15. Microscopic observations of H2 sample; a) assembly of the entire sample under annular lighting; b) voids in HSC ply, with a maximum length of 401 µm, under coaxial lighting c) plies stacking sequence and thickness measurements

With measurements of the UTS plies in the same region with a high ply waviness as for HSC plies, the thickness of the UTS plies has a smaller variation, between 229-309 µm, with a

relative percentage difference with respect to the expected value between 63% and 120%. The thickness variation from all measurements can be observed in Fig. 2.16b. The UTS ply thickness values are similar to H1 material, with an average of 242 µm, and a min. value of 217 µm, and a max. of 264 µm, giving a relative percentage difference with respect to the expected thickness value between +55% and +89%, close to the values from H1. Therefore, in the hybrid laminates, while the thick HSC plies have an actual thickness closer to the expected values, the thinner UTS plies are significantly thicker in both hybrid configurations, while in the reference UTS laminates, the relative percentage difference with respect to the expected value is between -7% and +27%. This fact suggests that the interaction between HSC and UTS plies can block proper resin extraction from the UTS plies during the manufacturing process.

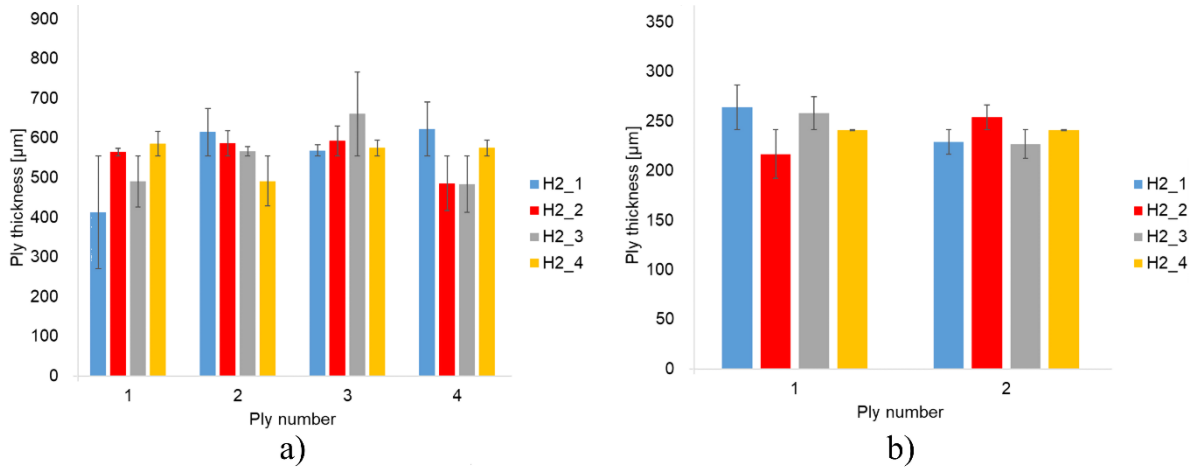

Fig. 2.16. H2 laminate ply thickness, with plies numbered from top to bottom and error bars representing the difference between the average measured thickness of the ply type and the actual thickness of the measured ply; a) HSC plies thickness; b) UTS plies thickness

2.3.4 Void content estimation

The average void content for the tested laminates is presented in Table 2.6 and Fig. 2.17. Because the void content estimation based on 2D micrography images is section-biased, there is high variability in the void content of the individual samples for each laminate configuration leading to very high standard deviations. This fact can be observed in Fig. 2.18, in which the void content estimation for the individual samples of two laminate configurations with similar average void content is presented. The average void content for UTS13 and H2 is approximately the same, around 0.22%. However, in the case of UTS13 samples, the presence of extreme values, particularly 0.002% and 0.858%, substantially elevates the standard deviation. This deviation is even greater than the average value itself. Conversely, for H2 samples, which lack such extreme values among individual samples, the standard deviation remains at approximately 0.086%.

Table 2.6. Average void content and standard deviation

Material	UTS13	UTS17	HSC3	HSC4	H1	H2
Average void content [%]	0.228	0.243	0.007	0.097	0.017	0.220
Standard deviation [%]	0.295	0.194	0.008	0.105	0.015	0.086

As mentioned in the previous section, part of the UTS13 and UTS17 samples showed an increased number of interply voids, which is considered to be due to air entrapment during manipulation of the increased number of plies, and is reflected as the highest average void content from all laminates. HSC3 samples have the least void content, and by adding an extra layer of HSC prepreg, thus increasing the overall thickness of the laminate, the estimated void content increased from 0.007% to 0.097%. This suggests that air removal from the laminates

during the process of curing in an autoclave is less efficient as the laminate thickness increases. In the same idea, H2 laminate has a higher void content than H1, with only one extra HSC ply.

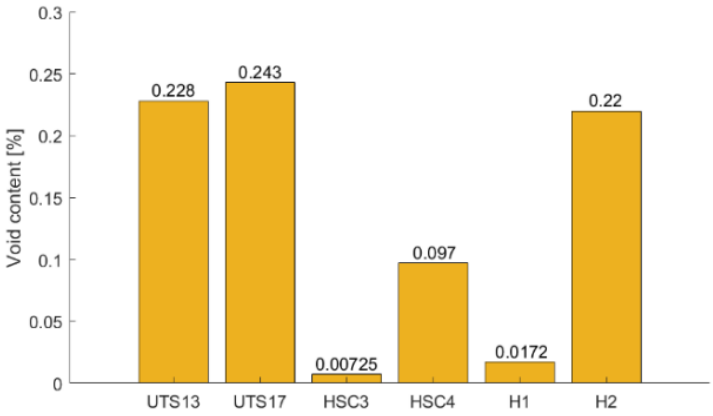

Fig. 2.17. Average void content of tested laminates

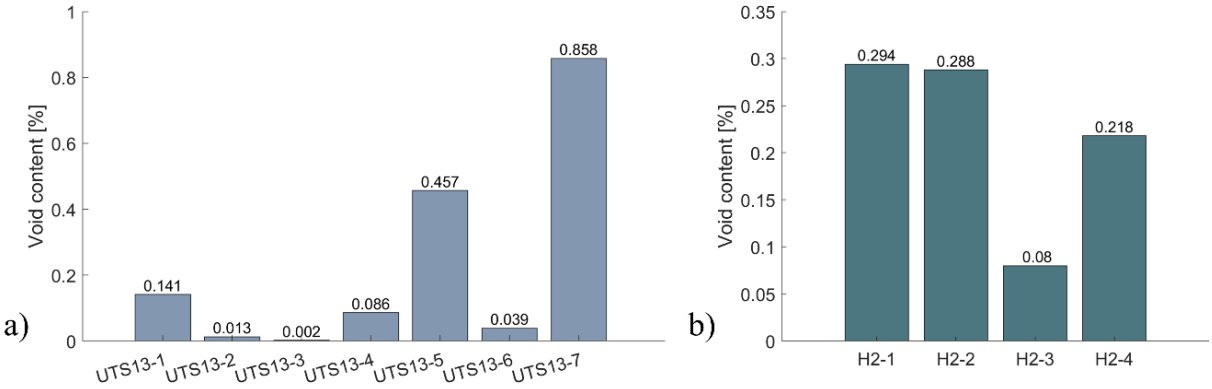

Fig. 2.18. Void content estimation of individual samples of laminates with similar average void content; a) void content of individual UTS13 samples; b) void content of individual H2 samples

After analyzing the micrographs of all samples, it was observed that the shape of the voids is irregular, mainly elongated rather than circular, especially for larger voids. For the hybrid configurations and HSC laminates, most voids are localized inside the thick HSC plies, and few voids were identified at the interface between plies. For UTS laminates, the voids are localized at interfaces between plies.

Using the chart in Table 2.3, H1, HSC3, and HSC4 materials are in the Grade A category with excellent quality in terms of void content. H2, UTS13, and UTS17 materials are grade B, still being very good composite materials. As the void content at which it can significantly affect the mechanical properties of the composite is above 1% [204], [219], it is concluded that for all materials in this study, the void content should not affect their mechanical properties.

SUMMARY

In this chapter, objective 1 was attained, and an experimental characterization of the internal structure and physical properties of both reference and ply-level hybrid unidirectional carbon fiber composites was carried out, contributing to the main objective of the thesis.

To realize this, the ply-level hybridization technique was adapted, which allowed to achieve hybridization not only in ply thickness but also in material quality. This was accomplished by combining high-quality carbon fiber prepreg plies with plies of lower quality within the same laminate. The primary motivation behind this hybridization was to achieve cost reduction. Two distinct stacking sequences for the hybrid laminates were explored: one symmetric by the midplane and the other unsymmetric. In addition, the creation of reference laminates served the dual purpose of establishing a foundational benchmark for comparing the hybrid laminates and

facilitating a comparison between UTS and HSC laminates. A comprehensive array of preliminary experimental characterization tests was conducted to examine the effects of hybridization on the internal structure and physical properties of the hybrid composites.

With a volume fraction ranging from 49% to 54%, the densities of the composites, determined using Archimedes' principle, exhibited similar values, with a maximum difference of only 1.42%. Archimedes' principle-based density values were identified as more reliable, and thus, they will serve as the basis for subsequent calculations requiring the density of the tested composites.

Microscopic observations revealed distinct characteristics of the UTS composites compared to the HSC counterparts. UTS composites demonstrated greater uniformity in their plies and reduced ply waviness, although they exhibited a higher percentage of interply voids compared to HSC composites. The internal structure analysis of the hybrid laminates indicated improvements in terms of ply mixing, resin-rich regions, and ply waviness when contrasted with HSC laminates. For all the composites under scrutiny, the estimated void content remained below 1%, which is indicative of good composite quality. This low void content suggests that the mechanical properties of these composites should remain unaffected by voids.

CHAPTER 3. QUASI-STATIC BEHAVIOR OF PLY-LEVEL HYBRID CARBON COMPOSITE MATERIAL

INTRODUCTION

This chapter provides a comprehensive analysis of the quasi-static mechanical performance of hybridized composite materials in comparison to high-standard reference materials. The main aim is to ascertain their suitability for cost-effective applications in the aerospace industry. Throughout this chapter, objectives 2, 3, and 4 are addressed.

The performance evaluation from a mechanical point of view involves monotonic on and off-axis quasi-static tests, conducted at a controlled displacement rate of 1 mm/min, to assess the in-plane behavior of both hybrid and reference laminates. On-axis tensile tests are carried out to determine in-plane properties, while off-axis tests reveal the nonlinear stress-strain behavior with varying off-axis angles. The impact of thickness on off-axis mechanical responses is also investigated, using reference laminates with different thicknesses.

For strain analysis, Digital Image Correlation is employed, supplemented by a successive linear regression method to assess the apparent Young modulus in off-axis samples, due to the nonlinearity of the stress-strain response.

Cyclic load-unload off-axis testing is undertaken to uncover the origins of nonlinear responses, and methods for residual strain and damage variable estimation are employed. Moreover, parameters required for nonlinear constitutive models are estimated, and predictions of off-axis behavior are carried out using a nonlinear coupled damage-plasticity model, offering insights into the predictive capabilities of the approach.

The chapter's subsequent structure comprises detailed accounts of the experimental methodologies, followed by the presentation and analysis of results for each test type. Additionally, discussions explore the particularities of the tested laminates and the effects of hybridization.

3.1 MATERIALS AND METHODS

3.1.1 Experimental setup

Quasi-static tension tests are performed to determine the on and off-axis response of the unidirectional laminates for three different fiber orientations: 15°, 30°, and 45°. Guidelines from EN ISO 527-5 [87] standard were followed to conduct these tests. All mechanical tests were carried out at ambient temperature (20° C) and controlled in displacement at 1 mm/min. The strain rate is approximated by dividing the crosshead displacement rate by the gauge length of the sample (~150mm), yielding an approximate strain rate of 10^{-4} s^{-1}.

Most 0° tensile tests were carried out on an ADAMEL® Lhomargy DY36 testing machine at ENSTA Bretagne with a load cell of 100 kN and wedge grips. Part of H1 and HSC3 0° tensile tests and all 90° and off-axis tensile tests were performed with an electromechanical testing machine INSTRON® 5960, with a load-cell of 50 kN and wedge grips, also at ENSTA Bretagne.

Strain measurements were performed with the use of Digital Image Correlation (DIC). GOM Aramis® 5M was used for most DIC measurements, post-processing, and extraction of the strain values. For part of the H1 0° tensile tests, a simple Retiga® 1300 camera was used to

record the images, and GOM Correlate® Software for post-processing and extraction of the strain values, as the GOM Aramis® 5M was unavailable at the time of the experimental tests.

GOM ARAMIS 5M is a non-contact, optical 3D measuring system that allows full-field displacements and strain measurements. The software package (ARAMIS Version 6.3) is designed to run the GOM sensor and controller, create the project files, process the recorded images, compute results, and perform the post-processing for data extraction. Using this system, out-of-plane displacements can be observed, along with in-plane displacements and strain fields of the target surface.

The GOM ARAMIS 5M sensor consists of two CCD cameras with a resolution of 2448 pixels × 2050 pixels. Lenses with a focal distance of 50 mm and no zoom were used. The calibration of the system was performed using a QCG 2045 32 mm × 24 mm calibration cube and instructions from the user manual. The images were acquired at a speed of 1 image per second. The tensile force from the tensile machine was imported via the Analog-to-Digital (A/D) input of the sensor controller for a better correlation of the force and corresponding displacement.

The DIC analysis requires a high-contrast stochastic pattern on the investigated sample. A reference image of the undeformed sample is recorded before the test, and sequential images of the deformed sample are recorded during the tensile test. In the postprocessing step, an analysis based on tracking the unique surface patterns is made using the ARAMIS V6.3 software, to provide a progressive measurement of surface deformation. For DIC processing, a subset size of 19 pixels × 19 pixels with a step size of 10 pixels, and an overlap area of 9 pixels was used. In standard conditions, the standard deviation for in-plane displacements is up to 0,4 µm, based on the user manual of the system.

The experimental setup is illustrated in Fig. 3.1.

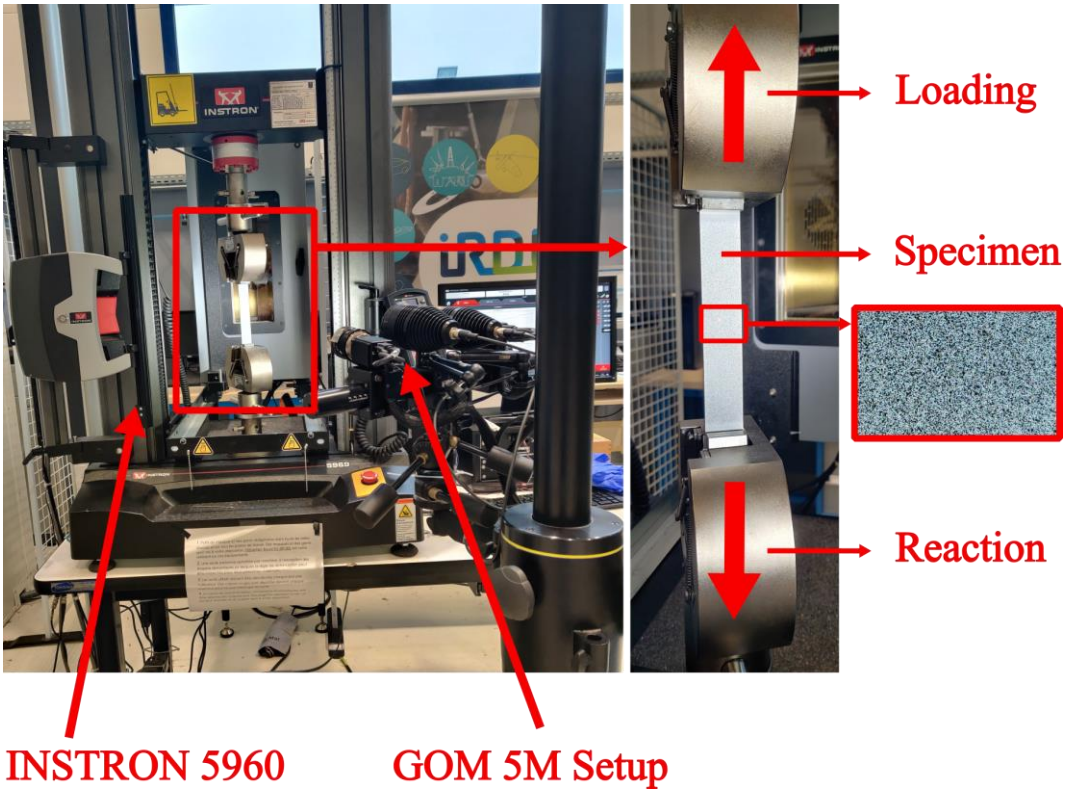

Fig. 3.1. Experimental setup for tensile testing

After calibrating the GOM system, only 75 mm of the sample's gauge length was within the field of view of the camera system, out of the total of 150 mm, as shown in Fig. 3.2a. An example of a displacement field based on post-processing image analysis at a certain timestep is illustrated in Fig. 3.2b. From the available field of view, inspection rectangles can be selected to extract the results based on an average over the inspection region.

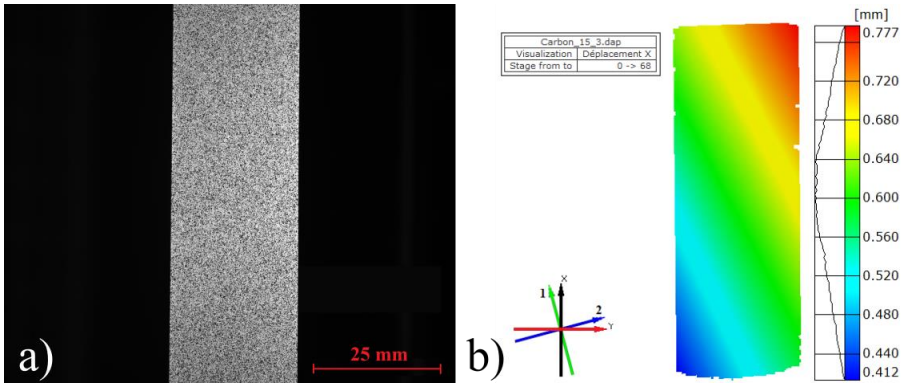

Fig. 3.2. DIC image acquisition and processing; a) recorded image; b) example of full-field measurement after post-processing the recorded images with X in the loading direction and 1 in the fiber direction (θ=15°)

3.1.2 Sample description and preparation

Because the materials were provided in two different batches, a year apart, they were cut using methods available at those specific times. Thus, H1 samples were provided first and were cut using a CNC milling machine at the manufacturer's facility, and all other laminates were cut using water-jet cutting at Université de Bretagne Occidentale in Brest, France. In all instances, the edges of the samples were visually inspected to ensure the absence of any noticeable irregularities that could potentially impact the tests.

The dimensions for the 0° test are shown in Fig. 3.3a, while for the 15°, 30°, 45°, and 90° tests, the sample dimensions are presented in Fig. 3.3b. Corresponding axis systems are designated as follows: X – the load direction, Y – transverse to the load direction, 1 – fiber direction, 2 – transverse to the fiber direction, and θ – the off-axis angle. In the case of the 0° tensile test, H1 samples exhibited a width of approximately 11 mm, while the width for all other laminates was around 15 mm. The actual dimensions of each sample showed slight deviations from the nominal dimension, falling within the margin of uncertainty of the measuring device.

Sample length and width were measured using a caliper with an accuracy of ±0.01mm, and thickness was measured using a micrometer with an accuracy of ±1μm. All calculations were based on the measured dimensions of each respective sample.

To reduce the gripping effects, aluminum tabs were bonded on the specimens using an Araldite 420 A/B Epoxy Adhesive System. For H1 samples, 2 mm thick aluminum tabs were used, and for all other samples, 1.5 mm thick aluminum tabs were used due to the unavailability of 2 mm aluminum plates during the preparation of the samples. The details of each test type, such as sample configuration and the number of samples that were used are also given in APPENDIX B.

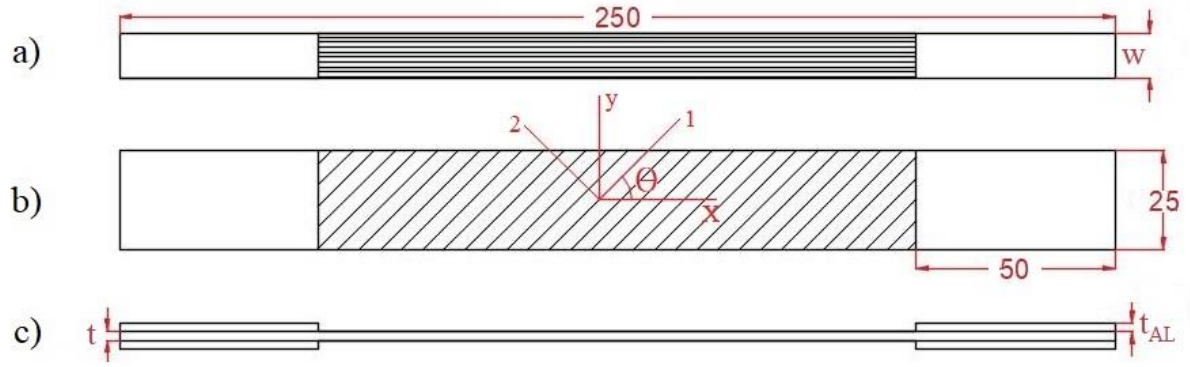

Fig. 3.3. Samples dimensions in mm; a) 0° tensile test b) off-axis and transverse tensile test c) side view of samples; all dimensions are in mm, w – width of the sample, t – thickness of the sample, t_{AL} – thickness of aluminum tabs

The speckle pattern for DIC measurement was obtained by first applying a white mat paint as a background, sprayed directly onto the specimen. After drying, mat black paint was sputtered over the white paint to create a random pattern of small black spots. It was accomplished by spraying the area next to the inclined placed specimen and using the drift of the overspray to create a fine speckle pattern. The pattern for each specimen was verified before starting the mechanical test to ensure that there were no saturated regions. The final specimens used for testing are illustrated in Fig. 3.4.

Fig. 3.4. Tensile test specimens with aluminum end tabs and speckle pattern

3.1.3 Data processing

DIC data were used to establish the evolution of stress versus strain. It outperforms traditional strain gauges since it is able to provide the whole strain field in 2D in the observed region. In all stress-strain graphs, the engineering stress and engineering strain are used because the tested composite samples do not deform as much as metals (the transverse deformation of the samples is very small, not noticeable with the naked eye) to have a reason to calculate true stress-strain. MATLAB® software was used for the linear fit and data extraction for both the Young modulus and Poisson ratio, according to sections 1.2.1 and 1.2.2.

For off-axis tensile tests, which exhibit a nonlinear stress-strain response, a successive linear regression procedure is proposed to select the linear stress-strain data at the origin, from which the apparent modulus E_x and Poisson ratio ν_{xy} are estimated. The schematic diagram of this method is detailed in Fig. 3.5.

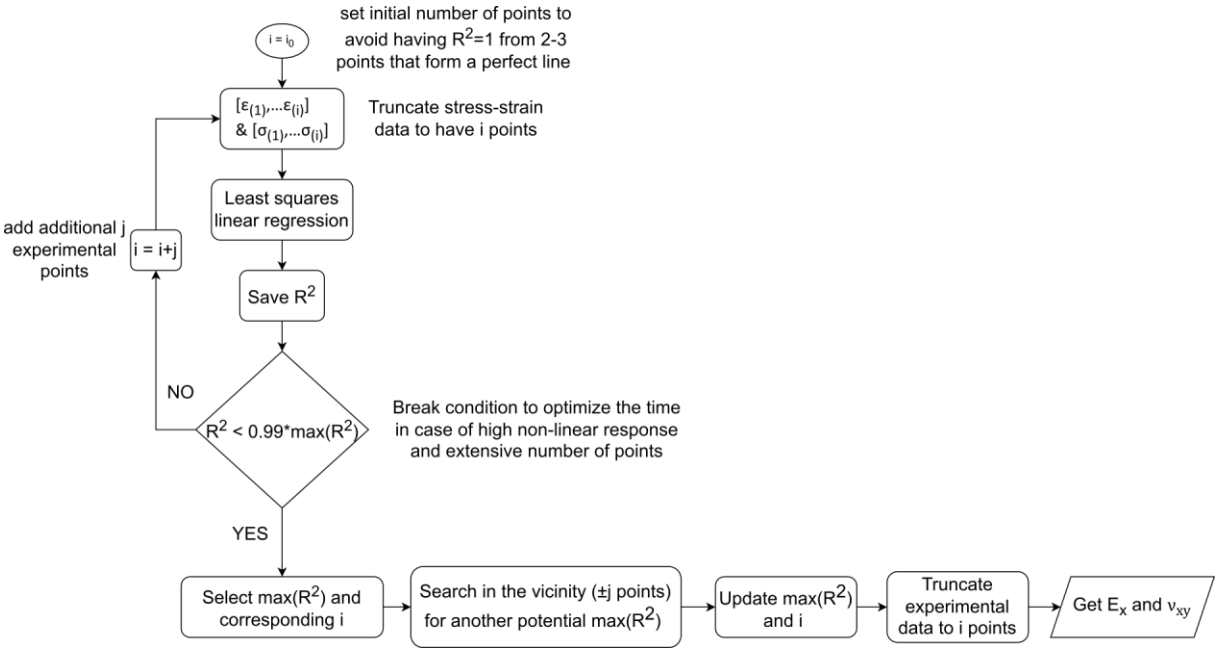

Fig. 3.5. Flowchart of the successive linear regression procedure on stress-strain relations obtained from experimental data extracted with DIC

The proposed method uses successive least-squares linear regressions and is similar to Castres's [84] proposal for the extraction of the cycle modulus in the cyclic load-unload curve. For this reason, it will be referred to as the Regression method, for cycle modulus extraction.

To employ the procedure, an initial regression is calculated using the first set of experimental points. Thereafter, the next regressions are calculated after adding additional experimental points to the initial dataset. For each regression, the coefficient of determination $R^2$is calculated. R^2 is a measurement of the correlation between a fitted model with the experiment data points. A value of 1 is an indication that the regression model fits perfectly the dataset. In the proposed procedure, the number of points from the dataset for which the regression has the maximum R^2 is saved and another potential maximum R^2 is searched in the vicinity, by adding or subtracting one data point. The apparent modulus is extracted as the slope of the linear fit for the stress-strain data points for which the regression had a maximum R^2. The apparent Poisson ratio ν_{xy} is the slope of the linear approximation of the $\varepsilon_y - \varepsilon_x$ curve, using the same number of data points as for the apparent modulus E_x.

Before employing the successive linear regression procedure, all stress-strain curves were smoothed using the 'Smooth' function in MATLAB® with the 'Lowess' method to minimize the influence of minor variations in the stress-strain data on the successive linear fits [220]. Furthermore, to avoid any influence of signal noise at the beginning of the tensile test due to grip/sample alignment on the extraction process, the stress-strain data below a strain value of 5.10^{-4} was not considered.

An illustration of the sequential stages involved in applying the procedure loop can be found in the APPENDIX C. The final data selection, obtained after exploring nearby possibilities for an additional maximum value of R^2, is shown in Fig. 3.6.

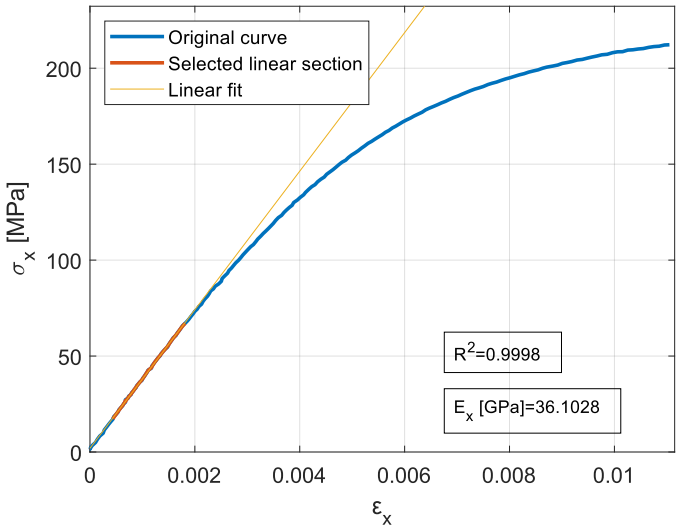

Fig. 3.6. Final selection of stress-strain data for elastic modulus extraction, based on max(R^2) criteria

3.2 EXPERIMENTAL RESULTS AND DISCUSSION

3.2.1 On-axis tensile tests – 0º and 90º

During the first 0° tensile tests, for certain samples, the aluminum tabs detached and slipped within the grips before the material's ultimate stress was reached. A test was even conducted without tabs, but the sample slipped within the grips at an earlier point, occurring sooner than with the tabbed sample. Additionally, the gripping area of the sample suffered considerable damage from the gripping force. It's important to note that two different machines were utilized for this test. Due to the issue of samples consistently slipping within the grip of the INSTRON® 5960 machine, a preliminary test on the ADAMEL® Lhomargy DY36 machine was carried out, and subsequently, the remaining samples were tested using the ADAMEL® Lhomargy DY36 machine. While failure was not encountered for all tested samples, valuable insights can still be derived from their behavior until the test is concluded.

The average values of the determined elastic constants and failure data from the longitudinal and transverse tensile loading are centralized in Table 3.1, including the number of tested samples for each configuration. The uncertainties in the values from the table represent half the range of measurements. At least 4 samples underwent testing, except for the H2 material, where only 2 samples were subjected to longitudinal tensile loading and 1 sample for transverse tensile loading. The reduced number of samples for H2 was due to challenges encountered during the cutting process, which resulted in damage to several samples. The particularities of the results for each parameter will be further discussed individually.

The axial stress-strain response figures for all tested samples under tensile loading in the fiber direction and perpendicular to the fiber direction are shown in APPENDIX D. All samples present a linear stress-strain response, and good reproducibility was obtained. Therefore, only representative samples from each test configuration were selected for further visualization, and illustrated in Fig. 3.7 for comparison purposes.

Table 3.1. Experimental results for longitudinal and transversal tensile testing

Material	UTS13	UTS17	HSC3	HSC4	H1	H2
0° tensile test - n° of samples	4	4	4	8	10	2
E_{11} [GPa]	125 ± 3	127 ± 5	114 ± 2	114 ± 4	117 ± 5	120.9 ± 0.4
Failure Stress σ_{11} [MPa]	1622 ± 174	1453 ± 201	1857 ± 252	-	1522 ± 170	1594 ± 14
Failure strain ε_{11}	0.013 ± 0.001	0.011 ± 0.002	0.015 ± 0.002	-	0.013 ± 0.002	0.0129 ± 0.0001
ν_{12}	0.32 ± 0.01	0.325 ± 0.006	0.31 ± 0.01	0.33 ± 0.01	0.32 ± 0.02	0.3090 ± 0.0004
90° tensile test - n° of samples	7	7	7	7	10	1
E_{22} [GPa]	6.9 ± 0.1	7.0 ± 0.1	7.0 ± 0.2	7.2 ± 0.2	7.0 ± 0.6	7.0
Failure Stress σ_{22} [MPa]	43 ± 10	46 ± 14	39 ± 8	36 ± 5	28 ± 7	38
Failure strain ε_{22}	0.006 ± 0.001	0.006 ± 0.002	0.0055 ± 0.0008	0.0049 ± 0.0005	0.003 ± 0.001	0.005

As reference laminates with different thicknesses were manufactured, thickness effects on the in-plane mechanical properties can be evaluated. In terms of the thickness effect on the elastic modulus of the tested laminates, the close results of the average Young modulus between

laminates manufactured from the same prepreg type with a different number of plies and different laminate thicknesses, presented in Table 3.1, indicate no thickness effect under both longitudinal and transverse tensile loading. This observation is also emphasized by the stress-strain response under 0° tensile loading illustrated in Fig. 3.7a for HSC3 and HSC4 and Fig. 3.7b for UTS13 and UTS17. For 90° tensile loading, the stress-strain response is presented in Fig. 3.7c for HSC3 and HSC4, and in Fig. 3.7d for UTS13 and UTS17.

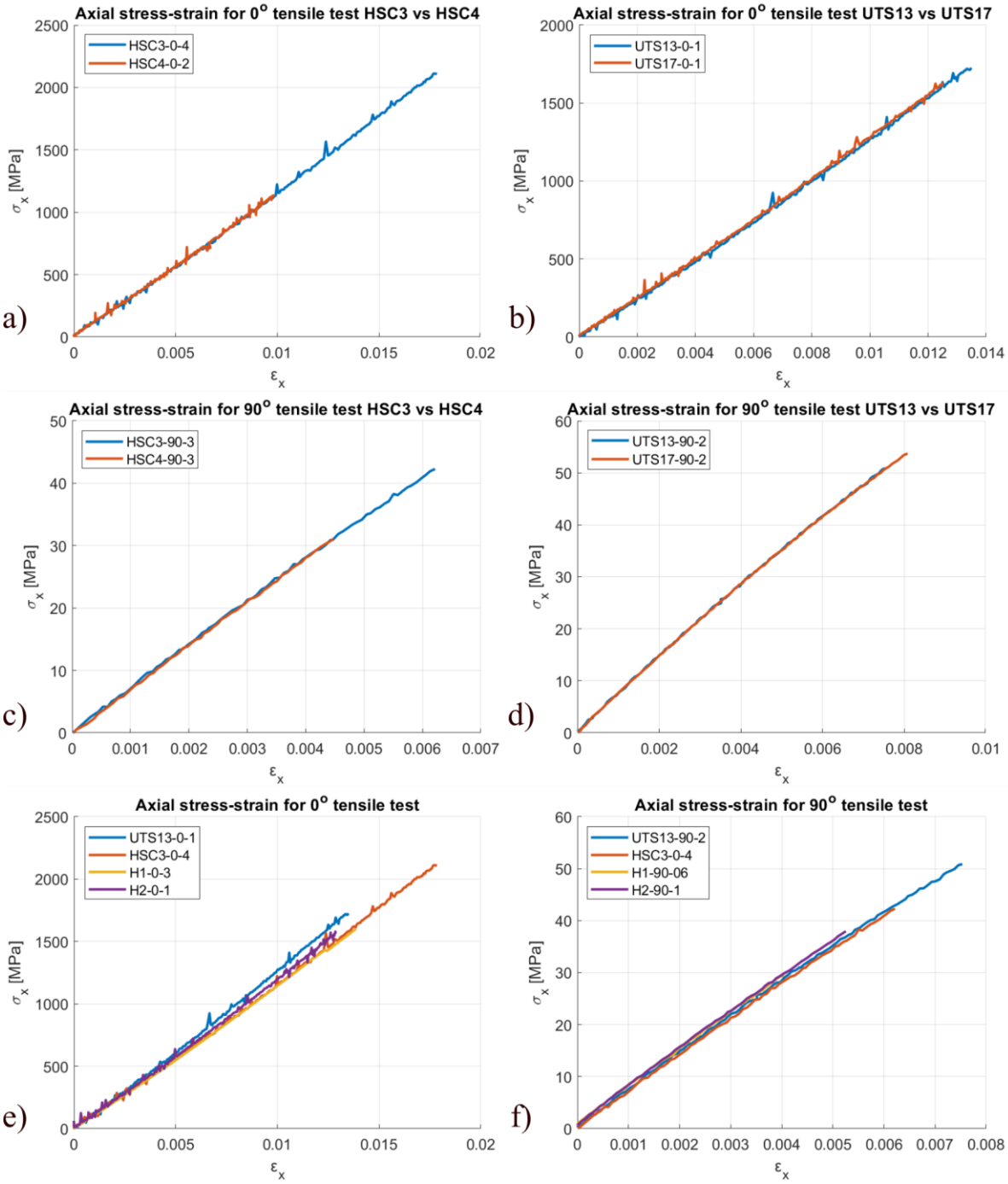

Fig. 3.7. Comparison of axial stress-strain response for representative samples of each testing configuration; a) HSC3 vs HSC4 under 0° tensile loading; b) UTS13 vs UTS17 under 0° tensile loading; c) HSC3 vs HSC4 under 90° tensile loading; d) UTS13 vs UTS17 under 90° tensile loading; e) Simple and hybrid configuration materials under 0° tensile loading; f) Simple and hybrid configuration materials under 90° tensile loading

In Fig. 3.7e, a comparison of the stress-strain response under 0° tensile loading of representative samples from both hybrid configurations and the reference materials is presented. By also analyzing the comparison of the longitudinal elastic modulus for all types of

laminates, presented in Fig. 3.8a, it can be seen that the HSC laminates have the smallest modulus, UTS laminates the highest and the hybrid configurations have intermediate elastic modulus, as previously reported in the literature for all carbon hybrid composites [50], [51]. Based on the average values of the longitudinal modulus from Table 3.1, H1 has a 2.63% increase in longitudinal modulus compared to HSC laminate, and H2 has a 5.59% increase in longitudinal modulus compared to HSC4 laminate. As no thickness effect was observed on the elastic modulus, the mentioned percentage increase in modulus is attributed to adding the two UTS plies to the HSC ones in creating the hybrid configurations. Moreover, for H2, a higher percentage increase was obtained than for H1, suggesting that blocking the UTS plies inside the laminate with the HSC plies might offer better results, as it was also indicated by Czel et al. [51].

In terms of transverse modulus, close results were obtained for all tested configurations, as shown in Table 3.1, Fig. 3.7f, and Fig. 3.8b, with a small range of values E_{22} = [6.9; 7.2] GPa that is within the error bars limit. This suggests that the epoxy resins used in the prepregs have similar quasi-static mechanical properties, and no effect of the hybridization on the transverse elastic modulus can be identified.

The values determined for the Poisson ratio for all tested configurations have close values between the different laminates and are in the range of values reported by other authors for unidirectional carbon fiber composites [39], [221], [222].

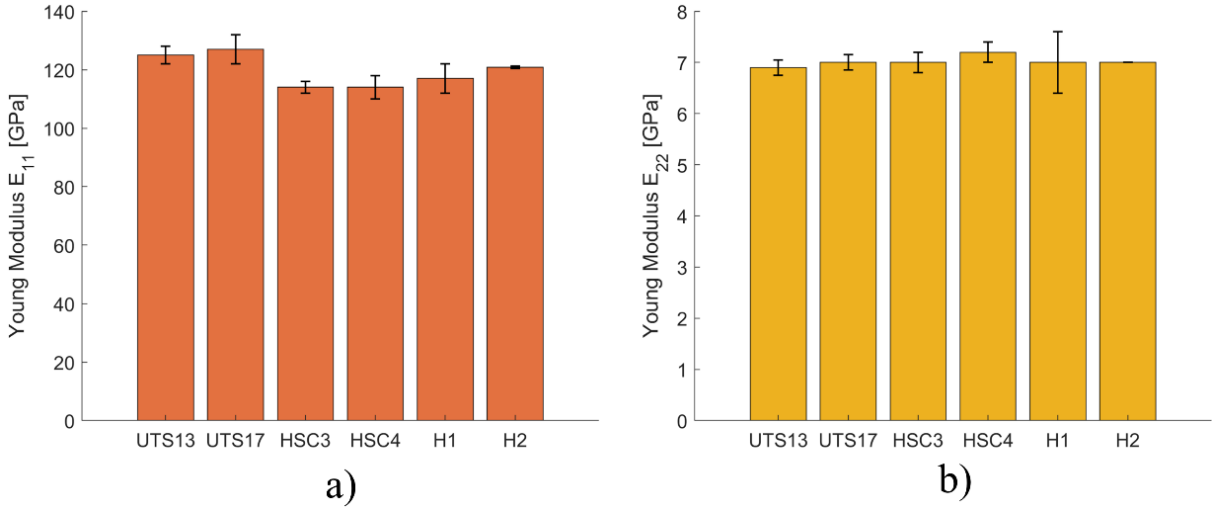

Fig. 3.8. Comparison of Young modulus for all laminate configurations, with error bars representing half the range of measurements; a) Longitudinal modulus of elasticity E_{11}; b) Transverse modulus of elasticity E_{22}

Concerning the failure stress, both tests encountered difficulties. As previously stated, in the case of tensile tests conducted along the fiber direction, not all samples experienced failure. This was attributed to the detachment of aluminum end tabs, causing the sample to slip within the gripping system, ultimately leading to the need for manual test termination.

An example of two 0° tensile tests, one that reached ultimate failure and one that was manually stopped, with the corresponding stress-crosshead displacement curves, is given in Fig. 3.9. Both tests are for H1 material and were performed on the ADAMEL® Lhomargy DY36 machine. For the case presented in Fig. 3.9a, an initial thin stripe detached from the sample also causing the detachment of the end tabs. The test could not be continued from this point on due to slipping within the grips, causing a continual force loss, and was manually stopped. In the other case, presented in Fig. 3.9b, after the initial crack, the tabs did not detach and the test could be continued. Each subsequent crack was followed by a sudden drop in force and a small increase afterward. The corresponding stress-crosshead displacement curve is also provided to support the statement. Ultimate failure was reached in the form of longitudinal splitting coupled

with ultimate fiber failure at the end tabs. This failure occurrence is also depicted in Fig. 3.10, showcasing an HSC3 sample that could be reassembled.

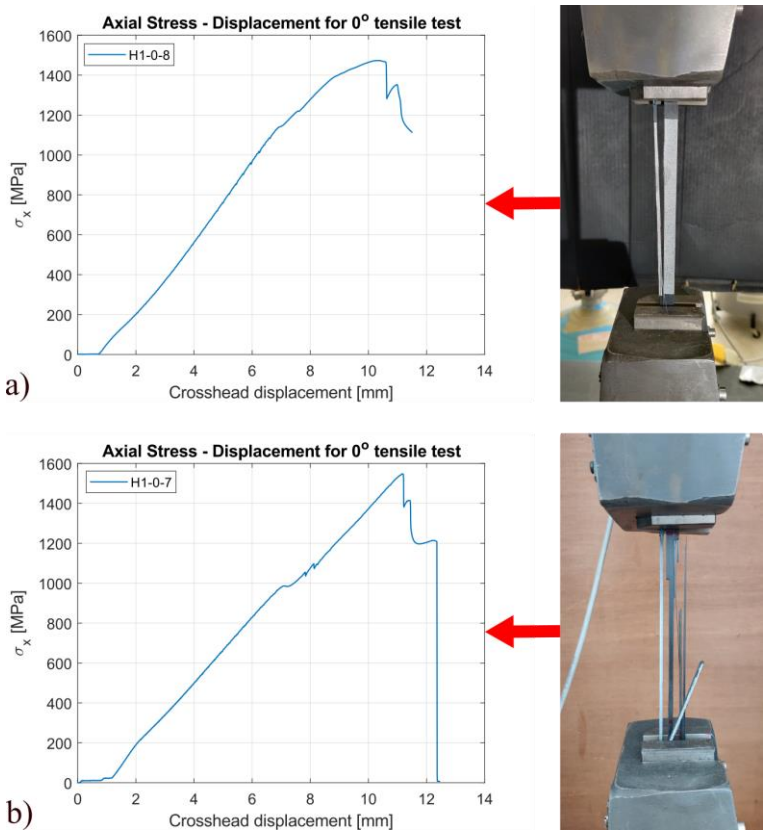

Fig. 3.9. Failure of 0° H1 test sample with corresponding Stress-Crosshead displacement curve; a) H1 - sample 8; b) H1 - sample 7

For H1, only 4 out of 10 samples reached failure when tested in the fiber direction, and for HSC3, 2 out of 4. For HSC4, only one sample had a longitudinal split at a stress level of 1200 MPa and it was not taken into consideration as a failure stress because the sample immediately slipped in the grip. All samples reached failure for UTS13, UTS17, and H2 laminates. Failure was in the form of longitudinal splitting with ultimate fiber failure at the end tabs. When averaging the failure stress, samples that reached failure were taken into consideration, as well as samples that reached a stress level above the failure stress of another sample of the same configuration.

Fig. 3.10.Example of failed HSC3 sample under 0° tensile test

For the tensile tests perpendicular to the fiber direction, almost 4 out of 7 samples fractured close to the end tabs at significantly lower stress levels compared to other samples that broke farther, thus leading to a high dispersion in failure stress data. The fracture positions of each sample are illustrated in APPENDIX E. Moreover, when fixing the sample in the gripping system, a small tension force was registered by the force cell which could not be set to zero before starting the test. That is why part of the stress-strain curves do not start from a zero-stress level.

To compare the failure stress of the composites for 0° tensile loading, as previously mentioned in section 1.2.1, a geometrical scaling was performed in advance. Because failure for HSC4 samples was not achieved, data from UTS13 and UTS17 was used as the reference for geometrical scaling. Therefore, m_{UTS} is obtained by fitting equation (1.6) to the failure stress data of UTS13 and UTS17, from the experimental results, with UTS13 data being the reference

one No experimental data is available for 0° tensile testing of UTS13 laminate with different specimen widths to estimate n_1 and n_2 parameters. Thus, the values from Kawai's work [96] were used. All coefficients and reference data used for geometrical scaling are detailed in Table 3.2.

Table 3.2. Coefficients and reference data used for geometrical scaling of failure stress for 0° tensile test

m_{UTS}	A_{UTS13}	σ_{UTS13}	t_{ref}	n_1	n_2
2.095	2205 mm^2	1622 MPa	2.17 mm	-0.386 [96]	0.399 [96]

The corresponding results of the geometrical scaling are presented in Fig. 3.11a. The first strength prediction based on Kawai's power law [96] using equation (1.6) was performed for a corresponding width of the samples of 15 mm. Although UTS13 and UTS17 data were used for determining the coefficients needed for the power law, it can be seen that the strength prediction also fits HSC3 failure stress data. When looking at H1 and H2 failure stress, H2 has increased failure stress compared to the strength prediction and compared to UTS17 as well (which has a similar thickness). However, H1 has a lower failure stress than the predicted one. This was concluded to be due to the H1 samples' smaller width, of 11 mm, compared to all other tested samples with a width of 15 mm. Therefore, an additional geometrical scaling of the initial strength prediction was performed to have a failure stress prediction for a corresponding sample width of 11 mm, using equations (1.7) and (1.8). By comparing the two failure stress predictions, the failure stress increases with the increasing width of the specimen, as also reported by Kawai [96]. When looking at the value of H1 failure stress compared to the prediction for a width of 11 mm, in this case, H1 has increased failure stress compared to the reference materials, as was also obtained for H2.

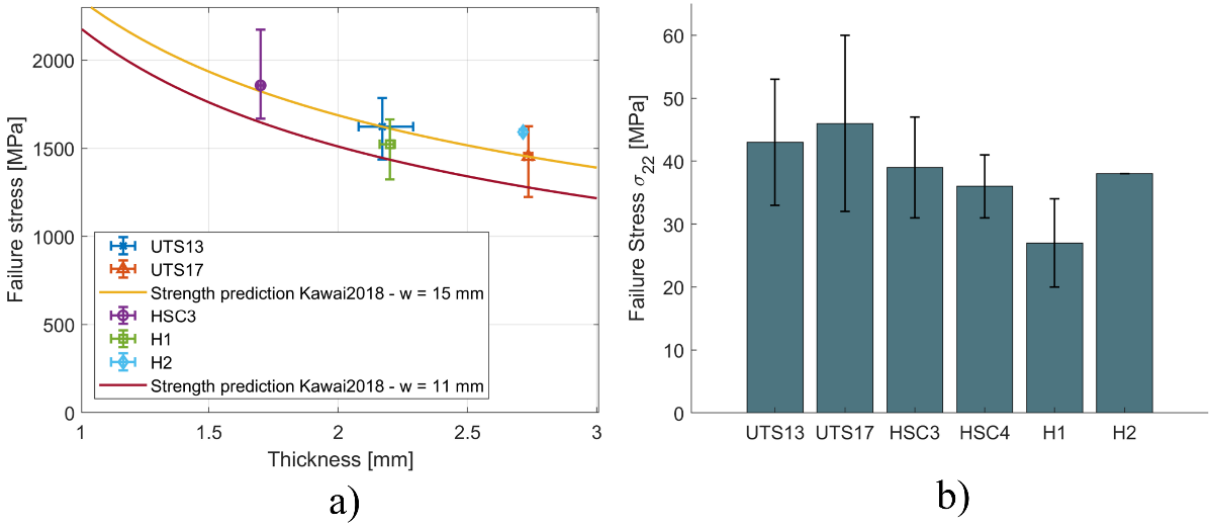

Fig. 3.11. a) Geometrical scaling of failure stress for longitudinal tensile loading, based on Kawai's [96] power law; b) Failure stress for transverse tensile loading, with error bars representing half the range of the measured values

Therefore, it can be concluded that the type of hybridization used in this work has a positive effect on both longitudinal elastic modulus and failure stress. In terms of the longitudinal stiffness-to-weight ratio related to the cost/fiber areal weight of the laminates, hybrid composites have an intermediate stiffness-to-weight ratio with intermediate costs, compared to simple laminates, as can be deduced from Fig. 3.12.

Fig. 3.11b shows the comparison of the failure stress under transverse tensile loading for the different laminates. As previously mentioned, the obtained failure stress data displayed a considerable dispersion, mainly attributed to samples failing near the end tabs. This phenomenon is also emphasized by the presence of high error bars. As a result of this issue,

there is a possibility that the transverse strength of the tested composites could be underestimated. Additionally, drawing meaningful conclusions regarding the impact of hybridization on transverse failure stress becomes challenging in light of these circumstances.

For each material configuration, the longitudinal failure strain was smaller than the fiber elongation at break reported by the manufacturer. Moreover, the failure strain for UTS17 was lower than for UTS13, suggesting that the laminate thickness could influence the failure strain, as it affects the failure stress. Kumar et al. [223] showed that the failure strain of unidirectional composites is influenced by the specimen's geometry. No information was found regarding the influence of specimen thickness on the failure strain. Due to the absence of failure data for HSC4, making a comparison with results from HSC3 and drawing a preliminary conclusion is not possible. To substantiate this statement, additional investigations would be necessary.

Although the hybrid configurations have more HSC fibers, their longitudinal failure strain is smaller than the one obtained for HSC3 and closer to the values obtained for UTS laminates. Still, the hybrid laminates have thicknesses closer to UTS reference samples rather than HSC3 laminates, which might influence the comparison, given the above-mentioned statement.

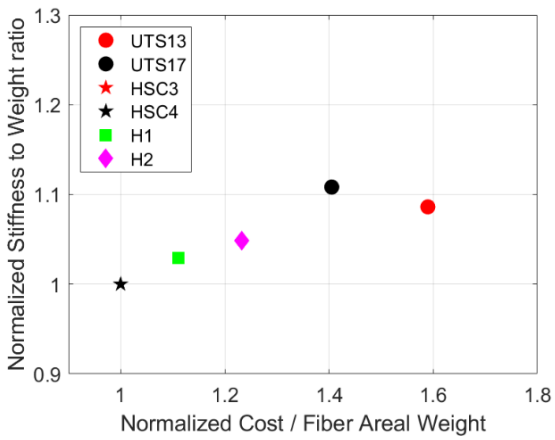

Fig. 3.12. Longitudinal stiffness to weight ratio of studied laminates and their cost/ fiber areal weight, normalized to the corresponding values of HSC3 laminate (HSC3 and HSC4 markers are overlapping)

By looking at transverse failure strain values in Table 3.1, UTS13 and UTS17 have the highest transverse failure strain, with values close to each other, while the hybrid configurations have the lowest transverse failure strain. H2 has a similar transverse failure strain to both UTS and HSC laminates (but only one sample was tested), while H1 has a significantly lower transverse failure strain. As also mentioned for the transverse failure stress, the transverse failure data could be underestimated since approximately 4 out of 7 samples broke near the end tabs, and no conclusion can be correctly drawn in terms of hybridization effects on the transverse failure strain.

3.2.2 Off-axis tensile tests

Three off-axis angles were tested, 15°, 30°, and 45°. The results will be presented for each angle individually as also an analysis of the influence of the off-axis angle will be performed. All testing configurations achieved good repeatability, with at least three tested samples, allowing the selection of representative tests for visualization and qualitative comparisons. For all off-axis tensile tests, no sliding was observed within the end-tabs during tensile testing.

The use of a 3D DIC system in this study enabled displacement measurements not only in the in-plane directions but also in the out-of-plane direction. Fig. 3.13 shows three out-of-plane (Z-axis) displacement fields, for different off-axis angle tests, at the same timestep (100s). The analysis of the displacement fields along the out-of-plane axis (Z) confirms the predominant in-plane response of the laminates, as evidenced by the minimal amplitude of out-of-plane displacements. However, a tendency of rotation by the loading axis is observed for the 15° off-

axis test (Fig. 3.13a). For the 45° off-axis angle, the rotation tendency follows a 45° line located at the center of the sample (Fig. 3.13c).

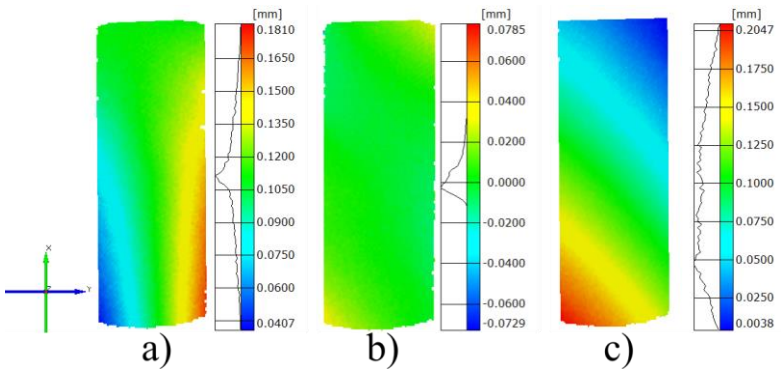

Fig. 3.13. Out-of-plane (Z-axis) displacement field, for different off-axis tests, at the same timestep (100s); a) 15° off-axis angle; b) 30° off-axis angle; c) 45° off-axis angle;

3.2.2.1 15° off-axis test

The axial stress-strain responses for all laminates and tested samples under 15° off-axis are presented in APPENDIX D, and the fracture position for each sample in APPENDIX E. Fig. 3.14 displays stress-strain responses of representative samples obtained with 15° off-axis tests.

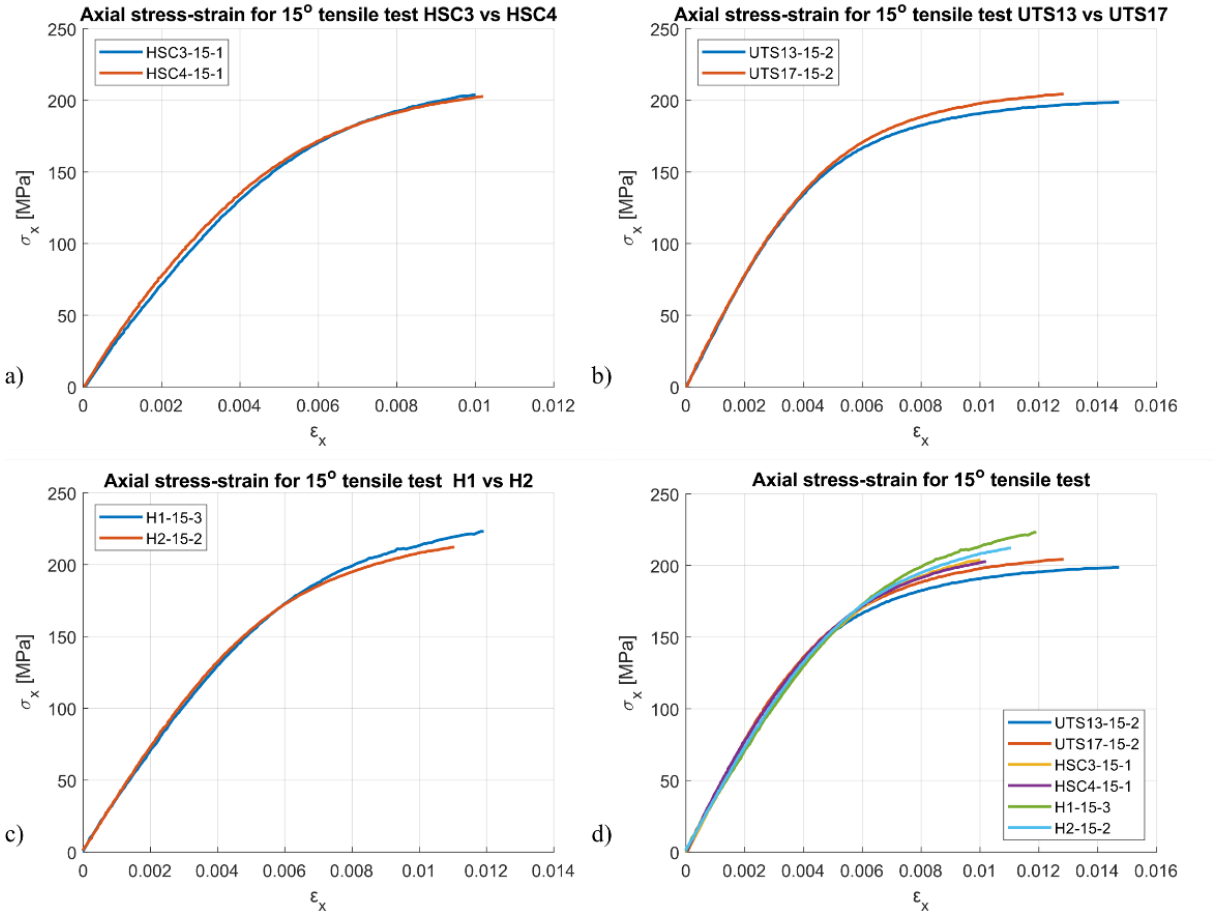

Fig. 3.14. Comparison of axial stress-strain response under 15° off-axis tensile test for representative samples of each laminate configuration; at 1 mm/min, from DIC analysis, a) HSC3 vs HSC4; b) UTS13 vs UTS17; c) H1vs H2; d) Simple and hybrid configuration materials

All laminates exhibit a high nonlinear stress-strain response, with the nonlinear regime starting at a stress level of 110-120 MPa. Notably, laminates HSC3 and HSC4, respectively 1.69 and 2.24 mm thick, manufactured from HSC plies, show no apparent thickness effect on the stress-strain response (Fig. 3.14a). Unlike HSC samples, UTS13 and UTS17 laminates

manufactured from UTS laminates, with respective thicknesses of 2.10 and 2.70 mm, exhibit a small difference in stress level in the nonlinear region (Fig. 3.14b), indicating a strain hardening for UTS17 laminates compared to UTS13.

The void content could influence the strain-hardening response of the materials, as the concentration of stress in the void vicinity can lead to localized deformation and internal failure, reducing the overall strain-hardening capacity of the material. However, UTS13 and UTS17 have similar fiber and void content [224], thus these properties do not represent a factor of influence on the difference in strain-hardening behavior. The thickness of the laminates could influence the strain hardening behavior, as in a thicker laminate there is more potential for fiber-dominated deformation mechanisms, such as fiber sliding and reorientation, which can enhance the strain hardening behavior. However, this response is not observed for the HSC thin-thick laminate pair. Among hybrid laminates, H2, the thicker laminate, exhibits less strain hardening than H1 (Fig. 3.14c), suggesting that the thickness of the laminate might not play a major role in the strain-hardening behavior for the tested laminates. Still, among other reasons, the different strain hardening responses between the hybrid laminates could be attributed to a difference in void content. Although under 1%, the average void content of H2 is twelve times higher than for H1 [224].

The comparison of the stress-strain response under 15° off-axis tensile loading using representative tests for each material configuration is presented in Fig. 3.14d. Differences in the linear response regime are negligible, but in the nonlinear response regime, HSC laminates show more strain hardening compared to UTS laminates, with a smaller failure strain. Both hybrid laminates reach higher stress levels than simple laminates and have intermediate failure strain. These different behaviors cannot be attributed only to the void content of the materials, as H2 and UTS laminates have similar void content, suggesting that ply-level hybridization triggers a strain-hardening effect.

Table 3.3. Experimental results 15° off-axis tensile testing at 1 mm/min, deduced from DIC analysis.

Material	UTS13	UTS17	HSC3	HSC4	H1	H2
E_x [GPa]	39± 2	40 ± 2	36± 2	39	34 ± 3	38 ± 2
Failure Stress σ_x [MPa]	199 ± 1	200 ± 11	204 ± 2	203	218 ± 12	212.2 ± 0.5
Failure strain ε_x	0.015 ± 0.001	0.012 ± 0.002	0.0100 ± 0.0002	0.0102	0.011 ± 0.002	0.0106 ± 0.0005
ν_{xy}	0.45 ± 0.01	0.47 ± 0.02	0.457 ± 0.005	0.46	0.44 ± 0.02	0.42 ± 0.02

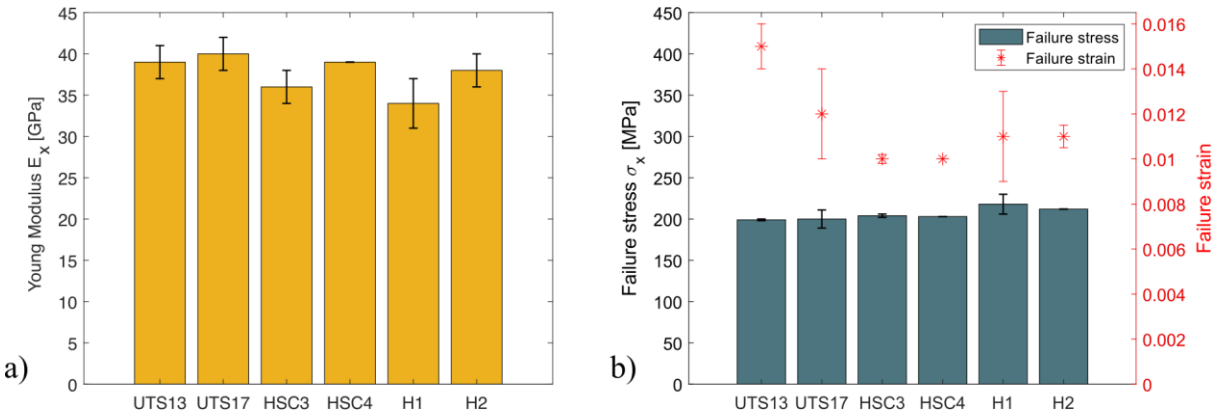

Fig. 3.15. 15° off-axis results comparison for all laminate configurations, with error bars representing half the range of measurements; a) Apparent modulus of elasticity E_x; b) Failure stress on the left axis and Failure strain on the right axis

The average values of the extracted apparent Young's modulus, failure stress, and failure strain as well as the Poisson ratio for all laminates are detailed in Table 3.3, with uncertainties as half the range of measurements. Discrepancies up to 6 GPa are found between the average values of the apparent modulus of all material configurations. A comparison of the average values of the apparent Young modulus is also shown in Fig. 3.15a, and small differences were found between the average values of the apparent modulus of all material configurations. It can be observed that the UTS laminates exhibit the highest apparent modulus, as expected given the fact that these laminates also have the highest in-plane modulus E_{11} of all tested laminates [224]. This is due to the fact that UTS carbon fibers have an inherently higher elastic modulus compared to HSC carbon fibers. Moreover, Wang et al. [225] showed that the fiber volume fraction also influences the elastic modulus of unidirectional composites. Considering the fiber volume fraction of the laminates, presented in section 2.2.2, the small differences in fiber content might represent an additional reason for variations in the elastic modulus. While it was expected for HSC laminates to have the lowest apparent modulus, as they have the lowest in-plane modulus E_{11} and fiber content [224], no clear trend is observed for HSC laminates and hybrid laminates. H1 has the lowest average apparent Young modulus, while H2 has an average value between the apparent modulus of HSC3 and HSC4. As a strong interfacial bond enhances load transfer and contributes to a higher apparent Young's modulus, while a weak or incompatible interface can result in stress concentration and reduced stiffness, for hybrid laminates, a lower apparent modulus could be due to a weaker interfacial bond at the interface between different types of plies. Compatibility of the matrix system should not represent an issue, as in the technical data of the matrix systems the manufacturer states that they are compatible for curing together. However, more investigations have to be conducted to assess the bond quality of the plies.

Regarding the failure stress and failure strain, also shown in Fig. 3.15b, the UTS laminates exhibit the lowest average failure stress and the highest failure strain, which is reflected in the stress-strain behavior as an almost plateau response before failure. These laminates also show the most pronounced nonlinear behavior of all. As previously mentioned, UTS17 shows a strain hardening compared to UTS13, and although the average failure stress is almost the same, the range of measurements for UTS17 was higher, potentially leading to higher failure stress. For failure strain, UTS13 has a higher failure strain by 16% (with uncertainties included). For HSC laminates, no significant difference is observed between HSC3 and HSC4 and compared to UTS laminates, they exhibit higher failure stress (approximately 2% increase) but lower failure strain (approximately 32% decrease compared to UTS13). For hybrid laminates, H1 has a higher average failure stress than H2, with a percentage increase of almost 3%, but also has a higher uncertainty. As more H1 samples were tested compared to H2, the possible occurrence of premature failure due to local material defects increases. Still, the increased scatter complicates the judgment and assessment of failure stress values, in comparison to the response of H2 material. Additional analysis is required to establish an appropriate criterion for judging the failure stress in H1, as compared to failure stress in H2. However, even if the lowest values of failure stress are considered, both hybrid configurations have higher failure stress compared to UTS and HSC laminates. In terms of the average value of the failure stress, H1 exhibits a 9% increase compared to UTS laminates and a 6% increase compared to HSC laminates, while for H2 the percentage increase is lower, with 6% compared to UTS laminates and 4% compared to HSC laminates. In terms of average failure strain, the values for the hybrid laminates are between the values for reference laminates, with an approximately 8% increase between H1 and HSC4, a 4% increase between H2 and HSC4, and a percentage decrease of 26% and 29% between UTS13 and H1 and H2, respectively.

3.2.2.2 30° off-axis test

Similar to the analysis performed for the 15° off-axis tensile test, the axial stress-strain response for all material configurations is presented in APPENDIX D, and the fracture position

for each sample in APPENDIX E. Good repeatability was obtained for all tested laminate types, with higher variations only for the failure stress and strain.

As for the 15° off-axis tensile test, a high nonlinear stress-strain response is observed in Fig. 3.16 for all laminates during the 30° off-axis test, with the nonlinear regime starting at a stress level of 50-60 MPa, which is half of the stress level observed in the 15° off-axis tensile test. No apparent thickness effect was observed for laminates made from the same material when analyzing the response of laminate pairs in Fig. 3.16a-c.

Fig. 3.16d displays a comparison of the stress-strain response under 30° off-axis tensile loading using representative tests for each material. The response in the linear regime is similar across all laminates, while in the nonlinear regime, UTS laminates exhibit a more pronounced nonlinear response than HSC laminates and hybrid configurations. Similar to the 15° off-axis test, hybrid laminates demonstrate strain hardening compared to reference laminates, reaching higher stress levels at the same strain value.

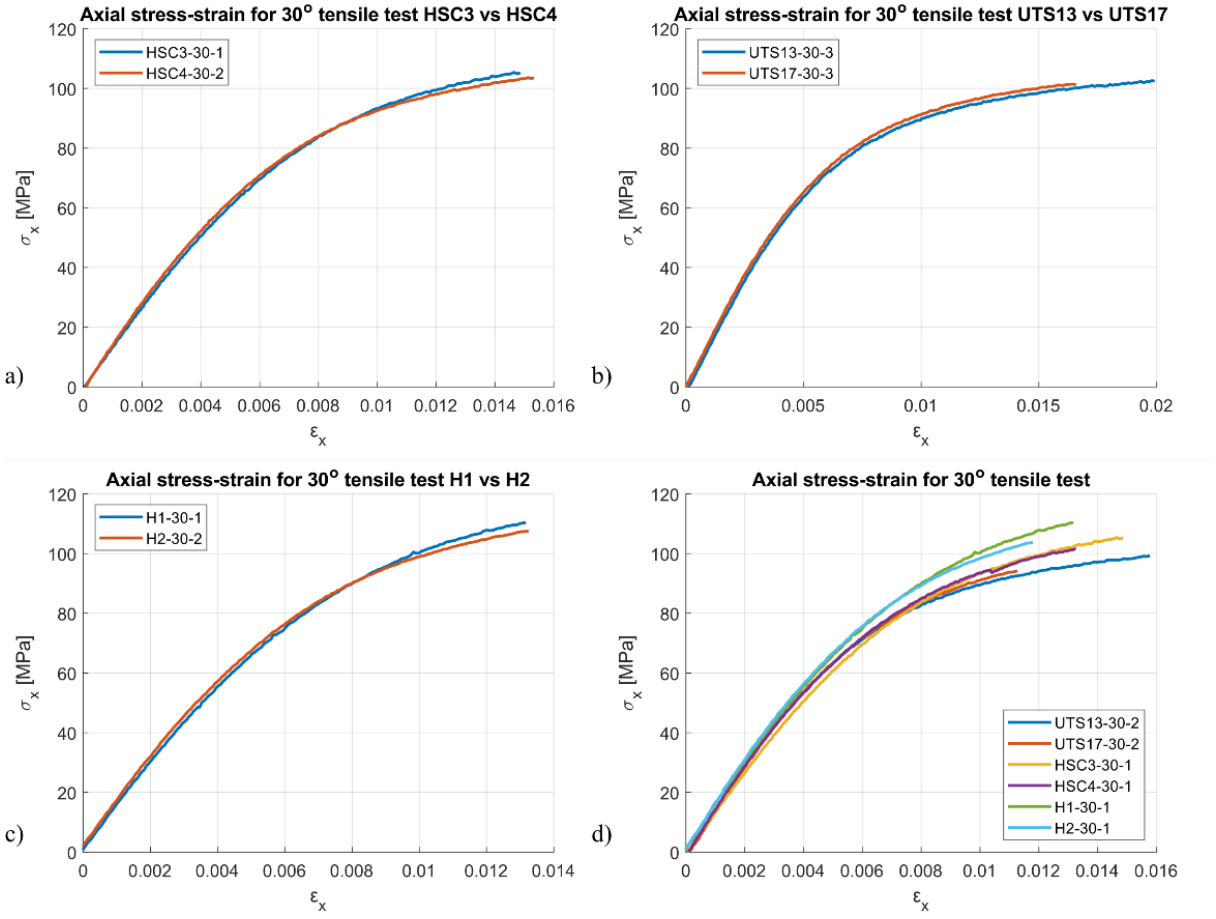

Fig. 3.16. Comparison of axial stress-strain response under 30° off-axis tensile test at 1 mm/min from DIC analysis, for representative samples of each laminate configuration; a) HSC3 vs HSC4; b) UTS13 vs UTS17; c) H1vs H2; d) Simple and hybrid configuration materials

Table 3.4 shows the average values of the extracted apparent Young's modulus, failure stress, failure strain, and Poisson ratio for all laminates during the 30° off-axis test, with uncertainties as half the range of measurements. Moreover, a comparison of the average values of the apparent Young modulus is also shown in Fig. 3.17a. Differences between the average values of the apparent modulus of all material configurations do not exceed 1.5 GPa, representing a 10% increase in the apparent elastic modulus for H2 (highest average apparent modulus) compared to HSC3 (lowest average apparent modulus).

For the failure stress and strain, the differences between sample groups are more pronounced, as can be seen in Fig. 3.17b. Samples H2-30-3 and HSC4-30-3 were not considered for the calculation of the average failure stress and strain because they failed at a much lower

stress value, compared to the other samples of the same materials. As was the case for the 15° off-axis tensile test, the UTS laminates have the lowest failure stress and the highest failure strain. HSC laminates have a higher failure stress and lower strain compared to UTS laminates but when looking at the hybrid configurations, they have the highest failure stress (a percentage increase of ~7% compared to UTS17) and lowest failure strain (a percentage decrease of ~47% between UTS13 and H2).

Table 3.4. Experimental results 30° off-axis tensile testing at 1 mm/min deduced from DIC analysis.

Material	UTS13	UTS17	HSC3	HSC4	H1	H2
E_x [GPa]	15.3± 0.2	15.1 ± 0.5	14± 0.5	14.8± 0.4	15 ± 1	15.4 ± 0.1
Failure Stress σ_x [MPa]	101 ± 2	99 ± 4	104 ± 2	103 ± 1	106 ± 6	105 ±2
Failure strain ε_x	0.019 ± 0.003	0.015 ± 0.003	0.0140 ± 0.001	0.013± 0.003	0.012 ± 0.002	0.010± 0.004
ν_{xy}	0.45± 0.01	0.46 ± 0.04	0.44 ± 0.02	0.40± 0.03	0.44 ± 0.02	0.43 ± 0.02

There is no significant difference between HSC3 and HSC4, while compared to UTS laminates, HSC laminates have higher failure stress with a percentage increase of approximately 4%. However, a percentage decrease of approximately 31% was found between UTS13 (this laminate was chosen for reference as it has the highest failure strain) and HSC laminates in terms of failure strain. Between hybrid laminates, no significant difference is observed in terms of failure stress, however, H1 exhibits a higher failure strain in comparison with H2, however, it is in the range of uncertainties for H2.

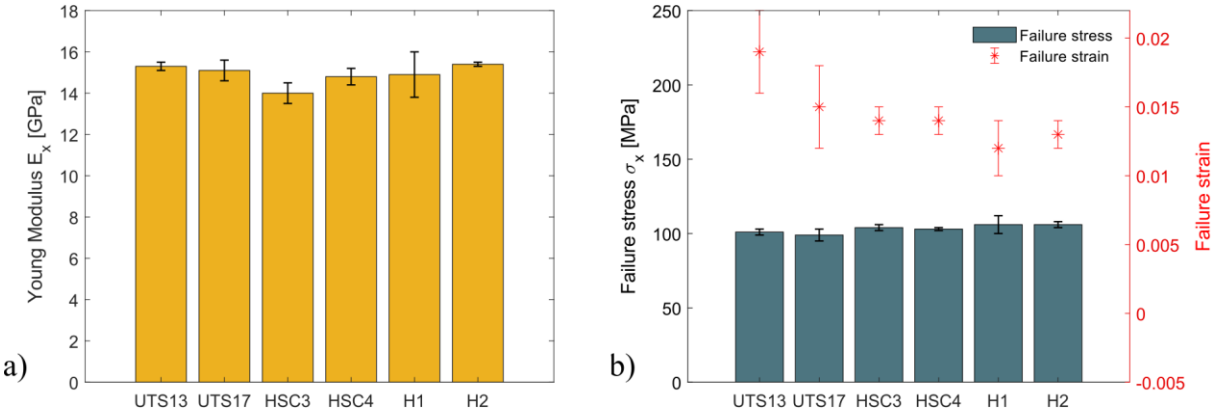

Fig. 3.17. 30° off-axis results comparison for all laminate configurations, with error bars representing half the range of measurements; a) Apparent modulus of elasticity E_x; b) Failure stress on the left axis and Failure strain on the right axis

Upon analyzing the strain distribution in the matrix direction (2) as shown in Fig. 3.18, which was calculated by rotating the original coordinate system at 30°, it becomes evident through DIC observations that at the sample's edge, denoted by a red circle, a matrix strain of 7.87% is present. This is in contrast to the strain of less than 1.5% observed in the remaining portion of the sample. Comparing the position of the strain concentration with the position of the fracture in the image after failure, it was concluded that failure started from the edge of the sample, with a matrix failure due to the high strain in the region. It may be assumed that for the other samples, including for other off-axis angles, the failure started similarly. In Hu's work [106], analysis of the strain fields obtained through DIC for the 45° specimens revealed that the highest strain occurs at the corner of the sample's edge as well.

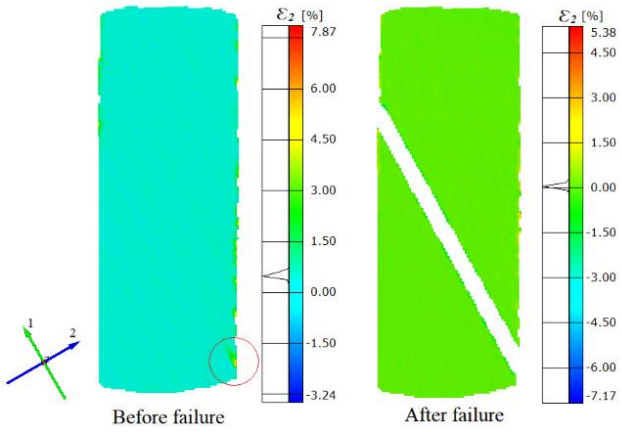

Fig. 3.18. Transverse strain field ε_2 deduced from the Digital Image Correlation for the H1-30-3 sample, under 30 off-axis tensile tests; before failure (left) and after failure (right)

3.2.2.3 45° off-axis test

Representative tests at 45° off-axis were selected for each material and comparisons are illustrated in Fig. 3.19, while the stress-strain response of all tested laminates is presented in APPENDIX D, and the fracture position for each sample in APPENDIX E. All material systems display a nonlinear regime beginning at around 30-40 MPa stress level, although this effect was less pronounced compared to the stress-strain response for 15° and 30° off-axis angles.

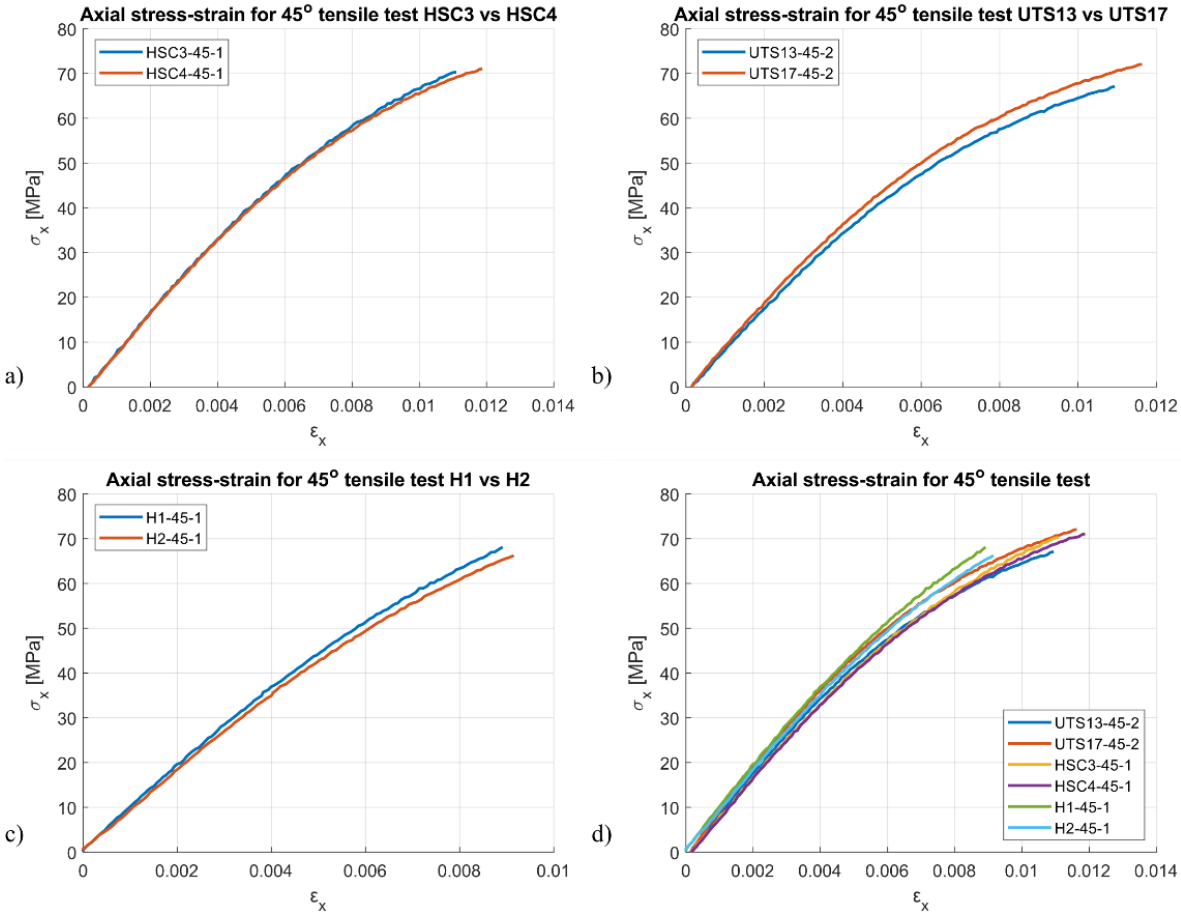

Fig. 3.19. Comparison of axial stress-strain response under 45° off-axis tensile test at 1 mm/min, measured by DIC, for representative samples of each laminate configuration; a) HSC3 vs HSC4; b) UTS13 vs UTS17; c) H1vs H2; d) Simple and hybrid configuration materials

There is no apparent thickness effect observed for UTS laminates and HSC laminates. Fig. 3.19d shows a comparison of the stress-strain response of representatives of all material types,

and the same strain hardening for the hybrid laminates compared to the reference ones can be observed. Although the difference in the value of the stress is not as high as for previously analyzed off-axis angles, the percentage increase in stress level is still around 10%.

Table 3.5 provides the average values of the apparent Young's modulus, failure stress, failure strain, and Poisson ratio for all laminates, with uncertainties as half the range of measurements. A comparison of the average values of the apparent Young modulus is also shown in Fig. 3.20a. The differences between the average values of the apparent modulus for all material configurations are very small, with less than 0.5 GPa difference. H2 has the highest apparent modulus, while HSC3 has the lowest, with a percentage increase of approximately 3% instead of 10%, as it was for the 30º off-axis angle test.

The differences in failure stress and failure strain are more noticeable, with UTS laminates displaying the highest values and both hybrid laminates having the lowest average failure stress and lowest failure strain, as illustrated in Fig. 3.20b. Although H1 and H2 reach higher stress levels compared to HSC and UTS laminates for the same strain value in the nonlinear response regime, the failure stress is also the lowest due to a very low failure strain. Additionally, 45° off-axis samples were more prone to fail near the grips than 15° and 30° off-axis samples, which could also influence the values of failure parameters.

Table 3.5. Experimental results 45° off-axis tensile testing at 1 mm/min from DIC.

Material	UTS13	UTS17	HSC3	HSC4	H1	H2
E_x [GPa]	9.3± 0.1	9.3 ± 0.5	9.1± 0.2	9.1± 0.1	9.2 ± 0.2	9.4 ± 0.4
Failure Stress σ_x [MPa]	70 ± 3	72 ± 2	67 ± 4	69 ± 5	60 ± 12	67 ± 2
Failure strain ε_x	0.012 ± 0.002	0.013 ± 0.001	0.010 ± 0.001	0.011 ± 0.002	0.008 ± 0.002	0.009 ± 0.001
ν_{xy}	0.34 ± 0.02	0.35 ± 0.01	0.35 ± 0.01	0.35 ± 0.01	0.34 ± 0.02	0.35 ± 0.01

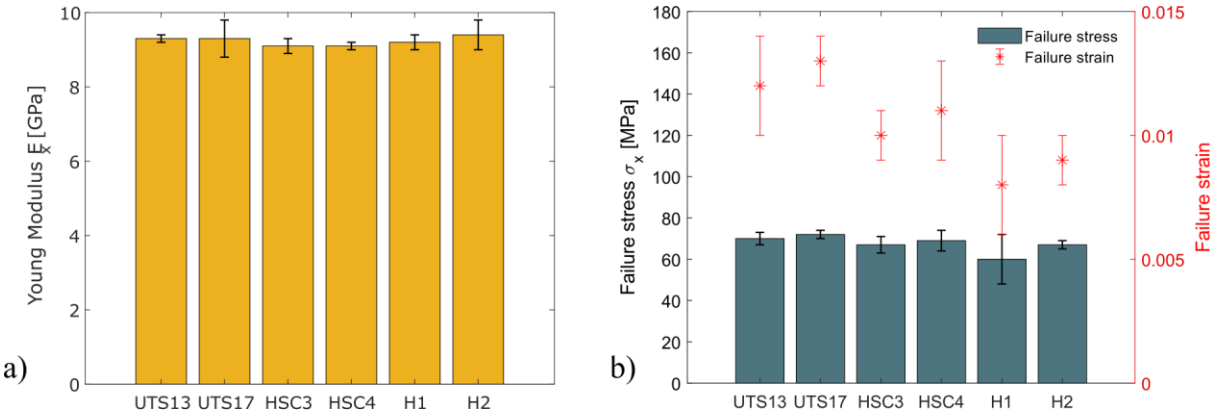

Fig. 3.20. 45° off-axis results comparison for all laminate configurations, with error bars representing half the range of measurements; a) Apparent modulus of elasticity E_x; b) Failure stress on the left axis and Failure strain on the right axis

3.2.2.4 Stress to fiber orientation response

Since the stress-strain response of each specimen in the same test configuration fluctuated slightly, for the sake of comparison of the results for various off-axis angles, only one specimen in each loading condition was selected as representative, for a qualitative comparison. Fig. 3.21 shows the stress-strain response under uniaxial tension at various angles for all material configurations. The response for the 0° test was truncated to have a clearer view of the response at the other angles. Each material shows an increased nonlinear response with decreasing off-

axis angle. Similar results were also reported by Zhao et al. [226] for T300/7901 unidirectional composite. Furthermore, there is a reduction in the apparent elastic modulus as the off-axis angle increases. It can also be observed that for all off-axis angles, in the nonlinear response region, the hybrid materials reach higher stress levels at the same strain value than the materials manufactured only from UTS or HSC plies, as previously mentioned. Furthermore, the stress level difference between the response of the materials increases with increasing nonlinearity in the stress-strain response - for the 15° tensile test the difference in the reached stress level is more visible compared to the response under the 45° tensile test.

For the ultimate strain reached, there is a downtrend with increasing angle, except the 30° test for which, both in individual and averaged comparison, the ultimate axial strain reached is higher than for the 15°. The lowest ultimate strain is for θ=90°, as expected.

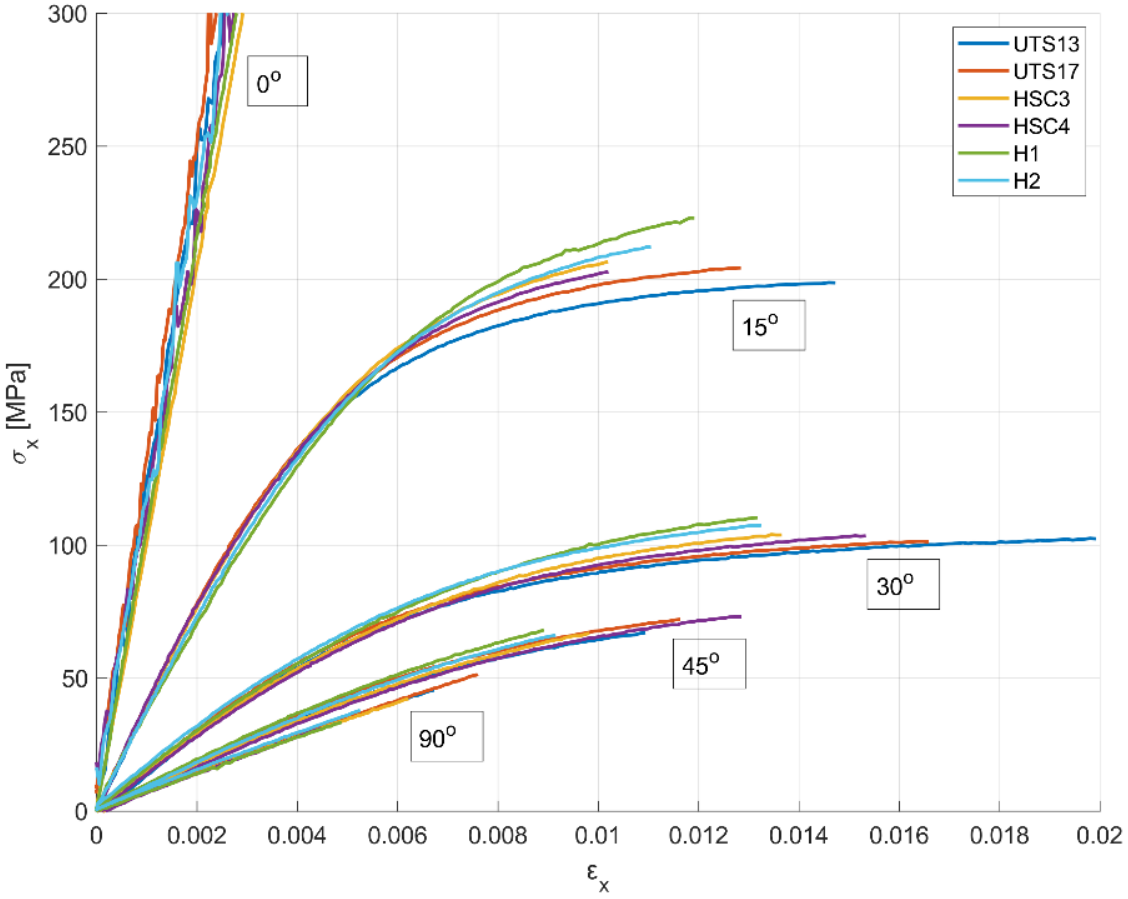

Fig. 3.21. Stress-strain curves obtained by DIC of on and off-axis specimens at 1 mm/min

The results of the apparent axial elastic moduli E_x obtained from each off-axis angle are summarized in Fig. 3.22, by using the average value for each test configuration. A significant difference in the value of the apparent elastic modulus with respect to the off-axis angle can be observed. The variation between 45° and 90° is less pronounced. However, when contrasted with the elastic modulus for the 0° orientation, the apparent modulus at 45° and 90° represents only 7.3-8% and 5.5-6.3%, respectively, of the elastic modulus for 0°. The percentage interval is calculated based on the individual percentage for each material configuration. The measured moduli were also compared with the prediction based on the transformation relation in equation (1.9) in which the elastic properties along the principal material direction are used. The prediction agrees well with the experimental results for all material configurations, with, in the worst case, an overestimation of less than 12 %.

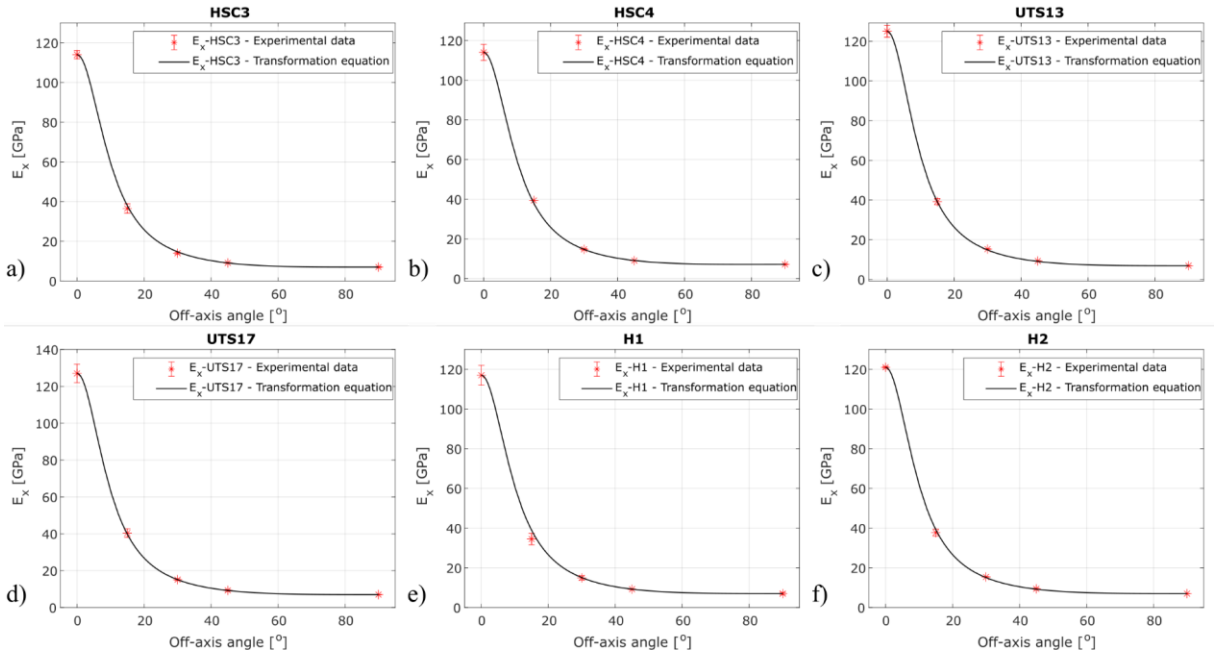

Fig. 3.22. Comparison of the apparent axial Young's modulus deduced from DIC (crosses) and calculated by the transformation equation (1.9) for various off-axis angles; a) HSC3; b) HSC4; c) UTS13; d) UTS17; e) H1; f) H2

For completeness, the results for apparent Poisson's ratio ν_{xy} are also presented in Fig. 3.23 and the experimental results are compared with the theoretical predictions of the transversely isotropic equation (1.10). Compared to the elastic moduli results, where the agreement is good between experimental data and prediction, for the apparent Poisson's ratio, there is a deviation in experimental data from the predicted response, for 15° and 30° off-axis angles. This deviation could be due to the end-constraint effects that were not accounted for, but further analysis must be employed in this regard. However, the trends observed in the experimental data are very similar to those predicted by the idealized model. Therefore, it can be concluded that both the reference materials as well as the ply-level hybrid carbon composite materials can be modeled as transversely isotropic systems.

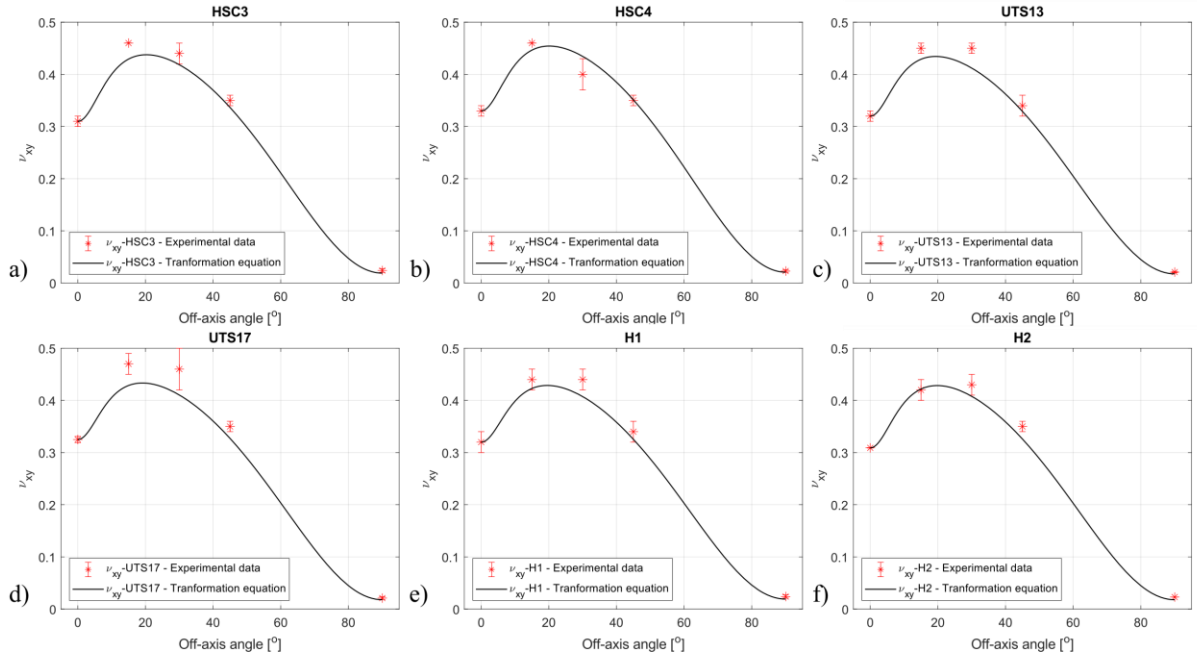

Fig. 3.23. Apparent Poisson ratio for various off-axis angles deduced from DIC (crosses) and determined by transformation equation (1.10); a) HSC3; b) HSC4; c) UTS13; d) UTS17

Regarding the failure stress, a significant reduction with increasing off-axis can be observed in Fig. 3.21 but the drop is better illustrated in Fig. 3.24, in which the averaged axial strength for each test configuration is presented. The same trend is observed for all laminate configurations. A sharp decline is observed when the off-axis angle increased from 0° to 15°, with a decrease in strength around 86-89%, depending on the material. Between the following consecutive off-axis angles, the decrease is not as significant as the first one, with 51-55% from 15° to 30°, 27-43% from 30° to 45° and 36-53% from 45° to 90°, but still, the lowest strength, for θ=90°, represents only 1.8-3% of the strength in 0°.

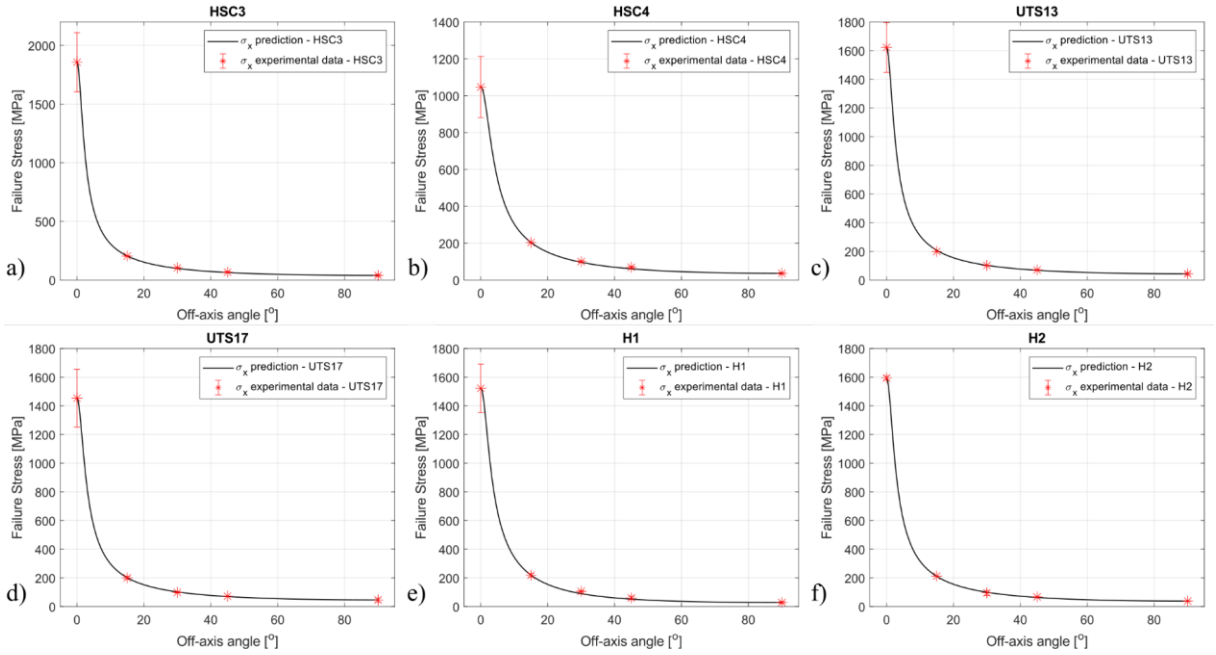

Fig. 3.24. Failure stress for various off-axis angles, with predictions based on Tsai-Hill criterion using equation (1.11) ; a) HSC3 – S=55 MPa; b) HSC4 – S=56 MPa; c) UTS13 – S=55 MPa; d) UTS17 – S=53 MPa; e) H1 – S=65 MPa; f) H2 – S=57 MPa

Predictions of the failure stress were also made using the Tsai-Hill failure criterion for uniaxial off-axis strength, detailed in equation (1.11). The predictions agree well with the experimental data for the adjusted shear strength *S* of each material configuration. The *S* values used for fitting the Tsai-Hill failure criterion to the experimental data are mentioned in the figure's caption, as well as in section 3.2.3.

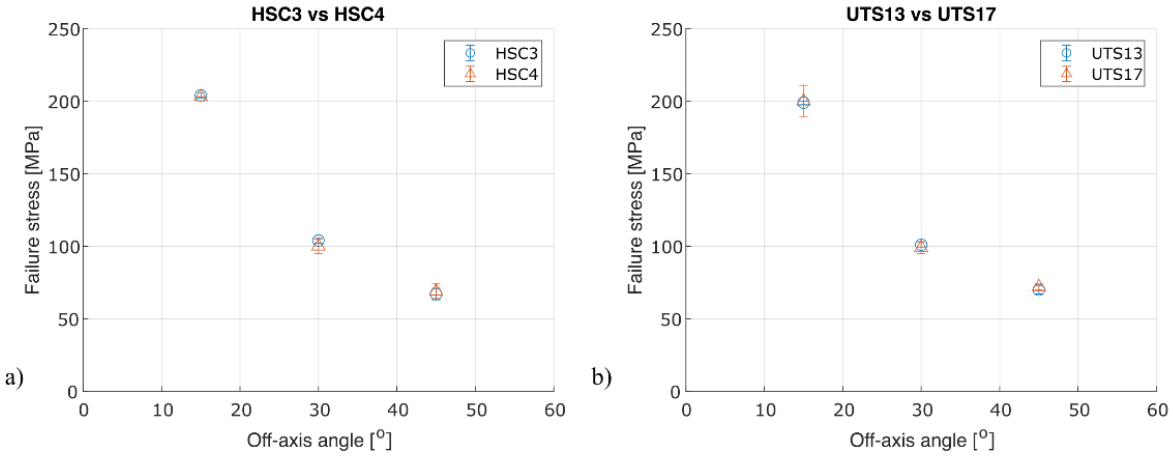

Fig. 3.25. Failure stress comparison for various off-axis angles for laminates with different thicknesses; a) HSC3 and HSC4 laminates of respective thicknesses of 1.69 and 2.24 mm; b) UTS13 and UTS17 laminates of respective thicknesses of 2.10 and 2.70 mm

Regarding the thickness effect on the failure stress under off-axis tensile testing, Fig. 3.25a shows a clearer comparison of the average failure stress of HSC laminates, and for UTS laminates the comparison is illustrated in Fig. 3.25b. Almost no difference in average off-axis strength is observed with increasing thickness of the laminate, for all tested angles.

3.2.3 In-plane shear properties results

As in this study one of the materials is a hybrid non-symmetric unidirectional composite material, ±45° test cannot be used for shear characterization. To easily obtain the in-plane shear modulus, the 45° off-axis test has been selected, based on Pindera's work [98], [99]. Because off-axis tensile tests are also performed for 15° and 30° off-axis angles, the shear modulus will also be evaluated from 15° and 30° off-axis tensile tests to compare the results with the modulus extracted from 45° off-axis test.

The shear properties results were extracted from off-axis tests as mentioned in section 1.2.3. The shear strain extracted from the GOM Aramis® software represents the tensorial shear strain ε_{xy} which is half the engineering shear strain γ_{xy}. The same applies to the strains in the local coordinate system of the sample, with 1–axis in the fiber direction. Therefore, when analyzing the DIC full-field contour plots, the values for shear strain represent the tensorial shear strain, leading to a difference in values compared to the shear stress-strain plots in which the engineering shear strain was considered.

The calculated shear strain γ_{12} based on equation (1.13), extracted from the 45° off-axis test was also compared with the shear strain extracted directly from the GOM Aramis® software after rotating the coordinate system with 45°, and a minor difference between the two was observed. Thus, the shear strain calculated with equation (1.13) was further used, regardless of the off-axis angle. For the employed coordinate system, shear strain values are represented as negative. Throughout all plots, the absolute values of the shear strain are employed.

As both shear stress τ_{12} and shear strain γ_{12} are extracted from axial stress and strain using coordinate transformation equations, the shear stress-shear strain curves for the tested samples of all materials have the same good reproducibility as for the off-axis tensile test from which they were extracted. Therefore, only representatives of each material configuration will be used to illustrate the shear response.

A comparison of the shear response extracted from different off-axis angles is shown in Fig. 3.26, for all tested materials. In every case the response is nonlinear and the nonlinear shear response for unidirectional carbon fiber reinforced composites was also reported in [101], [117], [134], [227]. It can be seen that the same observations made for the axial stress-strain response of corresponding tests are applicable. In all cases, the hybrid laminates present a strain hardening in the nonlinear response regime, which leads to higher stress levels at the same strain values compared to reference materials.

The average values of the in-plane shear modulus extracted from all off-axis test types are given in Table 3.6, with uncertainties as half the range of measurements. It can be observed that for all materials, except H1, the shear moduli extracted from 15° and 30° are higher than the ones extracted from the 45° off-axis test. A similar observation was also made by Pindera et al. [98] but with a higher difference in the values of the shear modulus extracted from different off-axis angle tests. They concluded that the 45° off-axis test is the most reliable in estimating the in-plane shear modulus, as the effects of end constraints are minimized compared to other angles. This is why, for further calculations, the modulus extracted from the 45° off-axis test will be used.

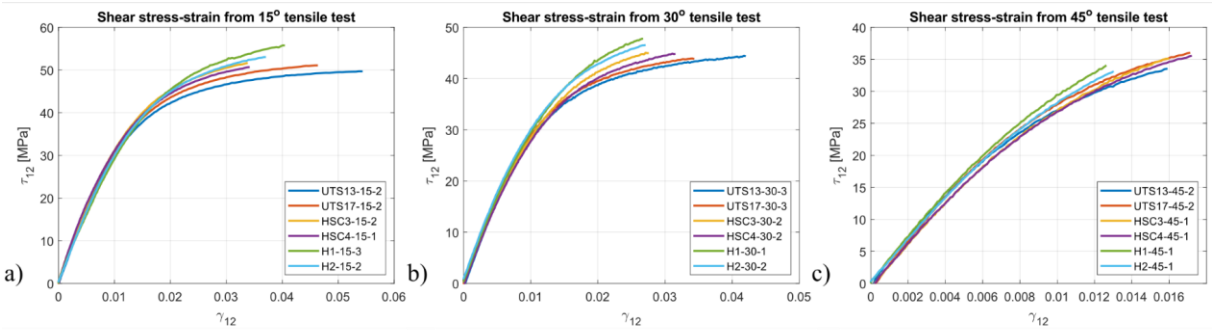

Fig. 3.26. Shear stress-strain response comparison using representative samples of each material configuration; a) θ=15°; b) θ=30°; c) θ=45°

Table 3.6. Shear modulus G_{12} values from off-axis tensile testing

Material	UTS13	UTS17	HSC3	HSC4	H1	H2
G_{12} from 45° [GPa]	3.42 ± 0.04	3.48 ± 0.22	3.40 ± 0.05	3.38 ± 0.02	3.49 ± 0.04	3.48 ± 0.17
G_{12} from 30° [GPa]	3.56 ± 0.01	3.49 ± 0.07	3.22 ± 0.12	3.42 ± 0.09	3.46 ± 0.21	3.56 ± 0.02
G_{12} from 15° [GPa]	3.74 ± 0.64	3.64 ± 0.20	3.64 ± 0.10	3.8	3.32 ± 0.95	3.50 ± 0.23
Shear failure stress τ_{12} from 45° [MPa]	35 ± 2	36 ± 1	33 ± 2	34 ± 3	30 ± 6	33 ± 1
Shear failure stress τ_{12} from 30° [MPa]	43.9 ± 0.7	43 ± 2	45± 0.7	43± 2.2	46 ± 3	41 ± 7
Shear failure stress τ_{12} from 15° [MPa]	49.8 ± 0.3	50± 3	51 ± 0.6	50.7	54 ±3	53.1 ±0.1
Shear failure stress estimation using Tsai-Hill failure criterion* [MPa]	55	53	55	56	65	57

**S* parameter that was adjusted to fit Tsai-Hill failure criterion to off-axis failure stress experimental data.

In the same Table 3.6, the average values of the shear failure stress are given, as well as the values used as the shear strength parameter *S* in Tsai-Hill failure criteria, in section 3.2.2.4. The shear stress extracted from the 15° off-axis tensile test is much higher than the one extracted from the 30° or 45° off-axis tensile test. Therefore, due to this high variation, the shear failure stress extracted from off-axis tensile tests is not reliable. It can also be observed that for all materials, the values of the experimental shear failure stress extracted from off-axis tensile tests are below the value of the shear strength for which the axial failure stress prediction using Tsai-Hill failure criteria fits the experimental data. Thus, the shear failure stress from off-axis tensile tests with $\theta \geq 15°$ is underestimated and not reliable.

An example of a full-field analysis of the shear strain distribution, for specific points selected from the shear stress-strain curve, is presented in Fig. 3.27 for a sample of H1 material, under 45° off-axis test. As the in-plane shear response is nonlinear, four points on the shear stress-strain curve of the sample were chosen for the analysis of in-plane shear distribution. These points are highlighted in Fig. 3.27. The first one was chosen to be in the linear response region, the second one near the beginning of the nonlinear region, the third point at a higher shear strain in the nonlinear response region, and the fourth point near the failure. Moreover, the original coordinate system (X – loading direction, Y – perpendicular to the loading direction) was rotated at 45°. Therefore, the coordinate system in the color maps represents the

coordinate system in the material principal direction, with 1 – in the fiber direction and 2 – perpendicular to the fiber direction.

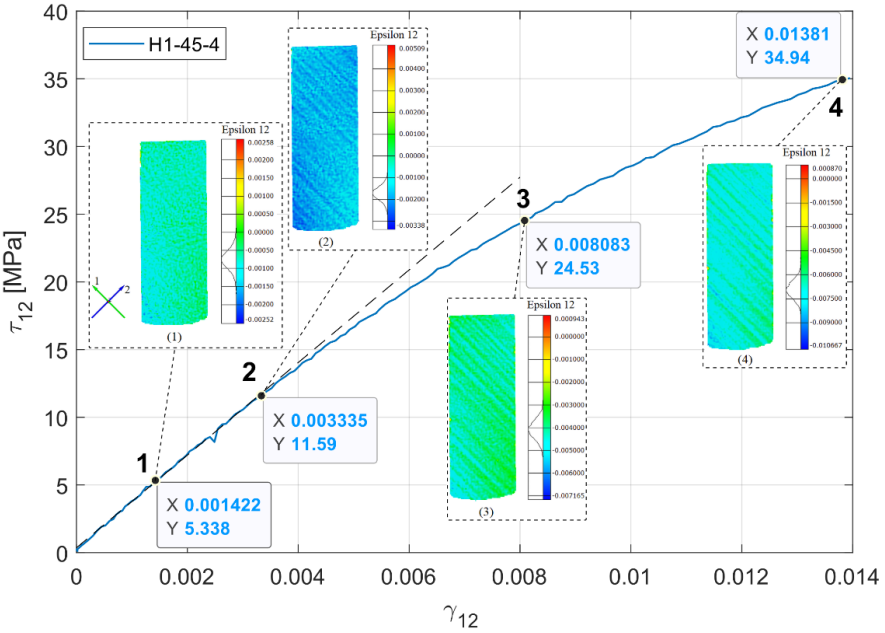

Fig. 3.27. In-plane shear stress-strain response with corresponding points for DIC full-field analysis, for tensile test on H1-45-4 sample at 1 mm/min. Color maps show in-plane ε_{12} full-field distribution from Digital Image Correlation analysis, at different time steps during 45° off-axis test

When comparing the shear values in Fig. 3.27 it must be mentioned that in the color maps, the values represent the tensorial strain ε_{12} which is half the engineering shear γ_{12}, used in all shear stress-strain plots. When looking at the in-plane shear distribution on the surface of the sample at different stages, it can be observed that at first, at point 1, the shear distribution is uneven, without a clear contour, compared to the other 3 points where the 45° angle of the fibers becomes visible in the distribution of shear strain. Near the failure point, in the fourth image, shear concentration points can be noted at the edges of the sample. This could imply that failure for these samples starts from their edge and propagates within the sample. Moreover, the lines of higher shear strain can be attributed to an increased shear strain in the matrix that bonds the fibers.

With the in-plane shear modulus determined, the compliance matrix can be determined for each laminate type, according to equation (1.1). The resulting matrices are given in APPENDIX F, using data from Table 3.1, G_{12} from 45° in Table 3.6, considering ν_{23}=0.4 from [228].

3.2.4 Damage assessment by Cyclic Load-Unload tensile tests

To investigate the nature of the nonlinear stress-strain response in off-axis tensile tests, cyclic load-unload tensile tests were performed for off-axis angles of 15°, 30°, and 45°. The number of cycles is limited to a maximum of six, to avoid low cycle fatigue phenomenon effects [129]. For 15° and 30° off-axis angles, a number of six cycles were considered, while for the 45° off-axis angle, only four were considered, as the maximum stress level reached was lower than for the other angles. To choose the unloading stress levels, the monotonic stress-strain response was analyzed. The first unloading stress level was chosen as being half the stress at which the nonlinear response begins. The second level was at the stress value where the nonlinear response begins and for the other unloading stress values, increments of 10 and 15 MPa were considered. Since the tests were conducted across two separate experimental campaigns, slight variations exist in the selected stress levels for each cycle for the H1 material in comparison to the other materials. This discrepancy arises because the H1 tests were conducted initially, and the stress levels chosen for this material proved excessive for certain reference materials. For the second experimental campaign, the stress levels were kept the same

for all tested materials, except the 30° off-axis angles test on UTS13. At first, higher values for the maximum stress of the cycle were set, and because not one UTS13 sample reached the 6th cycle, the maximum stress levels of the last cycles were decreased for the other materials. The actual values of the unloading stress levels that were imposed for each configuration are detailed in Table 3.7. From the cyclic load-unload tensile tests, the residual strains are evaluated and damage variables are estimated using the three methods mentioned in section 1.2.4. Details are also given in [229].

Table 3.7. Maximum load for each cycle of load-unload tests

Material	θ	C1 σ_{max} [MPa]	C2 σ_{max} [MPa]	C3 σ_{max} [MPa]	C4 σ_{max} [MPa]	C5 σ_{max} [MPa]	C6 σ_{max} [MPa]
H1	15°	72	145	160	175	190	205
	30°	30	60	70	80	90	100
	45°	22	44	55	65	-	-
H2, HSC3, HSC4, UTS13, UTS17	15°	65	120	140	160	180	190
	45°	20	40	50	60	-	-
H2, HSC3, HSC4, UTS17	30°	25	50	60	70	80	90
UTS13	30°	25	50	70	85	95	100

In general, good reproducibility was obtained for all configurations, thus, only representative samples are presented. The stress-strain response for all cyclic load-unload tests is shown in APPENDIX G. Fig. 3.28 shows the axial stress-strain response for representative samples of monotonic and cyclic load-unload, for each configuration. It can be observed that the cyclic envelope curve is coincident with the monotonic curve for all materials, at all tested off-axis angles. Only for the 15° off-axis angle, for UTS17, H1, and H2, the cyclic curve shows a small extent of strain hardening as the nonlinear deformation increases.

All cyclic load-unload tensile curves exhibit a nonlinear appearance, with residual strains with complete unloading. It suggests that the cause of the nonlinearity of the stress-strain response involves a plastic component. Moreover, the nonlinearity of the stress-strain curves during unloading was also observed, which leads to a decreased elastic modulus that has been attributed to internal damage [129], [132], [230]. Similar to monotonic off-axis results, UTS laminates exhibit a visible, more pronounced nonlinearity with increasing load, compared to HSC and hybrid laminates. Furthermore, for UTS13, the residual strain appears to be significantly higher than for other laminates, for the 15° and 30° off-axis angles. Moreover, all cyclic load-unload tensile curves exhibit hysteresis loops, with the width of the hysteresis loop decreasing with increasing off-axis angle.

A similar observation was made by Kawai and Negishi [231] for AS4/PEEK unidirectional composites. While studying the ratcheting behavior of unidirectional T300/7901carbon fiber composites loaded off-axis, Cheng et al. [232] observed that the nonlinear hysteresis behavior and ratcheting effect of each specimen under asymmetric stress cycles depend on the fiber orientation and peak loading stress. The size and shape of the hysteresis loop in each cycle remained unchanged for 100 cycles. Thus, it can be implied that the wider hysteresis loops with increasing cycle number, as well as decreasing off-axis angles are due to the increase in the maximum stress levels imposed for the cycles.

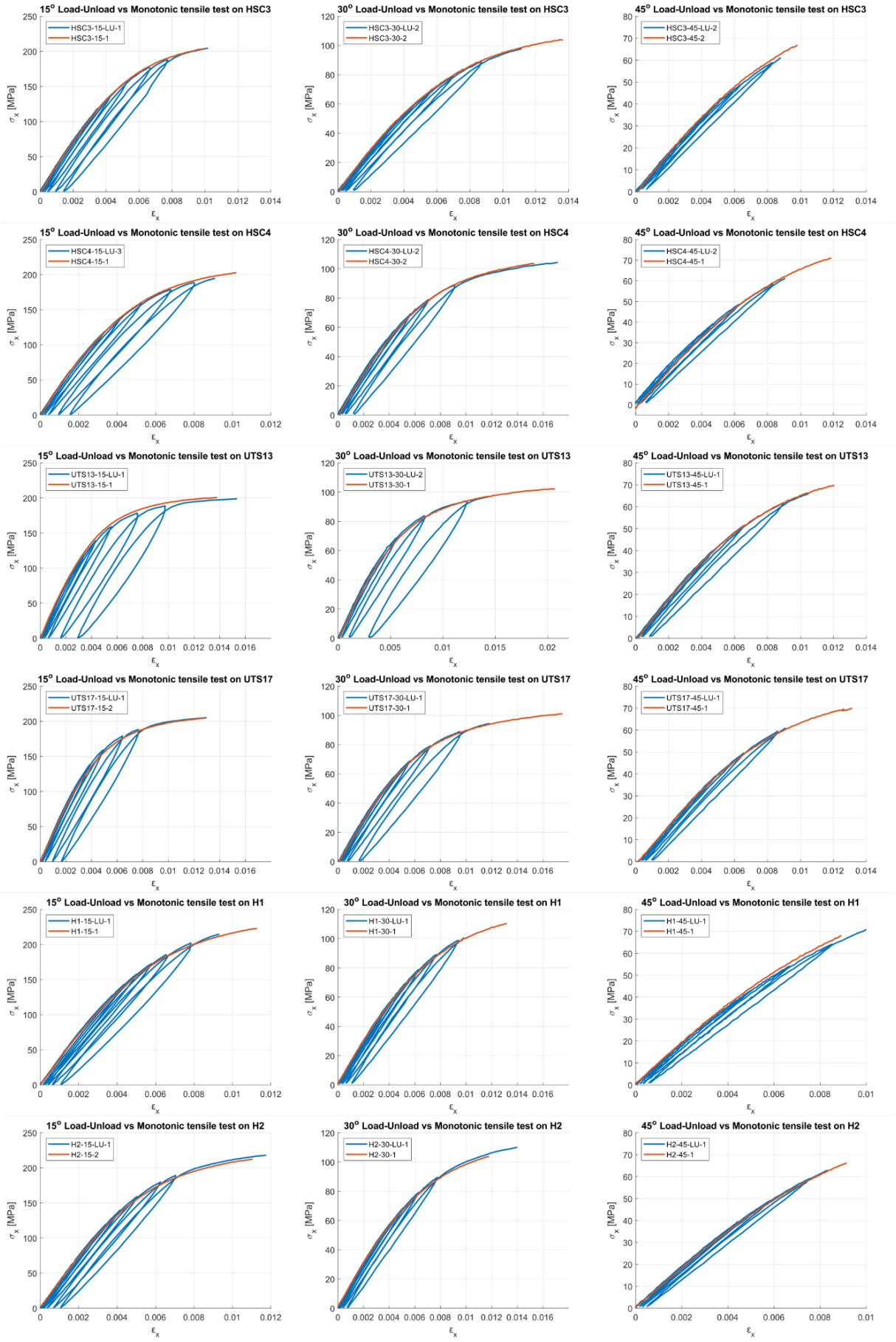

Fig. 3.28. Axial stress-strain response of representative samples for monotonic and load-unload off-axis tensile tests; Columns: 1st- 15°; 2nd - 30°; 3rd - 45°; Rows: 1st – HSC3; 2nd – HSC4; 3rd – UTS13; 4th – UTS17; 5th – H1; 6th – H2

3.2.4.1 Residual strain estimation

The first to be investigated is the residual strain. Fig. 3.29 illustrates the average residual strain at the unloading point versus the total strain of the cycle. The error bars represent half the measuring range.

For all configurations, the residual strain rapidly accumulates with each cycle, and its value increases as the prior maximum stress becomes larger, as also noted by Kawai and Negishi [231]. It also shows a dependence on the fiber orientation, as the residual strain in 15° samples is the highest and in 45° samples is the lowest. This could be due to the fact that for 15° off-axis tests, higher stress values for each cycle are imposed, compared to other off-axis angles. Moreover, for 15° samples, the residual strain has a sharp increase towards the last three cycles, while for 45° samples, the increase is almost linear after the second cycle. Again, the higher values imposed for 15° samples could be responsible. Moreover, a lower number of cycles was imposed for the 45°off-axis angle (4 cycles are imposed as opposed to 6 for the other angles). For all cases, the maximum stress for the first two cycles is chosen to be in the linear response regime, and as close to the transition point from linear to nonlinear response, leading to similar residual strain accumulation, regardless of the off-axis angle.

Furthermore, it was shown by Sinclair and Chamis [233] that when loaded off-axis, the fracture surfaces of unidirectional composites revealed resulted in distinct fracture modes based on the off-axis angles. Up to 30º, the fracture is mainly due to intralaminar shear stress, whereas fracture at 45° primarily indicates failure due to transverse tensile stress. Consequently, the different failure mechanisms could contribute to the observed differences in residual strain accumulation at different off-axis angles.

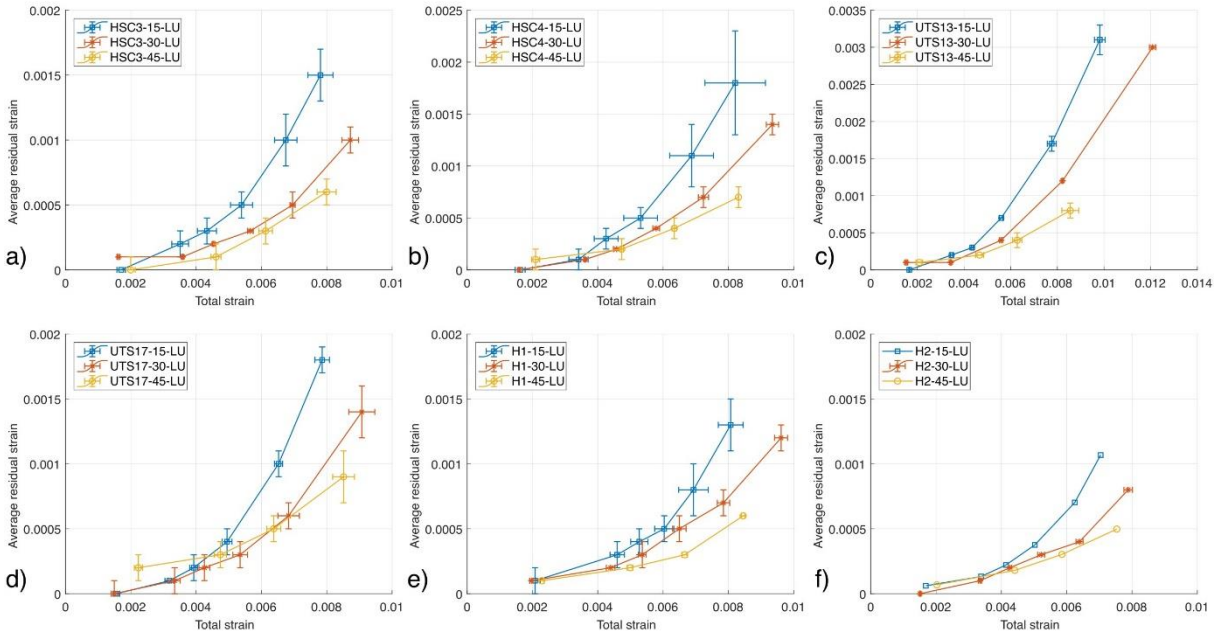

Fig. 3.29. Average Residual strain vs Average Total strain at 15° (blue), 30° (orange), 45° (yellow) off-axis angle; a) HSC3; b) HSC4; c) UTS13; d) UTS17; e) H1; f) H2

Fig. 3.30 shows in the first row a comparison of average residual strain versus average total strain between all tested materials, and in the second row, a comparison of average residual strain vs. cycle stress level is presented. By looking at the results from cyclic load-unload tests for 15° and 30° off-axis angles (1st column - 15°; 2nd column - 30°), it can be observed that in both cases UTS13 has the highest residual strain and it also reaches a significantly higher total strain by the last cycle, compared to other materials. Still, when analyzing the average residual strain versus average total strain (Fig. 3.30a and Fig. 3.30b), the evolution trend of the residual strain of UTS13 is similar to the evolution trend for UTS17, it only reaches higher values of both residual strain and total strain. If the evolution trend of average residual strain versus average maximum stress of the cycle (the value imposed in the test setup) is analyzed, for the

same stress levels, the residual strain of UTS13 has a sharper increase than UTS17, with a residual strain value of 1.7 times higher for the last cycle of 15° off-axis load-unload test. For the 45° off-axis angle (3rd column in Fig. 3.30), the shape of the residual strain evolution is similar for UTS13 and UTS17, with UTS17 having higher values. Overall, UTS laminates have the highest residual strains in all test cases, suggesting that the matrix in UTS prepreg has an inherent higher plasticity characteristic compared to HSC laminates.

The residual strains of HSC3 and HSC4 laminates have similar evolution for each off-axis angle, with very close values for the 15° off-axis angle. For the 30° and 45° off-axis angles, HSC4 has a higher increase in residual strain towards the last cycles compared to HSC3. A similar trend is also observed for the hybrid laminates, H1 and H2. In this case, the close values of residual strain are found for the 30° off-axis angle, while for 15° and 45° off-axis angles, H2 shows an increased residual strain towards the last cycles. Furthermore, it can be observed that in all cases, the hybrid laminates have lower residual strains compared to all reference laminates, for similar total strains. This fact suggests that the interaction between the different prepreg plies within the hybrid carbon laminates leads to a material with fewer residual strains, thus a more stable material, with a better ability to recover from displacements [234]. The lower residual strain for hybrid laminates, compared to HSC laminates could also be attributed to the fact that the hybrid laminates have less resin-rich regions compared to HSC laminates.

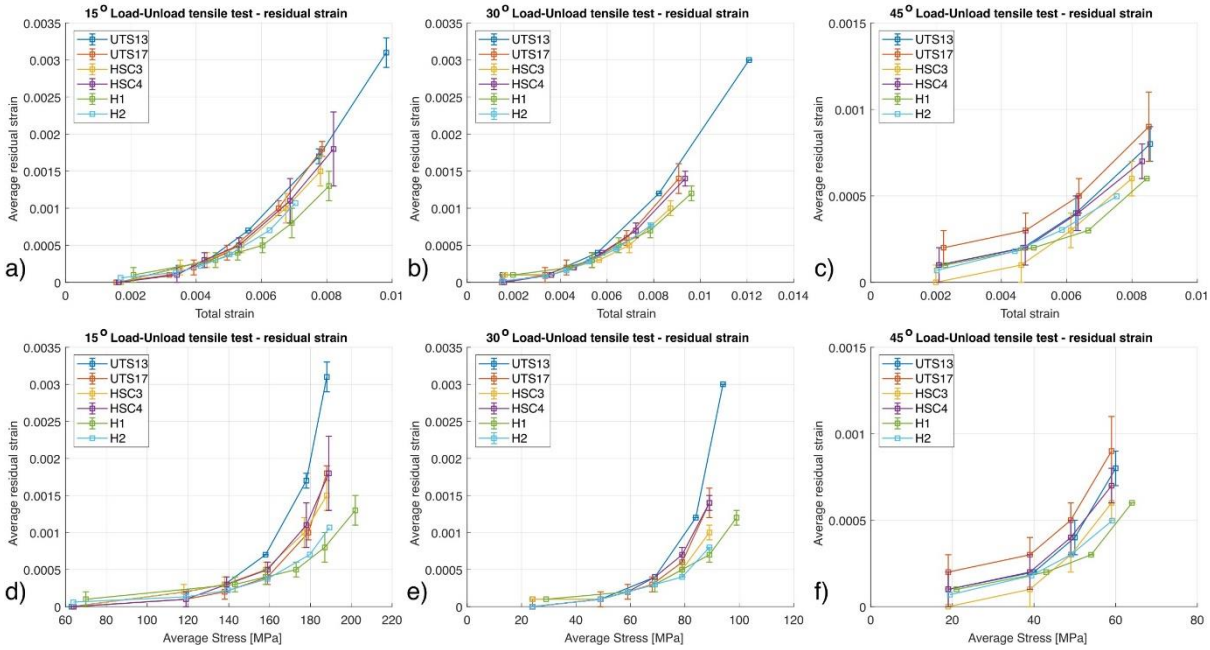

Fig. 3.30. Comparison of average residual strain vs cycle stress level; a) 15°; b) 30°; c) 45°; Comparison of average residual strain vs total strain; d) 15°; e) 30°; f) 45°

While there is a difference in the amount of accumulated residual strain for laminates of the same prepreg type with different thicknesses, for UTS laminates the thinner laminate exhibits a higher residual strain than the thicker laminate, and for HSC laminates the opposite occurs – the thicker laminate has a higher residual strain compared to the thinner one, for 15° and 30° off-axis angles, whereas for 45° off-axis angle, the thicker composite exhibits a higher residual strain than the thinner laminate, for both UTS and HSC composites. Although a thickness effect on the residual strain with complete unloading might exist, no clear conclusion can be drawn for the tested laminates, and additional testing at different angles and thicknesses would be required to observe a relevant trend.

3.2.4.2 Damage variable estimation

For the estimation of the damage variable, the three methods presented in section 1.2.4 are used. Examples of the results following the application of all three methods on three different individual samples are given in Fig. 3.31. For all three examples, it is observed that Ladeveze's

method gives overall higher damage variable values, with an almost linear increase with applied stress level. The damage variables calculated based on the Fitoussi and Regression model have lower values, closer to each other for the first cycles. This outcome was expected, as Ladeveze's method considers the unloading chord modulus of the cycle, which is lower in value than the modulus given by the loading curve of the cycle, considered in the other two methods.

It is also observed that for some cycles, the damage variable evaluated with Fitoussi's method or the Regression method presents negative values. Although the presence of negative damage variables when using the Fitoussi method was observed in Hug's work [138] as well, no explanation was provided. While the damage parameter accounts for stiffness loss due to internal damage, we consider that the negative values do not retain any physical meaning, as damage growth is an irreversible phenomenon [131], [235]. Therefore, the negative values of the damage variable represent a procedural error of the employed methods for evaluating the cycle modulus.

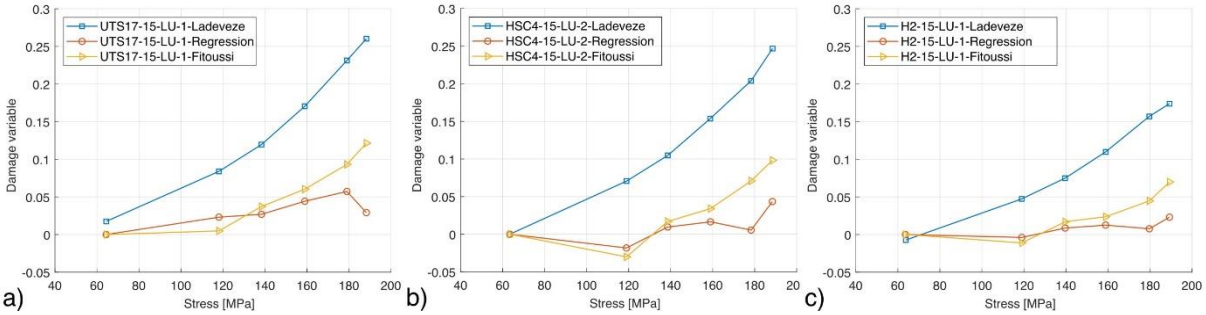

Fig. 3.31. Application of Ladeveze, Regression, and Fitoussi methods to evaluate the damage variable from 15° off-axis cyclic load-unload tensile test; a) UTS17 – sample 1; b) HSC4 – sample 2; c) H2 – sample 1

Due to the cycle hysteresis loop, as well as to noise in the data for the first two cycles, the modulus extracted with Fitoussi's method and the Regression model has a close value or even higher than the modulus extracted from the 1st cycle in some cases. This leads to negative values of the damage variable or lower values compared to previous cycles, when employing equation (1.14). Thus, the damage variable growth with increasing stress does not have a smooth evolution for the Fitoussi and Regression model, as it has for the Ladeveze method, with the Regression model having the most irregular progression. Although Eliopoulos and Philippidis [139] also employed a linear regression for each stress–strain loop to extract the cycle modulus of $[\pm 45]_s$ GFRP composites, they did not report a higher modulus evaluation for subsequent cycles.

Fig. 3.32 shows the average damage variable estimated using all three methods, for all off-axis angle/material configurations, with error bars as half of the measuring range. In the 1st column, results for 15° off-axis angle are presented, in the 2nd column for 30° off-axis angle, and in the 3rd column for 45° off-axis angle. Each row presents results for the same material, at different off-axis angles: 1st row– HSC3, 2nd row– HSC4, 3rd row– UTS13, 4th row– UTS17, 5th row– H1, and 6th row– H2. It can be observed that for all off-axis angles, the Ladeveze method gives the highest value for the damage variable, with a smooth increase with increasing applied stress. Based on the Fitoussi and Regression methods, the average damage variables have lower values compared to the Ladeveze method, and they are closer together in the first cycles, as previously mentioned for the analysis of the results on an individual sample.

The evolution of the damage variable estimated using the Regression and Fitoussi methods is smoother at 45° off-axis angle, pointing to a potential influence of the hysteresis loop width on the cycle elastic modulus extraction.

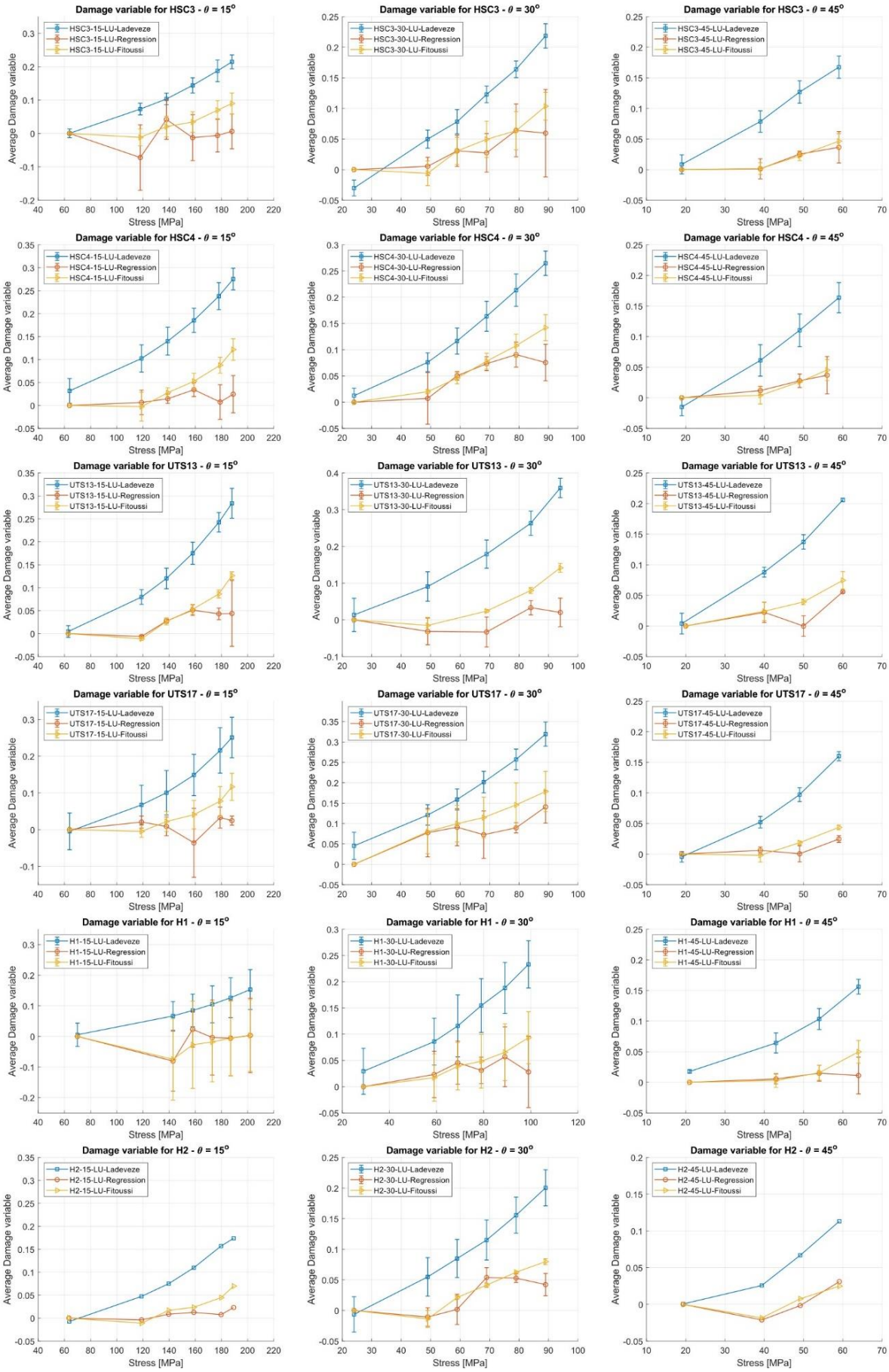

Fig. 3.32. Average damage variables estimated using Ladeveze, Fitoussi, and Regression methods; Columns: 1st- 15°; 2nd - 30°; 3rd - 45°; Rows: 1st – HSC3; 2nd – HSC4; 3rd – UTS13; 4th – UTS17; 5th – H1; 6th – H2

There are high error bars in the results of all three methods. This suggests that despite similar cycle-load-unload stress-strain responses between samples of the same configuration, there is a difference in stiffness reduction with increasing applied stress. Even though samples are of the same configuration, they might still exhibit slight variations in terms of material properties, imperfections, defects such as voids, or local variations in microstructure. These localized internal differences between samples could lead to early fiber/matrix interface debonding and matrix microcracks, which could lead to a loss in stiffness. A higher error bar is observed in the Regression method as compared with the other two methods, and the damage variable changes at an irregular rate when stress levels increase.

Given that both the Fitoussi method and the Regression method share the same fundamental approach to estimating the initial modulus, albeit with distinct data bounds for linear regression, it becomes evident that as the cycles progress, especially in the later cycles where the hysteresis loop widens, and lower off-axis angles (see Fig. 3.28), the selection of data points for cycle modulus estimation becomes a critical factor. Fig. 3.33 shows an example of elastic modulus extraction from the reloading curve of the 5th cycle of a UTS13 sample tested at a 15º off-axis angle, providing both the coefficient of correlation R^2 and the resultant modulus from the linear fit using the selected data. Applying Fitoussi's method with specified data bounds (Fig. 3.33b) yields a strong correlation with $R^2 = 0.9995$ and an apparent modulus $E_x = 34.78$ GPa.

Meanwhile, implementing the Regression method on the same reloading curve (Fig. 3.33c) also yields a correlation coefficient of $R^2 = 0.9995$, but with a different data selection closer to the start of the reloading curve, resulting in a higher apparent modulus $E_x = 35.54$ GPa.

Given the initial modulus for this sample ($E_0 = 37.70$ GPa), equation (1.14). calculates a damage variable of 0.07 with Fitoussi's method and 0.05 with the Regression method.

Moving on to the 6th cycle of the same sample, Fitoussi's method yields an apparent modulus of 33.05 GPa with $R^2 = 0.9992$, while the Regression method provides an apparent modulus of 35.24 GPa with $R^2 = 0.9998$, thus an even greater difference. Although the correlation coefficients remain highly favorable for both methods, the distinction in the data points selected for extraction, specifically the inclusion of experimental points closer to the start of the reloading curve, significantly impacts the modulus value and subsequently the damage variable value. When comparing the modulus extracted using the Fitoussi and the Regression models for all tested samples, percentage differences up to 24% are observed between the values obtained from both approaches.

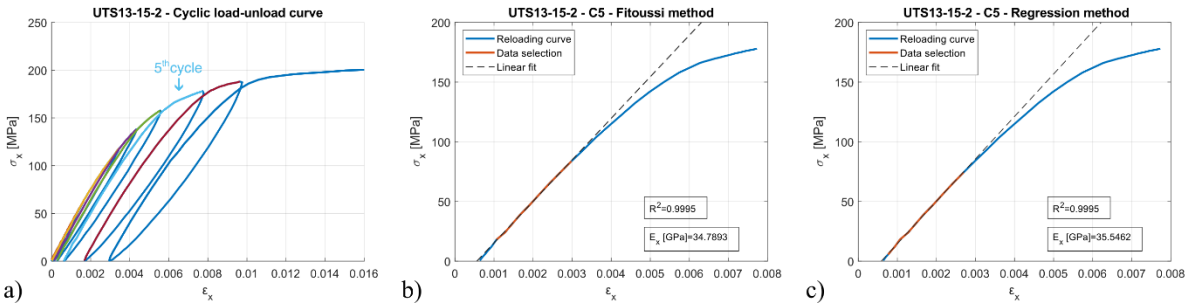

Fig. 3.33. Example of elastic modulus evaluation from the reloading curve; a) Cyclic load-unload stress-strain curve for UTS13 sample, 15º off-axis angle; b) Elastic modulus evaluation from the reloading curve of the 5th cycle with the Fitoussi method; c) Elastic modulus evaluation from the reloading curve of the 5th cycle with the Regression method

Thus, one contributing factor to potentially inconsistent results with the Regression method is the lower limit imposed for initiating the analysis. In this specific case, an inferior strain limit of 1e-4 above the first strain value of the reloading curve was established, to exclude just the initial few points of the reloading curve, aiming to prevent additional errors induced by potential instability at the start of the reloading curve. This approach avoids introducing instability-associated errors, as no recovery time is mandated in the cyclic test following unloading.

When applying the same lower strain limits to the Regression method as used in Fitoussi's method, the same results are obtained for the 5th cycle with both methods. However, for the 6th cycle, the Regression method chooses a distinct and shorter dataset, resulting in a stronger correlation and a higher cycle modulus compared to the Fitoussi method.

While effective in extracting the apparent elastic modulus in the case of nonlinear stress-strain curves from off-axis tensile testing [236], the influence of the chosen inferior limit for employing the regression method on the results highlights a need for a standardized method to evaluate the cycle apparent modulus for composite materials, for low cycle numbers (not fatigue analysis) and increasing cycle amplitude tests.

In Fig. 3.34, a comparison of the average damage variables evolution with total strain, obtained from different off-axis angles, is presented. The x-axis of this plot displays the total strain due to the varying stress levels applied to the cycles across different off-axis angles. This choice was made to accommodate the differences in stress levels among the cycles. The damage variables estimated using Ladeveze's method are shown in the first column, in the second column the damage variables estimated using Fitoussi's method are shown, and in the third column, the damage variables calculated using the Regression model are illustrated. Each row is dedicated to a type of material: 1st row for HSC3, 2nd row for HSC4, 3rd row for UTS13, 4th row for UTS17, 5th row for H1, and the 6th row for H2.

For all materials, it can be observed that the Regression method offers inconclusive results, with an erratic variation of the damage variable with the total strain. By analyzing the evolution with the total strain of the damage variable estimated using Ladeveze's method, for 15° and 30° off-axis angles, the damage variable evolutions are similar, almost linear, with a difference in value for most materials. For Fitoussi's method, the damage variables for 15° and 30° off-axis angles are almost coincident for HSC3 and HSC4, and for other materials, the variation has a similar shape, with a difference in the estimated values. After the second cycle, the evolution of the damage variable is almost linear. It can also be observed that using Ladeveze's method, for HSC3 and HSC4, the damage variable in the 15° off-axis angle case is the highest, while for UTS13 and UTS17 the highest values are found for the 30° off-axis angle. H1 follows the trend of UTS laminates, with a higher damage variable for 30º off-axis angle, while H2 shows close results for both angles. By using Fitoussi's method, this observation is valid for UTS17, H1, and H2, while for HSC3, HSC4, and UTS13, the results are reversed.

For the 45° off-axis angle, the values of the damage variable are lower compared to the other two angles, regardless of the method used for extracting the values, except for H1 for which the lowest values are found for the 15° off-axis angle (by using the Regression or Fitoussi's method), but with large error bars, implying that the presence of unaccounted-for microstructural variations and internal defects among samples likely influenced the final results for this specific case. When loaded at a 45° off-axis angle, fiber-matrix interfaces are the most loaded, leading to fiber-matrix interface debonding at lower stresses [226], compared to the other angles. Furthermore, interface debonding primarily affects the composite's ability to carry transverse loads, with a more pronounced negative impact at the 45° off-axis angle than at lower off-axis angles. Consequently, at the 45° angle, damage accumulation is constrained as the ultimate failure of the matrix promptly follows interface debonding. Thus, in the 45° off-axis angle case, the unidirectional composite is capable of sustaining a comparably larger loss in modulus and accumulation of residual strain before final failure. Therefore, the damage variable estimation is influenced by the off-axis angle.

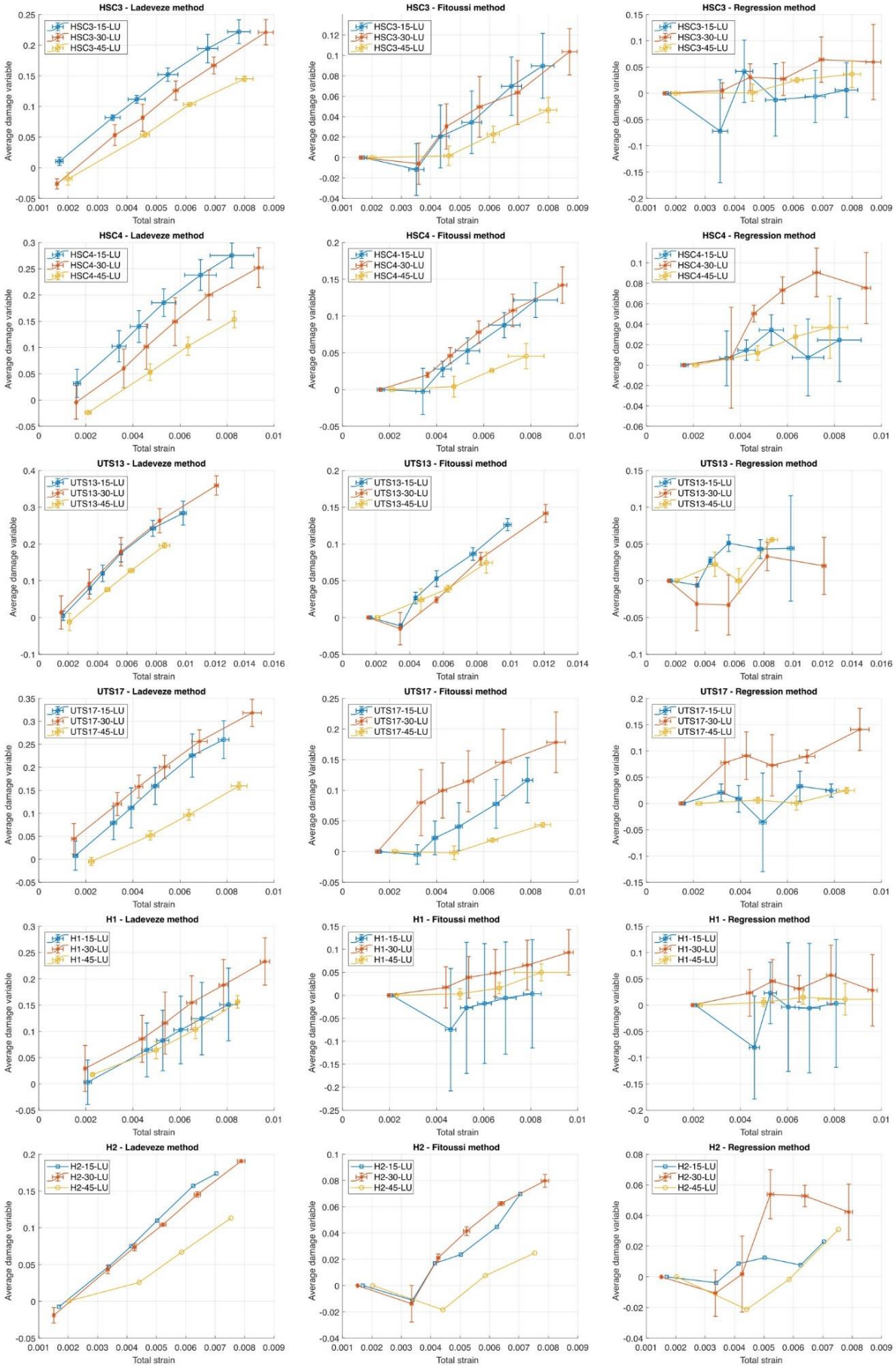

Fig. 3.34. Comparison of average damage variables estimated using Ladeveze, Fitoussi, and Regression methods, at different off-axis angles; Columns: 1st- Ladeveze's method; 2nd – Fitoussi's method; 3rd – Regression method; Rows: 1st – HSC3; 2nd – HSC4; 3rd – UTS13; 4th – UTS17; 5th – H1; 6th – H2

A comparison of the damage variables for all material types, at the same off-axis angle, using all three methods is given in Fig. 3.35. In the first column, the comparisons for the 15° off-axis angle are presented, in the second column for 30°, and in the third column for 45°. The first row shows the damage variables extracted using the Ladeveze method, the second row illustrates the damage variables using the Fitoussi method, and the third row is for the damage variables estimated using the Regression method. Again, due to the unpredictable evolution of the damage variable extracted using the Regression method, the results are inconclusive, with negative values for some materials and high error bars.

For the other two methods, it is clear that the hybrid laminates, H1 and H2, have the lowest damage variables, for all off-axis angles. The increase in damage variable with increasing maximum stress of the cycle is closer to a linear evolution for the hybrid laminates, as opposed to the reference laminates for which the damage variable has a sharper increase towards the last cycles. Moreover, it can be observed that for the 15° off-axis angle, the HSC3 and UTS laminates have similar damage variables, and starting with a stress level of 140 MPa, the damage variables of UTS13 and UTS17 diverge from the original path, having higher values than HSC3. For 30° off-axis angles, the damage variable evolutions are almost parallel to each other, with UTS laminates having the highest values. In the case of 45° off-axis angles, the reference laminates present a linear variation of the damage variable, with a higher slope compared to hybrid laminates.

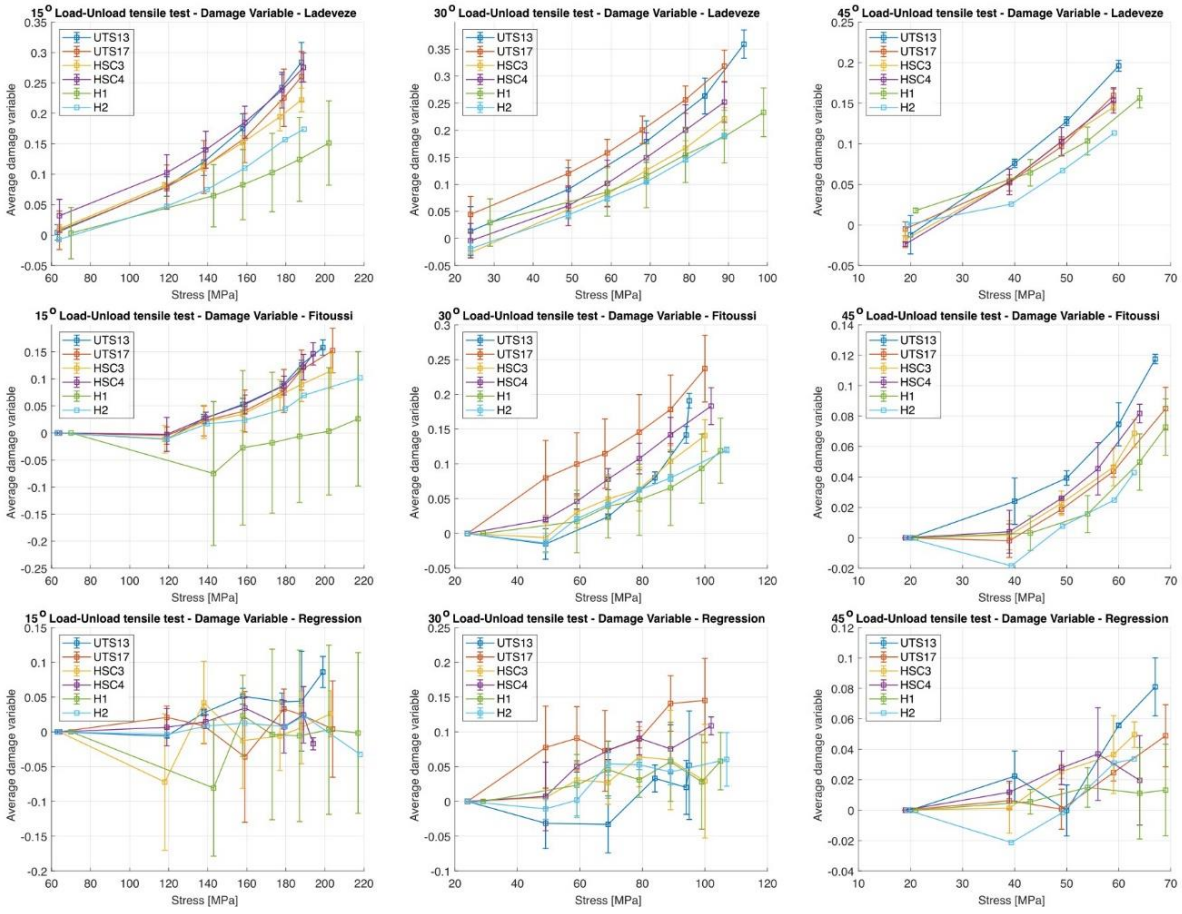

Fig. 3.35. Comparison of the average damage variables estimated using Ladeveze, Fitoussi, and Regression methods, for the different laminates, at the same off-axis angle; Columns: 1st- 15°; 2nd - 30°; 3rd - 45°; Rows: 1st – Ladeveze's method; 2nd – Fitoussi's method; 3rd – Regression method;

By coupling these observations with the ones for the evolution of the residual stress, illustrated in Fig. 3.30, an explanation can be drawn for the off-axis stress-strain response comparison, shown in Fig. 3.21. UTS laminates exhibit both the highest residual strain and damage variable, thus, with increasing stress levels, the nonlinear response is more pronounced due to internal damage and plasticity of the matrix. HSC laminates do not have such a strong

nonlinear off-axis response as UTS laminates and their residual strains and damage variables are also lower than for UTS laminates. By combining these two ply types into H1 and H2 hybrid configurations, lower residual strains and damage variables are obtained for all off-axis angles, compared to reference UTS and HSC laminates. Therefore, with less internal damage and plasticity of the matrix, the hybrid configurations show a strain hardening in the off-axis response, reaching a higher stress level at the same strain, for all off-axis angles, compared to reference laminates. Thus, a positive hybrid effect is obtained.

3.3 NONLINEAR CONSTITUTIVE MODEL FOR OFF-AXIS BEHAVIOR

3.3.1 Model parameters

To determine all the necessary parameters for the nonlinear constitutive model outlined in section 1.2.5, several sequential steps are essential. Initially, the values for parameters a_2 and b_2 from equation (1.18) were set for all materials at the values proposed by Cho et al. [120] for unidirectional carbon/epoxy composite, $a_2 = 0.2$ and $b_2 = 0.05$. Using these values, the $\bar{\sigma} - \bar{\varepsilon_p}$ (effective stress – effective plastic strain) curves from different off-axis angles collapse on one another, with small scatter for H1, HSC3, HSC4, and UTS17 materials. Therefore, they offer satisfactory results for different types of unidirectional carbon fiber composites. The $\bar{\sigma} - \bar{\varepsilon_p}$ curves, and the corresponding power law fittings (equation (1.24)) are shown in Fig. 3.36 for all tested materials. The values of the power law fitting parameters, A and n, are given in Table 3.8.

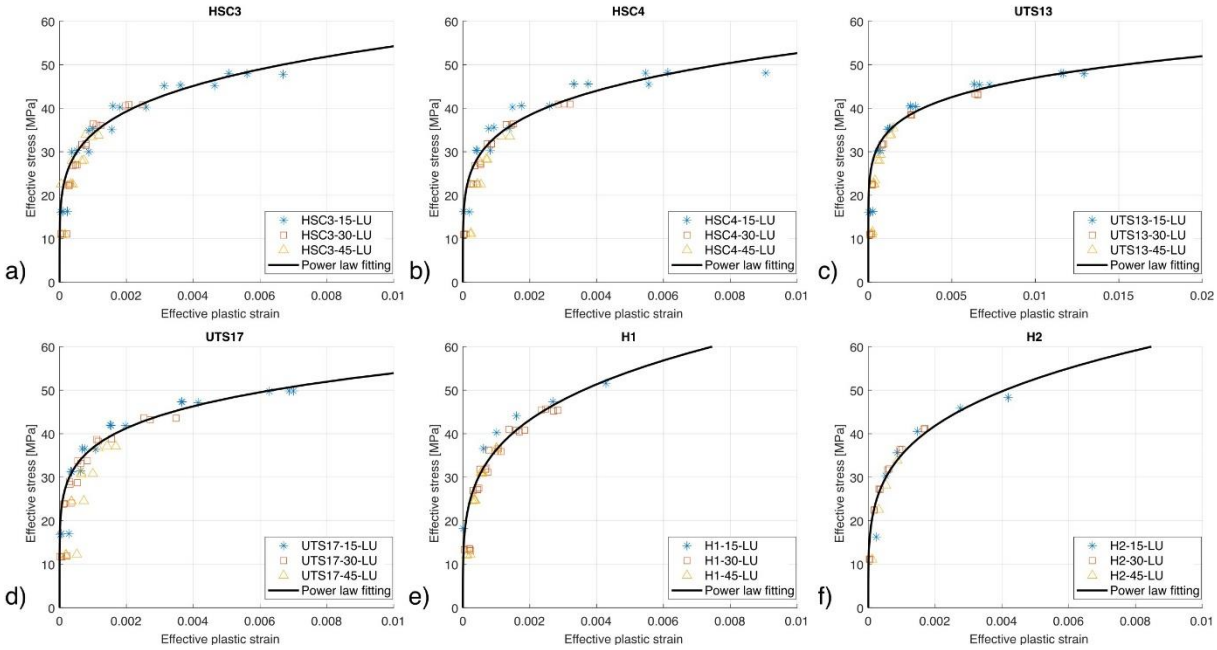

Fig. 3.36. Effective stress – effective plastic strain curves, with power-law fitting, a_2=0.2 and b_2=0.05; a) HSC3; b) HSC4; c) UTS13; d) UTS17; e) H1; f) H2

For the damage variable formulation, the values from both Ladeveze and Fitoussi methods were used, to compare the effect of the method for estimating the cycle elastic modulus on the prediction of the nonlinear off-axis stress-strain behavior. Fig. 3.37 shows the evolution of the damage variables with the effective stress, as well as the numerical fitting using equation (1.31). Damage variables estimated using both Ladeveze and Fitoussi methods are presented in the same figure. The data points for negative damage variables were removed, to not influence the fitting, as they do not have a physical meaning, as explained in section 3.2.4.2. For H1 material, only one 15° off-axis test was used, the one closest to the values from 30° and 45° tests, because the high differences from one test to another strongly influenced the numerical fitting. Fig. 3.38 displays numerical fittings both before and after excluding certain 15° off-axis tests. It is noticed in Fig. 3.38b that after removing part of the 15° off-axis tests, the fitting follows the increase of

the damage variable with effective stress more closely (and similar to the other tested materials), compared to the almost linear fitting result in Fig. 3.38a.

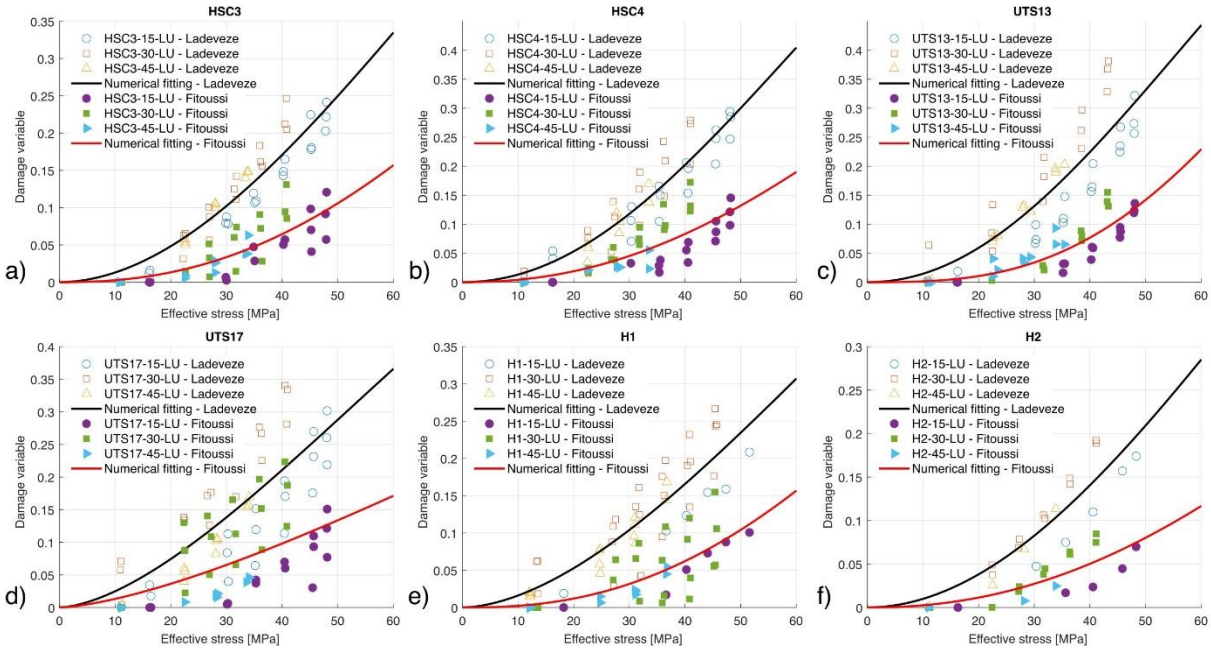

Fig. 3.37. Damage variable at 15°, 30°, and 45° off-axis angle - effective stress curves with numerical fitting, a_2=0.2 and b_2=0.05; a) HSC3; b) HSC4; c) UTS13; d) UTS17; e) H1; f) H2

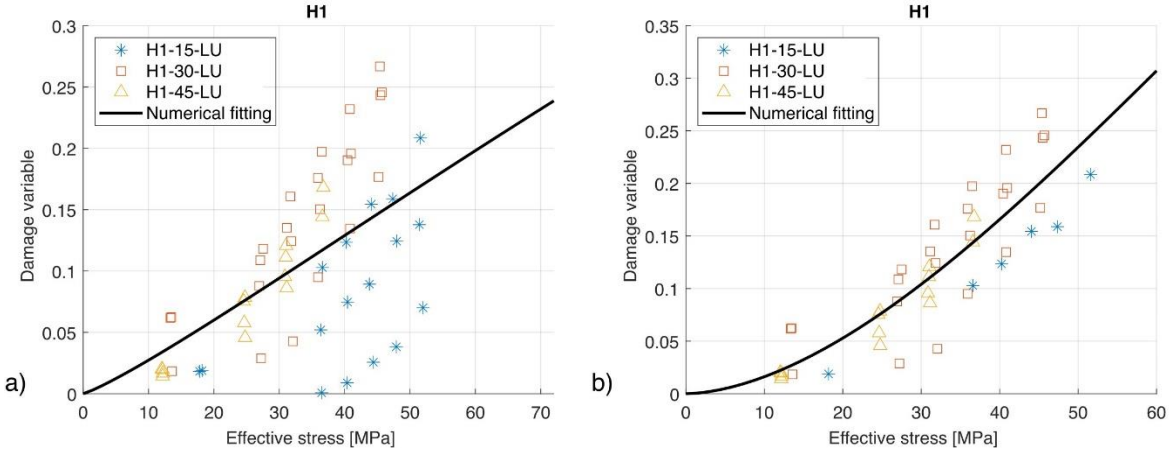

Fig. 3.38. Damage variable (Ladeveze's method) - effective stress curves with numerical fitting, for H1 material, a_2=0.2 and b_2=0.05; a) before removing part of 15° off-axis tests; b) after removing part of 15° off-axis tests

The resulting parameters σ_e and n_e are given in Table 3.8. It is observed that for all materials, the Fitoussi method gives smaller values for the damage variable, thus the numerical fitting does not have a sharp increase, as it does for the Ladeveze method. Moreover, by looking at the values for σ_e and n_e in Table 3.8, while n_e values are quite similar for both methods, σ_e has significantly higher values for Fitoussi's method compared to the Ladeveze method. Therefore, σ_e is the parameter in equation (1.31) that has the most influence on the increase of the damage variable with increasing effective stress. A higher value for σ_e leads to a softer increase of the damage variable with effective stress.

Table 3.8. Initial model parameters for all tested materials

Material	a_2	b_2	A	n	σ_e	n_e	σ_e	n_e
					Ladeveze		Fitoussi	
UTS13	0.2	0.05	2.50e-14	6.9	77.83	2.05	95.26	2.91
UTS17	0.2	0.05	1.79e-11	5.0	97.66	1.61	186.18	1.47
HSC3	0.2	0.05	2.29e-11	4.98	95.77	1.91	128.65	2.31
HSC4	0.2	0.05	1.60e-11	5.1	82.69	2.04	122.26	2.18
H1	0.2	0.05	5.75e-10	4	106.81	1.73	125.13	2.4
H2	0.2	0.05	6.53e-10	4	104.71	1.96	157.17	2.16

3.3.2 Predictions of off-axis nonlinear stress-strain response

Predictions using the coupled damage-plasticity model described in section 1.2.5, with a_2 = 0.2 and b_2 = 0.05, and both damage formulations, are shown in Fig. 3.39- Fig. 3.44, for all materials, using a representative experimental curve for each case. The corresponding percentage error between the anticipated stress and the actual experimental values is also provided for each strain measurement, determined using equation (1.14). The first few strain points data (up to 0.002) are left out from the percentage error plot as the values were high due to noise in the experimental data at the beginning of the tests. In the constitutive model, the applied stress is given, and the corresponding strain value is computed. However, when evaluating the discrepancies between the predicted curve and the experimental results, stress values matching the same strain values were employed. This approach was chosen for better intuitive analysis and correlation with the stress-strain graphs.

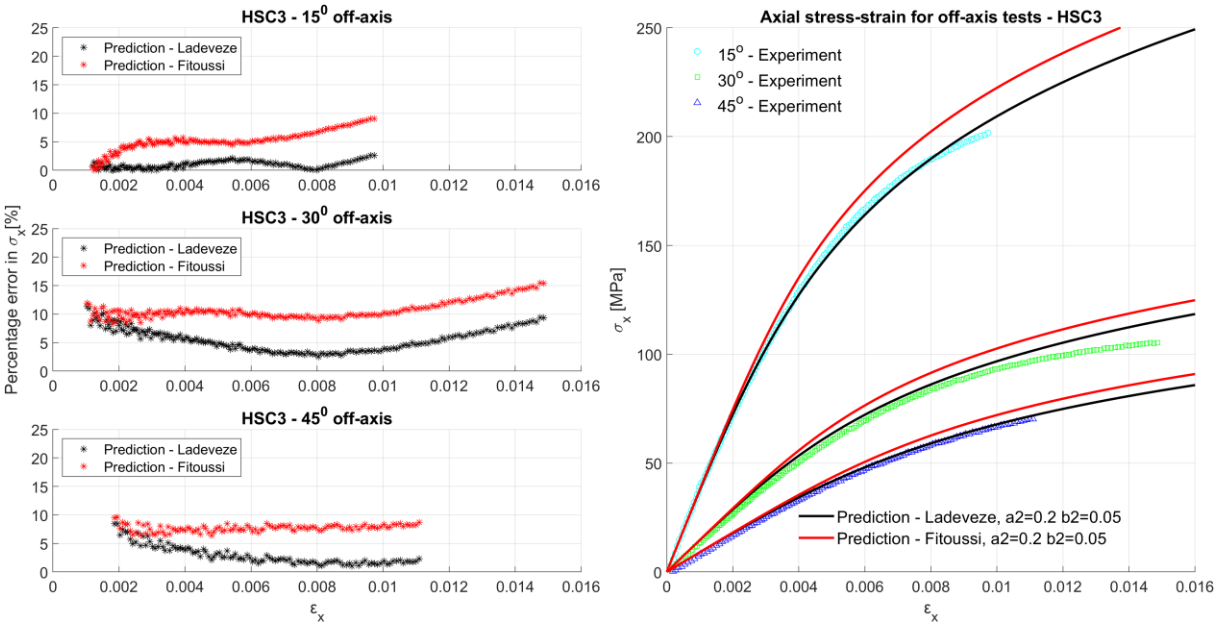

Fig. 3.39. Predictions of the off-axis nonlinear stress-strain of HSC3, with damage variable estimation from both Ladeveze and Fitoussi methods, a_2=0.2 and b_2=0.05 – with corresponding σ_x percentage error between predicted values and experimental results

$$\text{percentage error [\%]} = \frac{\left|\sigma_{x_{Experimental}} - \sigma_{x_{Predicted}}\right|}{\left|\sigma_{x_{Experimental}}\right|} \cdot 100 \qquad (3.1)$$

The maximum applied stress for the behavior prediction is set to 250 MPa for 15° off-axis angle, 120 MPa for 30° off-axis angle, and 80 MPa for 45° off-axis angle. For all materials and off-axis angles, a good prediction is obtained in the linear region of the stress-strain curve for

both methods and as the stress-strain curve becomes nonlinear, a gap between the prediction and the experimental curve is observed, with an underprediction of the total strain. This gap widens with decreasing off-axis angle. When looking at the percentage error (both methods included), for reference laminates the maximum percentage error is less than 15%, while for hybrid laminates the percentage error is higher, reaching 25% in some cases, but still offering satisfactory results. In the nonlinear response region, the percentage error in stress values between the predicted and measured values has an almost linear increase with increasing strain, suggesting that the prediction model with the determined parameters does not fully account for all damage-plasticity effects.

For HSC4 (Fig. 3.40), because the initial apparent modulus calculated using the transformation equation (1.9) is smaller than the apparent modulus determined experimentally, the prediction in the linear region has a smaller slope, thus leading to an increased percentage error between the prediction and the experimental stress-strain curve in the linear response region.

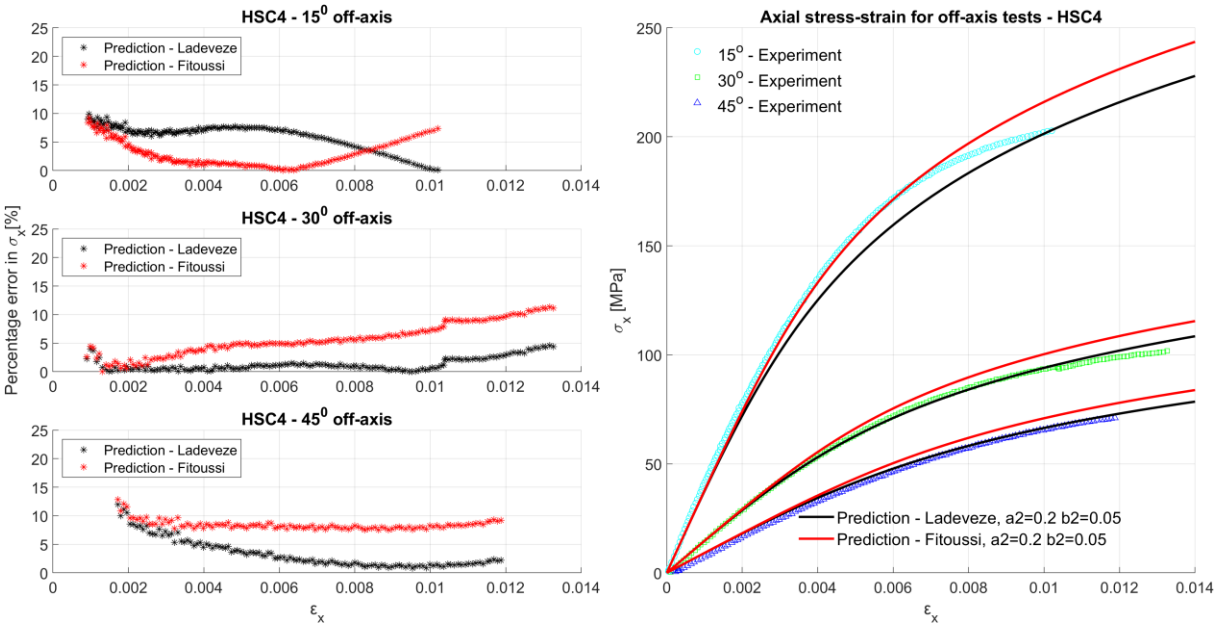

Fig. 3.40. Predictions of the off-axis nonlinear stress-strain of HSC4, with damage variable estimation from both Ladeveze and Fitoussi methods, a_2=0.2 and b_2=0.05 – with corresponding σ_x percentage error between predicted values and experimental results

Looking at predictions with the damage variable estimated from both methods, in all cases, the prediction using the Fitoussi method for damage formulation reaches higher stresses at the same axial strain, compared to the Ladeveze method. This was expected, as the Fitoussi method gives smaller values for the damage variable and a slower increase with increasing effective stress (Fig. 3.37). The slow accumulation of the damage, by the Fitoussi method, leads to a wider gap between the prediction and experimental curves, compared to the Ladeveze method, as the applied stress increases, in the sense of overestimating the strength. This is also reflected in the curves of the percentage error. For composite structures design, overestimating the material strength presents as a safety risk, thus following a more pessimistic approach (such as Ladeveze's damage formulation) is preferable. There are few cases in which the percentage error by the Fitoussi method is lower than the one given by the Ladeveze method (45º for H1 and H2), or one method offers a better prediction at the beginning of the tensile test, while the other gives a better prediction in the nonlinear response region (15º for UTS13 and UTS17).

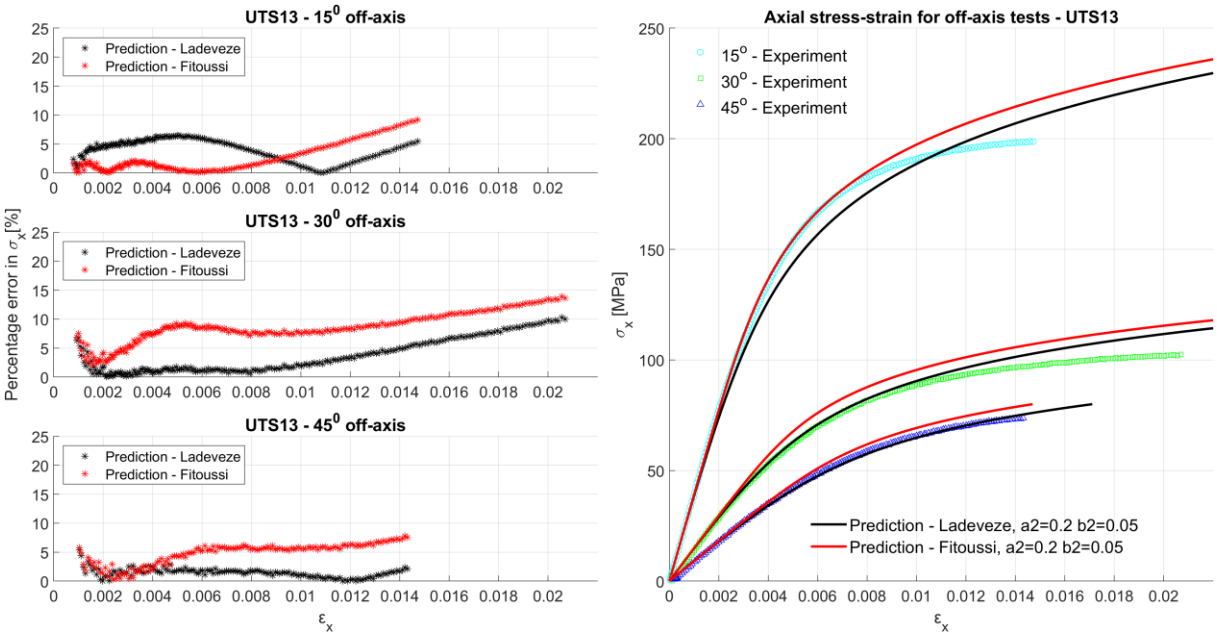

Fig. 3.41. Predictions of the off-axis nonlinear stress-strain of UTS13, with damage variable estimation from both Ladeveze and Fitoussi methods, a_2=0.2 and b_2=0.05 – with corresponding σ_x percentage error between predicted values and experimental results

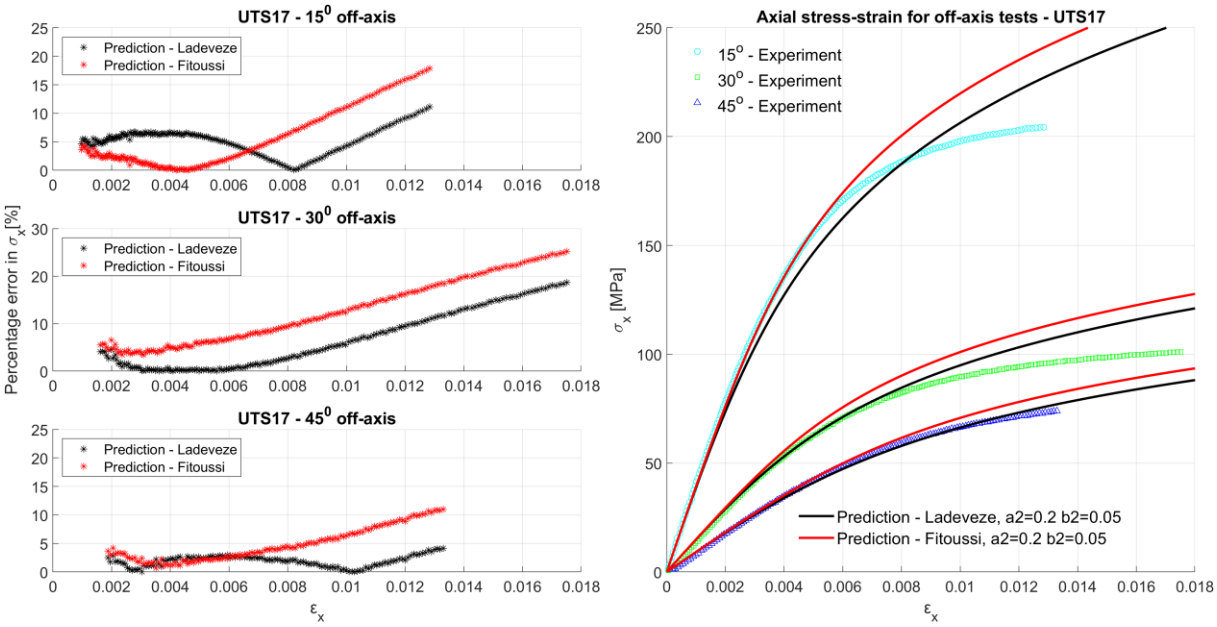

Fig. 3.42. Predictions of the off-axis nonlinear stress-strain of UTS17, with damage variable estimation from both Ladeveze and Fitoussi methods, a_2=0.2 and b_2=0.05 – with corresponding σ_x percentage error between predicted values and experimental results

Overall, the coupled damage-plasticity model with the Ladeveze method for extracting the damage variable offers a better prediction, with almost half the value of the percentage errors compared to the Fitoussi method, although it is unable to fully predict the nonlinear stress-strain behavior with the current parameters. In this regard, the choice of a_2 and b_2 could also influence the prediction, as they not only influence the plasticity and damage parameters but also the estimation of the axial strain in equation (1.32) as they are also included in $h(\theta)$ parameter. Therefore, multiple iterations were performed for different values of a_2 and b_2, and it was observed that to reduce the gap between the prediction and the experimental stress-strain curve, in the nonlinear region, a higher influence of the dilatational component of the plastic potential function is needed.

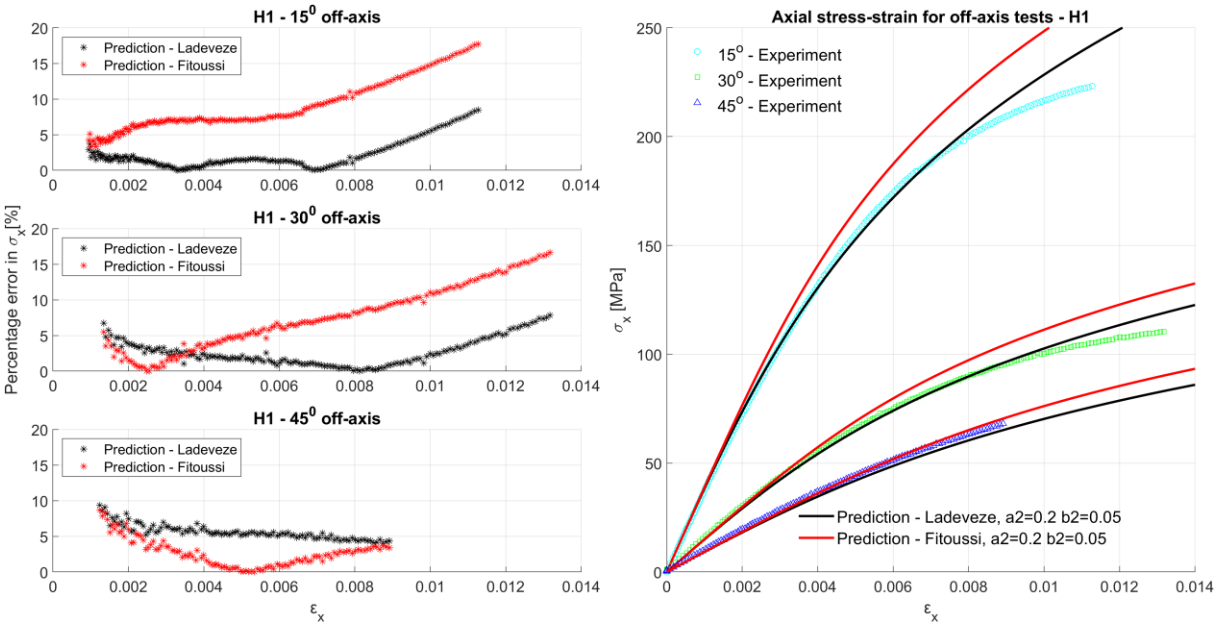

Fig. 3.43. Predictions of the off-axis nonlinear stress-strain of H1, with damage variable estimation from both Ladeveze and Fitoussi methods, a_2=0.2 and b_2=0.05 – with corresponding σ_x percentage error between predicted values and experimental results

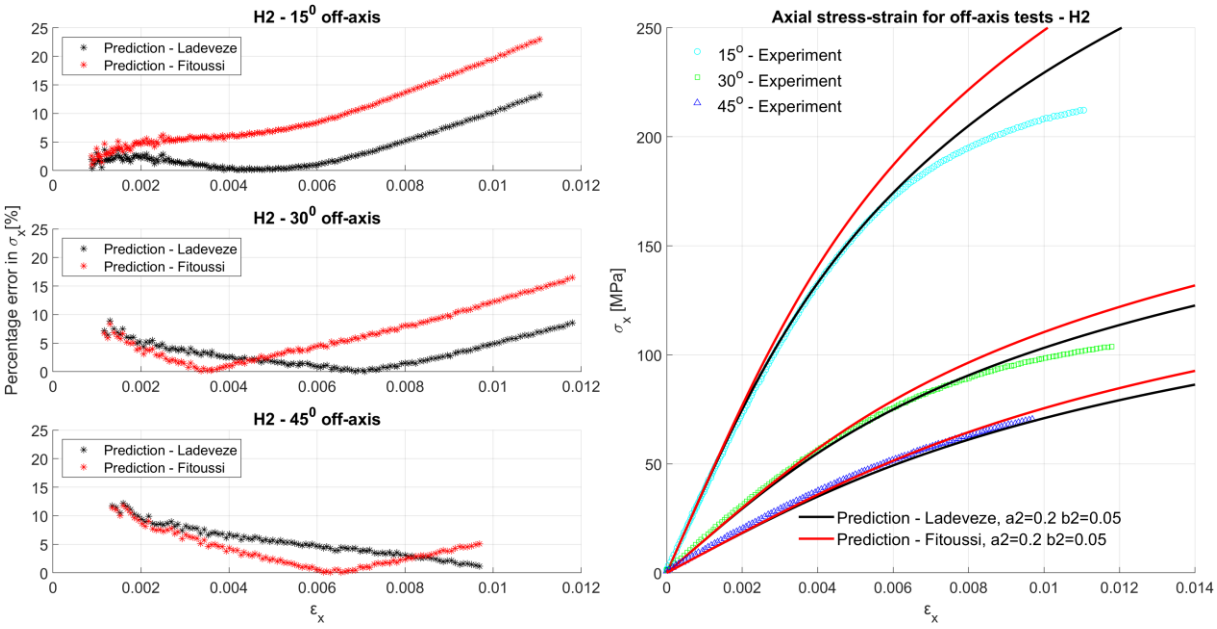

Fig. 3.44. Predictions of the off-axis nonlinear stress-strain of H2, with damage variable estimation from both Ladeveze and Fitoussi methods, a_2=0.2 and b_2=0.05 – with corresponding σ_x percentage error between predicted values and experimental results

After several iterations, it was observed that by increasing the value of b_2 to 0.2, better predictions are obtained for all laminates, for 15º and 30°, while for 45° the predicted values are not too different, and in some cases, the percentage error has a slight increase in value compared to previous prediction (with b_2=0.05). An illustration of the percentage errors with both sets of a_2 and b_2 parameters is given in APPENDIX H. The corresponding damage and plasticity parameters are given in Table 3.9. The effective stress–effective plastic strain curves collide on master curves similar to the ones presented in Fig. 3.36, thus only the fitting parameters are given.

Table 3.9. Adjusted model parameters for all tested materials

Material	a_2	b_2	A	n	σ_e	n_e	σ_e	n_e
					Ladeveze		Fitoussi	
UTS13	0.2	0.2	2.0e-17	8.68	75.38	2.37	86.29	3.58
UTS17	0.2	0.2	1.0e-13	6.35	93.18	1.81	169.90	1.63
HSC3	0.2	0.2	2.44e-12	5.50	92.28	2.14	117.18	2.66
HSC4	0.2	0.2	1.45e-13	6.25	81.58	2.26	111.43	2.51
H1	0.2	0.2	4.14e-10	4	104.30	1.92	120.52	2.66
H2	0.2	0.2	4.94e-10	4	99.09	2.21	137.44	2.52

The predictions with the adjusted model parameters are illustrated in Fig. 3.45 - Fig. 3.50, with corresponding percentage errors between the anticipated stress and the actual experimental values. The difference is not as significant for stiffer composites such as HSC and hybrid laminates, as it is for UTS laminates, which have a more pronounced nonlinear behavior.

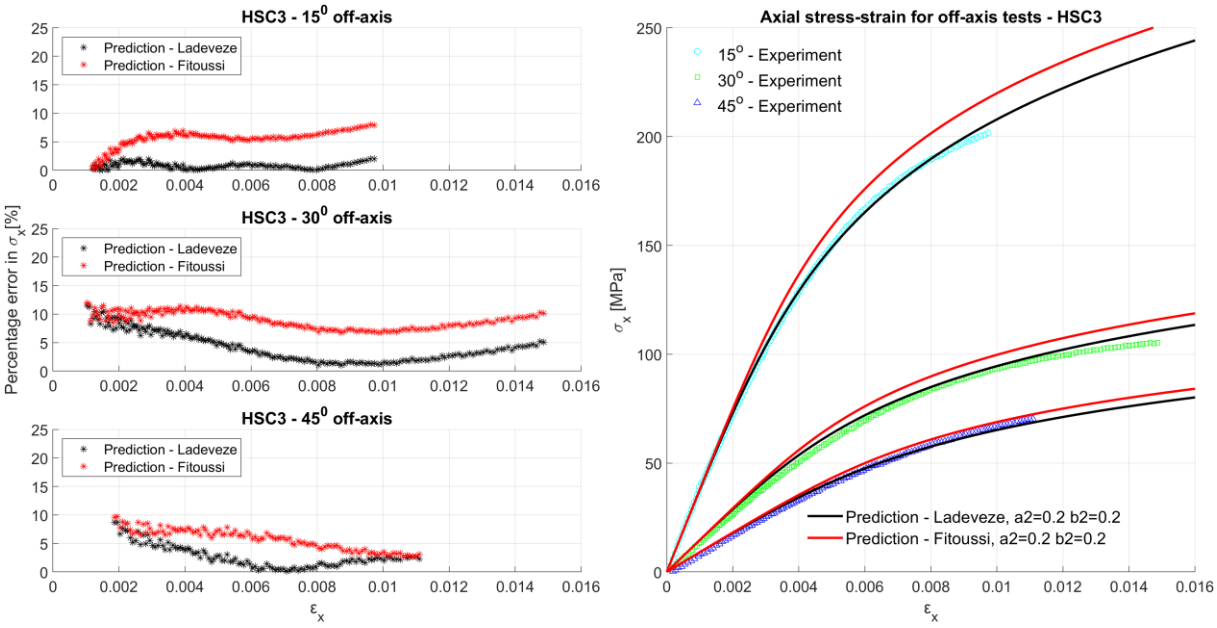

Fig. 3.45. Predictions of the off-axis nonlinear stress-strain of HSC3, with damage variable estimation from both Ladeveze and Fitoussi methods, a_2=0.2 and b_2=0.2 – with corresponding σ_x percentage error between predicted values and experimental results

Looking at the maximum percentage errors, some observations are drawn. Among the reference laminates, the decrease in maximum percentage error for HSC3 is up to 0.58% (Ladeveze method) and 4.08% (Fitoussi method). For HSC4, the maximum percentage errors dropped by a maximum of 2.58% (Ladeveze method) and 5.44% (Fitoussi method). However, in the case of UTS laminates, the reduction in maximum percentage errors was more substantial. For UTS13, the reduction reached 5.48% (Ladeveze method) and 3.08% (Fitoussi method), while for UTS17, the reduction was even more pronounced, at 7.11% (Ladeveze method) and 9.08% (Fitoussi method). Regarding the hybrid laminates, a minor variation of less than 0.1% was observed in the maximum percentage errors for the 15° off-axis angle. For the 30° off-axis angle, a more noticeable drop of 2.4% was observed, regardless of whether the Ladeveze or Fitoussi methods were employed. However, for the 45° off-axis angle, the percentage error slightly increased for H1, with ~0.9%, while a slight reduction of 0.14% (Ladeveze method) was noted for H2.

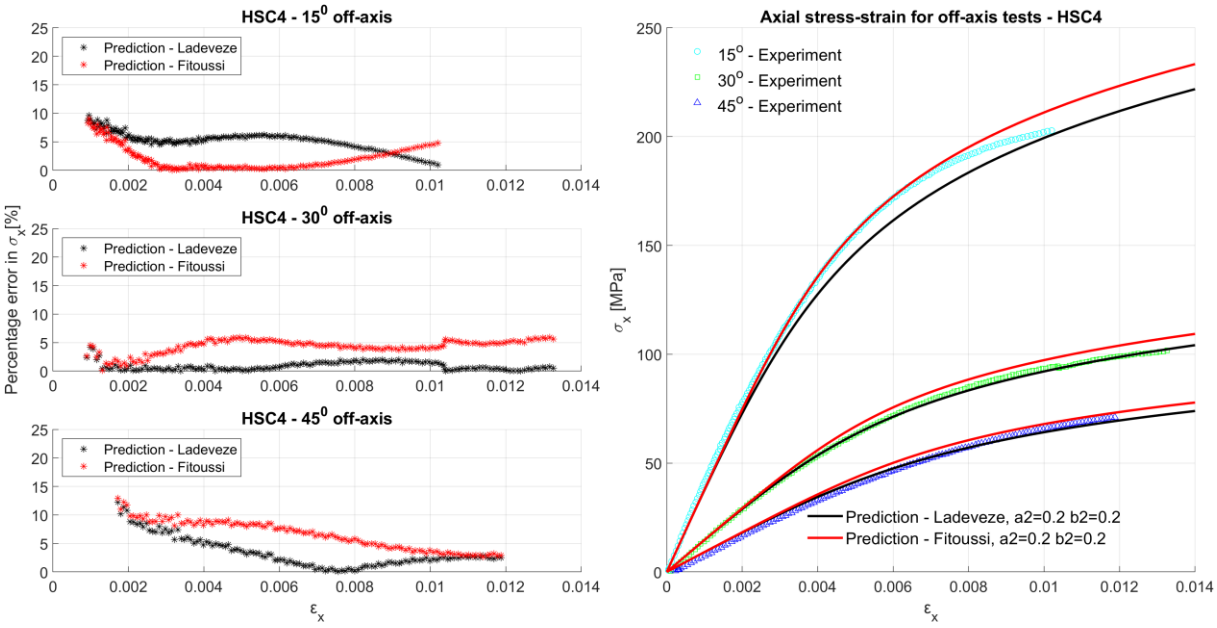

Fig. 3.46. Predictions of the off-axis nonlinear stress-strain of HSC4, with damage variable estimation from both Ladeveze and Fitoussi methods, a_2=0.2 and b_2=0.2 – with corresponding σ_x percentage error between predicted values and experimental results

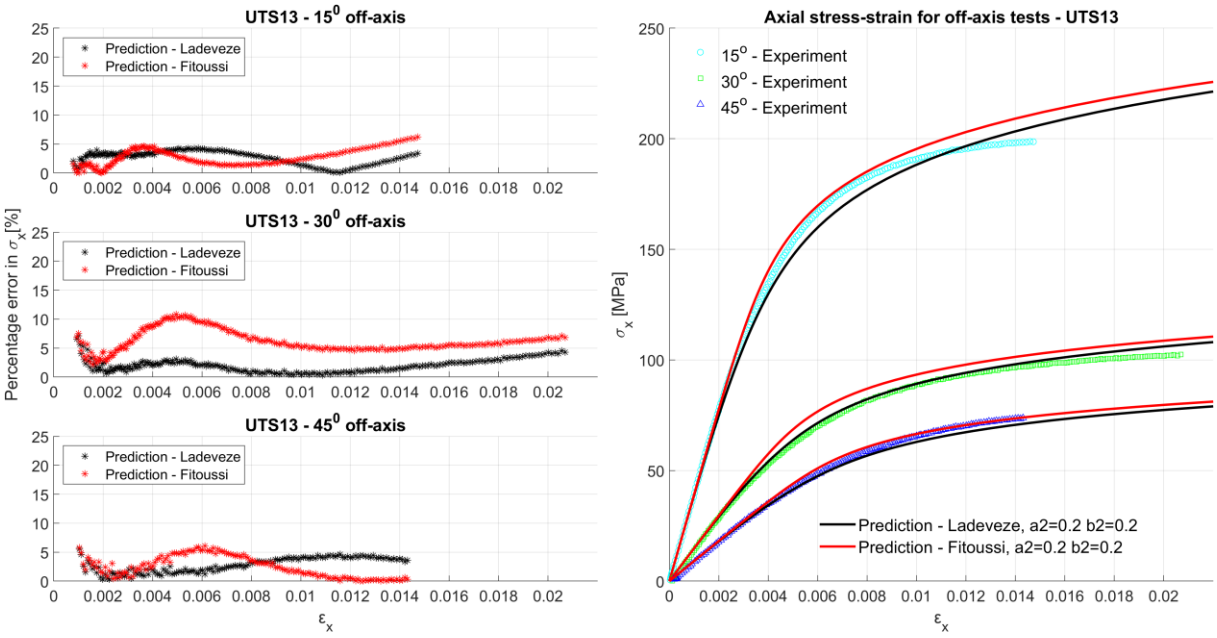

Fig. 3.47. Predictions of the off-axis nonlinear stress-strain of UTS13, with damage variable estimation from both Ladeveze and Fitoussi methods, a_2=0.2 and b_2=0.2 – with corresponding σ_x percentage error between predicted values and experimental results

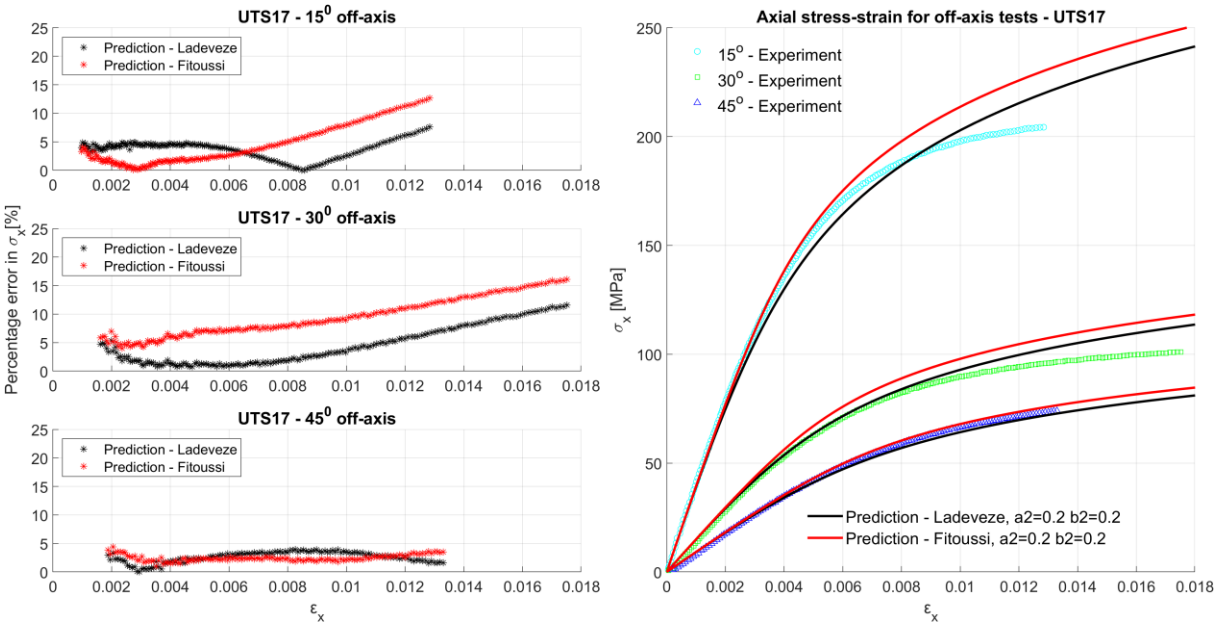

Fig. 3.48. Predictions of the off-axis nonlinear stress-strain of UTS17, with damage variable estimation from both Ladeveze and Fitoussi methods, a_2=0.2 and b_2=0.2 – with corresponding σ_x percentage error between predicted values and experimental results

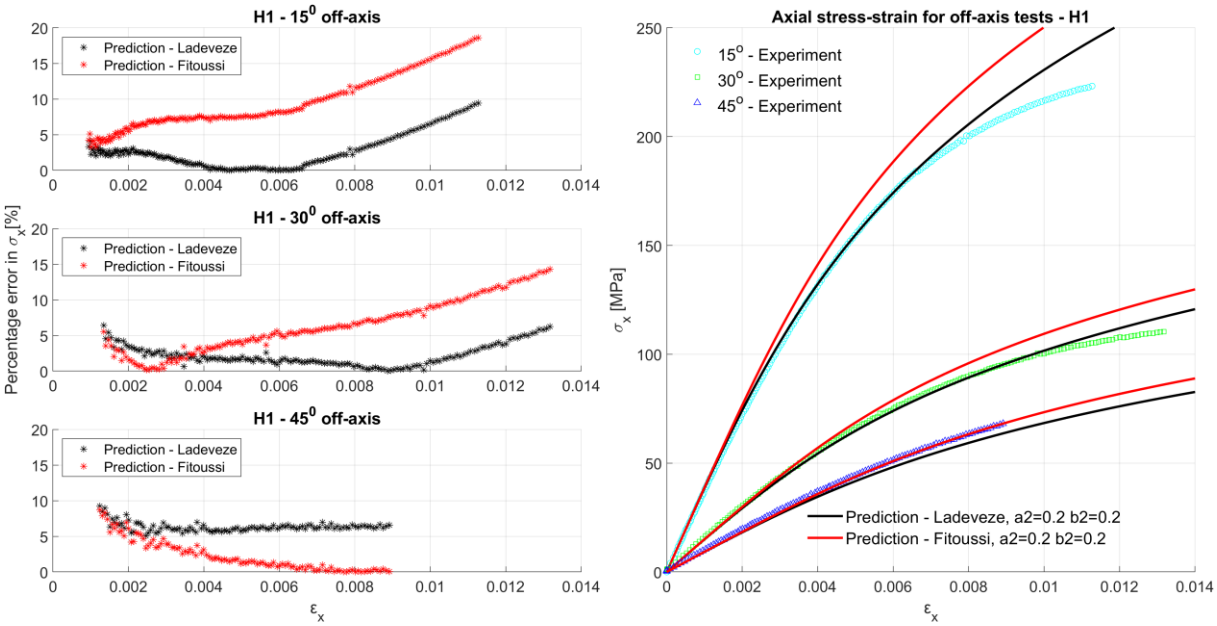

Fig. 3.49. Predictions of the off-axis nonlinear stress-strain of H1, with damage variable estimation from both Ladeveze and Fitoussi methods, a_2=0.2 and b_2=0.2 – with corresponding σ_x percentage error between predicted values and experimental results

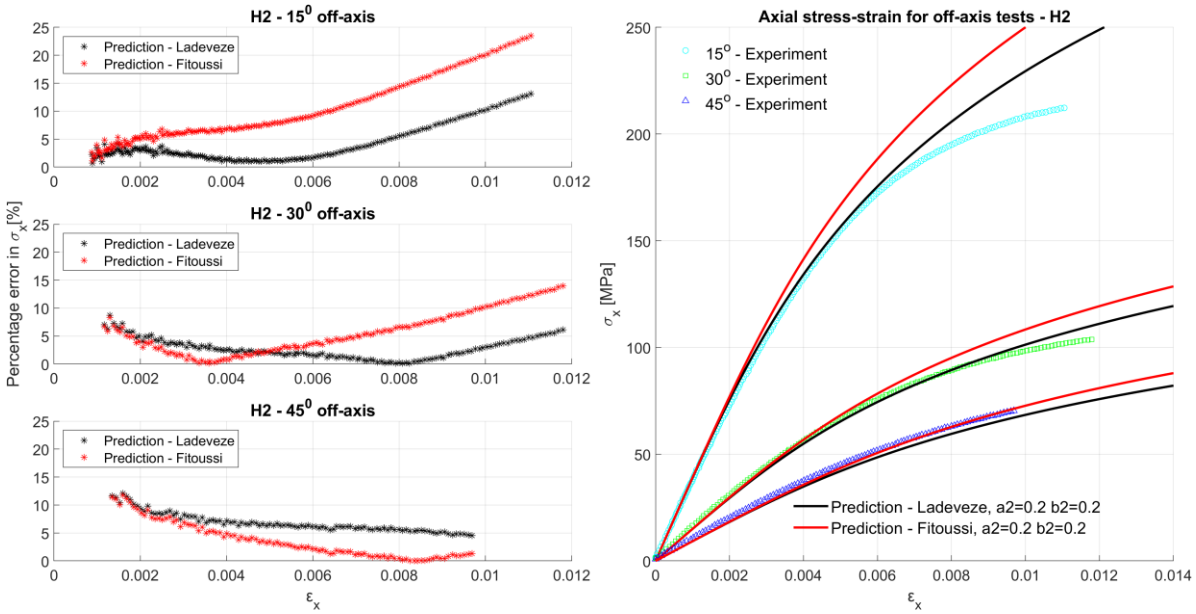

Fig. 3.50. Predictions of the off-axis nonlinear stress-strain of H2, with damage variable estimation from both Ladeveze and Fitoussi methods, a_2=0.2 and b_2=0.2 – with corresponding σ_x percentage error between predicted values and experimental results

Although better predictions are obtained for both UTS laminates, as seen in Fig. 3.47 and Fig. 3.48, in the case of UTS17, there remains a notable difference between the predicted and experimental curves, marked by a maximum percentage error of 11.5% (Ladeveze method) and 16.1% (Fitoussi method) at a 30° off-axis angle. This discrepancy is attributed to the scatter observed in both plasticity and damage variable data, extracted from distinct cyclic load-unload off-axis tests. In this regard, because UTS13 and UTS17 are manufactured from the same prepregs, a prediction of the response of UTS17 laminate using the damage and plasticity parameters from UTS17 is made. The result is presented in Fig. 3.51 and it shows that by using the in-plane mechanical properties of UTS17 and the damage-plasticity parameters from UTS13, which had less scatter in data, a good prediction is obtained for the off-axis response of UTS17, with a maximum percentage error less than 5% for the Ladeveze method, and less than 11% for Fitoussi method. However, it is observed that at 15° and 45° the stress level from the prediction with the Ladeveze method is lower than the experimental values, and the percentage error is higher than for the Fitoussi method.

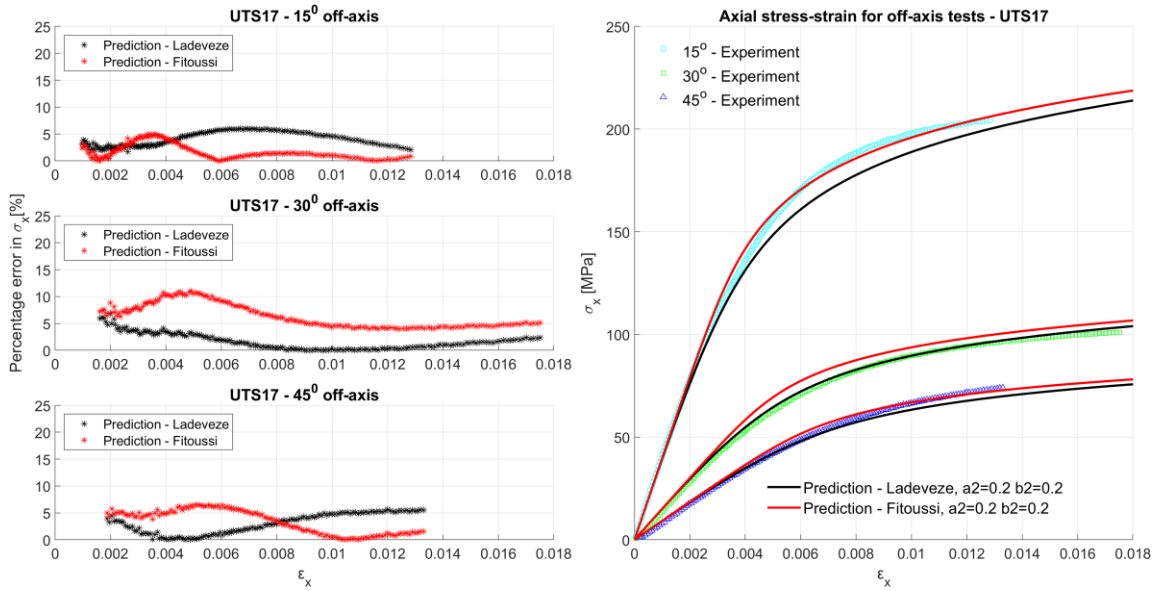

Fig. 3.51. Prediction for UTS17 using damage-plasticity parameters estimated from UTS13 data, a_2=0.2 and b_2=0.2 – with corresponding σ_x percentage error between predicted values and experimental results

The same approach was employed for HSC3 and HSC4 laminates, and although the prediction for HSC4 using damage and plasticity parameters estimated from HSC3 data is not necessarily better (Fig. 3.52), it is close to the original prediction. with small differences in the percentage errors. Thus, it confirms that for laminates with the same material and different thicknesses (differences up to 0.7 mm), using the same plasticity and damage parameters offers satisfactory results.

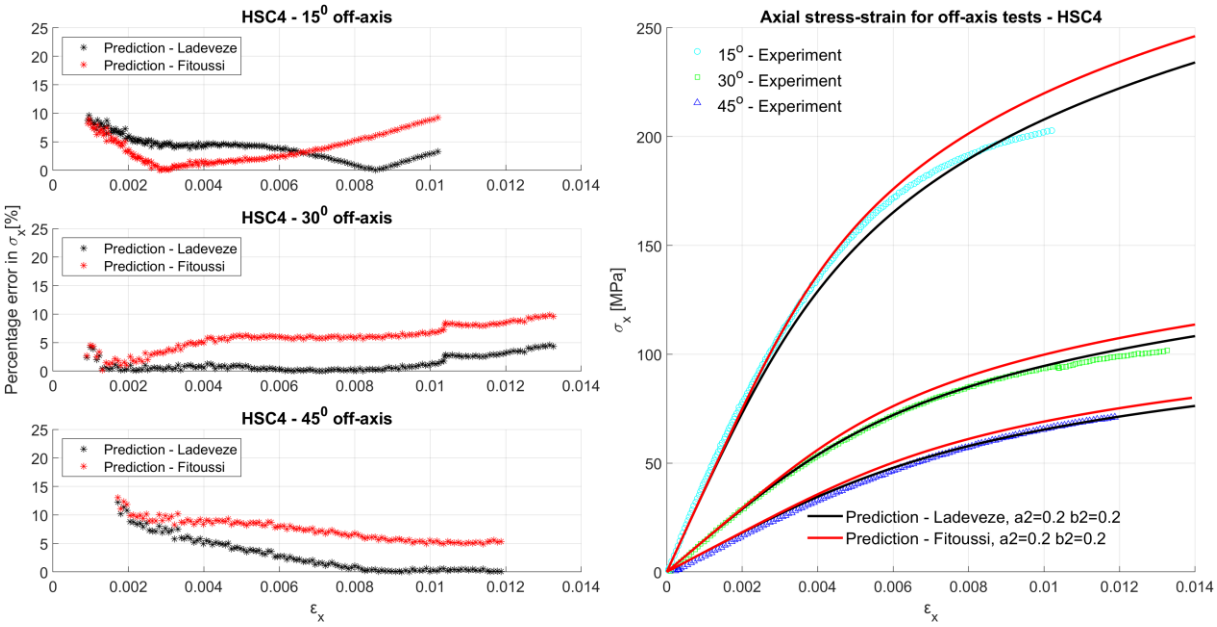

Fig. 3.52. Prediction for HSC4 using damage-plasticity parameters estimated from HSC3 data, a_2=0.2 and b_2=0.2 – with corresponding σ_x percentage error between predicted values and experimental results

While the prediction of the nonlinear off-axis stress-strain response for reference HSC and UTS laminates is good, for the hybrid laminates the stress level is still overpredicted for 15° and 30°. A possible reason is the lack of effective stress–effective plastic strain data for effective plastic strains above 0.0045, which could lead to an erroneous power law fitting. From the power law fittings shown for all materials in Fig. 3.36, the fitting for hybrid materials has the highest increase in effective stress for effective plastic strains above 0.0045, compared to reference materials which have a more flattened curve. Moreover, by looking at the plasticity and damage parameters from Table 3.8 and Table 3.9, it can be observed that close values are obtained for H1 and H2, while compared to the values for reference materials, A and σ_e have the highest values (except for UTS17, for Fitoussi formulation), n has the lowest values, and for n_e, the values are similar to the other materials. Hence, a straightforward approach to establishing a correlation between damage and plasticity parameters for hybrid configurations based on constituent parameters remains elusive. The hybridization of UTS and HSC plies yields a stiffer response in comparison to reference laminates, and the underlying factors behind this phenomenon are still not comprehensively understood. However, if H1 and H2 plasticity parameters are replaced with HSC parameters from the laminates with the same HSC ply number in the hybrid laminates, significantly better predictions are obtained for the nonlinear off-axis response of hybrid laminates, for 15° and 30° off-axis angles, with both damage formulations. Fig. 3.53 shows the predictions for H1, using its damage parameters and the plasticity parameters from HSC3, while Fig. 3.54 shows the predictions for H2, using its damage parameters and the plasticity parameters from HSC4 data.

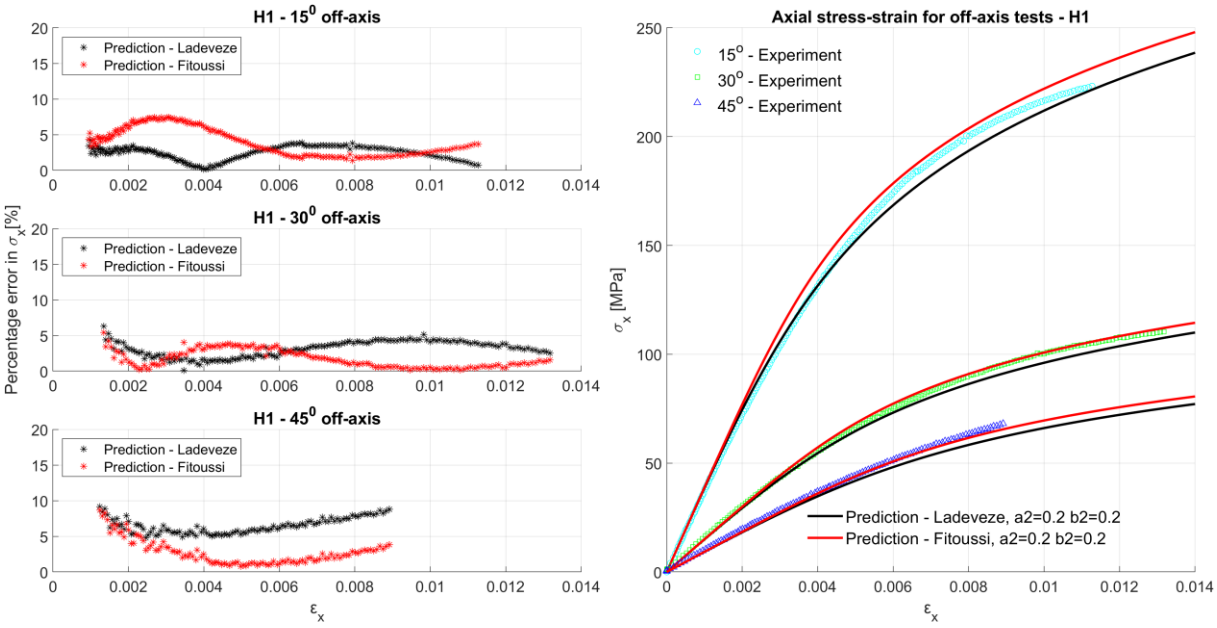

Fig. 3.53. Prediction for H1 using damage parameters from H1 data and plasticity parameters estimated from HSC3 data, a_2=0.2 and b_2=0.2 – with corresponding σ_x percentage error between predicted values and experimental results

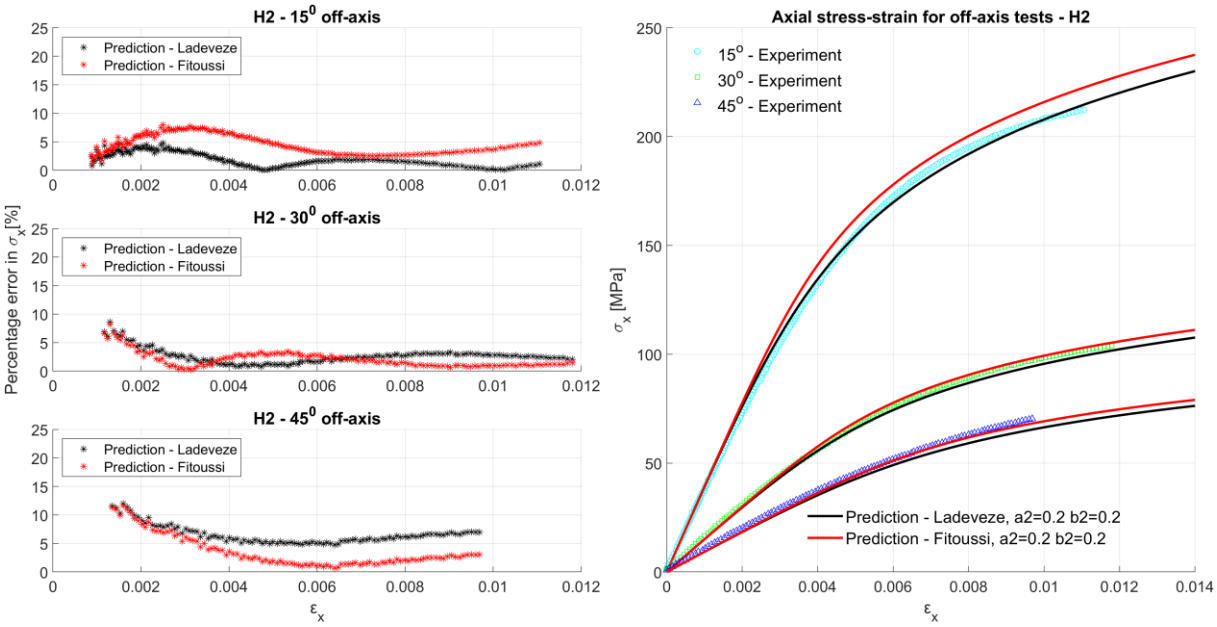

Fig. 3.54. Prediction for H2 using damage parameters from H2 data and plasticity parameters estimated from HSC4 data, a_2=0.2 and b_2=0.2 – with corresponding σ_x percentage error between predicted values and experimental results

For both laminates, the change in plasticity parameters with the corresponding ones from HSC laminates resulted in percentage errors between the predicted stress and experimental stress of less than 5% in the nonlinear response region, in the case of 15° and 30° off-axis angles, regardless of the damage formulation used. For 45º off-axis angle though, the response is slightly underpredicted, with a lower value of the stress value at the same strain, but the percentage error is still less than 10%. This observation suggests that the softening in the nonlinear response region is predominantly influenced by matrix plasticity. In the case of the tested hybrid laminates, the matrix in the HSC plies plays a significant role in governing the plastic response. Efforts were also made to predict outcomes using plasticity parameters from UTS laminates, but these predictions significantly deviated from experimental values at

corresponding strain levels. Consequently, with accurate plasticity parameters, both damage formulations provide satisfactory results, characterized by low percentage errors.

SUMMARY

This chapter aimed at evaluating the quasi-static mechanical performances of hybridized composite materials with respect to high-standard reference materials. The overall goal is to validate an economic choice based on safety justifications relying on a mechanical approach for structural applications in the aeronautic and aerospace industry. Throughout this chapter, objectives 2 (evaluate of the quasi-static mechanical response of hybrid and reference laminates under on and off-axis tensile testing), 3 (investigate the cause of the nonlinear off-axis response through off-axis cyclic load-unload tensile tests and evaluate residual strains and damage variables), and 4 (define a coupled damage-plasticity model to predict the nonlinear off-axis response of laminates) were achieved.

Monotonic quasi-static on and off-axis tests were performed and monitored in displacement at 1 mm/min, to evaluate the in-plane behavior of hybrid and reference laminates. Evaluating and analyzing the results led to achieving objective number 2. Reference laminates of different thicknesses were tested, for comparison purposes, and also to evaluate potential thickness effects on the off-axis mechanical response. Digital Image Correlation was used for full-field strain analysis. However, the setup only allowed for half of the laminate's gauge length to be in the DIC system field of view. A successive linear regression method was proposed and employed for the evaluation of the apparent Young modulus in off-axis samples. This method offers the advantage of minimizing errors induced by the manual selection of the data in the linear response region of the off-axis stress-strain response.

The in-plane tensile properties of the manufactured composites were obtained from quasi-static tensile testing. No thickness effects were noticed on the stress-strain response under both longitudinal and transverse quasi-static tensile loading. For equivalent thickness and sample geometry, hybrid composites exhibited an improved 0° failure stress compared to the estimated strength based on Kawai's scaling function. For the transverse failure stress, high dispersion of data was obtained because most samples failed close to the grips (~ 4 out of 7 samples). The in-plane properties of the studied materials are similar to other published works performed on similar unidirectional carbon fiber-reinforced composite materials [88], [222], [237]–[239].

The off-axis results showed that all tested composites exhibited nonlinear stress-strain behavior, with the degree of nonlinearity decreasing as the off-axis angle increased. In the linear response region, minor differences were observed among the laminates, while in the nonlinear response region, the HSC laminates demonstrated strain hardening compared to the UTS laminates, but had a smaller failure strain. Both hybrid laminates exhibited higher failure stress levels compared to simple laminates and had intermediate failure strains.

No significant thickness effects were observed in the stress-strain response during quasi-static off-axis tensile loading within the linear response region. However, slight differences in stress levels were noted for laminates with the same material but different thicknesses in the nonlinear response region.

The experimental results revealed a degradation of off-axis elastic moduli with increasing off-axis angles, in accordance with predictions using the transformation equation. Similar degradation was observed in the off-axis strength. The in-plane shear modulus was evaluated using tensile tests at various off-axis angles, and the modulus extracted from the 45° off-axis test was selected for further calculations, following the recommendations of Pindera et al. [98].

Overall, the hybridization approach exhibited notable benefits in terms of strain-hardening behavior and increased failure stress when compared to the reference laminates. Additionally, the hybrid laminates demonstrated behavior resembling that of a transversely isotropic system.

Furthermore, cyclic load-unload off-axis testing was performed to investigate the cause of the nonlinear response and achieve objective 3. After analyzing the results, it was concluded that the nonlinearity is caused by a combination of internal damage and residual strain. The

evolution of the damage variable and the accumulated residual strain were quantified by analyzing the incremental loading/unloading stress-strain response of the tested samples. Overall, UTS laminates have the highest residual strains in all test cases, suggesting that the matrix in UTS prepreg has an inherent higher plasticity characteristic compared to HSC laminates, while the hybrid laminates have the smaller residual strains of all materials. For the estimation of the damage variable, three methods are used: Ladeveze, Fitoussi, and Regression. Among these methods, the Regression method is unreliable for extracting the elastic modulus of the load-unload cycles and estimating the damage variables for the materials used in this study, because the damage variable changes at an irregular rate when stress levels increase, giving also negative values and high error bars.

The parameters required to define a nonlinear constitutive model for predicting the off-axis behavior of unidirectional ply-level hybrid composites were determined from the residual strain and damage variable experimental data, achieving objective 4. For predictions of the off-axis behavior of the studied composites, only the damage variables given by Ladeveze and Fitoussi methods are considered. Overall, a good prediction was obtained, with deviations from the experimental results in the nonlinear response region. By increasing the value of b_2 from 0.05 to 0.2, better predictions are obtained for all laminates. Moreover, predictions for thicker reference laminates were performed using the damage and plasticity parameters from thinner laminates of the same material prepregs. Prediction results were improved for UTS17 laminate and were satisfactory for HSC4, confirming that for laminates with a thickness difference up to 0.7mm, using the same plasticity and damage parameters offers satisfactory prediction results. Additionally, predictions of the hybrid laminates' off-axis response were made using the damage parameters of the hybrid laminates and plasticity parameters from the HSC laminates. In the nonlinear response region, the predictions were significantly improved, underlying the importance of the plasticity parameters, and suggesting that the softening in the nonlinear response region is mainly caused by the plasticity of the matrix and in the case of the tested hybrid laminates, the plastic response is mainly governed by the matrix in the HSC plies.

The quasi-static response of the reference and ply-level hybrid carbon fiber composite specimens has been deeply studied and understood from a constitutive as well as from a damage point of view. However, the question of strain-rate sensitivity remains legitime, given the fact that during service time, aircraft components are prone to high-strain rate impact loading.

CHAPTER 4. DYNAMIC RESPONSE OF PLY-LEVEL HYBRID COMPOSITE MATERIALS

INTRODUCTION

In the previous chapter, an analysis of the quasi-static response of the reference and ply-level hybrid carbon fiber composite materials was performed. The complement in the dynamic regime of the mechanical characterization of the studied materials is needed for the design of aircraft structure components, as they can be subjected to intense and impulsive loadings such as mechanical impacts at high velocity. These impacts can be encountered during the rupture of a fan blade, a ballistic or warhead attack for example. They could engender strain rates as high as 10^5 to 10^6 s^{-1} that are very difficult to obtain with Hopkinson bar, which is traditionally utilized for the study of dynamic behavior of materials. In this chapter, the dynamic response at very high strain rates (> 10^5 s^{-1}) is evaluated. As the composite material of interest is unidirectional, this study also considers the evaluation of shockwave propagation in the fiber direction.

In this approach, in the first part of the chapter, Laser-induced shockwaves are chosen to produce intense and impulsive mechanical loadings. Thus, two types of laser tests are performed: one in the fiber direction (in-plane), and one perpendicular to the fiber direction (out-of-plane), with strain rates as high as 10^6 s^{-1}. At least three characteristics are prospected by the use of laser-induced shock waves: 1) sound velocity in the shock direction; 2) material speed and thus corresponding strain rate; 3) damage threshold in laser density of power that can be estimated in term of stress and thus corresponding strain-rate.

The sample preparation for the laser-induced shockwaves tests as well as the experimental setup are described in this chapter. The methods used for data processing and analysis are detailed. The experimental results and discussions for each type of laser test are presented, along with an analysis of the hybrid material response compared to reference laminates.

In the second part of the chapter, the description of steel ball impact testing on an H2 composite plate is provided, along with few experimental data results. This type of test is explored as a means to provide additional insight into damage propagation during impact with a foreign object, as well as the energy absorption capacity of the unidirectional laminates. Results could be extensively used for numerical model validation that is out of the scope of this thesis work, but could be a relevant outlook of this work.

PART 1: LASER-INDUCED SHOCKWAVES

4.1 SAMPLE DESCRIPTION

Because of the anisotropic aspect of composite materials, several experimental characterizations are chosen: one in the sample's out-of-plane direction and one in the in-plane direction, mainly in the fiber direction. In this intention, two types of specimens were prepared.

Small plates of approximately 2.5 ×5 cm, with the fibers aligned with the longer edge, were used for the out-of-plane laser shock test. The thickness of the samples is similar to the material details in 2.1, with small variations. Lower average thickness values were obtained for part of the laminates used for laser-impact testing. The average value decreased for HSC3 laminates to 1.67 mm, for UTS13 it decreased to 2.04 mm, for UTS17 to 2.66 mm, while for H1 it increased

to 2.20 mm, and for H2 to 2.71. For the in-plane laser shock test, the thickness of the laminate plates was insufficient to accommodate the focal spot, as its diameter is about 3.5 – 4 mm. Therefore, thin stripes of ~ 2 mm thick composite material were precision-cut using a diamond cut-off saw. The actual thickness of the stripes varied between 1.7 mm and 2.2 mm, thus they were sorted in pairs of three, with similar thicknesses, and were bonded on top of each other with ethyl-cyanoacrylate (glue) from Sader, as illustrated in Fig. 4.1. Care was taken to have a similar stacking sequence oriented in the same direction for each stripe. Therefore, samples with a width of 6-8 mm and a length of 25 mm were obtained. The chosen glue has a similar shock impedance to the epoxy matrix [158], [240]–[242].

When manufacturing the in-plane samples, for H1 samples which have an asymmetric stacking sequence, care was taken to position the adjacent stripes in the same position. For reference laminates, only the thicker UTS and HSC laminates, UTS17 and HSC4 respectively, were used to manufacture the in-plane samples.

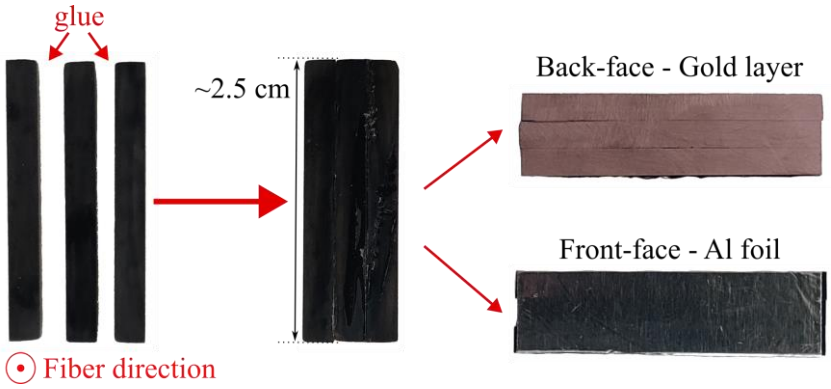

Fig. 4.1. Sample preparation for in-plane laser impact

To ensure uniform thickness and eliminate any residual glue, manual polishing was conducted on both faces of the samples. The samples were affixed to a resin block using double-face adhesive tape for improved handling. A water-lubricated SiC foil #500 was employed for polishing to achieve flat and smooth surfaces on the samples.

In both tests, a sacrificial layer of aluminum tape with 50 µm of aluminum and 30 µm of adhesive is used to have a mastered laser-matter interaction [243], [244], and also to be able to approximate the mechanical loading generated on the specimen's surface. Additionally, a reflective surface is necessary for measuring the back-face velocity. To achieve this, a thin gold layer was applied to the back face using a sputtering machine COXEM SPT-20 ION-COATER. The coating process utilized a current of 7 mA for a duration of 200 s. According to the manufacturer, the corresponding gold thickness in such a configuration is about 500 nm.

Fig. 4.1 presents the final test samples for in-plane laser impact and Fig. 4.2 illustrates the particularities of out-of-plane laser test samples. For in-plane tests, only one shot is performed on each sample, while for out-of-plane tests multiple shots are performed on the same sample, with an appropriate distance between them so that damage from one shot would not affect the wave propagation of another shot (Fig. 4.2c).

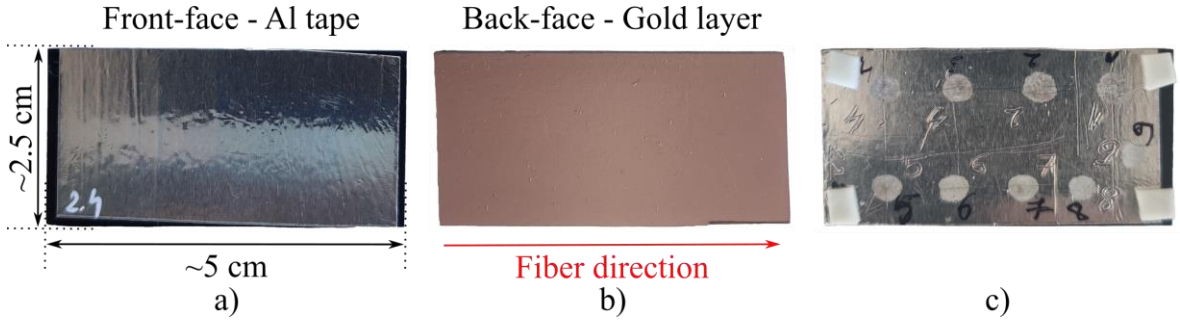

Fig. 4.2. Out-of-plane laser impact sample; a) Front-face with Al tape for sacrificial layer; b) Back-face coated with gold; c) Multiple laser shots on the same sample

4.2 EXPERIMENTAL SETUP

The laser source is an Nd: YAG Quanta-Ray Pro 350-10 delivering a Gaussian pulse of about 7.5 ns, with a maximum energy of 3.5 J at the output in its fundamental mode at a wavelength of 1064 nm, when warmed up at 10 Hz. This laser works in Q-Switch technology. It consists of an oscillation stage providing an 8 mm diameter laser beam of about 1 J, followed by an amplification stage, shaping the beam diameter to 12.7 mm with 3.5 J. This laser has been designed to work at a rate of 10 Hz, but it can also be used in single shots. A preheating time of 30 minutes is required for optimal performance. These parameters influence optimum functioning: temporal pulse, maximum values of the output energy, and energy repartition in the beam cross-section, as well as the repeatability of the shot characteristics.

The energy graduation can be continuously adjusted outside the laser source with a variable attenuator comprised of a quarter wave plate and a polarizer mounted in a rotative mount, at the Brewster angle of 56°. This ensures that the laser is working at its maximum energy and accounts for better laser pulse repeatability. By adjusting the angle shift from 0° to 45° between the quarter wave plate and the polarizer, the output energy can vary respectively from E_{max} = 2.9 J to about E_{min} = 100 mJ, with a beam diameter of 13 mm. The laser beam is thus separated into a direct beam of intensity I_1 and a deviated beam of intensity I_2. Their intensity summation equals the source beam intensity, including leaks of about 100 mJ: $I_{source} = I_1 + I_2 + I_{leaks}$.

To obtain better shot parameters, the continuous 10 Hz working mode is preferred, and a previously developed mechanical shutter is set in place to reflect the laser beam into a beam dump. The mechanical shutter is composed of a flag hosting a mirror moved by an electrical motor, is controlled by Arduino Uno [245], and can order a fast opening and closure so that only one pulse out of 10 per second passes out, and single shots on the target are obtained, with a warmed laser condition, much more favorable to a better shot to shot stability. The laser beam is then focused on a target using a lens with a focal distance of 200 mm, at a desired diameter so that the density of power in GW/cm² can be selected and create a laser-induced shock wave.

To achieve higher pressures and longer pulse duration, water confinement is used [246]. To ensure a proper water film, the target is placed horizontally and an O-ring is used to keep the water in the test area. Therefore, an additional mirror has to be used to deflect the laser beam at a 90-degree angle.

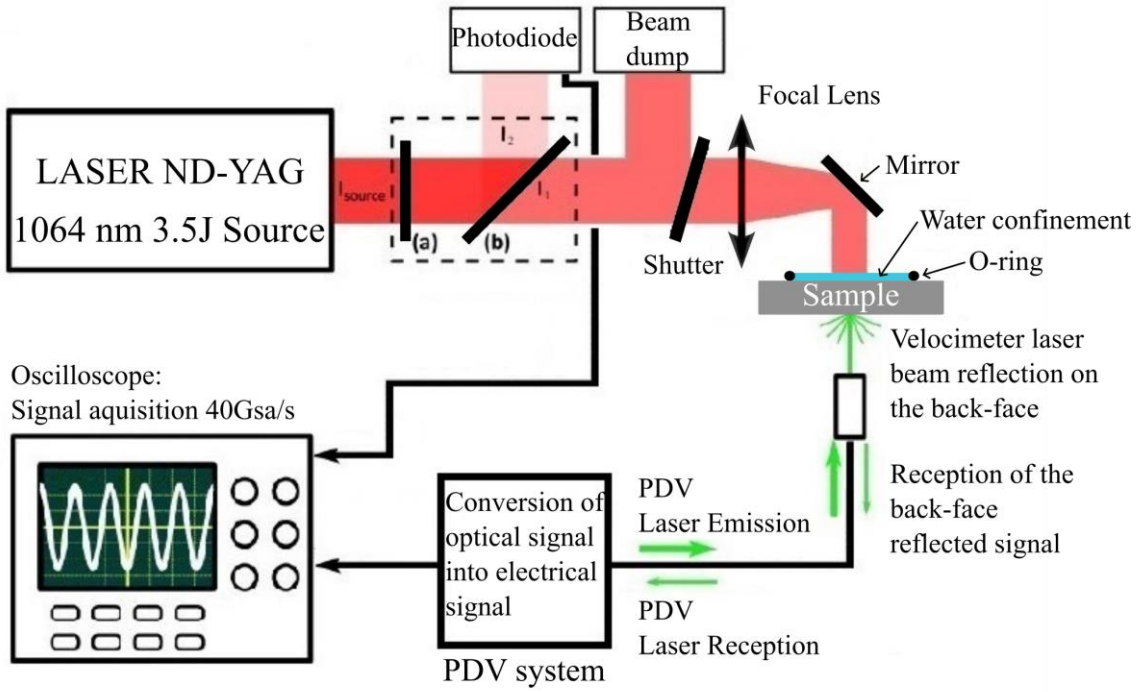

Fig. 4.3. Scheme of laser impact experimental setup (not at scale); (a) quarter-wave lens, (b) polarizer

Photon Doppler Velocimetry (PDV) manufactured by IDIL France is used for measuring the back-face velocity. The measured quantities are recorded by an acquisition chain triggered by a fast response time photodiode (<1ns) UPD300SD distributed by Alphalas. A fast oscilloscope Agilent DSO80604B (50 Ohm, 6GHz, 40 GS/s) is used for signal acquisition. The scheme of the described experimental setup with the laser impact shot and measurement chain is represented in Fig. 4.3.

4.3 LASER PULSE CHARACTERIZATION

The laser pulse characteristics are of paramount importance, as they are required to calculate the density of power of the laser shot (equation (1.37)). For this, a set of pulse duration and energy measurements were performed to characterize the laser pulse, and focal spot observations and measurements were made for each shot, to characterize the irradiated surface. To account for the uncertainties in the measurements and their influence on the density of power, a Monte Carlo analysis with 10000 trials was used to estimate the density of power and its standard deviation. The same analysis was performed to calculate other parameters as well, and more details are given in section 4.4.3

4.3.1 Pulse Duration and Time Shift

To measure the pulse duration of the laser shot, a fast response time photodiode UPD 300 SD (rising and falling time < 1 ns) is used. In previous work, this pulse was estimated at 9.2 ns [243]. Initially, the flashlamp of the laser source and the plasma light caused by the laser impact on the target surface were both captured by the photodiode. As a consequence, the pulse shape has a longer release, leading to an overestimation of the pulse duration. Thus, a soft-coated bandpass filter FL1064-3 from Thorlabs placed ahead of the photodiode allows only passing the light wavelength of 1064 ±0.6 nm. A different set of measurements was performed to estimate the pulse duration.

Fig. 4.4 presents results obtained for different energy levels: 25%, 50%, 75%, and 100% of maximum energy. The laser source is adjusted at 10 Hz at full power and the mechanical shutter is used to obtain single pulses. The pulse duration measurement is obtained from the reflection from the front face of the focusing lens. Its duration is fixed by the manufacturer and is not supposed to depend on the energy setup. Fig. 4.4a shows the signals digitized by a fast oscilloscope Agilent DSO80604B (50 Ohm, 6GHz, 40 GS/s) directly while Fig. 4.4b shows the signal after normalization, and illustrates the pulse-to-pulse repeatability of the laser beam. The pulse durations of these Gaussian are determined at half maximum - or full width at half maximum (FWHM). From 4 sets of measurements (10 for 100%, 10 for 75%, 5 for 50%, and 5 for 25%), the average pulse duration was evaluated at 7.35 ns, with a standard deviation of 0.36 ns. The obtained pulse duration is similar to the manufacturer's specification of 7.5 ns.

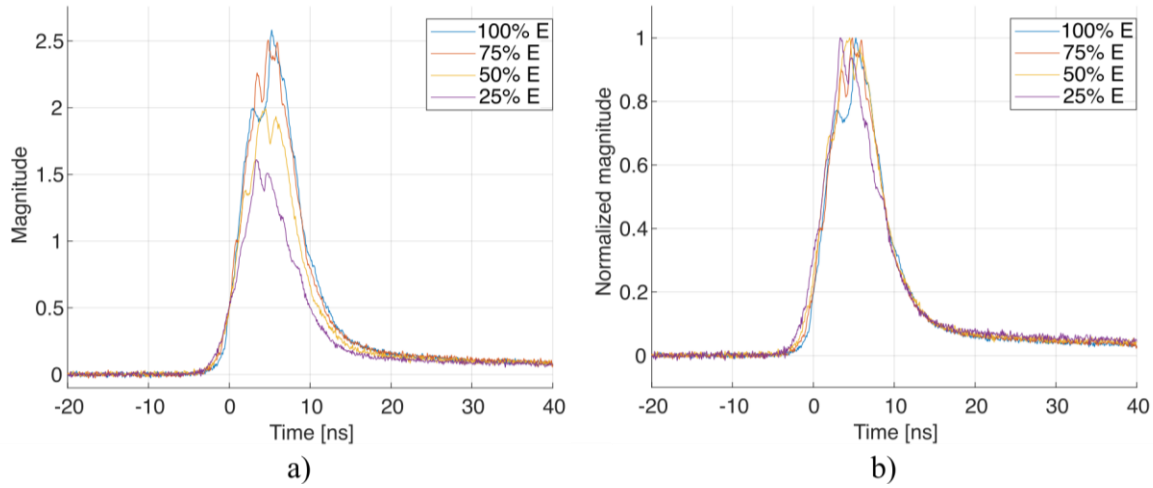

Fig. 4.4. Temporal form of the laser pulse for different energies recorded by the photodiode a) direct signal b) normalized signal.

Due to the delay in the chain of measurement, corresponding to the delay of the information transit in BNC cables and optical fibers, a time-shift must be considered for each laser shot, to set the start of the rising laser loading at zero time. To evaluate the required time shift for each test, an analysis is performed of the rising front of the laser pulse. Fig. 4.5 illustrates the procedure to extract the time shift from the laser pulse data. In the first step, a line is drawn between two points set at 10% of the magnitude above the baseline and at -10% of the magnitude below the maximum value, denoted as L_1. The intersection of L_1 with the baseline is marked as I_1. A vertical line passing through the I_1 line is further drawn and its intersection with the pulse data is marked as I_2. The coordinate of I_2 on the time scale represents the time at which the shockwave starts, thus, it also represents the required time shift. The time shift is calculated for each laser impact test. The actual trigger time results from the trigger level adjusted at the oscilloscope, on the rising edge of the photodiode signal. Therefore, the time scale of the corresponding back-face velocity signal is adjusted accordingly.

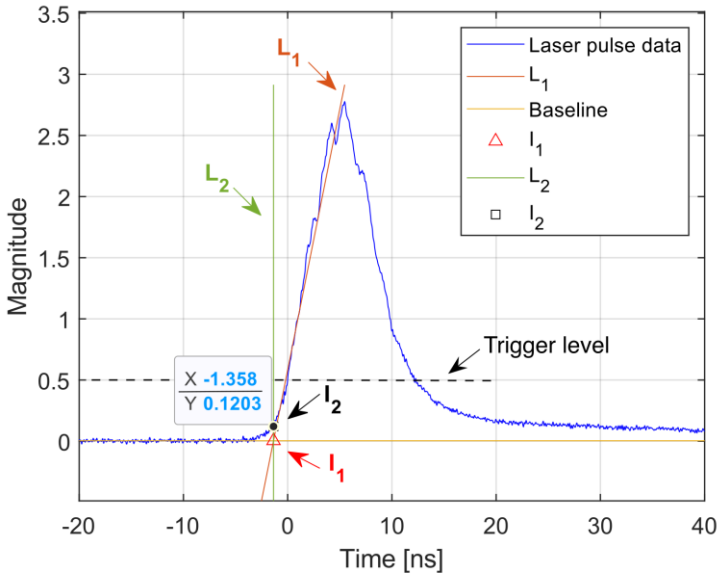

Fig. 4.5. Analysis of laser pulse data to extract required time shift

In addition to this correction, one shall consider the lens-target distance that differs from the lens-photodiode distance. Moreover, there is a loss of time in RG58 cables from the photodiode to the oscilloscope (~5 ns/m), and in the PDV system because of the length of optical fibers (~3 ns/m). To estimate this time loss, a shot is preliminarily performed on an Al target of 1000 µm thick with a known sound speed of 5390 m/s [189] and C_L=6300 m/s.

In Fig. 4.6, it can be seen that the time of arrival t_{oa} when the shock breaks out at the back face corresponds to 236 ns, and the back-and-forth time between two peaks is about t_2-t_1 = 0.33 µs and t_3-t_2 = 0.31 µs. The time of arrival for a moderate shock pressure just above the Hugoniot elastic limit (elastic precursor traveling at 6300 m/s) can be calculated using equation (4.1), where d represents the thickness of the aluminum target, and $C_{L_{AL}}$ is the longitudinal speed of sound (i.e. 1mm/6.300 mm µs^{-1} = 0.159 µs = 159 ns). This time shift is also to be corrected by the triggering time which takes between 2 to 3 ns because the trigger threshold is fixed at 550 mV on the photodiode signal. An additional time correction t_{lmi} should be considered because of the time taken by the pressure rise resulting from the laser-matter interaction (which is negligible). Also, the delay caused by the cable length, t_{cl}, and fiber length, t_{fl}, inside the interferometer should affect the actual triggering time and thus transit time. However, it was not possible to evaluate t_{lmi}, t_{cl}, and t_{fl} and it is then suggested to evaluate the global time shift which is the difference between the observed and the theoretical time of arrival and theoretical, based on equation (4.2). For the back-face velocity of a 1mm aluminum sample illustrated in Fig. 4.6, the resulting required time shift is then 236 ns – 159 ns = 77 ns. For different laser test

campaigns, different calibration tests were performed on aluminum targets, and the time shift was estimated and applied for the corresponding tests in the specific experimental campaign.

$$t_{oa_{th}} = \frac{d}{C_{L_{AL}}} \tag{4.1}$$

$$t_{shift} = t_{oa_{obs}} - t_{oa_{th}} \tag{4.2}$$

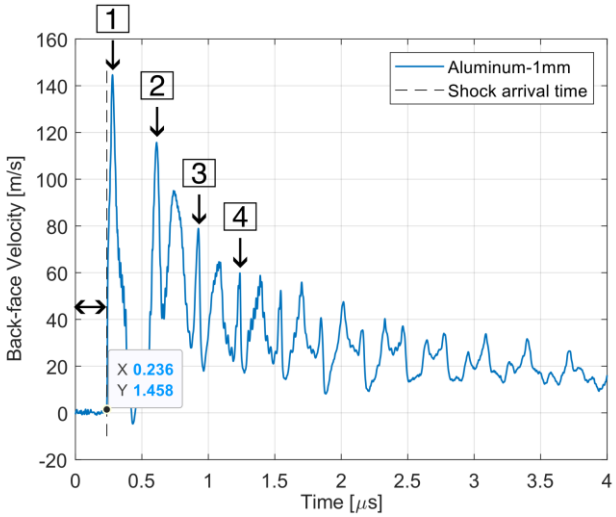

Fig. 4.6. Back-face velocity signal for 1 mm thick Aluminum Target, 100% of max energy

4.3.2 Energy Measurements

Two laser shock experimental campaigns were performed one in 2021, mainly on H1 material, and a second one in 2022. For both campaigns, energy measurements were made using a QE25LP-S-MB-QED-D0 Pyroelectric detector for laser energy measurement coupled with a MAESTRO interface, both manufactured by Gentec.

It must be noted that between these campaigns, maintenance was performed on the laser facility: The Nd:YAG Rods were replaced, and the photodiode for the trigger was replaced by a faster one equipped with an interferential filter. Another type of Joulemeter was tested and measured 3 J when the Gentec Maestro measured 2.9 J. Both direct energy measurements and measurements of the laser beam energy after passing through the optical chain were performed. The optical chain loss was estimated at ~0.3J between the laser output and the target.

The energy levels and corresponding angle of the polarizer and energy values in both experimental campaigns are presented in Table 4.1. All energy measurements have an uncertainty of ±0.01J. The values of the energy represent the energy deposited on the target.

Table 4.1. Laser energy measurements

Energy level [%]	Polarizer Angle [deg]	Energy value [J]	
		2021 Campaign	2022 campaign
100	0	2.63	2.94
85	11	2.24	-
75	14	1.97	2.22
50	22.5	1.31	1.54
35	27	0.92	1.10
25	30	0.66	0.85
15	35	0.39	-
10	36.5	0.26	-

4.3.3 Beam Energy Profile

The spatial repartition of the laser energy onto the target is not perfectly uniform. Tahan [199] performed an analysis of the spatial repartition of the density of power (intensity) of the laser used in this study, with the help of a Edmund Optics® Beam Profiler 4M. A smoothed spatial profile of the intensity of the laser beam over the radius of the laser beam was obtained along with a fitting function obtained by interpolation of a cross-section analysis provided by the beam profiler, and is described in equation (4.1). Fig. 4.7, adapted from Tahan's work [199], shows measurements of the distribution of the density of power of the laser source, with a fitting function using equation (4.1). It can be observed that a plateau of maximum intensity is obtained in the center, with a sudden drop and remanent energy towards the edges. The effects of the low density of power towards the edge can be observed on the focal spot as a faded shade on its perimeter.

This profile corresponds to measurements before focusing the laser beam onto the target. The spatial profile after focus is considered as a homothety of the profile at the output of the laser source. During the experimental campaigns that have been carried out, the laser beam was commonly focused on an almost circular, slightly oval shape. The ovality is due to a security measure which consists of tilting the optics slightly so as not to reflect the laser beam into the entrance of the laser source, which could damage the latter. Although the spatial distribution of the density of power is not considered in analytical calculations, it is of utmost importance for numerical simulations of the laser impact.

$$\phi(r) = \min\left(300.9\left(\frac{1}{\pi}\operatorname{atan}\left(-103.4 - abs\left(\frac{r}{2.917}\right)^{12}\right) + 0.5\right), 0.4488\right) \qquad (4.3)$$

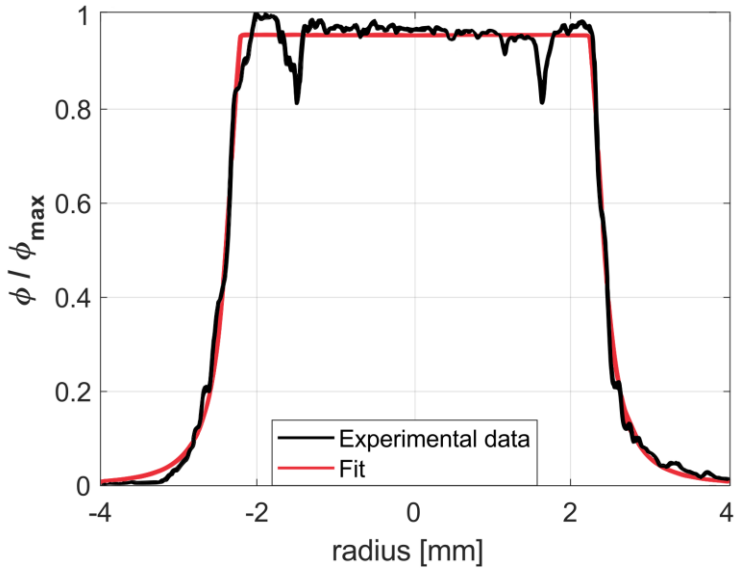

Fig. 4.7. Radial distribution of the density of power with a fitting function , adapted from Tahan [199]

4.3.4 Focal Spot Analysis

When the laser beam hits the target, a focal spot is imprinted on the target surface. The focal spot dimension influences the density of power of the shot. To limit edge effects on the shock propagation, the focal spot diameter should be 3-4 times larger than the thickness of the sample [247]. Below this threshold, back-face velocity signals may be affected by edge effects coming from the border of the spot irradiated by the laser.

Fig. 4.8a shows a focal spot example, for a target shot at 50% of max energy level with water confinement. It is observed that the focal spot is uniform, with an almost round shape. For calculation purposes, the focal spot is approximated as a circle with the diameter taken as

the average value between diameter measurements on two perpendicular axes. An uncertainty of 0.01 mm is considered to account for errors when choosing the focal spot boundary.

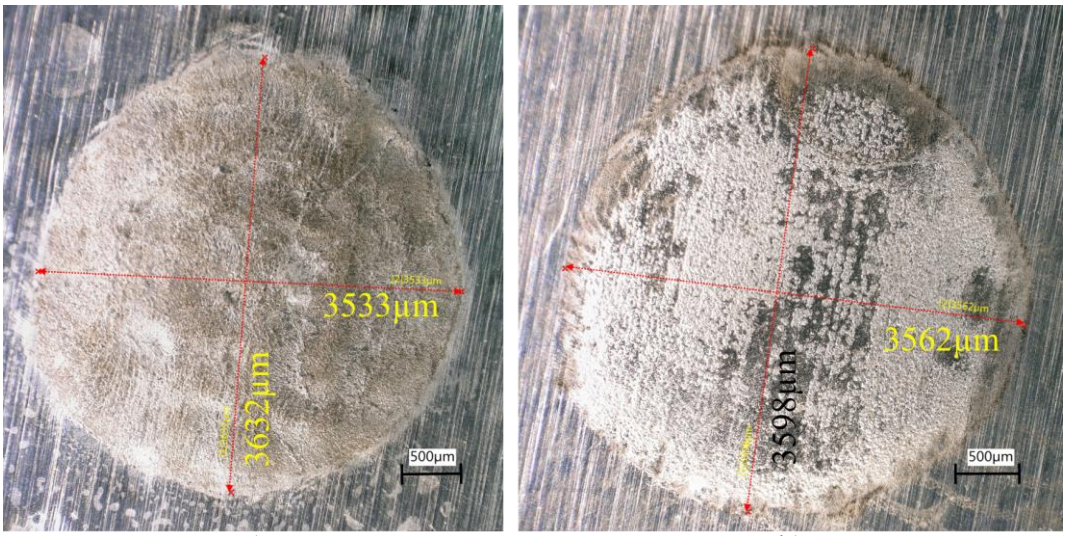

Fig. 4.8 Focal spot microscopic image for shots at 50% of max energy level; a) Water confinement; b) no confinement

The use of a confinement medium improves the uniformity of the focal spot, hence the laser energy distributed to the target, as can be seen when looking at Fig. 4.8b, which presents the focal spot of a direct shot with the same target type and energy level as Fig. 4.8a. The confinement medium does not affect significantly the focal spot diameter since care was taken to deposit a flat drop of water on the irradiated face.

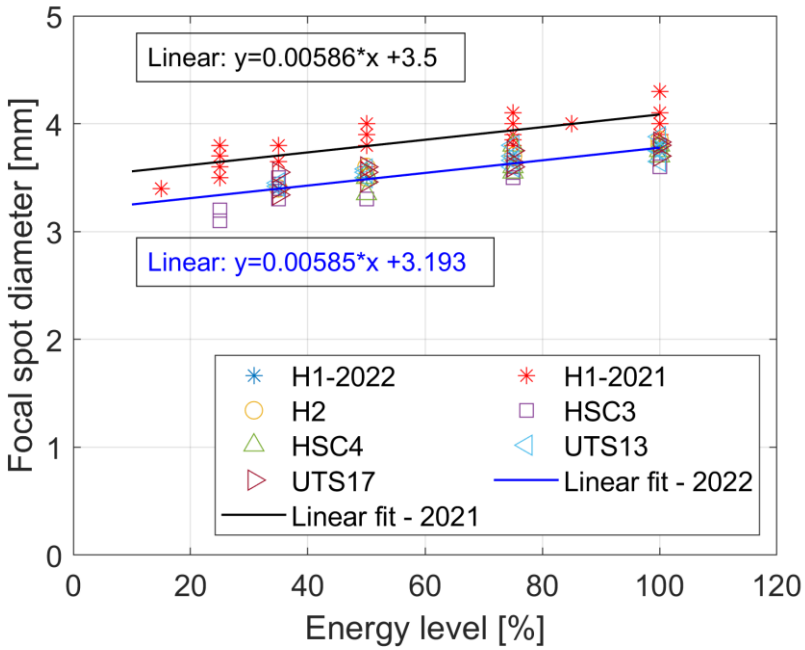

Fig. 4.9. Focal spot diameter versus laser energy level for out-of-plane tests

In the first experimental campaign (2021), a focal spot diameter at a maximum energy of 4 mm was set. In the experimental setup in the second experimental campaign (2022), the same focal spot was intended, but due to the optical chain involved, a maximum focal spot of 3.85mm was obtained. Although the same experimental setup was used for shots at different energy levels (in the respective campaigns), in both cases it was observed that the focal spot decreases with the energy level. Small variations in the diameter of the focal spot were found also for

shots at the same energy level. Fig. 4.9 shows the variation of the focal spot diameter with energy level, for both 2021 and 2022 experimental campaigns, with linear fits. It is observed that although the focal spot diameters for the 2021 campaign are higher than the ones obtained in the 2022 campaign, the trendline and the slope of the linear fit are mainly the same. This implies that the focal spot diameter decreases at the same rate, regardless of the focal spot diameter choice at maximum energy. This allows for predictions of the focal spot dimension at various energy levels, hence the prediction of the density of power, when the same laser source and setup are used.

4.4 HETERODYNE VELOCIMETRY

4.4.1 Signal Processing

Material velocity is one of the most accessible physical parameters in shock physics. Thanks to laser doppler interferometry it is possible to measure the back face velocity during shock experiments bringing extreme loadings in pressure intensity and briefness. In addition, it is a contactless (non-intrusive) technique. In this intention, the Photonic Doppler Velocimetry technique was used. For laser-induced shockwave experiments, back face velocity measurements are of high interest as this time-resolved measurement is fast enough to provide valuable information on shock propagation history, its effect on material, and velocity history.

The PDV signal was saved after each shot and processed with Cafeine software, provided by the French institution Commissariat à l'Energie Atomique. The software processes the digitized PDV signal using Short Time Fourier Transform (STFT), according to [248]. For this, temporal windows of fixed number of samples of the original signal are considered and a Fast Fourier Transform (FFT) is applied locally. One way that can be used to derive these segments is through windowing – the original signal is multiplied by a window function (for example rectangular window, Hann, Hamming, etc.), sample by sample, and a windowed signal is obtained. A spectrum is estimated with FFT and the operation is repeated by sliding the window function to the next segment of the signal. Overlapping the segments is needed to avoid losing signal data at the beginning and endpoints of the window frame when using other window function types, except for the rectangular one. Multiple spectra are obtained which are collected into a spectrogram of the whole signal. Besides the window function type, this method has additional entry parameters, which influence the quality of the spectrogram and the extracted velocity signal.

The width of the window, which represents the number of samples that windowing is applied, determines the ratio between temporal precision and accuracy of the velocity data. The larger the window, the more accurate the signal will be in terms of velocity value but at the cost of a loss of precision in the occurrence of events. A thinner window will allow a more precise description of the time of an event but with a higher uncertainty on the velocity value.

Another parameter represents the overlapping rate of the windows, which influences the discretization of the spectrogram. This represents the number of samples that are slid to the right when a new frame of the signal is taken. The lower the overlap rate, the fewer columns the spectrogram will contain. This parameter can smooth the events because it induces an average on the signal. Therefore, the overlapping rate can become detrimental in reading information on the velocity signal, such as distinguishing the elastic precursor on the rising front of the velocity signal. The first step of obtaining a spectrogram of the velocity signal after the required parameters are set is illustrated in Fig. 4.10, with examples for the same overlapping rate (Samples) but different window widths (Step).

After the spectrogram is obtained, the second step includes a selection of the region of interest (Fig. 4.11a), to extract velocity data (Fig. 4.11b). Polygon selection is preferred to the rectangular selection, as it enables a better choice of regions, therefore baseline induced artifacts can be avoided. The third step involves saving the data in a .txt file and processing it with MATLAB software to plot the back-face velocity history. A comparison of resulting velocity signals for the cases presented in Fig. 4.10 is shown in Fig. 4.12. It is observed that in signal

processing, the maximum velocity of the first peak is not affected by the step number, but in the region between 0.75 µs and 1 µs, a sort of plateau is visible and exhibits some peaks of much lower intensity. This pattern is actually the signature of delamination inside the sample provoked by tensile stress (spallation process). The lower step size induces additional noise in the back-face velocity data, compared to the case with a higher step size. The signal intensity exhibits some losses that are visible in the signal extraction as sharp edges. These edges are not physical since the sharpest signal feature should not exceed the loading characteristic frequency (around hundreds of MHz). These edges thus, should be carefully interpreted not as mechanical signals, but as lack of signal.

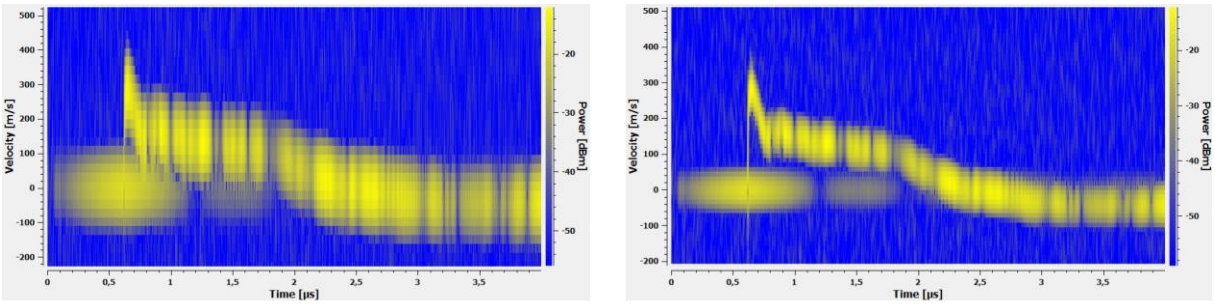

a) b)

Fig. 4.10. Back-face velocity signal processing using Cafeine with Hamming window type; a) Step: 400, Samples: 40; b) Step: 800, Samples: 40

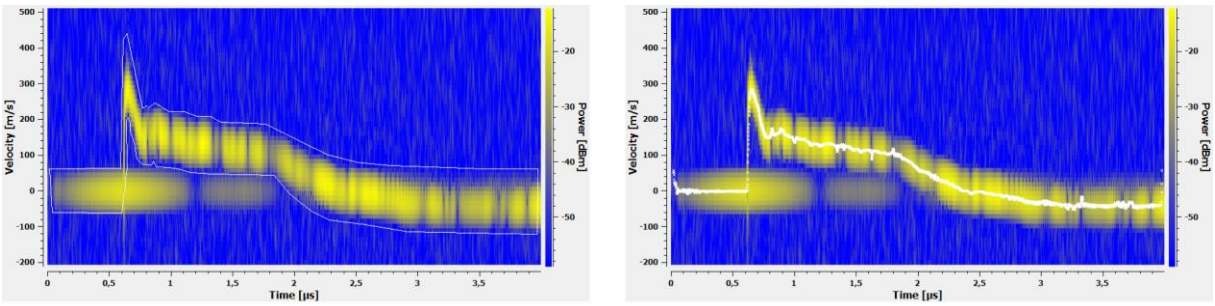

a) b)

Fig. 4.11. Back-face velocity signal processing using Cafeine, Hamming window, Step: 800, Samples: 40; a) Polygon selection for the signal of interest; b) Velocity extraction from PDV signal

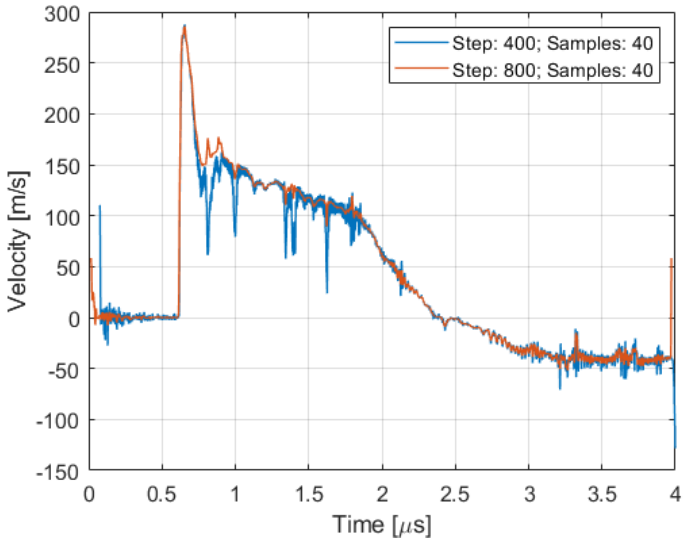

Fig. 4.12. Back-face velocity signals extracted using Cafeine

For processing the back-face velocity signals, Hamming window type with Step: 800, Samples: 40 was set as default, as it offered good results. For particular cases, these parameters were slightly adjusted to obtain satisfying results. One shall note that combining the extreme aspect of the loading (briefness and intensity), and the lack of reflectivity, these experimental results, although pointing out some limits, are at the frontier of the possible experimental methods available in shock physics.

4.4.2 Speed of Sound Estimation from BFV Signals

In section 1.4.3, a theoretical exemplification of back-face velocity analysis was presented. Fig. 4.13 shows the back-face velocity signal for an undamaged sample, shot in the out-of-plane direction at 35% of max energy, with a density of power of 1.06 GW/cm^2. In this figure, the first and second shockwave breakouts are identified from the back-face velocity signal, and the corresponding time values t_1 and t_3 are used for the speed of sound estimation. Because a sacrificial layer is used, to determine the propagation speed in the composite laminate, equation (1.51) is adapted to account for the propagation time in the aluminum and glue layers from the aluminum tape, giving equation (4.4), where L denotes the composite thickness without the aluminum layer, t_{AL} and t_{GL} represent the propagation time in the aluminum and glue layer respectively (from the aluminum foil). For the aluminum layer the shockwave speed is C_{LAL} = 6300 m/s, and C_{0GL} = 1200 m/s for glue [244]. The elastic wave in glue is neglected. The extraction of the time value for the 1st and 2nd shockwave breakout for out-of-plane samples is made using the *islocalmax* function in MATLAB. The *'MinProminence'* setting is adjusted to avoid selecting the local maxima from reflections in the composite plies (the first two peaks after the first shockwave breakout) and noise in the data.

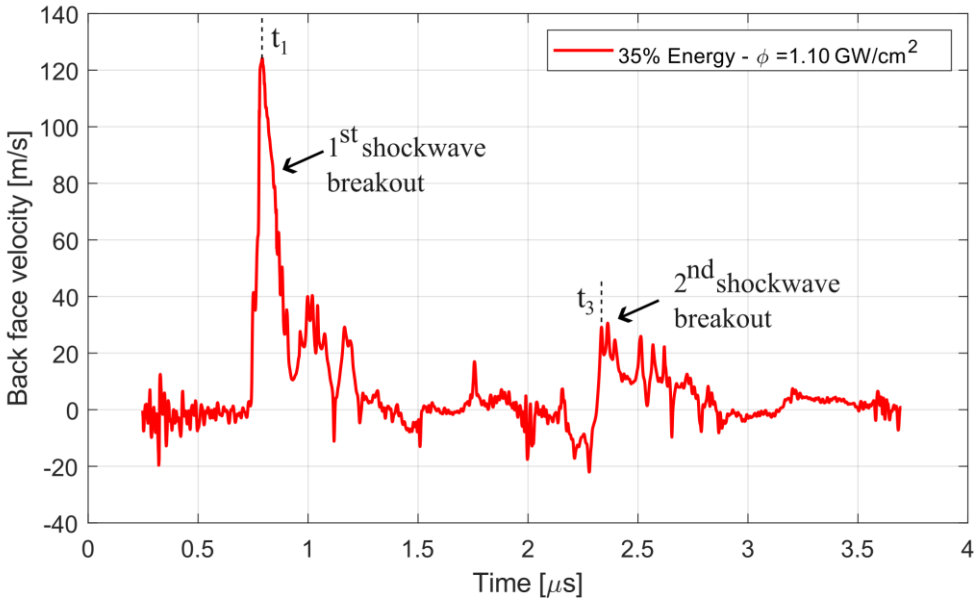

Fig. 4.13. Example of back-face velocity signal of an undamaged sample, shot in the out-of-plane direction, with data identification for calculating the speed of sound

According to the shock polar in Fig. 1.18, the material velocity for the maximum pressure load is half of the maximum back-face velocity. Thus, when evaluating the speed of sound, half of the back-face velocity is subtracted from the propagation speed determined from the back-and-forth propagation. Equation (4.5) is used to estimate the speed of sound, where u_{BFV} represents the maximum velocity of the first peak in the case of in-plane laser shots, and the average value between the maximum velocity of the first and second peak in the case of out-of-plane laser shots, as the shockwave is attenuated and the maximum velocity of the second peak is significantly lower than the first one.

$$C_L = \frac{2L}{t_3 - t_1 - t_{AL} - t_{GL}};\ t_{AL} = \frac{2L_{AL}}{C_{L_{AL}}};\ t_{GL} = \frac{2L_{GL}}{C_{0_{GL}}} \tag{4.4}$$

$$C_0 = C_L - \frac{1}{2}u_{BFV}; \tag{4.5}$$

For the back-face velocity of in-plane samples, the number of back-and-forth shockwave propagations within the 4 µs timeframe is much higher than for out-of-plane samples, for which only two shockwave breakouts are captured, suggesting a higher propagation speed. The shockwave is also less attenuated in one back-and-forth propagation for the in-plane shot, compared to the out-of-plane case. Fig. 4.14 illustrates an example of back-face velocity response in the case of an in-plane laser shot at maximum energy and a density of power of 3.2 GW/cm^2. Therefore, to have a more accurate propagation period, a Fast Fourier Transform (FFT) analysis is used for the back-face velocity signals of in-plane samples, to extract the period of oscillation.

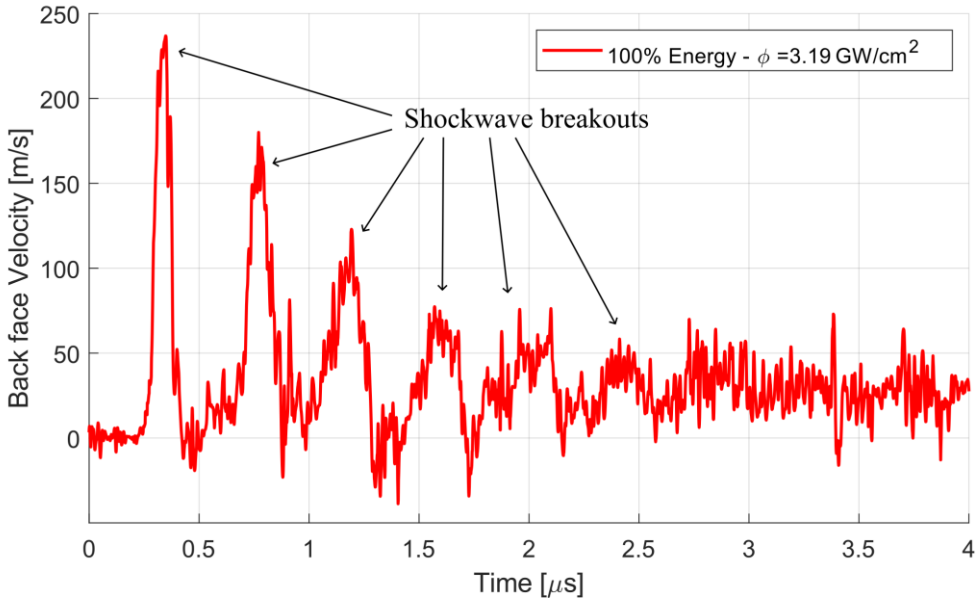

Fig. 4.14. Example of back-face velocity signal of an undamaged sample, shot in the in-plane direction, with identification of shockwave breakouts

The FFT analysis procedure is developed in MATLAB, and the code is provided in APPENDIX I. First, the DC component is removed from the velocity signal. The Sampling Interval (T) is calculated as the average of the time difference between consecutive data points, and the Sampling Frequency (F_s) represents the inverse of the sampling interval. The FFT is employed on the velocity signal without the DC component using the FFT function in MATLAB. The positive half of the spectrum is selected and multiplied by 2 to compensate for the loss of energy in the positive half of the magnitude spectrum due to the complex conjugate symmetry property of the Direct Fourier Transform (DFT). The frequency values are calculated using equation (4.6), where L represents the signal length, F_s is the sampling frequency, and n is a vector of consecutive values. An example of a frequency spectrum with the magnitude normalized to the signal length is shown in Fig. 4.15. The presented frequency spectrum corresponds to the in-plane back-face-velocity signal from Fig. 4.14.

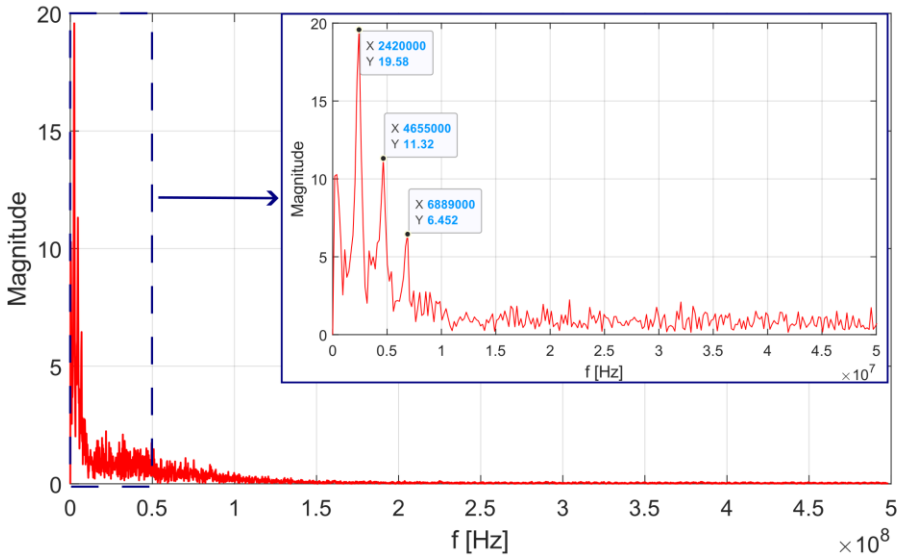

Fig. 4.15. Example of the frequency spectrum, with the magnitude normalized to the signal length

$$f = n \cdot \frac{F_s}{L}, n = 0 : \frac{L}{2} - 1 \tag{4.6}$$

The period of oscillations, hence the shockwave propagation time, is calculated as the reciprocal of the frequency corresponding to the peak value in the magnitude spectrum. For each type of material, multiple undamaged samples are used to calculate the speed of sound. The final speed of sound is determined as the average value of all measurements for each material type.

4.4.3 Dynamic Tensile Strength and Strain Rate Estimation from BFV Signals by Novikov's approach [195]

To estimate the dynamic tensile strength (or spall strength) with equation (1.53) and strain rate during delamination using equation (1.54), back-face velocity signals that exhibit spall signal, as presented in Fig. 4.12 are selected. In this work, a spall is represented by a crack occurring in a damage plane parallel to the back face due to high dynamic tensile stress. This spall can be either a crack in the matrix or a delamination at the interply.

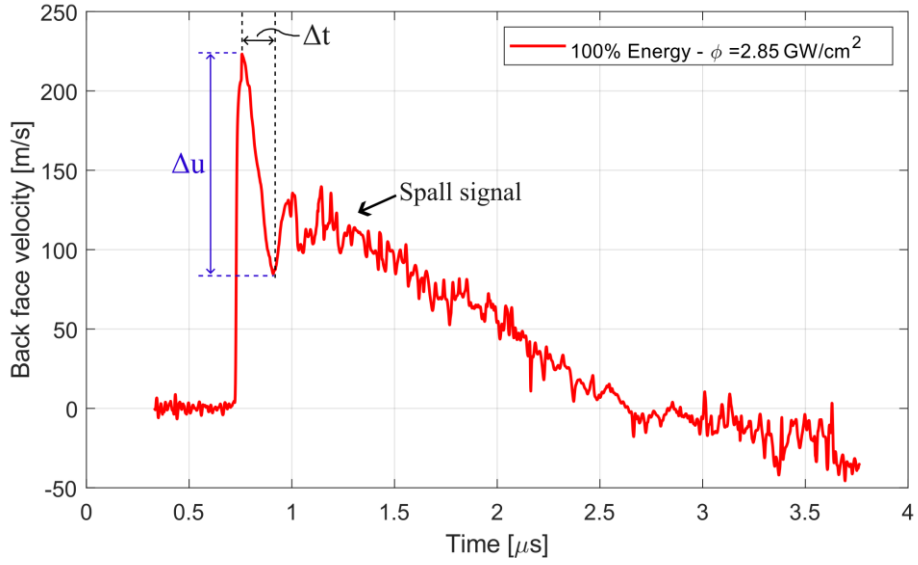

Fig. 4.16. Example of data identification for estimating the dynamic tensile strength and strain rate from a back-face velocity curve with a spall signal for a sample shot in the out-of-plane direction

Fig. 4.16 shows an example of the identification of back-face velocity pullback Δu and time interval Δt required for calculations, for a 100% of max energy shot in the out-of-plane direction, at a density of power of 2.85 GW/cm^2.

Given the fact that all required parameters to estimate the dynamic tensile strength and strain rate present a certain degree of uncertainty, a Monte Carlo analysis with 10000 trials was used to calculate the dynamic tensile strength and strain rate, using the average values and uncertainties of the parameters in equations (1.53) and (1.54). For the velocity pullback, an uncertainty of 1 m/s was used, to account for the influence of signal processing on the final back-face velocity values, while for the time difference, an uncertainty in measurement of 0.001 μs was employed.

To generate the random trials, the *normrnd* function from MATLAB was used, to consider a normal distribution of the parameters, considering their average value and standard deviation. Fig. 4.17 shows the distribution of the trial results in the form of a histogram with 100 bins for the test presented in Fig. 4.16. It can be observed that the same normal distribution employed to generate random parameters is found for the distribution of the Monte Carlo analysis.

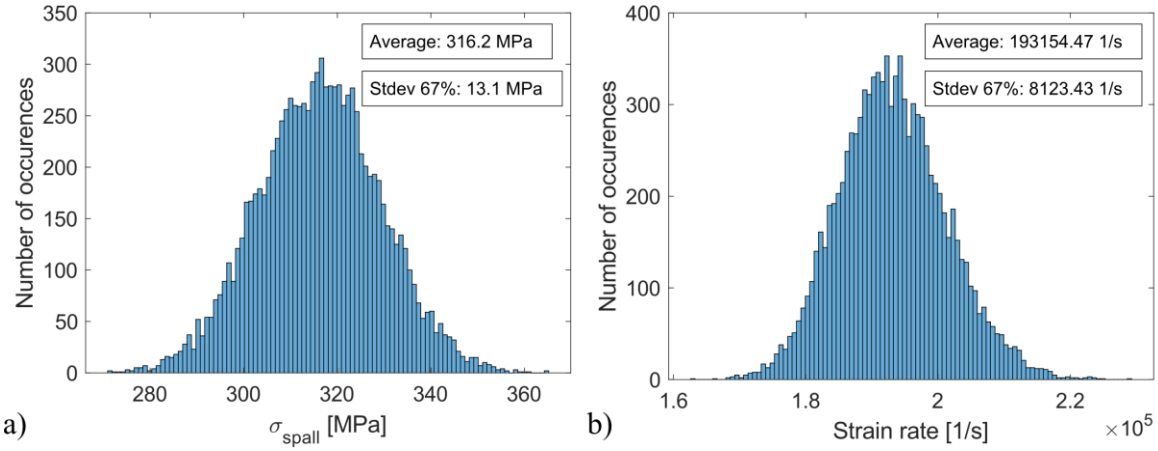

Fig. 4.17. Histogram with 100 bins for Monte Carlo trials; a) Dynamic tensile strength; b) Strain rate during spall fracture

4.5 DAMAGE ANALYSIS PROCEDURE

To further analyze the internal damage in out-of-plane samples, diagnosed through the back-face velocity signal, microscopic observations of the sample's cross-sections were made. The samples were prepared according to the sequence of steps illustrated in Fig. 4.18.

First, the out-of-plane samples on which multiple shots were performed were cut into smaller pieces to isolate individual shots (~1.2 cm) using a precision cut-off machine, Accutom-10 from Struers, equipped with an appropriate diamond cut-off wheel. The diameter of the impact spot is marked and its position relative to the edge is measured. The sample is fixed in position using a fixation clip, placed into a mounting cup, and embedded using a KM-U cold mounting powder resin kit with a liquid catalyst from Presi. The resulting specimen is placed into the cut-off machine and the blade is positioned as close as possible to the marked diameter plane. To remove the scratches caused by cutting, the sample is polished using a fine SiC foil (grit 1200) and afterward with diamond suspensions. The procedure is similar to the one described in section 2.2.3. A Keyence VHX-5000 series digital microscope was used to capture high-quality images at different magnification levels. For in-plane samples, the damage was assessed through microscopic observations of the back face.

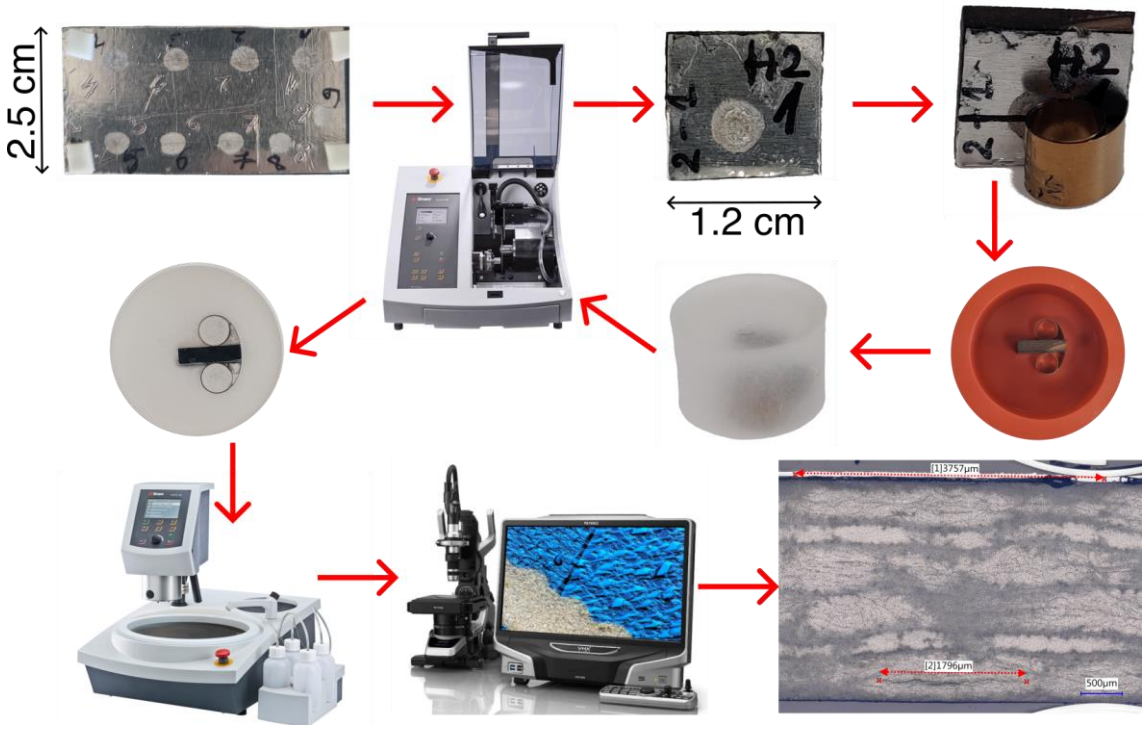

Fig. 4.18. The sequence of steps - from out-of-plane sample to microscopic observations

4.6 REPEATABILITY OF EXPERIMENTS

Two types of laser-induced shockwave experiments were performed: in-plane tests and out-of-plane tests, as also mentioned in section 4.1. As the samples for the in-plane tests were difficult to manufacture, the preliminary testing to ensure the repeatability of the experiment setup was made on a sample in the out-of-plane direction.

Shots with 100%, 50%, and 10% of max energy were performed on the same plate, at a distance between shots of ~1cm, and the back-face velocity was recorded. Fig. 4.19 shows that for each energy level, all three shots exhibit a similar velocity outline in the first peak region. 100% and 50% of max energy plots illustrate damage in the composite material. Therefore, the spall signal is present for all shots, with some minor differences in amplitude and frequency, which can be attributed to the composite internal structure irregularities (resin-rich regions, ply waviness, etc.). As for the 10% of max energy plots, no damage is present and the outline of the back-face velocity is almost the same for all three shots. Small differences in amplitude between back-face velocity signals from different shots can also be attributed to the influence of the signal noise in extracting the back-face velocity from the PDV signal but also to a small difference in the thickness of the sample. Therefore, it was concluded that the repeatability of the tests, regarding the peak velocities and chronology, is satisfactory. Additionally, for each testing configuration, a minimum number of two shots were performed.

In some back-face velocity signals, a sharp negative peak is visible, similar to the one in Fig. 4.19c, for the T-11 sample. This negative peak lacks a physical significance; it arises because the laser probe light no longer reaches the entrance of the PDV optical fiber. One must keep in mind that the dimension of the beam size of the PDV laser at the back face is of the order of 100 µm, very small compared to the size of a possible defect or dark sport on the back face. Possible reasons for negative peaks are: 1) the back-face deformation reflects the laser light out of the solid angle catchable by the PDV probe; 2) there is a lack of reflectivity of the back-face (absence of coated gold, dark region, dust); 3) a particle with high reflectivity and zero speed is pulling the PDV signal to zero.

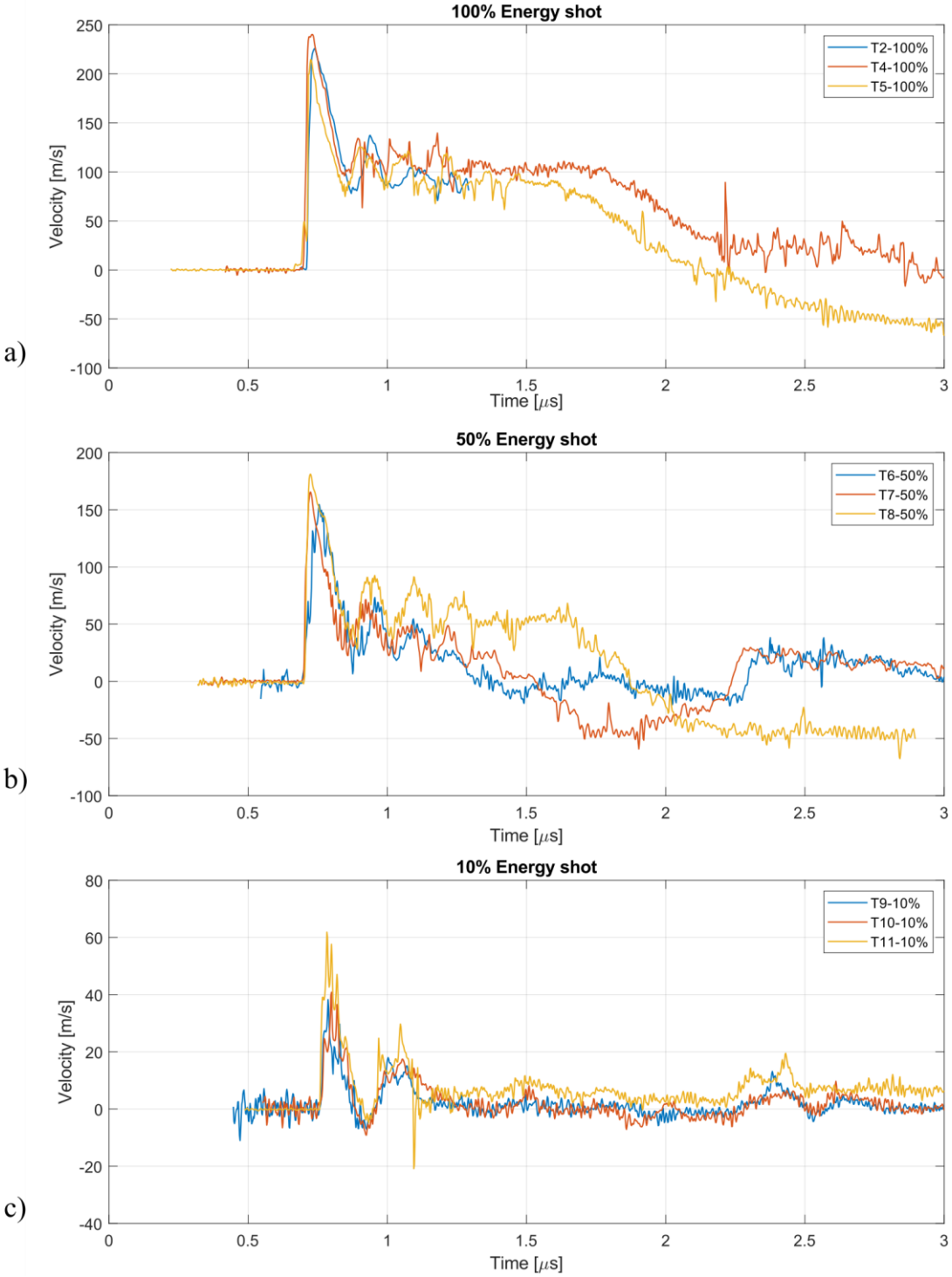

Fig. 4.19. Repeatability tests on out-of-plane carbon fiber composite sample; a) 100 % max energy; b) 50% max energy; c) 10% max energy

4.7 EXPERIMENTAL RESULTS AND DISCUSSION

4.7.1 Along the fiber-direction (in-plane) laser-induced shockwave test results

Laser impact tests were carried out at three different energy levels: 100%, 75%, and 50% of maximum energy level. For each configuration, a minimum of two samples were tested, except for H1 material - 75% of max energy level, for which only 1 experimental test was employed (due to a limited number of samples). In APPENDIX J the details of each test are provided, such as the material name, sample number, year of the experimental campaign, sample thickness, impact energy level, focal spot diameter, and density of power.

For each laser impact test, the required time shift was determined and implemented in the back-face velocity signal, using the procedure described in section 4.3.1.

4.7.1.1 Back-face velocity signal analysis for in-plane laser tests

a. Reference laminates UTS and HSC

Fig. 4.20 illustrates the back-face velocity signals for UTS samples, for different energy levels while Fig. 4.21 shows the back-face velocity signals for HSC samples. A good reproducibility is obtained for each tested configuration. For sample UTS17-IP-4, only the 1st peak could be extracted as the subsequent signal was of poor quality for an accurate extraction of the velocity. Although the back-face velocity signals were adjusted using the required time shift, there is still a small gap in the time scale in the response of HSC samples tested in the same conditions. These gaps could be attributed to the difference in sample thickness (less than 0.1 mm between samples). Furthermore, a high number of shockwave back-and-forth propagations with decreasing amplitudes are observed within the 4 µs timeframe, suggesting a high propagation velocity and shockwave attenuation.

Fig. 4.20d and Fig. 4.21d present the comparative back-face velocity response for shots at 100%, 75%, and 50% of max energy levels, for UTS laminates and HSC laminates respectively. The back-and-forth propagation period of the shockwave remains unaffected by the intensity of the laser shot, as the oscillations for different energy levels overlap. The only difference between the response at different laser intensities regards the amplitude of oscillations. For HSC laminates, the maximum velocity of the first peak decreases with decreasing energy level and density of power, while for the subsequent peaks, the 100% and 75% of max energy levels seem to reach the same amplitude, and it decreases only for 50% of max energy level.

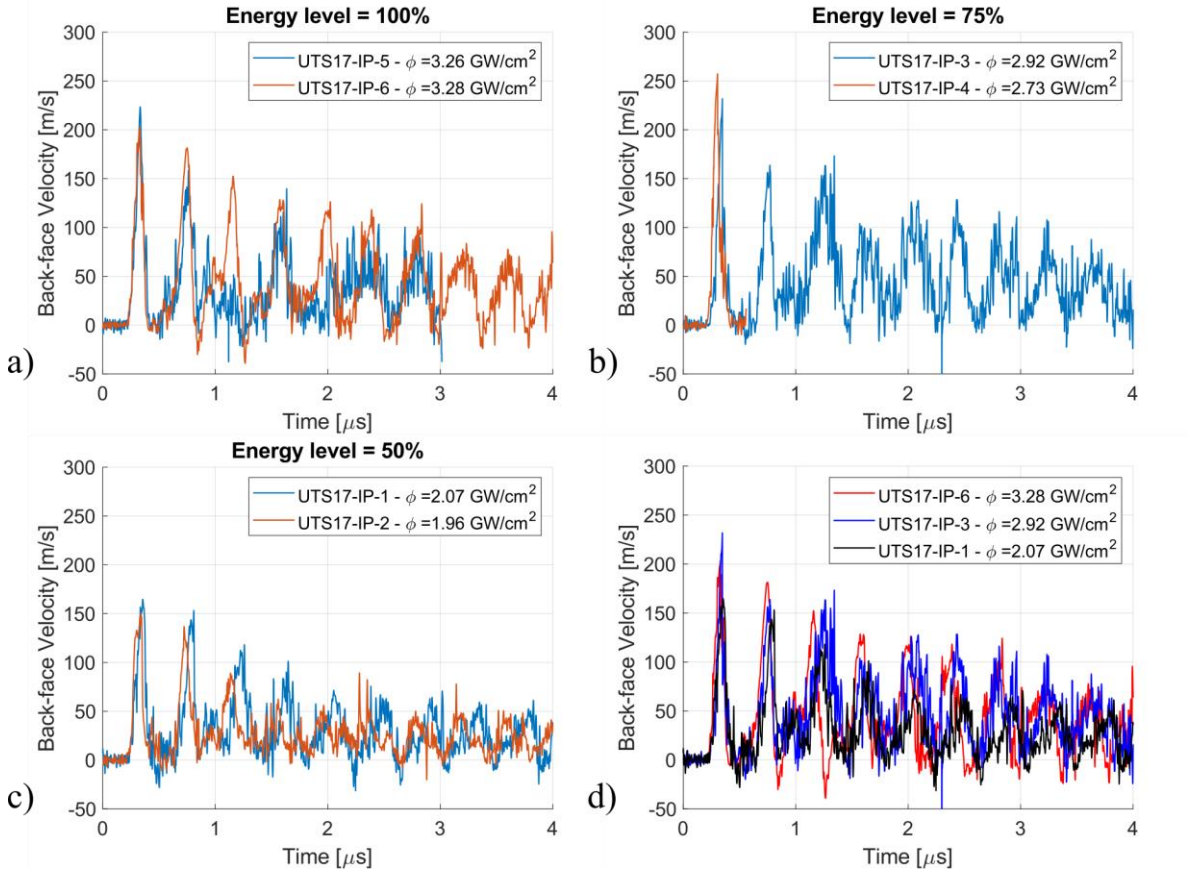

Fig. 4.20. Back-face velocity versus time for UTS laminates - in-plane laser tests; a) 100% of max energy; b) 75% of max energy; c) 50% of max energy; d) comparison of representative tests for each energy level

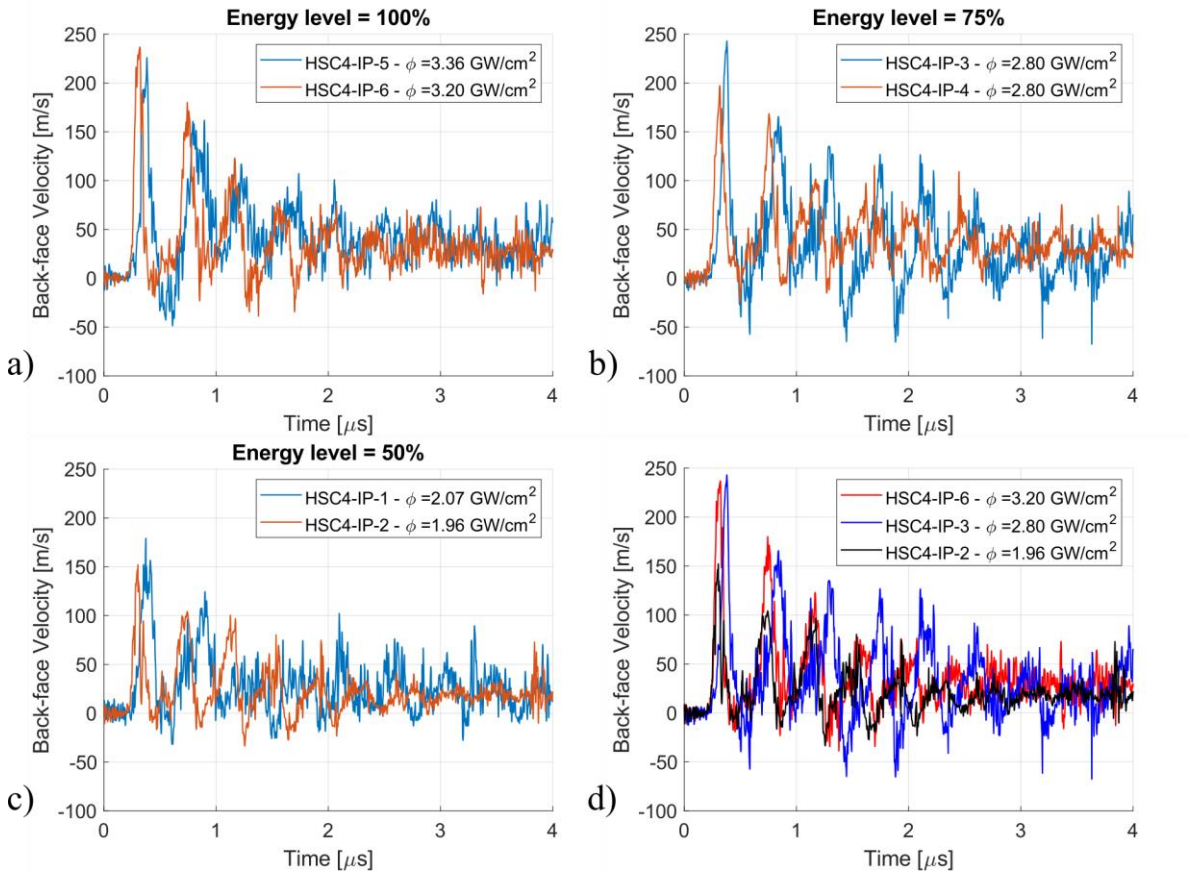

Fig. 4.21. Back-face velocity versus time for HSC laminates - in-plane laser tests; a) 100% of max energy; b) 75% of max energy; c) 50% of max energy; d) comparison of representative tests for each energy level

UTS laminates exhibit a slightly different response, with the maximum velocity of the first peak for 100% and 75% of max energy level being inverted: at a lower energy level and density of power, the 75% shot gives a higher maximum first velocity peak than the shot at 100%. For the subsequent peaks, the difference between 100% and 75% of max energy level is not notable. Overall, the 50% of max energy shot exhibits lower amplitudes. A clearer visualization of the evolution of the maximum velocity of the first peak with the density of power is given in Fig. 4.29.

When comparing the response of the UTS and HSC laminates (Fig. 4.22), it is noticed that while the maximum velocity of the first peak is similar for both laminate types, HSC laminate exhibits subsequent peaks with lower amplitudes compared to UTS laminates, suggesting a higher degree of shockwave attenuation with each back-and-forth propagation. For example, at 100% of max energy level, the peak value of the back-face velocity for HSC laminate within five consecutive back-and-forth propagations drops from 235 m/s to 48 m/s (79.5% percentage decrease), while for UTS laminates, after the same number of back-and-forth propagations, the peak value of the back-face velocity drops with a percentage decrease of 42.5 m/s (from 200 m/s to 115 m/s).

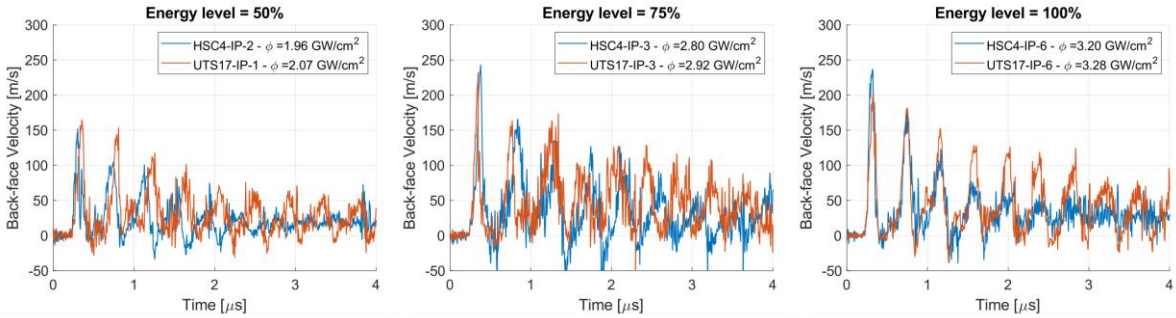

Fig. 4.22. Back-face velocity versus time comparison for UTS and HSC laminates, for different energy levels; a) 50%; b) 75%; c) 100%

To evaluate the hydrodynamic damping of the shockwave in UTS and HSC in-plane samples, the peaks of the back-face velocities were fitted with an exponential function (equation (4.7)). Fig. 4.23 shows examples of exponential fitting of the back-face velocity peaks for 100% of max energy shots on UTS17 and HSC4 laminates. When examining the shots on all samples at the tested energy levels, and identifying the peaks, we observe that the B coefficient for UTS17 ranges from -0.295 to -0.467, while for HSC4, it falls within the range of -0.422 to -0.716. The more negative B coefficients for HSC4 compared to UTS17 suggest that HSC exhibits a more pronounced hydrodynamic damping effect, causing the back-face velocity to decrease more rapidly over time.

$$Max_{BFV}(t) = A \cdot \exp(B \cdot t) \tag{4.7}$$

Despite UTS and HSC laminates having different fiber volume fractions, approximately 54% and 49% respectively, it is believed that shockwave attenuation is not strongly influenced by the fiber volume fraction. Alexander et al. [170] conducted plane plate impact tests on carbon fiber composites with 62% and 68% fiber volume fractions, both in the fiber direction. No significant difference was observed between them in the Stress-Particle velocity plot, suggesting that small variations in the fiber volume fraction did not affect shockwave attenuation in their context. However, the pulse duration in the case of laser-induced shockwaves is much smaller than for plane plate impact tests, and the influence of the fiber content cannot be ignored entirely. Thus, it is considered that the difference in the quality of the carbon fibers is mainly responsible for the different shockwave attenuation in the reference UTS and HSC laminates, coupled with the difference in density and fiber content Moreover, the presence of voids could also affect the shockwave propagation.

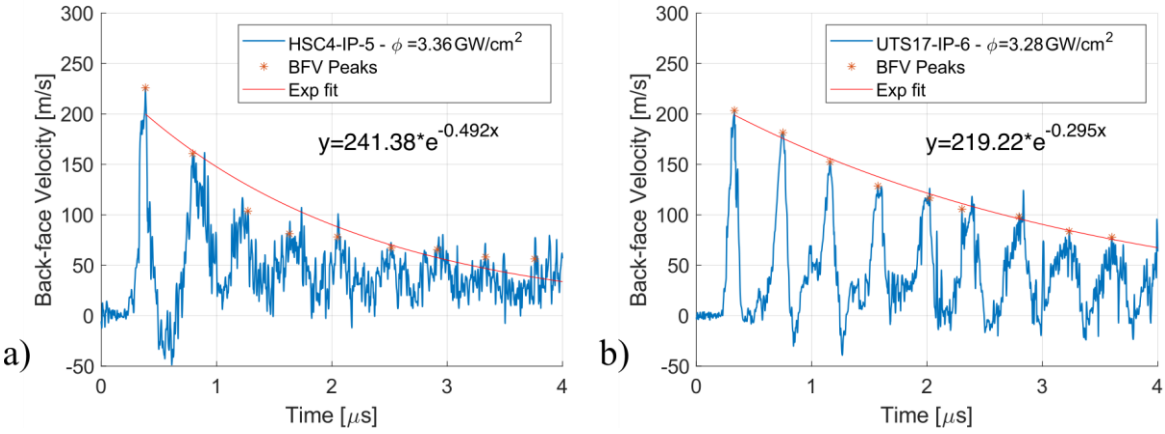

Fig. 4.23. Back-face velocity signals, with exponential fitting of the peaks; a) HSC4 shot at 100% E; b) UTS17 shot at 100% E.

The fact that the maximum velocity does not significantly change with the density of power of the shot could be due to the thickness of the sample. At the impacted face, the shock is strong (> 1 GPa), but as the sample is thick (~2 mm) with respect to the mechanical wavelength of the loading pulse (~0.45 mm), during its propagation, the shock is strongly attenuated because it is caught up by the release elastic waves from behind the shock front that are faster than the shockwave. As a result, the plastic wave turns rapidly into an elastic wave and the elastic propagation is less subjected to decay. Hence, UTS samples, being less susceptible to attenuation than HSC samples, show comparable maximum back-face velocities during impacts when the difference in power shot density is not substantial. However, a variation in the maximum back-face velocity becomes apparent when the difference in power shot density is significant.

b. Hybrid laminates H1 and H2

It is reminded that in order to obtain a better laser reflection at the back face, a thin layer of gold (about 500 nm) was sputtered on the sample back face. For in-plane laser tests, due to poor adhesion of the gold particles to the resin, part of the gold particles were expelled when the shockwave reached the back face. For a few H1 samples, for which the gold layer was slightly thicker, besides the signal due to the shockwave back-and-forth propagation, a plateau-like spall signal was also visible, as illustrated in Fig. 4.24. In all cases, the mean velocity of the plateau signal is very close to the velocity of the first peak. Thus, it is considered that the plateau signal is due to the expulsion of the gold particles and not due to damage in the sample. Also, according to Novikov's approach, it shows that the bond strength of the gold layer on the sample's back face is very poor. The presence of both types of signals posed problems in extracting the velocity signal, as it had to be considered separately from the back-and-forth propagation signal.

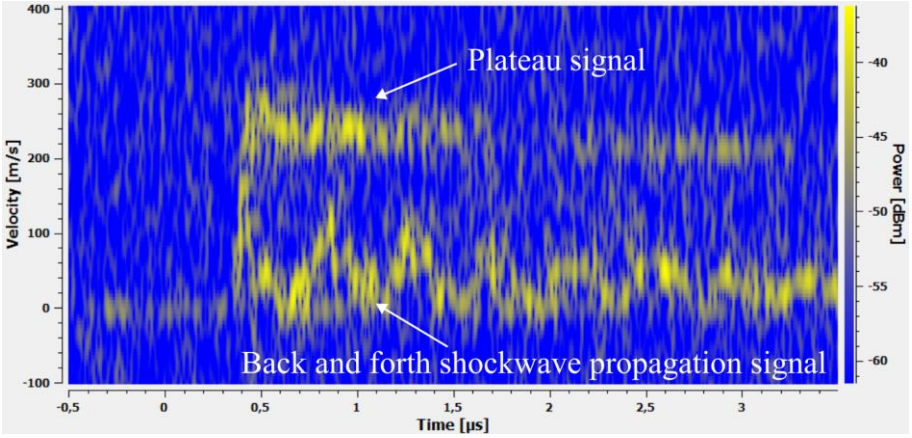

Fig. 4.24. Example of back face velocity signal for an in-plane shot showing both back-and-forth propagation of the shockwave and plateau signal due to gold expulsion

In Fig. 4.25a-c back-face velocity versus time plots are shown for H1 material, at different laser energy levels, with comparisons illustrated in Fig. 4.25d. As previously mentioned, two shots – at 100% and 75% of max energy levels – exhibited a plateau signal due to gold expulsion. The plateau signal and the back-and-forth propagation signal were extracted separately, which is why the plateau signal is plotted on top of the back-and-forth propagation signal in Fig. 4.25a and Fig. 4.25b, in a lighter shade. The rising front is the same in both extractions, with small differences in the maximum velocity of the first peak. Both signals are considered when evaluating the maximum velocity of the first peak.

Upon comparing the back-face velocity response of the two shots at 100% of max energy (Fig. 4.25a), it becomes evident that although the discrepancy in the first peak value is minimal (attributed to a higher density of power for the H1-IP-4 sample), a noticeable difference of up to 100 m/s emerges for the second velocity peak. This discrepancy is attributed to the presence of the spall signal, which impacted the acquisition of the velocity peaks, particularly in terms of their amplitude, leading to lower peak values.

At 50% of max energy level (Fig. 4.25c), the response is similar for all three shots. However, due to trigger and acquisition issues, precise positioning on the time axis of the initial rising front for samples H1-IP-2 and H1-IP-5 was not possible. The initial shock breakout should have a small temporal delay between the samples as the thickness of the tested samples varies slightly. In the absence of another tool to correct the trigger acquisition delay (~30μs)), the matching of the first peak method was adopted. Consequently, manual data manipulation was performed to align the signals closer to the axis origin, matching the first peak position with that of sample H1-IP-6.1. The impact of the thickness difference becomes evident in the second shockwave breakout. As the thinnest sample, H1-IP-5 exhibits a shorter back-and-forth shockwave propagation time compared to the other two samples, followed by sample H1-IP-6.1, and lastly, sample H1-IP-2, in accordance with their thickness.

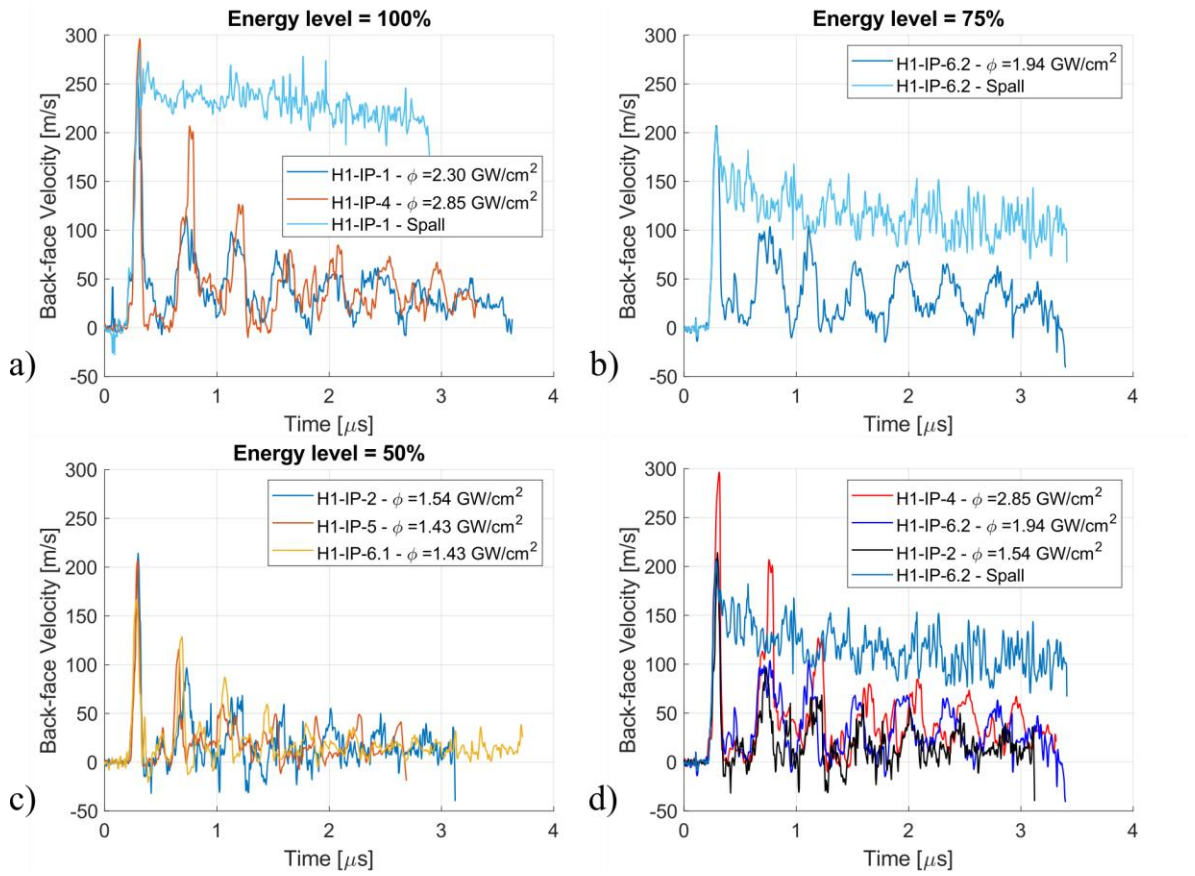

Fig. 4.25. Back-face velocity versus time for H1 laminates - in-plane laser tests; a) 100% of max energy; b) 75% of max energy; c) 50% of max energy; d) comparison of representative tests for each energy level

From Fig. 4.25d, a decrease in the maximum velocity of the first peak with the decrease in energy level can be observed. The second peak velocity for all three energy levels is almost the same, indicating the fact that for both 75% and 100% of max energy, the spall signal of the gold particle expulsion may have influenced the signal acquisition of the shockwave secondary breakouts. The gold expulsion occurs just after the first peak, but because of the Short Fourier Transform of the PDV treatment, it tends to attenuate the difference between the peak and the spall plateau.

The back-face velocity response of H2 hybrid material, at different energy levels, is illustrated in Fig. 4.26a-c, with a comparison between the response at all tested energy levels given in Fig. 4.26d. It is observed that the response at 100% and 75% of max energy levels is very similar, with almost no differences in the amplitude of the peaks. The 50% of max energy shot gives lower velocity amplitudes of the secondary peaks, while the maximum velocity of the first peak seems unchanged, at ~200m/s for all energy levels.

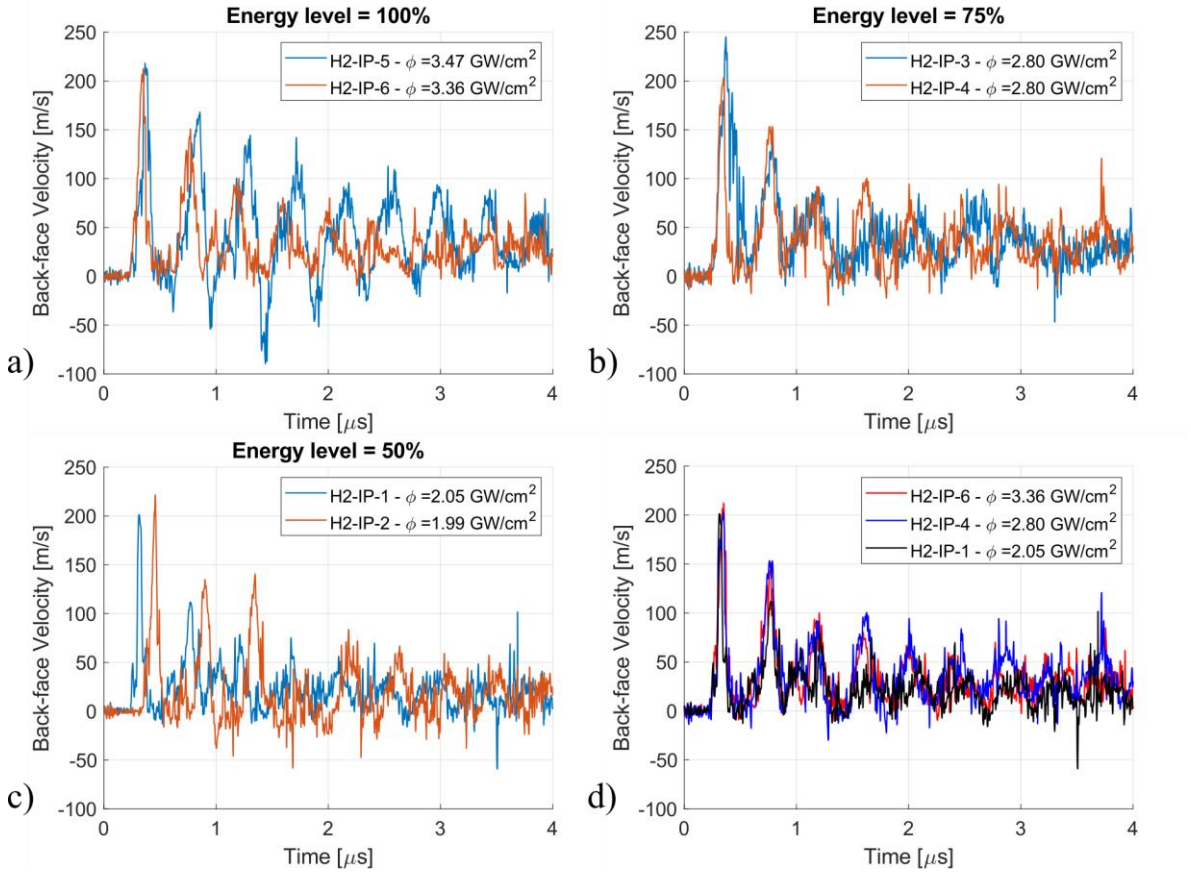

Fig. 4.26. Back-face velocity versus time for H2 laminates - in-plane laser tests; a) 100% of max energy; b) 75% of max energy; c) 50% of max energy; d) comparison of representative tests for each energy level

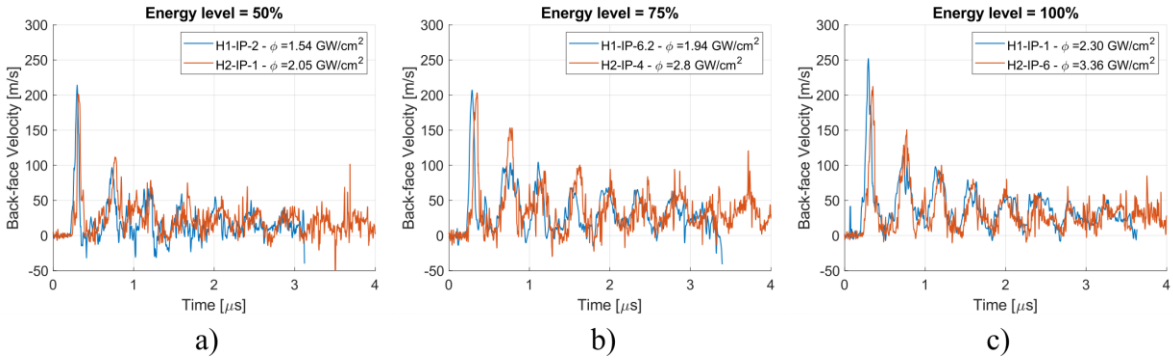

Fig. 4.27. Back-face velocity versus time comparison for H1 and H2 laminates, for different energy levels; a) 50%; b) 75%; c) 100%

Although H1 samples were shot at lower laser density of power, their back-face velocity response is close to the response of H2 material (except 100% shot and the presence of the plateau signal due to gold expulsion), as seen in Fig. 4.27. It emphasizes the fact that the wave propagation is rapidly attenuated to an elastic regime with a lower decay.

c. Reference and Hybrid laminates

Fig. 4.28 depicts a comparison of representative back-face velocity signals for both reference and hybrid laminates, for different energy levels. It must be noted that H1 samples, tested in 2021, were subjected to lower laser intensity shots, compared to all other samples tested in 2022. Despite this fact, the back-face velocity response of H1 samples is very similar to the other tested materials, with even higher maximum velocity peaks in certain cases.

Overall, the shockwave attenuation is more pronounced in hybrid laminates than in UTS reference laminates, having a response closer to HSC laminates. This outcome was anticipated since the hybrid laminates consist predominantly of HSC fibers.

Contrary to expectations, the maximum back-face velocity did not consistently increase with higher laser energy and power density for all the materials tested, as shown in Fig. 4.29a. In the 2021 campaign, the H1 samples, subjected to lower power density laser shots, exhibited a higher maximum velocity of the first peak compared to the response of other materials tested in 2022. As the number of shots is not enough for statistical analysis, this result is odd with possible explanations being attributed to the laser-matter interaction or some micro defects in the sample that are significant with respect to the spot size of the PDV laser. Moreover, this velocity increased with a higher density of power. However, in the 2022 campaign, all the other materials showed lower values of the maximum velocity of the first peak as power density exceeded ~2.8 GW cm^{-2} (primarily at the 100% of max energy level).

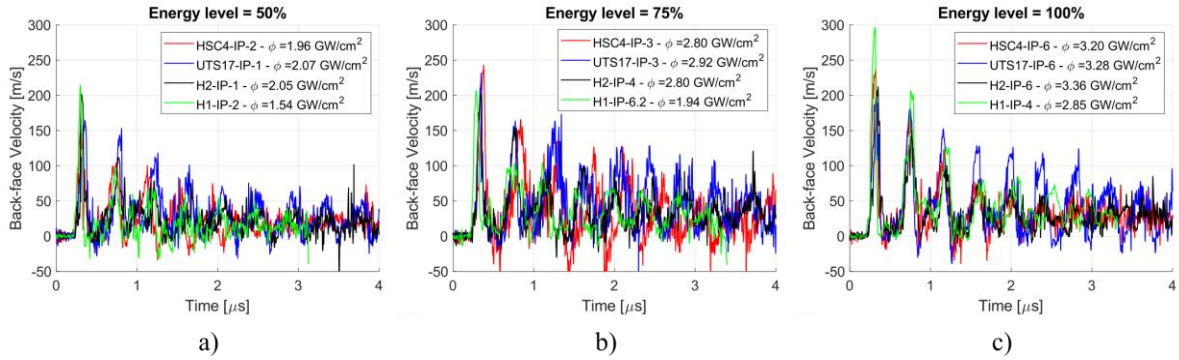

Fig. 4.28. Back-face velocity versus time comparison for all laminates, for different energy levels; a) 50%; b) 75%; c) 100%

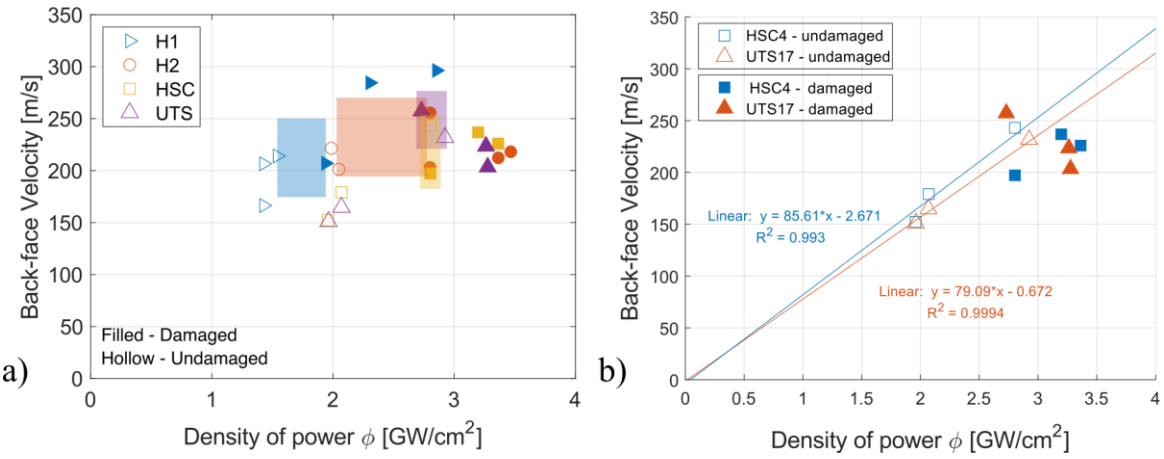

Fig. 4.29. a) Maximum BFV evolution with the density of power for all tested materials; b) Maximum BFV evolution with the density of power for UTS and HSC, including a linear fit for the undamaged samples

As also mentioned in [249], by excluding damaged samples, the BFV evolution with the density of power of reference laminates follows a linear shape, as seen in Fig. 4.29b, consistent with other works [250]. For hybrid laminates this assumption cannot be made, as all samples impacted at energy levels higher than 50% were damaged. Still, for H1, including the damaged samples, the linear increase with increasing density of power is valid.

4.7.1.2 Hugoniot Elastic Limit

In [170], Alexander et al. performed plane-plate impact experiments of carbon fiber laminates, in the fiber direction. Their results suggest that elastic waves travel along the fibers, with the bulk shock front coming from behind. Because of the high wave speed in the fibers,

the elastic wave will reverberate between the sample-window interface in their case and the bulk shock front, prior to bulk shock arrival at the PMMA window. At each successive arrival of the elastic wave, elastic loading is observed in their data. Similar observations were also made by Millet et al. [166]. In the case of laser-induced shockwaves in the sample, the same phenomenon is expected, with the sample-PMMA window interface being replaced with the back face of the sample.

The prior arrival of the elastic wave is seen in most in-plane samples as a small step below 50 m/s in the back-face velocity signal, ahead of the main shock front, and it represents the Hugoniot Elastic Limit (HEL). Two examples of the visible HEL are shown in Fig. 4.30.

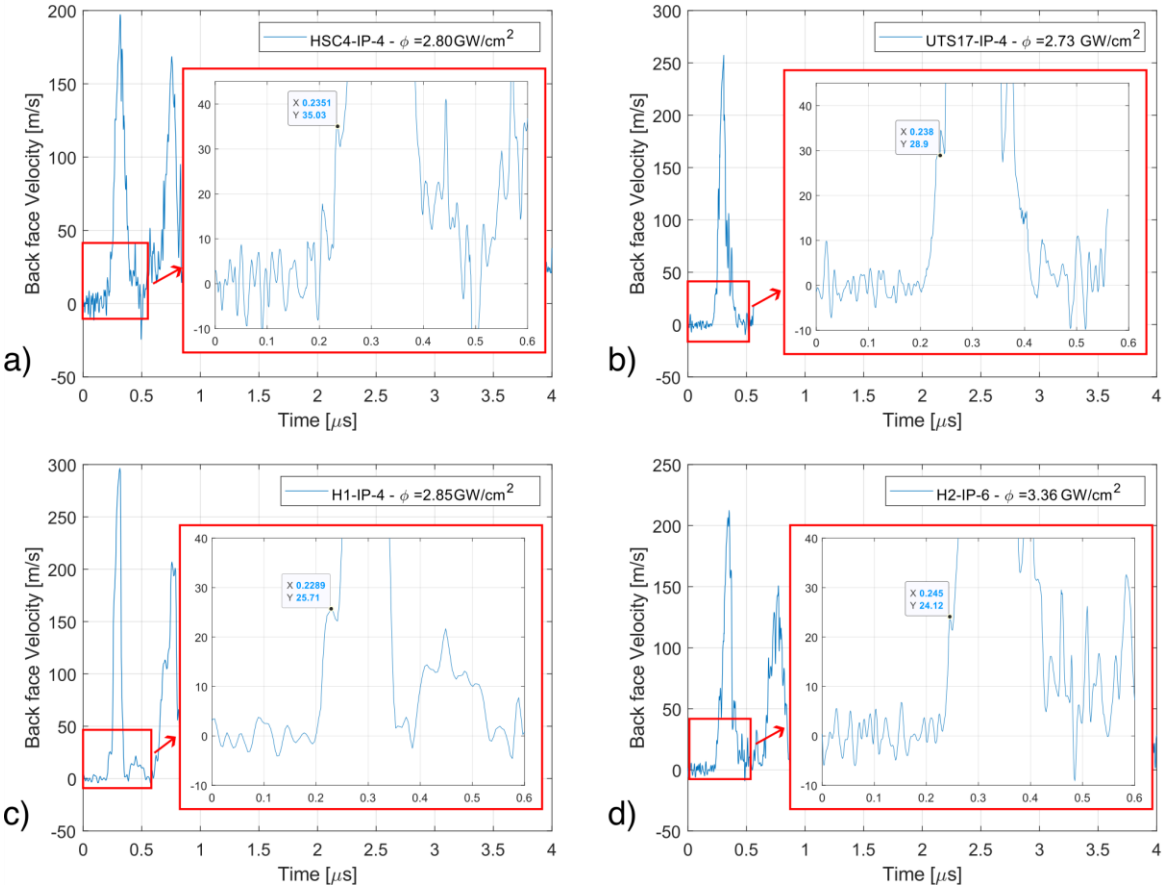

Fig. 4.30. HEL limit from in-plane back-face velocity signals; a) HSC sample – 75% E; b) UTS sample – 75% E; c) H1 sample – 100% E (2021 campaign); d) H2 sample – 100% E

From the samples where the HEL signature is observed, its value in terms of velocity threshold lies between 23 m/s and 47 m/s. A histogram with the distribution of the HEL values is presented in Fig. 4.31. It can be seen that most values lie in the interval [20; 35] m/s. However, uncertainties can be attributed to the fact that the experiments are not entirely reproducible as the results can be affected by local defects or parasites in the back-face velocity signals. Although for some samples the HEL limit was indiscernible and was not considered, for H1 samples that were impacted at lower densities of power, no HEL was visible when impacted at densities of power below 1.5 GW/cm^2.

Considering the velocity of the HEL at ~30 m/s, and a propagation speed of ~10 km/s, using equation (1.50), the resulting HEL limit would be 222 MPa. In the fiber direction, Alexander et al. [170] determined a HEL limit of 3.5 GPa for unidirectional carbon fiber composites, which is significantly higher than the value obtained from the in-plane laser tests. Thus, it leads to the idea that the observed HEL signature might be due to the elastic precursor formed in the aluminum sacrificial layer which further propagates through the composite layer. Smith et al. [251] identified the HEL on the back-face velocity trace from laser-induced shockwaves test on

aluminum samples at approximately 25 m/s, giving a HEL limit of 176 MPa, much closer to the one estimated here. Therefore, it is concluded that the discontinuity in the rising front of the back-face velocity, in the case of laser-induced shockwave tests in the fiber direction of the studied composite represents the HEL of the aluminum sacrificial layer and not the HEL of the carbon fiber composite.

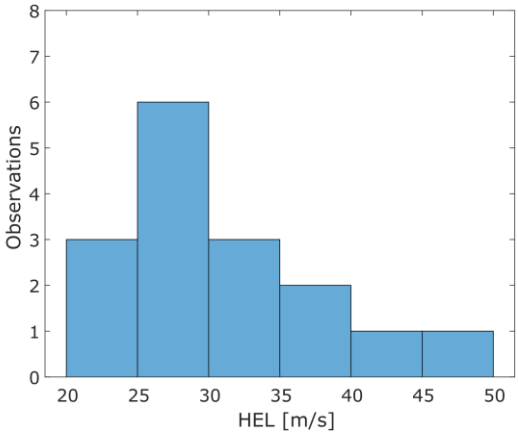

Fig. 4.31. Histogram displaying the distribution of HEL values

4.7.1.3 Speed of sound estimation from in-plane Laser-induced shockwave tests

By estimating the time difference between the first and second shockwave breakout and using equation (4.4), the propagation speed equivalent in this case with the longitudinal speed of sound is determined. The back-and-forth propagation period is extracted from the back-face velocity of the in-plane samples using FFT analysis, as described in section 4.4.2. Due to the manufacturing process, the tested samples exhibit slight differences in thickness, resulting in varying propagation times. The period versus the sample thickness is illustrated in Fig. 4.32a and varies from 0.38 µs to 0.45 µs. In general, the period increases with the thickness of the sample, as expected.

According to the shock polar approach, the material velocity u for the maximum pressure load should be half of the maximum value of the back-face velocity peak. Thus, to estimate the speed of sound, equation (4.5) where half of the maximum back-face velocity peak is subtracted from the propagation speed determined using equation (4.4). The resulting speed of sound is plotted against the density of power in Fig. 4.32b. The speed of sound evolution with the density of power is almost constant for each material, with small variations induced by the particularities of each sample.

Table 4.2 presents the average C_L and C_0 for each material type and the corresponding standard deviations. UTS laminates, with standardized and higher quality carbon fibers, have a higher speed of sound compared to HSC laminate by ~0.8 km/s. The hybrid materials exhibit values of the speed of sound closer to the average value of HSC laminate. This was expected as the hybrid materials have HSC plies in the middle. Moreover, the cross-section surface corresponding to HSC plies is higher than for UTS plies, leading to a higher probability of positioning the center of the laser spot (thus the measurement of the back-face velocity) on an HSC ply. Little data can be found regarding the speed of sound in fiber direction in unidirectional carbon fiber reinforced composites for comparing the results. Alexander [32] made ultrasonic measurements on unidirectional Hexcel IM7/8552 composite to determine ambient sound speeds along each of the principal directions, and the results indicated sound speeds of 10.763 km/s along the fibers (0°). The average values from Table 4.2 align with Alexander's measurements. The differences can be attributed to the variation in mechanical properties between the fibers used in Alexander's study and the ones employed in this research.

The theoretical C_L is also provided within Table 4.2, determined by using equation (1.47), the in-fiber-direction Young modulus and Poisson ratio of the laminates from the quasi-static

tensile tests in section 3.2.1, and the density of the laminate from section 2.3.1. It is observed that the values of the longitudinal speed of sound determined from the experimental data are higher than the theoretical values estimated using the properties of the laminate, having a percentage difference between 12.5-17.7%. If instead of the laminate properties, the fiber properties are used, for UTS laminate (for which the modulus and density of the fibers are known from the manufacturer and standardized) the theoretical speed of sound is ~11.7 km/s. In this case, the theoretical value is higher than the experimental-determined one, and the percentage error between the experimental and theoretically determined values decreases from 17.7% to 5.62 %. This is another confirmation that with the in-plane laser impact tests, the response of the fibers is mainly captured.

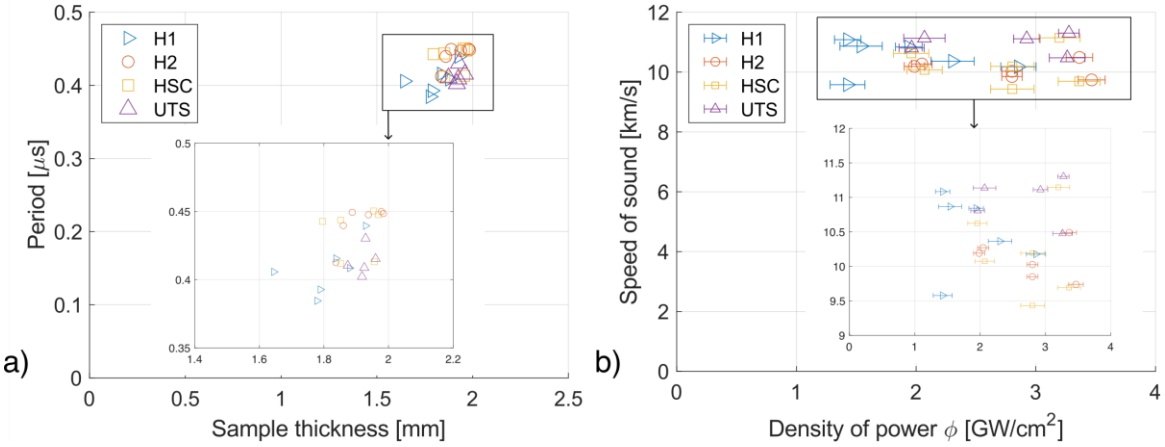

Fig. 4.32. a)Back-and-forth in-plane propagation period versus the thickness of the sample; b) Speed of sound versus density of power of the laser shot

Table 4.2. Average estimated speed of sound and theoretical values for in-plane laser tests

Material	Average C_L [km/s]	Standard deviation [km/s]	C_L [km/s] from (1.47)*	Average C_0 [km/s]	Standard deviation [km/s]	ρ_0 [g/cm^3]
HSC	10.29	0.62	8.79	10.19	0.62	1.483 ± 0.005
UTS	11.06	0.32	9.26	10.96	0.32	1.490 ± 0.004
H1	10.59	0.55	8.92	10.48	0.56	1.478 ± 0.007
H2	10.20	0.27	9.00	10.09	0.27	1.499 ± 0.011

*parameters from quasi-static experiments (laminate parameters)

4.7.1.4 Damage analysis

Although the back-face velocity signals showed only spallation of the gold particles (for two shots on H1 material), for all materials, samples shot at 75% and 100% of max energy showed visible signs of damage, not in the form of a spall but as flexural matrix crack and microcracks, as seen in Fig. 4.33. Besides the principal matrix crack, other thin lines of matrix microcracks were observed for all samples, and an example is highlighted in Fig. 4.33. Moreover, most samples shot at 75% or 100% of max energy levels exhibited a second flexural crack in a marginal stripe, located at a distance from the central crack that varied between 0.2 mm (Fig. 4.34a) and 2.7 mm (Fig. 4.35 – 100%E). Only two H2 samples exhibited secondary cracks in both marginal stripes, located at different distances from the central flexural crack (Fig. 4.34b and Fig. 4.34c), and one H1 sample broke entirely in half (Fig. 4.36). Furthermore, at all tested energy levels, weak glue bond failure caused stripe separation at either one or at

both stripe interfaces, as can be seen in the microscopic illustration in Fig. 4.35. This could not be attributed to PDV measurements, pointing out the fact that it could not be possible to determine chronologically at which instant they occurred after the first breakout. The 50% of max energy level shots on HSC were the only ones without stripe separation. The different position of the secondary flexural crack along with stripe separation suggests a potential influence of the weak glue bonding on the shockwave propagation in between the thin bonded stripes.

Gold expulsion from the back-face was also visible for all samples, on an almost circular surface vis-a-vis of the irradiated area with a diameter of approximately 2.9-3.5 mm. The gold expulsion is more pronounced at higher energy levels and at ply interfaces, where the resin is prominent. For HSC and hybrid laminates, lines of expelled gold can be observed at similar distances as the plies' thicknesses, while for UTS laminates the gold expulsion does not follow a pattern, as the plies are thinner and the ply interface is not easily distinguishable.

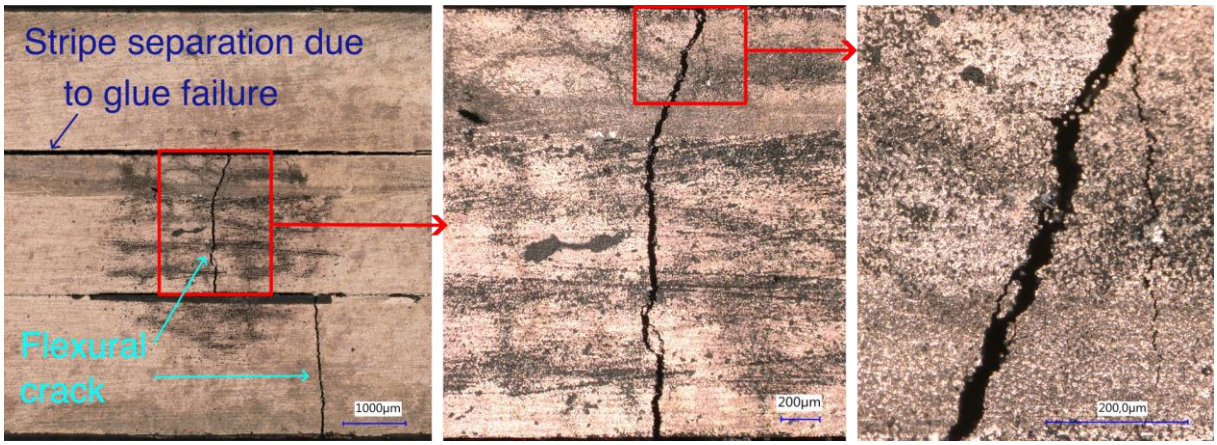

Fig. 4.33 Visible damage on the back-face of H1-IP-1 sample, shot at 100% of max energy level with ϕ=2.30 GW/cm^2

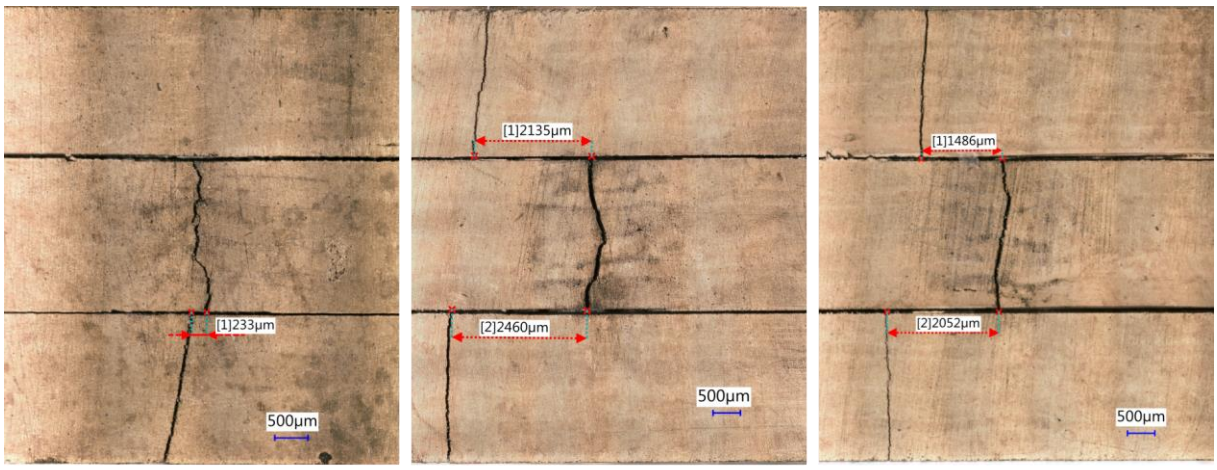

Fig. 4.34. Back face microscopic observations with measurements of secondary crack position relative to the middle crack; a) HSC4-IP-5 – 100% E, ϕ = 3.36 GW/cm^2 b) H2-IP-45 – 75% E, ϕ = 2.80 GW/cm^2 c) H2-IP-55 – 100% E, ϕ = 3.45 GW/cm^2

Although the back-face velocity signal is not very different from one energy level to another as it mainly reflects the shockwave propagation through the fibers, there is a difference in the resulting damage in the matrix. For example, for UTS laminates (Fig. 4.35), a flexural crack is observed on the back face for the 100% of max energy shot, near the middle of the shot, in the middle stripe. The crack propagated through the stripe bonding and also through the lower stripe, at a distance of ~2.7 mm from the middle one. For 75% of max energy level, only gold expulsion and stripe separation due to the weak glue bond failure between the stripes is

observed. When lowering the energy level to 50%, less gold is expelled and only one stripe bonding failed.

Since the H1-IP-4 sample broke in half, further observations were made in the rupture plane to identify if the fibers were also damaged, even though the back-face velocity signal showed no spall. As the surface was irregular, proper focusing of the microscope was possible only for small areas. Fig. 4.36 shows the back face microscopic observation of the H1-IP-4 sample, with the most relevant fiber images captured from the rupture plane A-A. Part of the fibers are broken, most of them closer to the back face. Also, broken fiber bundles can be observed. Although some fibers are broken, there is not a fracture plane for all of them, which is probably why no clear spall signal could be obtained for the back face velocity. The failure position relative to the rear face is different for most of the broken fibers. Moreover, in the same observation section, while some fibers were broken, the others appeared intact.

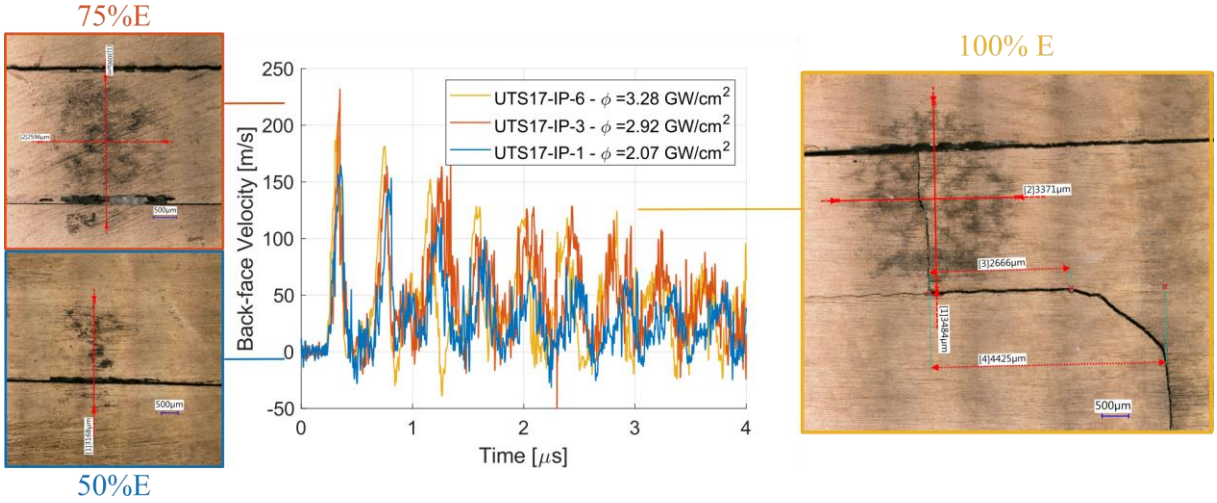

Fig. 4.35. Back-face velocity comparison for UTS17 laminate, at different energy levels, with corresponding microscopic images of the back-face

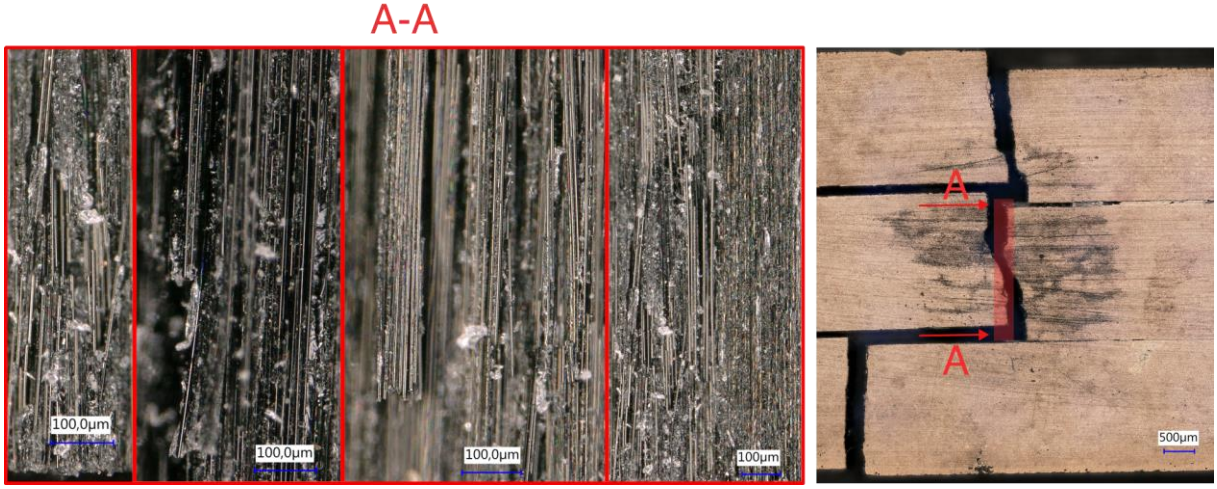

Fig. 4.36 Back-face microscopic observation of H1-IP-4 sample, with images captured from the rupture plane A-A

Based on microscopic observations of matrix cracks visible on the back face and the laser shot's density of power (excluding stripe separation), Fig. 4.37 presents the matrix failure threshold for the in-fiber direction laser shots for all tested materials. For UTS and HSC laminates, the matrix failure threshold is ~2.8 GW/cm^2, while for the hybrid laminates, the gap between the damaged and undamaged samples is wider. For H1, the matrix failure threshold is in the density of power interval of 2 – 2.8 GW/cm^2, while for H1 the matrix failure threshold is lower, at a density of power between 1.4 and 1.9 GW/cm^2.

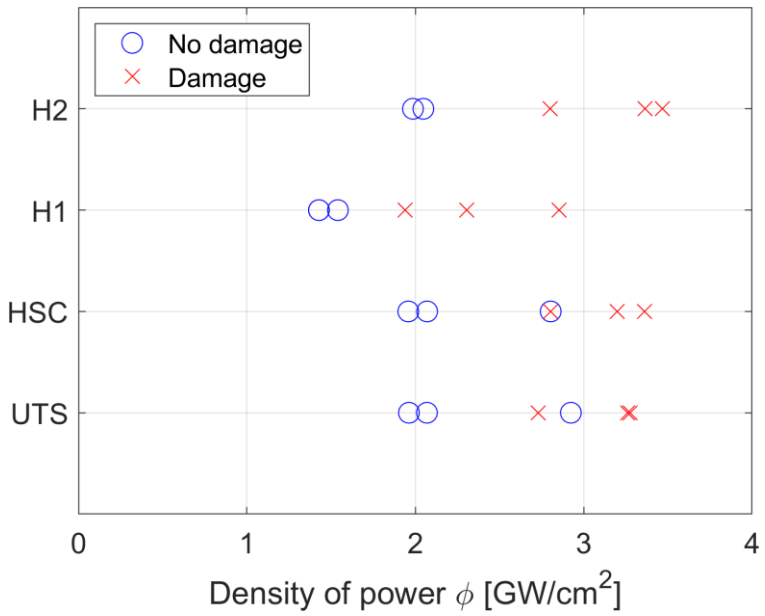

Fig. 4.37. Matrix failure threshold in-fiber direction based on microscopic inspection of the back face.

4.7.2 Out-of-plane laser-induced shockwave test results

4.7.2.1 Back-face velocity signal analysis for out-of-plane laser tests

The details for out-of-plane laser impact tests, with corresponding material name, sample and shot number, energy level, sample thickness, focal spot diameter, and density of power are presented in APPENDIX K. For each laser impact test, the required time shift was determined and implemented in the back-face velocity signal, using the procedure described in section 4.3.1.

a. Influence of density of power

Fig. 4.38 presents representative samples of all tested materials, for different energy levels (100%, 75%, 50%, and 35%; 25% - only for HSC3), with the corresponding density of power. By analyzing the back-face velocity signals, it can be observed that the first peak has a lower amplitude with decreasing energy level and density of power of the laser shot.

Moreover, clear spall signals, identified by a non-return to zero right after the first peak, can be observed for all materials, at the highest tested density of power, meaning that the material was damaged under out-of-plane laser impact. For lower values of the density of power, the presence of a spall signal depends on the tested material.

For the thinnest laminate, HSC3 (Fig. 4.38a), all laser shots, except for the one at 25% of max energy level and 1.53 GW/cm^2, exhibited a spall signal. The spall signal's mean value was not constant, implying that the internal damage might lack a distinct delamination plane. For the first two shots, at the highest densities of power, the spall signal follows the same path, although the maximum velocity of the first peak is different. This leads to a higher velocity drop, thus a different dynamic tensile strength for shots at different intensities. The influence of the density of power on the dynamic tensile strength will be discussed in detail in section 4.7.2.2. For the shot at 25% of max energy, following the velocity drop from the first shockwave breakout, the BFV signal captured remanent reflections in the last ply, while the secondary peak occurred at approximately 1.9 µs. HSC4 showed a similar response (Fig. 4.38b) with HSC3, but the back-and-forth propagation of the shockwave was observed for a laser shot at a higher power density of 1.65 GW/cm^2 (35% E shot). Moreover, the velocities for the spall signal decrease with decreasing density of power.

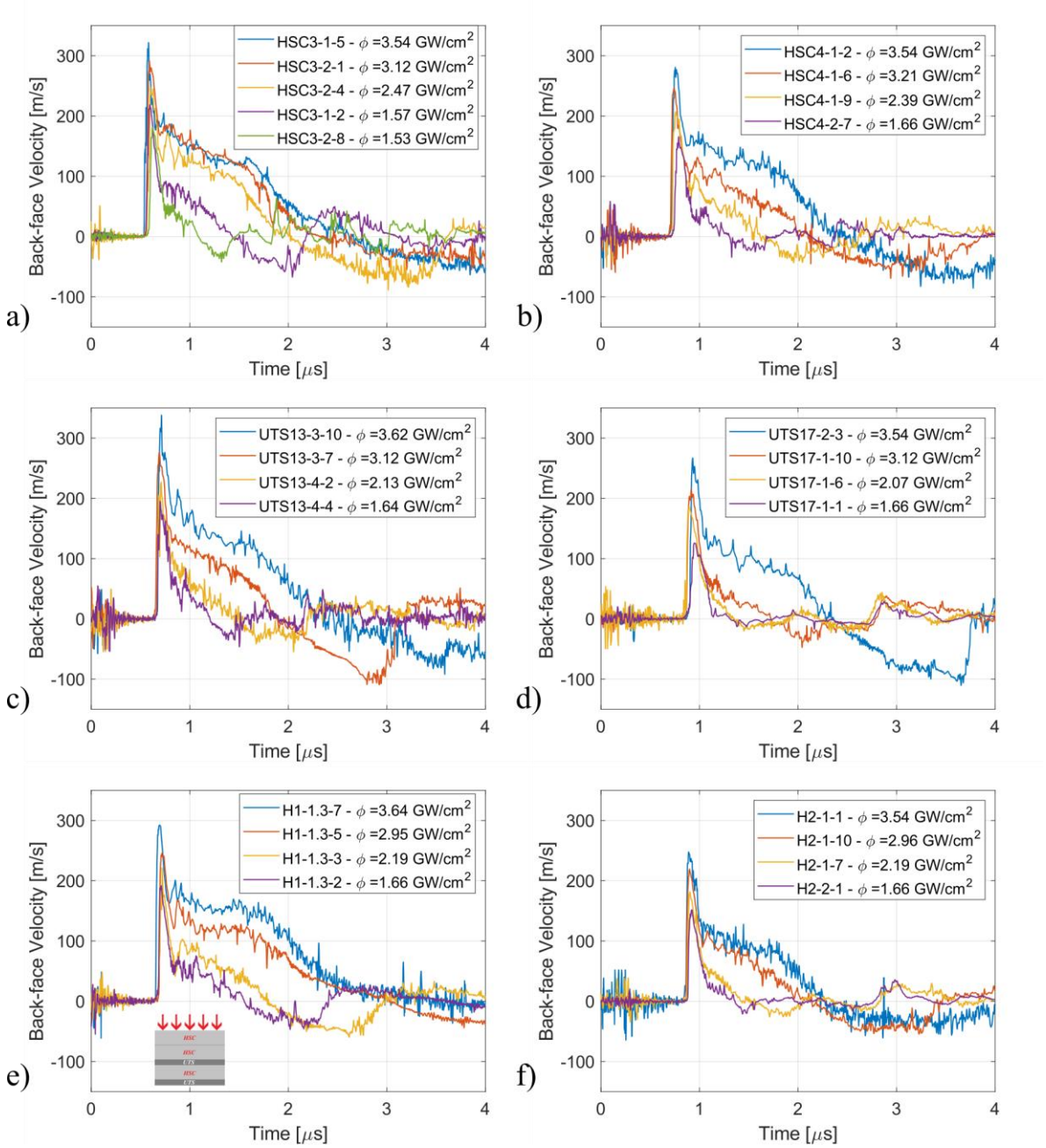

Fig. 4.38. Representative back-face velocity versus time signals for all tested materials, at different energy levels, with the corresponding density of power; a) HSC3; b) HSC4; c) UTS13; d) UTS17; e) H1 (2022 experimental campaign); f) H2

The response of the UTS13 laminate (Fig. 4.38c), characterized by thinner and more compact unidirectional plies, appears similar to that of HSC4, which has thicker plies. The spall signal shows a similar descending trend with no constant average value. Before the second shockwave breakout, reflections in the last plies are captured in the back-face velocity signal, in the form of small oscillations. The thick UTS17 laminate (Fig. 4.38d) exhibits a spall signal only for the laser impact at maximum energy level and a density of power above 3.5 GW/cm^2, without having a constant mean velocity for the spall signal. In the other shots, at lower densities of power, the second breakout of the shockwave can be easily identified at ~2.8 μs, attesting that the shockwave still propagates through a non-cracked sample. H2 laminate (Fig. 4.38e), with a similar thickness as UTS17, exhibits a spall signal for the second shot (at 75% of max energy level – 2.95 GW/cm^2), in addition to the shot at 100% of max energy. The spall signal follows the same descending path as the other UTS and HSC materials. The shockwave second arrival is captured at a similar position on the time scale, at ~ 2.9 μs.

The H1 laminate, when shot on the HSC face, shows a spall signal across the entire range of power densities depicted in Fig. 4.38d. Interestingly, it is the only configuration with an almost constant mean velocity in the spall signal before starting to decrease. Furthermore, the average spall velocity decreases as the intensity of the shot decreases. A detailed analysis of the influence of the stacking sequence on the BFV response for the H1 laminate is provided in a section 4.7.2.1.c.

b. Influence of sample thickness

Fig. 4.39 and Fig. 4.40 provide a qualitative comparison of the BFV response between thin and thick HSC laminates, and thin and thick UTS laminates, respectively. In both cases, the increased thickness leads to a delay in the shock arrival (Δt_a) and a decrease in the maximum velocity of the first peak (ΔMax_{BFV}).

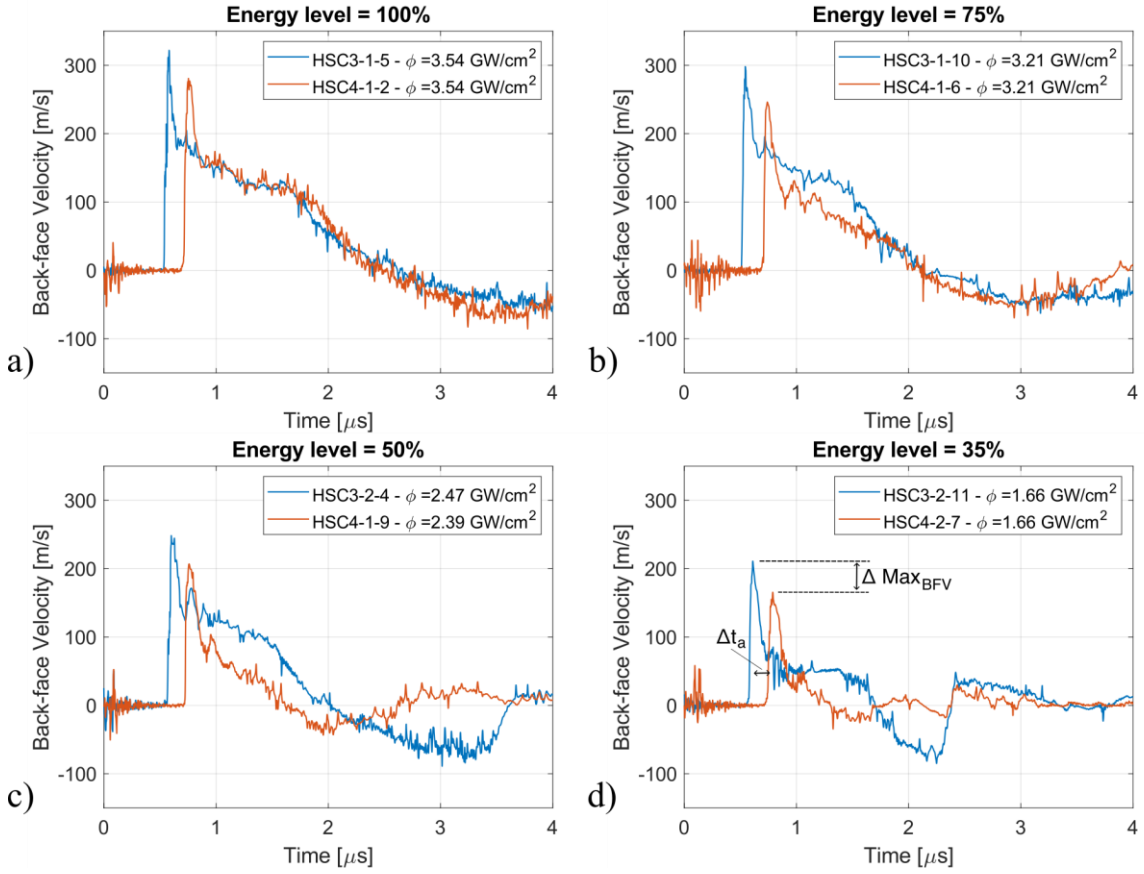

Fig. 4.39. BFV comparison between representative samples of HSC3 and HSC4; a) 100% of max energy; b) 75% of max energy; c) 50% of max energy; d) 35% of max energy

For HSC laminates, an increase of ~0.4 mm in the thickness of the sample leads to Δt_a between 0.16 and 0.19 µs, while for UTS laminates, an increase in the thickness of the sample with ~0.6 mm implies a shock arrival delay of ~0.21-0.24 µs. There are also small differences in the thickness of the same material laminate, leading to minor differences in the shock arrival time as well.

In terms of ΔMax_{BFV}, it depends on the samples chosen for comparison. In this regard, the differences between all possible combinations for the same energy level and prepreg type were determined.

UTS laminates display variations in the maximum velocity of the first peak among samples tested under the same configuration, resulting in data dispersion regarding the percentage decrease of the maximum velocity of the first peak between UTS13 and UTS17 laminates. At 100% of max energy level, the differences range from 14 m/s to 100 m/s (excluding very low differences), corresponding to a percentage decrease between 5% and 29%. Similarly, at 75% of max energy level, ΔMax_{BFV} varies between 7 m/s and 74 m/s, with a percentage decrease

ranging from 3% to 25%. When the energy level is further reduced to 50%, the differences in maximum BFV continue to exhibit variability, with ΔMax_{BFV} ranging from 3 m/s to 61 m/s and a percentage decrease between 2% and 25%. Lastly, at 35% of max energy level, ΔMax_{BFV} spans from 19 m/s to 74 m/s, resulting in a percentage decrease between 12% and 38%.

HSC laminates demonstrate less variation in the data, resulting in narrower intervals for ΔMax_{BFV} and, consequently, for the percentage decrease. At 100% of max energy level, ΔMax_{BFV} falls within the range of 39 m/s to 71 m/s, corresponding to a percentage difference of 12% to 21.5%. Similarly, at 75% of max energy level, the maximum velocity difference spans from 45 m/s to 65.5 m/s, with a percentage difference of 15% to 22%. As the energy level was diminished down to 50 % of the maximal energy, the interval gap further reduces, with ΔMax_{BFV} ranging between 37 m/s and 51.5 m/s, and percentage differences between 15% and 20.5%. Lastly, at 35% of max energy level, the range of ΔMax_{BFV} lies between 20 m/s and 55 m/s, resulting in a percentage difference between 10% and 25%.

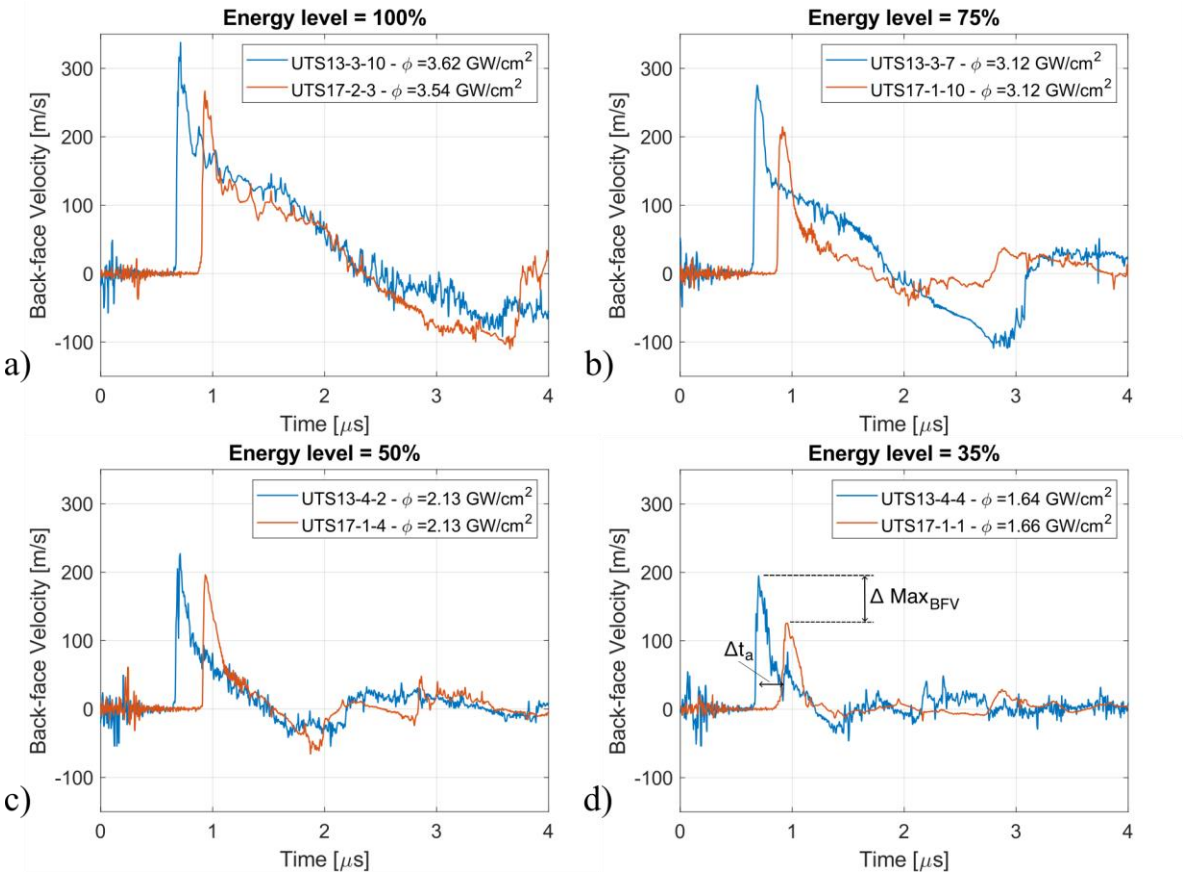

Fig. 4.40. BFV comparison between representative samples of UTS13 and UTS17; a) 100% E; b) 75% E; c) 50% E; d) 35% E

While the data for individual reference laminates may not appear informative due to the broad intervals for percentage decrease, a linear decreasing trend becomes apparent when plotting the maximum back-face velocity against the sample thickness for all reference laminates (both UTS and HSC laminates), as depicted in Fig. 4.41. With the exception of the 100% of max energy level, where UTS13 data for the maximum back-face velocity is either close to the values for the 75% of max energy level or lies above the linear trendline, the data for both UTS and HSC laminates appears to complement each other. When using the Pearson correlation coefficient to assess the relationship between the maximum back-face velocity and the thickness of the samples, considering data from all reference materials at each energy level, a strong to very strong negative correlation is consistently observed in all cases. Specifically, at the 100% of max energy level, the Pearson coefficient is the lowest at -0.74, attributed to the scattered data from UTS13. For the 75% of max energy level, the coefficient is -0.90, for the

50% of max energy level, it is -0.818, and for the 35% of max energy level, it is the highest at -0.947.

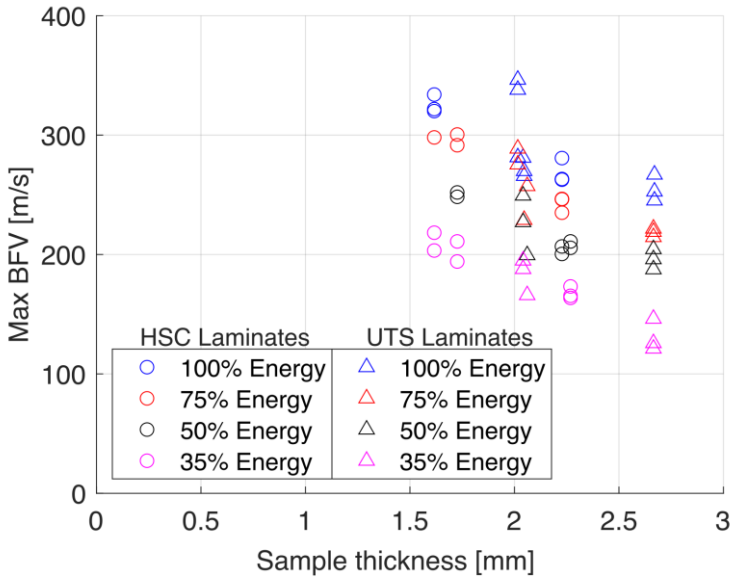

Fig. 4.41. Maximum back-face velocity versus samples' thickness, for UTS and HSC laminates, at different energy levels

The obtained Pearson coefficients confirm the presence of a linear decreasing trendline of the maximum back-face velocity with the thickness of the sample. Additionally, it appears that the type of carbon fiber composite does not exert any significant influence on the maximum back-face velocity within the range of tested thicknesses.

c. Influence of the stacking sequence (H1 material)

As the H1 composite has an unsymmetric stacking sequence, the influence of impacting the sample on one face or the other is studied. In this regard, pairs of samples with opposite stacking sequences were tested in both the 2021 and 2022 experimental campaigns. Fig. 4.42 provides a schematic illustration of the H1 stacking sequence, loading direction with respect to fiber direction and stacking sequence, and sample numbers for the corresponding stacking sequences.

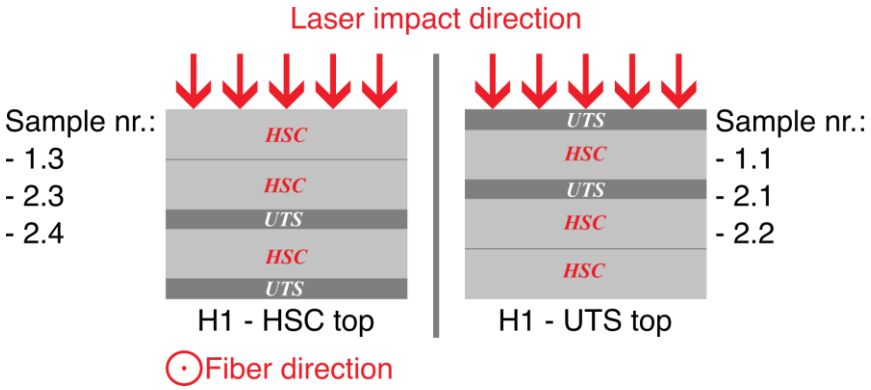

Fig. 4.42. Laser impact direction on H1 samples

The experimental data is presented in two sets: one from the 2021 campaign (Fig. 4.43), and the other from the 2022 experimental campaign (Fig. 4.44). The analysis involves comparing the back-face velocity signals for paired samples with opposite stacking sequences, considering various laser energy levels (100%, 75%, 50%, and 35% of max energy). Representative samples impacted on the UTS and HSC ply were selected for each energy level, and their responses are depicted in blue and orange, respectively, along with their respective stacking sequences.

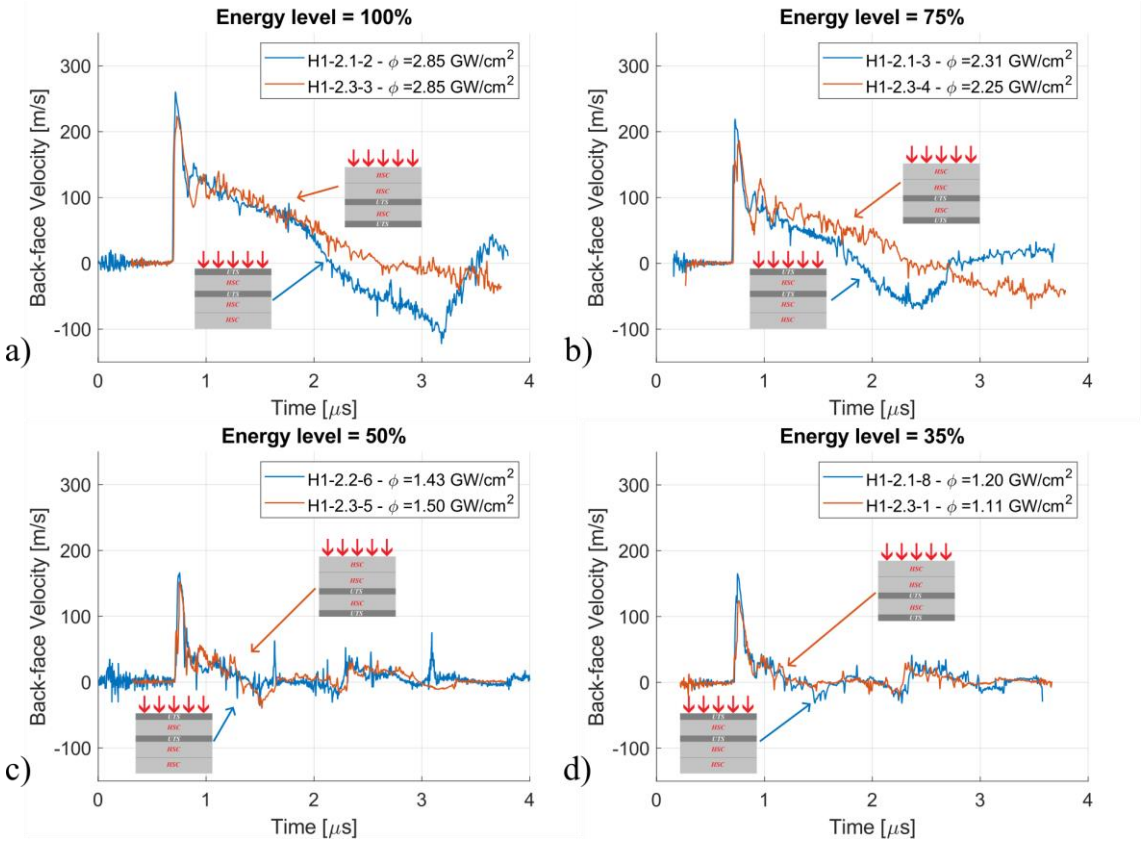

Fig. 4.43. BFV comparison between representative samples of H1, impacted on UTS face and HSC face, tested in 2021 experimental campaign; a) 100% of max energy; b) 75% of max energy; c) 50% of max energy; d) 35% of max energy

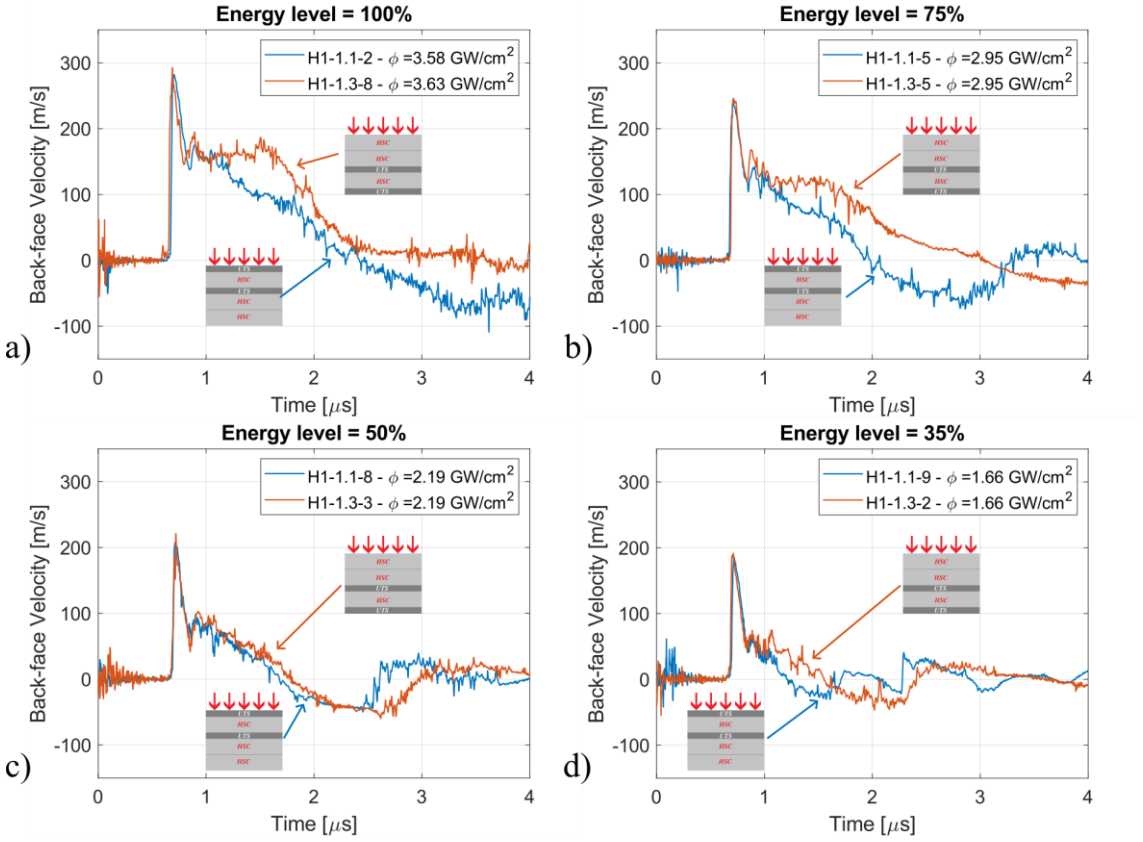

Fig. 4.44. BFV comparison between representative samples of H1, impacted on UTS face and HSC face, tested in 2022 experimental campaign; a) 100% of max energy; b) 75% of max energy; c) 50% of max energy; d) 35% of max energy

During the 2021 campaign, it was noticed that the maximum velocity of the first peak for samples impacted on the UTS ply was higher than those impacted on the HSC ply, despite a minimal difference in density of power. Even when a shot on the HSC ply had a higher density of power than the corresponding shot on the UTS ply, the latter still exhibited a higher maximum velocity of the first peak, though the difference was lower compared to cases with equal power densities. However, such behavior was not observed in the samples tested during the 2022 experimental campaign.

Fig. 4.45 provides a clearer depiction of the variation in the velocity of the first peak with the density of power of the laser shot. At lower densities of power, the difference between samples impacted on the HSC or UTS ply is negligible. As the density of power increases, the difference in the velocities' values also increases for the samples tested in the 2021 campaign. However, when incorporating the peak velocities from the 2022 campaign, the previously observed difference in the peak velocity is not present anymore. Furthermore, the 2022 results align with the trendline for 2021 samples impacted on the UTS face, which prompts the question of why the results in 2021 differed. This observation emphasizes the necessity of conducting a numerical analysis to delve deeper into the shockwave propagation inside the material. Such an analysis could help unravel the underlying factors contributing to the variation in the experimental results and provide valuable insights into the dynamic behavior of the laminates.

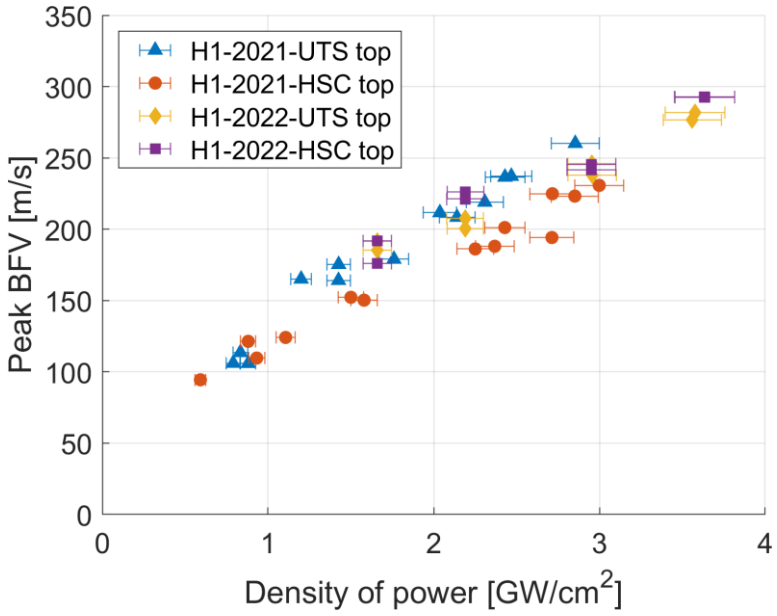

Fig. 4.45. Maximum velocity of the first peak of the back-face velocity with respect to the density of power, for samples impacted on opposite stacking sequences, in both 2021 and 2022 experimental campaigns

However, there is a difference in the damage mechanism. When examining the 100% and 75% of max energy shots for samples impacted on the UTS ply (Fig. 4.43a and b, Fig. 4.44a and b), the spall signal does not display a clear mean velocity before starting to decrease, in contrast to shots on samples impacted on the HSC ply. Furthermore, the mean spall velocity for samples tested in the 2021 campaign is not as distinct as those tested in 2022, particularly at higher intensities. These findings suggest that for H1 samples impacted on the HSC face, a clear plane rupture should exist, while for samples impacted on the UTS ply, the rupture plane might be irregular. Detailed information on the damage is available in section 4.7.2.3.

Since all other materials were tested in 2022, the back-face velocity results for H1 materials will also be selected from the 2022 experimental campaign to ensure a consistent basis for comparison.

d. Comparison of reference and hybrid laminates back-face velocity response

As the peak back-face velocity is influenced by the thickness of the sample, due to attenuation of the shockwave, to compare the back-face velocity response of reference and hybrid materials, laminates with closer thicknesses are selected for each figure set. Fig. 4.46 shows the back-face velocity response of representative samples of H1, HSC4, and UTS13, with thicknesses between 2.04 mm and 2.24 mm.

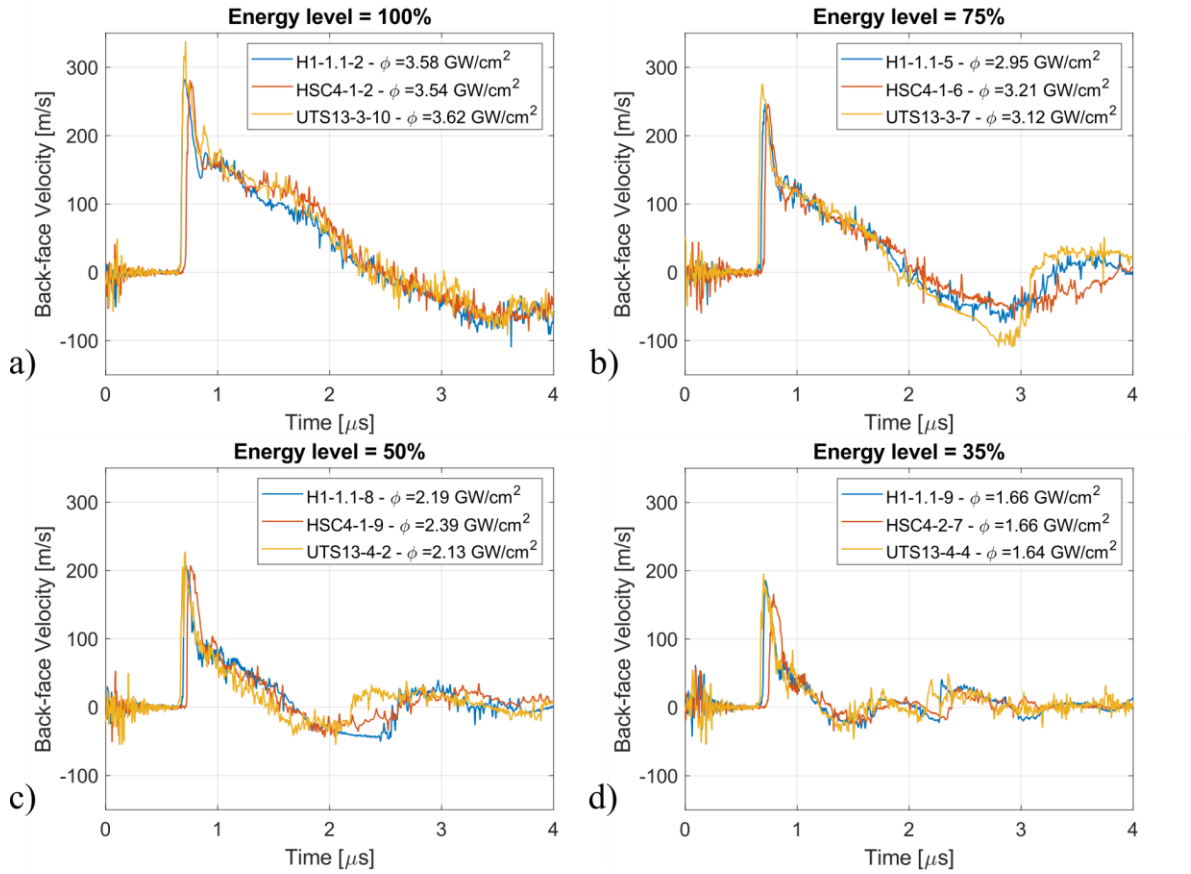

Fig. 4.46 BFV comparison between representative samples of H1, HSC4 and UTS13, at different energy levels; a) 100% of max energy; b) 75% of max energy; c) 50% of max energy; d) 35% of max energy

The outline of the back-face velocity signal is mostly the same for all three laminates, at all tested energy levels, with minor differences. A short time delay in the shockwave arrival is observed, due to the thickness difference. Moreover, the differences in the peaks of the back-face velocity are not significant, except for the 100% of max energy level case, where UTS13 (the thinnest laminate of the set), exhibits a peak velocity with ~40 m/s higher than the other two. It can be attributed to the thickness difference, as well as to the higher density of power of the laser shot, compared to the other two. Again, due to the thickness difference, the second shockwave arrival in Fig. 4.46d for UTS13 is at an earlier time, followed by H1 and HSC4.

For the second set, UTS17 and H2 representative samples were chosen for comparison, as they have similar thicknesses, and the back-face velocity comparison is shown in Fig. 4.47. As in the previous case, the back-face velocity traces are alike, with minor differences such as delay in shock arrival caused by the thickness of the samples, as well as little variances in peak velocity, also attributed to differences in sample thickness and density of power of the laser shot.

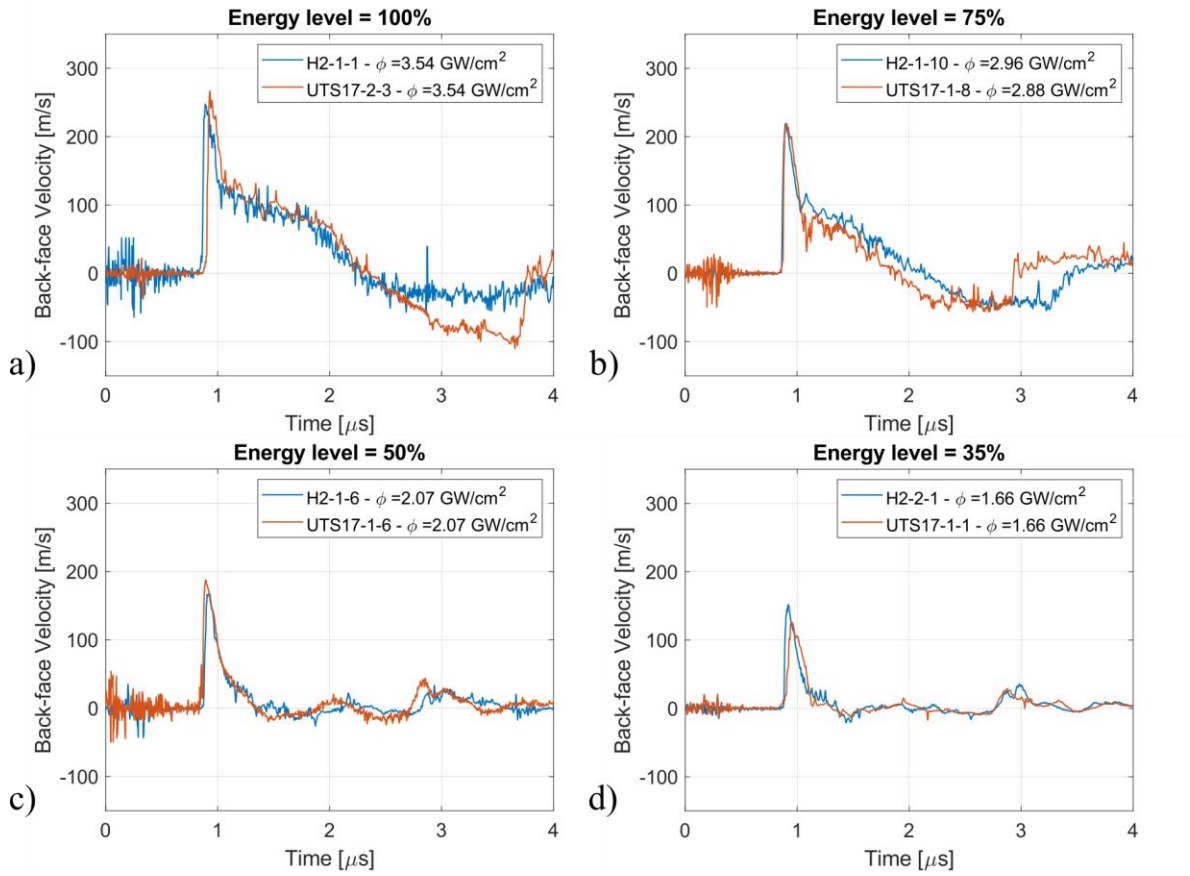

Fig. 4.47. BFV comparison between representative samples of H2 and UTS17 , at different energy levels; a) 100% of max energy; b) 75% of max energy; c) 50% of max energy; d) 35% of max energy

In Fig. 4.48, the evolution of the peak back-face velocity with the density of power is presented, individually for each laminate type, with a linear fit and 95% prediction interval. Normally, for a zero density of power, a zero back-face velocity should be obtained, and the evolution of the back-face velocity be fitted with a power law. However, no experimental data is available at very low densities of power in this case, which could lead to erroneous power law fitting. Thus, for the sake of clarity and comparison purposes, a linear fit was used for the range of densities of power studied. In Fig. 4.48, the fitting equation is also provided.

It is noticed that for all the carbon fiber composites, the slope of the linear fit is in the same range, with values between 50 and 59. This observation is highlighted in Fig. 4.49, in which the linear fits for all materials are plotted. It can be observed that the slope for the reference laminates is mainly the same, while H1 and H2 laminates have a higher and lower slope respectively, which could be due to reflections at the interface of different plies within the hybrid composites. Moreover, the amplitude of the peak back-face velocity increases with decreasing thickness of the laminate, which is expected due to the attenuation of the shockwave while propagating through the thick composite laminate.

In APPENDIX L, the evolution of the ablation pressure with the peak back-face velocity is presented. In the range of ablation pressures in these tests (~0.18 GPa to ~0.3 GPa), the evolution is mostly linear, suggesting an elastic response regime.

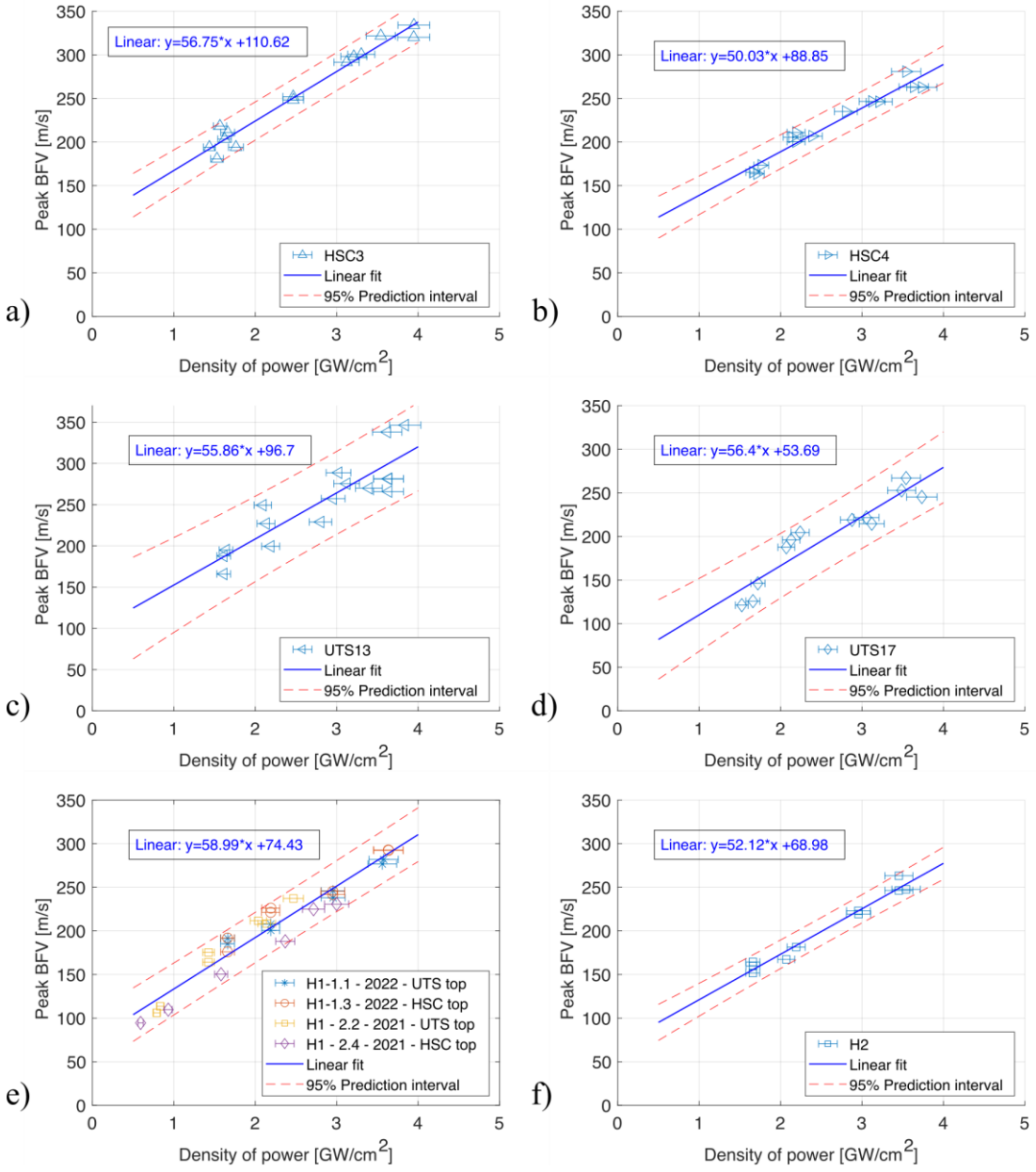

Fig. 4.48. Evolution of the maximum back-face velocity of the first peak with density of power, with linear fit; a) HSC3; b) HSC4; c) UTS13; d) UTS17; e) H1; f) H2

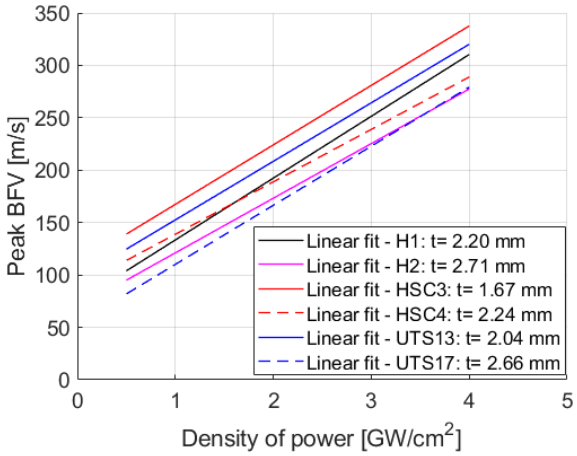

Fig. 4.49. Linear fits for maximum back-face velocity evolution with density of power, for all tested materials

4.7.2.2 Parameters estimation from Laser-induced shockwave tests

Derived from the back-face velocity signals from each shot, from shots that did not present a spall signal, and the second shockwave arrival is clearly identifiable, the propagation and sound speed in the samples were estimated as described in section 4.4.2.

The resulting speed of sound is plotted against the density of power in Fig. 4.50a. The speed of sound evolution with the density of power is almost constant for each material, with small variations induced by the particularities of each sample. This shows that the speed of sound evaluation from an undamaged sample is independent of the loading intensity, and reflects the material behavior.

Fig. 4.50b shows the average values of the speed of sound, with error bars representing the standard deviation when averaging the values from all samples of each corresponding material. Small differences are observed between the reference and hybrid materials, with H2 having the lowest average speed of sound and the highest error bar. Still, the small differences between the average speed of sound appear to be within the error bars, thus, they can be attributed to microstructure differences from one sample to the other. In the case of H1 material, even though for the back-face velocity signals for samples with opposing stacking sequences some differences were observed when analyzing the average speed of sound, no clear distinction between the two cases could be observed. Thus, results from both cases were used to determine the average speed of sound of H1 hybrid laminate.

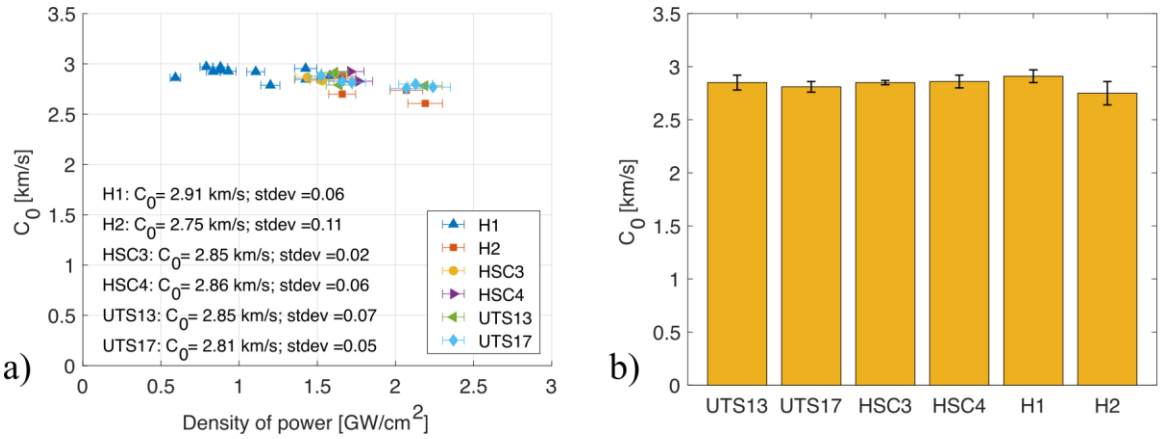

Fig. 4.50. Speed of sound evaluation from non-damaged samples; a) C_0 evolution with density of power of the laser shot; b) average C_0 values for each material type

The average C_L and C_0 for each material type and the corresponding standard deviations are also presented in Table 4.3, along with a theoretical longitudinal speed of sound in the out-of-plane direction, determined using equation (1.48) and the quasi-static laminate properties from section 3.2.1. Compared to the in-plane laser test results, where the different carbon fibers within the reference laminates affected the propagation speed, with UTS having a higher propagation speed compared to HSC laminates, in the case of out-of-plane laser tests, almost no difference is seen between the two laminate types. Thus, it is clear that the shockwave propagation is mainly governed by the epoxy resin and its properties. The average speed of sound varies between 2.75 km/s and 2.91 km/s, which is almost three times lower than the speed of sound in the fiber direction. Similar values were reported by Gay [202] and Alexander [170].

Table 4.3. Average estimated speed of sound and theoretical values for out-of-plane laser tests

Material	Average C_L [km/s]	Standard deviation [km/s]	C_L [km/s] from (equation)*	Average C_0 [km/s]	Standard deviation [km/s]	ρ_0 [g/cm^3]
HSC3	2.91	0.02	2.18	2.85	0.02	1.483 ± 0.005
HSC4	2.91	0.02	2.18	2.86	0.06	1.483 ± 0.005
UTS13	2.91	0.05	2.15	2.85	0.07	1.497 ± 0.009
UTS17	2.91	0.07	2.17	2.81	0.05	1.490 ± 0.004
H1	2.95	0.05	2.18	2.91	0.06	1.478 ± 0.007
H2	2.80	0.11	2.17	2.75	0.11	1.499 ± 0.011

*parameters from quasi-static experiments (laminate parameters)

From back-face velocities that exhibited a clear spall signal, the dynamic tensile strength (σ_{SPALL}) and strain rate during spall fracture were evaluated as described in section 4.4.3, using the evaluated speed of sound in the out-of-plane direction for each material type.

Fig. 4.51a shows the dynamic tensile strength evaluation versus the density of power for each viable sample. No clear trend can be observed for the evolution of σ_{SPALL} with the density of power for either material, although it tends to not be affected by the density of power of the laser shot. Although the data is quite scattered, it seems to revolve between 250 MPa and 350 MPa. For H1, the data was separated based on the year of the test, and Fig. 4.51c shows a separation of the dynamic tensile strength data based on the tested stacking sequence as well. Looking at 2022 data (circles), no apparent influence of the stacking sequence is seen. However, for 2021 data, where also differences in the maximum back-face velocities were observed, it seems that in the case where the H1 sample was shot on the UTS face, it exhibits a higher σ_{SPALL} than the case when it is shot on the HSC face.

When averaging the results for each material type, illustrated in Fig. 4.52a and also presented in Table 4.4, values between 290 MPa and 317 MPa are obtained, which are comparable to the 292 ± 15 MPa value evaluated by Gay et al. [172] for laser-induced shockwaves in a 4 ply unidirectional carbon fiber reinforced polymer material, with cross-ply stacking sequence. Other authors evaluated the dynamic strength of carbon fiber composites using plane-plate impact – Xie [82] showed that the spall strength has a linear variation with the loading strain rate for a unidirectional carbon fiber composite with quasi-isotropic layup, with similar quasi-static material properties as the composite used in this study and they found a maximum spall strength of 163.3 ± 10.2 MPa for a strain rate of 1.22e+05 s^{-1}, and Riedel [252] estimated the dynamic tensile strength at 250 ± 12 MPa for a strain rate of 1.5e+05 s^{-1}. However, in this study, no clear dependency between the dynamic tensile strength and strain rate during spall fracture was noticed.

The error bars in Fig. 4.52 represent the average standard deviation, which is also presented in Table 4.4, and is calculated using equation (4.8), where STD represents the average standard deviation, std is the standard deviation obtained for a sample after Monte Carlo analysis, and N represents the number of samples.

$$STD = \sqrt{\frac{\sum_{i=1}^{N} std_i}{N}}; \tag{4.8}$$

Among the tested laminates, H2 has the lowest σ_{SPALL} value, but also the highest error bar, followed closely by HSC3, while UTS laminates have the highest values. This could be due to

the fact that the matrix in UTS is a toughened epoxy, more resistant to impact loading. However, HSC4 exhibits a dynamic tensile strength similar to UTS laminates, thus it cannot be fully implied that the different results are due to the different matrix in the prepregs.

For H1, in Fig. 4.52a, the average value takes into account all samples, regardless of the impacted face. However, in Fig. 4.52b, the average results for each stacking sequence case are illustrated separately. It is noticed that when the H1 sample is impacted on the UTS face it exhibits a higher σ_{SPALL} value than when it is shot on the HSC face. It is explained in section 4.7.2.3 that the damage behavior is responsible for these different values.

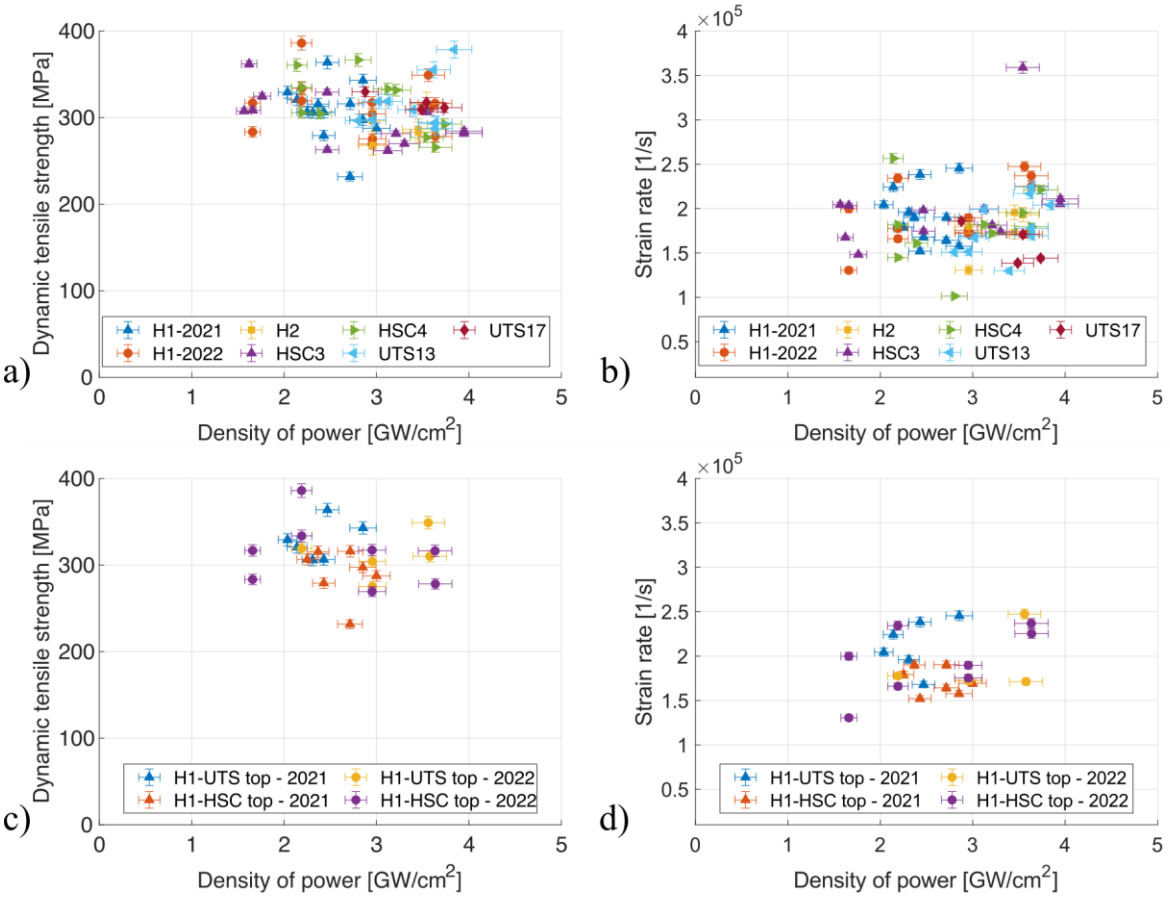

Fig. 4.51. Dynamic tensile strength and strain rate evaluation; a) Dynamic tensile strength for all tested materials; b) Strain rate for all tested materials; c) Dynamic tensile strength for H1 on samples tested on opposite stacking sequences; d) Strain rate for H1 on samples tested on opposite stacking sequences

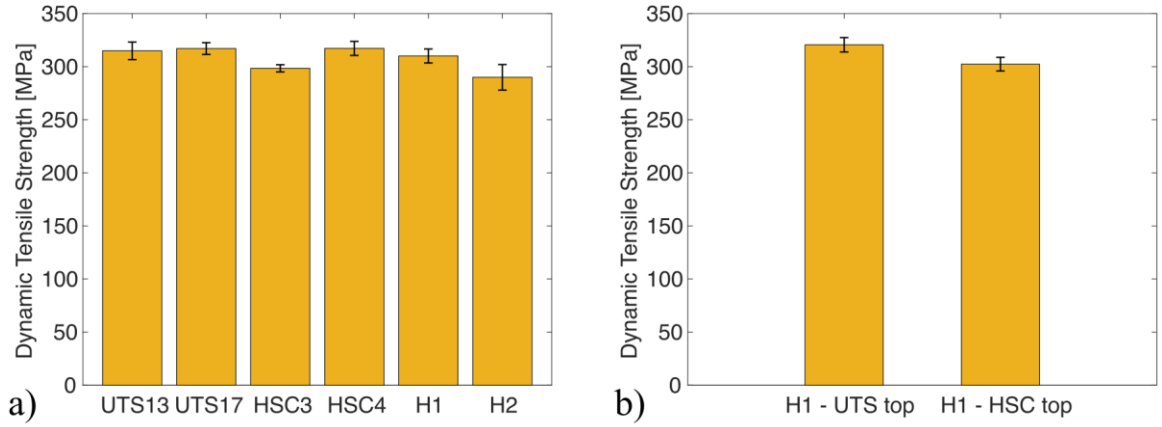

Fig. 4.52. Average dynamic tensile strength; a) all tested materials; b) H1 material, for both tested stacking sequences

Regarding the strain rate during spall fracture, Fig. 4.51b shows the strain rates evaluated for individual samples, versus the density of power of the laser shot. Similar to the results for the dynamic tensile strength, no clear evolution trend with the density of power can be identified. However. Most values appear to be concentrated in the [1.5e+05; 2e+05] s^{-1} interval. The isolated high value of 3.5e+05 s^{-1} for HSC3 materials was excluded from further analysis. For H1 material, the results were again divided by testing year and stacking sequence in Fig. 4.51d. While the results from 2022 for the two stacking sequences are intertwined, when looking at the results from 2021, H1 samples impacted on the UTS face exhibit a higher strain rate during spall fracture, compared to samples impacted on the HSC face, as observed for the dynamic tensile strength as well. This is due to the difference in the peak back-face velocity, detailed in section 4.7.2.1c.

When looking at average strain rate values, illustrated in Fig. 4.53a and presented in Table 4.4 as well, it is observed that UTS17 is subjected to lowest strain rates, followed by H2, but with a higher error bar, HSC4, UTS13, HSC3 and with H1 being subjected to the highest strain rates. The error bars represent the standard deviation calculated in the same manner as for the dynamic tensile strength, using equation (4.8).

It would appear that in the case of laser-induced shockwave tests in the out-of-plane direction, where the shockwave is highly attenuated when propagating towards the back face, the thickness of the sample affects the strain rate during spall fracture. To have conclusive results and determine a trendline, a higher range of thicknesses would require testing. It is important to notice that in Fig. 4.53a for H1 all samples were used for averaging, regardless of the stacking sequence. The results for the individual stacking sequences are shown in Fig. 4.53b. As already noticed in previous observations, the strain rate in the case where the H1 sample is impacted on the UTS face is higher than when impacted on the HSC face, suggesting different tensile loading conditions when damage is in the form of delamination or as a spallation (details about damage behavior in section 4.7.2.3).

Table 4.4. Average estimated dynamic tensile strength and strain rate during spall fracture

Material	Average σ_{SPALL} [MPa]	Standard deviation [MPa]	Average $\dot{\varepsilon}$ [s^{-1}]	Standard deviation [s^{-1}]	Average laminate thickness [mm]
HSC3	298.43	3.37	1.88e+05	2.56e+03	1.67
HSC4	317.20	6.60	1.80e+05	4.04e+03	2.24
UTS13	314.92	8.28	1.79e+05	4.86e+03	2.04
UTS17	317.06	5.54	1.60e+05	2.97e+03	2.66
H1	310.08	6.58	1.91e+05	4.33e+03	2.20
H1 – UTS top	320.61	6.78	2.01e+05	4.55e+03	2.20
H1 – HSC top	302.35	6.43	1.84e+05	4.16e+03	2.20
H2	289.96	12.03	1.75e+05	7.36e+03	2.71

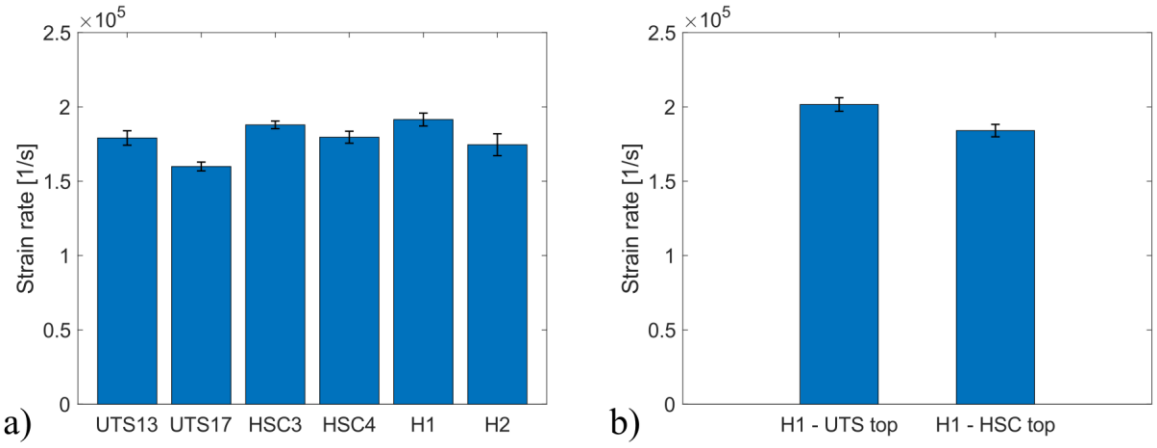

Fig. 4.53. Average strain rate during spall fracture; a) all tested materials; b) H1 material, for both tested stacking sequences

4.7.2.3 Damage analysis

Damaged samples diagnosed through the presence of a spall signal in the back-face velocity response were further subjected to microscopic observation of the cross-section of the samples. For all laminates, cross-sections perpendicular to the fiber direction were observed.

In Fig. 4.54, cross-sections of UTS17 samples are presented, along with the corresponding back-face velocity signal. The focal spot is marked on the impacted face with a thick red line. Because of the UTS17 laminate's thickness (~2.66 mm), the shockwave is highly attenuated upon reaching the back face, and the generated tensile stress at the intersection of the release wave and the reflected wave exceeds the damage threshold only in the case of a 100% of max energy level shot, at a density of power close to 3.5 GW/cm^2. Even in this case, the crack is barely visible at ~240 µm from the back face. Although a delamination between plies was expected, it appears that the spall formed inside the second last ply, and not at the interface between plies. In the laser shot at a lower intensity (marked with orange), no visible crack was identified, even at higher magnifications of the digital microscope. Thus, the small accelerations visible right after the main velocity peak are due to wave reflections within the interplies [172]. These reflections are also partly responsible for the shockwave attenuation.

When reducing the thickness of the sample, the effects of the shockwave propagation and wave intersections are more pronounced, leading to increased damage within the sample. Fig. 4.55 shows cross-section observation of UTS13 samples (~2 mm thick), impacted at various energy levels and density of power, with microscopic observation close-ups of the damaged sections and corresponding back-face velocity signals. It is observed that by reducing the thickness of the impacted sample by ~0.7 mm, from UTS17 to UTS13, damage is visible for shots with densities of power above 2.8 GW/cm^2. The laser shot at the highest intensity of ~ 3.4 GW/cm^2 (blue) leads to extensive damage within the second to last ply. It is again noticed that the spall is not in the form of delamination at the interface of adjacent plies but as matrix damage inside the ply. This leads to the assumption that for unidirectional composites with standard thickness plies, cured in autoclave, the bonding at the interface between plies is not weaker than the ply itself. It is observed that the crack propagates inside the ply following the regions with higher resin content and localized low fiber volume fraction. A thinner, less visible crack is also observed in the resin-rich region between the second and third ply from the back-face, at ~330 µm from the back-face.

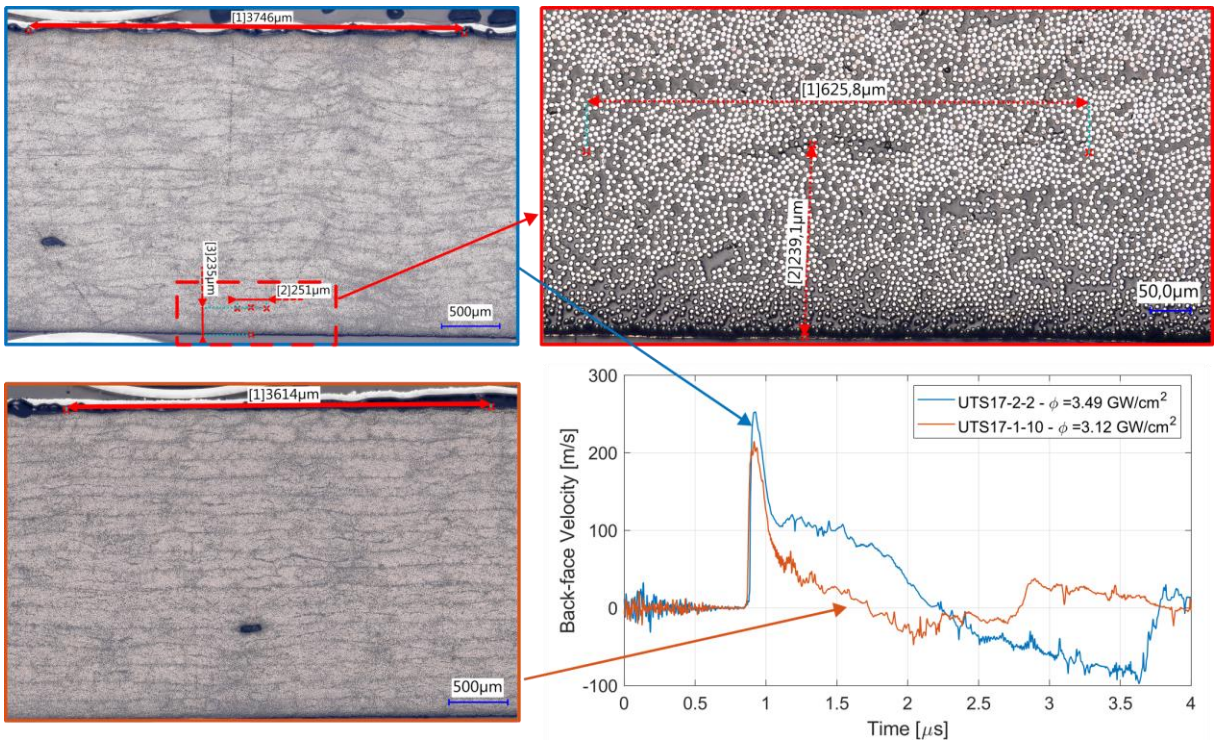

Fig. 4.54. Microscopic observations of damage induced by laser impact in UTS17 samples, cutting plane perpendicular to the fiber direction, with corresponding back-face velocity signals

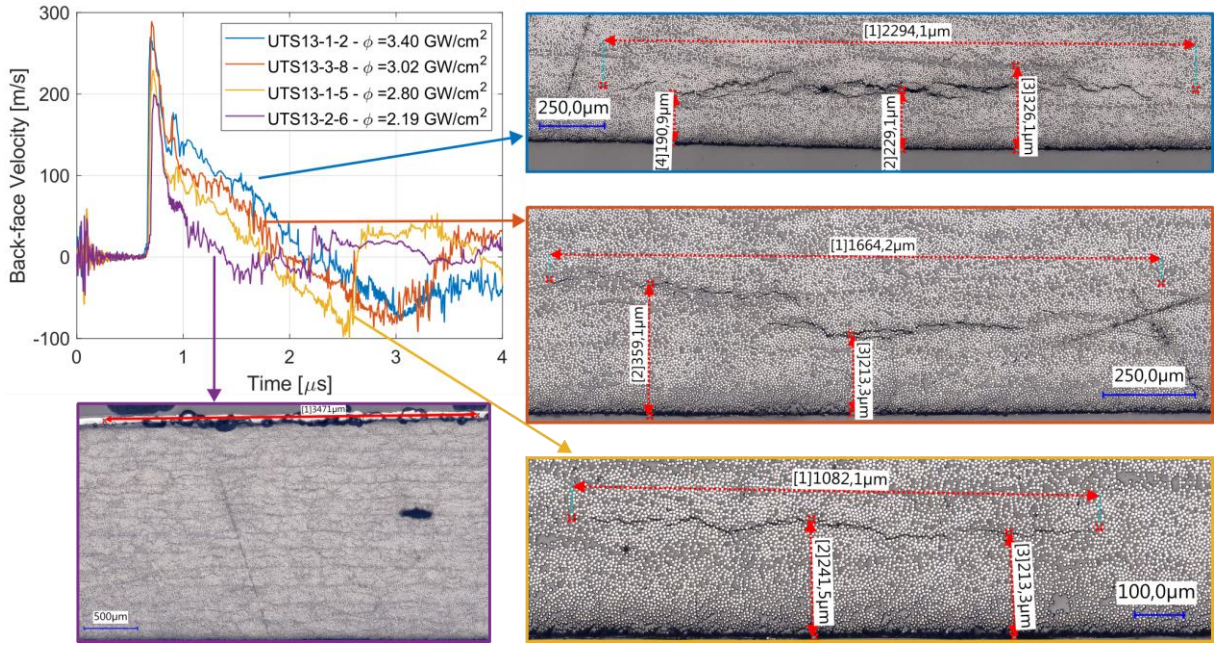

Fig. 4.55. Microscopic observations of damage induced by laser impact in UTS13 samples, cutting plane perpendicular to the fiber direction, with corresponding back-face velocity signals

Although UTS13 is thinner than UTS17, the crack position relative to the back face is similar, suggesting that the thickness of the laminate does not have a detrimental effect on the position of the wave intersection, hence on the tensile loading point.

For the next shot, at an intensity of ~3 GW/cm^2 (orange), the damage is localized inside the second to last ply, and at the interface between the second and third ply from the back face. In both sections, the matrix crack follows regions with higher resin content. Although localized at similar distances from the back face, in this case, the length of the damaged section is lower than for shots at higher intensities. When further reducing the intensity of the shot to ~2.8

GW/cm^2 (yellow), the length of the damaged section is almost half the length of the damage in the highest intensity shot, still being localized in the second to last ply.

At an intensity of the laser shot of ~2.2 GW/cm^2 (purple), no visible damage was identified in the tested sample, and it is considered again that the small acceleration after the first peak and before the secondary shock arrival at the back-face are due to wave reflections at the ply interfaces that ultimately reach the back-face.

For HSC samples, similar cross-section observations, perpendicular to the fiber direction, are shown in Fig. 4.56 for HSC4 and in Fig. 4.57 for HSC3. Having thick plies (~0.5 mm), for both laminates damage induced by the shockwaves is localized inside the last ply. Again, the spall signal from the back-face velocity response corresponds to matrix cracks inside the ply, and not to a delamination plane. For the HSC4 sample shot at ~3.5 GW/cm^2 (blue), the matrix crack is more pronounced and easily identifiable and follows the shape of a resin-rich region. At a lower density of power shot, with ~3.2 GW/cm^2 (orange), the crack follows a similar trend. However, its length is reduced and the crack is not as easily identifiable as the previous one. The crack position relative to the back face is similar for both shots, between 210 µm and 280 µm, and is in the same range as the position of the matrix crack for UTS laminates, suggesting similar shockwave propagation properties for the matrix of the two types of prepregs.

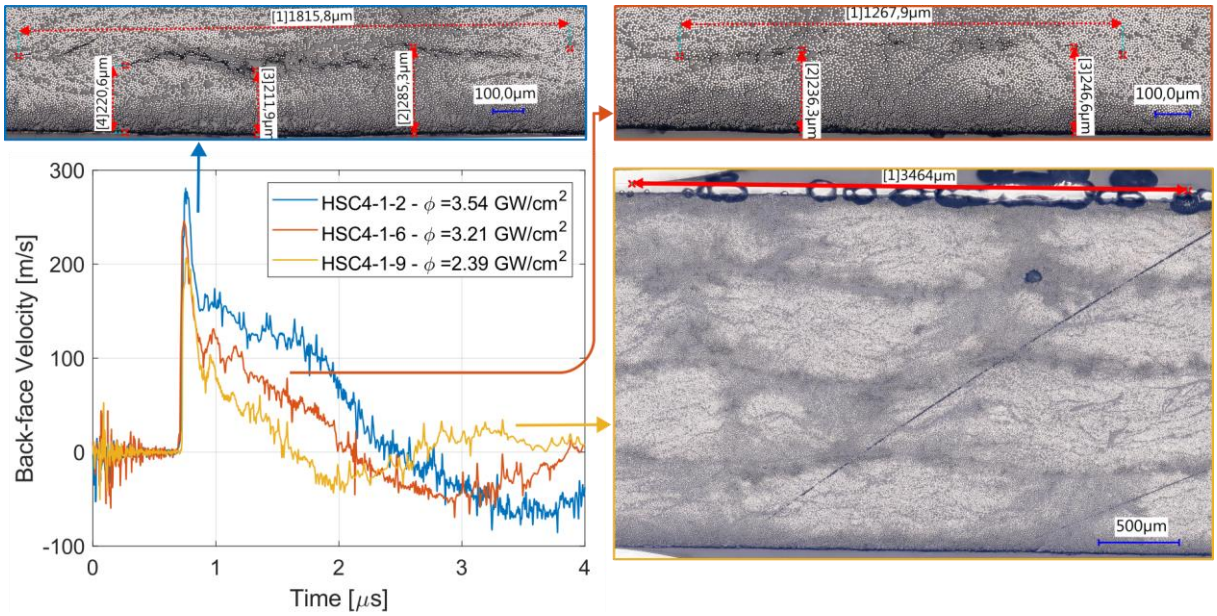

Fig. 4.56. Microscopic observations of damage induced by laser impact in HSC4, cutting plane perpendicular to the fiber direction, with corresponding back-face velocity signals

The HSC4 sample shot with a density of power of ~2.4 GW/cm^2 (yellow) does not exhibit any visible damage in the cross-section. However, on the corresponding back-face velocity signal, a spall-like shape after the first peak is observed. Considering that in the case of HSC samples, the plies are thick and the ply interface is more resin-rich than in the case of tightly packed UTS plies, the respective signal could be due to wave reflection at the last interface. Still, when analyzing Fig. 4.38b, the back-face velocity signal corresponding to a shot at a density of power of ~1.66 GW/cm^2 (purple) exhibits a second shockwave arrival, and also small accelerations after the 1st peak, similar to the ones observed for UTS laminates, that can be attributed to the reflections at the ply interfaces. Since microscopic observations are section-biased, and achieving a cross-section precisely in the middle of the impact proves to be rather challenging, there is a possibility that at lower shot intensities, the internal damage resulting from the intersection of the release wave with the reflected wave might be minimal and could be overlooked during cross-section examinations.

When looking at the microscopic observations for HSC3 samples in Fig. 4.57, the effect of the sample thickness on the damage induced by the laser shots is highlighted again, if compared with observations from HSC4 samples. By reducing the thickness from ~2.2 mm to ~1.7 mm,

the damage is visible within the samples for densities of power as low as 1.56 GW/cm^2. The matrix cracks are positioned inside the last plies in all cases, at a somewhat closer distance to the back-face compared to other laminates, but still between 170 µm and 230 µm near the middle of the shot. The length of the damaged section does not follow a clear decreasing trend with decreasing laser shot intensity and the crack mostly follows resin-rich regions in its propagation. In the sample impacted at the lowest density of power, ~1.53 GW/cm^2 (light blue), no visible damage was identified and an apparent second shock arrival and wave reflection accelerations are seen in the back-face velocity signal.

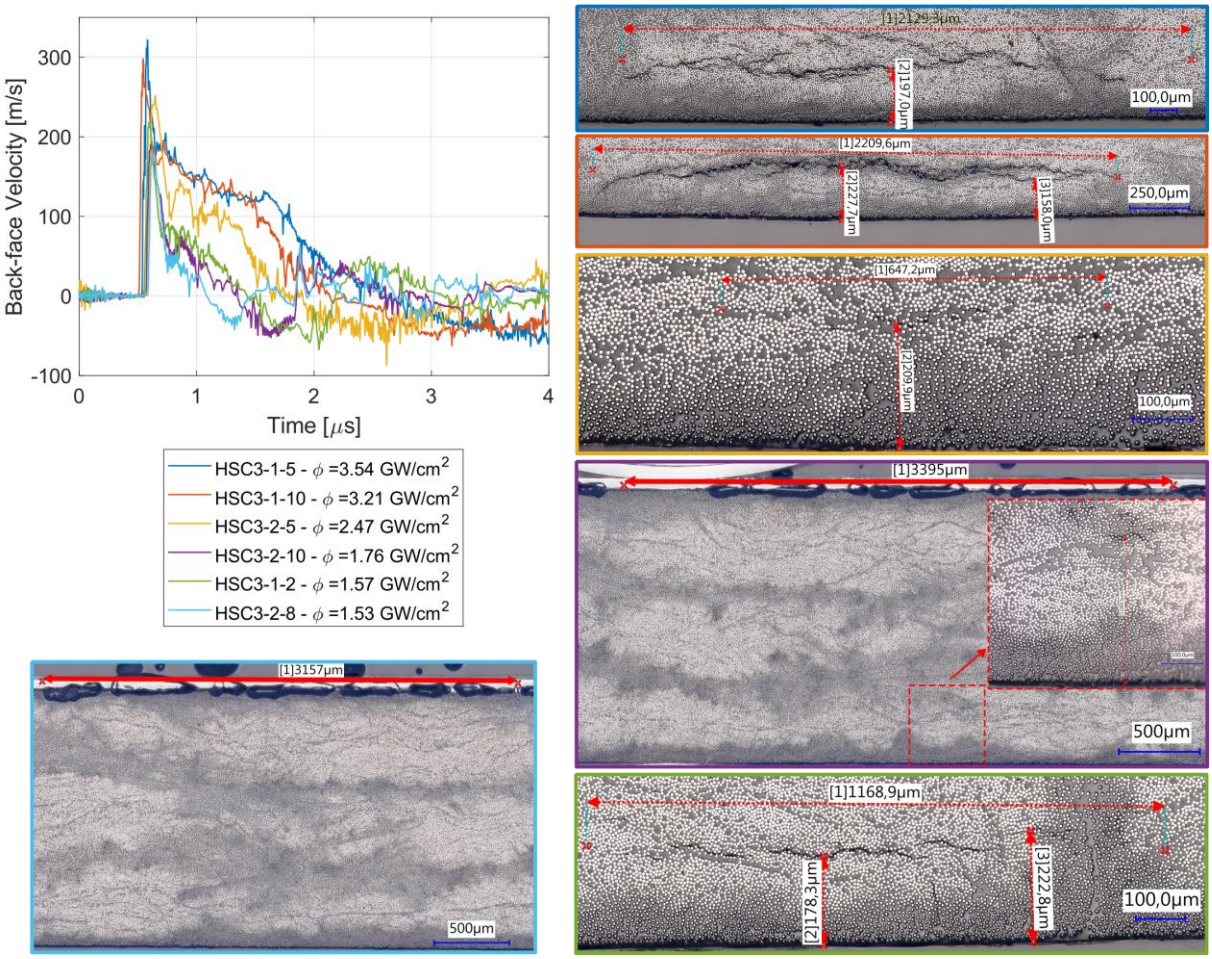

Fig. 4.57. Microscopic observations of damage induced by laser impact in HSC3 samples, cutting plane perpendicular to the fiber direction, with corresponding back-face velocity signals

Going further with analyzing the cross-sections of hybrid laminates, Fig. 4.58 shows the microscopic observations for H2 laminates, with a thickness (~2.72 mm) closer to that of UTS17. It is noticed that even at laser shot intensities of ~2.2 GW/cm^2 (yellow), damage is visible, and thin crack lines are observed, although the spall signal is not as clear. This suggests that the damage tolerance of HSC plies is lower than the one of UTS plies. Considering the position of the crack, it is localized inside the last HSC ply, at distances similar to those of HSC4 laminates. In terms of damage position and crack propagation, H2 laminates seem to have a similar behavior to HSC laminates.

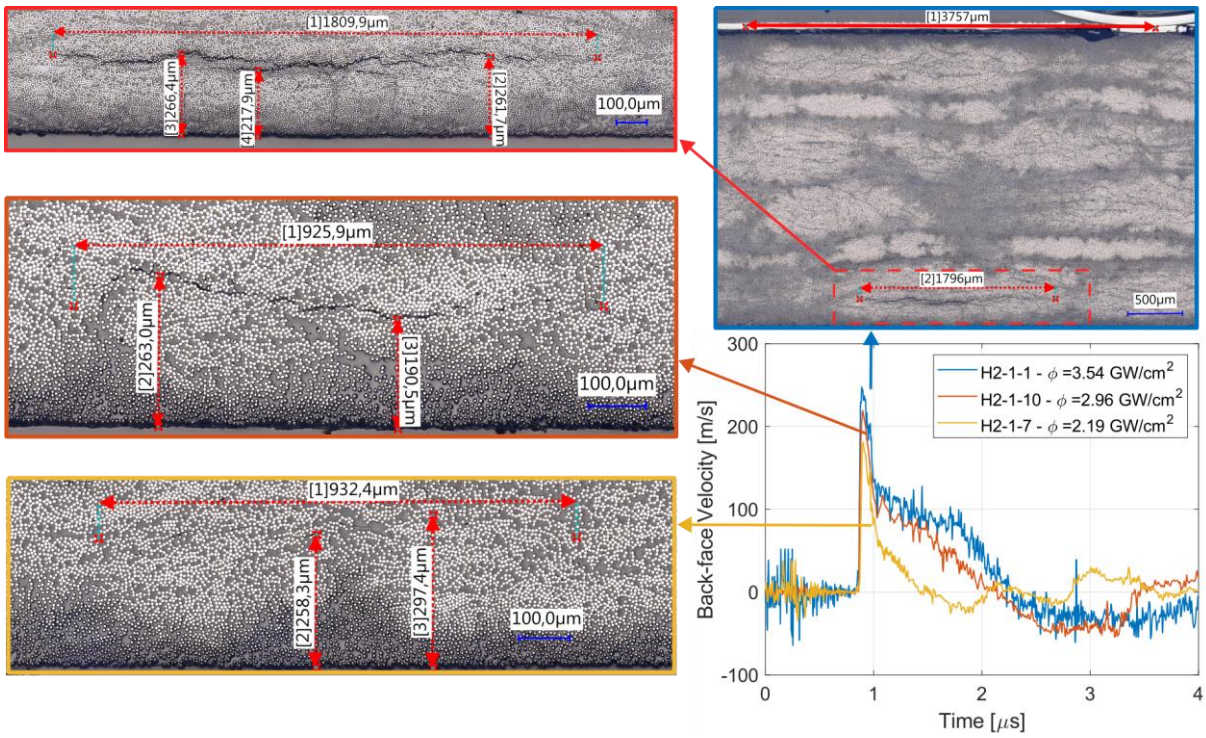

Fig. 4.58. Microscopic observations of damage induced by laser impact in H2 samples, cutting plane perpendicular to fiber direction, with corresponding back-face velocity signals

For H1 hybrid laminate though, having an asymmetric stacking sequence, the damage analysis was performed for two cases. First, for the case in which the sample is impacted on the UTS ply and the last ply is represented by an HSC ply, the cross-sections and corresponding back-face velocities are shown in Fig. 4.59. It is noticed that similar to HSC and H2 laminates, damage is localized inside the last ply and represents a matrix crack. The position relative to the back face is between ~160µm and ~230 µm, similar to previous results.

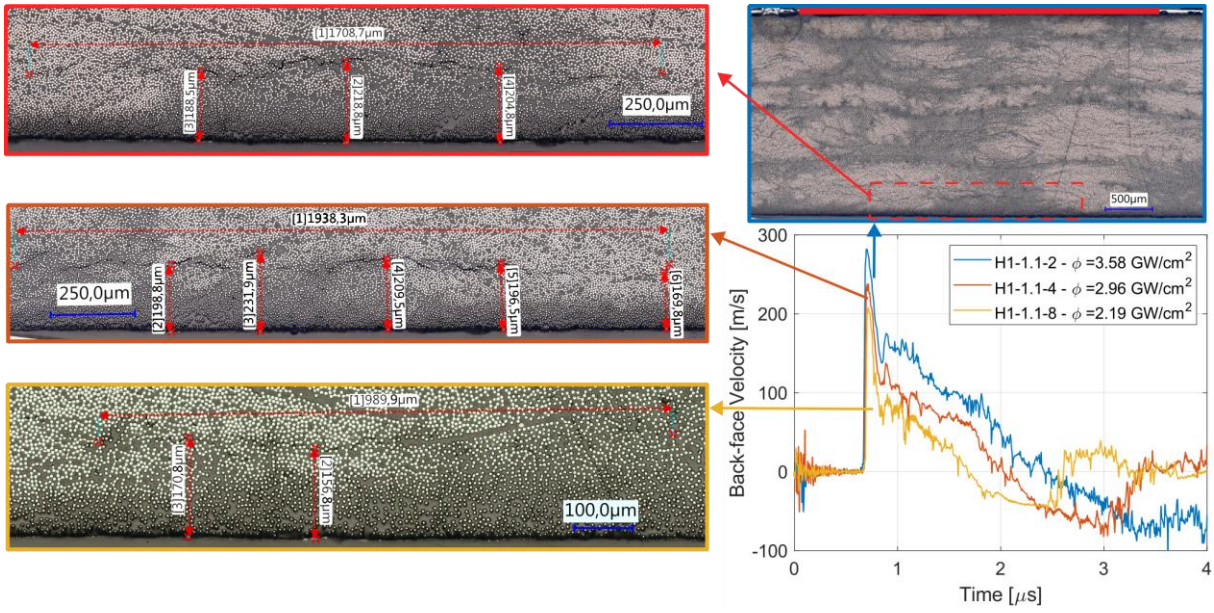

Fig. 4.59. Microscopic observations of damage induced by laser impact in H1 samples – laser impact on UTS face, cutting plane perpendicular to the fiber direction, with corresponding back-face velocity signals

However, when the H1 sample is shot on the HSC face and the last ply is a UTS ply, damage is in the form of delamination at the interface between the last UTS ply and the previous HSC ply, as can be observed in Fig. 4.60. As mentioned in section 2.3.3.3, due to inconsistent resin

removal during manufacturing, the thickness of the UTS plies in the hybrid laminates is higher than the thickness in the UTS laminates, reaching values of ~240 µm. In this case, it corresponds to previously observed positions of the damage inside the plies, thus, to the waves' intersection position.

While the interface between two adjacent UTS plies in UTS laminates is not weaker than the matrix inside the ply, it appears that the interface between UTS and HSC plies has a lower damage threshold, and the damage initiates at the interface and also propagates as delamination. Its shape is more regular, visible, and extensive, compared to the matrix crack inside the last HSC ply. Analyzing the dynamic tensile strength for these two cases, it was seen in the previous section that the dynamic tensile strength when the H1 sample is impacted on the UTS face (damage is in the last HSC ply) is higher than in the case where the H1 sample is shot on the HSC face (damage as delamination between the last two plies). This suggests that the bonding between the HSC and UTS ply is weaker than the matrix in the HSC ply.

The clear, horizontal delamination plane is reflected in the back-face velocity signal as a plateau-like spall signal. Moreover, the propagation of the shockwave within the delimited spall is more visible in the spall signal as well, compared to back-face velocity signals of other configurations.

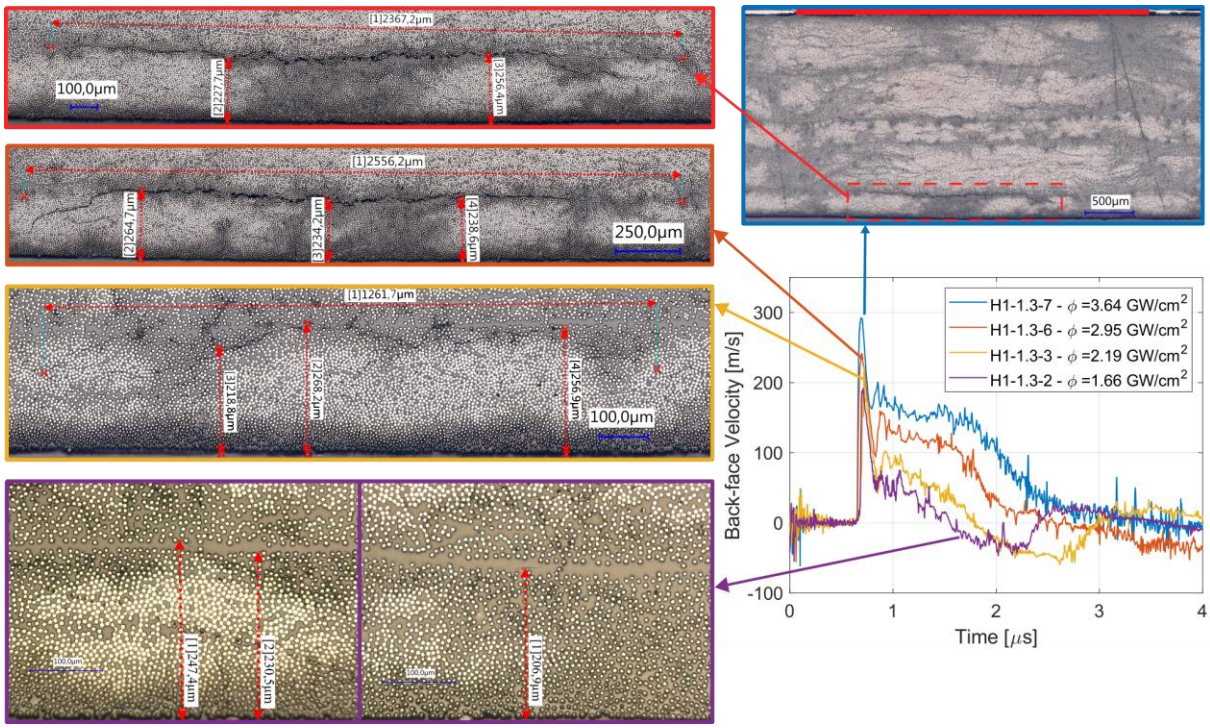

Fig. 4.60. Microscopic observations of damage induced by laser impact in H1 samples – laser impact on HSC face, cutting plane perpendicular to the fiber direction, with corresponding back-face velocity signals

Although not entirely successful, attempts were made to identify the damage position and length in cross-sections parallel to the fiber direction. Fig. 4.61 shows the microscopic observations for a laser shot at an intensity of ~3 GW/cm^2, on an H1 sample shot on the HSC face. As all the fibers are unidirectional, the plies of the composite are well bonded and there is no clear layer of resin at the interply, the damage plane is not easily identifiable in this cross-section, as it is in the form of a very thin line. A high magnification ratio had to be used in order to identify it (>1000x) using coaxial lightning.

Moreover, by analyzing the position of the damage with respect to the back-face of the sample and taking into account the stacking sequence of the sample and the average thickness of a UTS ply inside H1 laminate, the damage located at ~251 µm from the back-face represents a delamination between the last HSC and UTS plies. It is more extensive than the length observed in the cross-sections perpendicular to the fiber direction, with a measured length of

~4953 µm, compared to ~2556 µm for another sample shot at a similar intensity. It suggests that damage propagates mainly in the fiber direction, forming an oval shape, as also observed by Ecault [158].

However, to clearly observe and measure the shape of the damage plane inside the composite samples caused by laser-induced shockwaves, non-destructive testing such as micro-tomography would be required. Attempts were made with a micro-tomograph GE/Phoenix v|tome|xsv at CRT Morlaix, having a voxel resolution of 5 µm, but no clear results could be drawn. Considering that the diameter of the carbon fiber is of ~7 µm, and the matrix cracks generally appear as very thin lines between the fibers, a tomograph with a significantly higher resolution would be required for clear visualization, involving significantly higher analysis costs.

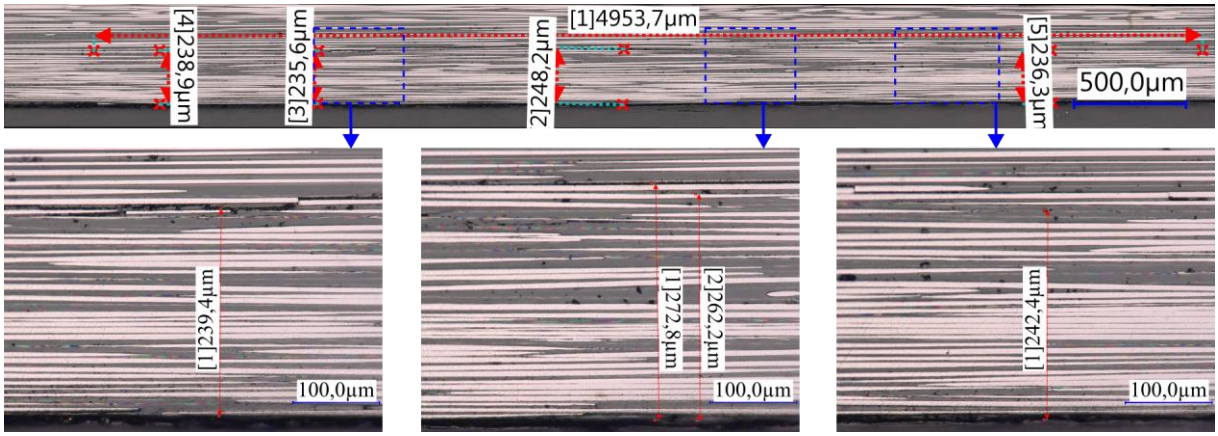

Fig. 4.61. Microscopic observations of damage induced by laser impact in H1 sample – laser impact on HSC face, cutting plane parallel to the fiber direction, φ = 3 GW/cm^2

Nevertheless, these observations show that a short duration, high energy loading is capable of inducing significant damage inside the composite sample, in the form of barely visible impact damage, that is difficult to identify with naked-eye and can also compromise the integrity of the structure.

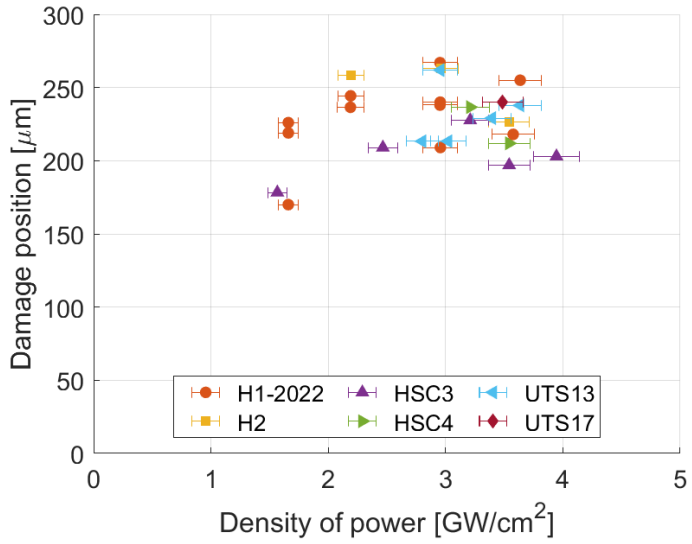

Fig. 4.62. Damage depth position with respect to the back face, for shots at different densities of power

The damage position variation with the density of power of the shot for all observed cross-sections is shown in Fig. 4.62. The damage position is taken as the distance between the back face of the sample and the position of the crack close to the center of the shot. Due to the irregular nature of the matrix cracks, errors might be induced by the manual selection of the position. The damage position mostly falls between 200 µm and 250 µm, regardless of the

tested laminate or the laser shot intensity. Again, this shows that the wave intersection position is not as affected by the thickness of the samples, and only depends on the pulse duration and propagation time [203].

Based on the presence of the spall signal on the back-face velocity response, and the confirmation of the presence of damage through microscopic observations that were performed for part of the tested samples, a damage threshold can be established for the different materials, as shown in Fig. 4.63a. The materials are organized on the Y axis in the crescent order of their thickness. Being the thinnest laminate, HSC3 has the lowest damage threshold, followed by H1 and HSC4 closely after. UTS laminates appear to have close thresholds. However, the gap in density of power between the No damage and Damage marks is quite high and further testing at intermediate densities of power would be required for a clear margin between the two. H2 follows the trend of the thick UTS17 laminate, with refinement needed for a clear threshold.

Because for H1 both opposite stacking sequences were tested and different damage behavior was observed, H1 damage threshold is further split in two cases and shown in Fig. 4.63b. When the sample is shot on the HSC face and damage is in the form of delamination between the last UTS ply and the previous HSC ply, the threshold appears to be lower than in the case of the sample impacted on the UTS face and damage in the form of matrix crack in the last HSC ply. meaning that the bonding between the HSC and UTS ply is weaker than the matrix in the HSC ply, meaning that the bonding between the HSC and UTS ply is weaker than the matrix in the HSC prepreg. For a clear conclusion and a precise threshold for the shot on the UTS face, the gap between the No damage and Damage marks should be filled by performing additional tests with designated densities of power.

Nevertheless, UTS laminates prove to have the highest damage threshold and the threshold is also influenced by sample thickness. Testing on multiple samples of the same material type, with different thicknesses would provide an evolution of the damage threshold with the thickness of the laminate, which would prove useful in composite structures design.

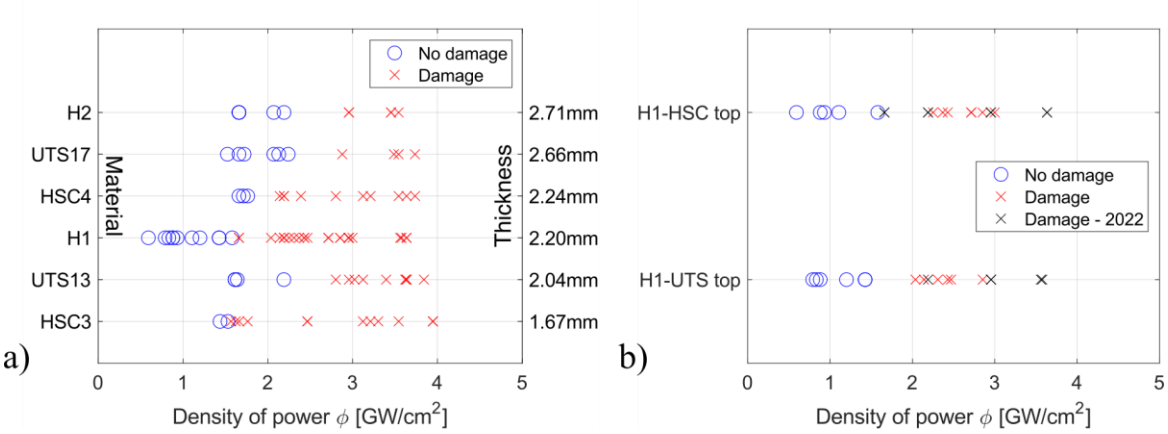

Fig. 4.63. Damage threshold in terms of density of power for laser shots in the out-of-plane directions; a) all tested material; b) threshold for H1 and opposite stacking sequences

PART 2: STEEL BALL IMPACT

High-velocity impact tests can be very expensive if they are performed at the scale of the structure. Such tests are commonly conducted on metallic structures. However, the scenario differs for composite materials, where impact behavior is influenced by factors like matrix-fiber combination, stacking sequence, and fiber orientation. As a result, initial tests often involve basic assessments on flat structures before transitioning to larger ones.

In the context of this study, impact tests are performed on flat specimens cut from laminate panels. Employing supposedly non-deformable steel ball projectiles enables the replication of impacts where the projectile's elastic deformation energy is negligible compared to the shot's energy. This approach permits the exclusive analysis of material behavior in the specimen.

This test aims to assess the ply-level hybrid composite material's capability to absorb impact energy, generating data for calibrating potential numerical simulations.

4.8 SAMPLE DESCRIPTION AND EXPERIMENTAL SETUP

To conduct the steel ball impact test, four flat panels measuring 250 × 210 mm (fiber direction on the long edge) were cut from a 500 × 500 mm composite panel. The ply-level hybrid material used for this test is H2, with a stacking sequence of HSC+UTS+2HSC+UTS+HSC [0°] (see Fig. 2.1). Rectangular aluminum end-tabs measuring 210 × 25 mm with a thickness of 1.5 mm were glued using Araldite 420 A/B Epoxy Adhesive System. The samples were securely held in place by a clamping system situated at both the top and bottom of the sample, as visually depicted in Fig. 4.64.

For this test, a single stage Taylor gun was used, with a maximum pressure of 20bar in the air tank. A stainless-steel ball (AISI 316) with a diameter of 10 mm and a mass of 4.171 g served as the projectile. This steel ball was positioned within a sabot and inserted into the gun's barrel. To gauge the speed of the sabot, two photodiodes were placed 7.3 cm apart near the barrel's end. In an effort to ascertain the ball's velocity both before and after impact, a high-speed Photron Fastcam SA-X2 camera was employed. The captured images were subsequently subjected to post-processing. The camera configuration and the assembly of the sabot with the projectile are illustrated in Fig. 4.65.

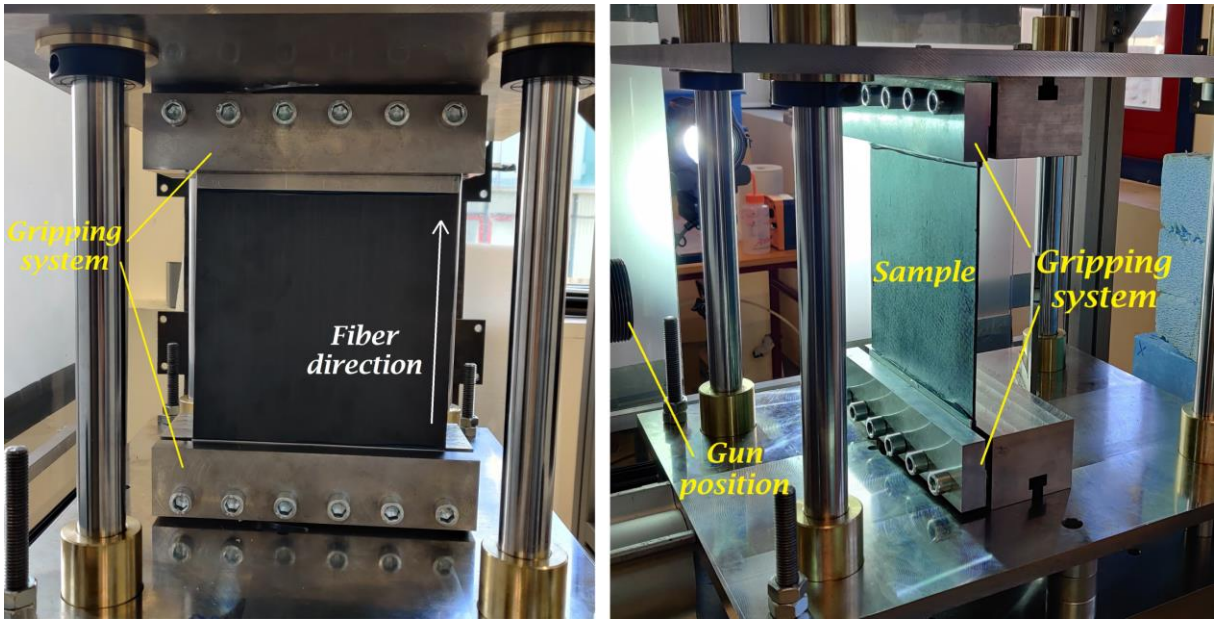

Fig. 4.64. Sample in gripping system for steel ball impact test

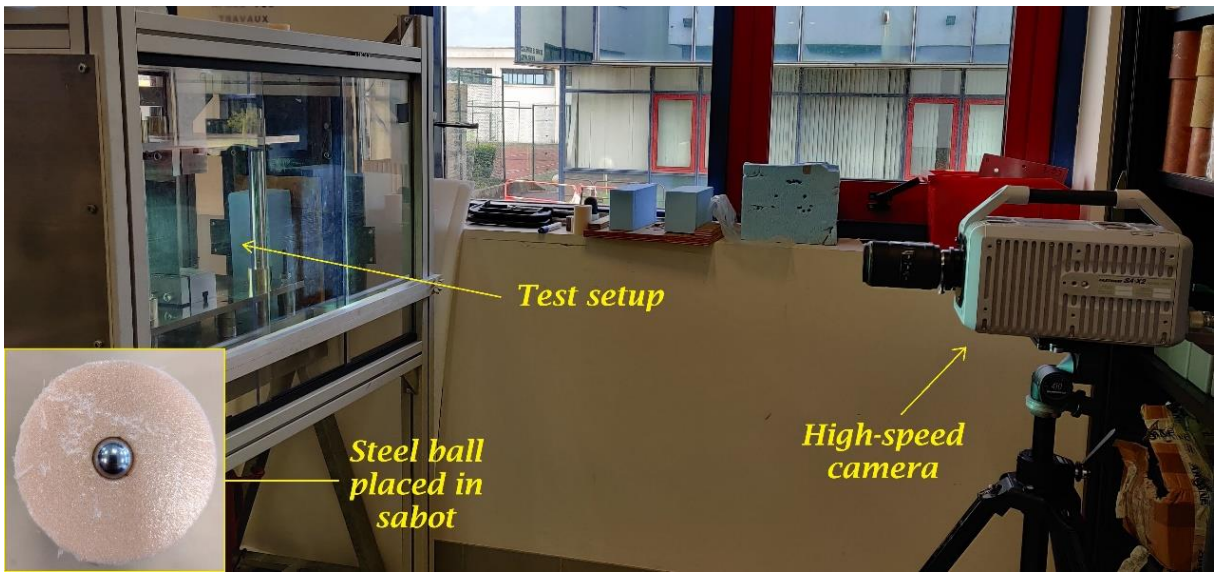

Fig. 4.65. Steel ball impact tests: high-speed camera setup and projectile placed in sabot

4.9 STEEL BALL IMPACT EXPERIMENTAL RESULTS

A series of four tests were conducted, each executed at distinct pressures within the air tank. Comprehensive information pertaining to each test, including the projectile's estimated velocity prior to and following impact, is outlined in Table 4.5. To derive these velocity estimations, an open-source video analysis tool, Tracker Video Analysis and Modeling Tool, was employed. This tool facilitates the tracking of the ball's trajectory within the video footage captured by the high-speed camera, thereby determining its velocity before and after the impact event.

The incident kinetic energy was determined using equation (1.33), the energy transferred to the composite panel, or absorbed energy E_t was calculated using equation (1.35) while the percentage change in kinetic energy was evaluated using equation (1.36).

In the first test, conducted at the air tank's maximum permissible pressure of 20 bar, the steel ball managed to penetrate through the plate. The progression of events is visually captured by the high-speed camera and depicted in Fig. 4.66. Subsequent to impact, notable damage in the composite panel extended to the end-tabs. Furthermore, deformation was evident in the portion of the aluminum tab that remained unclamped within the gripping system. This observation is illustrated in Fig. 4.67, and a more detailed view is presented in Fig. 4.68. The damage mechanism was characterized by both fiber breakage and matrix cracks. These manifested as slender strips, approximately 3 mm wide, that became detached from one another. Despite this, the strips retained their deformed state, seemingly held together by the bond with the end-tabs. In subsequent tests, lower pressures were employed to avoid damage reaching the end-tabs. The impact velocity for this particular test was determined to be 170 m/s. Following the ball's passage through the plate, its velocity decreased to 51 m/s. This resulted in an initial kinetic energy of 60.27 J and a residual energy of 5.42 J. Consequently, the composite plate absorbed 91% of the initial kinetic energy.

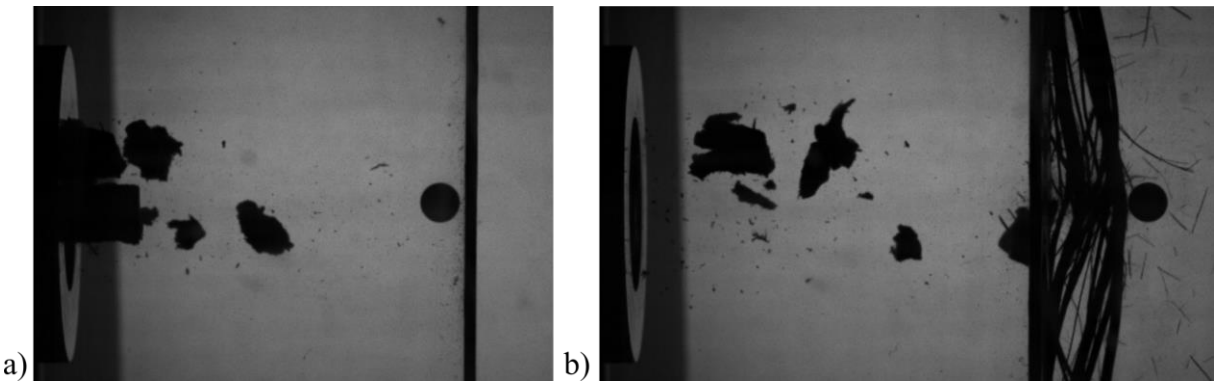

Fig. 4.66. High-speed camera capture of steel ball impact test on Sample 1, at 20 bar pressure; a) before impact, b) after impact

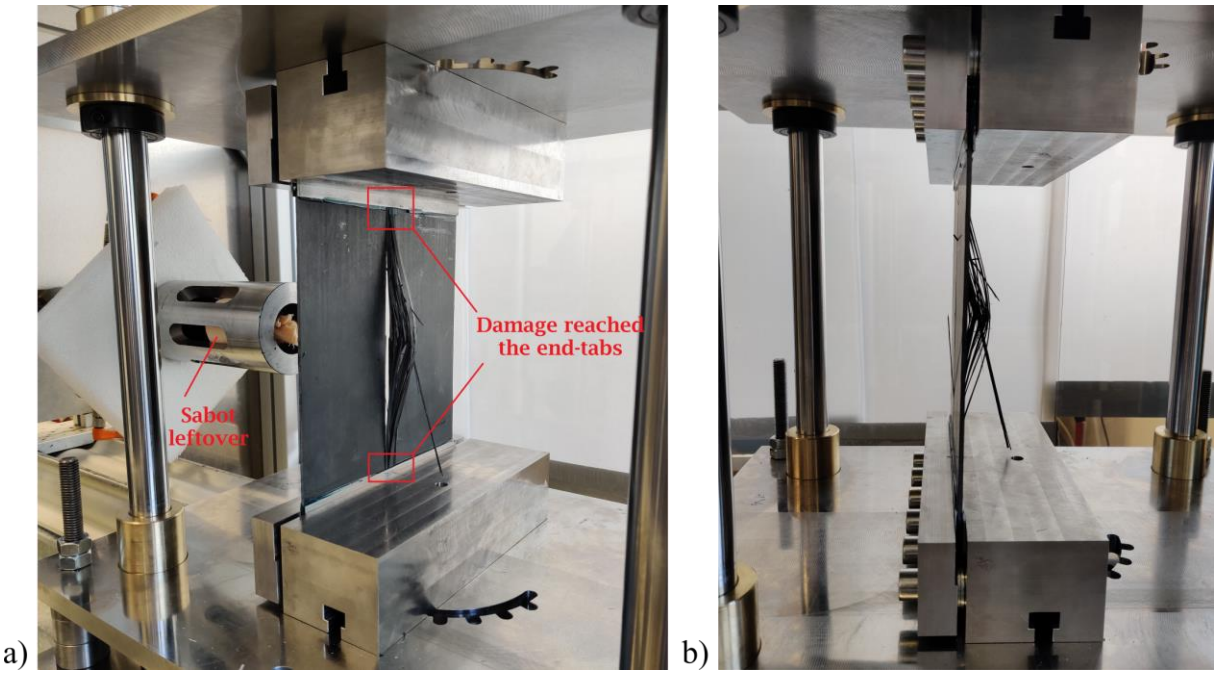

Fig. 4.67. Sample 1 after steel ball impact at 20 bar pressure in the air tank and impact velocity of 170m/s; a) back-view of the sample, b) side-view of the sample

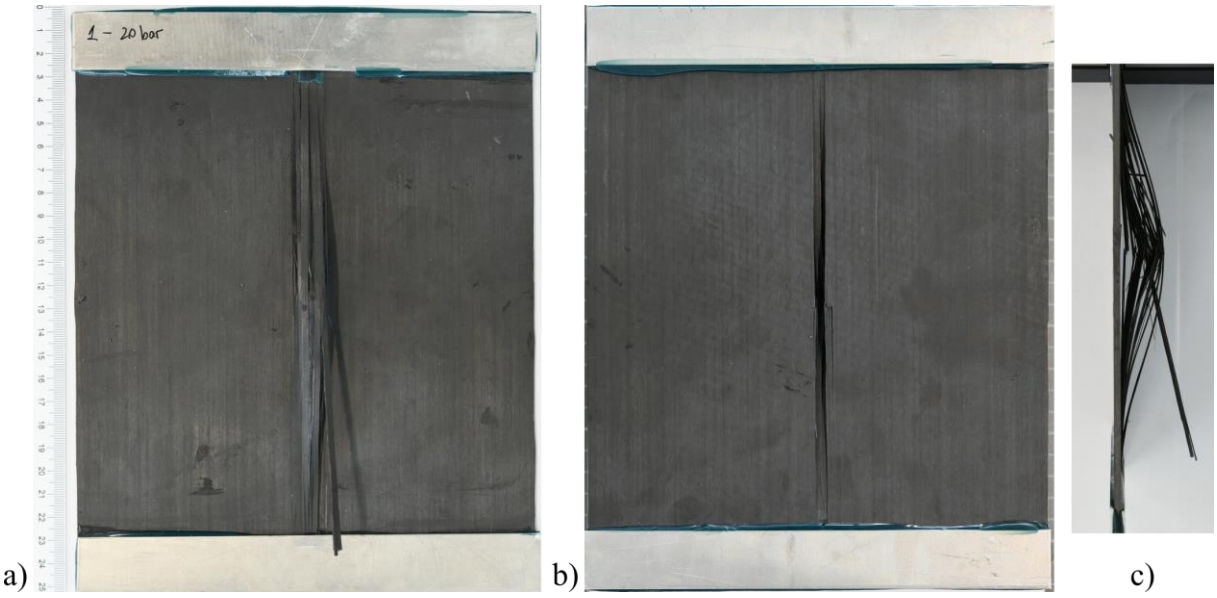

Fig. 4.68. Sample 1 after steel ball impact; a) back-view of the sample, b) front-view of the sample c) side-view of the sample

As the air tank pressure was reduced, there was a corresponding decline in impact velocity, causing the ball to rebound in each test instead of passing through the composite panel. The sequence of events for each test, encompassing the moments before impact, the maximum sample deflection, and the ball's rebound, has been documented through camera captures. These visual records are made available in Fig. 4.66, Fig. 4.69, Fig. 4.70, and Fig. 4.71.

For the 6 bar test, characterized by an impact velocity of 107 m/s and a maximum deflection of ~11.5 mm, matrix cracks oriented along the fiber direction were observed. These cracks, while not extending all the way to the end-tabs, came close, resulting in a damaged region approximately 2 cm wide. Following the ball's rebound, the resultant velocity was estimated at 35 m/s. In terms of energy, the incident kinetic energy was calculated at 23.88 J, while the ball's residual kinetic energy after rebound was 2.55 J. As a result, the composite plate demonstrated an 89% energy absorption capacity.

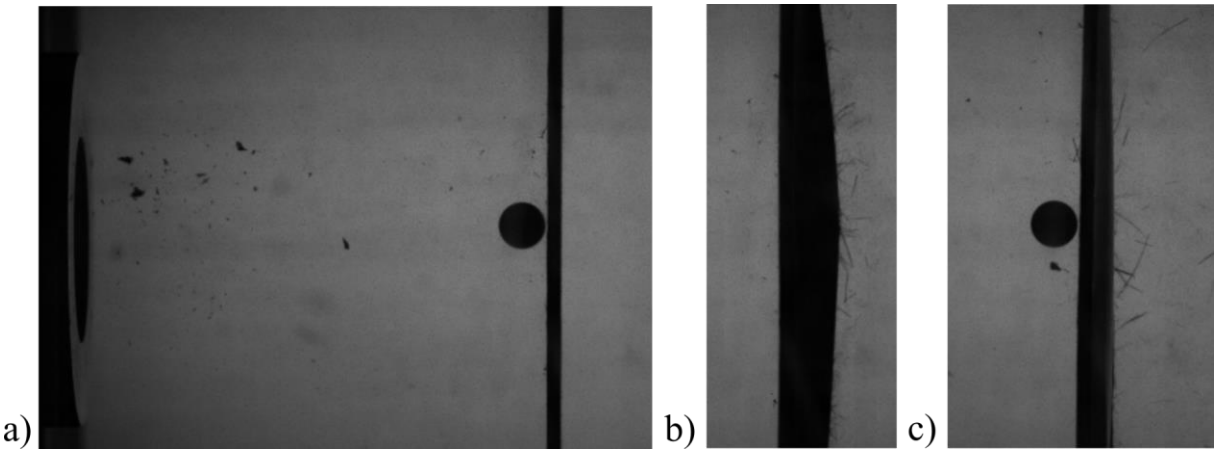

Fig. 4.69. High-speed camera capture of steel ball impact test on Sample 2, at 6 bar pressure; a) before impact, b) point of maximum deflection in the sample and turning point for the steel ball movement direction, c) after impact – the ball rebounded

In the case of tests conducted at 1.5 and 1 bar pressures, corresponding to impact velocities of 56 m/s and 39 m/s, with incident kinetic energy values of 6.54 J and 3.17 J respectively, no external damage aside from the ball's impact mark was evident. The maximum deflection is ~7.4 mm for 1.5 bar test and ~5.1 mm for the 1 bar test. After rebound, the velocities were determined to be 15 m/s and 11 m/s, yielding residual kinetic energy values of 0.47 J and 0.25 J. In both instances, the absorbed energy represented approximately 92% of the incident kinetic energy.

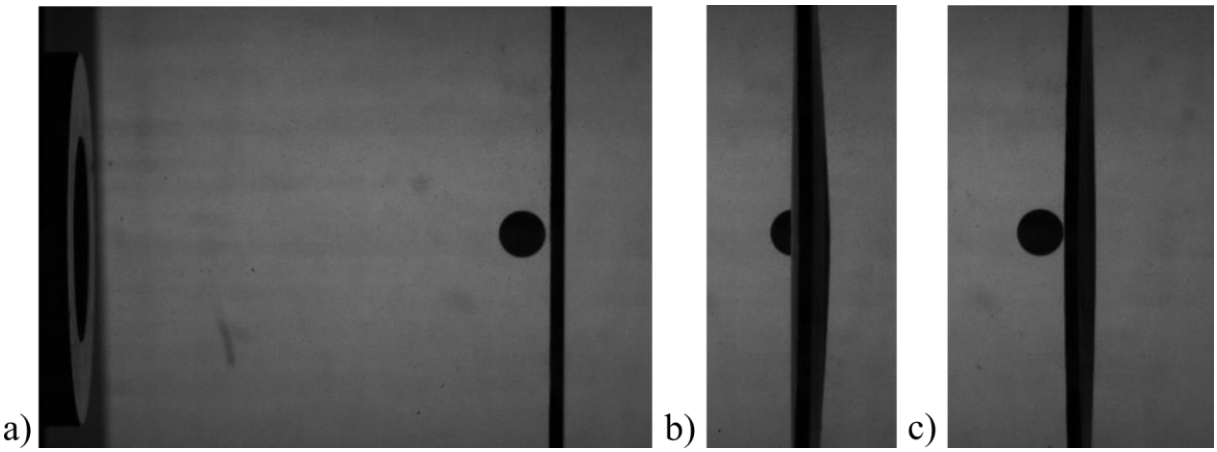

Fig. 4.70. High-speed camera capture of steel ball impact test on Sample 3, at 1.5 bar pressure; a) before impact, b) point of maximum deflection in the sample and turning point for the steel ball movement direction, c) after impact – the ball rebounded

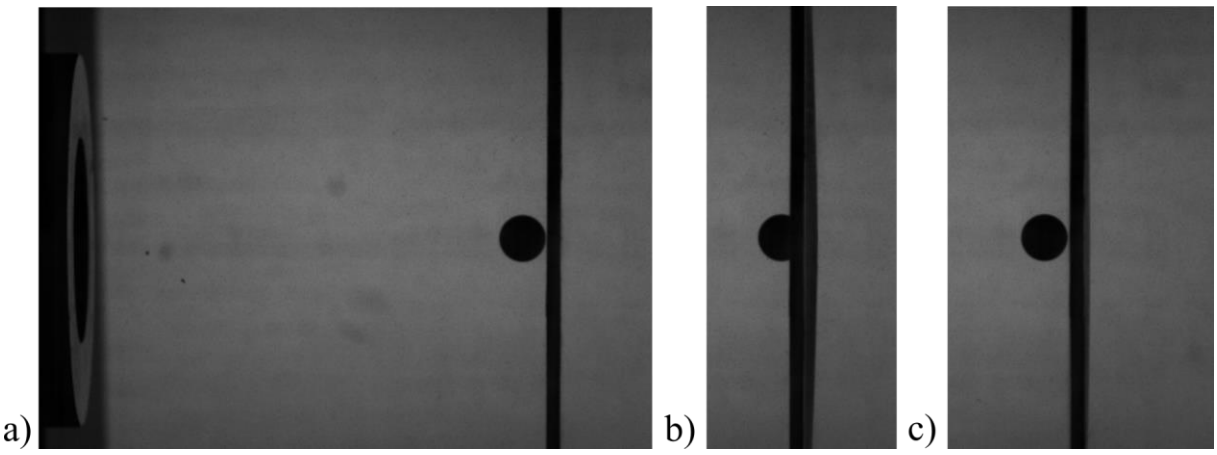

Fig. 4.71. High-speed camera capture of steel ball impact test on Sample 4, at 1 bar pressure; a) before impact, b) point of maximum deflection in the sample and turning point for the steel ball movement direction, c) after impact – the ball rebounded

Table 4.5. Steel ball high-velocity impact test details

Test nr.	Plate thickness [mm]	Pressure in air tank [bar]	V before impact [m/s]	V after impact [m/s]	Max deflection [mm]	Incident Kinetic Energy [J]	Residual Kinetic Energy [J]
1	2.72	20	170	51		60.27	5.42
2	2.7	6	107	-35	11.5	23.88	2.55
3	2.7	1.5	56	-15	7.5	6.54	0.47
4	2.71	1	39	-11	5.1	3.17	0.25

Fig. 4.72 illustrates the relationship between the percentage change in kinetic energy and the impact energy (depicted on the right y-axis). Notably, even with escalating impact energy, the absorbed energy percentage remains consistently around 90%. While this trend is apparent, it would require additional data at higher impact energies to establish with greater certainty. The figure also presents the evaluation of energy absorption per unit thickness, indicating a linear relationship that escalates as impact energy increases. A comparable linear trend was noted in Hazell's work [253], [254]. However, their study encompassed a wider range of impact velocities and energy levels than this research, and no additional comparative data was identified.

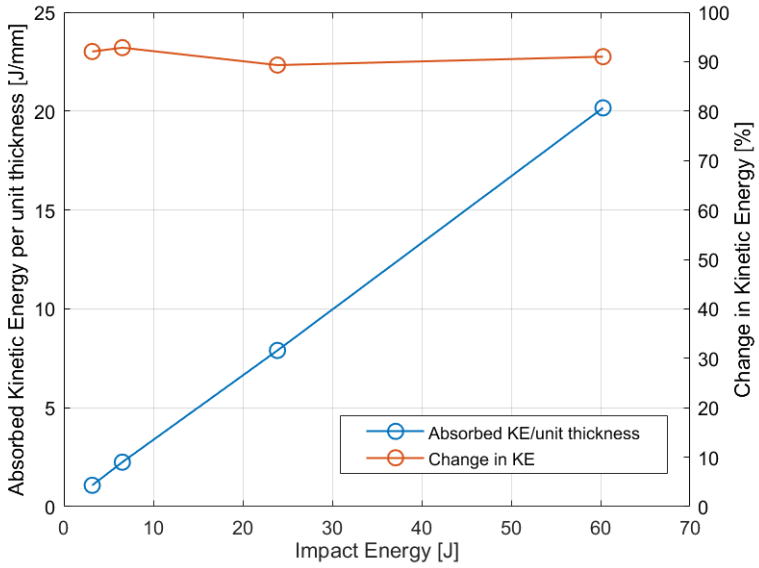

Fig. 4.72. Absorbed kinetic energy / unit thickness and percentage change in kinetic energy with respect to the impact energy

Because the results of the steel ball impact tests were not conclusive for the tested unidirectional material due to damage reaching the end-tabs at higher impact velocities, no further tests were conducted on the other materials used in this study. Nevertheless, the results should provide enough data for calibrating a potential numerical model that is falling as an obvious outlook of this thesis work.

SUMMARY

Through the analysis performed in this chapter, insight on the behavior of unidirectional carbon fiber composite materials under dynamic loading conditions, at high and very high strain rates was obtained, attaining objectives 5, 6 and 7. Laser-induced shockwaves tests in the fiber direction and in the out-of-plane direction were performed to analyze the composite behavior under very high strain rate loading as well as to evaluate damage, spallation and delamination within the composite, caused by shock propagation. Steel ball impact tests on H2 material were also performed, to address damage caused by foreign object impact at velocities below the ballistic regime (<200 m/s), as well as the absorbed energy by the composite plate.

In the fiber direction (in-plane) laser impact shots were performed on the materials at three different energy levels, and by analyzing the back-face velocity signal, recorded by laser-Doppler interferometry, a decrease in the maximum velocity of the first peak with the decrease of energy level was observed. A spall signal due to the expulsion of the gold layer deposited on the back-face for increased reflectivity was noticed for two H1 samples and it slightly influenced the extraction of the back-face velocity signal.

The propagation period was extracted through FFT analysis, and the speed of sound was evaluated between 10 km/s and 11 km/s, depending on the laminate type, with UTS laminates having the highest speed of sound in the fiber direction. By comparing the theoretical longitudinal speed of sound with experimental data, it was observed that by using the properties of the carbon fiber when estimating the longitudinal speed of sound rather than the laminate quasi-static properties, closer results are obtained.

Even though the back-face velocity signals showed only spallation of the gold particles, the samples shot at 75% and 100% of max energy showed visible signs of damage, but not in the form of a spall but as matrix cracking and fiber breakage. Besides the principal matrix crack, other thin lines of matrix crack propagation could be observed for all inspected samples shot with an energy level above 75%. As microscopic observations were performed in the rupture plane of one of the H1 samples, it was observed that part of the fibers were broken, most of them closer to the back face. Also broken fiber bundles could be identified. Although some fibers were broken, there was not a clear fracture plane for all of them, which is probably why a clear spall signal could not be obtained for the back face velocity.

By analyzing the back-face velocity signals for the out-of-plane laser impact tests (i.e., the direction of the shock propagation is normal to the ply plane), it was observed that the first peak has a lower amplitude with decreasing energy level and density of power of the laser shot. Moreover, laser shots at high energy levels exhibited a spall signal. When evaluating the sample thickness effects on the back-face velocity trace, it was observed that the increased thickness leads to a delay in the shock arrival, and a decrease in the maximum velocity of the first peak, caused by shockwave attenuation.

For H1 material, the influence of impacting the sample on one face or the other was also studied. By comparing the back-face velocity signals for shots on the UTS face with the signals for shots on HSC face of H1 material, a clear difference in values of the maximum velocity of the first peak was observed for all samples tested in 2021, with shots on UTS face having a higher maximum velocity. However, for shots performed in 2022 , no significant difference in the peak velocity was observed.

The sound speed in the out-of-plane direction was evaluated by measuring the time difference between the first and second shockwave breakout for shots that did not produce any damage in the composites, giving average values between 2.75 km/s and 2.91 km/s, with no significant differences between the reference laminates. The dynamic tensile strength was evaluated from shots that exhibited a clear spall signal according to Novikov approach [195] and was estimated between 289 MPa and 317 MPa, with average strain rates during spall fracture between 1.75e+05 s^{-1} and 1.91e+05 s^{-1}.

Through microscopic observation of cross-sections close to the centerline of the laser impact focal spot, part of the samples that presented a spall signal were further analyzed to confirm the presence of damage within the samples. Although a delamination between plies was expected in most cases, for all laminates except for H1 impacted on the HSC face, damage was in the form of intraply matrix crack, thus a spallation. UTS laminates exhibited spallation in the second to last ply, while HSC samples and hybrid laminates showed damage in the last HSC ply. Damage was mostly located at similar positions relative to the back-face, at around 250 μm. For H1 impacted on the HSC face, damage was in the form of delamination between the last HSC and UTS plies. It was more regular, visible and extended compared to the spallation observed in the case of H1 samples impacted on the UTS face.

Damage thresholds were established for each material, and UTS laminates prove to have the highest damage threshold and the threshold is also influenced by sample thickness.

Damage assessments reveal that short duration, high-energy loading can lead to substantial damage within the composite sample. This damage often manifests as barely visible impact-related issues that are challenging to detect with the naked eye. Furthermore, such damage has the potential to compromise the structural integrity of the material.

Steel ball impact tests were also performed on the hybrid material H2. Four tests were performed at various pressures in the Taylor gun. For the first shot, with a velocity before impact of 170m/s, the ball passed through the composite causing damage in the sample in form of stripes with an approximate width of 3mm that reached the end-tabs. For the second shot, a lower pressure was used to avoid damage reaching the end-tabs. The ball had an impact velocity of 107m/s and rebounded. Only matrix cracks along the fibers were observed, close to the end-tabs but without reaching them. For the next two shots, with even lower pressures and corresponding impact velocities of 56m/s and 39m/s, no apparent damage was observed, with the exception of the mark left by the ball at the impact point. The steel ball impact test was intended as a structural test for further numerical simulation validation and showed that H2 material absorbs almost 90% of the incident kinetic energy, for all impact velocities tested.

CONCLUSIONS, CONTRIBUTIONS, AND OUTLOOKS

CONCLUSIONS

The research work presented in this thesis contributes to the understanding of the mechanical behavior of unidirectional composite materials, and also introduces the concept of ply-level hybridization in both ply thickness and carbon fiber type, addressing the effects of such a hybridization as well. Referring back to the objectives of the thesis, mentioned in the Introduction section, the following aspects were addressed:

1. The experimental characterization of internal structure and physical properties of reference and ply-level hybrid unidirectional carbon composite materials
2. Evaluation of the quasi-static mechanical response of hybrid and reference laminates under on and off-axis tensile testing;
3. The cause of the nonlinear off-axis response, through off-axis cyclic load-unload tensile tests and the evaluation of residual strains and damage variables;
4. The definition of a coupled damage-plasticity model for predicting the nonlinear off-axis response of laminates
5. Evaluation of the shockwave propagation in the reference and ply-level hybrid materials, in the fiber direction and perpendicular to the fiber direction
6. Delamination and spall fracture at high-strain rates, and evaluation of dynamic tensile strength
7. Damage position and threshold evaluation for the different configurations of the studied composites

The objectives were attained, along with the primary aim of the study, and the following general conclusions can be drawn. In order to address the first objective, a comprehensive analysis of the properties of the studied materials was performed in Chapter 2, involving the measurement of density using two approaches - mass and dimensions measurements, and by Archimedes principle; measurements of fiber volume fraction by burn-off procedure; void content estimation by 2D microscopy and areal fraction measurements; internal structure analysis and identification of internal defects. Density measurements conducted through Archimedes' principle were deemed to be more reliable. This choice was driven by the understanding that slight irregularities in the flatness of the edges introduced measurement errors when using dimensional methods, impacting the accuracy of the overall density estimation. The studied composites exhibit similar densities with differences of up to 1.42%. The burn-off method for fiber volume content estimation proved to be suitable and safe for the tested carbon-fiber composites, with no resin residue visible on the fibers after a complete burn-off cycle. The fiber volume fraction was estimated between 49% and 54%, with HSC laminates having the lowest fiber content. Considering the prepregs datasheet, this outcome was expected. The microscopic observation of the laminates' cross-sections revealed that UTS composites, having thinner prepreg plies, display a more uniform distribution of the fibers, reduced ply-waviness, with a ply interface that is not rich in resin and easily identifiable. However, they exhibited a higher percentage of interply voids. The laminates with thicker HSC plies exhibited ply mixing, rich-resin regions, and ply waviness, along with intraply voids. The internal structure analysis of the hybrid laminates indicated improvements in terms of ply mixing, resin-

rich regions, and ply waviness when compared with HSC laminates. In all studied laminates, the estimated void content falls below 1%, suggesting that the mechanical properties of these composites should not be affected by the void content.

Moving forward to analyzing the mechanical response of the composites of interest, and addressing objectives 2, and 3, quasi-static tensile tests were performed in the fiber direction, perpendicular to the fiber direction, and at three off-axis angles: 15°, 30°, and 45°. For damage assessment and evaluation of parameters required for the definition of a coupled damage-plasticity model in order to predict the nonlinear behavior of unidirectional laminates loaded off-axis, quasi-static cyclic load-unload tests were performed for the same three off-axis angles. The results, presented in Chapter 3, show no significant thickness effects on the stress-strain response under both longitudinal and transverse quasi-static tensile loading. For equivalent thickness and sample geometry, hybrid composites exhibited an improved 0° failure stress compared to the estimated strength based on Kawai's scaling function.

For the transverse failure stress, high dispersion of data was obtained because most samples failed close to the grips, and the results presented high error bars. Off-axis tests exhibited nonlinear behavior with the degree of nonlinearity decreasing with increasing off-axis angles. Minor differences were found in the linear response region, but HSC laminates showed strain hardening in the nonlinear region, albeit with smaller failure strain than UTS laminates.

Hybrid laminates displayed higher failure stress and intermediate failure strains compared to simple laminates, also exhibiting a strain hardening compared to reference laminates. Laminate thickness did not significantly affect stress-strain responses in the linear region, but slight differences emerged in the nonlinear region for laminates of the same material but with different thicknesses. The experimental data aligned with predictions using theoretical equations, indicating off-axis elastic moduli and strength degradation with increasing off-axis angles.

In general, the hybridization approach demonstrated significant advantages, such as improved strain-hardening behavior and increased failure stress compared to the reference laminates. Furthermore, the behavior of hybrid laminates resembled that of a transversely isotropic system.

The cyclic load-unload tests revealed that the nonlinearity of off-axis response results from a combination of internal damage and residual strain. Damage variable evolution and accumulated residual strain were quantified by studying incremental loading/unloading stress-strain responses. Overall, UTS laminates exhibited the highest residual strains, suggesting the UTS matrix prepreg's inherent plasticity compared to HSC laminates. Hybrid laminates, on the other hand, exhibited lower residual strains across all scenarios. Three methods - Ladeveze, Fitoussi, and Regression - were used to estimate the damage variable. Regression proved unreliable due to irregular damage variable changes with increasing stress levels, yielding negative values and high error margins.

To fulfill objective 4 and define a nonlinear constitutive model for predicting off-axis behavior in unidirectional ply-level hybrid composites, parameters were derived from experimental data on residual strain and damage variables. Only damage variables obtained through Ladeveze and Fitoussi methods were considered for predicting off-axis behavior. These predictions generally matched experimental results in the linear response region and satisfactory results were obtained in the nonlinear response region. Furthermore, damage and plasticity parameters from thinner laminates of the same material prepregs were used to predict responses in thicker reference laminates, yielding improved results for UTS17 and satisfactory outcomes for HSC4. Predictions for hybrid laminates' off-axis responses, using damage parameters from hybrid laminates and plasticity parameters from HSC laminates, showed significant improvements in the nonlinear response region. This underscores the importance of plasticity parameters and suggests that matrix plasticity in HSC plies primarily governs the softening observed in the nonlinear response region of tested hybrid laminates.

Forwarding to more complex loadings, the mechanical response under very-high strain rate loading was analyzed using laser-induced shockwave tests (Chapter 4), to address objectives 5, 6, and 7. The propagation of shockwaves in the reference and hybrid laminates, in both longitudinal and transverse directions, was evaluated by employing back-face velocity analysis.

Laser impact tests were conducted in the fiber direction (in-plane) at three energy levels. Analysis of the back-face velocity signal, recorded through laser-Doppler interferometry, revealed a decrease in the maximum velocity of the first peak with decreasing energy level. Spallation of the gold layer on the back-face, used for enhanced reflectivity, was observed in two H1 samples and slightly affected the back-face velocity signal extraction.

The propagation period was determined through FFT analysis, yielding sound speeds between 10 km/s and 11 km/s, dependent on the laminate type, with UTS laminates exhibiting the highest speed of sound in the fiber direction. A comparison of the theoretical longitudinal speed of sound with experimental data indicated that using carbon fiber properties for estimating longitudinal sound speed provided more accurate results than using laminate quasi-static properties.

While the back-face velocity signals showed spallation of gold particles, samples subjected to 75% and 100% of max energy levels exhibited visible damage, including intralaminar matrix cracking and fiber breakage, rather than spallation. Microscopic examination revealed broken fibers, primarily closer to the back face, and broken fiber bundles. The lack of a clear fracture plane for all fibers likely contributed to the absence of a distinct spall signal.

For out-of-plane laser impact tests (shock propagation normal to the ply plane), two experimental campaigns were conducted, one in 2021 and the other in 2022. It was observed that the first peak in the back-face velocity signal had a lower amplitude with decreasing energy level and laser power density. High-energy laser shots produced spallation.

Sample thickness influenced the back-face velocity trace, with increased thickness causing delayed shock arrival and reduced maximum first peak velocity due to shockwave attenuation. The impact on either the UTS or HSC face of H1 material was compared. For tests performed in 2021, shots on the UTS face exhibited higher maximum first peak velocities, but this difference was not significant for tests performed in 2022.

Sound speed in the out-of-plane direction was evaluated by measuring the time difference between the first and second shockwave breakout for shots without composite damage, yielding average values between 2.75 km/s and 2.91 km/s, with no significant differences among reference laminates and hybrid ones. Dynamic tensile strength, determined using the Novikov approach from shots with clear spall signals, ranged between 289 MPa and 317 MPa, with close results between the reference and hybrid laminates.

Microscopic analysis of cross-sections near the center of the laser impact focal spot was performed on samples that exhibited spall signals. Contrary to the expected delamination between plies, all laminates except H1 impacted on the HSC face showed intraply matrix cracks, resembling spallation. UTS laminates had spallation in the second-to-last ply, while HSC samples and hybrid laminates had damage in the last HSC ply, typically around 250 μm from the back face. In the case of H1 impacted on the HSC face, delamination occurred between the last HSC and UTS plies, appearing more regular, visible, and extensive compared to spallation observed when impacted on the UTS face. Damage thresholds were determined for each material, with UTS laminates having the highest damage threshold, which was also influenced by sample thickness.

The assessments revealed that short-duration, high-energy loading could result in significant damage within the composite sample. This damage often presents as nearly imperceptible impact-related issues that are challenging to discern with the naked eye. Furthermore, such damage has the potential to compromise the structural integrity of the material, revealing the necessity for a better understanding of the phenomenon.

Additionally, steel ball impact tests were performed on H2 samples, to evaluate the energy absorption capacity of the unidirectional composite laminate and damage mechanism during

high-velocity impact loading with a foreign object. Four tests at different pressures in the Taylor gun were performed. In the first test, at maximum pressure, the steel ball penetrated the laminate plate. However, the induced damage in the laminate was constrained by the end-tabs, deeming the test unreliable for damage assessments. For subsequent tests, lower pressures were used to prevent damage from reaching the end-tabs. In these cases, the steel ball rebounded. No additional testing was performed for the other laminate configurations in this thesis, as the unidirectional laminate proved to be unsuitable for this type of test, requiring larger sample dimensions to avoid end-tab effects. However, these first results remain a set of experimental results to be matched with numerical modelling.

CONTRIBUTIONS

Considering the aim and objectives of this thesis, the following original contributions are highlighted:

1. Introduction of a novel approach to ply-level hybridization, by considering carbon fibers with different quality besides the different ply thickness, for cost reduction purposes;
2. Implementing a successive linear regression procedure, to determine the linear response region of nonlinear off-axis response, to determine the apparent Young modulus and Poisson ratio;
3. Use and comparison of three distinctive methods of evaluating the damage variable from cyclic load-unload tensile testing, and their effects on prediction models;
4. Use of damage and plasticity parameters from thinner laminates to predict the nonlinear behavior of thicker laminates of the same prepreg type;
5. Experimental testing using laser-induced shockwaves in the fiber direction, considering a new method of obtaining a viable testing sample from thin unidirectional laminates;
6. Analysis of laser impact on opposite faces of laminates with asymmetric stacking sequence;
7. Synthesis of the experimental campaigns and analysis of the all-carbon ply-level hybridization effects on the mechanical response of carbon fiber composites under quasi-static and high-strain rate dynamic loading.

OUTLOOKS

The work in this thesis leads to interesting perspectives. First, considering the improved response under quasi-static on and off-axis response of the hybrid laminates, prepregs with carbon fibers having detrimental differences in the mechanical properties could be combined, to assess the effects of the inherent properties of the fibers on the overall mechanical response.

As the coupled damage-plasticity model employed in Chapter 3 proved to be able to predict the nonlinear off-axis behavior of the composites with satisfactory error margins, another point would be to extend the analytical damage-plasticity model and include it in a numerical model, for more accurate predictions and structure optimization. By calibrating the numerical model using the experimental data from this work, additional laminate configurations can be explored, to optimize and tailor the hybrid composite response to specific applications,

From the laser-induced shockwave testing and results, some perspectives can also be discussed. Considering the fact that the back-face velocity measurement in this work is limited to one central point, it would be interesting to simultaneously measure the back-face velocity in several points along the diameter of the focal spot, to quantify the effects of the laser-energy distribution during impact.

The novel back-face velocity traces in the fiber direction from this thesis lack a spall trace even at the highest energy levels available in the testing facility. However, in one sample microscopic observations could be performed and broken fibers were observed. It would be of interest to manufacture thick unidirectional samples and test them at even higher energy values and densities of power, to assess if spallation can be obtained in purely unidirectional composites.

Moreover, the issue of damage detection is a critical aspect. This study demonstrates that measuring the back-face velocity provides significant insight. It facilitates an accurate description of phenomena and effectively distinguishes between damage and non-damage events. Moreover, for the first time, it was observed that laser-induced shockwaves can produce spallation inside the composite ply, and not only delamination at the ply interface. However, in terms of quantifying internal damage, the destructive microscopic cross-section analysis is section-biased, limited to one direction, and also prone to off-center positioning due to sensitive sample preparation. Although not available in this study, micro-tomography observation using a sufficiently high resolution could be a valuable addition to understanding spallation propagation in unidirectional composites.

Considering that damage caused by laser-induced shockwaves is internal and in the form of barely visible impact damage which is difficult to observe, for structural applications, it would be of interest to assess the mechanical properties of the laminate after such an impact, for example, the compression after impact strength.

Although not addressed in this work, numerical modeling of the laser impact, both in the fiber and in the out-of-plane direction, calibrated using the experimental data in this work, would provide valuable information and additional insight on shockwave propagation inside the laminates, the effects of fiber orientation, and additional hybridization effects on the propagation of the shockwaves. When testing the H1 samples on opposite stacking sequences, different back-face velocity amplitudes were observed between the configurations in one experimental campaign. However, in the second experimental campaign, the differences were not present. For now, this phenomenon is yet to be explained, and numerical simulations could provide valuable in understanding the underlying causes for the observed phenomenon.

PUBLICATIONS

Part of this thesis work was published in scientific journals and presented at scientific conferences. The author led the following publications:

Journal publications:

- **M. Casapu**, I. Fuiorea, and M. Arrigoni, *Experimental Characterization of Internal Structure and Physical Properties of Unidirectional Ply-Level Hybrid Carbon Composite Material*, Advanced Engineering Materials, 2023, DOI: 10.1002/ADEM.202201447.
- **M. Casapu**, M. Arrigoni, and I. Fuiorea, *Off-axis response and shear characterization of unidirectional ply-level hybrid carbon-fiber-reinforced polymer materials*, INCAS BULLETIN, vol. 15, no. 3, pp. 31–46, 2023, DOI: 10.13111/2066-8201.2023.15.3.3.
- **M. Casapu**, I. Fuiorea, and M. Arrigoni, *Damage assessment through cyclic load-unload tensile tests for ply-level hybrid carbon fiber composites*, Express Polymer Letters, vol. 18, no. 1, pp. 41-60, 2024, DOI: 10.3144/expresspolymlett.2024.4.
- **M. Casapu**, A. C. Casapu, M. Arrigoni, and I. Fuiorea, *Laser-induced Shockwaves for Damage Assessment and Characterization at High Strain Rates in the Fiber Direction of Unidirectional Composites*, Materials Letters - (Revision pending).

Conference presentations:

- **M. Casapu**, I. Fuiorea, and M. Arrigoni, *Experimental Characterization of Internal Structure and Physical Properties of Unidirectional Ply-Level Hybrid Carbon Composite Material*, 15th International Conference on Advanced Computational Engineering and Experimenting – ACEX2022, Florence, Italy, 2022.

— **M. Casapu**, A. C. Casapu, M. Arrigoni, and I. Fuiorea, *Laser-induced Shockwaves for Damage Assessment and Characterization at High Strain Rates in the Fiber Direction of Unidirectional Composites*, 27th DYMAT Technical Meeting, Colmar, France, 2023.

APPENDIX A

POLISHING METHOD FOR CARBON/EPOXY SAMPLES

The polishing machine used was Struers Labo-Pol-30 with a LaboForce-100 specimen mover. The polishing method applied is detailed in Table A. 1. Steps 1-4 represent the pre-polishing and 5-6 are the polishing steps. Except for step 6, where the tray and specimen mover had rotations in opposite directions, for all the other steps the tray and the specimen mover rotated in the same direction.

Table A. 1. Polishing method

Step number	Surface type	Tray rotational speed [rpm]	Samples support rotational speed [rpm]	Suspension	Suspension dosage	Lubrifiant	Time [min]	Applied force per sample [N]
1	SiC Foil #220	150`	150	-	-	Water	2	40
2	Sic Foil #500	150	150	-	-	Water	2	40
3	SiC Foil #1200	150	150	-	-	Water	2	40
4	MD-Largo	150	150	DiaPro Allegro/ Largo 9µm	3/8	-	6	30
5	MD-Mol	150	150	DiaPro MOL B 3µm	1/10	-	6	35
6	MD-Chem	150	150	OP-S NonDry	Manual distribution	Water at the end	1+1	30

APPENDIX B

SAMPLE DIMENSIONS FOR ALL TENSILE TEST CONFIGURATIONS

Table B. 1. Tensile tests - samples' dimension details

Laminate	Tensile test type	Number of samples	Nominal length [mm]	Nominal width w [mm]	Nominal thickness t [mm]	Aluminum tabs thickness t_{AL} [mm]
HSC3	0°	4	250	15	1.69	1.5
	15°	3	250	25	1.69	1.5
	30°	3	250	25	1.69	1.5
	45°	3	250	25	1.69	1.5
	90°	7	250	25	1.69	1.5
	15°-LU	3	250	25	1.69	1.5
	30°-LU	3	250	25	1.69	1.5
	45°-LU	3	250	25	1.69	1.5
HSC4	0°	8	250	15	2.24	1.5
	15°	3*	250	25	2.24	1.5
	30°	3	250	25	2.24	1.5
	45°	3	250	25	2.24	1.5
	90°	7	250	25	2.24	1.5
	15°-LU	3	250	25	2.24	1.5
	30°-LU	3	250	25	2.24	1.5
	45°-LU	3	250	25	2.24	1.5
UTS13	0°	4	250	15	2.1	1.5
	15°	3	250	25	2.1	1.5
	30°	3	250	25	2.1	1.5
	45°	3	250	25	2.1	1.5
	90°	7	250	25	2.1	1.5
	15°-LU	3	250	25	2.1	1.5
	30°-LU	3	250	25	2.1	1.5
	45°-LU	3	250	25	2.1	1.5
UTS17	0°	4	250	15	2.7	1.5
	15°	3	250	25	2.7	1.5
	30°	3	250	25	2.7	1.5
	45°	3	250	25	2.7	1.5
	90°	7	250	25	2.7	1.5
	15°-LU	3	250	25	2.7	1.5
	30°-LU	3	250	25	2.7	1.5
	45°-LU	3	250	25	2.7	1.5
H1	0°	10	250	11	2.19	2
	15°	6	250	25	2.19	2
	30°	6	250	25	2.19	2
	45°	6	250	25	2.19	2
	90°	10	250	25	2.19	2
	15°-LU	4	250	25	2.19	2
	30°-LU	4	250	25	2.19	2
	45°-LU	4	250	25	2.19	2
H2	0°	2	250	15	2.7	1.5

15°	3	250	25	2.7	1.5
30°	3	250	25	2.7	1.5
45°	3	250	25	2.7	1.5
90°	1	250	25	2.7	1.5
15°-LU	1	250	25	2.7	1.5
30°-LU	2	250	25	2.7	1.5
45°-LU	1	250	25	2.7	1.5

(*) the data file for two tests was corrupted and the strain values could not be retrieved

APPENDIX C

SEQUENTIAL STAGES FOR SUCCESIVE LINEAR REGRESSION PROCEDURE

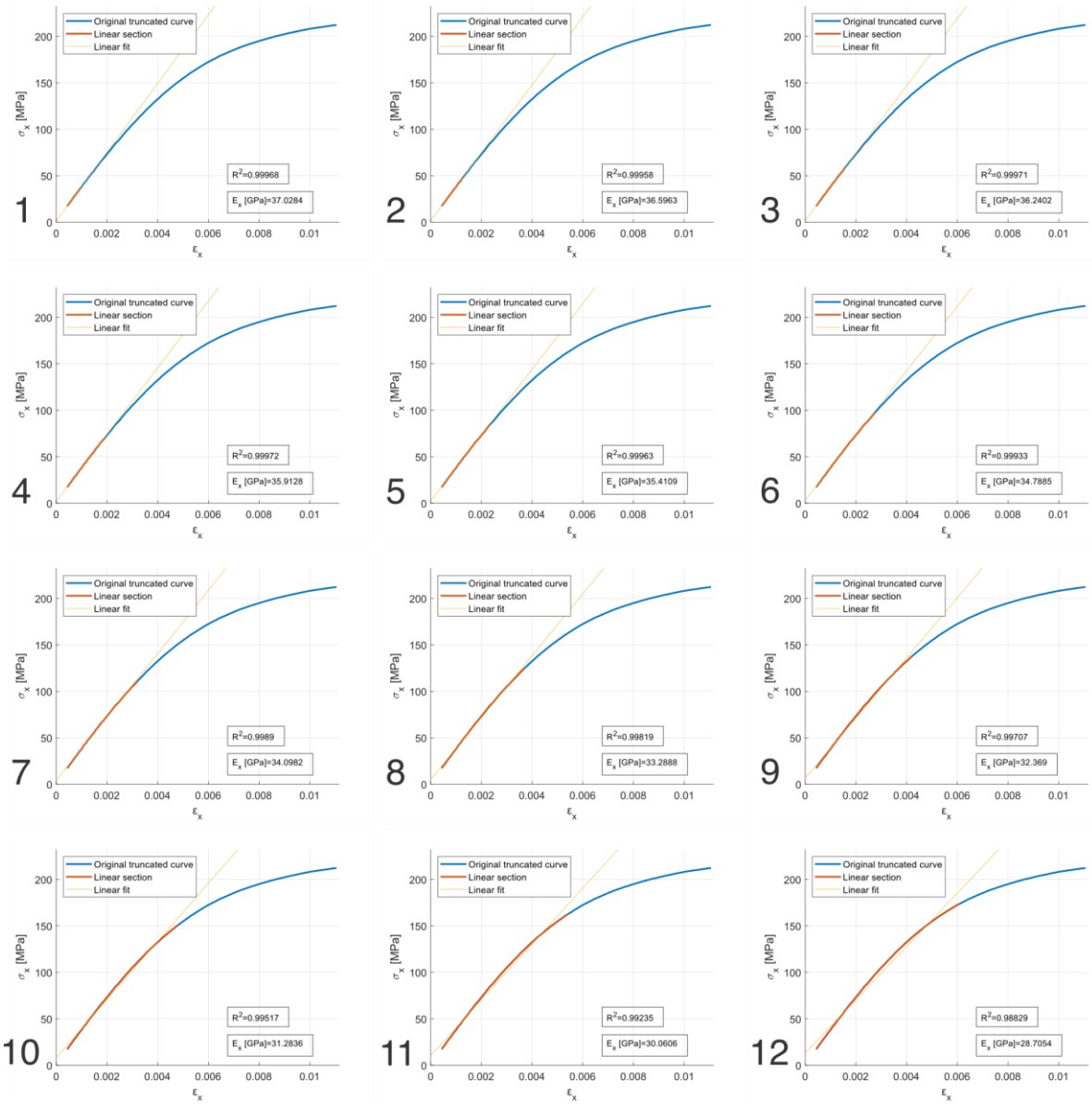

Fig. C. 1. Example of application of the successive linear regression procedure on the stress-strain response of a 15° off-axis tensile test, 1-12 – successive steps

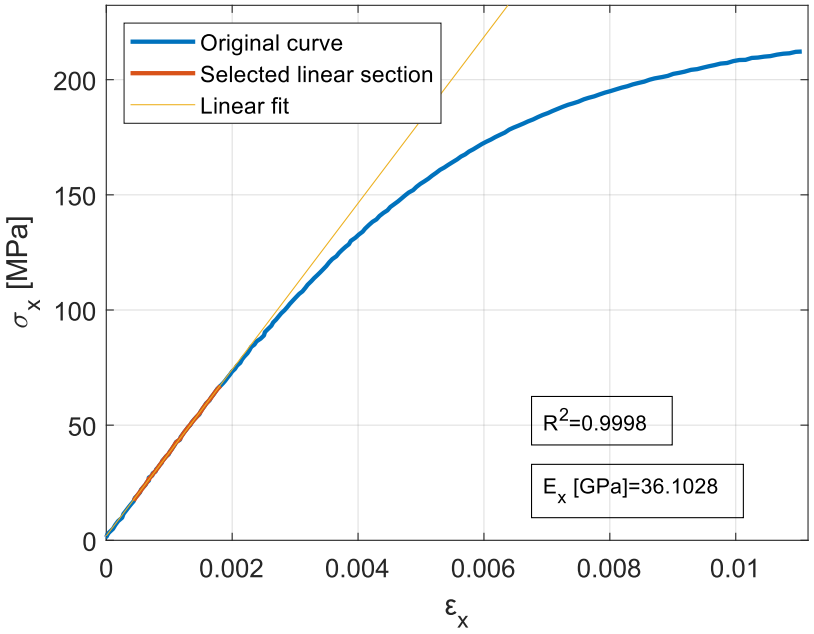

Fig. C. 2. Final selection of stress-strain data for elastic modulus extraction, based on max(R^2) criteria

APPENDIX D

AXIAL STRESS-STRAIN RESPONSE FOR ALL TESTED SAMPLES – MONOTONIC TENSILE TESTING

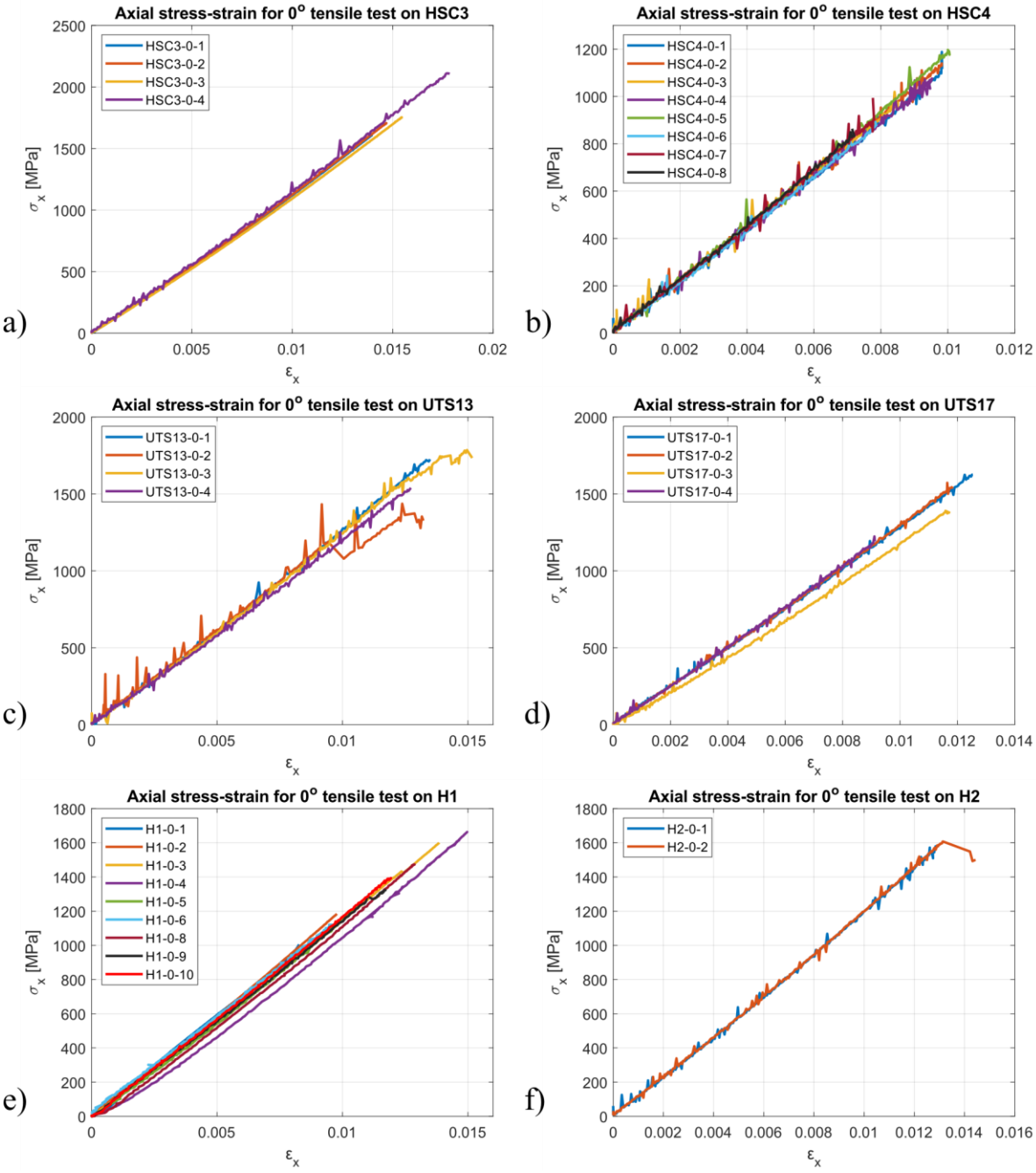

Fig. D. 1. Axial Stress-Strain response for all tested samples under tensile loading in the fiber direction; a) HSC3; b) HSC4; c) UTS13; d) UTS17; e) H1; f) H2

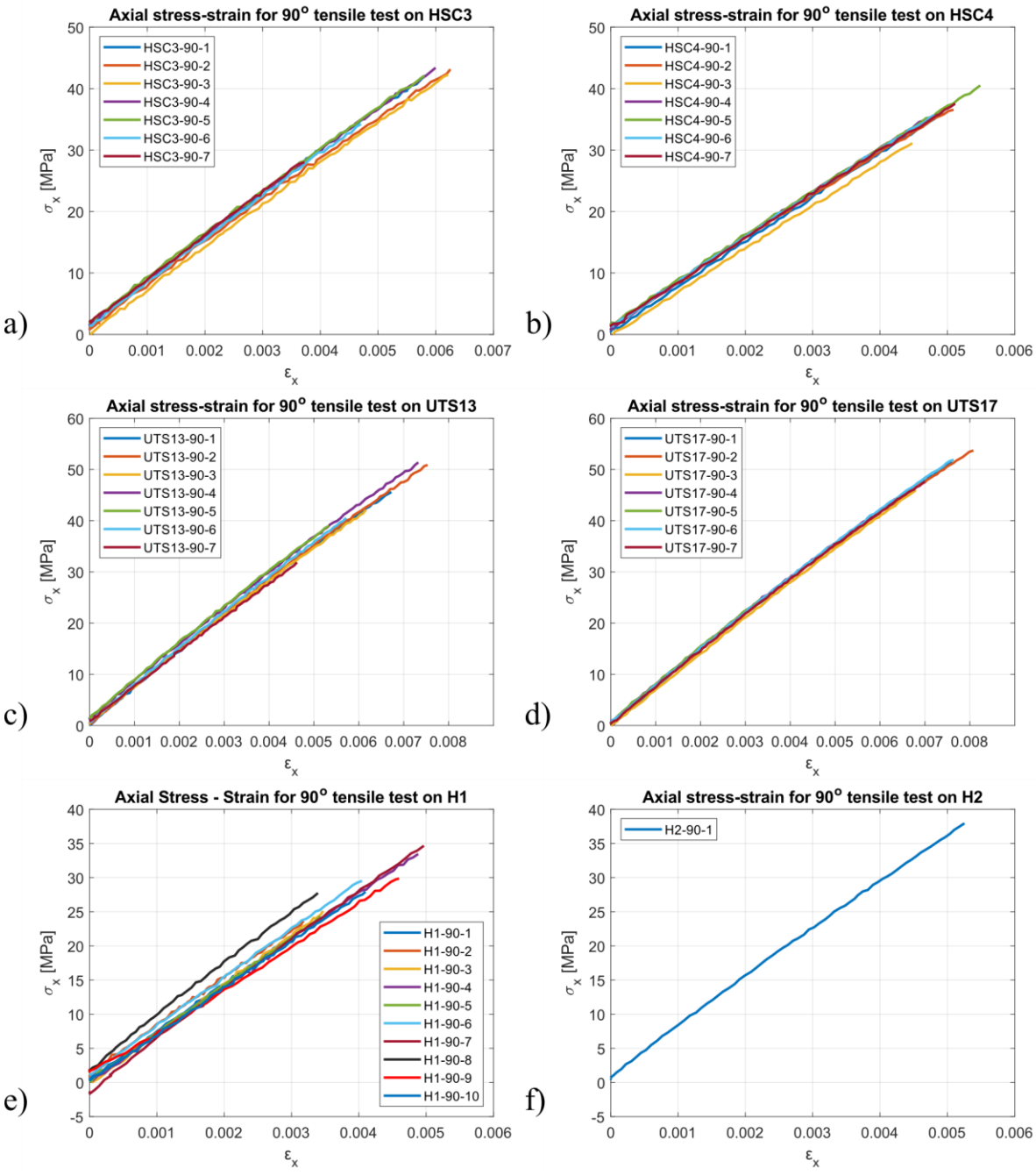

Fig. D. 2. Axial Stress-Strain response for all tested samples under tensile loading perpendicular to the fiber direction; a) HSC3; b) HSC4; c) UTS13; d) UTS17; e) H1; f) H2

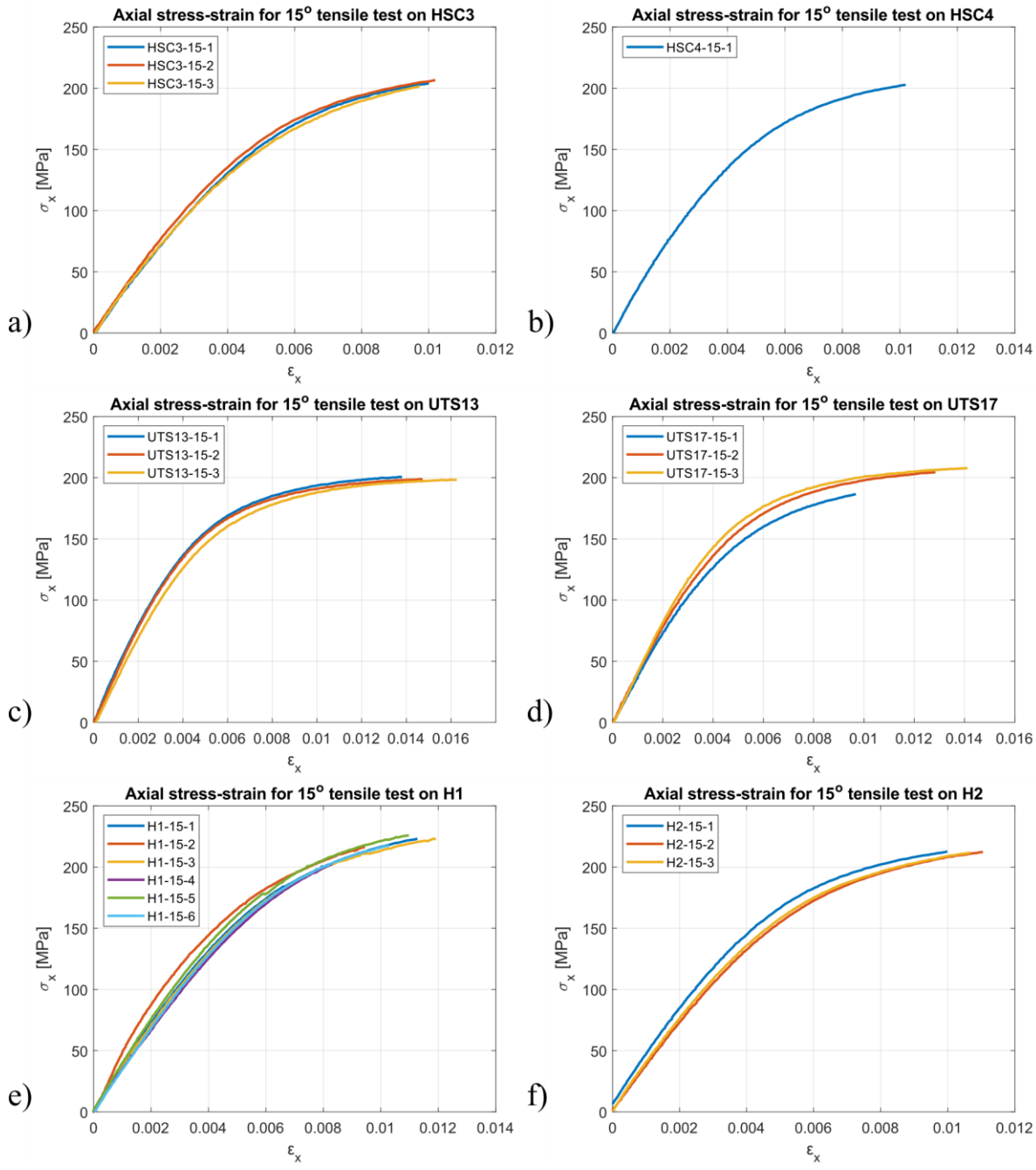

Fig. D. 3. Axial Stress-Strain response for all tested samples under off-axis tensile loading, θ=15°; a) HSC3; b) HSC4; c) UTS13; d) UTS17; e) H1; f) H2

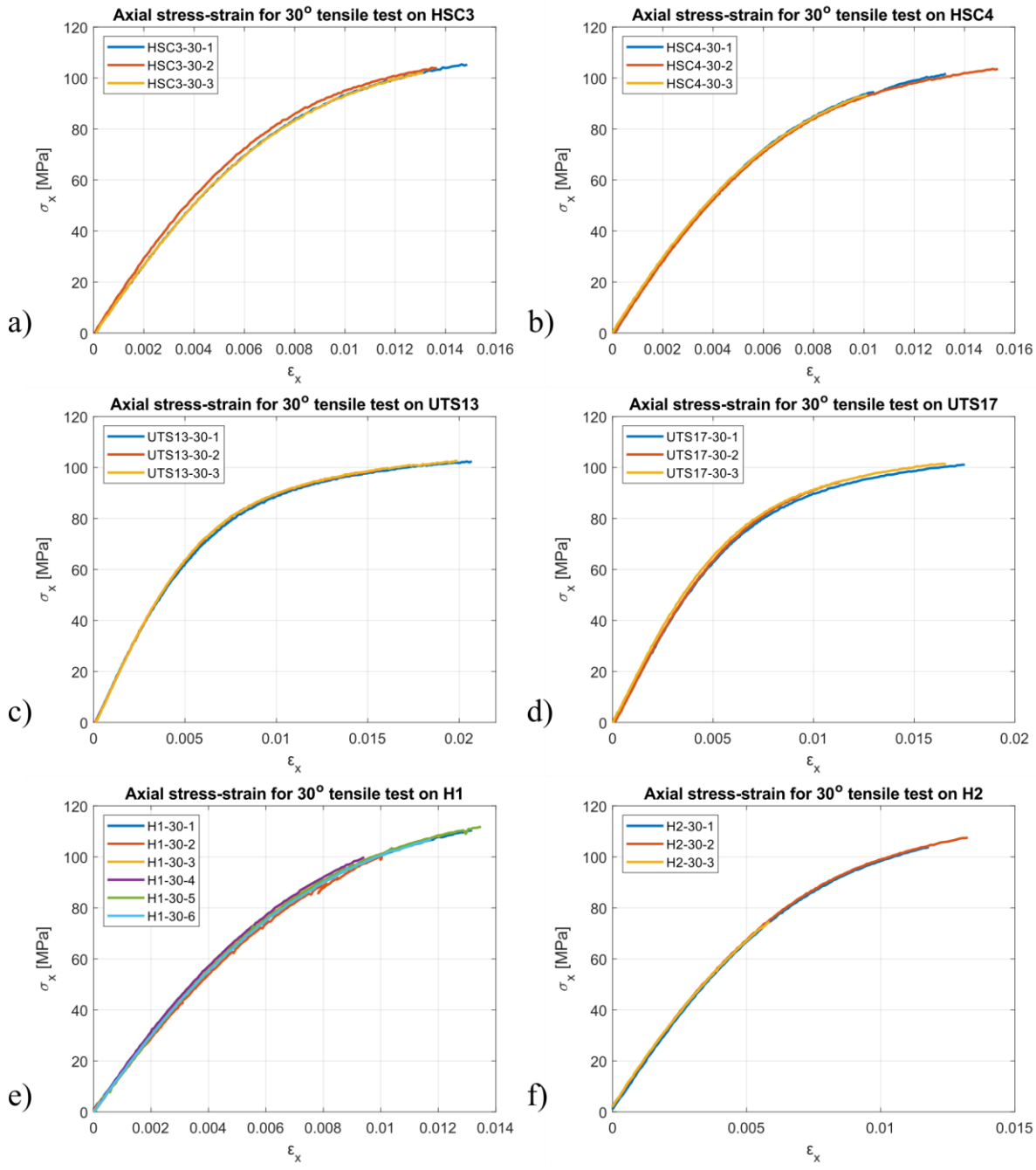

Fig. D. 4. Axial Stress-Strain response for all tested samples under off-axis tensile loading, θ=30°; a) HSC3; b) HSC4; c) UTS13; d) UTS17; e) H1; f) H2

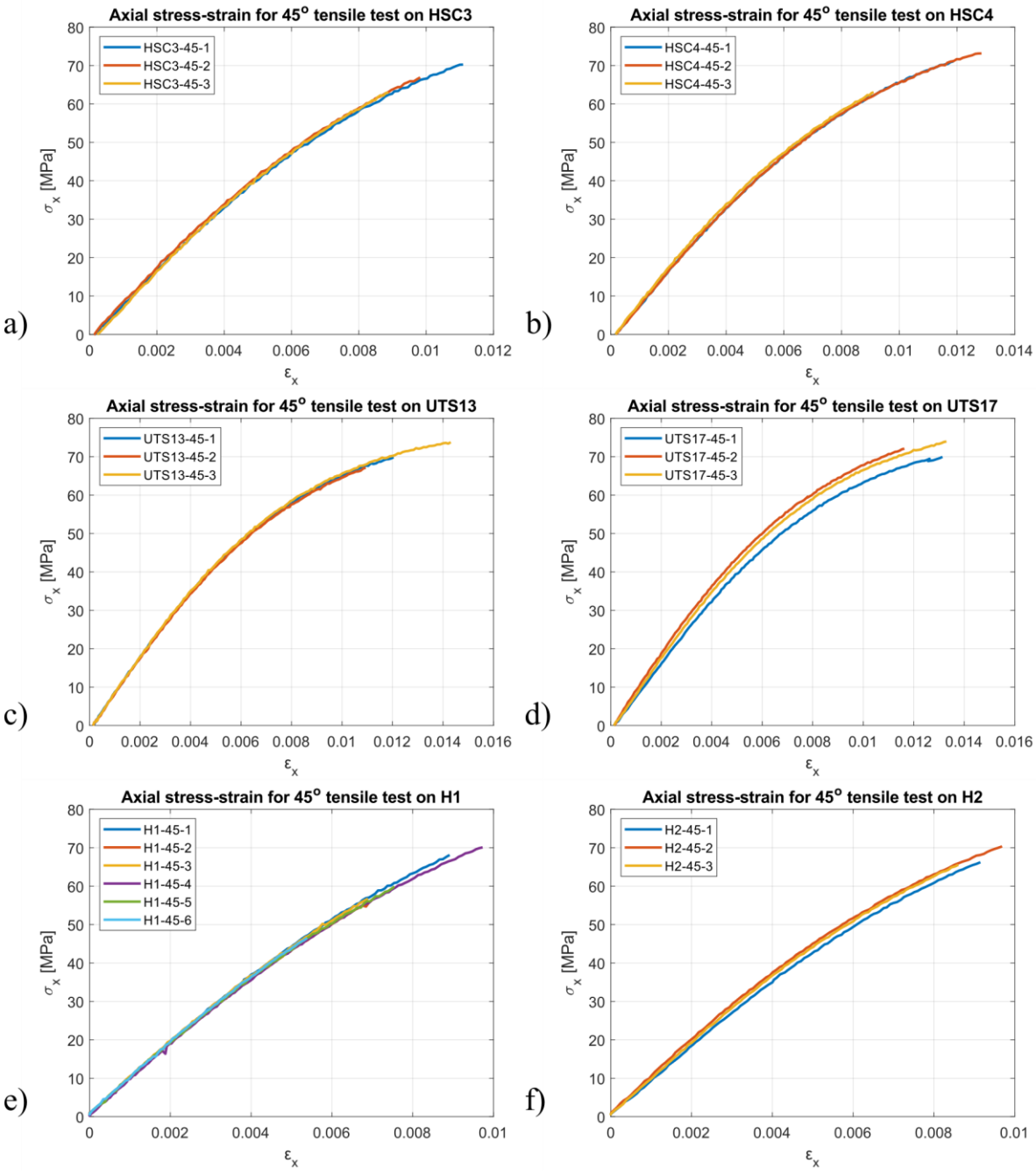

Fig. D. 5. Axial Stress-Strain response for all tested samples under off-axis tensile loading, θ=45°; a) HSC3; b) HSC4; c) UTS13; d) UTS17; e) H1; f) H2

APPENDIX E

FRACTURE POSITION FOR MONOTONIC TENSILE TEST SAMPLES

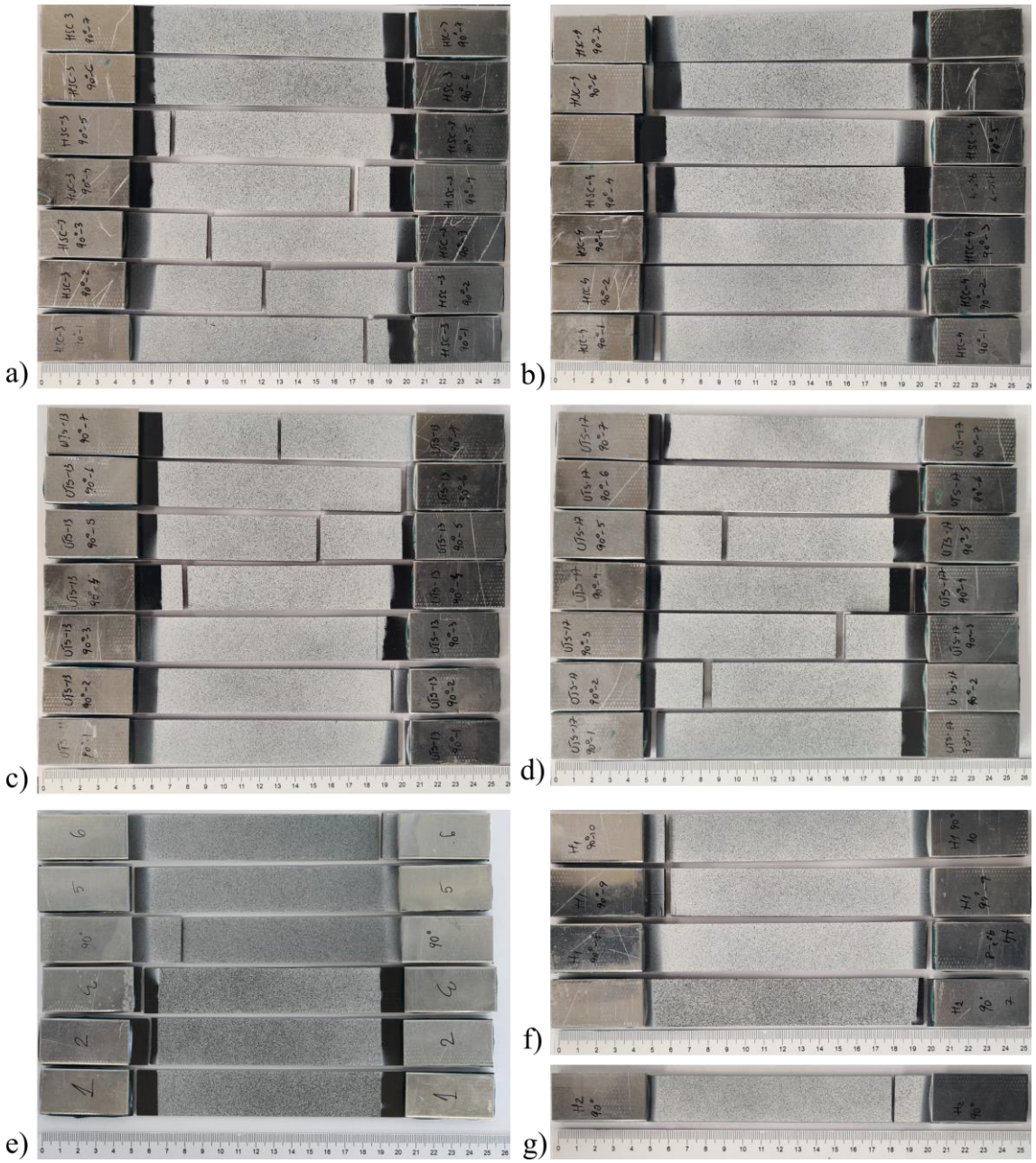

Fig. E. 1. Fracture position for 90° samples, with sample 1 starting from the ruler; a) HSC3; b) HSC4; c) UTS13; d) UTS17; e) H1 (Samples 1-6); f) H1 (Samples 7-10); g) H2

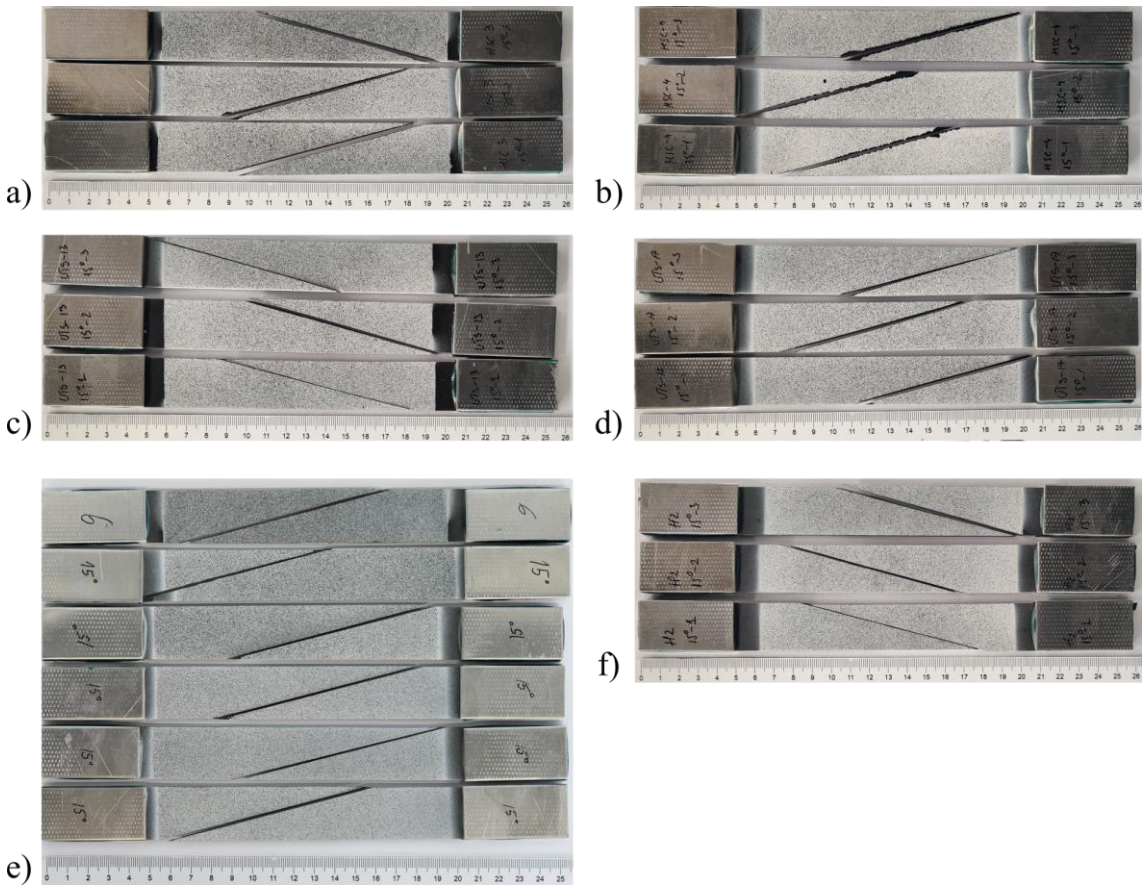

Fig. E. 2. Fracture position for 15° samples, with sample 1 starting from the ruler; a) HSC3; b) HSC4; c) UTS13; d) UTS17; e) H1; f) H2

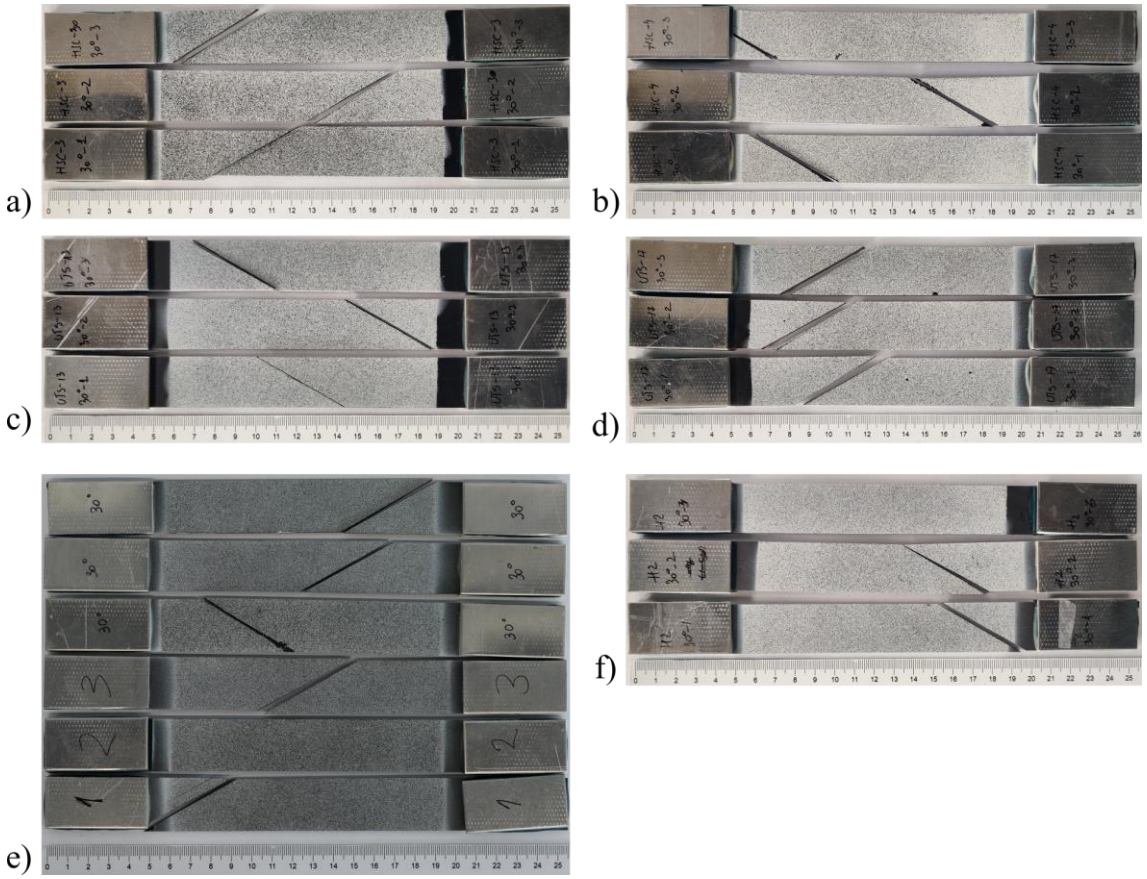

Fig. E. 3. Fracture position for 30° samples, with sample 1 starting from the ruler; a) HSC3; b) HSC4; c) UTS13; d) UTS17; e) H1; f) H2

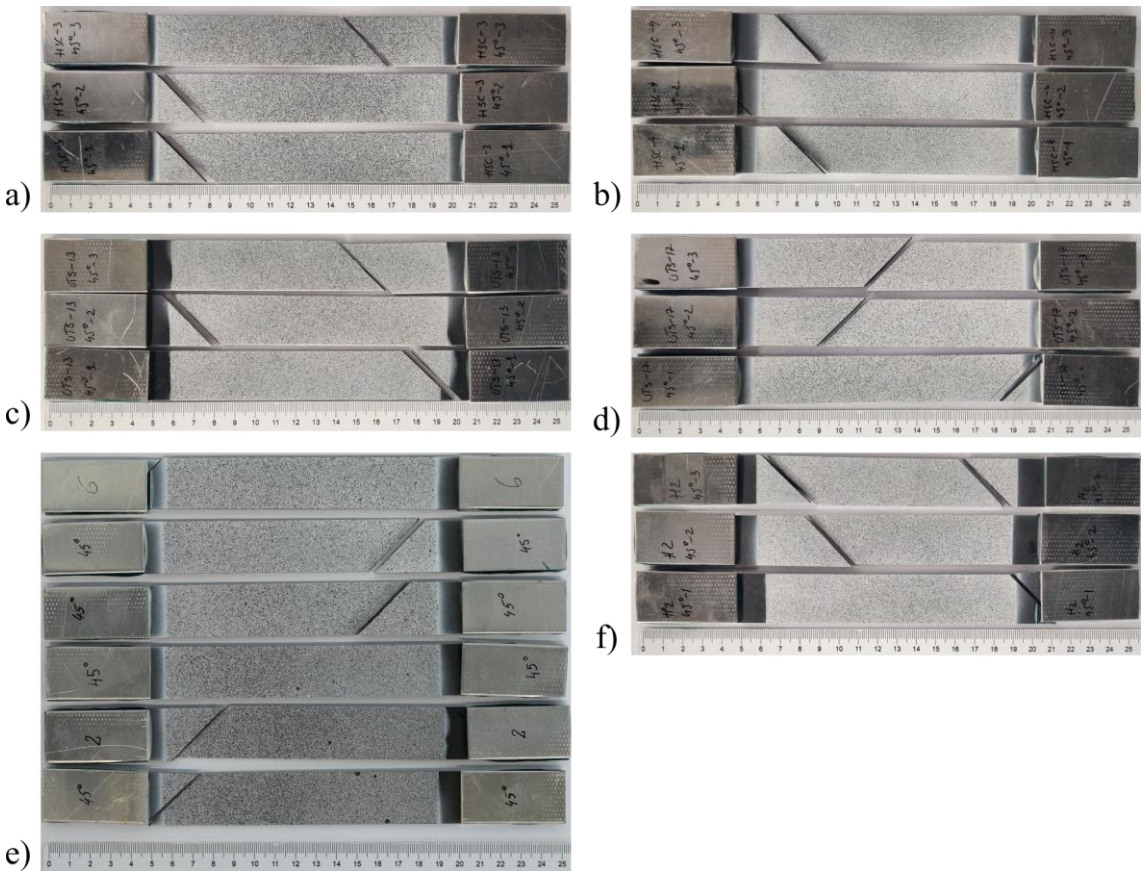

Fig. E. 4. Fracture position for 45° samples, with sample 1 starting from the ruler; a) HSC3; b) HSC4; c) UTS13; d) UTS17; e) H1; f) H2

APPENDIX F

COMPLIANCE MATRICES FOR ALL LAMINATES

$$C_{HSC3} = \begin{bmatrix} 8.77e-3 & -2.72e-3 & -2.72e-3 & 0 & 0 & 0 \\ -2.72e-3 & 0.143 & -0.057 & 0 & 0 & 0 \\ -2.72e-3 & -0.057 & 0.143 & 0 & 0 & 0 \\ 0 & 0 & 0 & 0.4 & 0 & 0 \\ 0 & 0 & 0 & 0 & 0.294 & 0 \\ 0 & 0 & 0 & 0 & 0 & 0.294 \end{bmatrix} \frac{1}{\text{GPa}}$$

$$C_{HSC4} = \begin{bmatrix} 8.77e-3 & -2.89e-3 & -2.89e-3 & 0 & 0 & 0 \\ -2.89e-3 & 0.139 & -0.056 & 0 & 0 & 0 \\ -2.89e-3 & -0.056 & 0.139 & 0 & 0 & 0 \\ 0 & 0 & 0 & 0.389 & 0 & 0 \\ 0 & 0 & 0 & 0 & 0.296 & 0 \\ 0 & 0 & 0 & 0 & 0 & 0.296 \end{bmatrix} \frac{1}{\text{GPa}}$$

$$C_{UTS13} = \begin{bmatrix} 8e-3 & -2.56e-3 & -2.56e-3 & 0 & 0 & 0 \\ -2.56e-3 & 0.145 & -0.058 & 0 & 0 & 0 \\ -2.56e-3 & -0.058 & 0.145 & 0 & 0 & 0 \\ 0 & 0 & 0 & 0.406 & 0 & 0 \\ 0 & 0 & 0 & 0 & 0.292 & 0 \\ 0 & 0 & 0 & 0 & 0 & 0.292 \end{bmatrix} \frac{1}{\text{GPa}}$$

$$C_{UTS17} = \begin{bmatrix} 7.87e-3 & -2.56e-3 & -2.56e-3 & 0 & 0 & 0 \\ -2.56e-3 & 0.143 & -0.057 & 0 & 0 & 0 \\ -2.56e-3 & -0.057 & 0.143 & 0 & 0 & 0 \\ 0 & 0 & 0 & 0.4 & 0 & 0 \\ 0 & 0 & 0 & 0 & 0.287 & 0 \\ 0 & 0 & 0 & 0 & 0 & 0.287 \end{bmatrix} \frac{1}{\text{GPa}}$$

$$C_{H1} = \begin{bmatrix} 8.54e-3 & -2.73e-3 & -2.73e-3 & 0 & 0 & 0 \\ -2.73e-3 & 0.143 & -0.057 & 0 & 0 & 0 \\ -2.73e-3 & -0.057 & 0.143 & 0 & 0 & 0 \\ 0 & 0 & 0 & 0.4 & 0 & 0 \\ 0 & 0 & 0 & 0 & 0.287 & 0 \\ 0 & 0 & 0 & 0 & 0 & 0.287 \end{bmatrix} \frac{1}{\text{GPa}}$$

$$C_{H2} = \begin{bmatrix} 8.27e-3 & -2.55e-3 & -2.55e-3 & 0 & 0 & 0 \\ -2.55e-3 & 0.143 & -0.057 & 0 & 0 & 0 \\ -2.55e-3 & -0.057 & 0.143 & 0 & 0 & 0 \\ 0 & 0 & 0 & 0.4 & 0 & 0 \\ 0 & 0 & 0 & 0 & 0.287 & 0 \\ 0 & 0 & 0 & 0 & 0 & 0.287 \end{bmatrix} \frac{1}{\text{GPa}}$$

APPENDIX G

AXIAL STRESS-STRAIN RESPONSE FOR ALL TESTED SAMPLES – CYCLIC LOAD-UNLOAD TENSILE TESTING

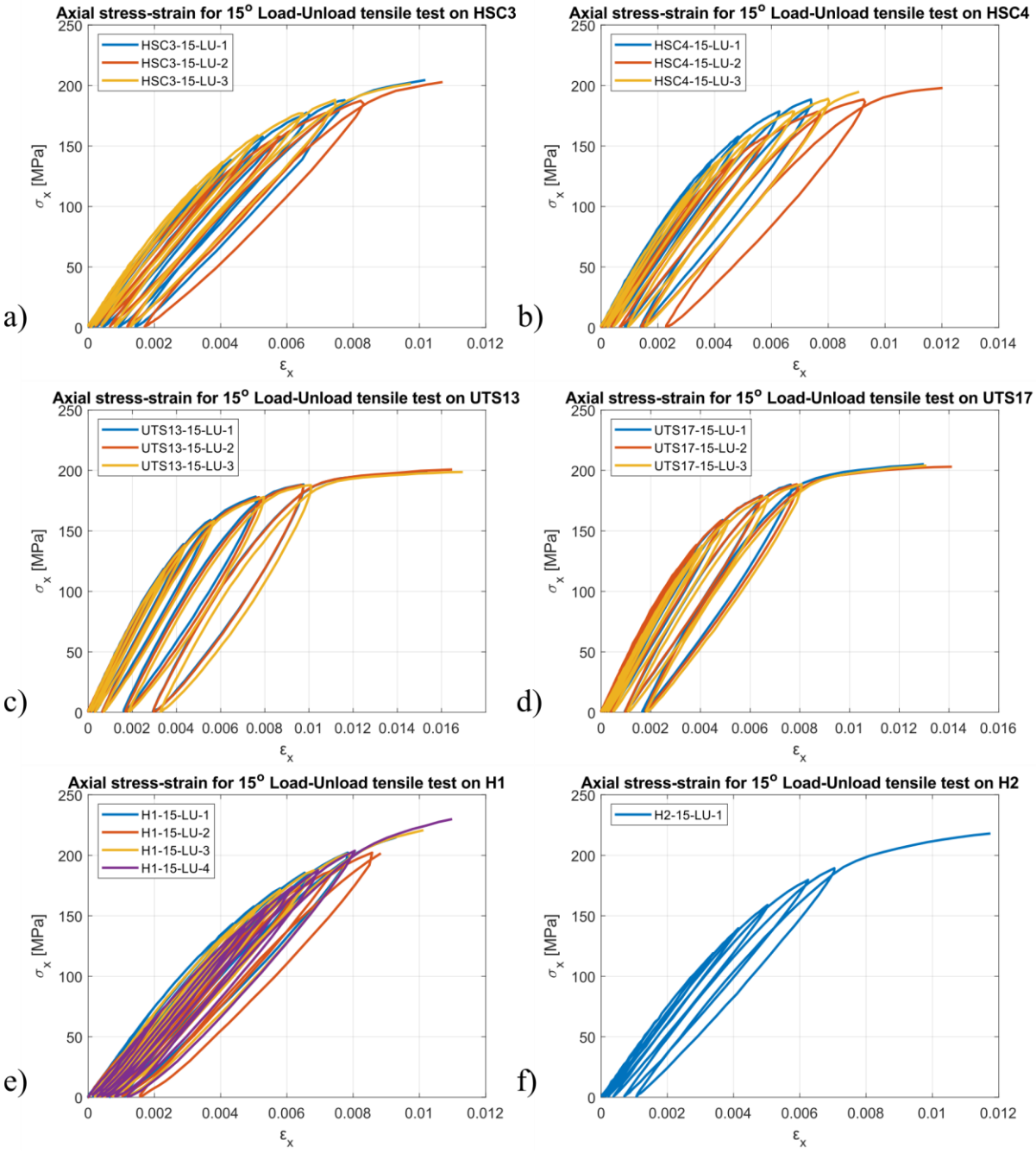

Fig. G. 1. Axial Stress-Strain response for all tested samples under off-axis load-unload tensile test, θ=15°; a) HSC3; b) HSC4; c) UTS13; d) UTS17; e) H1; f) H2

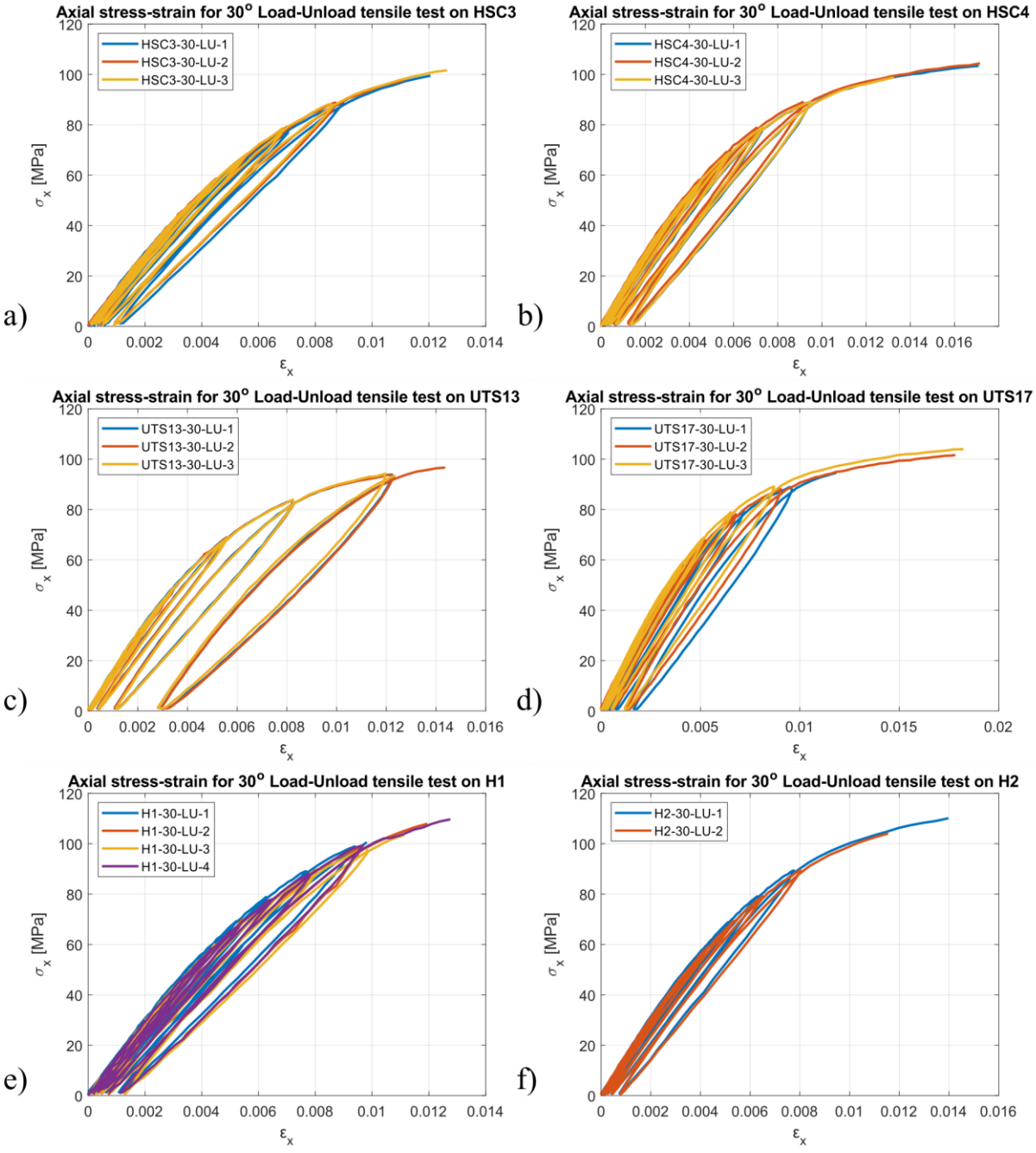

Fig. G. 2. Axial Stress-Strain response for all tested samples under off-axis load-unload tensile test, θ=30°; a) HSC3; b) HSC4; c) UTS13; d) UTS17; e) H1; f) H2

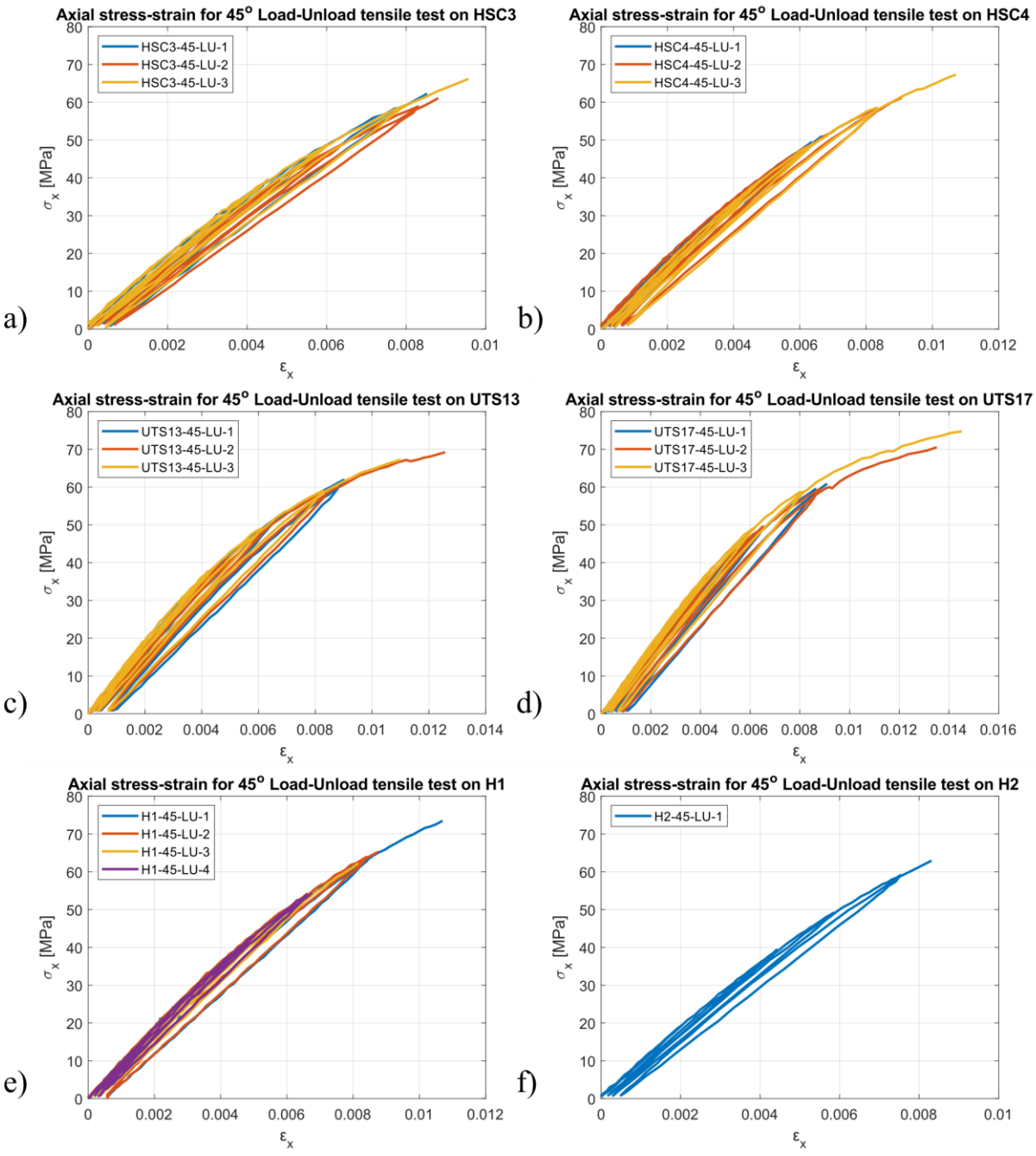

Fig. G. 3. Axial Stress-Strain response for all tested samples under off-axis load-unload tensile test, θ=45°; a) HSC3; b) HSC4; c) UTS13; d) UTS17; e) H1; f) H2

APPENDIX H

PREDICTION PERCENTAGE ERROR

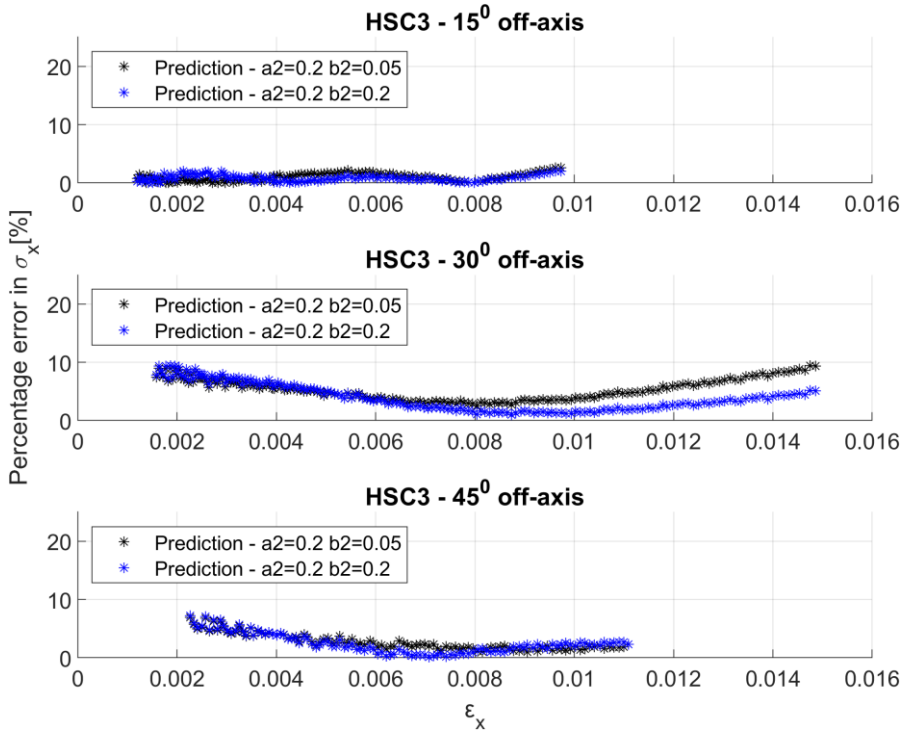

Fig. H. 1. Prediction percentage error comparison for HSC3, using a_2=0.2; b_2=0.05 or b_2=0.2

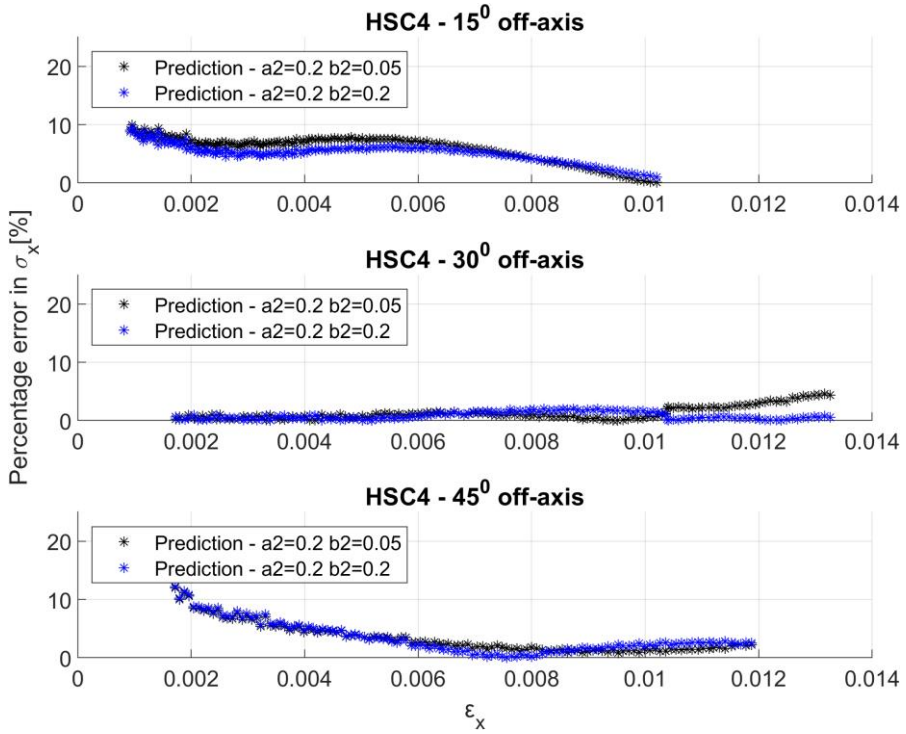

Fig. H. 2. Prediction percentage error comparison for HSC4, using a_2=0.2; b_2=0.05 or b_2=0.2

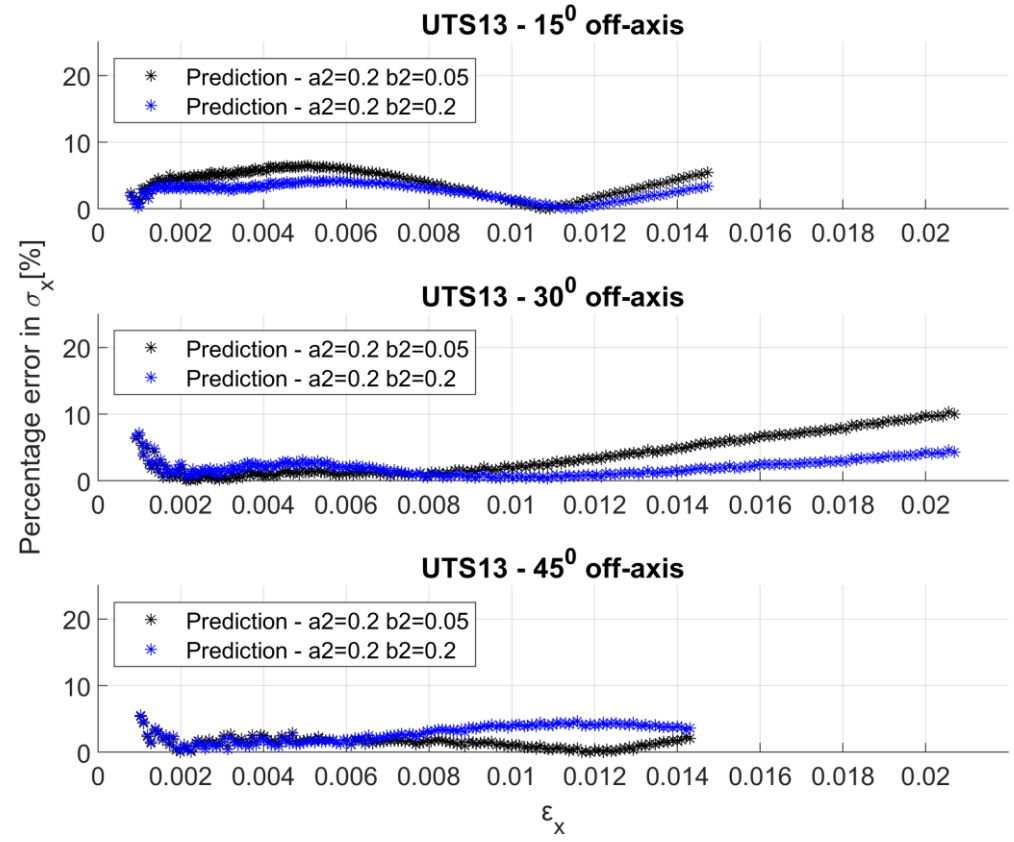

Fig. H. 3. Prediction percentage error comparison for UTS13, using a_2=0.2; b_2=0.05 or b_2=0.2

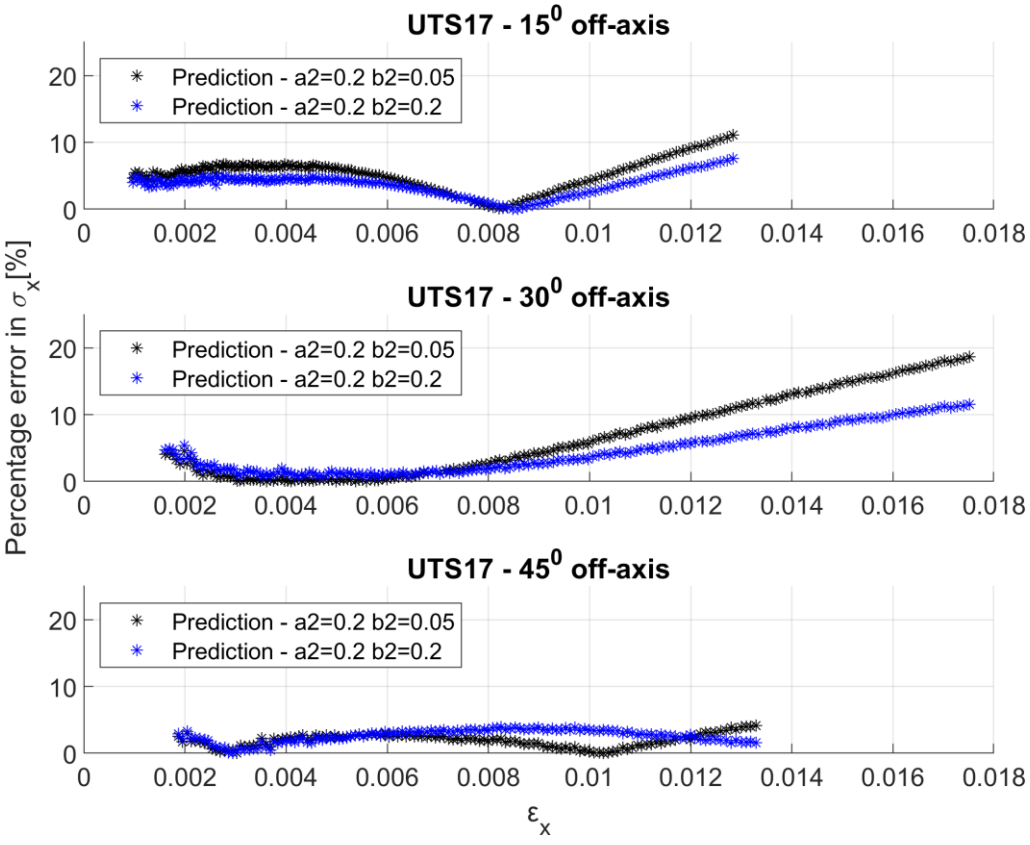

Fig. H. 4. Prediction percentage error comparison for UTS17, using a_2=0.2; b_2=0.05 or b_2=0.2

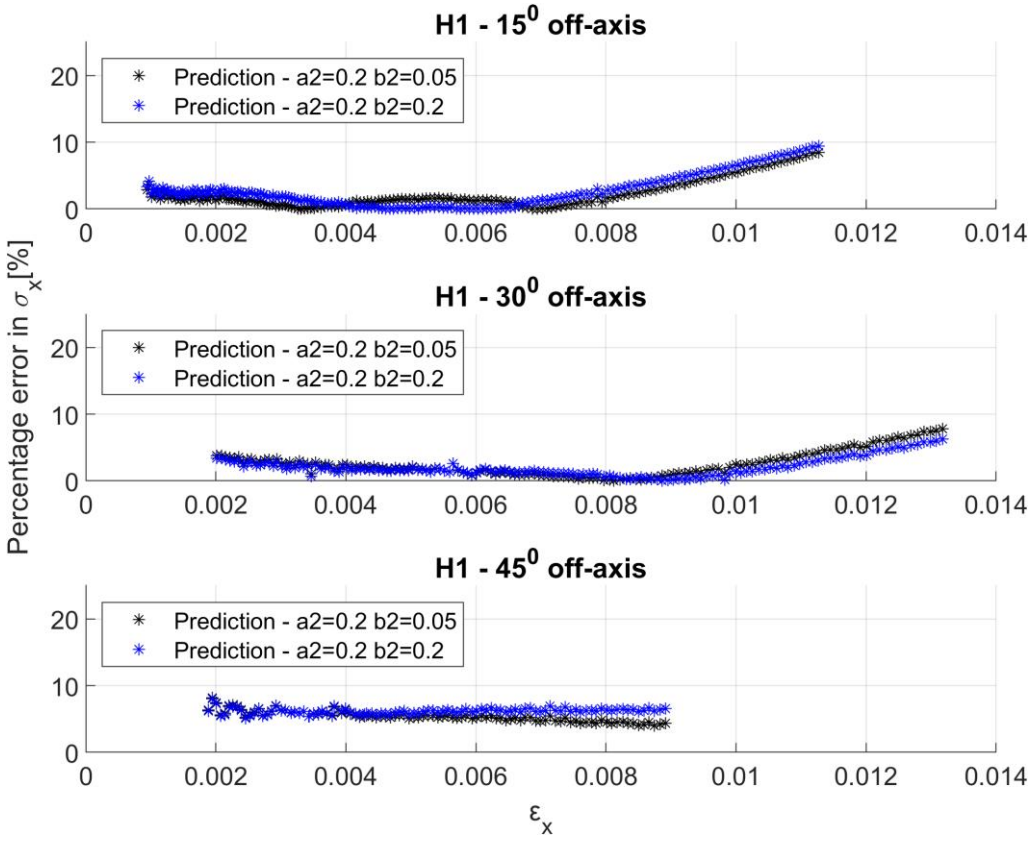

Fig. H. 5. Prediction percentage error comparison for H1, using a_2=0.2; b_2=0.05 or b_2=0.2

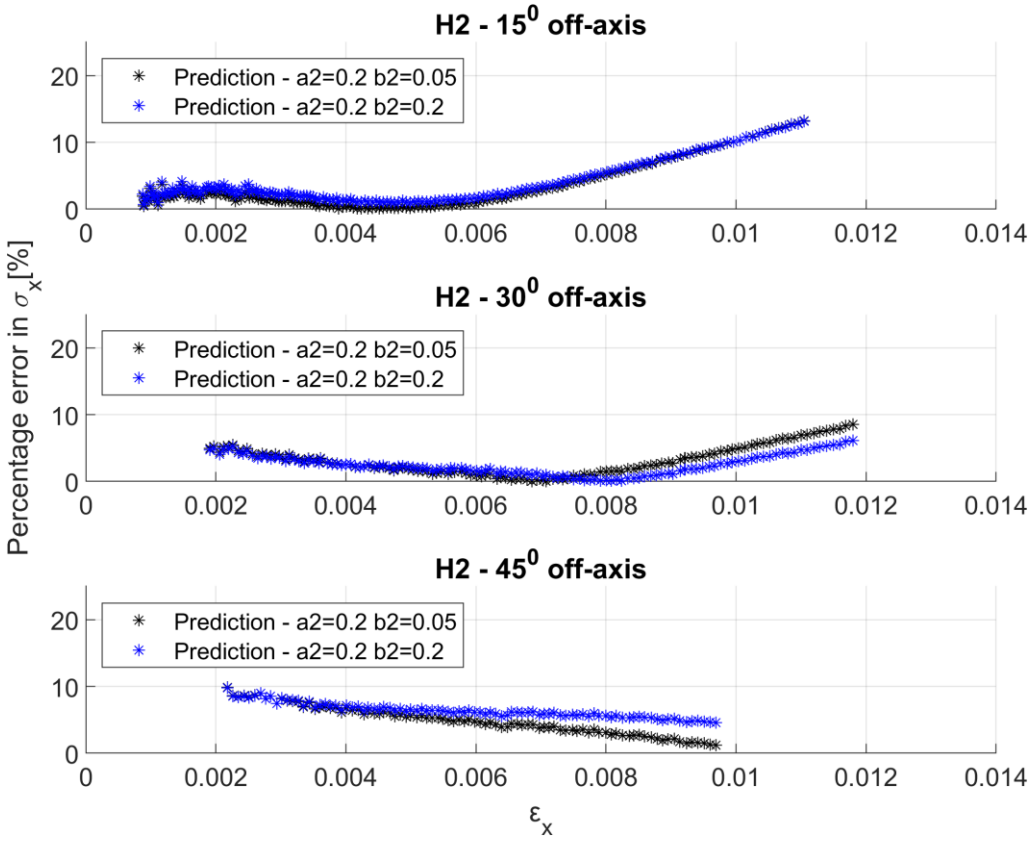

Fig. H. 6. Prediction percentage error comparison for H2, using a_2=0.2; b_2=0.05 or b_2=0.2

APPENDIX I

MATLAB CODE FOR FFT ANALYSIS

```
function [period_us]=FFT_IP(BF_VEL,name)
% BF_VEL – matrix of the back-face velocity of one tested sample
% name – name of the tested sample

t = BF_VEL(:,1)/1e+6;                          % Time Vector in seconds
s = BF_VEL(:,2);                               % signal Vector - Velocity in m/s
s_dc = s - mean(s);                                    % Remove DC component
L = numel(t);                                          % Signal Length
T = mean(diff(t));                                     % Sampling Interval
Fs = 1/T;                                              % Sampling Frequency
Fn = Fs/2;                                             % Nyquist Frequency

fig=figure('DefaultAxesFontSize',12);
plot(BF_VEL(:,1),BF_VEL(:,2))          % Plot the back-face velocity signal
xlabel('Time [\mus]')
ylabel('Back face velocity [m/s]')
title(strcat('Original signal: ', name))

% FFT
X = fft(s_dc);                                         % apply FFT
fig=figure('DefaultAxesFontSize',12);
plot(abs(X))                                          % plot full spectrum
title(strcat('Full spectrum FFT: ', name))

SSB = X(1:L/2);                % get only the positive half of the spectrum
SSB(1:end) = 2*SSB(1:end);     % multiply by 2 to compensate for the loss of
energy in the positive half of the magnitude spectrum due to the complex
conjugate symmetry property of the DFT
f = (0:L/2-1)*(Fs/L);             % get frequency axis for half the spectrum
f_full = (0:L-1)*(Fs/L);          % get frequency axis for the full spectrum

fig=figure('DefaultAxesFontSize',12);
plot(f,abs(SSB/L))                  % Plot normalized FFT, half the spectrum
xlabel('f [Hz]')
ylabel('Magnitude')
title(strcat('Normalized Frequency Spectrum: ', name))

[~,maxIndex] = max(SSB/L);  % find the index of the peak in the magnitude
spectrum
peakFrequency = f(maxIndex);        % find the frequency of the peak
period = 1/peakFrequency;           % calculate the period as the reciprocal
of the frequency

period_us=period*1e+6;                  % period in microseconds
```

APPENDIX J

IN-PLANE LASER IMPACT TEST DETAILS

Table J. 1. In-plane laser tests details

Material	Sample number	Experimental campaign session	Energy Level [%]	Sample initial thickness [mm]	Focal spot diameter [cm]	Density of power φ [GW/cm^2]	Standard deviation for φ [GW/cm^2]
H1	1	2021	100	1.837	0.445	2.3047	0.1133
	2		50	1.880	0.385	1.5403	0.0781
	4		100	1.929	0.400	2.8546	0.1421
	5		50	1.645	0.400	1.4274	0.0716
	6-1		50	1.779	0.400	1.4281	0.0721
	6-2		75	1.789	0.420	1.9392	0.0975
H2	1	2022	50	1.984	0.362	2.0478	0.1026
	2		50	1.978	0.367	1.9861	0.0990
	3		75	1.938	0.380	2.8012	0.1408
	4		75	1.860	0.380	2.8008	0.1377
	5		100	1.888	0.384	3.4665	0.1722
	6		100	1.837	0.390	3.3642	0.1693
HSC	1	2022	50	1.954	0.360	2.0704	0.1040
	2		50	1.852	0.370	1.9585	0.0983
	3		75	1.969	0.380	2.8041	0.1386
	4		75	1.796	0.380	2.8032	0.1386
	5		100	1.852	0.390	3.3625	0.1674
	6		100	1.956	0.400	3.1977	0.1606
UTS	1	2022	50	1.960	0.360	2.0693	0.1046
	2		50	1.874	0.370	1.9622	0.0996
	3		75	1.925	0.372	2.9240	0.1457
	4		75	1.829	0.385	2.7300	0.1360
	5		100	1.929	0.396	3.2621	0.1637
	6		100	1.918	0.395	3.2764	0.1635

APPENDIX K

OUT-OF-PLANE LASER IMPACT TEST DETAILS

Table K. 1. Out-of-plane laser tests details

Material	Sample number	Shot number	Experimental campaign session	Energy Level [%]	Sample initial thickness [mm]	Focal spot diameter [cm]	Density of power φ [GW/cm^2]	Standard deviation at 67% for φ [GW/cm^2]
H1	2.1	2	2021	100	2.200	0.4	2.8540	0.1435
		3		75		0.385	2.3083	0.1134
		4		50		0.36	1.7598	0.0892
		5		25		0.36	0.8805	0.0457
		7		85		0.4	2.4297	0.1198
		8		35		0.365	1.1997	0.0611
	2.2	2		100	2.215	0.43	2.4682	0.1231
		3		75		0.4	2.1402	0.1076
		4		75		0.41	2.0371	0.1002
		6		50		0.4	1.4253	0.0706
		7		50		0.4	1.4262	0.0712
		8		25		0.38	0.7898	0.0406
		9		25		0.37	0.8333	0.043
	2.3	1		35	2.226	0.38	1.1061	0.0568
		2		100		0.41	2.7131	0.1331
		3		100		0.4	2.8514	0.1424
		4		75		0.39	2.2505	0.1117
		5		50		0.39	1.5001	0.0755
		6		25		0.36	0.8802	0.046
		8		85		0.4	2.4290	0.121
	2.4	1		100	2.165	0.41	2.7157	0.1362
		4		25		0.35	0.9315	0.0485
		5		15		0.34	0.5920	0.0331
		6		100		0.39	2.9986	0.1486
		8		75		0.38	2.3681	0.1169
		9		50		0.38	1.5796	0.0794
H1	1.1	2	2022	100	2.175	0.38	3.5767	0.1800
		3		100		0.38	3.5604	0.1767
		4		75		0.37	2.9559	0.1472
		5		75		0.37	2.9542	0.1450
		7		50		0.35	2.1899	0.1101
		8		50		0.35	2.1894	0.1111
		9		35		0.34	1.6591	0.0857
		10		35		0.34	1.6599	0.0853
	1.3	1		35	2.155	0.34	1.6594	0.0855
		2		35		0.34	1.6593	0.0854
		3		50		0.35	2.1892	0.1120
		4		50		0.35	2.1908	0.1107
		5		75		0.37	2.9524	0.1477

Material	Sample number	Shot number	Experimental campaign session	Energy Level [%]	Sample initial thickness [mm]	Focal spot diameter [cm]	Density of power φ [GW/cm^2]	Standard deviation at 67% for φ [GW/cm^2]
		6		75		0.37	2.9524	0.1473
		7		100		0.38	3.6364	0.1802
		8		100		0.38	3.6336	0.1817
H2		1	2022	100		0.38	3.5412	0.1751
		2		100		0.39	3.4521	0.1717
		3		100		0.39	3.4525	0.1725
	1	6		50	2.711	0.36	2.0697	0.1045
		7		50		0.35	2.1908	0.1106
		8		75		0.37	2.9553	0.1453
		10		75		0.37	2.9573	0.1488
		1		35		0.34	1.6592	0.0858
	2	2		35	2.740	0.34	1.6607	0.0856
		3		35		0.34	1.6595	0.0869
HSC3		1	2022	35		0.34	1.6218	0.0833
		2		35		0.35	1.5661	0.0810
		5		100		0.38	3.5421	0.1787
	1	7		100	1.616	0.36	3.9452	0.1980
		8		100		0.36	3.9480	0.1950
		10		75		0.36	3.2102	0.1595
		1		75		0.36	3.1216	0.1551
		3		75		0.35	3.3021	0.1659
		4		50		0.33	2.4672	0.1249
		5		50		0.33	2.4657	0.1257
	2	7		25	1.726	0.32	1.4363	0.0734
		8		25		0.31	1.5298	0.0769
		10		35		0.33	1.7625	0.0918
		11		35		0.34	1.6609	0.0854
HSC4		2	2022	100		0.38	3.5426	0.1796
		4		100		0.37	3.7358	0.1847
		5		100		0.38	3.6353	0.1807
		6		75		0.36	3.2106	0.1609
	1	7		75	2.227	0.36	3.1228	0.1576
		8		75		0.38	2.8016	0.1403
		9		50		0.34	2.3907	0.1210
		10		50		0.35	2.1897	0.1106
		1		50		0.35	2.1401	0.1084
		2		50		0.35	2.1902	0.1104
	2	6		35	2.268	0.33	1.7630	0.0904
		7		35		0.34	1.6597	0.0853
		8		35		0.34	1.7111	0.0883
UTS13		2	2022	100		0.39	3.3954	0.1650
	1	4		100	2.046	0.38	3.6360	0.1833
		5		75		0.38	2.8014	0.1386
		6		50		0.35	2.1890	0.1100
	2	7		75	2.061	0.37	2.9561	0.1465
		9		35		0.35	1.6118	0.0837
		2		100		0.37	3.8408	0.1912
		5		100		0.38	3.6356	0.1828
	3	7		75	2.016	0.36	3.1227	0.1576
		8		75		0.37	3.0223	0.1516
		10		100		0.38	3.6198	0.1796

Material	Sample number	Shot number	Experimental campaign session	Energy Level [%]	Sample initial thickness [mm]	Focal spot diameter [cm]	Density of power φ [GW/cm^2]	Standard deviation at 67% for φ [GW/cm^2]
		1		100		0.38	3.6367	0.1819
		2		50		0.36	2.1312	0.1085
	4	3		50	2.041	0.36	2.0931	0.1064
		4		35		0.34	1.6407	0.0837
		5		35		0.35	1.6120	0.0835
UTS17		1	2022	35		0.34	1.6602	0.0861
		2		35		0.36	1.5234	0.0791
		3		35		0.33	1.7209	0.0876
		4		50		0.36	2.1289	0.1074
	1	6		50	2.665	0.36	2.0703	0.1042
		7		50		0.35	2.2402	0.1124
		8		75		0.38	2.8774	0.1423
		9		75		0.36	3.0538	0.1540
		10		75		0.36	3.1200	0.1534
		2		100		0.38	3.4867	0.1731
	2	3		100	2.67	0.38	3.5413	0.1771
		4		100		0.37	3.7352	0.1876

APPENDIX L

ABLATION PRESSURE VARIATION WITH PEAK BACK-FACE VELOCITY

The ablation pressure was determined using Berthe's formulation for laser impact test in water confinement, using equations (1.38) and (1.39). The evolution of the ablation pressure with the peak back-face velocity is illustrated in Fig. L. 1 for all tested material in 2022, in the out-of-plane direction, while Fig. L. 2 shows the results for each material, with a linear fit and corresponding equation. In the range of ablation pressures used for testing (~0.18 GPa to ~0.3 GPa), the evolution with the peak back-face velocity, hence the material velocity, appears linear, suggesting an elastic response regime.

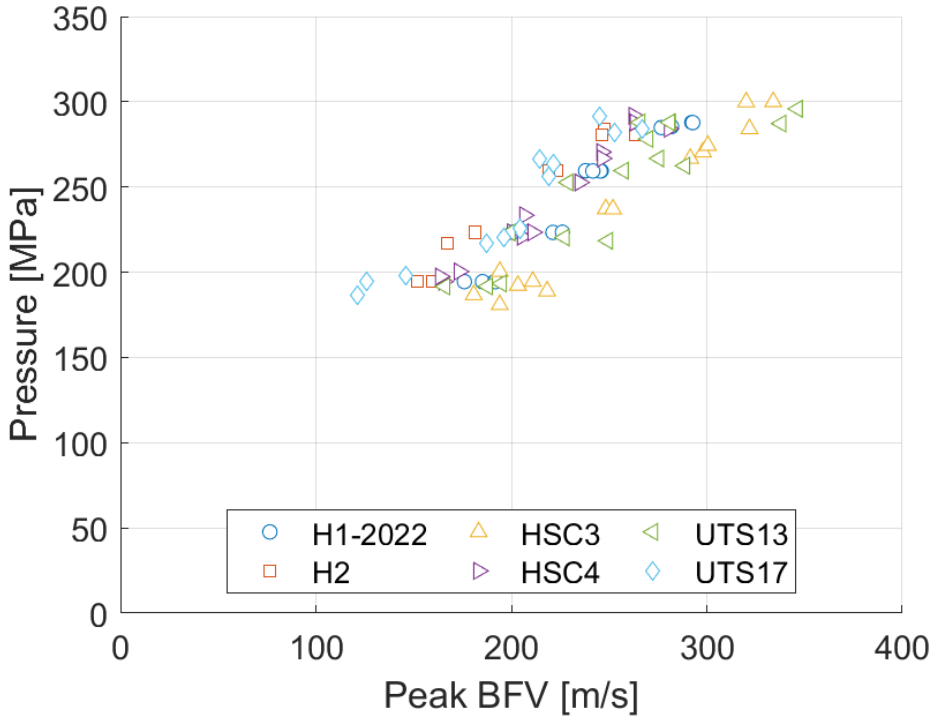

Fig. L. 1. Ablation pressure versus the peak back-face velocity, for out-of-plane laser impact tests

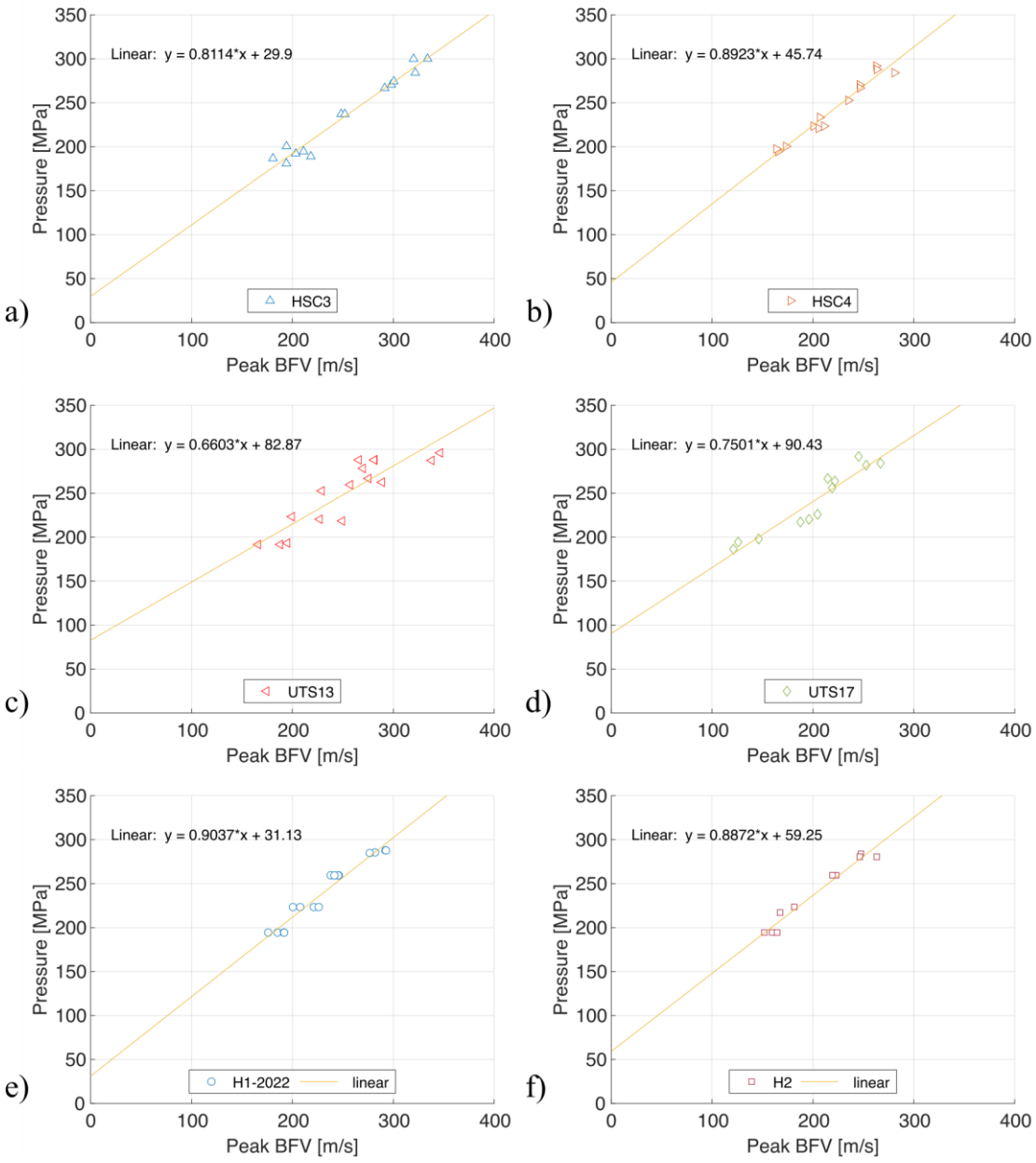

Fig. L. 2. Ablation pressure versus the peak back-face velocity, for out-of-plane laser impact tests with corresponding linear fittings; a) HSC3; b) HSC4; c) UTS13; d) UTS17; e) H1; f) H2

REFERENCES

[1] International Civil Aviation Organization, 2021 global air passenger totals show improvement from 2020, but still only half pre-pandemic levels. https://www.icao.int/Newsroom/Pages/2021-global-air-passenger-totals-show-improvement.aspx (accessed Jul. 26, 2022).

[2] C. Soutis, Carbon fiber reinforced plastics in aircraft construction, *Materials Science and Engineering: A*, vol. 412, no. 1–2, pp. 171–176, 2005, doi: 10.1016/J.MSEA.2005.08.064.

[3] IATA, CO2 EMISSIONS MEASUREMENT METHODOLOGY. Accessed: Jun. 22, 2022. [Online]. Available: https://www.iata.org/contentassets/34f5341668f14157ac55896f364e3451/rp-carbon-calculation.pdf

[4] D. Gay, *Composite materials : design and applications*, Third Edit. Boca Raton: CRC Press, 2015.

[5] T. Jollivet, C. Peyrac, and F. Lefebvre, Damage of composite materials, *Procedia Engineering*, vol. 66, pp. 746–758, 2013, doi: 10.1016/j.proeng.2013.12.128.

[6] I. M. Daniel and O. Ishai, *Engineering mechanics of composite materials*. Oxford University Press, 1994.

[7] C. Fualdes, X. Jolivet, and C. Chamfroy, Safe operations with composite aircraft, *The Airbus Safety Magazine*, no. 18, pp. 18–23, 2014. [Online]. Available: https://safetyfirst.airbus.com/safe-operations-with-composite-aircraft/

[8] T. Kellner, The Art of Engineering: The World's Largest Jet Engine Shows Off Composite Curves, 2016. https://www.ge.com/news/reports/the-art-of-engineering-the-worlds-largest-jet-engine-shows-off-composite-curves (accessed Jun. 22, 2022).

[9] Rolls Royce, Rolls-Royce starts manufacture of world's largest fan blades - made of composite material - for next-generation UltraFan demonstrator, 2020. https://www.rolls-royce.com/media/press-releases/2020/11-02-2020-intelligentengine-rr-starts-manufacture-of-world-largest-fan-blades.aspx (accessed Jun. 22, 2022).

[10] Safran Group, LEAP engine - Composite Fan Blades & Case. https://www.safran-group.com/videos/leap-engine-composite-fan-blades-case (accessed Jun. 22, 2022).

[11] C. Soutis, Fibre reinforced composites in aircraft construction, *Progress in Aerospace Sciences*, vol. 41, no. 2, pp. 143–151, 2005, doi: 10.1016/J.PAEROSCI.2005.02.004.

[12] M. V. Ramana and S. Ramprasad, Experimental Investigation on Jute/Carbon Fibre reinforced Epoxy based Hybrid Composites, *Materials Today: Proceedings*, vol. 4, no. 8, pp. 8654–8664, 2017, doi: 10.1016/J.MATPR.2017.07.214.

[13] E. Randjbaran, R. Zahari, A. A. N. Jalil, and D. L. A. A. Majid, Hybrid Composite Laminates Reinforced with Kevlar/Carbon/Glass Woven Fabrics for Ballistic Impact

Testing, 2014, doi: 10.1155/2014/413753.

[14] L. Ferrante, J. Tirillò, F. Sarasini, F. Touchard, R. Ecault, M. A. Vidal Urriza, L. Chocinski-Arnault, and D. Mellier, Behaviour of woven hybrid basalt-carbon/epoxy composites subjected to laser shock wave testing: Preliminary results, *Composites Part B: Engineering*, vol. 78, pp. 162–173, 2015, doi: 10.1016/j.compositesb.2015.03.084.

[15] A. Rajpurohit, S. Joannès, V. Singery, P. Sanial, and L. Laiarinandrasana, Hybrid Effect in In-Plane Loading of Carbon/Glass Fibre Based Inter- and Intraply Hybrid Composites, *Journal of Composites Science 2020, Vol. 4, Page 6*, vol. 4, no. 1, p. 6, 2020, doi: 10.3390/JCS4010006.

[16] J. H. Song, Pairing effect and tensile properties of laminated high-performance hybrid composites prepared using carbon/glass and carbon/aramid fibers, *Composites Part B: Engineering*, vol. 79, pp. 61–66, 2015, doi: 10.1016/J.COMPOSITESB.2015.04.015.

[17] D. W. Lee, B. J. Park, S. Y. Park, C. H. Choi, and J. Il Song, Fabrication of high-stiffness fiber-metal laminates and study of their behavior under low-velocity impact loadings, *Composite Structures*, vol. 189, pp. 61–69, 2018, doi: 10.1016/j.compstruct.2018.01.044.

[18] K. Dadej, J. Bienias, and B. Surowska, On the effect of glass and carbon fiber hybridization in fiber metal laminates: Analytical, numerical and experimental investigation, *Composite Structures*, vol. 220, pp. 250–260, 2019, doi: 10.1016/J.COMPSTRUCT.2019.03.051.

[19] A. R. Bunsell and B. Harris, Hybrid carbon and glass fibre composites, *Composites*, vol. 5, no. 4, pp. 157–164, 1974, doi: 10.1016/0010-4361(74)90107-4.

[20] G. Czél and M. R. Wisnom, Demonstration of pseudo-ductility in high performance glass/epoxy composites by hybridisation with thin-ply carbon prepreg, *Composites Part A: Applied Science and Manufacturing*, vol. 52, pp. 23–30, 2013, doi: 10.1016/J.COMPOSITESA.2013.04.006.

[21] G. Czél, M. Jalalvand, and M. R. Wisnom, Demonstration of pseudo-ductility in unidirectional hybrid composites made of discontinuous carbon/epoxy and continuous glass/epoxy plies, *Composites Part A: Applied Science and Manufacturing*, vol. 72, pp. 75–84, 2015, doi: 10.1016/J.COMPOSITESA.2015.01.019.

[22] A. Arteiro, C. Furtado, G. Catalanotti, P. Linde, and P. P. Camanho, Thin-ply polymer composite materials: A review, *Composites Part A: Applied Science and Manufacturing*, vol. 132, p. 105777, 2020, doi: 10.1016/J.COMPOSITESA.2020.105777.

[23] S. Sihn, R. Y. Kim, K. Kawabe, and S. W. Tsai, Experimental studies of thin-ply laminated composites, *Composites Science and Technology*, vol. 67, no. 6, pp. 996–1008, 2007, doi: 10.1016/J.COMPSCITECH.2006.06.008.

[24] I. Daniel and R. LaBedz, Method for Compression Testing of Composite Materials at High Strain Rates, *ASTM special technical publications*, pp. 121–139, 1983, doi: 10.1520/STP36200S.

[25] L. C. Alil, M. Arrigoni, M. Istrate, A. Kravcov, J. Le Pavic, and G. Tahan, Laser Induced Shockwave as Delaminator of Composite Material for Ballistic Protection at High Strain Rate, *NATO Science for Peace and Security Series C: Environmental Security*, pp. 15–33, 2020, doi: 10.1007/978-94-024-1755-5_2.

[26] S. Ekşi and K. Genel, Comparison of Mechanical Properties of Unidirectional and Woven Carbon, Glass and Aramid Fiber Reinforced Epoxy Composites, *Acta Physica Polonica Series A*, vol. 132, no. 3–II, pp. 879–882, 2017, doi: 10.12693/APhysPolA.132.879.

[27] Y. Zhong, M. Cheng, X. Zhang, H. Hu, D. Cao, and S. Li, Hygrothermal durability of glass and carbon fiber reinforced composites – A comparative study, *Composite Structures*, vol. 211, pp. 134–143, 2019, doi: 10.1016/J.COMPSTRUCT.2018.12.034.

[28] X. Li, A. B. Nia, X. Ma, M. Y. Yahya, and Z. Wang, Dynamic response of Kevlar ® 29/epoxy laminates under projectile impact-experimental investigation, *Mechanics of Advanced Materials and Structures*, 2015, doi: 10.1080/15376494.2015.1107670.

[29] P. Baldus, M. Jansen, and D. Sporn, Ceramic fibers for matrix composites in high-temperature engine applications, *Science*, vol. 285, no. 5428. pp. 699–703, Jul. 30, 1999. doi: 10.1126/science.285.5428.699.

[30] W. Krenkel, *Ceramic Matrix Composites: Fiber Reinforced Ceramics and their Applications*. John Wiley and Sons, 2008. doi: 10.1002/9783527622412.

[31] F. I. Hurwitz, Ceramic Matrix and Resin Matrix Composites: a Comparison., *NASA Technical Memorandum*, 1987.

[32] K. K. Chawla, *Ceramic Matrix Composites*. Boston, MA: Springer US, 2003. doi: 10.1007/978-1-4615-1029-1.

[33] D. U. Shah, Characterisation And Optimisation Of The Mechanical Performance Of Plant Fibre Composites For Structural Applications, University Of Nottingham, 2013.

[34] R. M. Rocha, C. A. A. Cairo, and M. L. A. Graça, Formation of carbon fiber-reinforced ceramic matrix composites with polysiloxane/silicon derived matrix, *Materials Science and Engineering A*, vol. 437, no. 2, pp. 268–273, 2006, doi: 10.1016/j.msea.2006.08.102.

[35] D. K. Rajak, D. D. Pagar, P. L. Menezes, and E. Linul, Fiber-Reinforced Polymer Composites: Manufacturing, Properties, and Applications, *Polymers 2019, Vol. 11, Page 1667*, vol. 11, no. 10, p. 1667, 2019, doi: 10.3390/POLYM11101667.

[36] B. Parveez, M. I. Kittur, I. A. Badruddin, S. Kamangar, M. Hussien, and M. A. Umarfarooq, Scientific Advancements in Composite Materials for Aircraft Applications: A Review, *Polymers*, vol. 14, no. 22, p. 5007, 2022, doi: 10.3390/POLYM14225007.

[37] Y. Chen, J. Zhang, Z. Li, H. Zhang, J. Chen, W. Yang, T. Yu, W. Liu, and Y. Li, Manufacturing Technology of Lightweight Fiber-Reinforced Composite Structures in Aerospace: Current Situation and toward Intellectualization, *Aerospace 2023, Vol. 10, Page 206*, vol. 10, no. 3, p. 206, 2023, doi: 10.3390/AEROSPACE10030206.

[38] G. Marsh, Prepregs — raw material for high-performance composites, *Reinforced Plastics*, vol. 46, no. 10, pp. 24–28, 2002, doi: 10.1016/S0034-3617(02)80172-2.

[39] P. T. Curtis and M. Browne, Cost-effective high performance composites, *Composites*, vol. 25, no. 4, pp. 273–280, 1994, doi: 10.1016/0010-4361(94)90219-4.

[40] C. Audibert, A. S. Andreani, É. Lainé, and J. C. Grandidier, Mechanical characterization and damage mechanism of a new flax-Kevlar hybrid/epoxy composite, *Composite Structures*, vol. 195, pp. 126–135, 2018, doi: 10.1016/J.COMPSTRUCT.2018.04.061.

[41] P. Zuo, D. V. Srinivasan, and A. P. Vassilopoulos, Review of hybrid composites fatigue, *Composite Structures*, vol. 274, 2021, doi: 10.1016/J.COMPSTRUCT.2021.114358.

[42] E. Rolfe, R. Quinn, G. Irven, D. Brick, R. E. Johnston, J. P. Dear, and H. Arora, Experimental investigation of the air blast performance of hybrid composite skinned sandwich panels with X-ray micro-CT damage assessment, *Thin-Walled Structures*, vol. 188, p. 110874, 2023, doi: 10.1016/J.TWS.2023.110874.

[43] C. Furtado, A. Arteiro, G. Catalanotti, J. Xavier, and P. P. Camanho, Selective ply-level hybridisation for improved notched response of composite laminates, *Composite*

Structures, vol. 145, pp. 1–14, 2016, doi: 10.1016/J.COMPSTRUCT.2016.02.050.

[44] A. Arteiro, G. Catalanotti, J. Xavier, P. Linde, and P. P. Camanho, A strategy to improve the structural performance of non-crimp fabric thin-ply laminates, *Composite Structures*, vol. 188, pp. 438–449, 2018, doi: 10.1016/J.COMPSTRUCT.2017.11.072.

[45] A. Sasikumar, D. Trias, J. Costa, N. Blanco, J. Orr, and P. Linde, Effect of ply thickness and ply level hybridization on the compression after impact strength of thin laminates, *Composites Part A: Applied Science and Manufacturing*, vol. 121, pp. 232–243, 2019, doi: 10.1016/J.COMPOSITESA.2019.03.022.

[46] W. McDonough, J. Dunkers, K. Flynn, and D. Hunston, A Test Method to Determine the Fiber and Void Contents of Carbon/Glass Hybrid Composites, *Journal of ASTM International*, vol. 1, no. 3, 2004, doi: 10.1520/JAI12076.

[47] K. S. Pandya, C. Veerraju, and N. K. Naik, Hybrid composites made of carbon and glass woven fabrics under quasi-static loading, *Materials & Design*, vol. 32, no. 7, pp. 4094–4099, 2011, doi: 10.1016/J.MATDES.2011.03.003.

[48] P. R. S. Reddy, T. S. Reddy, K. Mogulanna, I. Srikanth, V. Madhu, and K. V. Rao, Ballistic Impact Studies on Carbon and E-glass Fibre Based Hybrid Composite Laminates, in *Procedia Engineering*, Elsevier Ltd, 2017, pp. 293–298. doi: 10.1016/j.proeng.2016.12.017.

[49] W. Wu, Q. Wang, and W. Li, Comparison of Tensile and Compressive Properties of Carbon/Glass Interlayer and Intralayer Hybrid Composites, *Materials*, vol. 11, no. 7, p. 1105, 2018, doi: 10.3390/MA11071105.

[50] K. Naito, J. M. Yang, and Y. Kagawa, Tensile properties of high strength polyacrylonitrile (PAN)-based and high modulus pitch-based hybrid carbon fibers-reinforced epoxy matrix composite, *Journal of Materials Science*, vol. 47, no. 6, pp. 2743–2751, 2012, doi: 10.1007/S10853-011-6101-8.

[51] G. Czél, M. Jalalvand, M. R. Wisnom, and T. Czigány, Design and characterisation of high performance, pseudo-ductile all-carbon/epoxy unidirectional hybrid composites, *Composites Part B: Engineering*, vol. 111, pp. 348–356, 2017, doi: 10.1016/J.COMPOSITESB.2016.11.049.

[52] R. Amacher, J. Cugnoni, J. Brunner, E. Kramer, C. Dransfeld, W. Smith, K. Scobbie, L. Sorensen, and J. Botsis, Toward aerospace grade thin-ply composites, in *17th European Conference on Composite Materials. Munich, Germany*, 2016.

[53] T. A. Sebaey and E. Mahdi, Using thin-plies to improve the damage resistance and tolerance of aeronautical CFRP composites, *Composites Part A: Applied Science and Manufacturing*, vol. 86, pp. 31–38, 2016, doi: 10.1016/J.COMPOSITESA.2016.03.027.

[54] Y. Yuan, X. Li, Z. Zhang, and W. Liu, Thin/thick-ply hybrid gradient laminate for low-velocity impact and compression-after-impact behaviors, *Composites Communications*, vol. 25, p. 100743, 2021, doi: 10.1016/J.COCO.2021.100743.

[55] M. I. Lincon and V. Chalivendra, High strain rate damage sensing in intra-ply hybrid composites under dynamic shear loading, *International Journal of Impact Engineering*, vol. 173, p. 104439, 2023, doi: 10.1016/J.IJIMPENG.2022.104439.

[56] P. Zhu, J. Lu, Q. Ji, and Z. Cheng, Experimental study of in-plane mechanical performance of carbon/glass hybrid woven composite at different strain rates, *International Journal of Crashworthiness*, vol. 21, no. 6, pp. 542–554, 2016, doi: 10.1080/13588265.2016.1198000.

[57] C. Stephen, B. Shivamurthy, A. H. I. Mourad, R. Selvam, and M. Mohan, Experimental

and finite element study on high-velocity impact resistance and energy absorption of hybrid and non-hybrid fabric reinforced polymer composites, *Journal of Materials Research and Technology*, vol. 18, pp. 5406–5418, 2022, doi: 10.1016/J.JMRT.2022.05.007.

[58] B. Gaur, M. Patel, and S. Patel, Strain rate effect analysis of hybrid composites under the high-velocity impact, *Materials Today: Proceedings*, vol. 72, pp. 2811–2816, 2023, doi: 10.1016/J.MATPR.2022.07.082.

[59] H. Ahmadi, G. H. Liaghat, H. Sabouri, and E. Bidkhouri, Investigation on the high velocity impact properties of glass-reinforced fiber metal laminates, *Journal of Composite Materials*, vol. 47, no. 13, pp. 1605–1615, 2012, doi: 10.1177/0021998312449883.

[60] I. Annamalai, K. Karthik, N. Kumar, S. Muthuselvan, M. Vignesh, and Y. J. Dhanush, Experimental investigation of mechanical properties of GLARE composite with different layup sequences, *Materials Today: Proceedings*, vol. 46, pp. 1371–1375, 2021, doi: 10.1016/J.MATPR.2021.02.487.

[61] R. Amacher, J. Cugnoni, J. Botsis, L. Sorensen, W. Smith, and C. Dransfeld, Thin ply composites: experimental characterization and modeling of size-effects, *Composites Science and Technology*, vol. 101, pp. 121–132, 2014, doi: 10.1016/j.compscitech.2014.06.027.

[62] E. Abisset, Un mésomodèle d'endommagement des composites stratifiés pour le virtual testing : identification et validation, École normale supérieure de Cachan - ENS Cachan, 2012.

[63] G. Longo, Models and methods to simulate low-energy impact damage on composite aerospace structures, University of Pisa, 2011.

[64] M. Marjanović, G. Meschke, and D. Vuksanović, A finite element model for propagating delamination in laminated composite plates based on the Virtual Crack Closure method, *Composite Structures*, vol. 150, pp. 8–19, 2016, doi: 10.1016/j.compstruct.2016.04.044.

[65] S. Abrate, *Impact engineering of composite structures*. Springer, 2011.

[66] M. R. Wisnom, The role of delamination in failure of fibre-reinforced composites, *Philosophical Transactions of the Royal Society A: Mathematical, Physical and Engineering Sciences*, vol. 370, no. 1965, pp. 1850–1870, 2012, doi: 10.1098/rsta.2011.0441.

[67] T. W. Shyr and Y. H. Pan, Impact resistance and damage characteristics of composite laminates, *Composite Structures*, vol. 62, no. 2, pp. 193–203, 2003, doi: 10.1016/S0263-8223(03)00114-4.

[68] V. V. Silberschmidt, *Dynamic deformation, damage and fracture in composite materials and structures*, 1st ed. Elsevier Ltd, 2016.

[69] S. R. (Stephen R. Reid and G. (Gang) Zhou, *Impact behaviour of fibre-reinforced composite materials and structures*. CRC Press, 2000.

[70] J. Bieniaś, P. Jakubczak, B. Surowska, and K. Dragan, Low-energy impact behaviour and damage characterization of carbon fibre reinforced polymer and aluminium hybrid laminates, *Archives of Civil and Mechanical Engineering*, vol. 15, no. 4, pp. 925–932, 2015, doi: 10.1016/j.acme.2014.09.007.

[71] M. S. Rajput, M. Burman, and S. Hallström, Impact resistance and damage tolerance assessment of composite sandwich materials for aircraft, *12th International Conference on Sandwich Structures ICSS-12: Proceedings*, pp. 261–263, 2018, doi: 10.5075/epfl-

icss12-2018-261-263.

[72] N. K. Naik and P. Shrirao, Composite structures under ballistic impact, *Composite Structures*, vol. 66, no. 1–4, pp. 579–590, 2004, doi: 10.1016/j.compstruct.2004.05.006.

[73] W. J. Cantwell and J. Morton, The impact resistance of composite materials — a review, *Composites*, vol. 22, no. 5, pp. 347–362, 1991, doi: 10.1016/0010-4361(91)90549-V.

[74] M. P. Flanagan, M. A. Zikry, J. W. Wall, and A. El-Shiekh, Experimental investigation of high velocity impact and penetration failure modes in textile composites, *Journal of Composite Materials*, vol. 33, no. 12, pp. 1080–1103, 1999, doi: 10.1177/002199839903301202.

[75] N. K. Naik and A. V. Doshi, Ballistic impact behavior of thick composites: Analytical formulation, *AIAA Journal*, vol. 43, no. 7, pp. 1525–1536, 2005, doi: 10.2514/1.11993.

[76] D. Zhang, Y. Sun, L. Chen, S. Zhang, and N. Pan, Influence of fabric structure and thickness on the ballistic impact behavior of Ultrahigh molecular weight polyethylene composite laminate, *Materials & Design*, vol. 54, pp. 315–322, 2014, doi: 10.1016/J.MATDES.2013.08.074.

[77] S. Yashiro, K. Ogi, T. Nakamura, and A. Yoshimura, Characterization of high-velocity impact damage in CFRP laminates: Part I - Experiment, *Composites Part A: Applied Science and Manufacturing*, vol. 48, no. 1, pp. 93–100, 2013, doi: 10.1016/j.compositesa.2012.12.015.

[78] R. Velmurugan, K. Naresh, and K. Shankar, Influence of fibre orientation and thickness on the response of CFRP composites subjected to high velocity impact loading, *Advances in Materials and Processing Technologies*, vol. 4, no. 1, pp. 120–131, 2018, doi: 10.1080/2374068X.2017.1410688.

[79] Phadnis V. A., Pandya K. S., Naik N. K., Roy A., and Silberschmidt V. V., Ballistic impact behaviour of woven fabric composite: Finite element analysis and experiments, *Journal of Physics: Conference Series*, vol. 451, p. 012019, 2013, doi: 10.1088/1742-6596/451/1/012019.

[80] I. Gilath, D. Salzmann, M. Givon, M. Dariel, L. Kornblit, and T. Bar-Noy, Spallation as an effect of laser-induced shock waves, *Journal of Materials Science*, vol. 23, no. 5, pp. 1825–1828, 1988, doi: 10.1007/BF01115727/METRICS.

[81] R. Ecault, M. Boustie, F. Touchard, F. Pons, L. Berthe, L. Chocinski-Arnault, B. Ehrhart, and C. Bockenheimer, A study of composite material damage induced by laser shock waves, *Composites Part A: Applied Science and Manufacturing*, vol. 53, pp. 54–64, 2013, doi: 10.1016/J.COMPOSITESA.2013.05.015.

[82] W. Xie, W. Zhang, L. Guo, Y. Gao, D. Li, and X. Jiang, The shock and spallation behavior of a carbon fiber reinforced polymer composite, *Composites Part B: Engineering*, vol. 153, pp. 176–183, 2018, doi: 10.1016/J.COMPOSITESB.2018.07.047.

[83] E. Gay, L. Berthe, M. Boustie, M. Arrigoni, and E. Buzaud, Effects of the shock duration on the response of CFRP composite laminates, *Journal of Physics D: Applied Physics*, vol. 47, no. 45, p. 455303, 2014, doi: 10.1088/0022-3727/47/45/455303.

[84] M. Castres, Modélisation dynamique avancée des composites à matrice organique (CMO) pour l'étude de la vulnérabilité des structures aéronautiques, Ecole Centrale de Lille, 2018.

[85] H. Rahmani, S. H. M. Najaf, A. Ashori, and M. Golriz, Elastic Properties of Carbon Fibre-Reinforced Epoxy Composites, *Polymers and Polymer Composites*, vol. 23, no. 7,

pp. 475–482, 2015, doi: 10.1177/096739111502300706.

[86] ASTM International, ASTM D3039/D3039M - Standard Test Method for Tensile Properties of Polymer Matrix Composite Materials, 2000

[87] British Standards Institution, BS EN ISO 527-5:2009: Plastics. Determination of tensile properties. Test conditions for unidirectional fibre-reinforced plastic composites, 2009

[88] N. Tual, Durability of carbon / epoxy composites for tidal turbine blade applications, Université de Bretagne Occidentale, 2015.

[89] M. M. Shokrieh and M. J. Omidi, Tension behavior of unidirectional glass/epoxy composites under different strain rates, *Composite Structures*, vol. 88, no. 4, pp. 595–601, 2009, doi: 10.1016/J.COMPSTRUCT.2008.06.012.

[90] T. Yokozeki, Y. Aoki, and T. Ogasawara, Experimental characterization of strength and damage resistance properties of thin-ply carbon fiber/toughened epoxy laminates, *Composite Structures*, vol. 82, no. 3, pp. 382–389, 2008, doi: 10.1016/J.COMPSTRUCT.2007.01.015.

[91] R. Foroutan, High strain rate behaviour of woven composite materials, McGill University, Montreal, 2009.

[92] E. . Botelho, Ł. Figiel, M. . Rezende, and B. Lauke, Mechanical behavior of carbon fiber reinforced polyamide composites, *Composites Science and Technology*, vol. 63, no. 13, pp. 1843–1855, 2003, doi: 10.1016/S0266-3538(03)00119-2.

[93] Z. Li and J. Lambros, Determination of the dynamic response of brittle composites by the use of the split Hopkinson pressure bar, *Composites Science and Technology*, vol. 59, no. 7, pp. 1097–1107, 1999, doi: 10.1016/S0266-3538(98)00152-3.

[94] C. Cerbu, D. Xu, H. Wang, and I. C. Roşca, The use of Digital Image Correlation in determining the mechanical properties of materials, *IOP Conference Series: Materials Science and Engineering*, vol. 399, 2018, doi: 10.1088/1757-899X/399/1/012007.

[95] M. R. Wisnom, B. Khan, and S. R. Hallett, Size effects in unnotched tensile strength of unidirectional and quasi-isotropic carbon/epoxy composites, *Composite Structures*, vol. 84, no. 1, pp. 21–28, 2008, doi: 10.1016/J.COMPSTRUCT.2007.06.002.

[96] M. Kawai, K. Watanabe, H. Hoshi, E. Hara, and Y. Iwahori, Effect of specimen size on longitudinal strength of unidirectional carbon/epoxy composite laminates (part 1, unnotched strength), *Advanced Composite Materials*, vol. 28, pp. 53–71, 2019, doi: 10.1080/09243046.2018.1458269.

[97] R. M. Jones, *Mechanics Of Composite Materials*, 2nd ed. New York: Taylor & Francis, 1999. doi: 10.1201/9781498711067.

[98] M. J. Pindera and C. T. Herakovich, Shear characterization of unidirectional composites with the off-axis tension test, *Experimental Mechanics*, vol. 26, no. 1, pp. 103–112, 1986, doi: 10.1007/BF02319962.

[99] M. J. Pindera, G. Choksi, J. S. Hidde, and C. T. Herakovich, A Methodology for Accurate Shear Characterization of Unidirectional Composites, *Journal of Composite Materials*, vol. 21, no. 12, pp. 1164–1184, 1987, doi: 10.1177/002199838702101205.

[100] C. C. Chamis and J. H. Sinclair, Ten-deg Off-axis Test for Shear Properties in Fiber Composites, *Experimental Mechanics*, vol. 17, pp. 339–346, 1977.

[101] G. Vargas and F. Mujika, Determination of In-plane Shear Strength of Unidirectional Composite Materials Using the Off-axis Three-point Flexure and Off-axis Tensile Tests, *Journal of Composite Materials*, vol. 44, no. 21, pp. 2487–2507, 2010, doi:

10.1177/0021998310369601.

[102] H. T. Hahn and S. W. Tsai, Nonlinear elastic behavior of unidirectional composite laminae, *Journal of Composite Materials*, vol. 7, no. 1, pp. 102–118, 1973, doi: 10.1177/002199837300700108.

[103] Shinji Ogihara, Nonlinear mechanical response of CFRP laminates under off-axis tensile loading, *Science and Engineering of Composite Materials*, vol. 17, no. 2, pp. 133–141, 2010, doi: 10.1515/SECM.2010.17.2.133.

[104] T. Yokozeki, T. Ogasawara, and T. Ishikawa, Nonlinear behavior and compressive strength of unidirectional and multidirectional carbon fiber composite laminates, *Composites Part A: Applied Science and Manufacturing*, vol. 37, no. 11, pp. 2069–2079, 2006, doi: 10.1016/J.COMPOSITESA.2005.12.004.

[105] D. Cai, G. Zhou, X. Wang, C. Li, and J. Deng, Experimental investigation on mechanical properties of unidirectional and woven fabric glass/epoxy composites under off-axis tensile loading, *Polymer Testing*, vol. 58, pp. 142–152, 2017, doi: 10.1016/J.POLYMERTESTING.2016.12.023.

[106] Y. Ma, Y. Li, and L. Liu, Off-axis tension behaviour of unidirectional PEEK/AS4 thermoplastic composites, *Applied Sciences*, vol. 13, no. 6, p. 3476, 2023, doi: 10.3390/APP13063476.

[107] M. Vogler, H. Koerber, P. Kuhn, R. Rolfes, and P. Camanho, Constitutive modeling and experimental characterization of the non-linear stress-strain behavior of unidirectional carbon-epoxy under high strain rates, in *20th International Conference on Composite Materials*, Copenhagen, Denmark, 2015.

[108] H. Koerber, P. Kuhn, M. Ploeckl, F. Otero, P.-W. Gerbaud, R. Rolfes, and P. P. Camanho, Experimental characterization and constitutive modeling of the non-linear stress–strain behavior of unidirectional carbon–epoxy under high strain rate loading, *Advanced Modeling and Simulation in Engineering Sciences*, vol. 5, no. 1, 2018, doi: 10.1186/S40323-018-0111-X.

[109] M. M. Shokrieh and M. J. Omidi, Investigation of strain rate effects on in-plane shear properties of glass/epoxy composites, *Composite Structures*, vol. 91, no. 1, pp. 95–102, 2009, doi: 10.1016/J.COMPSTRUCT.2009.04.035.

[110] H. Koerber, J. Xavier, and P. P. Camanho, High strain rate characterisation of unidirectional carbon-epoxy IM7-8552 in transverse compression and in-plane shear using digital image correlation, *Mechanics of Materials*, vol. 42, no. 11, pp. 1004–1019, 2010, doi: 10.1016/j.mechmat.2010.09.003.

[111] Y. Liang, H. Wang, and X. Gu, In-plane shear response of unidirectional fiber reinforced and fabric reinforced carbon/epoxy composites, *Polymer Testing*, vol. 32, no. 3, pp. 594–601, 2013, doi: 10.1016/j.polymertesting.2013.01.015.

[112] A. K. Ditcher, F. E. Rhodes, and J. P. H. Webber, Non-Linear Stress-Strain Behaviour Of Carbon Fibre Reinforced Plastic Laminates, *Journal of Strain Analysis*, vol. 16, no. 1, pp. 43–51, 1981, doi: 10.1243/03093247V161043.

[113] ASTM International, ASTM D4255/D4255M-15a Standard Test Method for In-Plane Shear Properties of Polymer Matrix Composite Materials by the Rail Shear Method, 2020

[114] ASTM International, ASTM D5379/D5379M - Standard Test Method for Shear Properties of Composite Materials by the V-Notched Beam Method, 2019

[115] S. Yoon Park and W. Jong Choi, Review of material test standardization status for the

material qualification of laminated thermosetting composite structures, *Journal of Reinforced Plastics and Composites*, vol. 40, no. 5–6, pp. 235–258, 2020, doi: 10.1177/0731684420958107.

[116] ASTM International, ASTM D3518/D3518M - Standard Test Method for In-Plane Shear Response of Polymer Matrix Composite Materials by Tensile Test of a ±45° Laminate, 2018

[117] M. Merzkirch and T. Foecke, 10° off-axis testing of CFRP using DIC: A study on strength, strain and modulus, *Composites Part B: Engineering*, vol. 196, p. 108062, 2020, doi: 10.1016/j.compositesb.2020.108062.

[118] F. Pierron and A. Vautrin, Accurate comparative determination of the in-plane shear modulus of T300/914 by the iosipescu and 45° off-axis tests, *Composites Science and Technology*, vol. 52, no. 1, pp. 61–72, 1994, doi: 10.1016/0266-3538(94)90008-6.

[119] C. T. Sun and J. L. Chen, A Simple Flow Rule for Characterizing Nonlinear Behavior of Fiber Composites, *Journal of Composite Materials*, vol. 23, no. 10, pp. 1009–1020, 1989, doi: 10.1177/002199838902301004.

[120] J. Cho, J. Fenner, B. Werner, and I. M. Daniel, A Constitutive Model for Fiber-reinforced Polymer Composites, *Journal of Composite Materials*, vol. 44, no. 26, pp. 3133–3150, 2010, doi: 10.1177/0021998310371547.

[121] R. C. Batra, G. Gopinath, and J. Q. Zheng, Material parameters for pressure-dependent yielding of unidirectional fiber-reinforced polymeric composites, *Composites Part B: Engineering*, vol. 43, no. 6, pp. 2594–2604, 2012, doi: 10.1016/J.COMPOSITESB.2011.12.005.

[122] P. H. Petit and M. E. Waddoups, A Method of Predicting the Nonlinear Behavior of Laminated Composites, *Journal of Composite Materials*, vol. 3, no. 1, pp. 2–19, 2016, doi: 10.1177/002199836900300101.

[123] A. Matzenmiller, J. Lubliner, and R. L. Taylor, A constitutive model for anisotropic damage in fiber-composites, *Mechanics of Materials*, vol. 20, no. 2, pp. 125–152, 1995, doi: 10.1016/0167-6636(94)00053-0.

[124] Y. Chen, Y. Zhao, S. Ai, C. He, Y. Tao, Y. Yang, and D. Fang, A constitutive model for elastoplastic-damage coupling effect of unidirectional fiber-reinforced polymer matrix composites, *Composites Part A: Applied Science and Manufacturing*, vol. 130, 2020, doi: 10.1016/J.COMPOSITESA.2019.105736.

[125] D. Vasiukov, S. Panier, and A. Hachemi, Non-linear material modeling of fiber-reinforced polymers based on coupled viscoelasticity–viscoplasticity with anisotropic continuous damage mechanics, *Composite Structures*, vol. 132, pp. 527–535, 2015, doi: 10.1016/J.COMPSTRUCT.2015.05.027.

[126] Y. Wang, D. Chen, N. Li, H. Yuan, Z. Zhu, Y. Li, and Z. Huang, A micromechanics based elasto-plastic damage model for unidirectional composites under off-axis tensile loads, *Scientific Reports*, vol. 10, no. 1, 2020, doi: 10.1038/s41598-020-57771-8.

[127] C. Schuecker and H. E. Pettermann, Combining Elastic Brittle Damage with Plasticity to Model the Non-linear behavior of Fiber Reinforced Laminates, *Computational Methods in Applied Sciences*, vol. 10, pp. 99–117, 2008, doi: 10.1007/978-1-4020-8584-0_5.

[128] T. Wehrkamp-Richter, R. Hinterhölzl, and S. T. Pinho, Damage and failure of triaxial braided composites under multi-axial stress states, *Composites Science and Technology*, vol. 150, pp. 32–44, 2017, doi: 10.1016/J.COMPSCITECH.2017.07.002.

[129] P. Ladeveze and E. LeDantec, Damage modelling of the elementary ply for laminated composites, *Composites Science and Technology*, vol. 43, no. 3, pp. 257–267, 1992, doi: 10.1016/0266-3538(92)90097-M.

[130] B. Liu and L. B. Lessard, Fatique and damage-tolerance analysis of composite laminates: Stiffness loss, damage-modelling, and life prediction, *Composites Science and Technology*, vol. 51, no. 1, pp. 43–51, 1994, doi: 10.1016/0266-3538(94)90155-4.

[131] J. Lemaître and J.-L. Chaboche, *Mechanics of solid materials*. Cambridge: Cambridge University Press, 1990.

[132] Z. Zhai, B. Jiang, and D. Drummer, Characterization of nonlinear response in quasi-unidirectional E-glass fabric reinforced polypropylene composites under off-axis tensile loading, *Polymer Testing*, vol. 63, pp. 521–529, 2017, doi: 10.1016/J.POLYMERTESTING.2017.09.019.

[133] R. M. O'Higgins, C. T. McCarthy, and M. A. McCarthy, Identification of Damage and Plasticity Parameters for Continuum Damage Mechanics Modelling of Carbon and Glass Fibre-Reinforced Composite Materials, *Strain*, vol. 47, no. 1, pp. 105–115, 2011, doi: 10.1111/J.1475-1305.2009.00649.X.

[134] W. Van Paepegem, I. De Baere, and J. Degrieck, Modelling the nonlinear shear stress–strain response of glass fibre-reinforced composites. Part I: Experimental results, *Composites Science and Technology*, vol. 66, no. 10, pp. 1455–1464, 2006, doi: 10.1016/J.COMPSCITECH.2005.04.014.

[135] M. C. Lafarie-Frenot and F. Touchard, Comparative in-plane shear behaviour of long-carbon-fibre composites with thermoset or thermoplastic matrix, *Composites Science and Technology*, vol. 52, no. 3, pp. 417–425, 1994, doi: 10.1016/0266-3538(94)90176-7.

[136] J. D. Fuller and M. R. Wisnom, Ductility and pseudo-ductility of thin ply angle-ply CFRP laminates under quasi-static cyclic loading, *Composites Part A: Applied Science and Manufacturing*, vol. 107, pp. 31–38, 2018, doi: 10.1016/J.COMPOSITESA.2017.12.020.

[137] J. Fitoussi, F. Meraghni, Z. Jendli, G. Hug, and D. Baptiste, Experimental methodology for high strain-rates tensile behaviour analysis of polymer matrix composites, *Composites Science and Technology*, vol. 65, no. 14, pp. 2174–2188, 2005, doi: 10.1016/J.COMPSCITECH.2005.05.001.

[138] G. Hug, Behaviour analysis of carbon-epoxy laminates under high-speed loading: manufacture of the same materials by means of microwave curing for comparison, Arts et Métiers ParisTech, Paris, 2005.

[139] E. N. Eliopoulos and T. P. Philippidis, A progressive damage simulation algorithm for GFRP composites under cyclic loading. Part I: Material constitutive model, *Composites Science and Technology*, vol. 71, no. 5, pp. 742–749, 2011, doi: 10.1016/J.COMPSCITECH.2011.01.023.

[140] J. Xie, G. Fang, Z. Chen, and J. Liang, Modeling of Nonlinear Mechanical Behavior for 3D Needled C/C-SiC Composites Under Tensile Load, *Applied Composite Materials*, vol. 23, no. 4, pp. 783–797, 2016, doi: 10.1007/S10443-016-9485-4.

[141] Y. Liu, L. Li, Z. Zhang, and X. Xiong, Monotonic and Cyclic Loading/Unloading Tensile Behavior of 3D Needle-Punched C/SiC Ceramic-Matrix Composites, *Materials*, vol. 14, no. 1, p. 57, 2020, doi: 10.3390/MA14010057.

[142] Z. Zhai, B. Jiang, and D. Drummer, Temperature-dependent response of quasi-unidirectional E-glass fabric reinforced polypropylene composites under off-axis tensile

loading, *Composites Part B: Engineering*, vol. 148, pp. 180–187, 2018, doi: 10.1016/J.COMPOSITESB.2018.04.058.

[143] J. Wang, Y. Xiao, M. Kawai, and K. Inoue, Observation and modeling of loading–unloading hysteresis behavior of unidirectional composites in compression, *Journal of Reinforced Plastics and Composites*, vol. 37, no. 5, pp. 287–299, 2017, doi: 10.1177/0731684417743347.

[144] J. Wang, Y. Xiao, K. Inoue, M. Kawai, and Y. Xue, Modeling of nonlinear response in loading-unloading tests for fibrous composites under tension and compression, *Composite Structures*, vol. 207, pp. 894–908, 2019, doi: 10.1016/J.COMPSTRUCT.2018.09.054.

[145] C. N. O'Brien and A. E. Zaghi, Modelling the nonlinear shear stress-strain response of composites with metal and non-metal reinforcement, *Composites Part B: Engineering*, vol. 221, p. 109009, 2021, doi: 10.1016/J.COMPOSITESB.2021.109009.

[146] W. Van Paepegem, I. De Baere, and J. Degrieck, Modelling the nonlinear shear stress–strain response of glass fibre-reinforced composites. Part II: Model development and finite element simulations, *Composites Science and Technology*, vol. 66, no. 10, pp. 1465–1478, 2006, doi: 10.1016/J.COMPSCITECH.2005.04.018.

[147] H. Fallahi and F. Taheri-Behrooz, Phenomenological constitutive modeling of the non-linear loading-unloading response of UD fiber-reinforced polymers, *Composite Structures*, vol. 292, p. 115671, 2022, doi: 10.1016/J.COMPSTRUCT.2022.115671.

[148] J. L. Chen and C. T. Sun, A Plastic Potential Function Suitable for Anisotropic Fiber Composites, *Journal of Composite Materials*, vol. 27, no. 14, pp. 1379–1390, 2016, doi: 10.1177/002199839302701403.

[149] S. N. A. Safri, M. T. H. Sultan, N. Yidris, and F. Mustapha, Low Velocity and High Velocity Impact Test on Composite Materials-A review 1, *The International Journal Of Engineering And Science (IJES)*, vol. 3, no. 9, pp. 50–60, 2014.

[150] W. J. Cantwell and J. Morton, The influence of varying projectile mass on the impact response of CFRP, *Composite Structures*, vol. 13, no. 2, pp. 101–114, 1989, doi: 10.1016/0263-8223(89)90048-2.

[151] D. E. Frank, Ballistic Tests of Used Soft Body Armor, Gaithersburg, 1986. doi: 10.6028/NBS.IR.86-3444.

[152] M. G. Hebsur, R. D. Noebe, and D. M. Revilock, Impact resistance of lightweight hybrid structures for gas turbine engine fan containment applications, *Journal of Materials Engineering and Performance*, vol. 12, no. 4, pp. 470–479, 2003, doi: 10.1361/105994903770343033.

[153] M. Chandrasekar, M. R. Ishak, M. Jawaid, S. M. Sapuan, and Z. Leman, Low velocity impact properties of natural fiber-reinforced composite materials for aeronautical applications, in *Sustainable Composites for Aerospace Applications*, Elsevier, 2018, pp. 293–313. doi: 10.1016/B978-0-08-102131-6.00014-1.

[154] E. E. Haro, A. G. Odeshi, and J. A. Szpunar, The energy absorption behavior of hybrid composite laminates containing nano-fillers under ballistic impact, *International Journal of Impact Engineering*, vol. 96, pp. 11–22, 2016, doi: 10.1016/j.ijimpeng.2016.05.012.

[155] P. O. Sjoblom, J. T. Hartness, and T. M. Cordell, On Low-Velocity Impact Testing of Composite Materials, *Journal of Composite Materials*, vol. 22, no. 1, pp. 30–52, 1988, doi: 10.1177/002199838802200103.

[156] J. Liu, Y. Li, X. Yu, X. Gao, and Z. Liu, Design of aircraft structures against threat of

bird strikes, *Chinese Journal of Aeronautics*, vol. 31, no. 7, pp. 1535–1558, 2018, doi: 10.1016/J.CJA.2018.05.004.

[157] C. R. Siviour and J. L. Jordan, High Strain Rate Mechanics of Polymers: A Review, *Journal of Dynamic Behavior of Materials*, vol. 2, no. 1, pp. 15–32, 2016, doi: 10.1007/s40870-016-0052-8.

[158] R. Ecault, Etude expérimentale et numérique du comportement dynamique de composites aéronautiques sous choc laser . Optimisation du test d ' adhérence par ondes de choc sur les assemblages composites collées, Ecole Nationale Supérieure de Mécanique et d'Aérotechique - Poitiers, 2013.

[159] H. M. Hsiao and I. M. Daniel, Strain rate behavior of composite materials, *Composites Part B: Engineering*, vol. 29, no. 5, pp. 521–533, 1998, doi: 10.1016/S1359-8368(98)00008-0.

[160] J. Harding, Impact Damage in Composite Materials, *Science and Engineering of Composite Materials*, vol. 1, no. 2, 1989, doi: 10.1515/SECM.1989.1.2.41.

[161] J. Harding and L. M. Welsh, A tensile testing technique for fibre-reinforced composites at impact rates of strain, *Journal of Materials Science*, vol. 18, no. 6, pp. 1810–1826, 1983, doi: 10.1007/BF00542078.

[162] Razali N., Sultan M.T.H, Safri S.N.A, Basri S., Yidrid N., and Mustapha F., High Velocity Impact Test on Glass Fibre Reinforced Polymer (GFRP) Using a Single Stage Gas Gun (SSGG), *Applied Mechanics and Materials*, vol. 564, pp. 376–381, 2014, doi: 10.4028/www.scientific.net/amm.564.376.

[163] Mohammed I., Abu Talib A.R., Sultan M.T., and Saadon S., Ballistic impact velocity response of carbon fibre reinforced aluminium alloy laminates for aero-engine, *IOP Conf. Series: Materials Science and Engineering*, vol. 270, p. 012026, 2017, doi: 10.1088/1757-899X/270/1/012026.

[164] C. Kaboglu, I. Mohagheghian, J. Zhou, Z. Guan, W. Cantwell, S. John, B. R. K. Blackman, A. J. Kinloch, and J. P. Dear, High-velocity impact deformation and perforation of fibre metal laminates, *Journal of Materials Science*, vol. 53, no. 6, pp. 4209–4228, 2018, doi: 10.1007/s10853-017-1871-2.

[165] C. Caisso, N. Dagorn, W. Albouy, M. Arrigoni, and D. Thévenet, Experimental and numerical investigations of a soft projectile impact three-point bending (SPITPB) test for adhesion assessment under dynamic loading, *European Journal of Mechanics - A/Solids*, vol. 101, p. 105060, 2023, doi: 10.1016/J.EUROMECHSOL.2023.105060.

[166] J. C. F. Millett, N. K. Bourne, Y. J. E. Meziere, R. Vignjevic, and A. Lukyanov, The effect of orientation on the shock response of a carbon fibre–epoxy composite, *Composites Science and Technology*, vol. 67, no. 15–16, pp. 3253–3260, 2007, doi: 10.1016/J.COMPSCITECH.2007.03.034.

[167] V. Jaulin, J. M. Chevalier, M. Arrigoni, and E. Lescoute, Characterization of a carbon fiber composite material for space applications under high strains and stresses: Modeling and validation by experiments, *Journal of Applied Physics*, vol. 128, no. 19, 2020, doi: 10.1063/5.0010268/346750.

[168] T. Lässig, F. Bagusat, M. May, and S. Hiermaier, Analysis of the shock response of UHMWPE composites using the inverse planar plate impact test and the shock reverberation technique, *International Journal of Impact Engineering*, vol. 86, pp. 240–248, 2015, doi: 10.1016/J.IJIMPENG.2015.08.010.

[169] P. J. Hazell, C. Stennett, and G. Cooper, The effect of specimen thickness on the shock propagation along the in-fibre direction of an aerospace-grade CFRP laminate,

Composites Part A: Applied Science and Manufacturing, vol. 40, no. 2, pp. 204–209, 2009, doi: 10.1016/J.COMPOSITESA.2008.11.002.

[170] C. S. Alexander, C. T. Key, and S. C. Schumacher, Dynamic response and modeling of a carbon fiber - Epoxy composite subject to shock loading, *Journal of Applied Physics*, vol. 114, no. 22, p. 223515, 2013, doi: 10.1063/1.4846116.

[171] M. Perton, A. Blouin, and J.-P. Monchalin, Adhesive bond testing of carbon-epoxy composites by laser shockwave, *Journal of Physics D: Applied Physics*, vol. 44, no. 3, p. 34012, 2011, doi: 10.1088/0022-3727/44/3/034012.

[172] E. Gay, L. Berthe, M. Boustie, M. Arrigoni, and M. Trombini, Study of the response of CFRP composite laminates to a laser-induced shock, *Composites Part B: Engineering*, vol. 64, pp. 108–115, 2014, doi: 10.1016/j.compositesb.2014.04.004.

[173] M. Ghrib, L. Berthe, N. Mechbal, M. Rébillat, M. Guskov, R. Ecault, and N. Bedreddine, Generation of controlled delaminations in composites using symmetrical laser shock configuration, *Composite Structures*, vol. 171, pp. 286–297, 2017, doi: 10.1016/j.compstruct.2017.03.039.

[174] J. Kwon, J. Choi, H. Huh, and J. Lee, Evaluation of the effect of the strain rate on the tensile properties of carbon–epoxy composite laminates, *Journal of Composite Materials*, vol. 51, no. 22, pp. 3197–3210, 2017, doi: 10.1177/0021998316683439.

[175] Y. Ou and D. Zhu, Tensile behavior of glass fiber reinforced composite at different strain rates and temperatures, *Construction and Building Materials*, vol. 96, pp. 648–656, 2015, doi: 10.1016/j.conbuildmat.2015.08.044.

[176] A. Gilat, R. K. Goldberg, and G. D. Roberts, Experimental study of strain-rate-dependent behavior of carbon/epoxy composite, *Composites Science and Technology*, vol. 62, no. 10–11, pp. 1469–1476, 2002, doi: 10.1016/S0266-3538(02)00100-8.

[177] J. M. Lifshitz and H. Leber, Response of fiber-reinforced polymers to high strain-rate loading in interlaminar tension and combined tension/shear, *Composites Science and Technology*, vol. 58, no. 6, pp. 987–996, 1998, doi: 10.1016/S0266-3538(97)00226-1.

[178] R. M. White, Generation of elastic waves by transient surface heating, *Journal of Applied Physics*, vol. 34, no. 12, pp. 3559–3567, 1963, doi: 10.1063/1.1729258.

[179] J. P. Romain and D. Zagouri, Laser-shock studies using an electromagnetic gauge for particle measurements, in *Shock Compression of Condensed Matter–1991*, Elsevier, 1992, pp. 801–804. doi: 10.1016/b978-0-444-89732-9.50183-7.

[180] L. Tollier, E. Bartnicki, and R. Fabbro, Experimental and numerical study of laser-driven spallation with visar diagnostic, in *AIP Conference Proceedings*, AIP Publishing, 1996, pp. 1265–1268. doi: 10.1063/1.50867.

[181] F. Cottet and M. Boustie, Spallation studies in aluminum targets using shock waves induced by laser irradiation at various pulse durations, *Journal of Applied Physics*, vol. 66, no. 9, pp. 4067–4073, 1989, doi: 10.1063/1.343991.

[182] M. Boustie, F. Cottet, and J. P. Romain, Spalling due to a strong shock wave decay process in solid targets irradiated by a pulsed laser, in *Shock Compression of Condensed Matter–1991*, Elsevier, 1992, pp. 805–808. doi: 10.1016/b978-0-444-89732-9.50184-9.

[183] J. Yuan and V. Gupta, Measurement of interface strength by the modified laser spallation technique. I. Experiment and simulation of the spallation process, *Journal of Applied Physics*, vol. 74, no. 4, pp. 2388–2396, 1993, doi: 10.1063/1.354698.

[184] L. Berthe, M. Arrigoni, M. Boustie, J. P. Cuq-Lelandais, C. Broussillou, G. Fabre, M. Jeandin, V. Guipont, and M. Nivard, State-of-the-art laser adhesion test (LASAT),

Nondestructive Testing and Evaluation, vol. 26, no. 3–4. Taylor and Francis Ltd., pp. 303–317, 2011. doi: 10.1080/10589759.2011.573550.

[185] I. Gilath, R. Englman, Z. Jaeger, A. Buchman, and H. Dodiuk, Impact resistance of adhesive joints using laser-induced shock waves, *Journal of Laser Applications*, vol. 7, no. 3, pp. 169–176, 1995, doi: 10.2351/1.4745391.

[186] M. Ducousso, S. Bardy, Y. Rouchausse, T. Bergara, F. Jenson, L. Berthe, L. Videau, and N. Cuvillier, Quantitative evaluation of the mechanical strength of titanium/composite bonding using laser-generated shock waves, *Applied Physics Letters*, vol. 112, no. 11, p. 111904, 2018, doi: 10.1063/1.5020352.

[187] M. Sagnard, R. Ecault, F. Touchard, M. Boustie, and L. Berthe, Development of the symmetrical laser shock test for weak bond inspection, *Optics & Laser Technology*, vol. 111, pp. 644–652, 2019, doi: 10.1016/J.OPTLASTEC.2018.10.052.

[188] M. Boustie, L. Berthe, T. De Resseguier, and M. Arrigoni, Laser Shock Waves: Fundamentals and Applications, *1st International Symposium on Laser Ultrasonics: Science, Technology and Applications*, 2008, Accessed: Jun. 11, 2019. [Online]. Available: https://api.semanticscholar.org/CorpusID:3297265

[189] L. Berthe, R. Fabbro, P. Peyre, L. Tollier, and E. Bartnicki, Shock waves from a water-confined laser-generated plasma, *Journal of Applied Physics*, vol. 82, no. 6, pp. 2826–2832, 1997, doi: 10.1063/1.366113.

[190] D. Devaux, R. Fabbro, L. Tollier, and E. Bartnicki, Generation of shock waves by laser-induced plasma in confined geometry, *Journal of Applied Physics*, vol. 74, no. 4, pp. 2268–2273, 1993, doi: 10.1063/1.354710.

[191] M. Arrigoni, J. P. Monchalin, A. Blouin, S. E. Kruger, and M. Lord, Laser Doppler interferometer based on a solid Fabry-Perot etalon for measurement of surface velocity in shock experiments, *Measurement Science and Technology*, vol. 20, no. 1, 2009, doi: 10.1088/0957-0233/20/1/015302.

[192] J. C. J. Duke, E. G. I. Henneke, and W. W. Stinchcomb, Ultrasonic stress wave characterization of composite materials - NASA-CR-3976, Cleveland, Ohio, 1986.

[193] D. Lee, *Fundamentals of Shock Wave Propagation in Solids*, 1st ed. Springer Berlin Heidelberg, 2008. doi: 10.1007/978-3-540-74569-3/COVER.

[194] G. I. Kanel, V. E. Fortov, and S. V. Razorenov, *Shock-Wave Phenomena and the Properties of Condensed Matter*. New York: Springer New York, 2004. doi: 10.1007/978-1-4757-4282-4.

[195] I. A. . Novikov S.A., Divnov I.I., The Study of Fracture of Steel, Aluminum, and Copper under Explosive Loading, *Physics of Metals and Metallography*, vol. 21(4), pp. 608–6015, 1966.

[196] L. C. Alil, M. Arrigoni, L. Deleanu, and M. Istrate, Assessment of Delamination in Tensylon® UHMWPE Composites by Laser-induced Shock, *Materiale Plastice*, vol. 55, no. 3, p. 364, 2018, doi: 10.37358/MP.18.3.5031.

[197] L. M. Barker and R. E. Hollenbach, Laser interferometer for measuring high velocities of any reflecting surface, *Journal of Applied Physics*, vol. 43, no. 11, pp. 4669–4675, 1972, doi: 10.1063/1.1660986.

[198] P. D. Sargis, N. E. Molau, D. Sweider, M. E. Lowry, and O. T. Strand, Photonic Doppler Velocimetry, 1999.

[199] G. Tahan, Etude des assemblages collés sous choc – Propriétés mécaniques après choc laser, Ecole Nationale Superieure De Techniques Avancees Bretagne, 2018.

[200] D. H. Dolan, Accuracy and precision in photonic Doppler velocimetry, *Review of Scientific Instruments*, vol. 81, no. 5, p. 053905, 2010, doi: 10.1063/1.3429257.

[201] I. Gilath, S. Eliezer, and S. Shkolnik, Spall Behaviour of Carbon Epoxy Unidirectional Composites as Compared to Aluminum and Iron, *Journal of Composite Materials*, vol. 24, no. 11, pp. 1138–1151, 1990, doi: 10.1177/002199839002401102.

[202] E. Gay, Comportement de composites sous choc induit par laser : développement de l'essai d'adhérence par choc des assemblages de composites collés, 'École Nationale Supérieure d'Arts et Métiers Paris, 2011.

[203] M. Scius-Bertrand, Endommagements maîtrisés par chocs laser symétriques et désassemblages des collages, HESAM Université, 2021.

[204] B. D. Agarwal, L. J. Broutman, and K. Chandrashekhara, *Analysis and performance of fiber composites*, 3rd ed. John Wiley and Sons, 2015.

[205] C. Larco, R. Pahonie, and I. Edu, The Effects of Fibre Volume Fraction on a Glass-Epoxy Composite Material, *IIncas Bulletin*, vol. 7, no. 3, pp. 113–119, 2015, doi: 10.13111/2066-8201.2015.7.3.10.

[206] Z. Han, S. Jeong, J. Noh, and D. Oh, Comparative Study of Glass Fiber Content Measurement Methods for Inspecting Fabrication Quality of Composite Ship Structures, *Applied Sciences*, vol. 10, no. 15, p. 5130, 2020, doi: 10.3390/APP10155130.

[207] Ravikumar and M. S. S. Prasad, Fracture Toughness and Mechanical Properties of Aluminum Oxide Filled Chopped Strand Mat E-Glass Fiber Reinforced-Epoxy Composites, *International Journal of Scientific and Research Publications*, vol. 4, no. 7, 2014.

[208] S. Francis, T. Bru, L. E. Asp, M. Wysocki, and C. Cameron, Characterisation of tape-based carbon fibre thermoplastic discontinuous composites for energy absorption, *Plastics, Rubber and Composites*, vol. 50, no. 7, pp. 351–361, 2021, doi: 10.1080/14658011.2021.1902119.

[209] ASTM International, ASTM D3171 Standard test methods for constituent content of composite materials, 2011

[210] D. Purslow, On the optical assessment of the void content in composite materials, *Composites*, vol. 15, no. 3, pp. 207–210, 1984, doi: 10.1016/0010-4361(84)90276-3.

[211] D. Saenz-Castillo, M. I. Martín, S. Calvo, F. Rodriguez-Lence, and A. Güemes, Effect of processing parameters and void content on mechanical properties and NDI of thermoplastic composites, *Composites Part A: Applied Science and Manufacturing*, vol. 121, pp. 308–320, 2019, doi: 10.1016/J.COMPOSITESA.2019.03.035.

[212] L. Liu, Z. Wu, B.-M. Zhang, D.-F. Wang, and Z.-J. Wu, Effects of cure cycles on void content and mechanical properties of composite laminates, *Composite Structures*, vol. 73, no. 3, pp. 303–309, 2006, doi: 10.1016/j.compstruct.2005.02.001.

[213] H. Liu, H. Cui, W. Wen, X. Su, H. Kang, and C. Engler-Pinto, The effect of voids on the quasi-static tensile properties of carbon fiber/polymer-laminated composites, *Journal of Composite Materials*, vol. 52, no. 15, pp. 1997–2015, 2018, doi: 10.1177/0021998317737827.

[214] S. F. M. de Almeida and Z. dos S. N. Neto, Effect of void content on the strength of composite laminates, *Composite Structures*, vol. 28, no. 2, pp. 139–148, 1994, doi: 10.1016/0263-8223(94)90044-2.

[215] A. Y. Zhang and D. X. Zhang, The Static Mechanical Properties of Carbon/Epoxy Composite Laminates with Voids, *Advanced Materials Research*, vol. 652–654, pp. 29–

32, 2013, doi: 10.4028/WWW.SCIENTIFIC.NET/AMR.652-654.29.

[216] ASTM International, Astm D2734-94 Standard Test Methods for Void Content of Reinforced Plastics, 1994 doi: 10.1520/D2734-94.

[217] S. Paciornik and J. d'Almeida, Digital microscopy and image analysis applied to composite materials characterization, *Matéria (Rio de Janeiro)*, vol. 15, no. 2, pp. 172–181, 2010, doi: 10.1590/S1517-70762010000200013.

[218] ImageJ. https://imagej.nih.gov/ij/

[219] M. Mehdikhani, L. Gorbatikh, I. Verpoest, and S. V. Lomov, Voids in fiber-reinforced polymer composites: A review on their formation, characteristics, and effects on mechanical performance:, *Journal of Composite Materials*, vol. 53, no. 12, pp. 1579–1669, 2018, doi: 10.1177/0021998318772152.

[220] MATLAB, *version 9.8.0.1417392 (R2020a)*. Natick, Massachusetts: The MathWorks Inc., 2020.

[221] V. Munoz, M. Perrin, M. L. Pastor, H. Welemane, A. Cantarel, and M. Karama, Determination of the elastic properties in CFRP composites: comparison of different approaches based on tensile tests and ultrasonic characterization, *Advances in Aircraft and Spacecraft Science*, vol. 2, no. 3, pp. 249–260, 2014, doi: 10.12989/AAS.2015.2.3.249.

[222] J. Bora and S. Kirtania, Comparative study of elastic properties and mode I fracture energy of carbon nanotube/epoxy and carbon fibre/epoxy laminated composites, *Micro and Nano Systems Letters*, vol. 8, no. 1, pp. 1–10, 2020, doi: 10.1186/S40486-020-00120-1.

[223] R. Kumar, L. P. Mikkelsen, H. Lilholt, and B. Madsen, Experimental Method for Tensile Testing of Unidirectional Carbon Fibre Composites Using Improved Specimen Type and Data Analysis, *Materials*, vol. 14, no. 14, 2021, doi: 10.3390/MA14143939.

[224] M. Casapu, I. Fuiorea, and M. Arrigoni, Experimental Characterization of Internal Structure and Physical Properties of Unidirectional Ply-Level Hybrid Carbon Composite Material, *Advanced Engineering Materials*, 2023, doi: 10.1002/ADEM.202201447.

[225] H. W. Wang, H. W. Zhou, L. L. Gui, H. W. Ji, and X. C. Zhang, Analysis of effect of fiber orientation on Young's modulus for unidirectional fiber reinforced composites, *Composites Part B: Engineering*, vol. 56, pp. 733–739, 2014, doi: 10.1016/J.COMPOSITESB.2013.09.020.

[226] Y. Q. Zhao, Y. Zhou, Z. M. Huang, and R. C. Batra, Experimental and micromechanical investigation of T300/7901 unidirectional composite strength, *Polymer Composites*, vol. 40, no. 7, pp. 2639–2652, 2019, doi: 10.1002/PC.25059.

[227] A. Fathi, J.-H. Keller, and V. Altstaedt, Full-field shear analyses of sandwich core materials using Digital Image Correlation (DIC), *Composites Part B*, vol. 70, pp. 156–166, 2015, doi: 10.1016/J.COMPOSITESB.2014.10.045.

[228] M. J. Hinton, A. S. Kaddour, and P. D. Soden, *Failure Criteria in Fibre-Reinforced-Polymer Composites*. Oxford, UK: Elsevier Ltd, 2004. doi: 10.1016/B978-0-080-44475-8.X5000-8.

[229] M. Casapu, I. Fuiorea, and M. Arrigoni, Damage assessment through cyclic load-unload tensile tests for ply-level hybrid carbon fiber composites, *Express Polymer Letters*, vol. 18, no. 1, pp. 41–60, 2024, doi: 10.3144/expresspolymlett.2024.4.

[230] C. Basaran and S. Nie, An irreversible thermodynamics theory for damage mechanics of solids, *International Journal of Damage Mechanics*, vol. 13, no. 3, pp. 205–223, 2004,

doi: 10.1177/1056789504041058.

[231] M. Kawai and R. Negishi, Micromechanical Analysis for Off-Axis Nonlinear Behavior of Unidirectional Carbon Fiber Composite at Room and High Temperatures, *Key Engineering Materials*, vol. 177–180, no. 180 PART 1, pp. 309–314, 2000, doi: 10.4028/WWW.SCIENTIFIC.NET/KEM.177-180.309.

[232] L. Cheng, Y. Xiao, J. Wang, J. Zhao, Z. Zhang, and Y. Xue, Characterization and modeling of the ratcheting behavior of unidirectional off-axis composites, *Composite Structures*, vol. 273, p. 114305, 2021, doi: 10.1016/J.COMPSTRUCT.2021.114305.

[233] J. H. Sinclair and C. C. Chamis, Mechanical Behavior and Fracture Characteristics of Off-Axis Fiber Composites I - Experimental Investigation, Cleveland, Ohio, 1977.

[234] Z. Al-Hajaj, A. Sarwar, R. Zdero, and H. Bougherara, In-situ damage assessment of a novel carbon/flax/epoxy hybrid composite under tensile and compressive loading, *Journal of Composite Materials*, vol. 53, no. 19, pp. 2701–2714, 2019, doi: 10.1177/0021998319839129.

[235] R. D. Machado, J. E. A. Filho, and M. P. da Silva, Stiffness loss of laminated composite plates with distributed damage by the modified local Green's function method, *Composite Structures*, vol. 84, no. 3, pp. 220–227, 2008, doi: 10.1016/J.COMPSTRUCT.2007.08.001.

[236] M. Casapu, M. Arrigoni, and I. Fuiorea, Off-axis response and shear characterization of unidirectional ply-level hybrid carbon-fiber-reinforced polymer materials, *Incas Bulletin*, vol. 15, no. 3, pp. 31–46, 2023, doi: 10.13111/2066-8201.2023.15.3.3.

[237] V. M. Cuartas, M. Perrin, M.-L. Pastor, H. Welemane, A. Cantarel, M. Karama, and V. Munoz, Determination of the elastic properties in CFRP composites: comparison of different approaches based on tensile tests and ultrasonic characterization, *Advances in Aircraft and Spacecraft Science*, vol. 2, no. 3, pp. 249–260, 2014, doi: 10.12989/aas.2015.2.3.249ï.

[238] C. Venkateshwar Reddy, C. Joseph S Raju, P. Ramesh Babu, and R. Ramnarayan, Mechanical Characterization of Carbon/Epoxy Unidirectional and Bidirectional Composites for Structural Application, *Journal of Engineering Research and Application*, vol. 8, no. 7–III, pp. 21–24, 2018, doi: 10.9790/9622-080703212421|P.

[239] G. A. Bibo, P. J. Hogg, and M. Kempb, Mechanical Characterisation Of Glass-and Carbon-Fibre-Reinforced Composites Made With Non-Crimp Fabrics, *Composite Science and Technology*, vol. 57, no. 9–10, pp. 1221–1241, 1997, doi: 10.1016/S0266-3538(97)00053-5.

[240] R. Hevroni, N. Karaev, E. Gudinetsky, V. Paris, and A. Yosef-Hai, Studying the dynamic properties of ethyl-cyanoacrylate adhesive up to 6.5 GPa, *AIP Conference Proceedings*, vol. 2272, p. 040005, 2020, doi: 10.1063/12.0001014.

[241] N. K. Bourne, On the Shock Response of Polymers to Extreme Loading, *Journal of Dynamic Behavior of Materials*, vol. 2, no. 1, pp. 33–42, 2016, doi: 10.1007/s40870-016-0055-5.

[242] P. J. Hazell, C. Stennett, and G. Cooper, The shock and release behavior of an aerospace-grade cured aromatic amine epoxy resin, *Polymer Composites*, vol. 29, no. 10, pp. 1106–1110, 2008, doi: 10.1002/pc.20614.

[243] G. Tahan, M. Arrigoni, P. Bidaud, L. Videau, and D. Thévenet, Evolution of failure pattern by laser induced shockwave within an adhesive bond, *Optics & Laser Technology*, vol. 129, p. 106224, 2020, doi: 10.1016/J.OPTLASTEC.2020.106224.

[244] M. Ayad, S. Ünaldi, M. Scius-Bertrand, C. Le Bras, B. Fayolle, and L. Berthe, Dynamical modeling of bi-layer Aluminium adhesive tape for laser shock applications, *Optics & Laser Technology*, vol. 163, p. 109366, 2023, doi: 10.1016/J.OPTLASTEC.2023.109366.

[245] G. H. Zhang, B. Braverman, A. Kawasaki, and V. Vuletić, Note: Fast compact laser shutter using a direct current motor and three-dimensional printing, *Review of Scientific Instruments*, vol. 86, no. 12, p. 126105, 2015, doi: https://doi.org/10.1063/1.4937614.

[246] R. Fabbro, J. Fournier, P. Ballard, D. Devaux, and J. Virmont, Physical study of laser-produced plasma in confined geometry, *Journal of Applied Physics*, vol. 68, no. 2, pp. 775–784, 1990, doi: 10.1063/1.346783.

[247] M. Boustie, J. P. Cuq-Lelandais, C. Bolis, L. Berthe, S. Barradas, M. Arrigoni, T. De Resseguier, and M. Jeandin, Study of damage phenomena induced by edge effects into materials under laser driven shocks, *Journal of Physics D: Applied Physics*, vol. 40, no. 22, p. 7103, 2007, doi: 10.1088/0022-3727/40/22/036.

[248] G. Prudhomme, Étude du nuage de particules éjectées sous choc : apports de la Vélocimétrie Hétérodyne, ENSAM Paris, 2014.

[249] M. Casapu, A. C. Casapu, M. Arrigoni, and I. Fuiorea, Laser-induced Shockwaves for Damage Assessment and Characterization at High Strain Rates in the Fiber Direction of Unidirectional Composites, in *27th DYMAT Technical Meeting*, Colmar, France, 2023.

[250] R. Bensaada, A. El Malki Alaoui, G. Darut, S. Costil, and M. Arrigoni, Towards hybridization of ultra-high molecular weight polyethylene composites by thermally sprayed alumina: Feasibility and bond strength assessment, *Materials and Design*, vol. 227, p. 111779, 2023, doi: 10.1016/j.matdes.2023.111779.

[251] J. A. Smith, J. M. Lacy, D. Lévesque, J. P. Monchalin, and M. Lord, Use of the Hugoniot elastic limit in laser shockwave experiments to relate velocity measurements, *AIP Conference Proceedings*, vol. 1706, no. 1, p. 47, 2016, doi: 10.1063/1.4940537/585873.

[252] W. Riedel, H. Nahme, and K. Thoma, Equation of State Properties of Modern Composite Materials: Modeling Shock, Release and Spallation, *AIP Conference Proceedings*, vol. 706, no. 1, p. 701, 2004, doi: 10.1063/1.1780335.

[253] P. J. Hazell, G. J. Appleby-Thomas, and G. Kister, Impact, penetration, and perforation of a bonded carbon-fibre-reinforced plastic composite panel by a high-velocity steel sphere: An experimental study, *Journal of Strain Analysis for Engineering Design*, vol. 45, no. 6, pp. 439–450, 2010, doi: 10.1243/03093247JSA604.

[254] P. J. Hazell, G. Kister, C. Stennett, P. Bourque, and G. Cooper, Normal and oblique penetration of woven CFRP laminates by a high velocity steel sphere, *Composites Part A: Applied Science and Manufacturing*, vol. 39, no. 5, pp. 866–874, 2008, doi: 10.1016/J.COMPOSITESA.2008.01.007.

Titre : Evaluation expérimentale de l'hybridation des composites en fibre carbone unidirectionnelles à matrice polymère : comportement mécanique sous chargements quasi-statiques et dynamiques

Mots clés : hybridation au niveau des plis, fibre de carbone, propriétés mécaniques, ondes de choc induites par laser

Résumé : Dans le contexte de l'utilisation croissante des composites renforcés à fibres de carbone dans l'industrie aérospatiale, cette thèse examine l'influence de l'hybridation entre plis, impliquant des variations de type de fibre de carbone et d'épaisseur de pli, sur la structure interne, les propriétés mécaniques et les réponses dynamiques des composites renforcés à fibres de carbone unidirectionnelles. Axée sur les applications aérospatiales, l'étude utilise deux types de préimprégnés de fibres de carbone unidirectionnelles avec des types de fibres et des épaisseurs de pli distincts, permettant la fabrication de laminés de référence et hybrides.

Les objectifs de la recherche englobent une caractérisation complète des matériaux dans des conditions de chargement quasi-statique et dynamique. Les analyses expérimentales comprennent des essais quasi-statiques monotones en traction selon les axes et hors axes, des essais de traction cycliques hors axes avec chargement et déchargement, le développement d'un modèle couplé de dommage-plasticité, une évaluation de la propagation des ondes de choc, une évaluation de la résistance dynamique à la traction, et l'examen des localisations de dommage et des variations de seuil d'efforts à la rupture.

Au-delà de contribuer à la compréhension fondamentale des composites unidirectionnels, cette recherche apporte des éclairages sur l'hybridation au niveau des plis, offrant des applications potentielles dans des structures complexes. Alors que l'industrie aérospatiale demande des matériaux avec des performances mécaniques améliorées, cette thèse fournit des perspectives précieuses pour faire progresser la conception et l'application des matériaux composites.

Title : Study of the mechanical response of ply-level hybrid composites under quasi-static and dynamic loadings

Keywords : ply-level hybridization, carbon fiber, mechanical properties, laser-induced shockwaves

Abstract : In the context of the increased use of carbon fiber-reinforced composites in the aerospace industry, this thesis investigates the influence of inter-ply hybridization, involving variations in carbon fiber type and ply thickness, on the internal structure, mechanical properties, and dynamic responses of unidirectional carbon fiber-reinforced composites. Focused on aerospace applications, the study utilizes two types of unidirectional carbon fiber prepregs with distinct fiber types and ply thicknesses, manufacturing both reference and hybrid laminates.

The research objectives encompass comprehensive material characterization under quasi-static and dynamic loading conditions. Experimental analyses include monotonic on and off-axis quasi-static tests, off-axis cyclic load-unload tensile tests, coupled damage-plasticity model development, shockwave propagation assessment, dynamic tensile strength evaluation, and examination of damage position and threshold variations.

Beyond contributing to the fundamental understanding of unidirectional composites, this research introduces insights into ply-level hybridization, offering potential applications in complex structures. As the aerospace industry demands materials with enhanced mechanical performance, this thesis provides valuable insights for advancing composite material design and application.